SYNTHESIS OF CORE-SHELL NANOPARTICLES AND STUDIES ON THEIR PROPERTIES AND APPLICATIONS

Ph.D. THESIS

by

SYAM KANDULA

DEPARTMENT OF CHEMISTRY
INDIAN INSTITUTE OF TECHNOLOGY ROORKEE
ROORKEE - 247 667 (INDIA)
APRIL, 2016

SYNTHESIS OF CORE-SHELL NANOPARTICLES AND STUDIES ON THEIR PROPERTIES AND APPLICATIONS

A THESIS

Submitted in partial fulfilment of the requirements of the award of the degree of

DOCTOR OF PHILOSOPHY

in

CHEMISTRY

by

SYAM KANDULA

DEPARTMENT OF CHEMISTRY
INDIAN INSTITUTE OF TECHNOLOGY ROORKEE
ROORKEE - 247 667 (INDIA)
APRIL, 2016

INDIAN INSTITUTE OF TECHNOLOGY ROORKEE
ROORKEE

CANDIDATE'S DECLARATION

I hereby certify that the work which is being presented in the thesis entitled **"SYNTHESIS OF CORE-SHELL NANOPARTICLES AND STUDIES ON THEIR PROPERTIES AND APPLICATIONS"** in partial fulfilment of the requirements for the award of the Degree of Doctor of Philosophy and submitted in the Department of Chemistry of the Indian Institute of Technology Roorkee, Roorkee is an authentic record of my own work carried out during a period from December, 2011 to April, 2016 under the supervision of Dr. P. Jeevanandam, Associate Professor, Department of Chemistry, Indian Institute of Technology Roorkee, Roorkee.

The matter presented in the thesis has not been submitted by me for the award of any other degree of this or any other Institute.

(SYAM KANDULA)

This is to certify that the above statement made by the candidate is correct to the best of my knowledge.

(P. Jeevanandam)
Supervisor

The Ph.D. Viva-Voce Examination of **Mr. SYAM KANDULA**, Research Scholar, has been held on _____

Chairman, SRC

Signature of External Examiner

This is to certify that the student has made all the corrections in the thesis.

Supervisor

Head of the Department

Dated:

CONTENTS

Abstract

Nanoparticles exhibit size and shape dependent optical, magnetic and other physicochemical properties, which are different from that of bulk materials. Among the nanoparticles, core-shell nanoparticles are receiving immense interest due to their versatile physicochemical properties and various potential applications. The properties of core-shell nanoparticles strongly depend on composition, size of the core, shell and ratio of core to shell. These materials show improved properties compared to their individual components and this has been attributed to synergistic interaction between the core and shell. Due to their improved properties, core-shell nanoparticles have been used in various applications such as photocatalysis, adsorption, data storage, supercapacitors, solar cells, drug delivery, bio-imaging, tumor therapy, etc. Various physical and chemical methods have been reported for the synthesis of core-shell nanoparticles. But, the synthesis of core-shell nanoparticles with uniform and controlled shell thickness is still a challenge.

In the present study, different core-shell nanoparticles were synthesized and the nanoparticles that have been investigated are: (i) SiO_2@CdS (Type-I) and ZnO@CdS (Type-II), (ii) semiconductor-metal based core-shell nanoparticles (ZnO@Ag and Cu_2O@Ag), and (iii) nanorattle type core-shell nanoparticles (SiO_2@Co_3O_4 and SiO_2@Ni-Co mixed metal oxides). The core materials with different shapes were first synthesized by StÖber's process, homogeneous precipitation, and solution route. In the next step, deposition of shell nanoparticles with different thickness was carried out *via* novel and economical methods such as homogeneous precipitation and thermal decomposition. The synthesized core-shell nanoparticles were characterized by an array of analytical techniques. After thorough characterization, optical properties of the core-shell nanoparticles were studied. Some of the interesting applications of synthesized core-shell nanoparticles have also been demonstrated. The present thesis consists of seven chapters and a brief description of each chapter is as follows.

Chapter 1 deals with a brief historical perspective of nanotechnology, an introduction to core-shell nanoparticles, classification of core-shell nanoparticles, and their various synthetic methods. Different examples elucidating the optical, magnetic and electrochemcial properties of core-shell nanoparticles have been discussed. At the end, some of the multi-functional applications of core-shell nanoparticles in different fields have been briefly described.

Chapter 2 deals with various analytical techniques which were used to characterize the core-shell nanoparticles and the sample preparation methods for the measurements. The analytical techniques include powder X-ray diffraction, Fourier transform infrared spectroscopy, thermal gravimetric analysis, field emission scanning electron microscopy, energy dispersive X-ray analysis, transmission electron microscopy, selected area electron diffraction, X-ray photoelectron spectroscopy, zeta potential and BET surface area analysis. Optical properties of the core-shell nanoparticles were studied using UV-Visible diffuse reflectance spectroscopy and photoluminescence spectroscopy.

Chapter 3 deals with the synthesis of SiO_2@CdS (Type-I) and ZnO@CdS (Type-II) core-shell nanoparticles *via* a novel thermal decomposition approach. This chapter contains two sections and each one of them has been discussed separately.

In the first section, SiO_2@CdS core-shell nanoparticles have been synthesized by a simple thermal decomposition approach. The synthesis involves two steps. In the first step, SiO_2 spheres were synthesized using StÖber's process. Then, cadmium sulfide nanoparticles were deposited on the SiO_2 spheres by the thermal decomposition of cadmium acetate and thiourea in ethylene glycol at 180 ^oC. XRD results indicate the presence of CdS nanocrystallites in all the SiO_2@CdS samples. Electron microscopy images show uniform deposition of cadmium sulfide nanoparticles on the surface of SiO_2 spheres. Electron diffraction patterns confirm crystalline nature of cadmium sulfide nanoparticles on the surface of silica and HRTEM images clearly show the lattice fringes due to cubic cadmium sulfide. Diffuse reflectance spectroscopy results show blue shift of band gap absorption of SiO_2@CdS core-shell nanoparticles with respect to bulk cadmium sulfide and this is attributed to quantum size effect. Photoluminescence results show enhancement in intensity of band edge emission of CdS and weaker emission due to surface defects in the SiO_2@CdS core-shell nanoparticles compared to pure cadmium sulfide nanoparticles.

In the second section, ZnO@CdS core-shell heteronanostructures with different shell thickness (20 nm to 45 nm) have been successfully synthesized by a novel thermal decomposition approach and the synthesis involves three steps. In the first step, ZnO nanorods were synthesized by homogeneous precipitation method. Then, the surface of ZnO nanorods was functionalized using citric acid as the surface modifying agent. Finally, cadmium sulfide shell was deposited on the surface modified ZnO nanorods by the thermal decomposition of cadmium acetate and thiourea in ethylene glycol at 180 ^oC. XRD results indicate the presence

of ZnO and CdS in all the ZnO@CdS samples. SEM and TEM results prove the deposition of CdS shell on the surface of ZnO nanorods. SAED patterns indicate crystalline nature of the ZnO@CdS core-shell nanoparticles. DRS results show blue shift of CdS band gap absorption in ZnO@CdS with respect to bulk CdS and PL results show evidence for synergistic interaction between ZnO and CdS nanoparticles.

Chapter 4 deals with the synthesis of semiconductor-metal based core-shell nanoparticles (ZnO@Ag and Cu_2O@Ag) *via* a novel thermal decomposition approach. This chapter contains two sections and each one of them has been discussed separately.

In the first section, ZnO@Ag core-shell heteronanostructures with varying amounts of silver nanoparticles on ZnO nanorods were synthesized *via* a novel and economical thermal decomposition approach. ZnO nanorods were first synthesized by homogeneous precipitation method and silver nanoparticles were subsequently deposited on the surface of ZnO nanorods by the thermal decomposition of silver acetate in diphenyl ether at 220 ^oC. The amount of silver nanoparticles on the ZnO nanorods was controlled by varying the concentration of silver acetate during the thermal decomposition. XRD results confirm the presence of silver nanoparticles (size = 24-31 nm) in the ZnO@Ag samples. SEM and TEM images prove the presence of silver nanoparticles on the surface of ZnO nanorods. XPS results indicate the presence of metallic silver in the ZnO@Ag core-shell heteronanostructures. DRS results show characteristic surface plasmon resonance absorption due to silver nanoparticles and PL results indicate an effective separation of photogenerated electron-hole pairs in the ZnO@Ag core-shell heteronanostructures as compared to that in pristine ZnO nanorods.

In the second section, Cu_2O@Ag polyhedral core-shell nanoparticles with different morphologies (rhombicuboctahedron, cuboctahedron, truncated octahedron, and octahedron) have been successfully synthesized *via* a novel thermal decomposition approach and the synthesis involves two steps. In the first step, Cu_2O polyhedral microcrystals with various morphologies were synthesized *via* a solution route. In the second step, silver shell was deposited on Cu_2O samples by thermal decomposition of silver acetate at 220 ^oC followed by growth at 150 ^oC in diphenyl ether. XRD results confirm the presence of Cu_2O and silver in the Cu_2O@Ag samples. SEM images show rhombicuboctahedron, cuboctahedron, truncated octahedron, and octahedron morphologies for Cu_2O samples. SEM and TEM studies prove the formation of silver nanoparticles shell on the Cu_2O polyhedral microcrystals. SAED patterns confirm the crystalline nature of Cu_2O@Ag samples and diffuse reflectance spectra of

Cu_2O@Ag polyhedral core-shell nanoparticles show band gap absorption due to Cu_2O as well as surface plasmon resonance due to silver nanoparticles.

Chapter 5 deals with the synthesis of SiO_2@Co_3O_4 and SiO_2@Ni-Co mixed metal oxide core-shell nanorattles *via* homogeneous precipitation method. This chapter contains two sections and each one of them has been discussed separately.

In the first section, SiO_2@Co_3O_4 core-shell nanorattles with different Co_3O_4 shell thickness have been synthesized by calcination of SiO_2@α-$Co(OH)_2$ at 500 ^oC and the synthesis involves two steps. In the first step, SiO_2 microspheres were synthesized using StÖber's process. In the second step, α-$Co(OH)_2$ was deposited on SiO_2 microspheres *via* homogeneous precipitation and the obtained samples were calcined at 500 ^oC to get SiO_2@Co_3O_4 core-shell nanorattles. The shell thickness was controlled by varying the concentration of cobaltous nitrate ($[Co^{2+}]$ = 5, 10 and 15 mM) used during the synthesis. XRD results indicate the presence of Co_3O_4 in all the SiO_2@Co_3O_4 samples. SEM analysis indicates hierarchical core-shell morphology for SiO_2@Co_3O_4 and TEM results indicate core-shell nanorattle morphology for the particles. SAED patterns demonstrate polycrystalline nature of Co_3O_4 shell on the SiO_2. BET surface area measurements show higher surface area for SiO_2@Co_3O_4 samples as compared to that for pure SiO_2 and Co_3O_4 nanoparticles which is attributed to the nanorattle morphology of SiO_2@Co_3O_4. Diffuse reflectance spectroscopy studies indicate that SiO_2@Co_3O_4 core-shell nanorattles exhibit two absorption bands in the range 420-450 nm and 700-750 nm attributed to two ligand to metal charge transfer transitions ($O^{2-} \rightarrow Co^{2+}$ and $O^{2-} \rightarrow Co^{3+}$).

In the second section, SiO_2@Ni-Co mixed metal oxide core-shell nanorattles with different Ni^{2+}:Co^{2+} molar ratios have been synthesized through a facile, inexpensive and self-template route by the calcination of SiO_2@Ni-Co layered double hydroxides at 500 ^oC. The synthesis involves two steps. In the first step, SiO_2 microspheres were synthesized using StÖber's process. In the second step, Ni-Co layer double hydroxide shell was deposited on the SiO_2 microspheres *via* homogeneous precipitation and the obtained samples were calcined in air at 500 ^oC to get SiO_2@Ni-Co mixed metal oxide core-shell nanorattles. The shell composition was controlled by varying the molar ratio of cobaltous nitrate and nickel nitrate ($[Ni^{2+}]$: $[Co^{2+}]$ = 7:3, 5:5, 3:7; total concentration = 10 mmol) during the synthesis. XRD results confirm the formation of Ni-Co mixed metal oxides (NiO, Co_3O_4, $NiCo_2O_4$) in all the SiO_2@Ni-Co mixed metal oxide core-shell nanorattles. Field emission scanning electron microscopy analysis indicates hierarchical flower-like morphology for the SiO_2@Ni-Co mixed metal oxide core-

shell nanorattles and transmission electron microscopy analysis confirms the formation of core-shell nanorattles. BET surface area analysis indicates higher surface area for SiO_2@Ni-Co mixed metal oxide core-shell nanorattles compared to their counter parts and diffuse reflectance spectra show two band gap absorptions in the mixed metal oxide core-shell nanorattles attributed to metal to ligand charge transfer transitions ($M^{n+} \rightarrow O^{2-}$).

Chapter 6 deals with the applications of core-shell nanoparticles/nanorattles, synthesized in the present study. ZnO@CdS and ZnO@Ag core-shell heteronanostructures were explored as photocatalysts for the degradation of methylene blue in aqueous solutions under sunlight. The ZnO@CdS and ZnO@Ag core-shell heteronanostructures exhibit better photocatalytic activity compared to their individual counter parts. Cu_2O@Ag polyhedral core-shell nanoparticles were explored as catalysts for the reduction of 4-nitrophenol and methylene blue in aqueous solutions. The Cu_2O@Ag polyhedral core-shell nanoparticles were better catalysts compared to their individual counter parts as well as previously reported catalysts. SiO_2@Co_3O_4 core-shell nanorattles were explored as an artificial peroxidase-like enzyme mimic. The SiO_2@Co_3O_4 core-shell nanorattles exhibit enhanced peroxidase-like activity compared to pure Co_3O_4 nanoparticles. The SiO_2@Ni-Co mixed metal oxide core-shell nanorattles were explored as adsorbents for the removal of rhodamine B and methylene blue and their mixture in aqueous solutions. The SiO_2@Ni-Co mixed metal oxide core-shell nanorattles exhibit higher adsorption capacity as compared to pure components as well as physical mixture of NiO and Co_3O_4.

Chapter 7 deals with an overall summary of the work done in the present study and future prospects.

ACKNOWLEDGEMENTS

I am wholeheartedly thankful and express my gratitude to all those people whoever helped me directly or indirectly to accomplish my dream and their massive support in each and every moment of my personal as well as professional life.

First and foremost, I would like to take this opportunity to express my deep sense of gratitude to my supervisor, Dr. P. Jeevanandam. I am immensely fortunate to have a skillful and splendid person as my supervisor. He is not only an example of best teacher but also a person with prodigious soul and humanity. Completion of Ph.D. is not an easy task without his innovative guidance and moral support combined with encouragement. His scientific and keen interest towards research helped me a lot in motivating, thinking and designing new research ideas. His timely suggestions and help towards many experimental and practical problems put me into right track of research. His training made me as a proper scientific researcher with broad vision. I am enthusiastically thankful for his care shown on my personal life and what I have learned from him will benefit my entire life.

I pay my persistent respect and gratitude to my father Sh. Rajendra Prasad, my mother Smt. Venkata Vijaya Kumari for their incredible care, love, affection, and strong support in tough situations of my life. I am strongly motivated and adopted many things from my parents and their understandable nature and freedom makes my life more and more beautiful and thoughtful. My dream may not be possible without their caring and utmost support. I am thankful to my brother, Lakshminarayana and his wife Sri Latha, who are always with me on my career aspiration. I much appreciate my nephews, Yuktesh and Yogesh, for their cherished smile and sweet words about me. Most importantly, I appreciate my beloved would be Lakshmi Parvathi (Chinni) for her uncountable love, support, and understanding of my struggling and responsibilities. I am very thankful to my cousin Mrudula for her immense motivation and care. My utmost respect to my grand-father, Sh. Gopal Rao, for his love and hope on me. I extend my sincere thanks to my grand-father, Sh. Sai Babu, and his whole family members for their moral support and financial help. I am thankful to my uncles Sh. Ram Mohan Rao, Sh. Satyanarayana, Sh. Srinivasa Rao and their whole family members for their continuous support. I thank all my family members and relatives for their love, care, faith and support in each and every moment of my life.

I am highly gratified and express my sincere thanks to Prof. M. R. Maurya, Head of the Department of Chemistry and all other faculty members for their timely support and help. I am

obliged to all the SRC members, Prof. M. R. Maurya (Chairman), Dr. Tapas Kumar Mandal (Internal expert), Department of Chemistry and Prof. Ramesh Chandra (External expert), Institute Instrumentation Centre, IIT Roorkee for their suggestions and reinforcement to carry out this work.

I extend my special thanks to Prof. Ramesh Chandra, Head, Institute Instrumentation Centre (IIC) for providing all the essential instrumental facilities. I am extremely indebted to Mr. S. D. Sharma, in-charge of FE-SEM for his support and timely help. I am also thankful to Mr. Shiv Kumar Sharma for his help for the FE-SEM measurements. I would like to thank Mr. Shiv Kumar Saini, in-charge of XRD, Mr. A. K. Saini, in-charge of TGA/DTA, Mr. Akshay and Mr. Mukesh for their help during TEM measurements. My special thanks to Dr. P. A. Joy, Senior Principal Scientist, Physical and Materials Chemistry Division, CSIR-National Chemical Laboratory, Pune for carrying out XPS measurements for my samples. I express my sincere thanks to Mr. Madan Pal, Department of Chemistry, for his technical arrangements during my presentations in the department. I also thankful to Mr. D. C. Meena and Mr. Abdul Haq, for their technical assistance.

I would like to express my heartfelt gratitude to Ministry of Human Resource Development, Government of India for providing fellowship during the course of my Ph.D.

I am very fortunate to have such a nice, wonderful and friendly seniors, Dr. Manu Sharma, Dr. P. N. R. Kishore, Dr. Geetu Sharma, Dr. Nisha Bayal and Mr. Sudheer Kumar Yadav. I am thankful to all of them for their valuable guidance, suggestions and care regarding my personal life as well as professional sphere. My sincere gratitude to Dr. P. N. R. Kishore for his immense help and training during my initial period of Ph.D. I am thankful to Mr. Sudheer Kumar Yadav, my senior, brother, and one of my well-wishers for his kind help and suggestions in each and every moment of my cherished life. I extend my thanks to all of my beloved juniors, Rama Gaur, Urvashi Sharma, Vanita Sharma, Jatin Mahajan, Rahul Goyal, Amit Kumar, Pankaj Verma, Sourav Sarkar, Gananath, Revathi Ramachandran, Abhishek Sachan, Uddipta Kundu, Megha Sharma, Silambarasan, Souvick Biswas, Rajendra for their help, co-operation, encouragement and friendly environment in the lab.

I would like to thank my school friends, Late. Sunil, Girish, Swaroop, Prasad, Yagnu, Yuva, Pavan, Sathish, Vanaja, Jyothirmai, Madhuri, Mahesh, Bala, Chandra, Venku, Leela, Rajesh, Chaitu and others for their heartfelt moral support and encouragement. I would like to thank my college friends, Siva Rama Krishna, V. V. Reddy, Lakshmi Prasad, Jahnavi, Sirisha, Adi

Seshu, Nagarju, Sudheer, Satya, Surendar, Vamshi, Naveen Reddy, Dr. Naveen Merugu, Suresh, Sudhakar and Jagadeesh for their support. I am extremely happy to convey my gratitude to my best friends, Sandeep, Koti, Shankar, Anusha, Bhuvaneswari and Keerthi for their immense encouragement. My special thanks to my best friend, Naresh Gollapally, for his strong support, understanding nature and I extremely delighted for all of his endeavors. I thank my colleagues, Govardhan, Rupam, Dr. Ravi, Monu, Amit, Soumita, Aarti, Shubra Bhardwaj, Pallavi, Dr. Koteswara Rao, Dr. Bhavani Prasad, Dr. B. M. N. K. Prasad, Dr. Venkateswara Rao, Santhosh, Balu, Rajendra, Nishant, Arun, Shivangi, Tikemani, Rahul, Sujit, Saurabh, Pankaj, Gulab, Karthik, and Joesph for being around all the time. I would like to thank all of my seniors and juniors for their hope, support, help and care one me. I am thankful to almighty of the God, for giving a strong health.

Finally, the entire work what I have done during my Ph.D. is solely dedicated to my beloved parents.

(SYAM KANDULA)

List of Figures

6.3.1 (a) Time dependent UV-Visible spectral results indicating the peroxidase-like activity on TMB using SiO_2, Co_3O_4 nanoparticles, and SiO_2@Co_3O_4 core-shell nanorattles (S1, S2 and S3) as the catalyst (λ_{max} = 652 nm), (b) Comparison of peroxidase activity of SiO_2@Co_3O_4 core-shell nanorattles (S1, S2 and S3) with that of SiO_2 and Co_3O_4 nanoparticles. For more details on the samples, see Section 5.1.2.2.

6.3.2 The effect of physicochemical conditions on peroxidase-like activity of SiO_2@Co_3O_4 core-shell nanorattles (S2): (a) amount of catalyst, (b) pH, (c) temperature, (d) H_2O_2 concentration, and (e) the effect of leaching.

6.3.3 Steady state kinetic analysis for SiO_2@Co_3O_4 core-shell nanorattles (S2) under various conditions: (a) [TMB] = 0.3 mM; [H_2O_2] = 20-200 mM, (b) [H_2O_2] = 100 mM; [TMB] = 0.015-0.4 mM, and (c and d) are the Lineweaver-Burk double reciprocal plots corresponding to conditions (a) and (b). Other conditions: 30 μg catalyst per 3 mL of 0.1 M acetate buffer, pH = 5, and temperature = 30 ^oC.

6.4.1 UV-Vis spectra for monitoring the adsorption of mixture of rhodamine B and methylene blue from an aqueous solution using different adsorbents (e.g. SiO_2, $NiCo_2O_4$, Co_3O_4, NiO, physical mixtures (Co_3O_4:NiO as 3:7, 5:5, and 7:3), SiO_2@Ni-Co mixed metal oxide core-shell nanorattles (M1, M2, and M3), SiO_2@Co_3O_4, and SiO_2@NiO core-shell nanorattles).

6.4.2 (a and b) Kinetics of adsorption of rhodamine B and methylene blue from their mixture in an aqueous solution using different adsorbents; (c and d) comparison of rhodamine B and methylene blue removal efficiency from their mixture using different adsorbents.

6.4.3 Effect of external factors on the adsorption of rhodamine B and methylene blue dye mixture on SiO_2@Ni-Co mixed metal oxide core-shell nanorattles (M1); (a) the amount of adsorbent, (b) initial concentration of mixture of rhodamine B and methylene blue, (c) pH and (d) zeta potential of sample M1 at different pH values.

6.4.4 Langmuir isotherms for the adsorption of rhodamine B (a and c) and methylene blue (b and d) from pure aqueous solutions using SiO_2@Ni-Co mixed metal oxide core-shell nanorattles.

6.4.5 Freundlich isotherms for the adsorption of (a) rhodamine B and (b) methylene blue from pure aqueous solutions using SiO_2@Ni-Co mixed metal oxide core-shell nanorattles.

List of Schemes

List of Tables

6.4.1 Langmuir and Freundlich adsorption isotherm parameters for rhodamine B and methylene blue in single dye systems using SiO_2@Ni-Co mixed metal oxide core-shell nanorattles.

6.4.2 Langmuir adsorption isotherm parameters using a competitive binary Langmuir model for the adsorption of rhodamine B and methylene blue from a mixture in an aqueous solution using SiO_2@Ni-Co mixed metal oxide core-shell nanorattles.

6.4.3 Kinetic parameters for the adsorption of rhodamine B and methylene blue in a single and mixed dye systems using SiO_2@Ni-Co mixed metal oxide core-shell nanorattles.

List of Publications

1 Syam Kandula and Pethaiyan Jeevanandam, "Synthesis of Cu_2O@Ag polyhedral core-shell nanoparticles by a novel thermal decomposition approach for catalytic applications", *European Journal of Inorganic Chemistry*, 2016, 1548-1557 **(2016)**.

2 Syam Kandula and Pethaiyan Jeevanandam, "Sun-light-driven photocatalytic activity by ZnO/Ag heteronanostructures synthesized *via* a facile thermal decomposition approach", *RSC Advances*, 5, 76150-76159 **(2015)**.

3 Syam Kandula and Pethaiyan Jeevanandam, "Synthesis of silica@Ni-Co mixed metal oxide core-shell nanorattles and their potential use as effective adsorbents for waste water treatment", *European Journal of Inorganic Chemistry*, 2015, 4260-4274 **(2015)**.

4 Syam Kandula and Pethaiyan Jeevanandam, "A facile synthetic approach for SiO_2@Co_3O_4 core-shell nanorattles with enhanced peroxidase-like activity", *RSC Advances*, 5, 5295-5306 **(2015)**.

5 Syam Kandula and P. Jeevanandam, "Synthesis of SiO_x@CdS core-shell nanoparticles by simple thermal decomposition approach and studies on their optical properties", *Journal of Alloys and* Compounds, 615, 167-176 **(2014)**.

6 Syam Kandula and P. Jeevanandam, "Visible-light-induced photodegradation of methylene blue using ZnO/CdS heteronanostructures synthesized through a novel thermal decomposition approach", *Journal of Nanoparticle* Research, 16, 2452/1-18 **(2014)**.

List of Conference Proceedings

1 Syam Kandula and P. Jeevanandam, Poster presentation on "Thermal decomposition approach for the synthesis of ZnO/Ag heteronanostructures and their use as photocatalyst for the degradation of methylene blue", *Fourth International Conference on Frontiers in Nanoscience and Technology (Cochin Nano-2016),* Cochin University of Science and Technology, Cochin, India, February 20-23, 2016.

2 Syam Kandula and P. Jeevanandam, Poster presentation on "ZnO@CdS core-shell heteronanostructures as photocatalyst for the degradation of methylene blue", *17th Chemical Research Society of India (CRSI) National Symposium in Chemistry*, CSIR-National Chemical Laboratory, Pune, India, February 6-8, 2015.

3 Syam Kandula and P. Jeevanandam, Poster presentation on “Synthesis of silica@cadmium sulfide core-shell nanoparticles by simple thermal decomposition approach”, *International Conference on Directions in Materials Science*, Jawaharlal Nehru Centre for Advanced Scientific Research, Bangalore and Indian Institute of Science, Bangalore, India, 30th November-01st December, 2013.

1 Introduction

DEDICATED TO
MY PARENTS

Chapter-1

Introduction

1.1 Nanotechnology: Historical perspectives

The term 'nano' was derived from the Greek word '*nanos'* which means 'dwarf'. "Nano" designates a billionth fraction of a meter, i.e. 10^{-9} m [1]. Now a days, nanotechnology is an emerging technology and it comprises many different fields such as chemistry, physics, engineering, materials science, biology, medicine, etc [2–5]. With regards to historical perspectives of nanotechnology, in the fourth century, Romans had made the 'Lycurgus cup' which is an example of dichroic glass [6]. It is made up of gold and silver nanoparticles in a glass matrix which allow it to look translucent red when light shines through inside and opaque green when light shines from outside. In 6^{th} – 15^{th} centuries, 'vibrant stained glass windows' were used in European cathedrals which owe their rich colors to incorporation of gold nanoparticles in mixed metal oxides (Figure 1.1a). In these windows, gold nanoparticles act as photocatalytic air purifiers [7]. In 9^{th} – 17^{th} centuries, 'luster ceramic glazes' were used in the Islamic world, and later in Europe. The glowing or glittering luster is due to silver or copper atoms (Figure 1.1b) [8]. In 13^{th} – 18^{th} centuries, 'Damascus saber sword' was used and it consists of carbon nanotubes and cementite nanowires, which provide strength, and resilience to the sword [9]. In the modern era, Michael Faraday discovered colloidal 'ruby' gold in 1856, and he called it as 'divided metal' and this colloidal solution is still preserved in the Royal Institution [10].

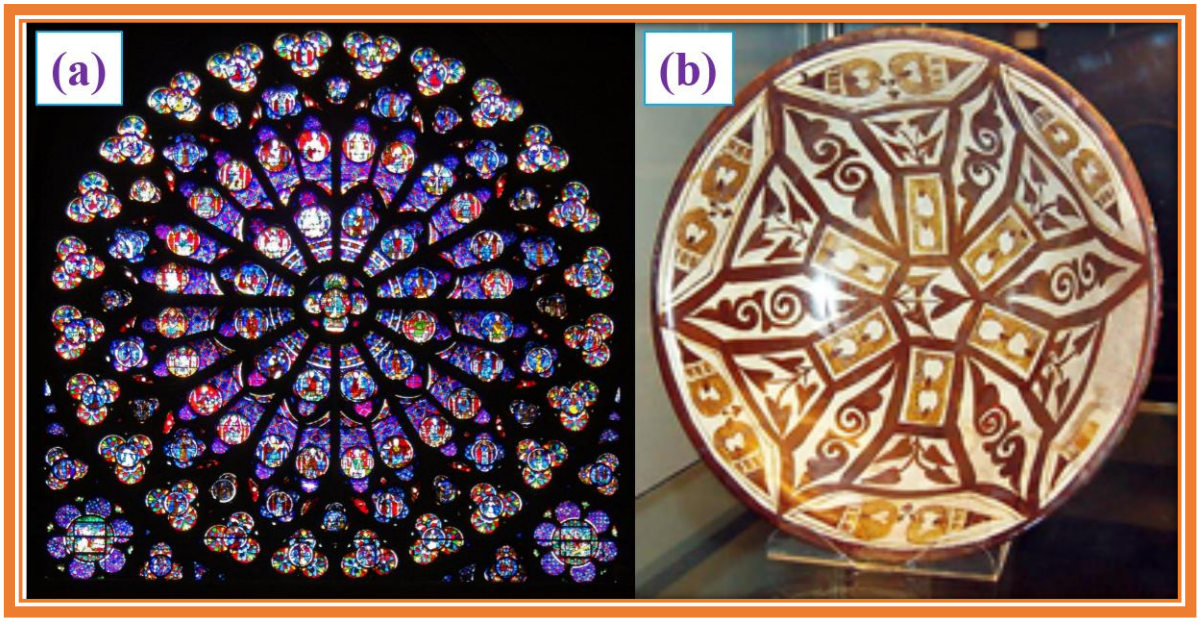

Fig. 1.1: (a) The south rose window of Notre Dame Cathedral, 12^{th} century, Paris [7], and **(b)** polychrome lustreware bowl, 9^{th} century, Iraq, British Museum [8].

Physics Nobel Laureate Richard Feynman delivered a lecture at the Annual American Physical Society meeting held on 29 December 1959 at California Institute of Technology regarding the problems of manipulating things on small scale for the first time [11]. His talk was entitled 'There is Plenty of Room at the Bottom: Invitation to Enter a New Field of Physics'. The entire talk theoretically suggested 'manipulation of atoms the way you want'. After over a decade, the term 'nanotechnology' was first coined by Professor Norio Taniguchi in 1974 at the International Conference on Production Engineering (ICPE), Tokyo in his talk entitled "On the Basic Concept of 'Nano-Technology'" [12]. In 1981, Scanning Tunneling Microscope was invented by IBM Zurich scientists Gerd Binnig and Heinrich Rohrer and they received Nobel prize in 1986 for their great invention [13]. In 1981, the 'founding father of nanotechnology', Eric Drexler introduced the concept of nanotechnology in his seminar proceedings paper at the National Academy of Sciences. He wrote two books on fundamental principles of molecular engineering entitled 'Engines of Creation: The Coming Era of Nanotechnology' and 'Nanosystems: Molecular Machinery, Manufacturing, and Computation' [14,15].

1.2 Nanoparticles and nanomaterials

Nanoparticle is the fundamental component in construction of a nanostructure or nanomaterial. It is typically defined as a particle which has one or more dimensions in the length scale range of 1-100 nm [16]. Nanomaterials possess different physicochemical properties (e.g. optical, electrical, mechanical, and magnetic) compared to their bulk materials [17]. The properties of nanoparticles are greatly influenced by size and shape of the particles [18]. As the particle size decreases from bulk to the nano range, surface area of nanoparticles increases due to exposure a of large fraction of atoms on their surface. This leads to an enhancement in surface to volume ratio [19]. Nature provides a huge number of nanoscale materials and organization of nanoarchitectures is considered to be central to biology. Inspired from Mother nature, human beings have made nanostructured materials which are comparable with the things present in nature (Figure 1.2) [20]. The diameter of DNA molecule is about 2 nm and an ATP synthase biochemical motor is about 10 nm whereas the diameter of manmade nanostructures is about 1 nm for iron atoms on copper surface, 1 nm for a carbon bucky ball, and 1.2 nm for a single-wall carbon nanotube. In the length scale of micrometers, the diameter of red blood cells is about 7-8 μm, fly ash is about 10-20 μm, human hair is between 60 and 120 μm, dust mite is about 200 μm, and an ant is about 5 mm whereas the diameter of zone plate X-ray lens is about

35 μm, micro electro mechanical device (MEMS) is about 10-100 μm, and the head of a pin is about 1-2 mm.

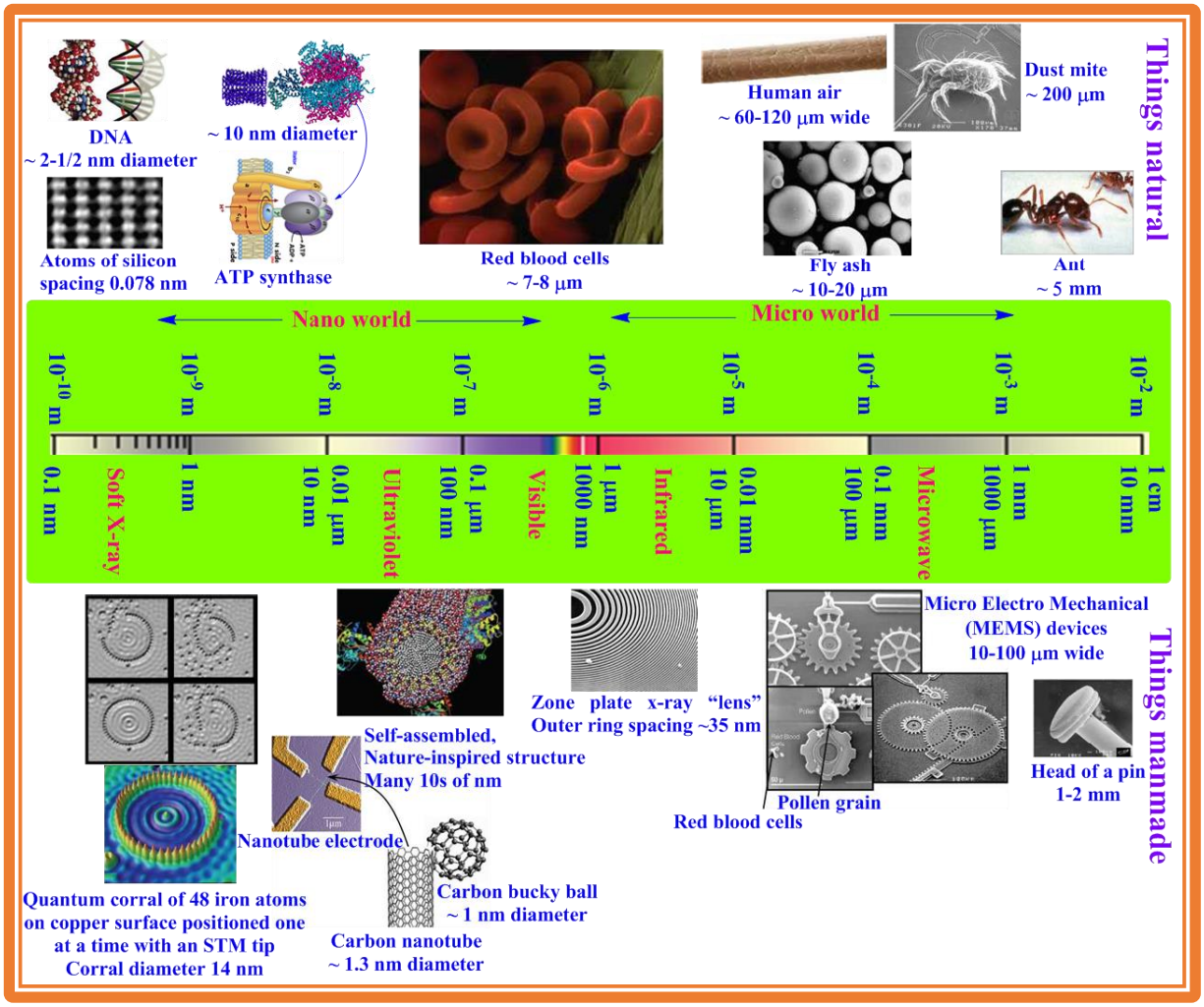

Fig. 1.2: The scale of things present in nature and those made by human [20].

1.2.1 Classification of nanomaterials

Nanomaterials are broadly classified into two main categories.

(i) Organic nanomaterials

e.g. Fullerenes, carbon nanotubes, graphenes, and dendrimers [21–25].

(ii) Inorganic nanomaterials

e.g. Self-assembled monolayers, clusters, metals, metal oxides, quantum dots, nanocomposites, core-shell/yolk-shell nanoparticles, and nanoshells [26–33].

1.2.2 General synthetic methods for the preparation of nanoparticles

In general, nanoparticles are synthesized *via* two main approaches.

(i) Top-down approach
(ii) Bottom-up approach

A schematic illustration of top-down and bottom-up approach for the synthesis of nanoparticles is shown in Figure 1.3 [34].

Top-down approach

In top-down approach, nanoparticles are synthesized *via* thermal, chemical or mechanical disintegration of bulk materials into nanoparticles [35]. Examples for top-down synthetic approach are physical vapour deposition (PVD), pulsed laser method, high energy ball milling, laser ablation, ion implantation, sputter deposition, electric arc deposition, thermolysis, melt mixing, and microwave-assisted synthesis [36,37].

Bottom-up approach

In a bottom-up approach, nanoparticles are synthesized through chemical reactions among atoms and/or molecules [36]. Examples for bottom-up synthetic approach are co-precipitation, sol-gel, micro emulsion, chemical reduction, thermal decomposition, hydrothermal, chemical vapour deposition, and sonochemcial synthesis [36,38,39].

The bottom-up approach has several advantages as compared to the top-down approach. The bottom-up approach is simple, versatile, and economical whereas the top-down approach requires expensive equipments, and also need a longer reaction time to complete the synthesis. The bottom-up approach has a good control on size and shape of the nanoparticles.

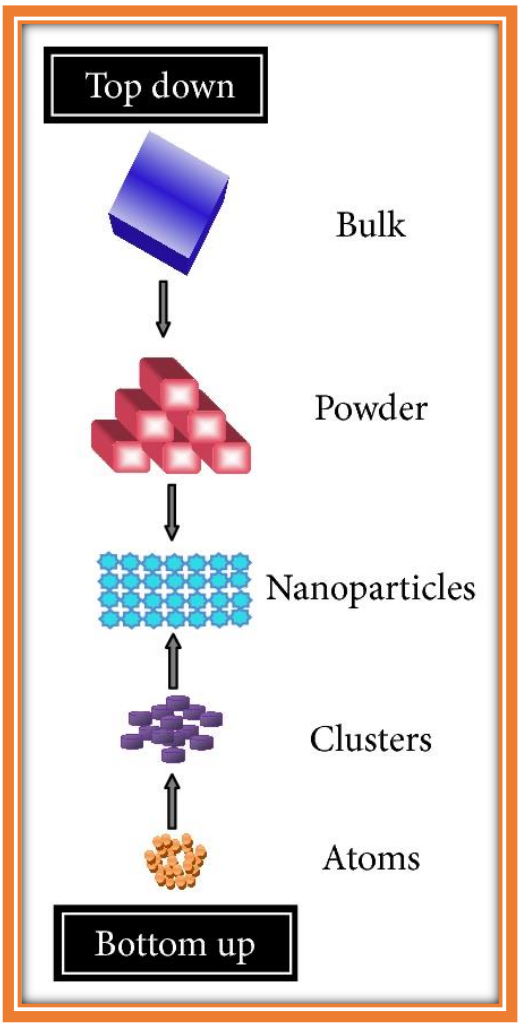

Fig. 1.3: Schematic illustration of top-down and bottom-up approaches for the synthesis of nanoparticles [34].

1.3 Introduction to core-shell nanoparticles

Historically, the term, "core-shell nanoparticles" was coined for the concentric multilayer semiconductor nanoparticles [40,41]. Core-shell nanoparticles are constructed with cores (inner material) and shells (outer materials) in which either the core or the shell or both are at nanoscale range [30]. This definition is extended to the class of nanomaterials, in which the shell material covers either fully or partially the core material as long as they can be separately distinguished [30]. Different shaped core-shell nanoparticles such as spherical core-shell nanoparticles, hexagonal core-shell nanoparticles, multiple core materials coated by a single shell material, nanomatryushkas, and movable core-hollow shell nanoparticles have been made by the scientists and a schematic representation of various shaped core-shell nanoparticles is given in Figure 1.4.

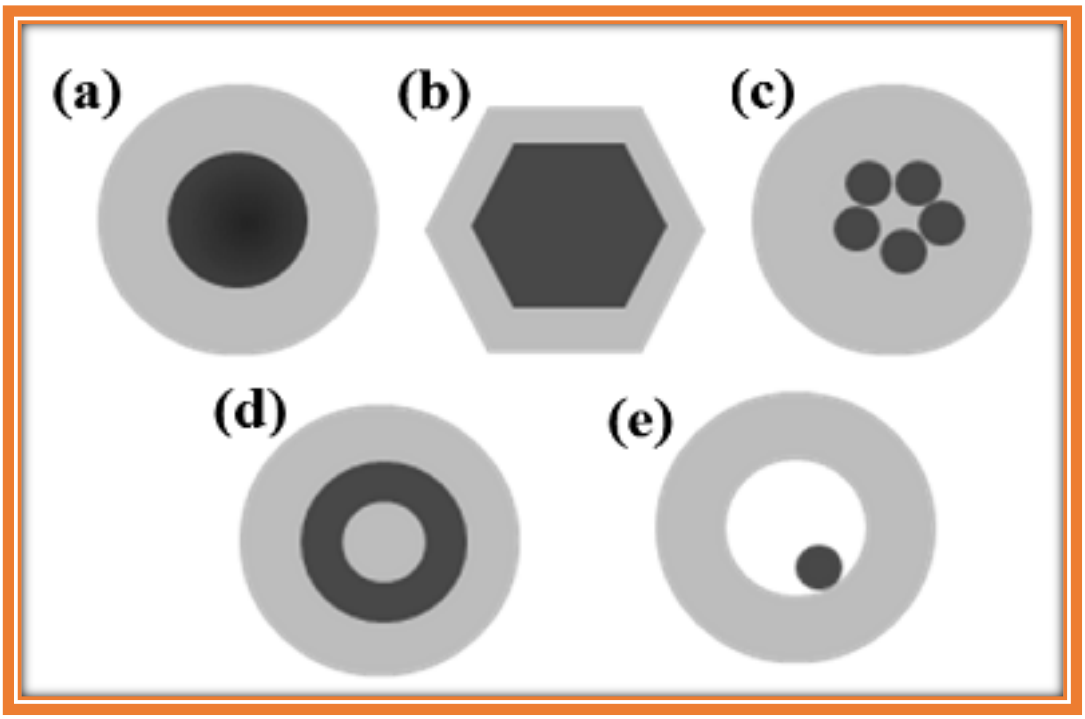

Fig. 1.4: Representation of **(a)** spherical core-shell nanoparticles, **(b)** hexagonal core-shell nanoparticles, **(c)** multiple cores coated by a single shell material, **(d)** nanomatryushka type core-shell nanoparticles, and **(e)** movable core-hollow shell nanoparticles [42].

The core-shell nanoparticles are broadly classified into several classes based on their composition and arrangement of the two components in them.

(i) Inorganic/inorganic core-shell nanoparticles
(ii) Inorganic/organic core-shell nanoparticles
(iii) Organic/inorganic core-shell nanoparticles
(iv) Organic/organic core-shell nanoparticles
(v) Core-multi shell nanoparticles
(vi) Movable core-hollow shell nanoparticles
(vii) Janus type core-shell nanoparticles

1.3.1 Inorganic/inorganic core-shell nanoparticles

In this type of nanoparticles, both the core and the shell are made up of inorganic materials such as metals, metal oxides, metal chalcogenides, or silica [42,43]. Based on the nature of the shell material, the inorganic/inorganic core-shell nanoparticles are further broadly classified into two main categories.

(i) Inorganic/inorganic (silica) core-shell nanoparticles

(ii) Inorganic/inorganic (non-silica) core-shell nanoparticles

1.3.1.1 Inorganic/inorganic (silica) core-shell nanoparticles

In these core-shell nanoparticles, the inorganic core material is coated with silica and coating silica on an inorganic core material has several advantages [42]. Silica is a chemically inert material which reduces bulk conductivity and increases suspension stability of the core material [44]. In addition, silica also blocks redox reactions at the core surface [42]. Silica shell has been coated on various inorganic core materials such as metals, binary metals, metal oxides, and metal salts/chalcogenides. Examples are FeNi@SiO_2, Fe_3O_4@SiO_2, AgI@SiO_2, CdSe@SiO_2, Au@TiO_2, etc [45–49].

1.3.1.2 Inorganic/inorganic (non-silica) core-shell nanoparticles

In this type of nanoparticles, the inorganic core material is coated with another inorganic material such as metals, metal oxides, metal salts, or metal chalcogenides except silica [42]. Examples are Au@Ag, FePt@CdS, Fe@Fe_2O_3, $Fe_{58}Pt_{42}$@Fe_3O_4, Au@CuI, Ag@Ag_2S, Fe_3O_4@TiO_2, etc [50–57].

1.3.2 Inorganic/organic core-shell nanoparticles

In the case of inorganic/organic core-shell nanoparticles, the core materials are mostly made up of metals and metal oxides whereas the shell material is made up of organic materials such as carbon and its derivatives, polymers, or any other high density organic material [42]. Coating of an organic material on an inorganic material has several advantages. For example, the oxidation stability of the metal core is greatly enhanced simply by preventing the oxidation of surface atoms from air. Also, organic shell molecules are bio-compatible [42]. Based on the properties of the core material, inorganic/organic core-shell nanoparticles are broadly classified into two main groups.

(i) Magnetic/organic core-shell nanoparticles

(ii) Non-magnetic/organic core-shell nanoparticles

1.3.2.1 Magnetic/organic core-shell nanoparticles

In this type of core-shell nanoparticles, the core material is made up of inorganic magnetic materials such as metals and metal oxides while the shell is composed of organic materials

such as carbon, polymers, etc. Examples are Fe@a-PEG, Fe@PS, Fe_3O_4@MPEG, Fe_3O_4@PLA, γ-Fe_2O_3@PEI-PEO-PEG, etc [58–62], where a-PEG-amine-terminated-poly(ethylene glycol), PS-polystyrene, MPEG-methoxypoly(ethylene glycol), PLA-polylactide, PEI-poly(ethylene imine), and PEO-poly(ethylene oxide).

1.3.2.2 Non-magnetic/organic core-shell nanoparticles

In this type of core-shell nanoparticles, the core is made up of non-magnetic materials such as metals and metal oxides while the shell is composed of organic materials such as carbon and their derivatives, and polymers. Examples are Au@C, Ag-Au@PEG, SnO_2@graphene, ZrO_2@PMMA, $BaTiO_3$@PMMA/PS, etc [63–67], where PMMA-poly(methyl methacrylate).

1.3.3 Organic/inorganic core-shell nanoparticles

In organic/inorganic core-shell nanoparticles, the core is composed of organic materials whereas the shell is made up of inorganic materials such as metals, metal oxides, metal chalcogenides, or silica [42]. The organic/inorganic core-shell nanoparticles have several advantages. These materials show high strength, increased thermal and colloidal stability, enhanced optical properties, flexibility, toughness, and brittleness [42,68]. Examples are PS@Ag, PU@SiO_2, PVBC@Pd, Dextrose@TiO_2, CTAB@Ag_2S, etc [69–73] where PU-polyurethane, PVBC-poly(vinyl benzyl chloride), and CTAB-cetyltrimethyl ammonium bromide.

1.3.4 Organic/organic core-shell nanoparticles

In organic/organic core-shell nanoparticles, the core as well as the shell are composed of organic materials such as carbon and their derivatives, or polymers. This type of core-shell nanoparticles are called as “smart particles” [42]. These materials have some advantages; polymer coating over another polymer leads to changes in the physical properties such as improvement in toughness, change in the glass transition temperature (T_g), and improvement in mechanical properties [74]. Examples are PEGDMA@PS, PS@PMMA, PEI@mPEG, PANI@PDVB, etc [75–79], where PEGDMA- poly(ethylene glycol dimethacrylate), PANI-polyaniline, and PDVB-poly(divinyl benzene).

1.3.5 Core-multi shell nanoparticles

In core-multi shell nanoparticles, the core is composed of mostly inorganic materials such as metals, metal oxides or metal chalcogenides whereas the different shells are composed of metals, metal oxides, metal chalcogenides, polymers, etc. The final shape of the material depends on shape of the core. Examples are α-Fe_2O_3@Ag@SnO_2, SiO_2@Ag@@SiO_2@TiO_2, Fe_3O_4@Ag@SiO_2@Au, n-GaAs@InGaP@p-GaAs, CdSe@CdS@CdS@$Cd_{0.75}Zn_{0.25}S$@$Cd_{0.5}Zn_{0.5}S$@$Cd_{0.25}Zn_{0.75}S$@ZnS@ZnSQDs@PMMA, CdSe@ZnSe@CdS, etc [80–85].

1.3.6 Movable core-hollow shell nanoparticles

This type of core-shell nanoparticles are generally referred to as 'yolk-shells' or 'nanorattles' [86]. The core and the shell are made up of either inorganic or organic materials. In general, they are denoted as either core@void@shell or core@shell1@shell2 [87,88]. The core is made up of metals, metal oxides, metalloids, doped oxides or sulfides whereas the shell is made up of metals, metal oxides, polymers, and carbon or nitrogen doped carbon [87]. Based on properties of the shell material, these core-shell nanoparticles are broadly classified into two main categories [30].

(i) Hollow core-shell nanoparticles
(ii) Core-porous shell nanoparticles

1.3.6.1 Hollow core-shell nanoparticles

In this type of core-shell nanoparticles, the core is sacrificed using various methods. For example, organic cores are removed by either calcination or dissolution in suitable organic solvents whereas inorganic cores are removed by reaction with a strong acid or a base [30,86]. Examples are SiO_2@void@TiO_2, ZrO_2@void@$BiVO_4$, hollow MFe_2O_4 (M= Zn, Co, Ni, Cd), α-Fe_2O_3@SnO_2, etc [89–92].

1.3.6.2 Core-porous shell nanoparticles

In this type of nanoparticles, the core and shell are made up of either inorganic or organic materials but the shells possess porous nature. Examples are SiO_2@Au@SiO_2, Ca-Pd@SiO_2, α-Fe_2O_3@SnO_2@C, Au-M (M = Au, Pd, and Pt), Fe_3O_4@SiO_2@mSiO_2, etc [93–96].

1.3.7 Janus type core-shell nanoparticles

In this type of nanoparticles, single crystal shells (either atomic or mesoscale ones) are coated on the core materials [97]. These materials possess asymmetric morphology and provide different physicochemical properties within a single nanoparticle. The name janus originates from the Roman God janus, the God of beginning and ending, doors and gates. The term 'janus' is first coined by Nobel Laureate P. G. de Gennes in his lecture entitled "Soft Matter" in 1991 [98]. Examples are SiO_2@α-Fe_2O_3, MNP's@PS-b-PAA, Pd/Au@Fe_3O_4, CdSe@Pt, etc [99–102].

1.3.8 Miscellaneous core-shell nanoparticles

In recent years, new heterostructured materials such as core-satellite nanoparticles and core@MOF's have been developed. In the case of core-satellite nanoparticles, the shell is immobilized on core surface *via* coupling agents [103]. In most of the cases, inorganic materials are used as the core as well as the shell. Examples are Dy-SiO_2@Fe_3O_4, Fe_3O_4@SiO_2@Au@mSiO_2, Au@Ag, Ag@$BaTiO_3$, etc [103–106]. In the case of core@MOF's, the core is made up of mostly metal and metal oxides whereas the shell is composed of metal organic frameworks (MOF's) which possess porous nature. Examples are M@MOF-5 (M = Pd, Au, Ru, Cu, Pt, Ni, and Ag), Fe_3O_4@[Cu_3(btc)$_2$], ZnO@ZIF-8, Cu/ZnO@MOF-5, Fe_3O_4@ZIF-8, Co_3O_4@MOF, Pd/ZnO@ZIF-8, etc [107–110].

1.4 Synthesis of core-shell nanoparticles

In general, core-shell nanoparticles are synthesized in two or more steps. The core nanoparticles are synthesized in the first step and the shell nanoparticles are synthesized in the next step [30]. Depending on availability of the core materials, the synthesis of core-shell nanoparticles is broadly classified into two types. In the first type, the core particles are synthesized and used in the second step with or without surface modification to coat the shell. In the second type, core particles are synthesized and this is followed by coating of shell material carried out *in situ*. Among the two methods, the first method is more versatile and superior because the shell is coated after proper cleaning of core surface. This results in enhancement in properties of the overall material as compared to the materials synthesized *via in situ* process [30,42]. Uniform coating of shell with controlled thickness on the core is difficult due to different physicochemical properties of the core and shell. In general, core-shell nanoparticles are synthesized in two ways.

(i) Top-down approach (physical route)

(ii) Bottom-up approach (chemical route)

Synthesis of core-shell nanoparticles has been reported in the literature using various synthetic methods such as reduction/transmetalation, thermal decomposition, chemical vapour deposition, sol-gel, precipitation, reverse micro-emulsion, sonochemical, hydro/solvothermal, microwave, polymerization, spray pyrolysis, galvanic displacement, template route, wire electrical explosion, and photo laser deposition. Some of the reported synthetic methods are explained in brief as follows.

1.4.1 Physical routes

1.4.1.1 Pulsed laser deposition

This method is used for the synthesis of either metal/metal oxide/metal chalcogenide core or shell nanoparticles. In this method, glass or quartz is used as a support. Before starting the PLD process, the chamber is purged with either helium or argon gas to eliminate residual oxygen or air present in the chamber. All the reactions are carried out inside the vacuum chamber at a residual pressure of about 10^{-8} Torr. Target pellet is prepared using a manual pellet presser and the pellet is used as a deposition source. In the PLD process, mostly, two types of lasers (Nd:YAG laser source (λ= 355 nm) and KrF laser (λ = 248 nm)) are used. The laser pulse width used is about 20-25 ns with a repetition rate of 5-10 Hz and the deposition is carried out for several minutes. The target to substrate distance is maintained at several centimeters and the target is continuously rotated during the deposition to produce uniform deposition. The energy of the laser pulse, used for the deposition, depends on respective ablation threshold of the substrate. The core-shell nanoparticles, prepared using this method, are Ge@GeO_2, CdS@ZnTe, ZnO@SnO_2, Ga@graphene, etc [111–114]. A schematic illustration for the synthesis of Ga@G core-shell nanoparticles using pulsed laser deposition is shown in Figure 1.5.

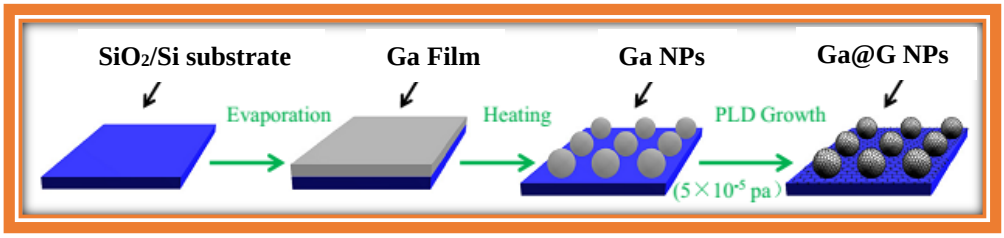

Fig. 1.5: Schematic illustration using PLD process for the synthesis of Ga@G core-shell nanoparticles [114].

1.4.1.2 Chemical vapour deposition

Chemical vapour deposition is used mostly for the synthesis of either semiconductor core or shell (thin film) nanoparticles. It is classified into different types based on the nature of precursors employed during the synthesis. They are local laser assisted chemical vapour deposition (LCVD), metal-organic chemical vapour deposition (MOCVD), and organo-metallic chemical vapour deposition (OMCVD). The CVD chamber is of cylindrical shape, made up of stainless steel with inlet and outlet connections for the precursor gaseous molecules as well as residual gases. The precursors used in the CVD process are volatile and they are put into a quartz boat and placed inside a quartz tube. The whole process is carried out under low vacuum of about 1 Torr in the presence of argon or nitrogen atmosphere to avoid chemical reactions with water or oxygen inside the chamber. The deposition undergoes near the hot surfaces inside the chamber and after the deposition, the sample chamber is allowed to cool to room temperature under the flow of either argon or nitrogen gas with the formation of thin film of nanoparticles. In the CVD process, the growth rate is effective due to three dimensional mass transport of the gaseous precursor molecules into the deposition zone. The core-shell nanoparticles, prepared using this method, are Ag@ZnO, Ni-Sn@C, SiC@Si, NiSi@SiC, etc [115–118].

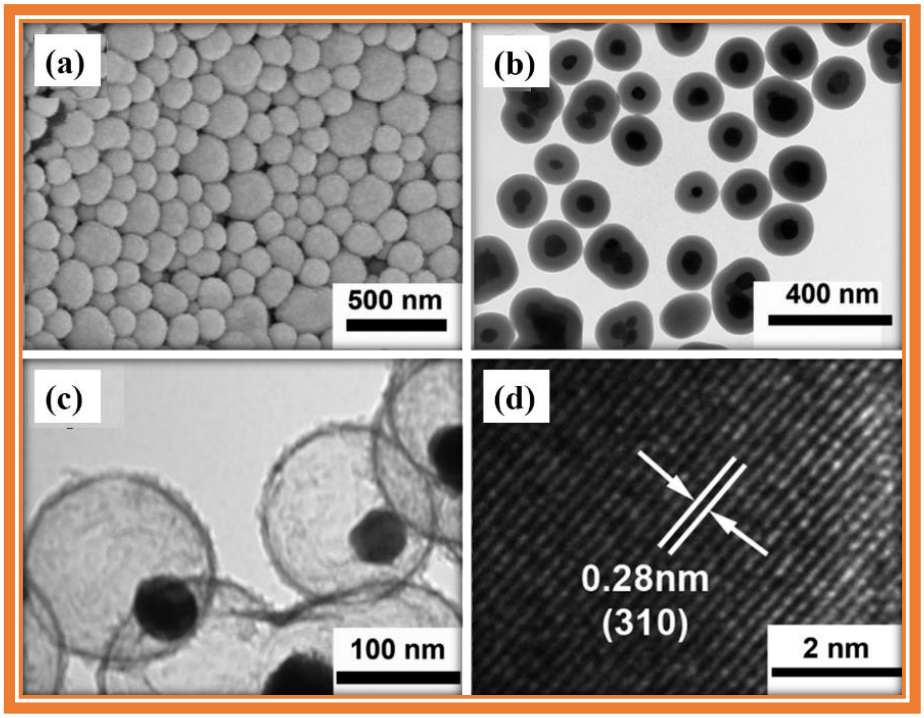

Fig. 1.6: (a, b) SEM and TEM images of Ni-Sn@SiO_2 core-shell nanoparticles, and **(c, d)** TEM and HRTEM images of Ni-Sn@C core-shell nanoparticles prepared by chemical vapour deposition [116].

1.4.1.3 Spray pyrolysis

This method is mostly used to prepare metal oxide core or shell nanoparticles. In this method, metal precursors are dissolved in diluted nitric acid to get a clear solution. The spray pyrolysis system contains a quartz reactor, droplet generator, and powder collector. All the reactions are carried out under vacuum after removing water vapour and exhausted gases by means of a vacuum pump. The metal precursor solutions are fed from a burette to an atomizer, which are nebulized by an ultrasonic atomizer (1.7 MHz). The nebulized spray is carried to the reaction tube chamber by air flow at a certain rate. The temperature in the reaction chamber is monitored using thermocouples placed near surface of the atomizer, reactor and the sample holder. These droplets are ignited by supported inverse diffusion of hydrogen/air flames and the flow rate of hydrogen/air is kept at a certain rate. During the spray pyrolysis, nanoparticles are deposited on the substrate placed in the tube chamber while water vapour and exhausted gases are discharged through a vent line. The core-shell nanoparticles synthesized using this method are Co_3Fe_7@$CoFe_2O_4$, $Ce_{0.7}Zr_{0.3}O_2$@Al_2O_3, Fe_2O_3@SnO_2, Ag@SiO_2, etc [119–122]. A schematic setup of flame spray pyrolysis for the synthesis of core-shell nanoparticles and TEM images of $Ce_{0.7}Zr_{0.3}O_2$@Al_2O_3 core-shell nanoparticles, synthesized using spray pyrolysis, are shown in Figure 1.7.

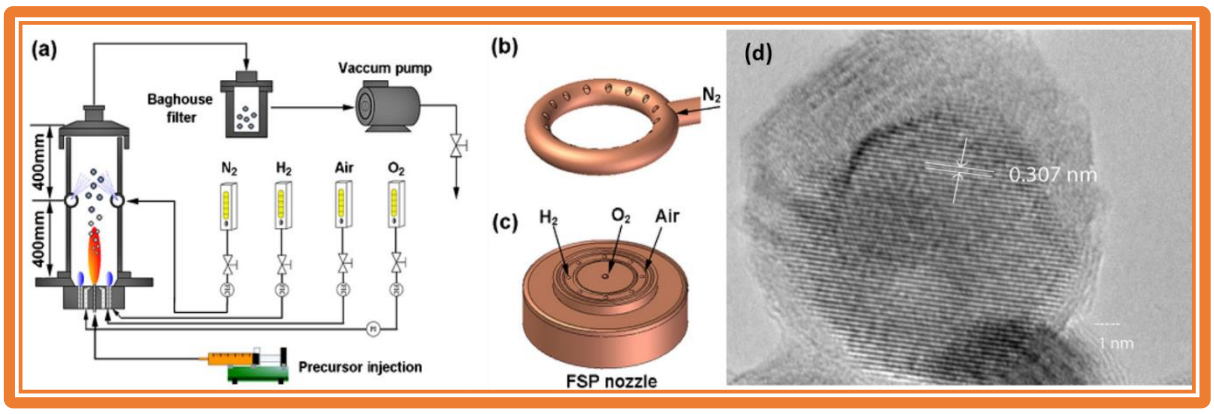

Fig. 1.7: (a) Schematic setup of flame spray pyrolysis, **(b)** 3D model of the cooling ring, **(c)** 3D model of the nozzle [119], and **(d)** HRTEM image of $Ce_{0.7}Zr_{0.3}O_2$@Al_2O_3 core-shell nanoparticles synthesized using spray pyrolysis [120].

1.4.1.4 Microwave synthesis

This method is used for the synthesis of either metal/metal oxide/metal chalcogenide core or shell nanoparticles. The microwave reactor operates at a frequency of 2.45 GHz which is too

low to break chemical bonds in a molecule. So this method is unable to induce chemical reactions but it generates efficient heating. Under microwave irradiation of the reaction mixture, ion or dipole alignment occurs. The ions or dipoles of the precursors, present in the reaction mixture, realign themself according to oscillation of the microwaves resulting in production of heat energy in a reaction system *via* molecular friction and dielectric loss. The fast energy transfer between the reactants allow fast decomposition of precursors and create highly supersaturated solutions. The ability of heat generation in the reaction mixture depends on dielectric property of the solvent used. The commonly used solvents are dimethylsulfoxide, isopropanol, formic acid, etc. The core-shell nanoparticles, synthesized using this method, are Ni@C@Ag_3PO_4, Fe_3O_4@C@CdS, CdTe@CdS, Ag@Ag_2SO_4, etc [123–126]. The TEM and HRTEM images of Fe_3O_4@C@CdS core-shell nanoparticles, synthesized using microwave synthesis, are shown in Figure 1.8.

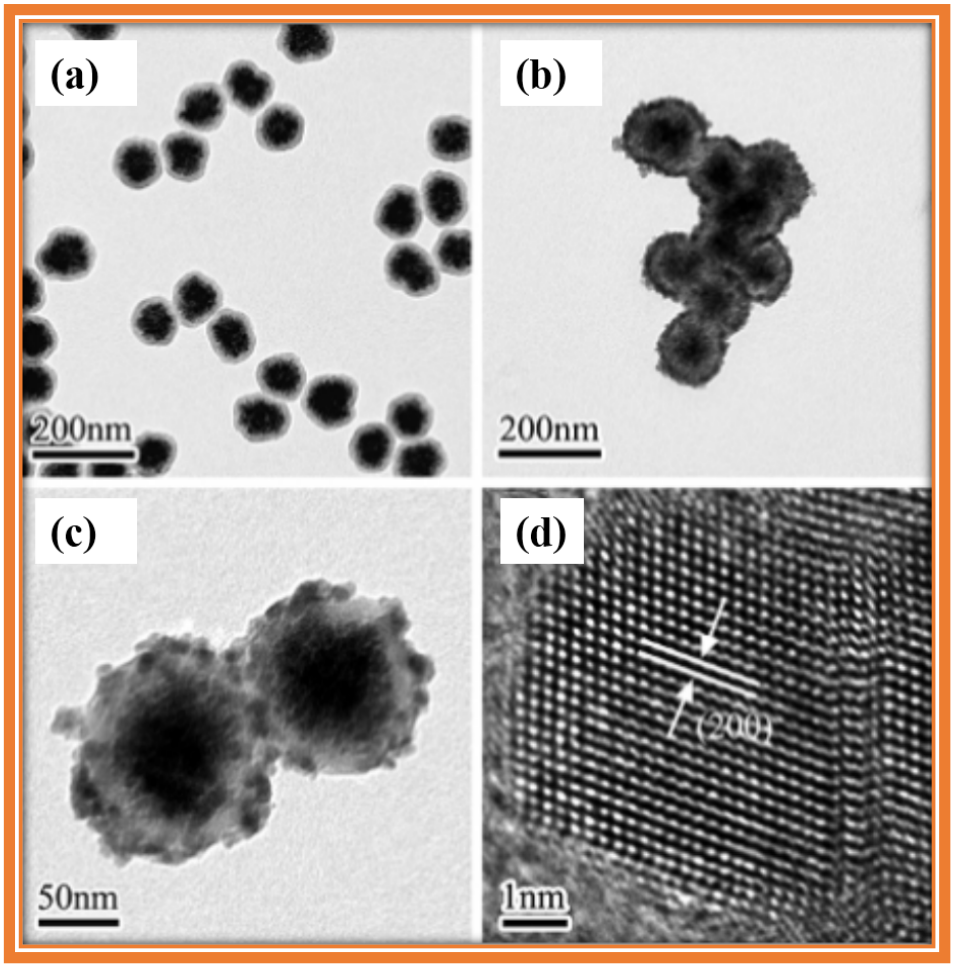

Fig. 1.8: (a) TEM image of Fe_3O_4@C core-shell nanoparticles, **(b, c)** TEM images of Fe_3O_4@C@CdS core-shell nanoparticles, and **(d)** HRTEM image of CdS nanoparticles in the Fe_3O_4@C@CdS core-shell nanoparticles [124].

1.4.2 Chemical routes

1.4.2.1 Reduction/Transmetalation

Generally, either core or shell of metal nanoparticles are synthesized using this method. Aqueous or organic solutions are used as the reaction media and metal salts are used as the precursors. Either sodium borohydride or hydrazine is used as a reducing agent. Surfactants or capping agents are also used to control the particle size as well as to coat a uniform shell of another metal on the metal core surface. Sodium borohydride is the most commonly used reducing agent due to its high solubility in both aqueous and organic media. It possesses high reduction potential of -1.24 V *vs.* NHE at pH =14 and decreases to 0.48 V at pH= 0 indicating that the reduction potential depends on pH of the reaction media. The reducing agent provides electrons to metal salts and the reduction proceeds to produce either metal core or shell nanoparticles. Transmetalation is an advanced method to produce bimetallic core-shell nanoparticles. In this method, core particles are synthesized using common reduction method and after that, reactants corresponding to the shell material are added to the reaction media without any reducing agent. Once the metal core surface atoms come into contact with the reactants of the shell, they are reduced by surface atoms of the metal core and deposited on the core surface to produce a uniform shell. The limitation of this method is that the reduction potential of shell material should be higher than that of the core material. The core-shell nanoparticles, synthesized using this method, are Ni@Ag/Au, Ru@Pt, Pd@Pt, etc [127–129]. A schematic indicating the reduction-transmetalation route for the synthesis of Sn@Cu core-shell nanoparticles is shown in Figure 1.9 [130].

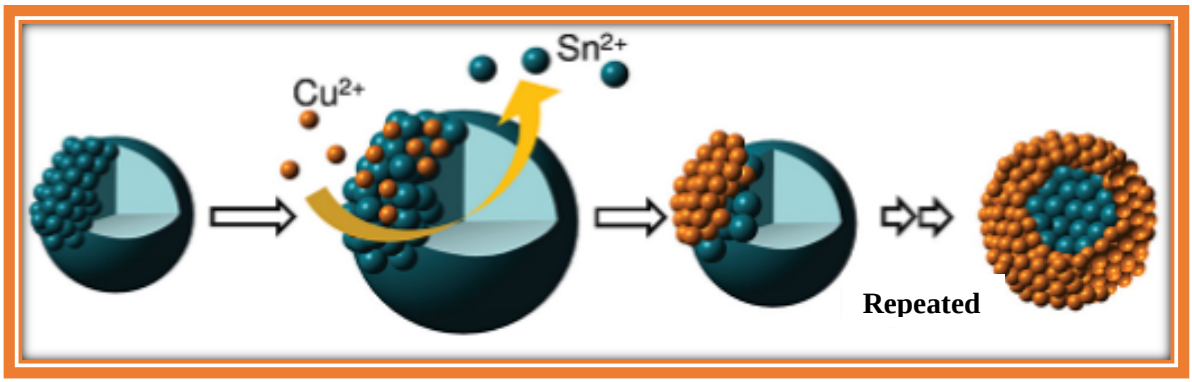

Fig. 1.9: Schematic illustration of the synthesis of Sn@Cu core-shell nanoparticles *via* reduction-transmetalation route [130].

1.4.2.2 Thermal decomposition

This method is used to synthesize either metal/metal oxide/metal chalcogenide core or shell nanoparticles. Organometallic compounds are used as metal precursors but their high decomposition temperature as well as toxic nature limit their use. To reduce decomposition temperature of the precursors, the organometallic precursors are replaced by metal-complexes or metal acetates. All the reactions are carried out in high boiling organic solvents under either air or an inert atmosphere. Surfactants such as oleic acid, oleylamine, hexadecanediol, or triphenylphosphine are used as stabilizing agents which control either the core morphology or particle size of the shell. The core-shell nanoparticles, synthesized using this method, are $Co@Fe_3O_4$, Pt-rich@Pt-Ni alloy, $Co_xFe_{1-x}O@Co_yFe_{3-y}O_4$, CdSe@ZnO, etc [131–134]. A schematic illustration of CdSe@ZnO core-shell nanoparticles synthesized using thermal decomposition approach is shown in Figure 1.10 [134].

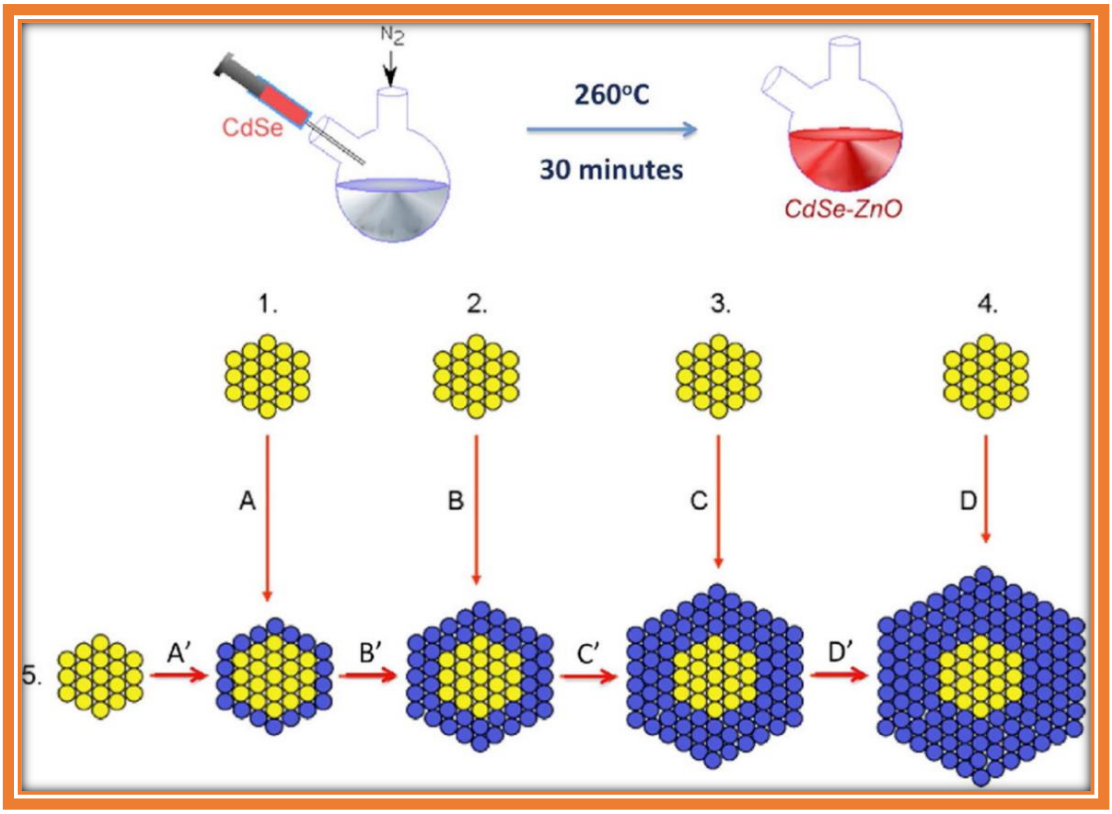

Fig. 1.10: Schematic illustration of the synthesis of CdSe@ZnO core-shell nanoparticles *via* thermal decomposition approach. Routes 1-4 are one-pot shelling reactions. A, B, C, and D represent equimolar amounts of one, two, three, and four monolayers of shelling precursor, respectively. Route 5 is monolayer-by-monolayer deposition, A´, B´, C´, and D´ represent amount of Zn precursor needed for each monolayer, respectively [134].

1.4.2.3 Sol-gel

This method is a wet-chemical technique and it is mostly used to prepare metal oxide core or shell nanoparticles. Metal alkoxides and metal chlorides are used as precursors to synthesize the metal oxide core or shell nanoparticles. Two steps are involved in this method; they are hydrolysis and polycondensation. Metal alkoxide precursors undergo hydrolysis in the presence of water and produce hydrated metal hydroxides which subsequently undergo condensation to form a sol. This sol contains –M–O–M– network with low viscous nature which casts into gel under heating. During gelation, the –M–O–M– network makes a bond with colloidal particles to form a 3D network with high viscosity. The obtained high viscous liquid is allowed to dry *via* xero-gel or aero-gel process. Solid powders are obtained which are calcined under air or oxygen atmosphere to produce metal oxide core or shell nanoparticles. The core-shell nanoparticles, synthesized using this method, are V_2O_5@TiO_2 loaded on graphene sheets, Au@mesoporous Si-Al shells, Fe_2O_3@SiO_2, FePt@SiO_2-Au, etc [135–138]. TEM and HRTEM images of the V_2O_5@TiO_2 core-shell nanoparticles loaded on graphene sheets are shown in Figure 1.11.

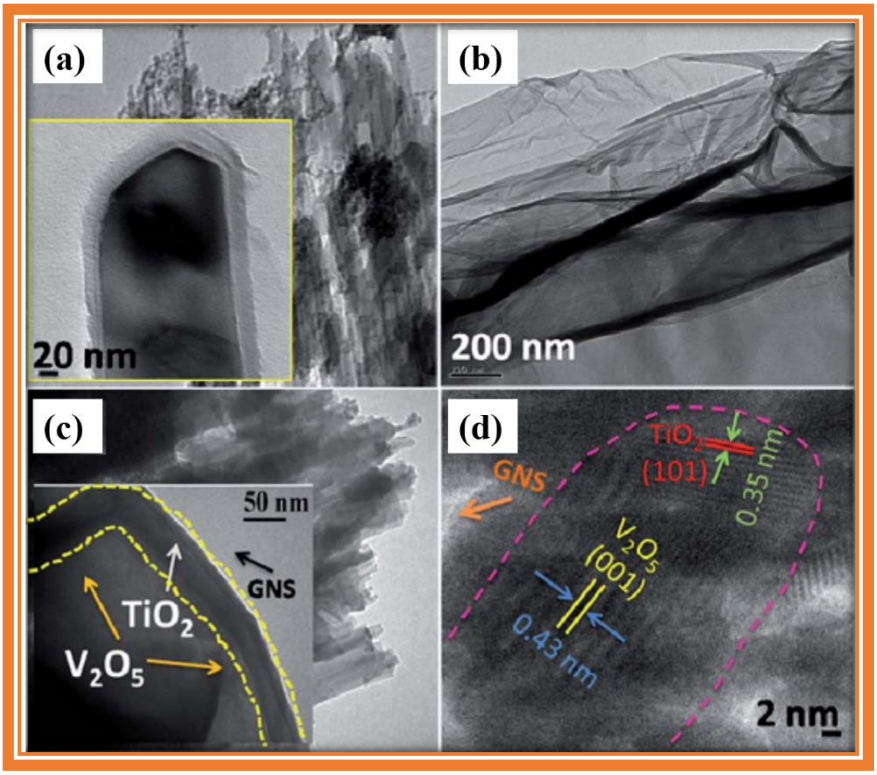

Fig. 1.11: (a-c) TEM images of V_2O_5@TiO_2 core-shell nanoparticles, graphene sheets, V_2O_5@TiO_2 core-shell nanoparticles loaded on graphene sheets, and **(d)** HRTEM image of V_2O_5@TiO_2 core-shell nanoparticles loaded on graphene sheets [135]. The core-shell nanoparticles were prepared by sol-gel method.

1.4.2.4 Precipitation method

This is another wet-chemical method and metal oxide/metal chalcogenide core or shell nanoparticles are synthesized using this method. Generally, precipitation reactions are divided into two types; one is homogenous precipitation and the other one is co-precipitation. In both the methods, metal salts such as metal chlorides, nitrates, or sulfates are used as metal precursors. In homogeneous precipitation, urea is generally used as the precipitating agent whereas sodium hydroxide or ammonium hydroxide is used as a precipitating agent in co-precipitation. Homogeneous precipitation reactions are carried out at about 80 ^{o}C while co-precipitation reactions are carried out either at room temperature or at slightly high temperature. In both the reactions, metal precursors react with the precipitating agent and precipitate out a water insoluble compound from the reaction media. The important factor for these reactions is the solubility product. When the concentration of a product crosses its solubility product, it gets precipitated from the reaction media and produce either core or shell nanoparticles. The core-shell nanoparticles, synthesized using this method, are CuO@NiO, ZnO@ZnS, CeO_2@ZnO@SiO_2, etc [139–141]. The schematic illustration for the formation of CuO@NiO core-shell nanoparticles by homogeneous precipitation is shown in Figure 1.12 [139].

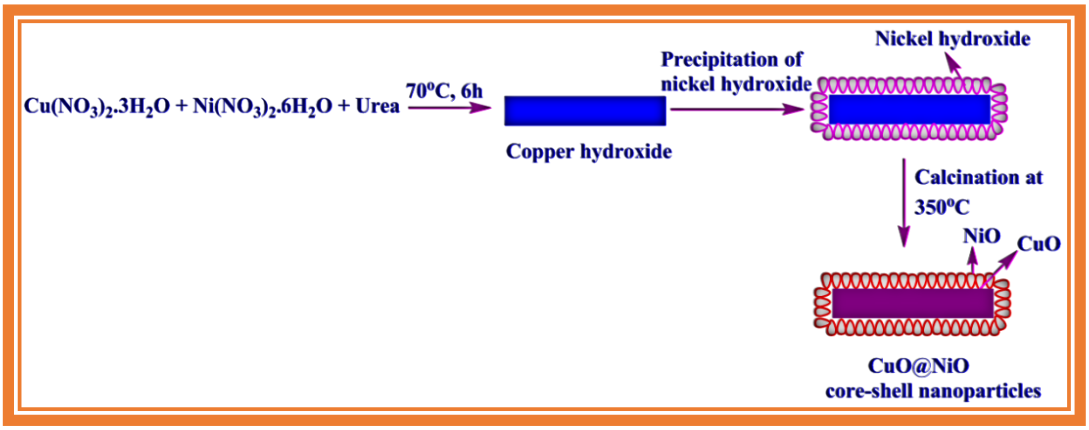

Fig. 1.12: Schematic illustration of the synthesis of CuO@NiO core-shell nanoparticles using homogeneous precipitation [139].

1.4.2.5 Microemulsion technique

This method is used for the preparation of either metal/metal oxide/metal chalcogenide core or shell nanoparticles. A microemulsion contains a ternary mixture of water, oil, surfactant and co-surfactant. Sodium dodecyl sulfate (SDS) and bis(2-ethylhexyl) sulfosuccinate sodium

(AOT) are usually used as the surfactants. The hydrophobic groups of the surfactant are nonpolar and they face towards the oil phase and the hydrophilic groups (polar) face towards the water phase. The surfactant molecules form reverse micelles and stabilize the water droplets whereas co-surfactant reduces the electrostatic repulsive forces between the charged head groups of the surfactant and facilitate the micellization process. During the reaction, interchange of the reactants takes place by means of collision of water droplets and the nanoparticles are produced. The final particle size and morphology of the nanoparticles depend on reduction, nucleation, and growth of particles inside the droplet. The size of the droplet depends on water to surfactant ratio and chain length of the surfactant. Examples for the core-shell nanoparticles, synthesized using this method, are ZnO@Ag, Fe_3O_4@SiO_2, $Cs_2[Mo_6Br_{14}]$@SiO_2, In_2O_3@SiO_2, etc [142–145]. The La Mer diagram and TEM images of Fe_3O_4@SiO_2 core-shell nanoparticles prepared using various amounts of TEOS are shown in Figure 1.13.

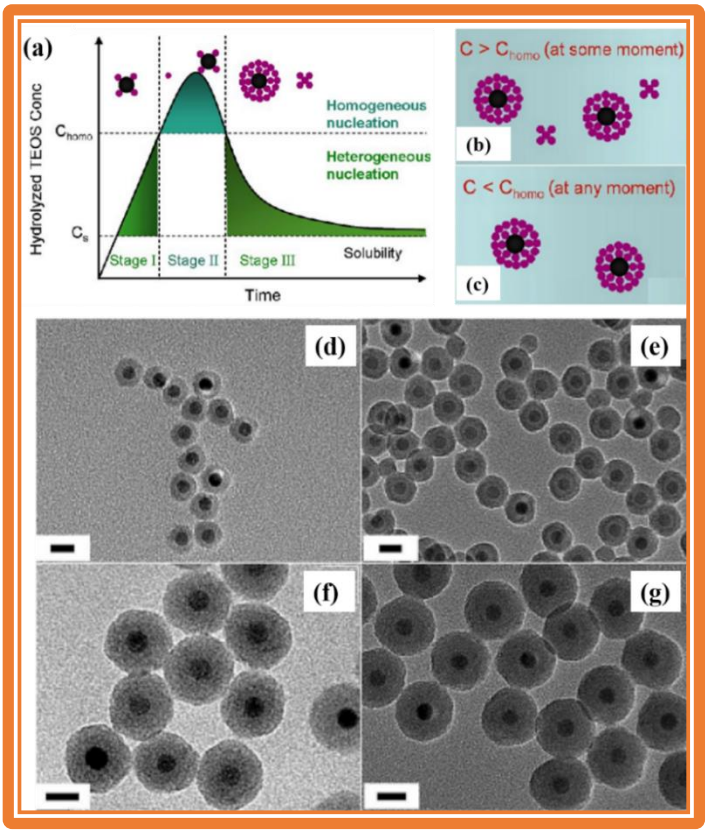

Fig. 1.13: (a) La Mer diagram indicating the hydrolyzed TEOS concentration with time, **(b)** the existence of both Fe_3O_4@SiO_2 core-shell nanoparticles and SiO_2 particles in the reaction media, **(c)** the existence of only Fe_3O_4@SiO_2 core-shell nanoparticles, and **(d-g)** TEM images of Fe_3O_4@SiO_2 core-shell nanoparticles prepared using 75, 150, 300 and 600 μL of TEOS [143].

1.4.2.6 Hydrothermal method

This method is used for the synthesis of either metal/metal oxide/metal chalcogenide core or shell nanoparticles. In this method, metal salts, metal acetates, or metal complexes are used as the precursors. Capping agents such as long chain amines, thiols, and trioctylphospine oxide are used to prevent aggregation as well hindering the irregular growth of particles. All the reactants are mixed in certain amount in an aqueous solution along with capping agents and stirred at room temperature to get a uniform mixture. Then, the contents are transferred into a Teflon lined stainless steel autoclave and heated at elevated temperatures (e.g. 150-250 ^{o}C) for several hours to get the core-shell nanoparticles. The core-shell nanoparticles, synthesized using this method, are SnO_2@graphene, α-Fe_2O_3@Ag@SnO_2, α-Fe_2O_3@SnO_2, Fe_3O_4@ZIF-8, etc [65,80,92,108]. The TEM image, EDX plot, FFT pattern, and HRTEM image of α-Fe_2O_3@SnO_2 core-shell nanoparticles, synthesized using the hydrothermal method, are shown in Figure 1.14.

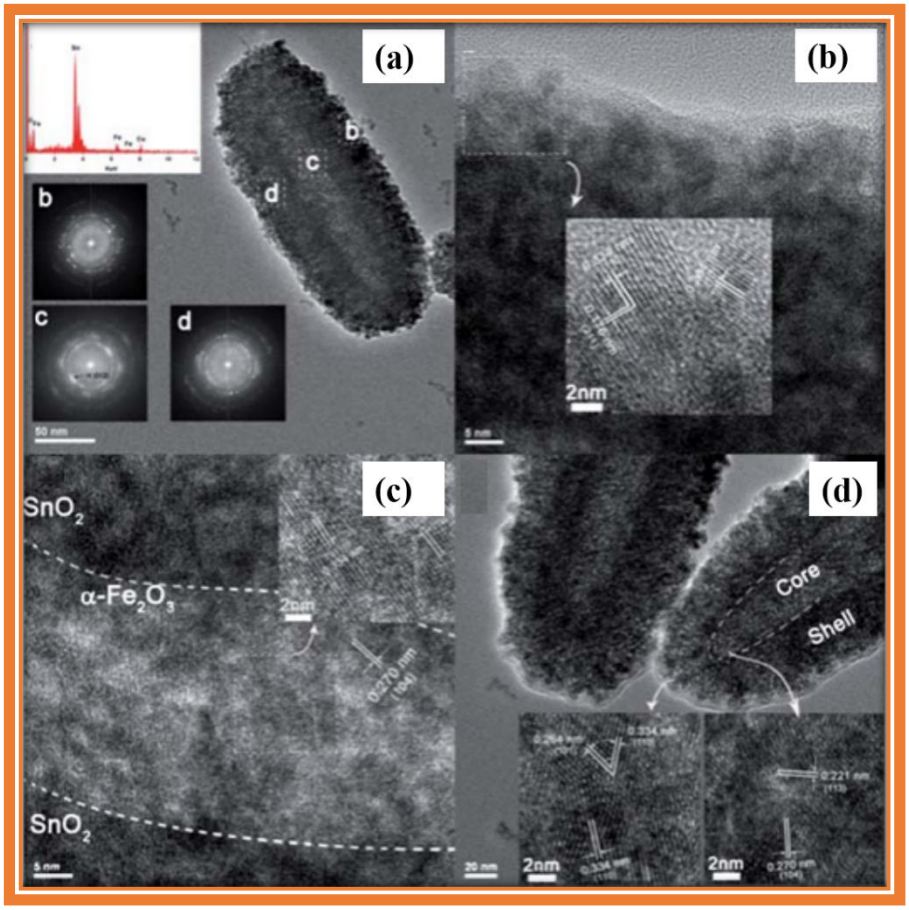

Fig. 1.14: (a) TEM image of α-Fe_2O_3@SnO_2 core-shell nanoparticles. Insets show the EDX spectrum and FFT patterns at the regions b, c, and d, respectively, and **(b-d)** HRTEM images of α-Fe_2O_3@SnO_2 core-shell nanoparticles at edge, center, and tip regions, respectively [92].

1.4.2.7 Sonochemical synthesis

This method is used for the synthesis of metal/metal oxide/metal chalcogenide/carbon core as well as the shell. The basic phenomenon involved in a sonochemical synthesis is breaking of a chemical bond by applying high power ultrasound ranging between 20 kHz and 10 MHz and the main physical phenomenon involved is acoustic cavitation. During the synthesis, three major events occur. They are creation, growth, and collapse of bubbles in a liquid. All the reactions occur in cavities or bubbles and they serve as microreactors. Initially, solute vapour diffuses into the bubbles and reach to certain size. Then, collapse of bubbles take place in less than a nanosecond. During the collapse, high temperature of 5000 to 25000 K is generated in the bubble which is sufficient enough to break the chemical bonds of solute in the gas phase. The shock waves generated during the synthesis hinder agglomeration and produce nanoparticles with either amorphous or crystalline nature. The physical nature of nanoparticles depends on the temperature present inside the bubble. The core-shell nanoparticles, synthesized using this method, are ZnO@SiO_2, Ag@TiO_2, Au@SnO_2, Fe@PtRu, etc [146–149].

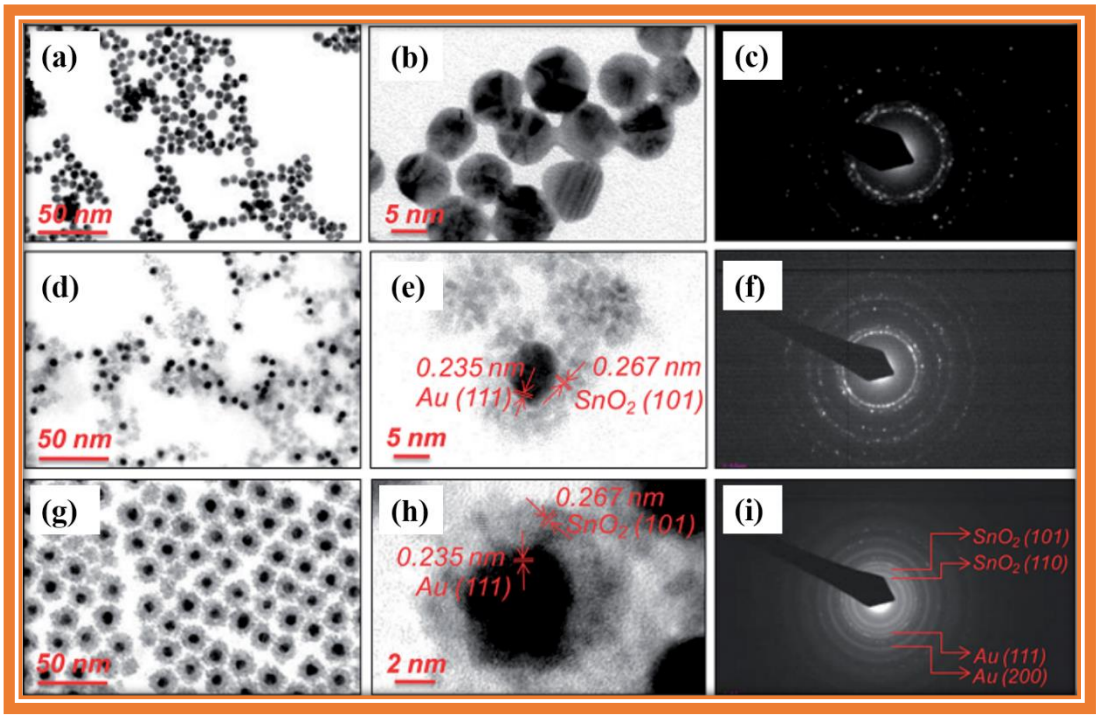

Fig. 1.15: (a, b) TEM image of Au nanoparticles, **(c)** the corresponding SAED pattern, **(d, e)** TEM images of Au@SnO_2 core-shell nanoparticles prepared at 30 min, **(f)** the corresponding SAED pattern, and **(g, h)** TEM images of Au@SnO_2 core-shell nanoparticles prepared at 90 min, and **(i)** the corresponding SAED pattern [148].

1.4.2.8 Polymerization technique

This method is used for the preparation of organic core or shell nanoparticles. The core-shell nanoparticles are prepared in two ways. The first one is called "grafting-from" and other one is "grafting-to". In both the types, living radical polymerization such as atom transfer radical polymerization (ATRP) and reversible addition fragmentation chain transfer (RAFT) occur. In the "grafting-from" method, initially, the core nanoparticle surface is functionalized using initiation sites and then the polymerization of monomers is carried out *in situ* on initiator functionalized core surface. In "grafting-to" method, the polymer monomer chains are grafted on surface of the core *via* a reaction between the functional groups of core nanoparticle surface and end-groups of the polymer. In the polymerization process, initially the monomers form oligomers. These oligomers crosslink together and form aggregates which grow bigger. During the crosslinking of oligomers, two mechanisms occur; enthalpy precipitation and entropy precipitation. In enthalpy precipitation, monomer grows upto its solubility limit in the organic solution and then it precipitates out from the solution. Monomers grow further by capturing other polymer nuclei and makes a bigger polymer. In entropy polymerization, the crosslinking groups of the polymers (e.g. vinyl) react with soluble oligomers leading to crosslinking of polymers with further growth. The core-shell nanoparticles, prepared using the polymerization method, are Ag-Au@PEG-HA, ZrO_2@PMMA, $BaTiO_3$@PMMA, PS-*co*-PMMA@PMMA, etc [64,66,67,76].

1.4.2.9 Template route

This is the most commonly used method to prepare nanorattles or yolk-shell nanoparticles containing hollow cores or hollow multi-shells. Template route is divided into hard template and soft template routes. Hard template method is frequently used to prepare nanorattles and in this method, the core material (metal, metal oxide, or polymer) is coated with one or more layers of the shell material. The shell coating is controlled by several factors such as hydrolysis and condensation, for example, in the case of silica and seeded distillation-precipitation, e.g. in the case of polymerization. If the core is an inorganic material, it is etched using either acids (hydrofluoric acid, hydrochloric acid, sulfuric acid, nitric acid) or bases (sodium hydroxide, ammonium hydroxide). If the core is an organic material, it is removed by simple calcination at high temperatures under air or inert gas atmosphere. In soft template route, micelles, microemulsion or vesicles formed by surfactants are used as the soft templates. In this method, either the core nanoparticles are encapsulated into the shell or shell is coated on the core

particles. Most of the multi shelled nanorattles are prepared using this approach. Examples for the core-shell nanoparticles, synthesized using this method, are MFe_2O_4 (M = Zn, Co, Ni, and Cd), α-Fe_2O_3@SnO_2, Au@SiO_2, Ca-Pd@SiO_2, γ-Fe_2O_3@SnO_2@C, Au-M (M = Au, Pt, and Pd), etc [91–96]. The schematic illustration of synthesis of core-shell nanoparticles using hard template route is shown in Figure 1.16 and that for the core-shell nanoparticles synthesized using soft template route is shown in Figure 1.17.

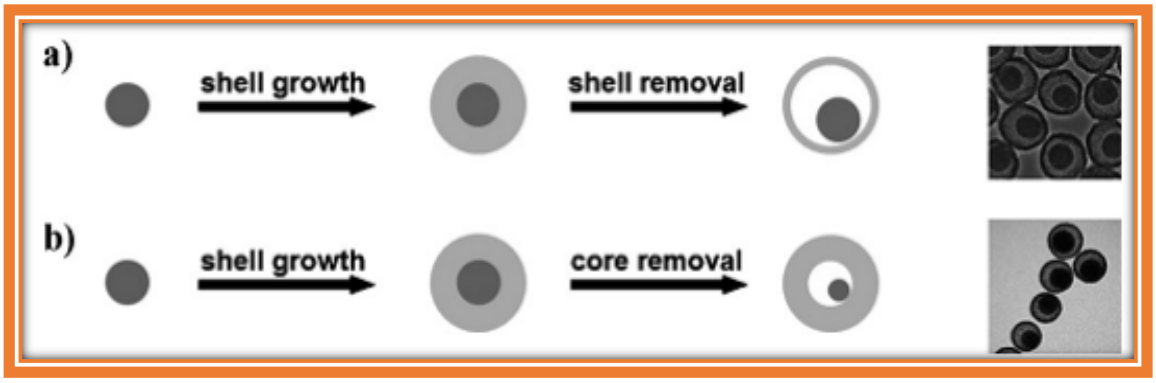

Fig. 1.16: Schematic illustration of the synthesis of core-shell nanoparticles *via* hard template route. The void is obtained by **(a)** removal of the interlayer [150], and **(b)** partial removal of the core [151].

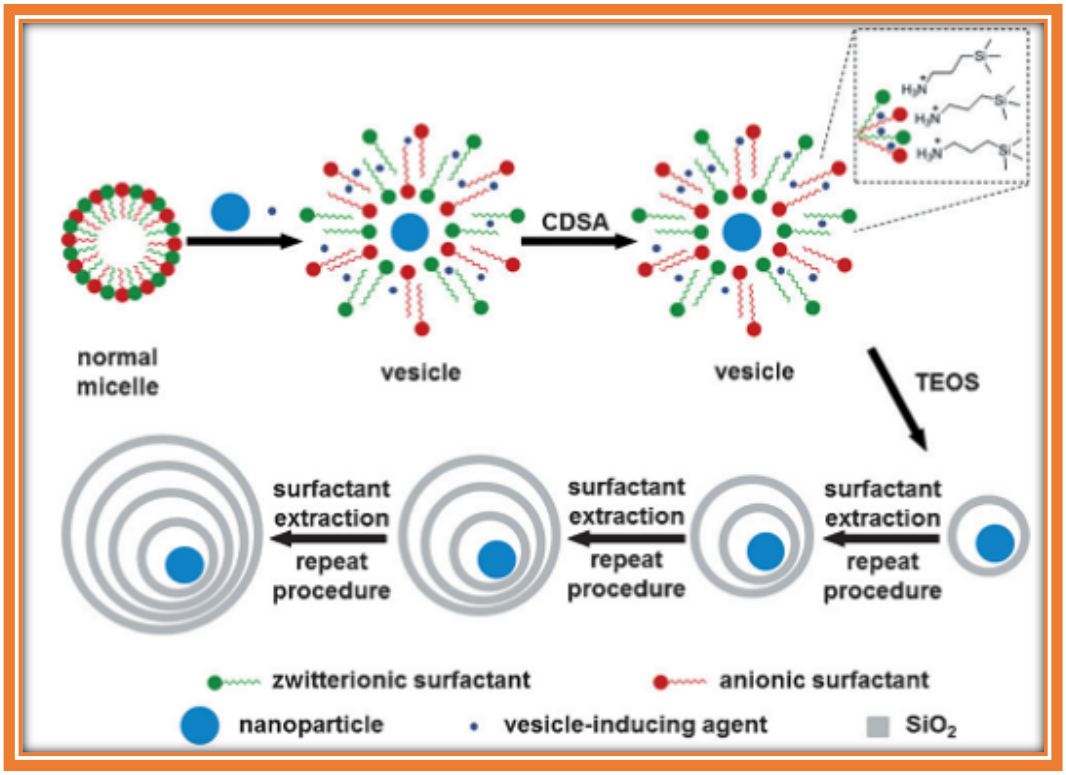

Fig. 1.17: Schematic illustration of the synthesis of core-multi shell nanoparticles using surfactants as the soft templates [152].

1.5 Properties of core-shell nanoparticles

In the following sections, the most interesting properties of core-shell nanoparticles have been discussed.

1.5.1 Optical properties of core-shell nanoparticles

Semiconductor nanoparticles exhibit size and shape dependent optical properties which are different from that of bulk materials [153,154]. The band gap (E_g) of semiconductor nanoparticles is strongly dependent on particle size as well as Bohr radius. On illumination with light whose energy is higher than the band gap of the semiconductor, electrons in the valence band are excited to the conduction band and electron-hole pairs called excitons are formed. The distance between the electron-hole pair is called as exciton Bohr radius. When the size of semiconductor nanoparticles is smaller than Bohr radius of the semiconductor, quantum confinement occurs which results in an increase in the band gap of the semiconductor nanoparticles [153]. Brus equation is used to calculate the particle size of semiconductor nanoparticles which is expressed as follows [155].

$$\Delta E = E_g^{nano} - E_g^{bulk} = \frac{\hbar^2 \pi^2}{2R^2}\left(\frac{1}{m_e^*} + \frac{1}{m_h^*}\right) - \frac{1.86\, e^2}{\epsilon R}$$

where, ΔE_g = Shift in the band gap of semiconductor nanoparticles from that of bulk semiconductor

R = Radius of the semiconductor nanoparticles

m_e^* = Effective mass of electron

m_h^* = Effective mass of hole

m_o = Mass of electron (9.11×10^{-28} g)

ε = Relative permittivity of the semiconductor

e = Charge of an electron (1.60×10^{-19} C)

h = Planck's constant ($4.1l \times 10^{-15}$ eV or 6.62×10^{-34} JS).

Semiconductor nanoparticles exhibit either direct or indirect band gap which is dependent on conduction and valence band edge alignment. In general, the band gap of semiconductor nanoparticles is calculated using Tauc equation which is expressed as follows [156].

$$(\alpha h\nu)^{1/n} = A\left(h\nu - E_g\right)$$

where, h = The Planck's constant

ν = Frequency of light

α = Absorption coefficient

E_g = Band gap of the semiconductor nanoparticles

A = Proportional constant

n = Type of transition in the semiconductor

n = ½ for direct allowed transition and n = 2 for indirect allowed transition.

Based on band edge alignment of valence band and conduction band as well as the band gap of core and shell nanoparticles, the optical properties of core-shell nanoparticles are classified into three categories. They are type-I, reverse type-I, and type-II. A schematic representation of band edge alignment in type-I and type-II core-shell nanoparticles is shown in Figure 1.18.

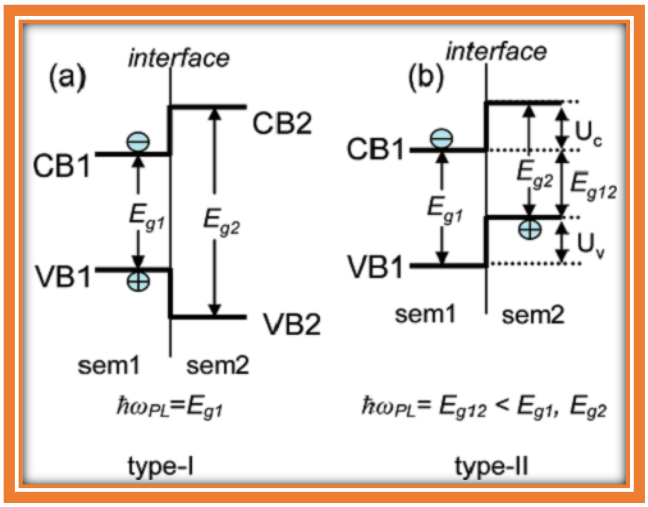

Fig. 1.18: Schematic representation of band edge alignment at the interface of semiconductor core-shell nanoparticles; **(a)** type-I and **(b)** type-II. Sem1 = semiconductor 1 and sem2 = semiconductor 2 [42].

1.5.1.1 Type-I core-shell nanoparticles

In the case of type-I core-shell nanoparticles, the shell nanomaterial has wider band gap than the core nanomaterial. The excitons are confined within the core due to band edge alignment. Both valence band and conduction band of the core nanomaterial are placed within the band gap energy of the shell nanomaterial. The valence band of the shell nanomaterial is located below than that of the core and this type of alignment confines excitons within the core [42,153]. The coating of a wider band gap shell material over a core material with narrow band gap passivates the core surface leading to enhancement in photostability as well as fluorescence quantum yield. On coating a thicker shell on the core surface, strain occurs at the interface due to lattice mismatch between the core and shell nanoparticles which leads to reduction in fluorescence quantum yield [42]. Examples for type-I core-shell nanoparticles are CdSe@ZnS, CdSe@CdS, CdTe@CdS, InP@ZnS, InAs@InP/ZnS/CdSe/ZnSe/GaAs, and PbSe@PbS [157–159]. Zhang et al. have studied optical properties of CdSe@$Zn_xCd_{1-x}S$ type-I core-shell nanoparticles [153]. They observed that as the reaction time increases from 0 to 180 min, the UV-Visible absorption and PL emissions are red shifted (Figure 1.19a). The CdSe@$Zn_xCd_{1-x}S$ type-I core-shell nanoparticles show about 80 % quantum yield within 30 min and this is stabilized up to 2 h (Figure 1.19b) indicating almost no change in particle size of the core-shell nanoparticles. Nan et al. have studied the optical properties of CdSe@CdS type-I core-shell nanoparticles [154]. PL studies showed shift of emission wavelength from about 500 to 650 nm on increasing the CdS shell monolayer coating on the CdSe core (Figure 1.19c). The CdSe@CdS core-shell nanoparticles with two CdS monolayer coatings on the CdSe core exhibit higher quantum yield than the core-shell nanoparticles with more number of CdS monolayer coatings on the CdSe core (Figure 1.19d). More number of CdS monolayer shell coating on the CdSe core induces more defects at the interface of CdSe core and CdS shell with reduction in quantum yield.

1.5.1.2 Reverse type-I core-shell nanoparticles

In reverse type-I core-shell nanoparticles, a narrow band gap shell nanomaterial is coated on a wider band gap core nanomaterial. In this type, both the electrons and holes are confined in the shell and the optical properties of core-shell nanoparticles are tuned by controlling thickness of the shell [42,157]. The most extensively studied core-shell systems that belong to this type are CdS@HgS, ZnS@CdSe, ZnSe@CdSe, In_2O_3@In_2S_3 and CdS@CdSe [157,160,161]. These core-shell nanoparticles exhibit lower quantum yield as compared to type-I core-shell nanopart-

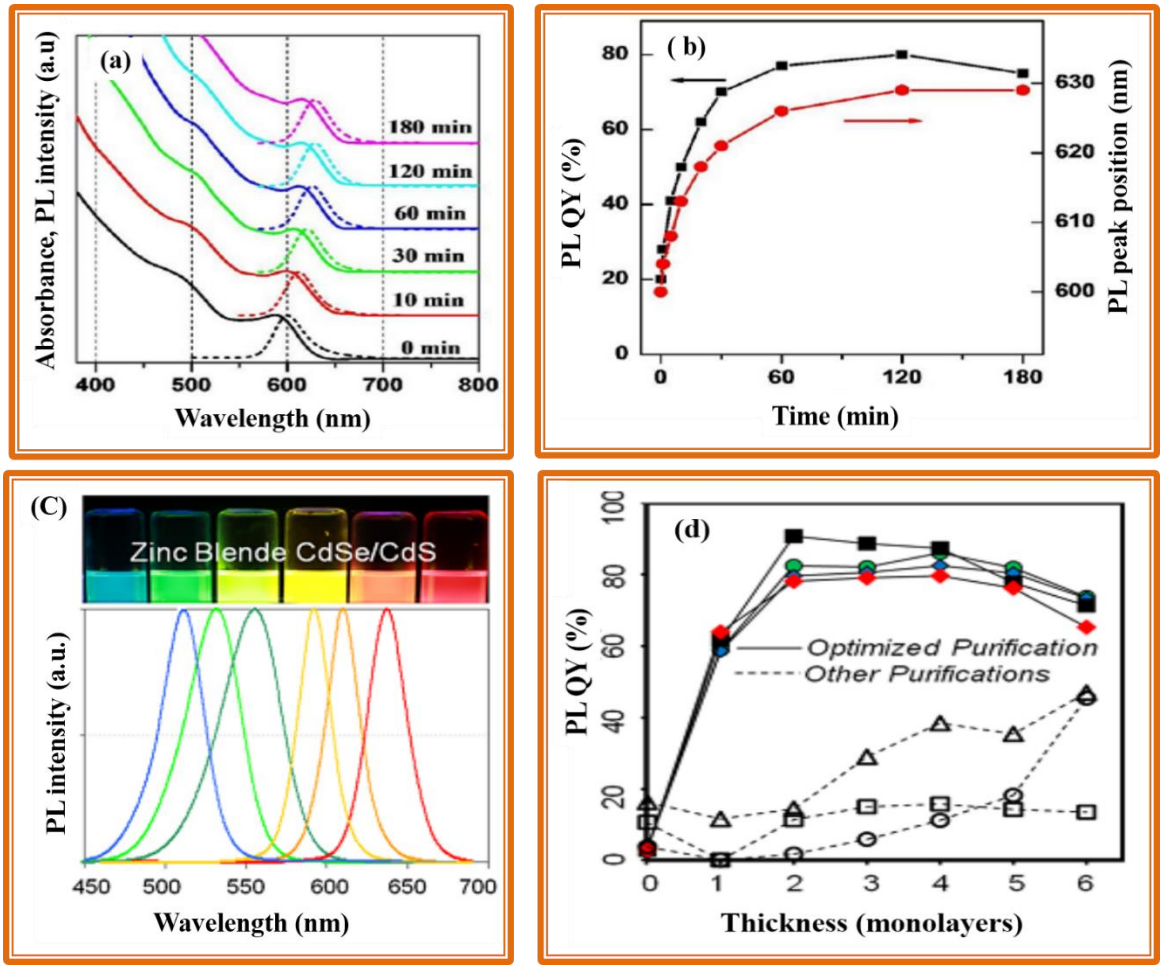

Fig. 1.19: (a) UV-Visible absorption and PL emission spectra of type-I CdSe@$Zn_xCd_{1-x}S$ core-shell nanoparticles, **(b)** PL quantum yield and peak positions at different growth times of CdSe@$Zn_xCd_{1-x}S$ [153], **(c)** luminescence of CdSe@CdS core-shell nanoparticles under UV light illumination (top) and PL emission spectra with different monolayer thicknesses of CdS shell, and **(d)** PL quantum yields of CdSe@CdS core-shell nanoparticles with different thicknesses of CdS shell on CdSe core [154].

icles but they exhibit higher resistance against photobleaching. Coating of a shell with wider band gap improves quantum yield of the core-shell nanomaterials [42]. Zhong et al. have reported that the PL emission of ZnSe@CdSe core-shell nanoparticles is red shifted from 375 to 674 nm on increasing the CdSe monolayer shell coating on the ZnSe core (2.8 nm) [160].The UV-Visible absorbance is red shifted from about 370 to 700 nm on increasing the coating of the CdSe shell on the ZnSe core. These results prove the role of CdSe shell thickness on the emission properties of ZnSe@CdSe core-shell nanoparticles [160]. The PL and UV-Visible spectra of ZnSe@CdSe core-shell nanoparticles are shown in Figure 1.20.

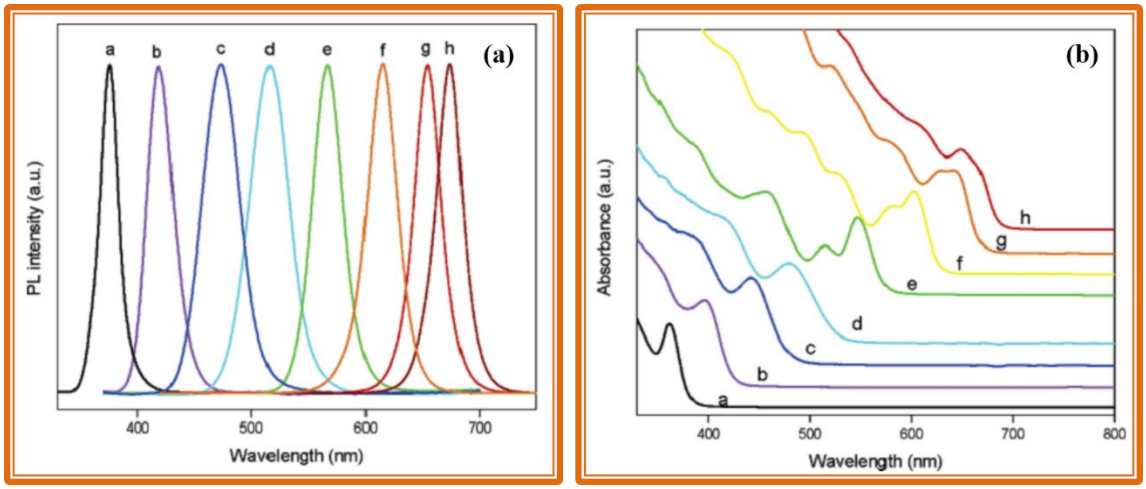

Fig. 1.20: (a) PL emission spectra, and **(b)** UV-Visible absorption spectra of ZnSe@CdSe core-shell nanoparticles (Reverse type-I) with 0.1, 0.2, 0.5, 1.0, 2.0, 4.0, and 6.0 monolayers of CdSe shell [160].

1.5.1.3 Type-II core-shell nanoparticles

In type-II core-shell nanoparticles, the band edge of valence band and conduction band of the core are located either lower or higher than that of the shell. This type of band alignment results in confinement of one of the charge carriers in the core and the other one is confined in the shell. The optical properties of this type of core-shell nanoparticles are tuned by controlling the size of either the core or the shell or both [42,157,162]. Figure 1.21 (a, b) illustrates the UV-Visible and PL spectra of CdS@ZnSe type-II core shell nanoparticles [163]. The diameters of the CdS cores are 3 nm and 6 nm with two monolayer ZnSe shell coating and the samples were annealed at 300 ^{o}C for different timings. UV-Visible spectral results show disappearance of absorbance hump besides the PL emission band. The broadening of the absorbance tail towards longer wavelength indicates type-II band alignment in these core-shell nanoparticles [163]. The PL spectra of CdS (3 nm)@ZnSe and CdS (6 nm)@ZnSe core-shell nanoparticles show red shift from 475 nm to 520 nm and 575 nm to 590 nm as the reaction time increases from 0 to 180 min. On changing the diameter of CdS core from 3 to 6 nm, the PL emission is shifted from 475 to 575 nm in the CdS@ZnSe core-shell nanoparticles. These results indicate that tuning of PL emission is possible by changing either the core diameter or the shell thickness [163]. The PL decay kinetics profile of CdS (5 nm)@ZnSe with five ZnSe monolayer coating and CdS (6 nm)@ZnSe with two ZnSe monolayer coating annealed at 300 ^{o}C for 0-180 min are shown in Figure 1.21 (c, d). The mean decay life time values of CdS (5 nm)@ZnSe with five ZnSe monolayer coating are about four times greater than that of the corresponding CdS

cores. In the case of CdS (6 nm)@ZnSe with two ZnSe monolayer coating annealed at 300 ºC for 0-180 min, about ten times increase in mean decay life time than that of CdS core is observed. These results suggest that slow recombination of electron-hole pairs of excitons as a consequence of effective separation of electrons and holes in the CdS cores and ZnSe shells [163].

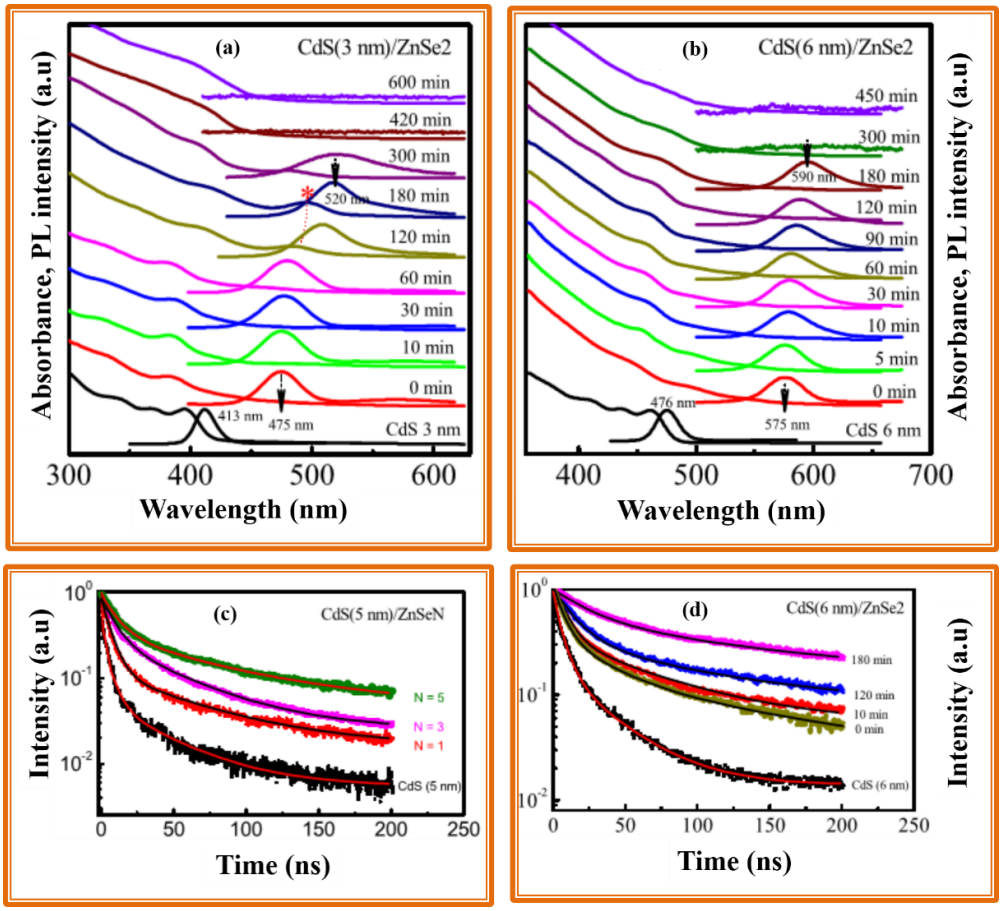

Fig. 1.21: (a, b) UV-Visible and PL emission spectra of CdS@ZnSe core-shell nanoparticles with CdS core diameters of 3 and 6 nm at different annealing timings (temperature = 300 ºC), and **(c, d)** PL decay kinetics of CdS(5 nm)@ZnSe core-shell nanoparticles with different monolayers of ZnSe shell and CdS(6 nm)@ZnSe core-shell nanoparticles with two monolayers of ZnSe shell annealed at 300 ºC for different timings [163].

1.5.2 Magnetic properties of core-shell nanoparticles

The magnetic properties of core-shell nanoparticles are dependent on shape, size, composition, interparticle and intraparticle interactions which are controlled by controlling either the core size or the shell thickness. Core-shell magnetic nanoparticles show phase transition at about blocking temperature (T_B) and mathematically it is expressed as follows [164].

$$T_B = \frac{kV}{25k_B}$$

where, k = Magnetic anisotropic constant

V = Average volume of the magnetic core-shell nanoparticles and

k_B= Boltzmann constant

The core-shell nanoparticles with different core size show dramatic effect on their magnetic properties. Figure 1.22 (a, b) shows the core ($Mn_xFe_{3-x}O_4$) size dependent zero field cooling (ZFC) and field cooling (FC) curves and the M-H hysteresis loops at 10 K for $Mn_xFe_{3-x}O_4$@ $Fe_xMn_{3-x}O_4$ core-shell nanoparticles [165]. The blocking temperature (T_B) and saturation magnetization (M_S) are directly proportional to volume or size of the core. The $Mn_xFe_{3-x}O_4$ soft ferrimagnetic core with 7.5 nm diameter (CS2) shows lower blocking temperature (115 K) and lower M_S (40 emu/g) while $Mn_xFe_{3-x}O_4$ soft ferrimagnetic core with 11.5 nm diameter (CS1) shows higher blocking temperature (205 K) and higher M_S (48 emu/g). These samples show another blocking transition at about 40 K and this is due to hard antiferromagnetic $Fe_xMn_{3-x}O_4$ shell. In the case of antiferromagnetic and ferrimagnetic systems, coercivity (H_C) and exchange bias (H_E) are inversely proportional to size of the soft ferrimagnetic material [165]. In the case of $Mn_xFe_{3-x}O_4$@$Fe_xMn_{3-x}O_4$ core-shell nanoparticles, the sample with smaller core size (CS2) shows higher H_C and H_E than the sample with bigger core size (CS1). These results suggest that the magnetic properties (T_B, M_S, H_C, and H_E) of $Mn_xFe_{3-x}O_4$@$Fe_xMn_{3-x}O_4$ core-shell nanoparticles are strongly dependent on soft ferrimagnetic core size [165].

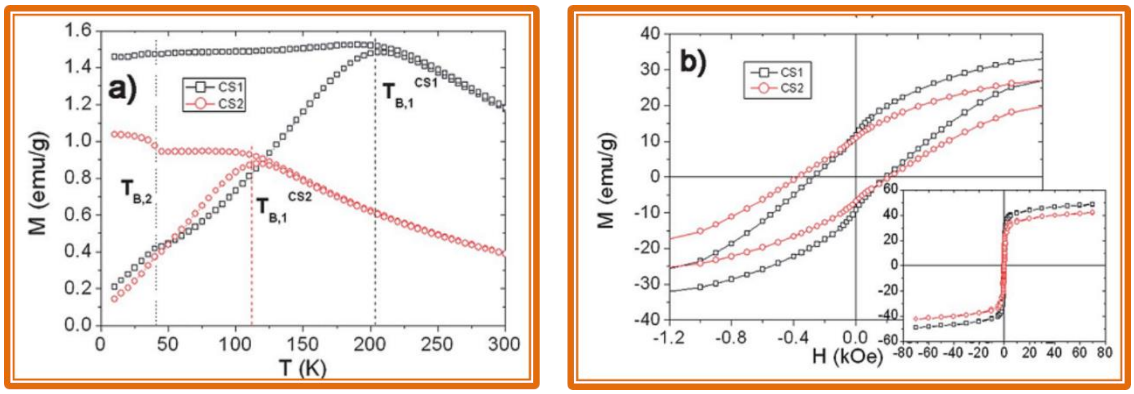

Fig. 1.22: (a) Temperature dependent ZFC-FC curves, and **(b)** M-H hysteresis curves at 10 K for $Mn_xFe_{3-x}O_4$@$Fe_xMn_{3-x}O_4$ core-shell nanoparticle samples CS1 and CS2 with 11.5 nm and 7.5 nm $Mn_xFe_{3-x}O_4$ core diameter. The inset shows the full M-H hysteresis loops [165].

Ding et al. have explained the core and shell thickness dependent magnetic properties of Fe_3O_4@SiO_2 core-shell nanoparticles [143]. Figure 1.23 (a, b) shows the TEM images of Fe_3O_4@SiO_2 core-shell nanoparticles with different thickness (14.1 and 19.8 nm) of SiO_2 shell. Figure 1.23 (c, d) shows the field dependent magnetization at 300 K and ZFC-FC curves of Fe_3O_4@SiO_2 core-shell nanoparticles with different thickness of silica shell and capping of Fe_3O_4 core with oleic acid. The oleate capped Fe_3O_4 core nanoparticles show saturation magnetization of about 27.7 emu/g whereas Fe_3O_4 core nanoparticles coated with SiO_2 shell thickness of 2.0, 12.1, and 18.5 nm show saturation magnetization of 30.0, 5.2 and 1.9 emu/g, respectively. The blocking temperature (T_B) of oleate capped Fe_3O_4 core nanoparticles is 155 K and SiO_2 coated Fe_3O_4 core-shell nanoparticles show 146, 135 and 133 K as the blocking temperatures for 2.0, 12.1, and 18.5 nm thickness of silica shell. The decrease in saturation magnetization and blocking temperature of silica coated Fe_3O_4 core-shell nanoparticles by increasing the shell thickness as compared to oleate capped Fe_3O_4 core nanoparticles is attributed to decrease in the dipolar interaction of Fe_3O_4 core nanoparticles, which is due to increased interparticle distance with increased silica shell thickness [143].

Figure 1.24a shows the field dependent magnetization of $La_{1-x}Sr_xMnO_3$ core nanoparticles and $La_{1-x}Sr_xMnO_3$@Au core-shell nanoparticles at 300 K. Figure 1.24b shows the field dependent magnetization of $La_{1-x}Sr_xMnO_3$@Au core-shell nanoparticles at 395, 300 and 5 K [166]. At 300 K, the $La_{1-x}Sr_xMnO_3$@Au core-shell nanoparticles show superparamagnetic behavior with a coercivity of 9.0 Oe and saturation magnetization of 18.26 emu/g whereas $La_{1-x}Sr_xMnO_3$ core nanoparticles show soft ferromagnetic or near superparamagnetic behavior with a coercivity of 15.2 Oe and saturation magnetization of 36.31 emu/g. The $La_{1-x}Sr_xMnO_3$@Au core-shell nanoparticles show lower coercivity as well as lower saturation magnetization as compared to $La_{1-x}Sr_xMnO_3$ core nanoparticles, which is attributed to unique spatial configurations and proximity effects [166]. The coercivity and saturation magnetization of $La_{1-x}Sr_xMnO_3$@Au core-shell nanoparticles increases with decreasing temperature, which is attributed to overcoming of the magnetic anisotropic energy over the thermal energy. Figure 1.24 (c, d) shows the ZFC and FC curves of $La_{1-x}Sr_xMnO_3$@Au core- shell nanoparticles and $La_{1-x}Sr_xMnO_3$ core nanoparticles under a magnetic field of 500 Oe. Both $La_{1-x}Sr_xMnO_3$@Au core-shell nanoparticles and $La_{1-x}Sr_xMnO_3$ core nanoparticles show superparamagnetic behavior at temperatures above 355 K and they show sharp ferromagnetic phase transition in a narrow temperature range 355-320 K. As compared to $La_{1-x}Sr_xMnO_3$ core nanoparticles, the $La_{1-x}Sr_xMnO_3$@Au core-shell nanoparticles show lower saturation magnetization, lower Curie

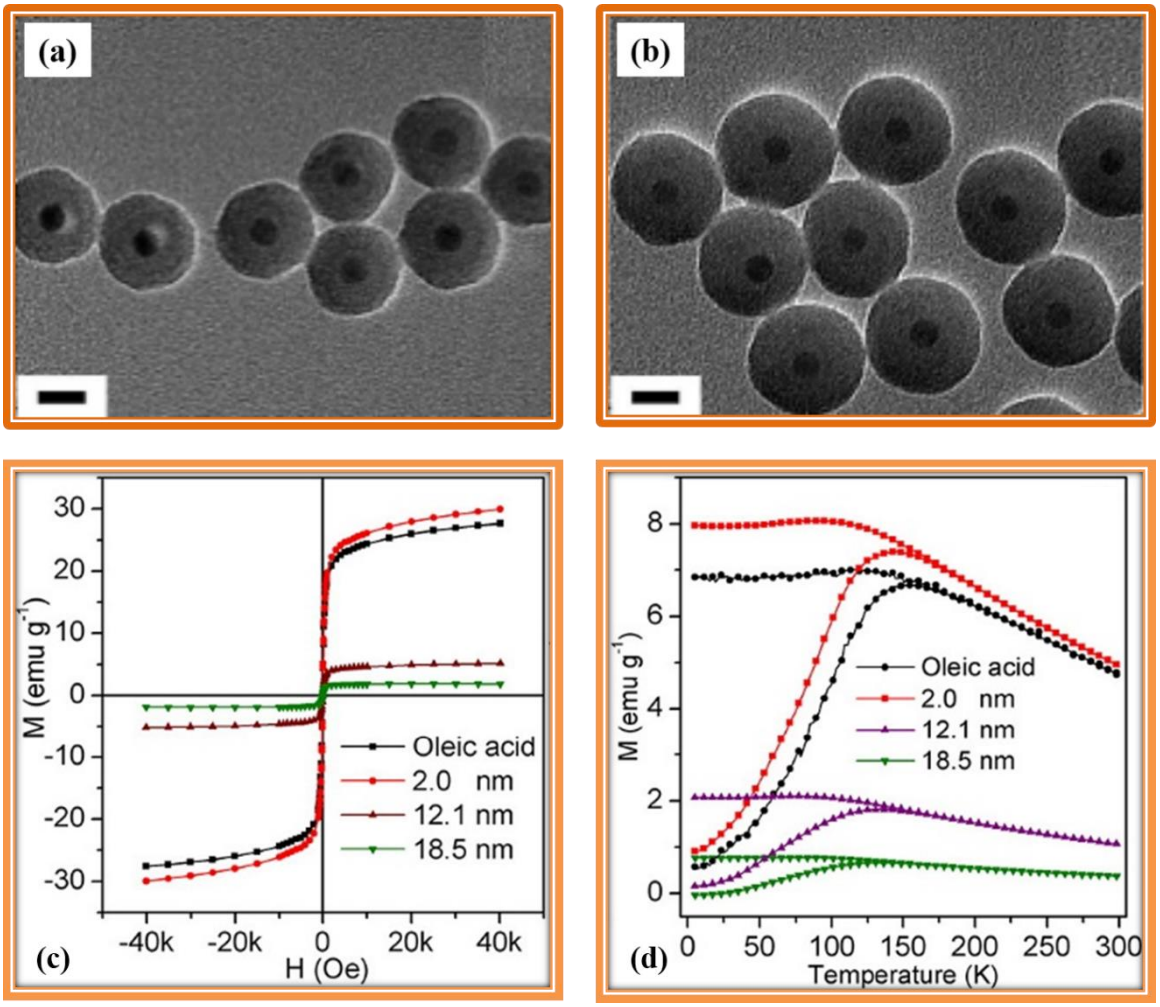

Fig. 1.23: (a, b) TEM images of Fe_3O_4@SiO_2 core-shell nanoparticles with 14.1 nm and 19.8 nm thicknesses of SiO_2 shell, and **(c, d)** the field dependent M-H hysteresis plots at 300 K and ZFC-FC curves of Fe_3O_4@SiO_2 core-shell nanoparticles with different thickness of silica shell along with oleate capped Fe_3O_4 core nanoparticles [143].

temperature (T_C) and lower blocking temperature, which is attributed to reduced volume fraction of $La_{1-x}Sr_xMnO_3$ core as well as particle size effect [166].

Patange et al. have studied the magnetic properties of graphitic carbon coated Ni@NiO core-shell nanoparticles and the corresponding TEM image and SAED pattern are shown in Figure 1.25 (a, b) [164]. The ZFC-FC and M-H hysteresis curves of graphitic carbon coated Ni@NiO core-shell nanoparticles are shown in Figure 1.25 (c-e). The ZFC-FC curves show irreversibility behavior, which is attributed to either clustered glassy system or magnetically frustrated spin disordered system. These sample show flat FC curves indicating strong inter particle dipolar interactions. These samples show blocking temperature above room temperatu-

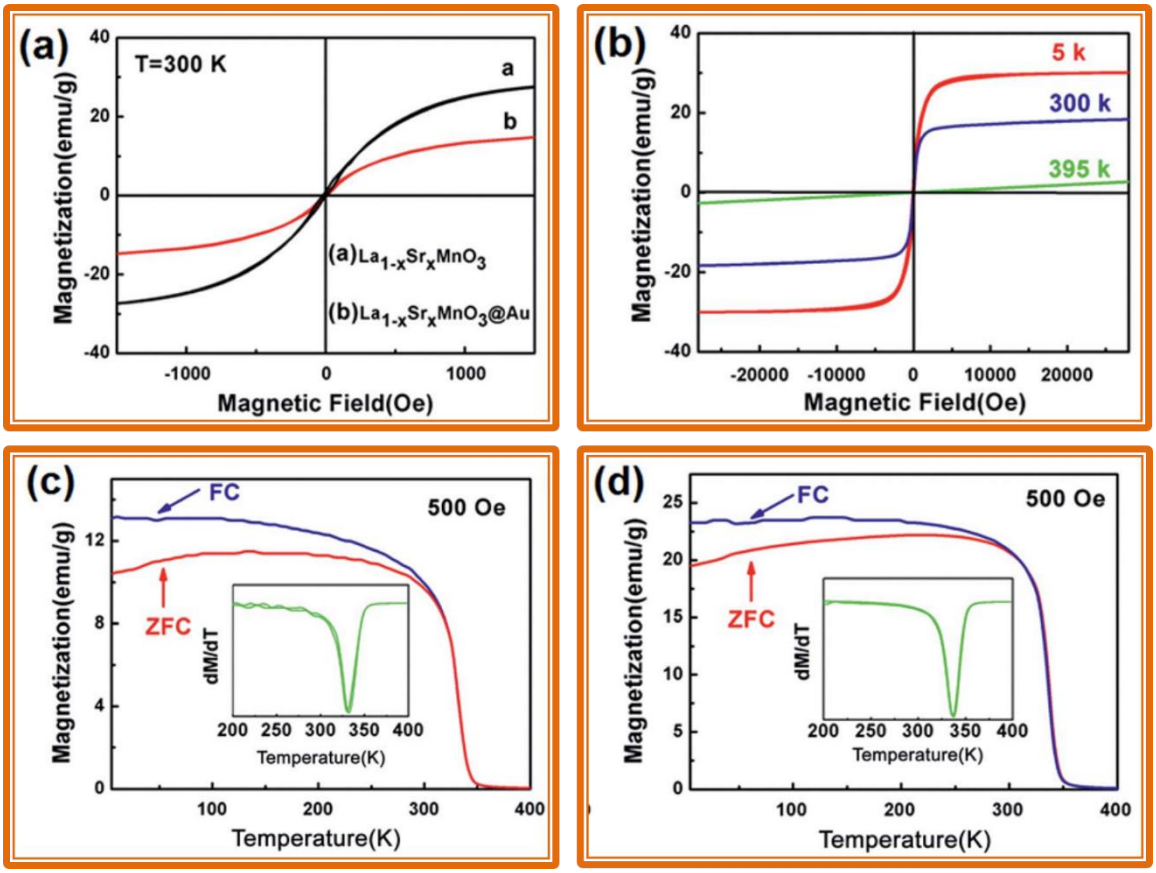

Fig. 1.24: (a) Field dependent M-H hysteresis plots for $La_{1-x}Sr_xMnO_3$ and $La_{1-x}Sr_xMnO_3$@Au core-shell nanoparticles at 300 K, **(b)** M-H hysteresis plots of $La_{1-x}Sr_xMnO_3$@Au core-shell nanoparticles at 395, 300, and 5 K, and **(c, d)** temperature dependent ZFC-FC curves of $La_{1-x}Sr_xMnO_3$@Au core-shell nanoparticles and $La_{1-x}Sr_xMnO_3$ core nanoparticles [166].

re, which is due to the smaller crystallite size of Ni core (21 nm and 31 nm) compared to critical size of pure Ni nanoparticles. This indicates the existence of superparamagnetic behavior at room temperature [164]. The increase in saturation magnetization and remanence (M_R) of graphitic carbon coated Ni@NiO core-shell nanoparticles on increasing the calcination temperature from 400 ^oC to 600 ^oC are attributed to increase in Ni content as well as crystallinity of the particles [164]. The saturation magnetization of graphitic carbon coated Ni@NiO core-shell nanoparticles is lower as compared to that of bulk ferromagnetic Ni (M_S = 55 emu/g). This is attributed to disordered magnetic orientation of large percentage of surface spins and proximity effects between ferromagnetic Ni and carbon [164].

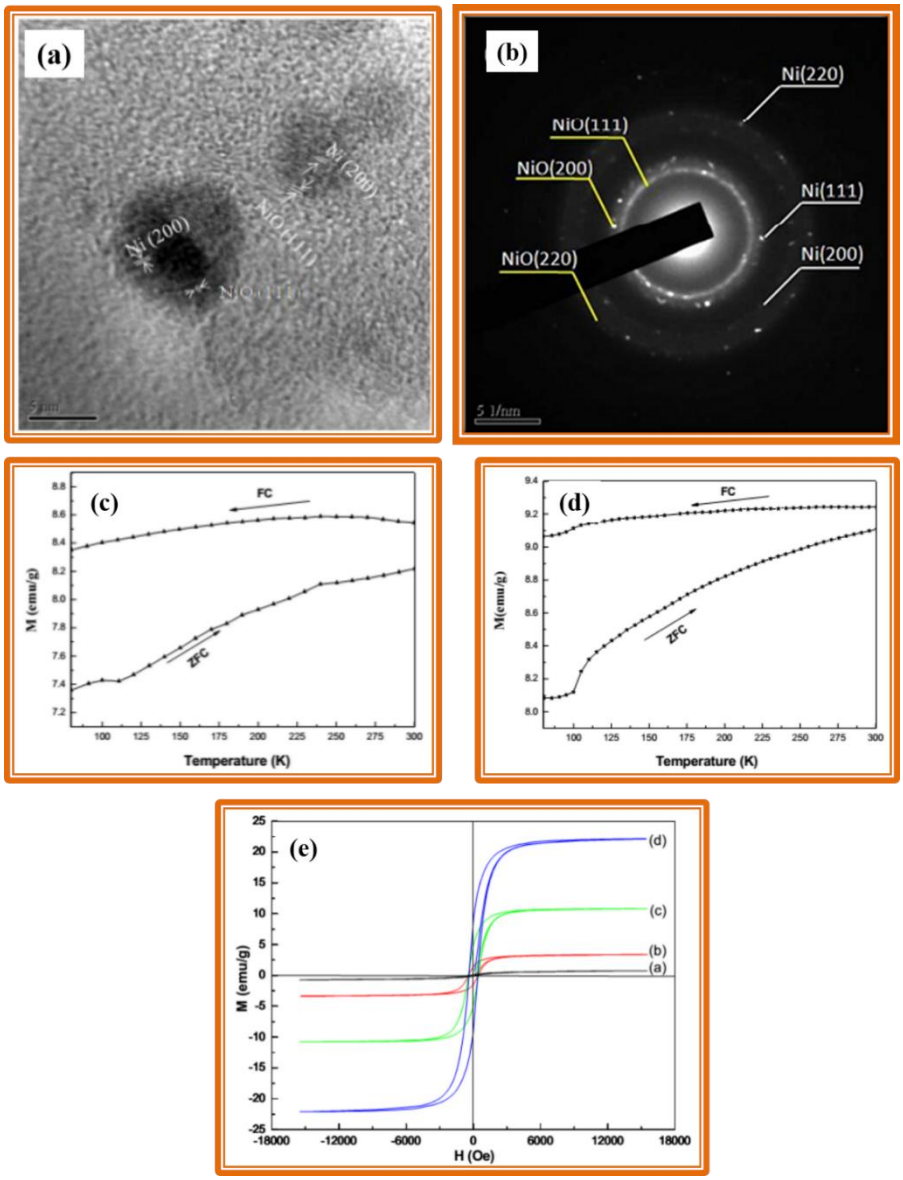

Fig. 1.25: (a, b) TEM and SAED pattern of graphitic carbon coated Ni@NiO core-shell nanoparticles, **(c, d)** ZFC-FC curves of graphitic carbon coated Ni@NiO core-shell nanoparticles annealed at 500 and 600 ^{o}C, and **(e)** field dependent M-H hysteresis plots of graphitic carbon coated Ni@NiO core-shell nanoparticles annealed at 400, 450, 500 and 600 ^{o}C [164].

1.5.3 Electrochemical properties of core-shell nanoparticles

Core-shell and core-multi shell nanoparticles show enhanced electrochemical properties as compared to their counter parts. For example, ZnO@Au@NiO core-shell nanoparticles show enhanced electrochemical properties compared to ZnO@NiO core-shell nanoparticles. Figure 1.26a shows the TEM image of ZnO@Au@NiO core-shell nanoparticles and the

corresponding HRTEM images are shown in Figure 1.26 (b, c). A schematic illustration of energy level diagram at the interface of ZnO/Au/NiO during charge and discharge processes is shown in Figure 1.26 (d, e). The cyclic voltammetry (CV) curves of ZnO@NiO and ZnO@Au@NiO core-shell nanoparticles in the voltage range of 0-0.5 V are shown in Figure 1.26f. The CV curves of ZnO@Au@NiO core-shell nanoparticles shift much as compared to the ZnO@NiO core-shell nanoparticles, which is ascribed to decreased energy barrier due to the formation of localized Schottky barrier at the interface [167]. The discharge curves and specific capacitance of ZnO@Au@NiO and ZnO@NiO core-shell nanoparticles at different current densities are shown in Figure 1.26 (g, h). During the charging, electrons are temporarily trapped and accumulated at the Fermi level until the gap between NiO and ZnO is filled. During the discharge process, additional electrons at the Fermi level are released, which leads to enhanced capacitance in the case of ZnO@Au@NiO core-shell nanoparticles as compared to that of ZnO@NiO core-shell nanoparticles [167].

Zhu et al. have reported the dielectric and energy storage properties of $BaTiO_3$@polymer (PHEMA, PMMA, and PGMA) shell/PVDF core-shell nanoparticles [168]. The dielectric constants of $BaTiO_3$@polymer (PHEMA, PMMA, and PGMA) shell/PVDF core-shell nanoparticles are higher than that of pure PVDF. $BaTiO_3$@PHEMA/PVDF core-shell nanoparticles show higher dielectric constant, which is attributed to suppression of macromolecular movement at the interfacial region due to strong polymer interaction and also restricted dipole movement of grafted polymer chains [168]. $BaTiO_3$@PGMA/PVDF core-shell nanoparticles show high discharge energy density with higher energy storage efficiency, owing to low leakage currents and low remanant polarization compared to pure PVDF [168].

Huang et al. have studied ultraviolet photodetection properties of ZnS@SnO_2 core-shell nanoribbons and the TEM and SAED patterns for these core-shell nanoparticles are shown in Figure 1.27 (a, b). A schematic diagram of an electrochemcial measurement specimen is shown in Figure 1.27c and I-V curves of pure ZnS nanoribbons and ZnS@SnO_2 core-shell nanoribbons with Au or ITO contact are shown in Figure 1.27d. The ZnS@SnO_2 core-shell nanoribbon with ITO contact shows very high conduction current of 3.5 μA at 5 V as compared to pure ZnS nanoribbon (10^{-7} μA). This is attributed to better contact of ZnS@SnO_2 core-shell nanoribbons with ITO substrate [169]. Annealing process induces diffusion of indium ions at the interface which leads to decrease in the contact barrier and enhances the electron transport by means of thermionic-field emission [169]. The source drain voltage (V_{ds}) and source drain

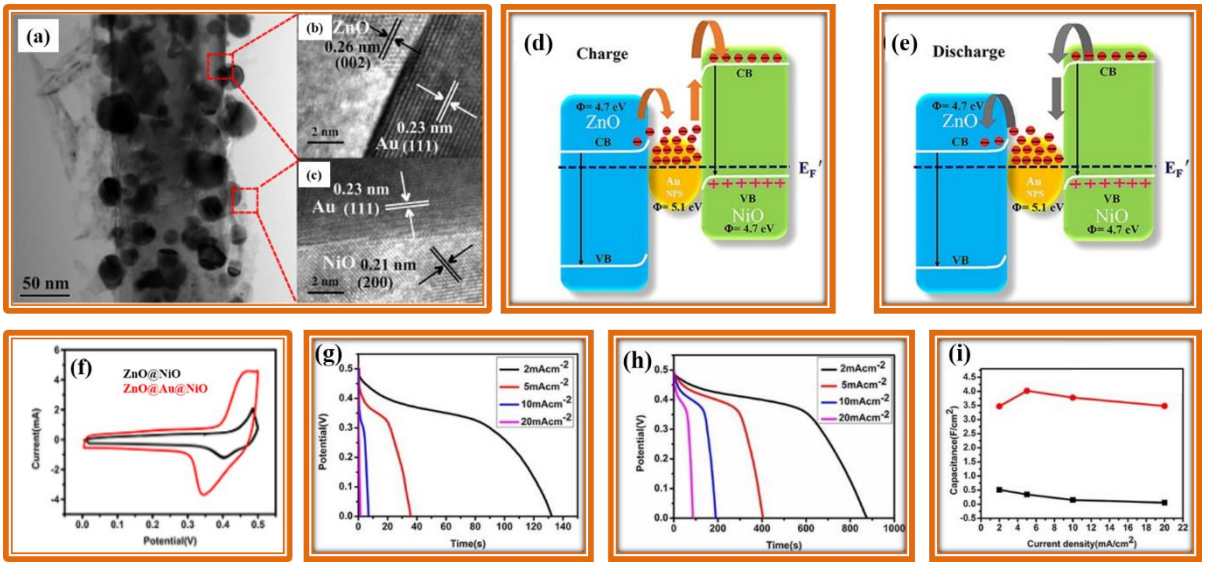

Fig. 1.26: (a) TEM and **(b, c)** HRTEM image of ZnO@Au@NiO core-shell nanoparticles, **(d, e)** charge and discharge process in ZnO@Au@NiO core-shell nanoparticles, **(f)** CV curves of ZnO@NiO and ZnO@Au@NiO core-shell nanoparticles, **(g, h)** discharge curves for ZnO@NiO and ZnO@Au@NiO core-shell nanoparticles at various current densities, and **(i)** specific capacitance curves of ZnO@NiO and ZnO@Au@NiO core-shell nanoparticles [167].

current (I_{ds}) of ZnS@SnO_2 core-shell nanoribbons with ITO substrate at different gate voltages (V_g) are shown in Figure 1.27e. These results suggest that ZnS@SnO_2 core-shell nanoribbons show n-type characteristics. The source drain current (I_{ds}) reaches its maximum value of about 11 μA at an applied gate voltage (V_g) of + 40 V which is turned off at an applied voltage of -40 V [169]. The I-V curves of ZnS@SnO_2 core-shell nanoribbons illuminated at different wavelengths are shown in Figure 1.27f. Illumination of UV light on the electrochemical device results in higher current (17.4 μA) compared to the device illuminated under visible light (3.6 μA). Figure 1.27g shows the photoresponse of the electrochemical device at various incident light wavelengths at a bias voltage of 1 V. The photoresponse of the device is about six orders of magnitude higher in the UV region as compared to that in the visible region. This is due to effective generation of electron-hole pairs in the ZnS@SnO_2 core-shell nanoribbons under the UV light illumination. These results indicate that ZnS@SnO_2 core-shell nanoribbons can act as either visible-blind or ultraviolet photodetectors [169]. Time resolved response of the electrochemical device at an applied voltage of 1 V is shown in Figure 1.27h. Under the illumination of UV light, photocurrent of the device reaches about 3.2 μA and it drops down to about 0.4 μA when the light is turned off with good stability and reproducibility. The photocurrent to dark current ratio is about 8 and the higher photoconductivity in these samples

is due to enhanced adsorption and desorption rates of oxygen molecules on the surface of ZnS@SnO_2 core-shell nanoribbons [169].

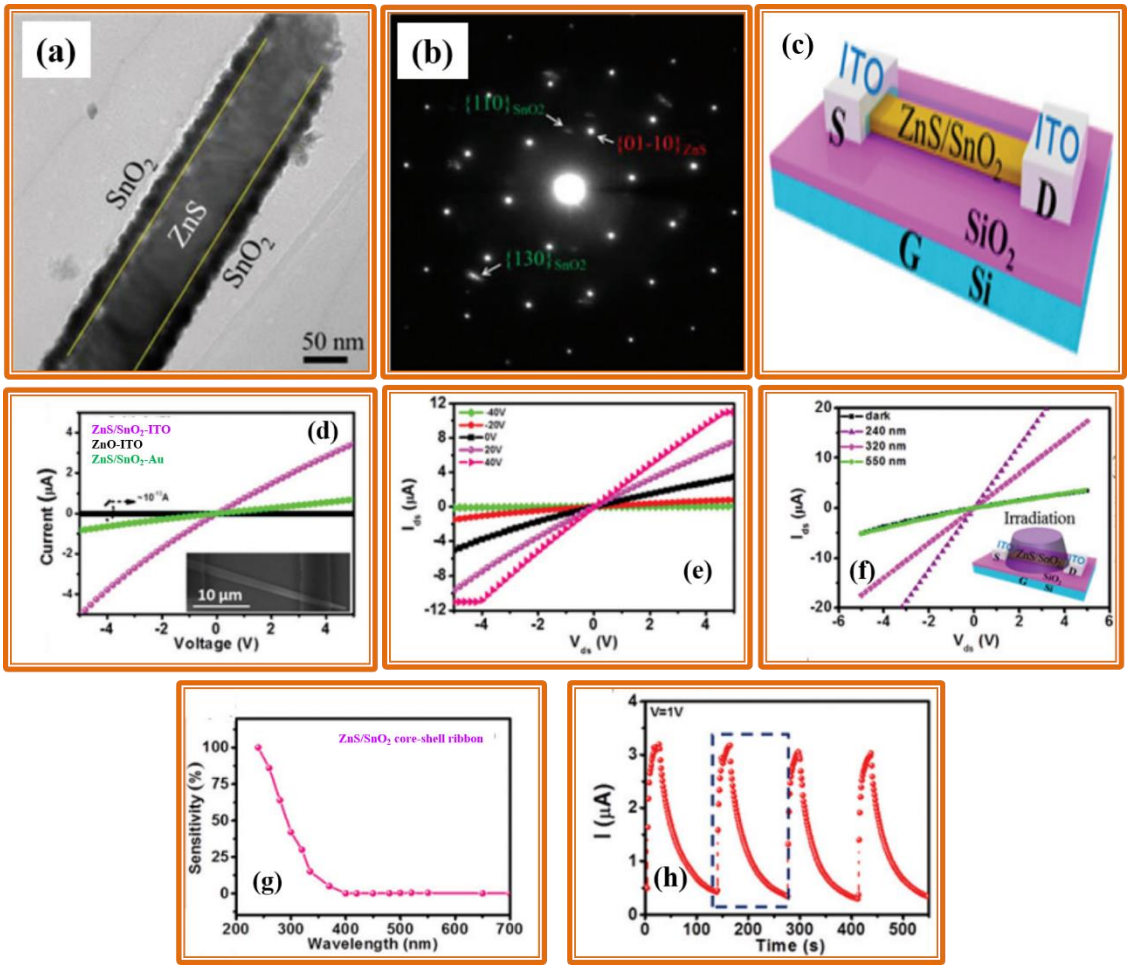

Fig. 1.27: (a, b) TEM and SAED pattern of ZnS@SnO_2 core-shell nanoribbons, **(c)** schematic diagram of an electrochemical measurement specimen, **(d)** I-V curves of ZnS@SnO_2 core-shell nanoribbons and ZnS nanoribbons, **(e)** I_{ds}-V_{ds} curves at different gate voltages (V_g), **(f)** I-V curves of the electrochemical device on illumination at different wavelengths, **(g)** sensitivity of the electrochemical device at various wavelengths at an applied voltage of + 1.0 V, and **(h)** time resolved photoresponse of the electrochemical device [169].

1.6 Applications of core-shell nanoparticles

Core-shell nanoparticles have received considerable attention as compared to their counter parts because they have potential applications in various fields such as catalysis, environmental remediation, pharmaceutics, electronics, data or energy storage devices, solar cells, fuel cells, supercapacitors, light emitting diodes, and bio-medicine [30,42,170,171]. A schematic

representation of various applications of the core-shell nanoparticles is given in Figure 1.28 and some of them are discussed in brief as follows [30].

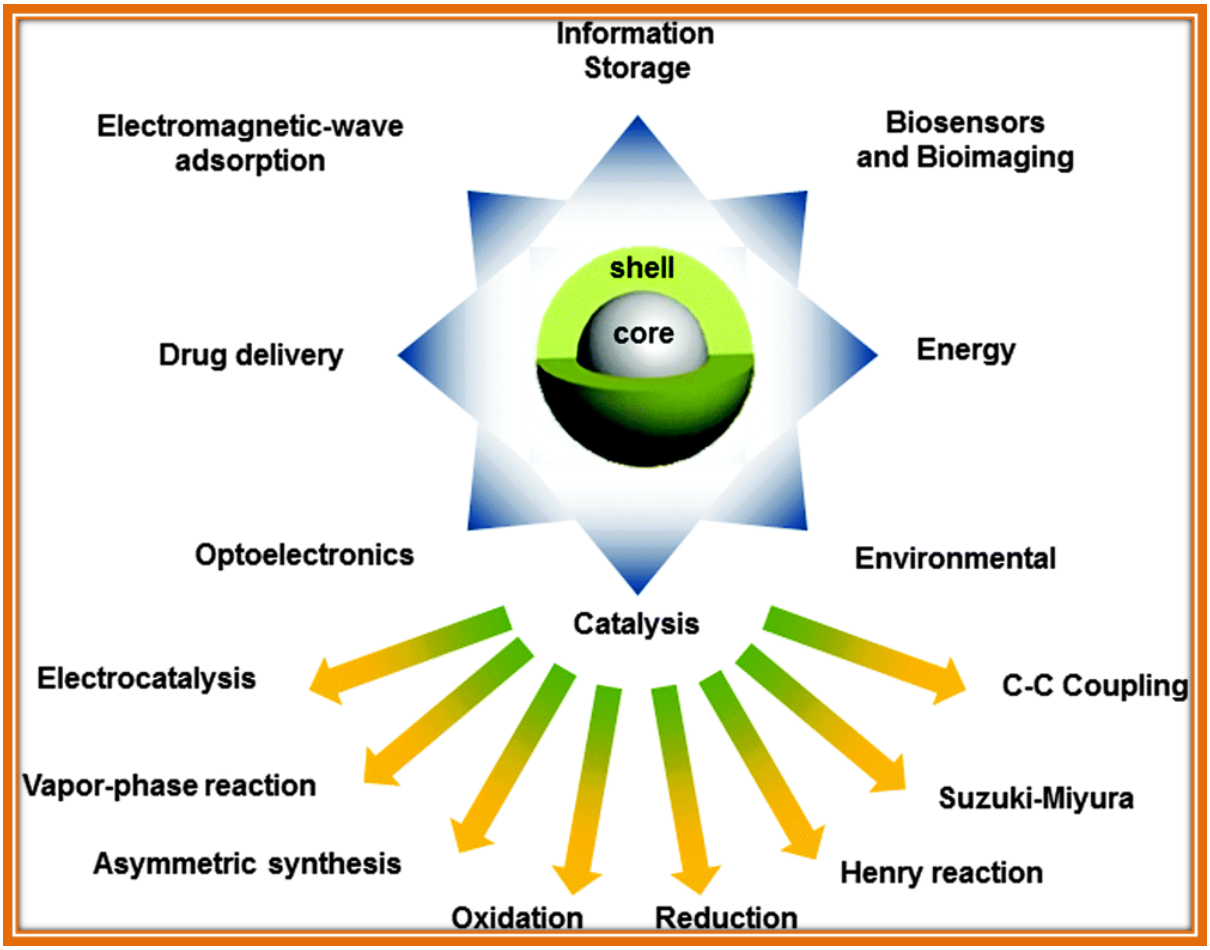

Fig. 1.28: Applications of core-shell nanoparticles in various fields [30].

1.6.1 Catalysis

Core-shell nanoparticles exhibit enhanced catalytic activity as compared to the core or shell nanoparticles. This is attributed to high surface area, porosity, surface charge, stability, and synergistic interaction between the core and shell. The catalytic properties of core-shell nanoparticles are affected by their structural and compositional features as well as the surface features of the core and shell (Figure 1.29 (a, b)) [30,172,173]. Core-shell nanoparticles have been used in different catalytic applications such as oxidation or hydrogenation reactions, cross-coupling reactions, Henry reaction, tandem deprotection-Knoevenagel reaction, aerobic oxidative esterification, etc.

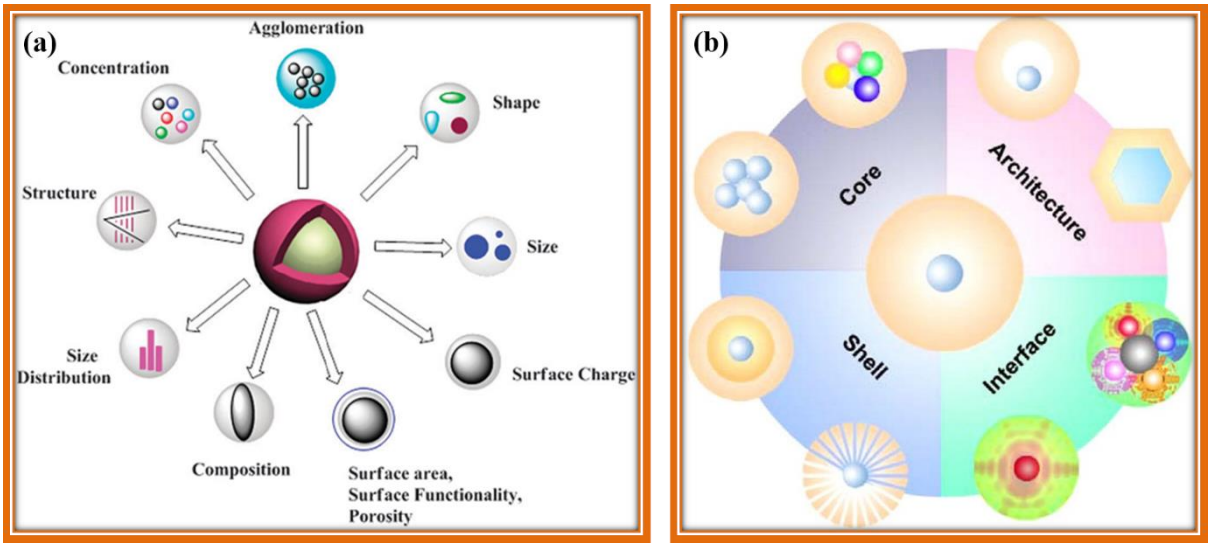

Fig. 1.29: (a) Various factors that can affect the catalytic properties of the core-shell nanoparticles, and **(b)** type of core, shell, interface and architecture of core-shell nanoparticles that can affect the catalytic activity [30,172].

1.6.1.1 Hydrogenation

Hydrogenation of alkenes, alkynes and aromatic nitro compounds play an important role in various industrial applications. As compared to traditional catalysts, core-shell nanoparticles have received great attention in catalytic applications due to their high chemo and regio selectivity, ease of separation and recyclability [30,42]. Haldar et al. have demonstrated the core size dependent catalytic activity of Au@Ag core-shell nanoparticles towards the reduction of 4-nitrophenol in an aqueous solution in the presence of $NaBH_4$ [50]. Figure 1.30a shows the TEM image of Au_{100}@Ag core-shell nanoparticles. Figure 1.30 (b-d) shows the absorbance spectra, kinetics plots and catalytic reaction efficiency plots for the reduction of 4-nitrophenol to 4-aminophenol using the Au@Ag core-shell nanoparticles. On increasing the Au core size from 20 to 100 nm, the catalytic activity of Au@Ag core-shell nanoparticles increases. As compared to pure components, the Au_{100}@Ag core-shell nanoparticles show enhanced catalytic activity, which is attributed to strong electronic effect and ligand effect. The capacitance increases with core size and accordingly electron density increases in the Au@Ag core-shell nanoparticles. The higher electron density enhances the overall catalytic activity of Au@Ag core-shell nanoparticles as compared to that of the constituents [50]. These results indicate that Au@Ag core-shell nanoparticles are useful in various industrial catalytic applications with tunable activity by changing the core size.

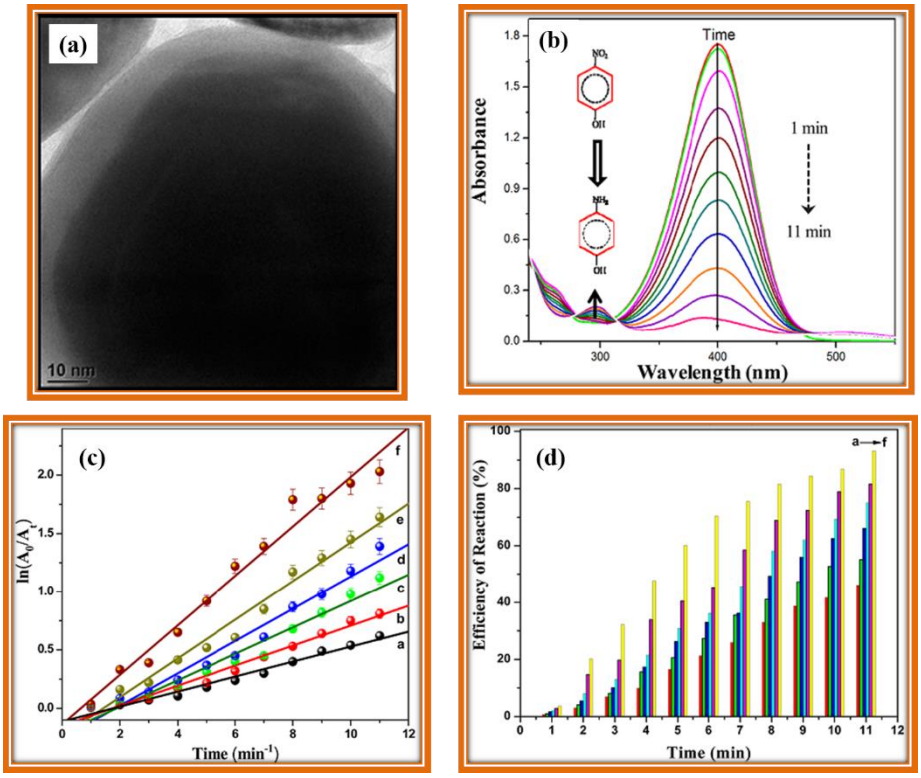

Fig. 1.30: (a) TEM image of Au_{100}@Ag core-shell nanoparticles, **(b)** UV-Visible spectral results indicating the reduction of 4-nitrophenol using Au_{100}@Ag core-shell nanoparticles, **(c)** plot of *ln* (A_o/A_t) *vs.* time for the reduction of 4-nitrophenol using Au@Ag core-shell nanoparticles with various Au core size (a = 10, b = 20, c = 40, d = 60, e = 80, and f = 100 nm), and **(d)** catalytic efficiency of Au@Ag core-shell nanoparticles with various Au core size [50].

1.6.1.2 Oxidation

Oxidation reactions have great importance in industrial applications like hydrogenation. For example, Chen et al. have investigated the catalytic activity of Pd@hollow mesoporous CeO_2 yolk-shell nanoparticles (calcined at 350 and 550 ^oC) towards CO oxidation as well as aerobic oxidation of cinnamyl alcohol to cinnamaldehyde [174]. Figure 1.31a shows the synthetic scheme for the synthesis of Pd@hollow mesoporous CeO_2 yolk-shell nanoparticles and Figure 1.31 (b, c) shows the low and high magnification TEM images of the yolk-shell nanoparticles. The Pd@hollow mesoporous CeO_2 yolk-shell nanoparticles calcined at 550 ^oC show better CO conversion at low temperature (80-100 ^oC) than the Pd@hollow mesoporous CeO_2 yolk-shell nanoparticles calcined at 350 ^oC. This is due to enhanced surface cleaning of Pd nanoparticles during calcination at 550 ^oC than at 350 ^oC [174]. As compared to pure Pd nanoparticles and Pd@SiO_2 core-shell nanoparticles, and Pd@hollow mesoporous CeO_2 yolk-shell nanoparticles (calcined at 550 ^oC) show enhanced catalytic activity. This is attributed to enhanced stability

of Pd nanoparticles in the CeO_2 matrix at elevated temperatures *via* synergistic interaction [174].

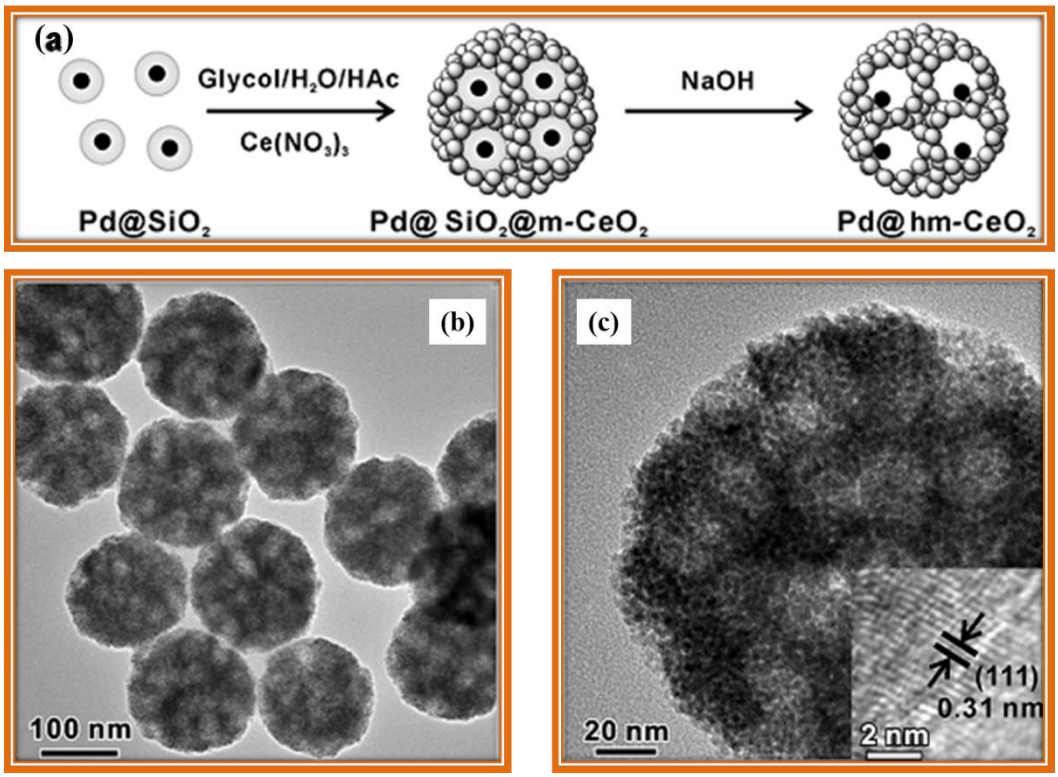

Fig. 1.31: (a) Schematic representation of synthesis of Pd@hm-CeO_2 yolk-shell nanoparticles, **(b, c)** high and low magnification TEM images of the yolk-shell nanoparticles. Inset shows the HRTEM image of Pd@hm-CeO_2 yolk-shell nanoparticles [174].

In the case of aerobic oxidation of cinnamyl alcohol to cinnamaldehyde, the Pd@hollow mesoporous CeO_2 yolk-shell nanoparticles show enhanced selectivity compared to Pd/C, Pd/CeO_2 and Pd nanoparticles (4.9 nm) supported on hm-CeO_2. A comparison of catalytic conversion using different catalysts is given in Table 1.1. These results indicate Pd@hollow mesoporous CeO_2 yolk-shell nanoparticles show higher catalytic activity compared to the other catalysts. In the Pd@hollow mesoporous CeO_2 yolk-shell nanoparticles, the reactants easily access the Pd nanoparticles *via* permeable porous CeO_2 shell which enhances the catalytic activity [174]. The Pd@hollow mesoporous CeO_2 yolk-shell nanoparticles show greater than 99.9 % conversion up to three cycles indicating high stability with good recyclability of the catalyst. These results indicate that Pd@hollow mesoporous CeO_2 yolk-shell nanoparticles are useful in various catalytic applications.

Table 1.1. Aerobic oxidation of cinnamyl alcohol to cinnamaldehyde using Pd@hm-CeO_2 yolk-shell nanoparticles, Pd/hm-CeO_2, Pd/CeO_2, and Pd/C nanoparticles [174].

Catalyst	No. of cycles	Time (h)	Conversion (%)
Pd@hm-CeO_2	First	1.5	> 99.9
	Second	1.5	> 99.9
	Third	1.5	> 99.9
Pd/hm-CeO_2		1.5	42.1
Pd/CeO_2		1.5	24.5
Pd/C		1.5	62.6

1.6.1.3 Coupling reactions

Coupling reactions play a crucial role in the synthesis of many pharmaceutical precursors and drug intermediates. The most studied coupling reactions are Suzuki-Miyaura, Henry, Sonogashira, and Ullmann coupling reactions. In all the reactions, precious metals (Pd, Pt, Au, etc.) are used as the catalysts [30,88,175,176]. To make these reactions more economical, Kou et al. have synthesized inexpensive Cu@Cu_2O inside-out core-shell nanoparticles *via* solution-phase strategy and have used them as the catalyst in Sonogashira reaction of aryl halides and phenyl acetylenes [177]. Pure Cu and Cu_2O does not catalyze the reaction and the conversion occurs only when Cu@Cu_2O core-shell nanoparticles are used as the catalyst. They show 85-94 % yield in the absence of precious metals and ligands. In addition to this, the recovered catalyst retains its core-shell morphology and exhibits significant catalytic activity without any loss in the multiple runs. The Cu@Cu_2O core-shell nanoparticles act as noble metal free and ligand free catalyst for Sonogashira coupling reaction with good efficiency [177]. These results suggests an alternative, economic and good sustainable pathway for Pd catalyzed reactions.

1.6.2 Photocatalysis

1.6.2.1 Photodegradation of organic dyes

The contamination of water sources by various industrial pollutants make a serious threat to aquatic life and environment. To degrade the organic pollutants, photocatalysis has been used in which, semiconductor nanoparticles such as ZnO, TiO_2, SnO_2, CdS are used as the photocatalysts but their fast recombination limits their use [80,81,178]. To overcome this problem, in recent years, heterostructures have been developed and they exhibit enhanced

catalytic activity towards the degradation of organic dyes (rhodamine B, methylene blue, methyl orange, malachite green, etc.) as well as water splitting reactions [92,109,135]. Schematic diagrams of core-shell nanoparticles towards photocatalysis based on their core or shell interactions and based on their hierarchical structure are given in Figure 1.32 (a, b).

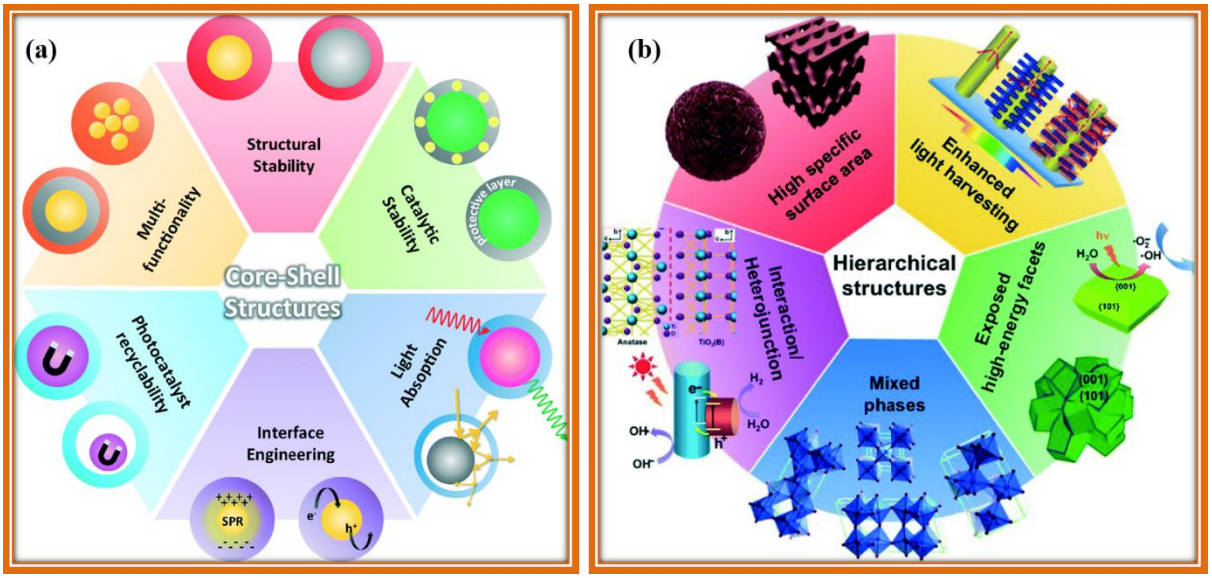

Fig. 1.32: Schematic diagrams of core-shell nanoparticles towards photocatalysis **(a)** based on core or shell interactions, and **(b)** based on hierarchical structure functions [179].

For example, Kumar et al. have reported the photodegradation of rhodamine B in an aqueous solution using nitrogen doped ZnO@g-C_3N_4 core-shell nanoparticles under sun light [180]. As compared to the pure components, the nitrogen doped ZnO@g-C_3N_4 core-shell nanoparticles show enhanced apparent rate constant (k_{app}), indicating higher catalytic activity. The higher catalytic activity of nitrogen doped ZnO@g-C_3N_4 core-shell nanoparticles is due to effective separation of charge carriers at the interface of nitrogen doped ZnO and g-C_3N_4 [180]. Under sun light irradiation, the photogenerated electrons in the conduction band of nitrogen doped ZnO are unable to produce $O_2^{\bullet-}$ from dissolved O_2 by photoreduction process due to more positive conduction band edge level of nitrogen doped ZnO (– 0.2 eV *vs.* NHE) than the standard redox potential of $O_2/O_2^{\bullet-}$ (– 0.3 eV *vs.* NHE). On the other hand, the photogenerated holes in the valence band of g-C_3N_4 is unable to oxidize the adsorbed H_2O molecules to $^{\bullet}OH$ due to the fact that the valence band edge of g-C_3N_4 is more negative (+ 1.3 eV *vs.* NHE) than the standard reduction potential of $-OH/H_2O$ (+ 2.8 eV *vs.* NHE) [180]. An efficient electron-hole separation is achieved based on Z-scheme mechanism which is responsible for higher catalytic activity of nitrogen doped ZnO@g-C_3N_4 core-shell nanoparticles [180]. A comparison

of photocatalytic activity using various catalysts and the plots of *ln* (C_t/C_o) *vs.* time are shown in Figure 1.33 (a, b). The mechanism of degradation of rhodamine B using nitrogen doped ZnO@g-C_3N_4 core-shell nanoparticles is shown in Figure 1.33c.

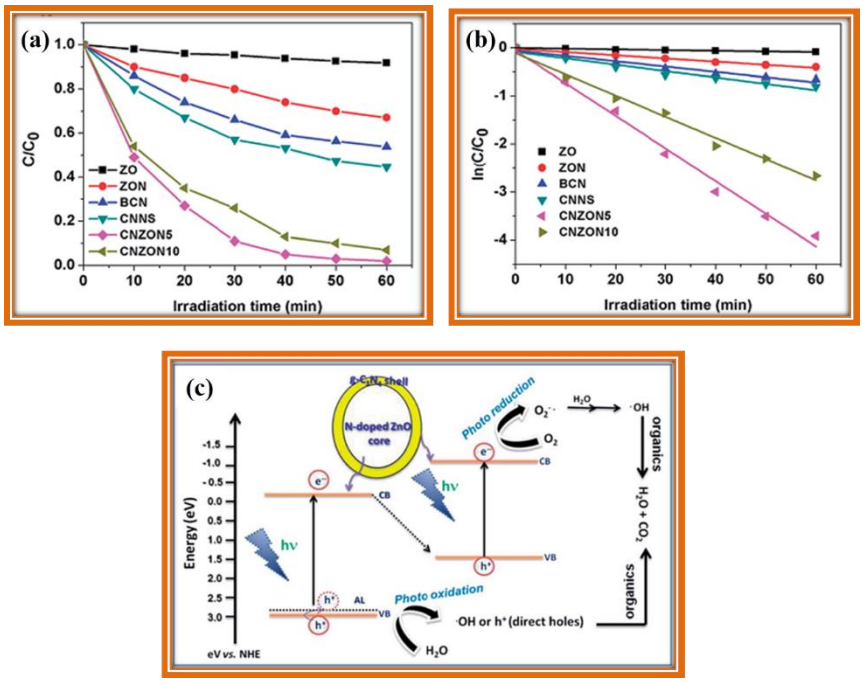

Fig. 1.33: (a) Photocatalytic activity of various catalysts (ZnO, nitrogen doped ZnO (ZON), bulk g-C_3N_4 (BCN), g-C_3N_4 nanosheets (CNNS), and nitrogen doped ZnO@g-C_3N_4 core-shell nanoparticles (CNZON5 and CNZON10)) towards photodegradation of rhodamine B in an aqueous solution, **(b)** *ln* (C_t/C_o) *vs.* time plots using the various catalysts, and **(c)** Z-scheme mechanism for the photodegradation of rhodamine B using nitrogen doped ZnO@g-C_3N_4 core-shell nanoparticles [180].

1.6.2.2 Water splitting

In 1972, Fujishima and Honda discovered catalytic hydrogen production using TiO_2 as the catalyst [181]. The fundamental principle to choose a suitable semiconductor for water splitting is that the valence band edge is more negative than 0 V *vs.* NHE and the conduction band edge is more positive than +1.23 V *vs.* NHE at pH =0. Thermodynamically, water splitting reaction requires a minimum energy of 1.23 eV and the Gibbs free energy change (ΔG) for water splitting reaction is 237.2 kJ/mol or 2.46 eV per molecule of H_2O [181]. The core-shell nanoparticles exhibit better catalytic activity towards water splitting compared to their counter parts. Recently, Chen et al. have reported that the Pd@Co@MIL-101 core-shell nanoparticles acts as efficient catalysts for water splitting reaction. Ammonia borane (AB) is used as the

reducing agent which is introduced into water along with various catalysts to produce hydrogen (H_2) [182]. Pd@Co@MIL-101 (the Pd/Co molar ratio is 0.3 and (Pd + Co)/AB is 0.011) achieves 100 % H_2 production with higher catalytic activity than pure Pd, Co, PdCo alloy, Pd@Co/MIL-101, and MIL-101. The core-shell nanoparticles show higher turnover frequency (51 $mol_{H_2}.mol_{cat}^{-1}.min^{-1}$) than the noble metal catalyst Ru (36.3 $mol_{H_2}.mol_{cat}^{-1}.min^{-1}$) and non-noble metal catalysts such as Ni (8.8 $mol_{H_2}.mol_{cat}^{-1}.min^{-1}$) and CuCo (9.18 $mol_{H_2}.mol_{cat}^{-1}.min^{-1}$) [182]. They show the lowest activation energy (E_a) of 22 kJ/mol compared to Ni@Ru (44 kJ/mol) and Ru (39 kJ/mol). The core-shell nanoparticles show similar catalytic activity up to five cycles without any loss indicating high durability of the catalyst. The higher catalytic activity of Pd@Co@MIL-101 core-shell nanoparticles is due to synergistic effects of Pd and Co as well as confinement effect of MIL-101 [182]. The plots of volume of hydrogen evolution *vs.* time and durability of Pd@Co@MIL-101 core-shell nanoparticles are shown in Figure 1.34 (a, b).

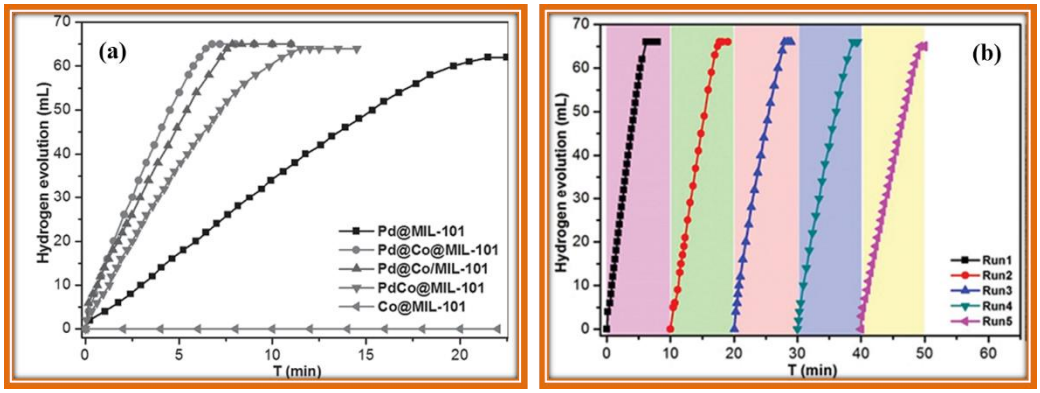

Fig. 1.34: (a) Volume of hydrogen evolution *vs.* time from ammonia borane aqueous solution using various catalysts, and **(b)** recyclability and stability of Pd@Co@MIL-101 yolk-shell nanoparticles for hydrogen evolution from ammonia borane aqueous solution [182].

1.6.3 Sensors

Sensors play a crucial role in the detection of hazardous volatile gases present in environment and they have a great impact in biological applications. Metal oxide nanoparticles are used as sensors and the sensing properties depend on size, shape, surface property, electronic structure, etc [87,183]. As compared to pure metal oxide semiconductors, heterostructures show better sensing activity with good selectivity [91,183]. For example, Majhi et al. have investigated the gas sensing activity of Au@ZnO core-shell nanoparticles towards various gases such as hydrogen, acetaldehyde, ethanol and CO [184]. The Au@ZnO core-shell nanoparticles exhibit

enhanced response for all the gases than that of pure ZnO nanoparticles at 300 ^{o}C. Among the gases, the Au@ZnO core-shell nanoparticles show higher response for H_2 indicating its better ability to distinguish H_2 in the environment [184]. The gas sensing mechanism is shown in Figure 1.35. The higher sensing activity of Au@ZnO core-shell nanoparticles is due to electronic and chemical sensitization effects. The electronic sensitization effect is responsible for higher sensitivity and the chemical sensitization effect is responsible for higher selectivity [184]. The Au core nanoparticles enhance the overall gas sensor activity of Au@ZnO core-shell nanoparticles *via* spillover effect [184]. These results suggest that Au@ZnO core-shell nanoparticles can be used as an effective and selective sensor to detect H_2 in the environmental applications.

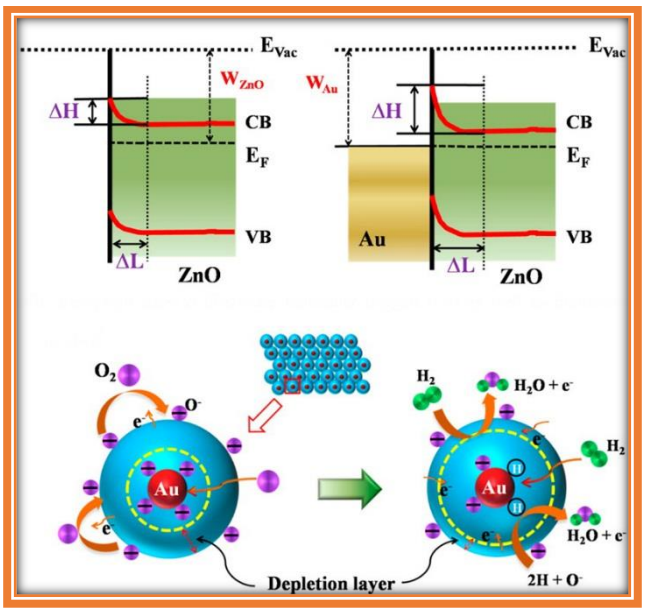

Fig. 1.35: Sensing mechanism of various gases using Au@ZnO core-shell nanoparticles under air and targeted gas [184].

1.6.4 Quantum dots sensitized solar cells

For the last two decades, dye sensitized solar cells are receiving much attraction due to their high conversion efficiency of solar energy to electricity. But their high cost, tricky synthesis procedure of organic dyes, and limited solar to electricity conversion efficiency restricts their commercial use in the market [185]. To overcome this problem, third generation quantum dots sensitized solar cells (QDSCs) have been developed and they are more cost effective with good photo conversion efficiency [185,186]. The quantum dots with higher conduction band edge level with free trap states enhance the photo conversion efficiency. A schematic representation of quantum dots sensitized solar cells and charge separation process is shown in Figure 1.36

(a, b) [185]. The QDSCs consist of QD sensitized photoanode, counter electrode, and redox electrolyte couple of S^{2-}/S_n^{2-}. The QDs are coated on wide band gap semiconductor (e.g. TiO_2, ZnO). On illumination with light, electrons in the valence band of semiconductor are excited to the conduction band and the excited electrons are transferred to the conduction band of TiO_2. These electrons are transferred to the transparent conductive oxide (TCO) *via* an external TiO_2 network. The electrolyte acts as a hole transport medium, which reduces the QD and regenerate the QD. Finally, the holes are transported to the counter electrode, which reduce the oxidized counterpart of the redox system. As compared to DSSC, the photo conversion efficiency is still lower, which is due to insufficient light absorption, fast recombination of electrons with holes in the electrolytes, and slow charge transfer between the counter electrode and electrolyte [185]. Type–II core-shell nanoparticles show better photo conversion efficiency due to confinement of holes in the core and electrons in the shell. Such an interface enables enhanced electron injection rate by reducing the charge recombination process [187]. Type –II ZnTe@CdSe core-shell nanoparticles show higher photo conversion efficiency (η) of 7.17 % with short circuit current (J_{sc}) of 19.65 mA/cm^2 and open circuit voltage (V_{oc}) of 0.642 V compared to that of CdTe@CdSe core-shell nanoparticles (η = 6.67 %, J_{sc} = 18.53 mA/cm^2, V_{oc} = 0.597 V). The higher photo conversion efficiency of ZnTe@CdSe core-shell nanoparticles is due to relatively larger conduction band offset (1.22 eV) compared to that of CdTe@CdSe (0.27 eV). This induces a strong dipole effect at the interface of TiO_2 and ZnTe@CdSe core-shell nanoparticles resulting in high photo conversion efficiency compared to CdTe@CdSe core-shell nanoparticles [187]. These results indicate that by tuning the conduction band edge alignment with free trap states can enhance the photo current efficiency of the quantum dots sensitized solar cells. The cost effective QDSCs can be used in the commercial market.

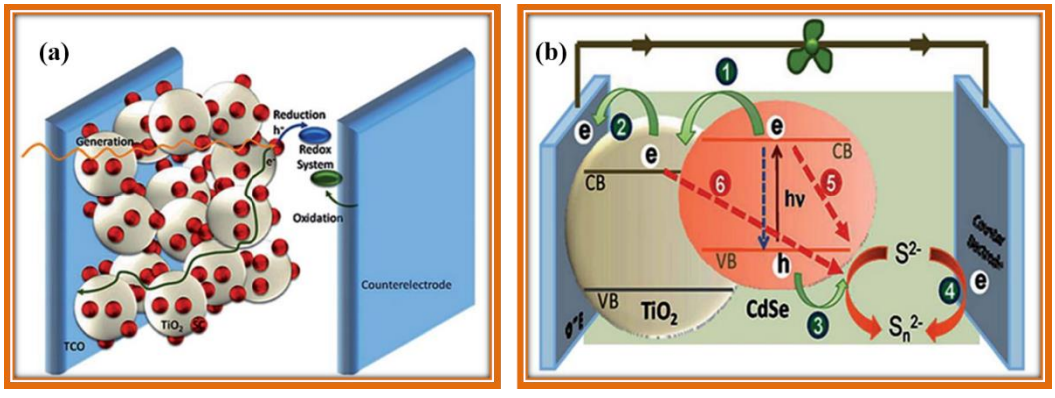

Fig. 1.36: (a) Schematic representation of quantum dots sensitized solar cell (QDSCs), and **(b)** interfacial charge transfer mechanism in QDSCs [185].

1.6.5 Microwave absorbers

Microwave absorbing materials have received great attention due to their wide range of applications in electronic industries, commerce, and defence. Magnetic loss materials such as ferrite, nickel, cobalt, and dielectric materials such as metal oxides, carbon, and conducting polymers have been used to develop the microwave absorbing materials [188]. Liu et al. have investigated the microwave absorbing properties of double shelled Fe_3O_4@SnO_2 yolk-shell nanorattles. They exhibit enhanced microwave absorption as compared to their counter parts, solid Fe_3O_4@SiO_2 core-shell nanoparticles, and single shell Fe_3O_4@SnO_2 nanorattles. By tuning the core, void size and the shell thickness, the microwave absorption is greatly enhanced in double shelled Fe_3O_4@SnO_2 yolk-shell nanorattles [189]. The enhanced microwave absorption of Fe_3O_4@SnO_2 yolk-shell nanorattles is due to synergistic effect of Fe_3O_4 core and SnO_2 shell as well as the presence of increased void space [189]. The SEM and TEM images of double shelled Fe_3O_4@SnO_2 core-shell nanorattles are shown in Figure 1.37 (a, b) and microwave loss curves using the various materials are shown in Figure 1.37c.

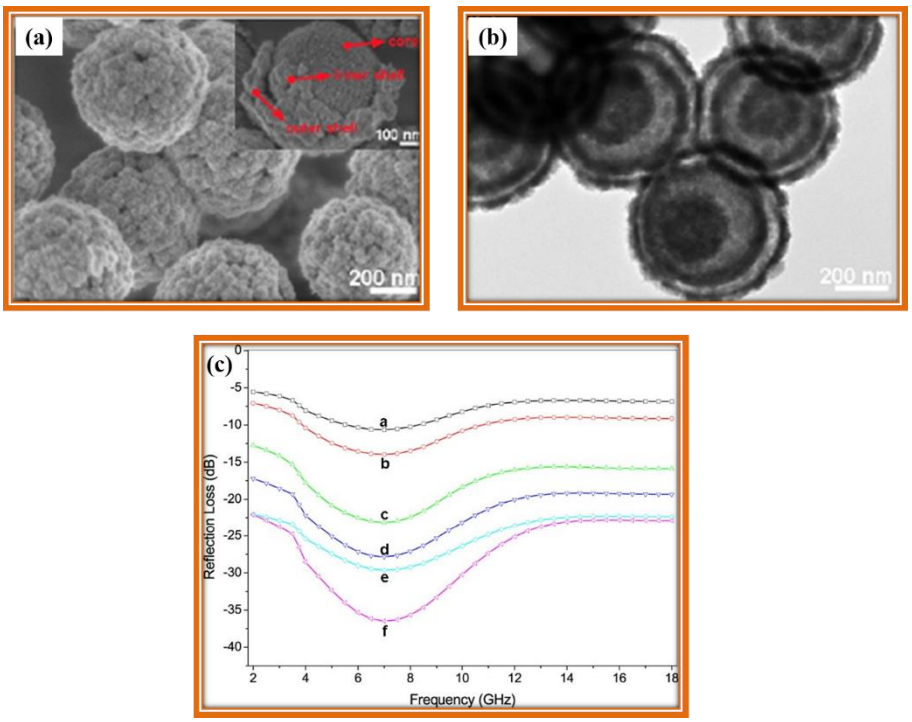

Fig. 1.37: (a, b) SEM and TEM images of double shelled Fe_3O_4@SiO_2 core-shell nanorattles, and **(c)** microwave reflection loss curves of various materials (a = Fe_3O_4 nanoparticles, b = Fe_3O_4@SiO_2 microspheres, c = single shelled Fe_3O_4@SnO_2 yolk-shell nanorattles, and **(d-f)** = double shelled Fe_3O_4@SnO_2 yolk-shell nanorattles with various core size, void size and shell thickness) [189].

1.6.6 Bio-medical applications

Core-shell nanoparticles have important applications in bio-medical field such as targeted drug delivery, bio-imaging, cell labelling, sensing, gene delivery, etc. Within the past decade, some of the applications have already been well explored and some are still under investigation [42,88,190]. Recently, Chen et al. have investigated the photo-chemo combination therapy using g-C_3N_4@ZIF-8 core-shell nanoparticles [191]. The g-C_3N_4@ZIF-8 core-shell nanoparticles exhibit higher amount of DOX (doxorubicin) release at pH 5.0 (~ 85 %) than that at pH 7.4 (~ 25 %) in 70 hours as compared to free DOX. The higher DOX release at pH 5.0 is attributed to acid-prompted dissolution of ZIF-8 [191]. The g-C_3N_4@ZIF-8 core-shell nanoparticles exhibit dual color fluorescence, in which red fluorescence arises from DOX in the nuclei and blue fluorescence arises from g-C_3N_4 in cytoplasm of human alveolar cancer cells A549. These results indicate effective delivery of DOX at cancer cell nucleus [191]. A schematic illustration of mechanism for photo-chemo therapy is shown in Figure 1.38. The higher DOX release at pH 5.0 with better florescence suggest that the g-C_3N_4@ZIF-8 core-shell nanoparticles are very promising targeted drug candidate to release DOX at acidic tumor sites with enhanced fluorescence.

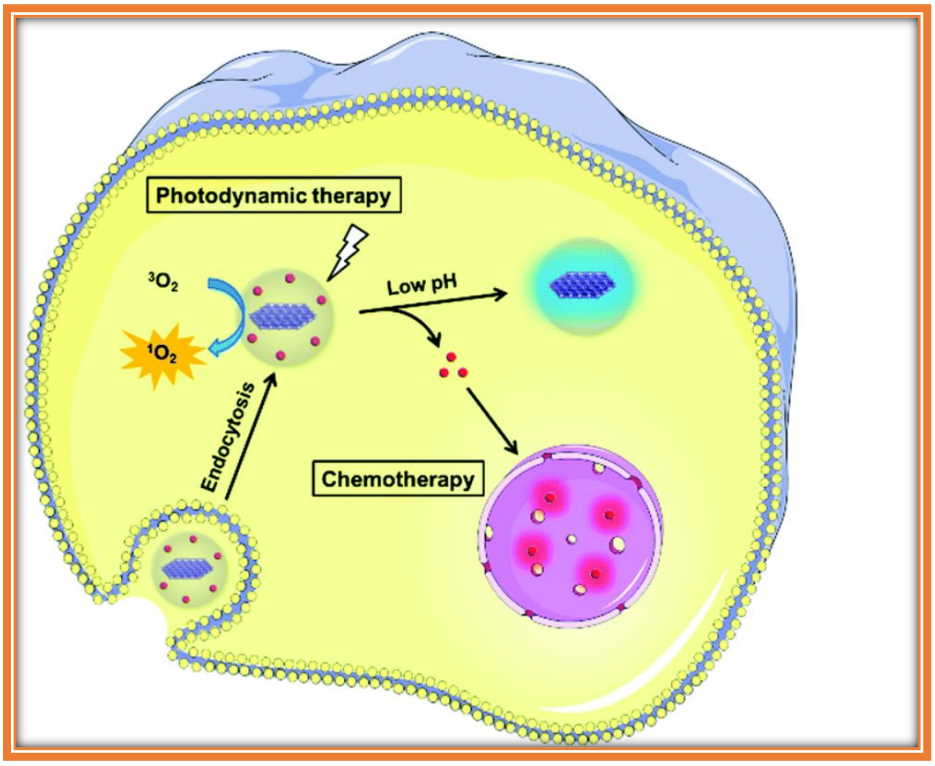

Fig. 1.38: Schematic representation of mechanism for photo-chemo therapy of human alveolar cancer cells A549 using DOX loaded g-C_3N_4@ZIF-8 core-shell nanoparticles [191].

Aim of the present study

Core-shell nanoparticles with different sizes and shapes play an important role in tuning their physicochemical properties. The uniform deposition of shell nanoparticles with controlled thickness on various shaped core materials is difficult. In the present study, various shaped core materials have been synthesized by StÖber's process, homogeneous precipitation, and solution route. Successful deposition of different shell nanoparticles with different thickness was carried out *via* novel and economical methods such as homogeneous precipitation and thermal decomposition. The core-shell nanoparticles that have been investigated are (i) type-I and type-II semiconducting core-shell nanoparticles (SiO_2@CdS and ZnO@CdS), (ii) semiconductor-metal core-shell nanoparticles (ZnO@Ag and Cu_2O@Ag), and (iii) nanorattle type core-shell nanoparticles (SiO_2@Co_3O_4 and SiO_2@Ni-Co mixed metal oxides). The synthesized core-shell nanoparticles were characterized by an array of techniques such as powder XRD, FT-IR, TGA, FE-SEM, EDXA, TEM, XPS, BET surface area and zeta potential measurements. After thorough characterization, optical properties of the core-shell nanoparticles were studied using UV-Visible DRS and PL spectroscopy techniques. Applications of synthesized core-shell nanoparticles have been demonstrated using photocatalytic degradation of methylene blue in an aqueous solution, the reduction of 4-nitrophenol and methylene blue in presence of $NaBH_4$ in an aqueous solution, an artificial peroxidase-like enzyme mimic activity, and adsorption of mixture of rhodamine B and methylene blue in aqueous solutions.

References

1. Schaefer H. E., 'Nanoscience: The science of the small in physics, engineering, chemistry, biology and medicine', *Springer* (2010).

2. Yao J., Sun Y., Yang M., Duan Y., 'Chemistry, physics and biology of graphene-based nanomaterials: New horizons for sensing, imaging and medicine', *Journal of Materials Chemistry,* **22**, 14313–14329 (2012).

3. Ray P. C., 'Size and shape dependent second order nonlinear optical properties of nanomaterials and their application in biological and chemical sensing', *Chemical Reviews,* **110**, 5332–5365 (2010).

4. Luo B., Liu S., Zhi L., 'Chemical approaches toward graphene-based nanomaterials and their applications in energy-related areas', *Small*, **8**, 630–646 (2012).

5. Chang H., Wu H., 'Graphene-based nanomaterials: Synthesis, properties, and optical and optoelectronic applications', *Advanced Functional Materials,* **23**, 1984–1997 (2013).

6. Freestone I., Meeks N., Sax M., Higgitt C., 'The Lycurgus cup-A Roman nanotechnology', *Gold Bulletin,* **40**, 270–277 (2007).

7. Horikoshi S., Serpone N., 'Introduction to nanoparticles', *Wiley-VCH Verlag GmbH & Co. KGaA* (2013).

8. Pradell T., Molera J., Smith A. D., Tite M. S., 'The invention of lustre: Iraq 9th and 10th centuries AD', *Journal of Archaeological Science,* **35**, 1201–1215 (2008).

9. Reibold M., Paufler P., Levin A. A., Kochmann W., Pätzke N., Meyer D. C., 'Materials: Carbon nanotubes in an ancient Damascus sabre', *Nature,* **444**, 286 (2006).

10. Thompson D., 'Michael Faraday's recognition of ruby's gold: The birth of modern nanotechnology', *Gold Bulletin,* **40**, 267–269 (2007).

11. Feynman R. P., 'There's plenty of room at the bottom, an invitation to enter a new field of physics', *Engineering and Science,* **23**, 22–36 (1960).

12. Taniguchi N., 'On the basic concept of 'nano-technology'', *Proceedings of the*

International Conference of Production Engineering, Tokyo, Japan Society of Precision Engineering, (1974).

13. Binnig G., Rohrer H., 'Scanning tunnelling microscopy', *IBM Journal of Research and Development*, **30**, 355–369 (1986).

14. Drexler K. E., 'Engines of creation: The coming era of nanotechnology', *Anchor Books* (1986).

15. Drexler K. E., 'Nanosystems: Molecular machinery, manufacturing and computation', *Wiley & Sons, Inc.* (1992).

16. Nagarajan R., 'Nanoparticles: Building blocks for nanotechnology', *ACS Symposium Series*, **996**, 2–14 (2008).

17. Zubarev E. R., 'Nanoparticle synthesis-any way you want it', *Nature Nanotechnology*, **8**, 396–397 (2013).

18. Leong G. J., Ebnonnasir A., Schulze M. C., Strand M. B., Ngo C., Maloney D., Frisco S. L., Dinh H. N., Pivovar B., Gilmer G. H., Kodambaka S., Ciobanu C. V., Richards R. M., 'Shape-directional growth of Pt and Pd nanoparticles', *Nanoscale*, **6**, 11364–11371 (2014).

19. Roduner E., 'Size matters: Why nanomaterials are different', *Chemical Society Reviews*, **35**, 583–592 (2006).

20. http://orise.orau.gov/ihos/tech-topics/nanotechnology-scale.html

21. Yan Y., Miao J., Yang Z., Xiao F. X., Yang H. B., Liu B., Yang Y., 'Carbon nanotube catalysts: Recent advances in synthesis, characterization and applications', *Chemical Society Reviews*, **44**, 3295–3346 (2015).

22. Li Z., Liu Z., Sun H., Gao C., 'Superstructured assembly of nanocarbons: Fullerenes, nanotubes, and graphene', *Chemical Reviews*, **115**, 7046–7117 (2015).

23. Caminade A. M., Ouali A., Laurent R., Turrin C. O., Majoral J. P., 'The dendritic effect illustrated with phosphorus dendrimers', *Chemical Society Reviews*, **44**, 3890–3899 (2015).

24. Ahmad R., Soni U., Srivastava R., Singh V. N., Chand S., Sapra S., 'Investigation of the photophysical and electrical characteristics of $CuInS_2$ QDs/SWCNT hybrid nanostructure', *The Journal of Physical Chemistry C*, **118**, 11409–11416 (2014).

25. Singh D. K., Giri P. K., Iyer P. K., 'Evidence for defect-enhanced photoluminescence quenching of fluorescein by carbon nanotubes', *The Journal of Physical Chemistry C*, **115**, 24067–24072 (2011).

26. Cheng X., Lowe S. B., Reece P. J., Gooding J. J., 'Colloidal silicon quantum dots: From preparation to the modification of self-assembled monolayers (SAMs) for bio-applications', *Chemical Society Reviews*, **43**, 2680–2700 (2014).

27. Jackson M. N. J., Kamunde-Devonish M. K., Hammann B. A., Wills L. A., Fullmer L. B., Hayes S. E., Cheong P. H. Y., Casey W. H., Nyman M., Johnson D. W., 'An overview of selected current approaches to the characterization of aqueous inorganic clusters', *Dalton Transactions*, **44**, 16982–17006 (2015).

28. Pal J., Pal T., 'Faceted metal and metal oxide nanoparticles: Design, fabrication and catalysis', *Nanoscale*, **7**, 14159–14190 (2015).

29. Zhou J., Yang Y., Zhang C., 'Toward biocompatible semiconductor quantum dots: From biosynthesis and bioconjugation to biomedical application', *Chemical Reviews*, **115**, 11669–11717 (2015).

30. Gawande M. B., Goswami A., Asefa T., Guo H., Biradar A. V, Peng D. L., Zboril R., Varma R. S., 'Core-shell nanoparticles: Synthesis and applications in catalysis and electrocatalysis', *Chemical Society Reviews*, **44**, 7540–7590 (2015).

31. Jin Y., 'Multifunctional compact hybrid Au nanoshells: A new generation of nanoplasmonic probes for biosensing, imaging, and controlled release', *Accounts of Chemical Research*, **47**, 138–148 (2014).

32. Karanjit S., Jinasan A., Samsook E., Dhital R. N., Motomiya K., Sato Y., Tohji K., Sakurai H., 'Significant stabilization of palladium by gold in the bimetallic nanocatalyst leading to an enhanced activity in the hydrodechlorination of aryl chlorides', *Chemical Communications*, **51**, 12724–12727 (2015).

33. Murugadoss A., Kai N., Sakurai H., 'Synthesis of bimetallic gold–silver alloy nanoclusters by simple mortar grinding', *Nanoscale*, **4**, 1280–1282 (2012).

34. Madhumitha G., Roopan S. M., 'Devastated crops: Multifunctional efficacy for the production of nanoparticles', *Journal of Nanomaterials*, **2013**, 1–12 (2013).

35. Birol H., Rambo C. R., Guiotoku M., Hotza D., 'Preparation of ceramic nanoparticles *via* cellulose-assisted glycine nitrate process: A review', *RSC Advances*, **3**, 2873–2884 (2013).

36. Thunugunta T., Reddy A. C., Reddy D. C. L., 'Green synthesis of nanoparticles: Current prospectus', *Nanotechnology Reviews*, **4**, 303–323 (2015).

37. Georgakilas V., Perman J. A., Tucek J., Zboril R., 'Broad family of carbon nanoallotropes: Classification, chemistry, and applications of fullerenes, carbon dots, nanotubes, graphene, nanodiamonds, and combined superstructures', *Chemical Reviews*, **115**, 4744–4822 (2015).

38. Chen A., Ostrom C., 'Palladium-based nanomaterials: Synthesis and electrochemical applications', *Chemical Reviews*, **115**, 11999–12044 (2015).

39. Cargnello M., Gordon T. R., Murray C. B., 'Solution-phase synthesis of titanium dioxide nanoparticles and nanocrystals', *Chemical Reviews*, **114**, 9319–9345 (2014).

40. Hoener C. F., Allan K. A., Bard A. J., Campion A., Fox M. A., Mallouk T. E., Webber S. E., White J. M., 'Demonstration of a shell-core structure in layered CdSe-ZnSe small particles by X-ray photoelectron and Auger spectroscopies', *The Journal of Physical Chemistry*, **96**, 3812–3817 (1992).

41. Honma I., Sano T., Komiyama H., 'Surface-enhanced Raman scattering (SERS) for semiconductor microcrystallites observed in Ag-CdS hybrid particles', *The Journal of Physical Chemistry*, **97**, 6692–6695 (1993).

42. Chaudhuri R. G., Paria S., 'Core/shell nanoparticles: Classes, properties, synthesis mechanisms, characterization, and applications', *Chemical Reviews*, **112**, 2373–2433 (2012).

43. Li W., Zhao D., 'Extension of the Stöber method to construct mesoporous SiO_2 and TiO_2

shells for uniform multifunctional core-shell structures', *Advanced Materials*, **25**, 142–149 (2013).

44. Jankiewicz B. J., Jamiola D., Choma J., Jaroniec M., 'Silica–metal core–shell nanostructures', *Advances in Colloid and Interface Science*, **170**, 28–47 (2012).

45. Mazaleyrat F., Ammar M., LoBue M., Bonnet J. P., Audebert P., Wang G. Y., Champion Y., Hÿtch M., Snoeck E., 'Silica coated nanoparticles: Synthesis, magnetic properties and spin structure', *Journal of Alloys and Compounds*, **483**, 473–478 (2009).

46. Guo X., Mao F., Wang W., Yang Y., Bai Z., 'Sulfhydryl-modified Fe_3O_4@SiO_2 core/shell nanocomposite: Synthesis and toxicity assessment in vitro', *ACS Applied Materials and Interfaces*, **7**, 14983–14991 (2015).

47. Kobayashi Y., Minato M., Ihara K., Nakagawa T., Gonda K., Takeda M., Ohuchi N., Kasuya A., 'Synthesis of high concentration colloid solution of silica-coated AgI nanoparticles', *Journal of Nanoscience and Nanotechnology*, **12**, 6741–6745 (2012).

48. Li H., Li Y., Cheng J., 'Molecularly imprinted silica nanospheres embedded Cdse quantum dots for highly selective and sensitive optosensing of pyrethroids', *Chemistry of Materials*, **22**, 2451–2457 (2010).

49. Peerakiatkhajohn P., Butburee T., Yun J. H., Chen H., Richards R. M., Wang L., 'A hybrid photoelectrode with plasmonic Au@TiO_2 nanoparticles for enhanced photoelectrochemical water splitting', *Journal of Materials Chemistry A*, **3**, 20127–20133 (2015).

50. Haldar K. K., Kundu S., Patra A., 'Core-size-dependent catalytic properties of bimetallic Au/Ag core–shell nanoparticles', *ACS Applied Materials and Interfaces*, **6**, 21946–21953 (2014).

51. Son J. S., Lee J., Shevchenko E. V, Talapin D. V., 'Magnet-in-the-semiconductor nanomaterials: High electron mobility in all-inorganic arrays of FePt/CdSe and FePt/CdS core−shell heterostructures', *The Journal of Physical Chemistry Letters*, **4**, 1918–1923 (2013).

52. Zeng H., Li J., Wang Z. L., Liu J. P., Sun S., 'Bimagnetic core/shell FePt/Fe_3O_4

nanoparticles', *Nano Letters*, **4**, 187–190 (2004).

53. Gu C., Xu H., Park M., Shannon C., 'Synthesis of metal-semiconductor core-shell nanoparticles using electrochemical surface-limited reactions', *Langmuir*, **25**, 410–414 (2009).

54. Shan Z., Clayton D., Pan S., Archana P. S., Gupta A., 'Visible light driven photoelectrochemical properties of Ti@TiO_2 nanowire electrodes sensitized with core-shell Ag@Ag_2S nanoparticles', *The Journal of Physical Chemistry B*, **118**, 14037–14046 (2014).

55. Stefan M., Pana O., Leostean C., Bele C., Silipasl D., Senila M., Gautron E., 'Synthesis and characterization of Fe_3O_4-TiO_2 core-shell nanoparticles', *Journal of Applied Physics*, **116**, 114312/1–11 (2014).

56. Narayanamoorthy B., Datta K. K. R., Eswaramoorthy M., Balaji S., 'Self-stabilized Pt–Rh bimetallic nanoclusters as durable electrocatalysts for dioxygen reduction in PEM fuel cells', *RSC Advances*, **4**, 55571–55579 (2014).

57. Wang H., Hodgson J., Shrestha T. B., Thapa P. S., Moore D., Wu X., Ikenberry M., Troyer D. L., Wang D., Hohn K. L., Bossmann S. H., 'Carbon dioxide hydrogenation to aromatic hydrocarbons by using an iron/iron oxide nanocatalyst', *Beilstein Journal of Nanotechnology*, **5**, 760–769 (2014).

58. Balakrishnan S., Bonder M. J., Hadjipanayis G. C., 'Particle size effect on phase and magnetic properties of polymer-coated magnetic nanoparticles', *Journal of Magnetism and Magnetic Materials*, **321**, 117–122 (2009).

59. Burke N. A. D., Stover H. D. H., Dawson F. P., 'Magnetic nanocomposites : Preparation and characterization of polymer-coated iron nanoparticles', *Chemistry of Materials*, **14**, 4752–4761 (2002).

60. Mikhaylova M., Kim D. K., Bobrysheva N., Osmolowsky M., Semenov V., Tsakalakos T., Muhammed M., 'Superparamagnetism of magnetite nanoparticles: Dependence on surface modification', *Langmuir*, **20**, 2472–2477 (2004).

61. Chen F., Gao Q., Hong G., Ni J., 'Synthesis of magnetite core–shell nanoparticles by

surface-initiated ring-opening polymerization of L-lactide', *Journal of Magnetism and Magnetic Materials*, **320**, 1921–1927 (2008).

62. Thunemann A. F., Schutt D., Kaufner L., Pison U., Mohwald H., 'Maghemite nanoparticles protectively coated with poly(ethylene imine) and poly(ethylene oxide)-block-poly(glutamic acid)', *Langmuir*, **15**, 2351–2357 (2006).

63. Liu R., Qu F., Guo Y., Yao N., Priestley R. D., 'Au@carbon yolk–shell nanostructures *via* one-step core–shell–shell template', *Chemical Communications*, **50**, 478–480 (2014).

64. Wu W., Shen J., Banerjee P., Zhou S., 'Core–shell hybrid nanogels for integration of optical temperature-sensing, targeted tumor cell imaging, and combined chemo-photothermal treatment', *Biomaterials*, **31**, 7555–7566 (2010).

65. Liu Y., Liu P., Wu D., Huang Y., Tang Y., Su Y., Zhang F., Feng X., 'Boron-doped, carbon-coated SnO_2/graphene nanosheets for enhanced lithium storage', *Chemistry - A European Journal*, **21**, 5617–5622 (2015).

66. Haldorai Y., Zong T., Shim J. J., 'Core-shell ZrO_2/PMMA composites *via* dispersion polymerization in superctitical fluid: Synthesis, characterization and mechanism', *Journal of Applied Polymer Science*, **123**, 1176–1183 (2012).

67. Xie L., Huang X., Wu C., Jiang P., 'Core-shell structured poly(methyl methacrylate)/$BaTiO_3$ nanocomposites prepared by in situ atom transfer radical polymerization: A route to high dielectric constant materials with the inherent low loss of the base polymer', *Journal of Materials Chemistry*, **21**, 5897–5906 (2011).

68. Huang X., Jiang P., 'Core-shell structured high-k polymer nanocomposites for energy storage and dielectric applications', *Advanced Materials*, **27**, 546–554 (2015).

69. Wang W., Jiang Y., Wen S., Liu L., Zhang L., 'Preparation and characterization of polystyrene/Ag core–shell microspheres – A bio-inspired poly(dopamine) approach', *Journal of Colloid and Interface Science*, **368**, 241–249 (2012).

70. Wang Z., Zhou Y., Yao Q., Sun Y., 'Preparation, characterization and infrared emissivity study of helical polyurethane@SiO_2 core-shell composite', *Applied Surface*

Science, **256**, 1404–1408 (2009).

71. Cheng Z., Zhang L., Zhu X., Kang E. T., Neoh K. G., 'Organic/inorganic hybrid nanospheres coated with palladium/P4VP shells from surface-initiated atom transfer radical polymerization', *Journal of Polymer Science Part A-Polymer Chemistry*, **46**, 2119–2131 (2008).

72. Nadagouda M. N., Varma R. S., 'Dextrose-templated microwave-assisted combustion synthesis of spongy metal oxides', *Smart Materials and Structures*, **15**, 1260–1265 (2006).

73. Sun Y., Zhou B., 'Single-crystalline Ag_2S hollow nanohexagons and their assembly into ordered arrays', *Materials Letters*, **64**, 1347–1349 (2010).

74. Li G. L., Möhwald H., Shchukin D. G., 'Precipitation polymerization for fabrication of complex core-shell hybrid particles and hollow structures', *Chemical Society Reviews*, **42**, 3628–3646 (2013).

75. Cai X., Yuan H., Blencowe A., Qiao G. G., Genzer J., Spontak R. J., 'Film-stabilizing attributes of polymeric core-shell nanoparticles', *ACS Nano*, **9**, 7940–7949 (2015).

76. Chicoma D. L., Carranza V., Giudici R., 'Synthesis of core-shell particles of polystyrene and poly(methyl methacrylate) using emulsion photopolymerization', *Macromolecular Symposia*, **324**, 124–133 (2013).

77. Quadir M. A., Radowski M. R., Kratz F., Licha K., Hauff P., Haag R., 'Dendritic multishell architectures for drug and dye transport', *Journal of Controlled Release*, **132**, 289–294 (2008).

78. Molberg M., Crespy D., Rupper P., Nüesch F., Månson J. A. E., Löwe C., Opris D. M., 'High breakdown field dielectric elastomer actuators using encapsulated polyaniline as high dielectric constant filler', *Advanced Functional Materials*, **20**, 3280–3291 (2010).

79. Ratha R., Goutam P. J., Iyer P. K., 'Photo stability enhancement of Poly(3-hexylthiophene)-PCBM nanocomposites by addition of multi walled carbon nanotubes under ambient conditions', *Organic Electronics*, **15**, 1650–1656 (2014).

80. Sun L., Wu W., Yang S., Zhou J., Hong M., Xiao X., Ren F., Jiang C., 'Template and

silica interlayer tailorable synthesis of spindle-like multilayer α-Fe_2O_3/Ag/SnO_2 ternary hybrid architectures and their enhanced photocatalytic activity', *ACS Applied Materials and Interfaces*, **6**, 1113–1124 (2014).

81. Zhou J., Ren F., Zhang S., Wu W., Xiao X., Liu Y., Jiang C., 'SiO_2–Ag–SiO_2–TiO_2 multi-shell structures: Plasmon enhanced photocatalysts with wide-spectral-response', *Journal of Materials Chemistry A*, **1**, 13128–13138 (2013).

82. Shen J., Zhu Y., Yang X., Zong J., Li C., 'Multifunctional Fe_3O_4@Ag/SiO_2/Au core-shell microspheres as a novel SERS-activity label *via* long-range plasmon coupling', *Langmuir*, **29**, 690–695 (2013).

83. Gutsche C., Lysov A., Braam D., Regolin I., Keller G., Li Z. A., Geller M., Spasova M., Prost W., Tegude F., 'n-GaAs/InGaP/p-GaAs core-multishell nanowire diodes for efficient light-to-current conversion', *Advanced Functional Materials*, **22**, 929–936 (2012).

84. Ma Y., Zhang B., Gu M., Huang S., Liu X., Liu B., Ni C., 'Bulk synthesis of homogeneous and transparent bulk core/multishell quantum dots/PMMA nanocomposites with bright luminescence', *Journal of Applied Polymer Science*, **130**, 1548–1553 (2013).

85. Yadav S., Chowdhury A., Sapra S., 'Thickness-dependent charge carrier dynamics in CdSe/ZnSe/CdS core/barrier/shell nanoheterostructures', *ChemPhysChem*, **17**, 692–698 (2016).

86. Li G., Tang Z., 'Noble metal nanoparticle@metal oxide core/yolk-shell nanostructures as catalysts: Recent progress and perspective', *Nanoscale*, **6**, 3995–4011 (2014).

87. Priebe M., Fromm K. M., 'Nanorattles or yolk-shell nanoparticles-what are they, how are they made, and what are they good for?', *Chemistry - A European Journal*, **21**, 3854–3874 (2014).

88. Liu J., Qiao S. Z., Chen J. S., Lou X. W., Xing X., Lu G. Q., 'Yolk/shell nanoparticles: New platforms for nanoreactors, drug delivery and lithium-ion batteries', *Chemical Communications*, **47**, 12578–12591 (2011).

89. Chandren S., Ohtani B., 'Preparation, characterization and photocatalytic performance of titania particles encapsulated in hollow silica shells as an efficient photocatalyst for redox-combined stereoselective synthesis of L-pipecolinic acid from L-lysine', *Journal of Photochemistry and Photobiology, A: Chemistry*, **246**, 50–59 (2012).

90. Yao B., Min L., Ma Z., Cheng W., 'Synthesis and characterization of hollow core-shell ZrO_2@void@$BiVO_4$ visible-light photocatalyst', *Advanced Materials Research*, **148-149**, 1331–1338 (2011).

91. Zhenmin L., Xiaoyong L., Hong W., Dan M., Chaojian X., Dan W., 'General synthesis of homogeneous hollow core-shell ferrite microspheres', *The Journal of Physical Chemistry C*, **113**, 2792–2797 (2009).

92. Wu W., Zhang S., Ren F., Xiao X., Zhou J., Jiang C., 'Controlled synthesis of magnetic iron oxides@SnO_2 quasi-hollow core-shell heterostructures: Formation mechanism, and enhanced photocatalytic activity', *Nanoscale*, **3**, 4676–4684 (2011).

93. Das S., Asefa T., 'Core–shell–shell microsphere catalysts containing Au nanoparticles for styrene epoxidation', *Topics in Catalysis*, **55**, 587–594 (2012).

94. Song J. R., Wen L. X., Shao L., Chen J. F., 'Preparation and characterization of novel Pd/SiO_2 and Ca-Pd/SiO_2 egg-shell catalysts with porous hollow silica', *Applied Surface Science*, **253**, 2678–2684 (2006).

95. Du N., Chen Y., Zhai C., Zhang H., Yang D., 'Layer-by-layer synthesis of γ-Fe_2O_3@SnO_2@C porous core-shell nanorods with high reversible capacity in lithium-ion batteries', *Nanoscale*, **5**, 4744–4750 (2013).

96. Kuai L., Geng B., Wang S., Sang Y., 'A general and high-yield galvanic displacement approach to Au-M (M=Au, Pd, and Pt) core-shell nanostructures with porous shells and enhanced electrocatalytic performances', *Chemistry - A European Journal*, **18**, 9423–9429 (2012).

97. Walther A., Muller A. H. E., 'Janus particles: Synthesis, self-assembly, physical properties, and applications', *Chemical Reviews*, **113**, 5194–5261 (2013).

98. De Gennes P. G., 'Soft Matter', *Science*, **256**, 495–497 (1992).

99. Feyen M., Weidenthaler C., Schüth F., Lu A. H., 'Regioselectively controlled synthesis of colloidal mushroom nanostructures and their hollow derivatives', *Journal of the American Chemical Society*, **132**, 6791–6799 (2010).

100. Hu S. H., Gao X., 'Nanocomposites with spatially separated functionalities for combined imaging and magnetolytic therapy', *Journal of the American Chemical Society*, **132**, 7234–7237 (2010).

101. Kim M., Song H., 'Precise adjustment of structural anisotropy and crystallinity on metal–Fe_3O_4 hybrid nanoparticles and its influence on magnetic and catalytic properties', *Journal of Materials Chemistry C*, **2**, 4997–5004 (2014).

102. Bang J. U., Lee S. J., Jang J. S., Choi W., Song H., 'Geometric effect of single or double metal-tipped CdSe nanorods on photocatalytic H_2 generation', *The Journal of Physical Chemistry Letters*, **3**, 3781–3785 (2012).

103. Lee J. H., Jun Y. W., Yeon S. I., Shin J. S., Cheon J., 'Dual-mode nanoparticle probes for high-performance magnetic resonance and fluorescence imaging of neuroblastoma', *Angewandte Chemie International Edition*, **45**, 8160–8162 (2006).

104. Ge J., Zhang Q., Zhang T., Yin Y., 'Core-satellite nanocomposite catalysts protected by a porous silica shell: Controllable reactivity, high stability, and magnetic recyclability', *Angewandte Chemie International Edition*, **47**, 8924–8928 (2008).

105. Choi I., Song H. D., Lee S., Yang Y. I., Kang T., Yi J., 'Core-satellites assembly of silver nanoparticles on a single gold nanoparticle *via* metal ion-mediated complex', *Journal of the American Chemical Society*, **134**, 12083–12090 (2012).

106. Xie L., Huang X., Li B. W., Zhi C., Tanaka T., Jiang P., 'Core-satellite Ag@$BaTiO_3$ nanoassemblies for fabrication of polymer nanocomposites with high discharged energy density, high breakdown strength and low dielectric loss', *Physical Chemistry Chemical Physics*, **15**, 17560–17569 (2013).

107. Liu Y., Tang Z., 'Multifunctional nanoparticle@MOF core-shell nanostructures', *Advanced Materials*, **25**, 5819–5825 (2013).

108. Zheng J., Cheng C., Fang W., Chen C., Yan R. W., Huai H. X., Wang C. C., 'Surfactant-

free synthesis of a Fe_3O_4@ZIF-8 core–shell heterostructure for adsorption of methylene blue', *CrystEngComm*, **16**, 3960–3964 (2014).

109. Zeng T., Zhang X., Wang S., Niu H., Cai Y., 'Spatial confinement of a Co_3O_4 catalyst in hollow metal-organic frameworks as a nanoreactor for improved degradation of organic pollutants', *Environmental Science and Technology*, **49**, 2350–2357 (2015).

110. Lin L., Zhang T., Liu H., Qiu J., Zhang X., 'In situ fabrication of a perfect Pd/ZnO@ZIF-8 core–shell microsphere as an efficient catalyst by a ZnO support-induced ZIF-8 growth strategy', *Nanoscale*, **7**, 7615–7623 (2015).

111. Yuan C., Zhang Y., He J., Ye S., Lei W., Liu X., Gu G., 'Strain-gradient facilitated formation of confined Ge/GeO_2 nanoparticles with a cracked shell and enhanced two-photon absorption', *Journal of Materials Chemistry C*, **2**, 8768–8772 (2014).

112. Wang K., Rai S. C., Marmon J., Chen J., Yao K., Wozny S., Cao B., Yan Y., Zhang Y., Zhou W., 'Nearly lattice matched all wurtzite CdSe/ZnTe type II core-shell nanowires with epitaxial interfaces for photovoltaics', *Nanoscale*, **6**, 3679–3685 (2014).

113. Ju D. X., Xu H. Y., Qiu Z. W., Zhang Z. C., Xu Q., Zhang J., Wang J. Q., Cao B. Q., 'Near room temperature, fast-response, and highly sensitive triethylamine sensor assembled with Au-loaded ZnO/SnO_2 core–shell nanorods on flat alumina substrates', *ACS Applied Materials and Interfaces*, **7**, 19163–19171 (2015).

114. Ren X., Zi W., Wei Q., Liu S., 'Fabrication gallium/graphene core–shell nanoparticles by pulsed laser deposition and their applications in surface enhanced Raman scattering', *Materials Letters*, **143**, 194–196 (2015).

115. Macias-Montero M., Pelaez R. J., Rico V. J., Saghi Z., Midgley P., Afonso C. N., Gonzalea-Elipe R., Borras A., 'Laser treatment of Ag@ZnO nanorods as long-life-span SERS surfaces', *ACS Applied Materials and Interfaces*, **7**, 2331–2339 (2015).

116. Lang L., Shi Y., Wang J., Wang F. Bin, Xia X. H., 'Hollow core–shell structured Ni–Sn@C nanoparticles: A novel electrocatalyst for the hydrogen evolution reaction', *ACS Applied Materials and Interfaces*, **7**, 9098–9102 (2015).

117. Wang W., Wang Y., Gu L., Lu R., Qian H., Peng X., Sha J., 'SiC@Si core–shell

nanowires on carbon paper as a hybrid anode for lithium-ion batteries', *Journal of Power Sources*, **293**, 492–497 (2015).

118. Hamzan N. B., Nordin F. N. B., Rahman S. A., Huang N. M., Goh B. T., 'Effects of substrate temperature on the growth, structural and optical properties of NiSi/SiC core–shell nanowires', *Applied Surface Science*, **343**, 70–76 (2015).

119. Li Y., Hu Y., Huo J., Jiang H., Li C., Huang C. J., 'Stable core shell Co_3Fe_7−$CoFe_2O_4$ nanoparticles synthesized *via* flame spray pyrolysis approach', *Industrial and Engineering Chemistry Research*, **51**, 11157–11162 (2012).

120. Kim M., Laine R. M., 'One-step synthesis of core-shell $(Ce_{0.7}Zr_{0.3}O_2)_x(Al_2O_3)_{1-x}$ [$(Ce_{0.7}Zr_{0.3}O_2)@Al_2O_3$] nanopowders *via* liquid-feed flame spray pyrolysis (LF-FSP)', *Journal of the American Chemical Society*, **131**, 9220–9229 (2009).

121. Li Y., Hu Y., Jiang H., Hou X., Li C., 'Construction of core–shell $Fe_2O_3@SnO_2$ nanohybrids for gas sensors by a simple flame-assisted spray process', *RSC Advances*, **3**, 22373–22379 (2013).

122. Hu Y., Shi Y., Jiang H., Huang G., Li C., 'Scalable preparation of ultrathin silica-coated Ag nanoparticles for SERS application', *ACS Applied Materials and Interfaces*, **5**, 10643–10649 (2013).

123. Cui C., Zhou P., Wu N., Lv Y., Liu X., 'Microwave absorption properties of Ag_3PO_4 nanoparticles-modified Ni@C nanocapsules', *Materials Letters*, **161**, 325–327 (2015).

124. Li D., Xie J., Zhang Y., Qiao R., Li S., Li Z., 'Convenient synthesis of magnetically recyclable Fe_3O_4@C@CdS photocatalysts by depositing CdS nanocrystals on carbonized ferrocene', *Journal of Alloys and Compounds*, **646**, 978–982 (2015).

125. Chen J., Xiao A., Zhang Z., Yu Y., Yan Z., 'The synthesis and modification of CdTe/CdS core shell quantum dots', *Spectrochimica Acta Part A: Molecular and Biomolecular Spectroscopy*, **151**, 506–509 (2015).

126. Zarghami Z., Maddahfar M., Ramezani M., '$Ag@Ag_2SO_4$ nanoparticles: Simple microwave-assistance synthesis, characterization and its co-photocatalytic degradation of methylene blue', *Journal of Materials Science: Materials in Electronics*, **26**, 6339–

6343 (2015).

127. Sardar D., Neogi S. K., Bandyopadhyay S., Satpati B., Ahir M., Adhikary A., Jain R., Gopinath C. S., Bala T., 'Multifaceted core–shell nanoparticles: Superparamagnetism and biocompatibility', *New Journal of Chemistry*, **39**, 8513–8521 (2015).

128. Hwang B. J., Sarma L. S., Chen C. H., Bock C., Lai F. J., Chang S. H., Yen S. C., Liu D. G., Sheu H. S., Lee J. F., 'Controlled synthesis and characterization of Ru_{core}-Pt_{shell} bimetallic nanoparticles', *The Journal of Physical Chemistry C*, **112**, 19922–19929 (2008).

129. Taufany F., Pan C. J., Rick J., Chou H. L., Tsai M. C., Hwang B. J., Liu D. G., Lee J. F., Tang M. T., Lee Y. C., Chen C. I., 'Kinetically controlled autocatalytic chemical process for bulk production of bimetallic core–shell structured nanoparticles', *ACS Nano*, **5**, 9370–9381 (2011).

130. Kim M. G., Sim S., Cho J., 'Novel core-shell Sn-Cu anodes for lithium rechargeable batteries prepared by a redox-transmetalation reaction', *Advanced Materials*, **22**, 5154–5158 (2010).

131. Knappett B. R., Abdulkin P., Ringe E., Jefferson D. A., Lozano-Perez S., Rojas T. C., Fernández A., Wheatley A. E. H., 'Characterisation of Co@Fe_3O_4 core@shell nanoparticles using advanced electron microscopy', *Nanoscale*, **5**, 5765–5772 (2013).

132. Hwang E. T., Lee Y. W., Park H. C., Kwak D. H., Kim D. M., Kim S. J., Kim M. C., Lee J. Y., Lee S., Park K. W., 'Synthesis of Pt-rich@Pt–Ni alloy core–shell nanoparticles using halides', *RSC Advances*, **5**, 8301–8306 (2015).

133. Baaziz W., Pichon B. P., Liu Y., Greneche J. M., Ulhaq-Bouillet C., Terrier E., Bergeard N., Halte V., Boeglin C., Choueikani F., Toumi M., Mhiri T., Begin-Colin S., 'Tuning of synthesis conditions by thermal decomposition toward core−shell $Co_xFe_{1-x}O$@$Co_yFe_{3-y}O_4$ and $CoFe_2O_4$ nanoparticles with spherical and cubic shapes', *Chemistry of Materials*, **26**, 5063–5073 (2014).

134. Nguyen T., Michael M., Mulvaney P., 'Synthesis of highly crystalline CdSe@ZnO nanocrystals *via* monolayer-by-monolayer epitaxial shell deposition', *Chemistry of Materials*, **26**, 4274–4279 (2014).

135. Rakkesh R. A., Durgalakshmi D., Balakumar S., 'Nanostructuring of a GNS-V_2O_5–TiO_2 core–shell photocatalyst for water remediation applications under sun-light irradiation', *RSC Advances*, **5**, 18633–18641 (2015).

136. Zhang Y., Xiang S., Zhou Y., Xu Y., Zhang Z., Sheng X., Wang Q., Zhang C., 'Enhanced catalytic activity with high thermal stability based on multiple Au cores in the interior of mesoporous Si–Al shells', *RSC Advances*, **5**, 48187–48193 (2015).

137. Zhang M., Fang K., Lin M., Hou B., Zhong L., Zhu Y., Wei W., Sun Y., 'Controlled fabrication of iron oxide/mesoporous silica core-shell nanostructures', *The Journal of Physical Chemistry C*, **117**, 21529–21538 (2013).

138. Hardiansyah A., Chen A. Y., Liao H. L., Yang M. C., Liu T. Y., Chan T. Y., Tsou H. M., Kuo C. Y., Wang J. K., Wang Y. L., 'Core-shell of FePt@SiO_2-Au magnetic nanoparticles for rapid SERS detection', *Nanoscale Research Letters*, **10**, 412/1–10 (2015).

139. Bayal N., Jeevanandam P., 'Synthesis of CuO@NiO core-shell nanoparticles by homogeneous precipitation method', *Journal of Alloys and Compounds*, **537**, 232–241 (2012).

140. Sadollahkhani A., Kazeminezhad I., Lu J., Nur O., Hultman L., Willander M., 'Synthesis, structural characterization and photocatalytic application of ZnO@ZnS core–shell nanoparticles', *RSC Advances*, **4**, 36940–36950 (2014).

141. Selvi N., Padmanathan N., Dinakaran K., Sankar S., 'Effect of ZnO, SiO_2 dual shells on CeO_2 hybrid core–shell nanostructures and their structural, optical and magnetic properties', *RSC Advances*, **4**, 55745–55751 (2014).

142. Satter S. S., Hoque M., Rahman M. M., Mollah M. Y. A., Susan M. A. B. H., 'An approach towards the synthesis and characterization of ZnO@Ag core@shell nanoparticles in water-in-oil microemulsion', *RSC Advances*, **4**, 20612–20615 (2014).

143. Ding H. L., Zhang Y. X., Wang S., Xu J. M., Xu S. C., Li G. H., 'Fe_3O_4@SiO_2 core/shell nanoparticles: The silica coating regulations with a single-core for different core sizes and shell thicknesses', *Chemistry of Materials*, **24**, 4572–4580 (2012).

144. Aubert T., Cabello-Hurtado F., Esnault M. A., Neaime C., Lebret-Chauvel D., Jeanne S., Pellen P., Roiland C., Le Polles L., Saito N., Kimoto K., Haneda H., Ohashi N., Grasset F., Cordier S., 'Extended investigations on luminescent $Cs_2[Mo_6Br_{14}]@SiO_2$ nanoparticles: Physico-structural characterizations and toxicity studies', *The Journal of Physical Chemistry C*, **117**, 20154–20163 (2013).

145. Fang Y., Loc W. S., Lu W., Fang J., 'Synthesis of $In_2O_3@SiO_2$ core-shell nanoparticles with enhanced deeper energy level emissions of In_2O_3', *Langmuir*, **27**, 14091–14095 (2011).

146. Kumar V. B., Gedanken A., Paik P., 'Triangular core-shell $ZnO@SiO_2$ nanoparticles', *ChemPhysChem*, **14**, 3215–3220 (2013).

147. Jhuang Y. Y., Cheng W. T., 'Fabrication and characterization of silver/titanium dioxide composite nanoparticles in ethylene glycol with alkaline solution through sonochemical process', *Ultrasonics Sonochemistry*, **28**, 327–333 (2016).

148. Tripathy S. K., Mishra A., Jha S. K., Wahab R., Al-Khedhairy A. A., 'Synthesis of thermally stable monodispersed $Au@SnO_2$ core-shell structure nanoparticles by a sonochemical technique for detection and degradation of acetaldehyde', *Analytical Methods*, **5**, 1456–1462 (2013).

149. Matin M. A., Lee E., Kim H., Yoon W., Kwon Y., 'Rational syntheses of Fe@(PtRu) nanoparticle electrocatalysts for methanol oxidation reaction with complete suppression of CO-poisoning and highly enhanced activity', *Journal of Materials Chemistry A*, **3**, 17154–17164 (2015).

150. Liu B., Wang J., Sun S., Wang X., Zhao M., Zhang W., Zhang H., Yang X., 'A general method for the synthesis of various rattle-type microspheres and their diverse applications', *RSC Advances*, **3**, 18506–18518 (2013).

151. Zeng T., Zhang X., Ma Y., Wang S., Niu H., Cai Y., 'A functional rattle-type microsphere with a magnetic-carbon double-layered shell for enhanced extraction of organic targets', *Chemical Communications*, **49**, 6039–6041 (2013).

152. Wu X. J., Xu D., 'Soft template synthesis of yolk/silica shell particles', *Advanced Materials*, **22**, 1516–1520 (2010).

153. Zhang W., Zhang H., Feng Y., Zhong X., 'Scalable single-step noninjection synthesis of high-quality core/shell quantum dots with emission tunable from violet to near infrared', *ACS Nano*, **6**, 11066–11073 (2012).

154. Nan W., Niu Y., Qin H., Cui F., Yang Y., Lai R., Lin W., Peng X., 'Crystal structure control of zinc-blende CdSe/CdS core/shell nanocrystals: Synthesis and structure-dependent optical properties', *Journal of the American Chemical Society*, **134**, 19685–19693 (2012).

155. Brus L., 'Electronic wave functions in semiconductor clusters: Experiment and theory', *The Journal of Physical Chemistry*, **90**, 2555–2560 (1986).

156. Li H., Yao C., Meng L., Sun H., Huang J., Gong Q., 'Photoelectrochemical performance of hydrogenated ZnO/CdS core-shell nanorod arrays', *Electrochimica Acta*, **108**, 45–50 (2013).

157. Reiss P., Protière M., Li L., 'Core/shell semiconductor nanocrystals', *Small*, **5**, 154–168 (2009).

158. Pal A., Srivastava S., Gupta R., Sapra S., 'Electron transfer from CdSe-ZnS core-shell quantum dots to cobalt (III) complexes', *Physical Chemistry Chemical Physics*, **15**, 15888–15895 (2013).

159. Yanover D., Vaxenburg R., Tilchin J., Rubin-brusilovski A., Zaiats G., Richard K. C., Sashchiuk A., Lifshitz E., 'Signifi cance of small-sized PbSe/PbS core/shell colloidal quantum dots for optoelectronic applications', *The Journal of Physical Chemistry C*, **118**, 17001–17009 (2014).

160. Zhong X., Xie R., Zhang Y., Basche T., Knoll W., 'High-quality violet- to red-emitting ZnSe/CdSe core/shell nanocrystals', *Chemistry of Materials*, **17**, 4038–4042 (2005).

161. Sun Z., Kumbhar A., Sun K., Liu Q., Fang J., 'One-pot synthesis of reverse type-I In_2O_3@In_2S_3 core–shell nanoparticles', *Chemical Communications*, 1920–1922 (2008).

162. Soni U., Pal A., Singh S., Mittal M., Yadav S., Elangovan R., Sapra S., 'Simultaneous type-I/type-II emission from CdSe/CdS/ZnSe nano-heterostructures', *ACS Nano*, **8**, 113–123 (2014).

163. Ca N. X., Lien V. T. K., Nghia N. X., Chi T. T. K., Phan T. L., 'Tunable luminescent emission characterization of type-I and type-II systems in CdS–ZnSe core–shell nanoparticles: Raman and photoluminescence study', *Nanotechnology*, **26**, 445701/1–8 (2015).

164. Patange M., Biswas S., Yadav A. K., Jha S. N., Bhattacharyya D., 'Morphology-controlled synthesis of monodispersed graphitic carbon coated core/shell structured Ni/NiO nanoparticles with enhanced magnetoresistance', *Physical Chemistry Chemical Physics*, **17**, 32398–32412 (2015).

165. López-Ortega A., Estrader M., Salazar-Alvarez G., Estradé S., Golosovsky I. V., Dumas R. K., Keavney D. J., Vasilakaki M., Trohidou K. N., Sort J., Peiró F., Suriñach S., Baró M. D., Nogués J., 'Strongly exchange coupled inverse ferrimagnetic soft/hard, $Mn_xFe_{3-x}O_4/Fe_xMn_{3-x}O_4$, core/shell heterostructured nanoparticles', *Nanoscale*, **4**, 5138–5147 (2012).

166. Liu X., Liu H. L., Fang N., Li X. M., Guo W. H., Wu J. H., Zhao M. X., 'Facile synthesis of multifunctional $La_{1-x}Sr_xMnO_3$@Au core–shell nanoparticles for biomedical applications', *RSC Advances*, **5**, 95454–95462 (2015).

167. Zheng X., Yan X., Sun Y., Bai Z., Zhang G., Shen Y., Liang Q., Zhang Y., 'Au-embedded ZnO/NiO hybrid with excellent electrochemical performance as advanced electrode materials for supercapacitor', *ACS Applied Materials and Interfaces*, **7**, 2480–2485 (2015).

168. Zhu M., Huang X., Yang K., Zhai X., Zhang J., He J., Jiang P., 'Energy storage in ferroelectric polymer nanocomposites filled with core−shell structured polymer@$BaTiO_3$ nanoparticles: Understanding the role of polymer shells in the interfacial regions', *ACS Applied Materials and Interfaces*, **6**, 19644–19654 (2014).

169. Huang X., Yu Y. Q., Xia J., Fan H., Wang L., Willinger M. G., Yang X. P., Jiang Y., Zhang T. R., Meng X. M., 'Ultraviolet photodetectors with high photosensitivity based on type-II ZnS/SnO_2 core/shell heterostructured ribbons', *Nanoscale*, **7**, 5311–5319 (2015).

170. Narayanamoorthy B., Kumar B. V. V. S. P., Eswaramoorthy M., Balaji S., 'Oxygen

reduction reaction catalyzed by platinum nanonetwork prepared by template free one step synthesis for polymer electrolyte membrane fuel cells', *Materials Research Bulletin*, **55**, 137–145 (2014).

171. Pramod P. S., Shah R., Chaphekar S., Balasubramanian N., Jayakannan M., 'Polysaccharide nano-vesicular multidrug carriers for synergistic killing of cancer cells.', *Nanoscale*, **6**, 11841–11855 (2014).

172. Zhang Q., Lee I., Joo J. B., Zaera F., Yin Y., 'Core-shell nanostructured catalysts', *Accounts of Chemical Research*, **46**, 1816–1824 (2013).

173. Ikenberry M., Peña L., Wei D., Wang H., Bossmann S. H., Wilke T., Wang D., Komreddy V. R., Rillema D. P., Hohn K. L., 'Acid monolayer functionalized iron oxide nanoparticles as catalysts for carbohydrate hydrolysis', *Green Chemistry*, **16**, 836–843 (2014).

174. Chen C., Fang X., Wu B., Huang L., Zheng N., 'A multi-yolk-shell structured nanocatalyst containing sub-10 nm Pd nanoparticles in porous CeO_2', *ChemCatChem*, **4**, 1578–1586 (2012).

175. Kumar A. S., Datta K. K. R., Rao T. S., Raghavan K. V, Eswaramoorthy M., Reddy B. V. S., 'Pd-aminoclay nanocomposite as an efficient recyclable catalyst for hydrogenation and Suzuki cross coupling reactions', *Journal of Nanoscience and Nanotechnology*, **12**, 2000–2007 (2012).

176. Dhital R. N., Kamonsatikul C., Somsook E., Sakurai H., 'Bimetallic gold–palladium alloy nanoclusters: An effective catalyst for Ullmann coupling of chloropyridines under ambient conditions', *Catalysis Science and Technology*, **3**, 3030–3035 (2013).

177. Kou J., Saha A., Bennett-Stamper C., Varma R. S., 'Inside-out core-shell architecture: Controllable fabrication of Cu_2O@Cu with high activity for the Sonogashira coupling reaction', *Chemical Communications*, **48**, 5862–5864 (2012).

178. Prasad K., Ashokkumar M., 'Photocatalytic properties of CdS nanoparticles synthesized under various ultrasonic operating conditions', *Industrial and Engineering Chemistry*, **53**, 715–722 (2014).

179. Gao M., Zhu L., Ong W., Wang J., Wei Ho G., 'Structural design of TiO_2-based photocatalyst for H_2 production and degradation applications', *Catalysis Science and Technology*, **5**, 4703–4726 (2015).

180. Kumar S., Baruah A., Tonda S., Kumar B., Shanker V., Sreedhar B., 'Cost-effective and eco-friendly synthesis of novel and stable N-doped ZnO/g-C_3N_4 core–shell nanoplates with excellent visible-light responsive photocatalysis', *Nanoscale*, **6**, 4830–4842 (2014).

181. Moniz S. J. A., Shevlin S. A., Martin D. J., Guo Z. X., Tang J., 'Visible-light driven heterojunction photocatalysts for water splitting–a critical review', *Energy and Environmental Science*, **8**, 731–759 (2015).

182. Chen Y. Z., Xu Q., Yu S. H., Jiang H. L., 'Tiny Pd@Co core-shell nanoparticles confined inside a metal-organic framework for highly efficient catalysis', *Small*, **11**, 71–76 (2015).

183. Rai P., Majhi S. M., Yu Y. T., Lee J. H., 'Noble metal@metal oxide semiconductor core@shell nano-architectures as a new platform for gas sensor applications', *RSC Advances*, **5**, 76229–76248 (2015).

184. Majhi S. M., Rai P., Yu Y., 'Facile approach to synthesize Au@ZnO core–shell nanoparticles and their application for highly sensitive and selective gas sensors', *ACS Applied Materials and Interfaces*, **7**, 9462–9468 (2015).

185. Duan J., Zhang H., Tang Q., He B., Yu L., 'Recent advances in critical materials for quantum dot-sensitized solar cells: A review', *Journal of Materials Chemistry A*, **3**, 17497–17510 (2015).

186. Etgar L., Yanover D., Capek R. K., Vaxenburg R., Xue Z., Liu B., Nazeeruddin M. K., Lifshitz E., Gratzel M., 'Core/shell PbSe/PbS QDs TiO_2 heterojunction solar cell', *Advanced Functional Materials*, **23**, 2736–2741 (2013).

187. Jiao S., Shen Q., Mora-Sero I., Wang J., Pan Z., Zhao K., Kuga Y., Zhong X., Bisquert J., 'Band engineering in core/shell ZnTe/CdSe for photovoltage and efficiency enhancement in exciplex quantum dot sensitized solar cells', *ACS Nano*, **9**, 908–915 (2015).

188. Purbia R., Paria S., 'Yolk/shell nanoparticles: Classifications, synthesis, properties, and applications', *Nanoscale,* **7**, 19789–19873 (2015).

189. Liu J., Cheng J., Che R., Xu J., Liu M., Liu Z., 'Double-shelled yolk−shell microspheres with Fe_3O_4 cores and SnO_2 double shells as high-performance microwave absorbers', *The Journal of Physical Chemistry C,* **117**, 489–495 (2013).

190. Pramod P. S., Shah R., Jayakannan M., 'Dual stimuli polysaccharide nanovesicles for conjugated and physically loaded doxorubicin delivery in breast cancer cells', *Nanoscale,* **7**, 6636–6652 (2015).

191. Chen R., Zhang J., Wang Y., Chen X., Zapien J. A., Lee C. S., 'Graphitic carbon nitride nanosheet@metal–organic framework core–shell nanoparticles for photo-chemo combination therapy', *Nanoscale,* **7**, 17299–17305 (2015).

Chapter-2

Experimental Techniques

To investigate the properties of core-shell nanoparticles in depth, various analytical techniques are required. In the present study, the synthesized core-shell nanoparticles were investigated using a set of techniques such as powder X-ray diffraction (PXRD), Fourier transform infrared spectroscopy (FT-IR), thermal gravimetric analysis (TGA), field emission scanning electron microscopy (FE-SEM), energy dispersive X-ray analysis (EDXA), transmission electron microscopy (TEM) and selected area electron diffraction (SAED). The oxidation state of metal and atomic composition were investigated using X-ray photoelectron spectroscopy (XPS). The surface charge of the core-shell nanoparticles was studied using zeta potential measurements. The surface area analysis was carried out using BET surface area analyzer. After thorough characterization, optical properties of the core-shell nanoparticles were investigated using UV-Visible diffuse reflectance spectroscopy (DRS) and photoluminescence spectroscopy (PL). To monitor the concentration of various dyes during photodegradation, adsorption and reduction experiments, UV-Visible spectroscopy was employed. A brief description of the analytical techniques used and the corresponding sample preparation methods have been discussed below.

2.1. Powder X-ray Diffraction (PXRD)

Powder X-ray diffraction is an important tool to identify the state of solid sample (amorphous or crystalline), phase purity, crystallographic structure, and crystallite size. Powder XRD is a non-destructive technique [1]. According to Bragg's law, when X-ray radiation is incident on a sample surface, diffraction takes place with an angle of diffraction equal to angle of incidence. The diffracted beam undergoes constructive interference when the path length between the beams is an integral multiple of the incident X-ray wavelength. It is expressed as follows.

$$n\lambda = 2d\ sin\theta \qquad (1)$$

where n is the order of diffraction (n = 1, 2, 3), λ is wavelength of the X-ray radiation, d is the interplanar spacing between the planes, and θ is the angle of diffraction [1].

In the case of core-shell nanoparticles, XRD results give an indirect evidence for the presence of a shell on the core surface. On coating of a complete shell on the core, the XRD peak intensity of core nanoparticles usually reduces as compared to that of pure core nanoparticles [2]. In some of the cases, XRD peaks of core nanoparticles completely vanish due to thicker coating of shell nanoparticles [2].

In the present work, the XRD patterns of all the synthesized core-shell nanoparticles were recorded on a Brucker AXS-D8 diffractometer at room temperature. About 100 mg of powder sample was filled in the sample groove and the sample surface was flattened using a glass slide. Then, the sample groove is placed on the sample holder to run the XRD measurements. All the XRD input parameters were given using DIFFRAC^{plus} software and the data evolution was carried out using EVA® software. The following instrumental parameters were employed during the XRD measurements; the X-ray source used was Cu-K_α radiation (λ = 1.5406 Å) and the instrument was operating at 40 kV and 40 mA. All the XRD patterns were recorded in the 2θ range of 5-90^o with a goniometer speed of 1^o/min. The obtained XRD patterns were analyzed using JCPDS (Joint committee on powder diffraction standards) database. The effect of finite crystallite size or grain size on the core-shell nanoparticles is measured by peak broadening and change in intensity of the peaks in the X-ray diffraction pattern, which is explained by the Debye-Scherrer equation and it is expressed as follows [3].

$$\delta = \frac{K\lambda}{\beta\, Cos\theta} \qquad (2)$$

where, δ is the average crystallite size of nanoparticles in nm, K is a dimensionless constant and it varies between 0.89 to 1.39 (for most of the two dimensional lattices, it is taken as 0.89), λ is the wavelength of Cu-K_α X-ray radiation, β is the full width at half maximum, and θ is the Bragg angle. In the present study, the most intense XRD peaks of either the core or the shell nanoparticles were chosen for the crystallite size calculations.

2.2. Fourier Transform Infrared Spectroscopy (FT-IR)

FT-IR spectroscopy is a sensitive technique and it gives information about surface functional groups, ligands, intercalated molecules, and nature of metal-oxygen interactions in inorganic materials. The basic principle of FT-IR spectroscopy is that when IR radiation (400-4000 cm^{-1}) falls on the sample surface, vibrational transitions occur in molecules [4]. The frequency of the absorbed IR radiation is equal to the vibrational transition energy of a group of the molecules. In the case of core-shell nanoparticles, FT-IR results give information on surface functional groups present on the core surface. Appropriate functional groups can be coated on a core surface using various ligands to deposit a uniform shell of interest which can be analyzed using FT-IR spectroscopy [5].

In the present study, FT-IR spectra of the synthesized core-shell nanoparticles were carried out on a Thermo Nicolet infrared spectrometer in the range of 400-4000 cm^{-1} with 16 scans.

Initially, the background was corrected using potassium bromide (Aldrich®) pellet. All the sample powders were prepared using KBr pellet method (KBr: sample = 100: 1). To prepare the pellet, the samples were mixed with potassium bromide and grounded into a fine powder in a mortar and the pellet was prepared using a hydraulic press. All the instrumental input parameters were given using Omnic® software. The baseline correction was carried out for all the samples using automatic baseline correction.

2.3. Thermal Gravimetric Analysis (TGA)

Thermogravimetry is a destructive technique, in which change in the weight of a sample is recorded as a function of time or temperature [6]. It provides quantitative information about the sample which is based on weight loss of the sample. The plot between percentage weight loss and temperature or time is called a thermogram. The important requirement for this technique is precision balance with a programmed furnace for a linear rise of temperature with respect to time. The derivative thermogravimetric (DTG) curve is obtained by measuring the first derivative of thermogravimetric (TG) curve [6]. A few milligrams of the sample was placed in a precision balance and heated to high temperatures (e.g. 1000 ^{o}C) under air or inert atmosphere. In the present study, TGA patterns of silica, surface modified ZnO, SiO_2@α-$Co(OH)_2$, SiO_2@Ni-Co mixed metal hydroxides and Cu_2O samples were recorded on a EXSTAR TG/DTA 3600 instrument. About 10 mg of the sample was used for the TG analysis. All the samples were heated under air in the temperature range of 25-1000 ^{o}C and the heating rate was 10 ^{o}/min.

2.4. Field Emission Scanning Electron Microscopy (FE-SEM) and Energy Dispersive X-ray Analysis (EDXA)

FE-SEM is an important analytical tool to investigate the sample topography, and morphology. An electron beam passes through narrow magnetic lenses and reach to LaB_6 electron gun tip (electric field at the tip is about 10^7 V/cm). The primary electron beam and the sample surface moves in a raster pattern (point-by-point) and form a three dimensional image [7]. FE-SEM has higher magnification, greater resolution, and large depth of field. The interaction of electron beam on a sample surface results in emission of characteristic X-rays, secondary electrons, back scattered electrons, Auger electrons and cathode luminescence [7]. The emitted back scattered electrons are detected by surface barrier detector, secondary electrons are detected by Everhurt-Thronley detector, and the X-rays are detected by photomultiplier tube. The emitted X-rays have characteristic energy for a particular element and its intensity is

directly proportional to the concentration of a particular element [7]. In the case of core-shell nanoparticles, FE-SEM analysis cannot distinguish clearly core from the shell and it provides only a surface image. But when it is coupled with EDX analysis, determination of elemental composition is possible [2].

In the present study, FE-SEM images of all the synthesized core-shell nanoparticles were recorded using a FEI Quanta 200F or Carl Zeiss ULTRA plus field emission electron microscopes operating at 15 or 20 kV. The sample chamber was maintained under high vacuum of about 10^{-7} Torr, which avoids reduction in the electron beam intensity and reduction in contrast of the images caused by gaseous molecules present in the chamber. Very fine FE-SEM images were recorded by adjusting the stigmator, which controls the optical aberrations. The elemental composition (atomic percent and weight percent) of all the core-shell nanoparticles were estimated at different spots and areas in the FE-SEM images. The sample preparation for SEM or EDX analysis was as follows. Initially, isoamyl alcohol was taken on a smooth cloth and bras stubs were cleaned thoroughly. After that, conducting carbon tape was stuck on the bras stub and the sample powder was smeared on the stub. To avoid charging during the SEM measurements, gold sputtering was carried out for about 100 seconds at 30 mA of current density.

2.5. Transmission Electron Microscopy (TEM)

TEM is a perfect analytical tool to confirm the formation of a core-shell structure based on contrast difference between the core and the shell. It gives information about core size, shell thickness, and the overall shape and mean diameter of the particles. A high energetic (e.g. 200 kV) and narrow electron beam passes through the magnetic lenses and strikes the sample surface under high vacuum. The transmitted electrons from the sample surface forms a two-dimensional image on a charge coupled device (CCD) or a scintillation screen [2, 7]. In recent years, high resolution transmission electron microscopy (HRTEM) has been introduced which is able to provide images at a point resolution of 0.24 nm and a line resolution of 0.14 nm. HRTEM gives the information about lattice fringes and lattice planes of both the core and shell nanoparticles. The selected area electron diffraction (SAED) provides information about the crystallinity and lattice planes [7].

In the present study, TEM images of all the core-shell nanoparticles were recorded on a TECHNAI G^2 20 S-TWIN transmission electron microscope operating at a voltage of 200 kV. A LaB_6 thermionic cathode was used as a high energetic electron source. The sample

preparation for the TEM measurements is as follows. About 2 mg each of the synthesized core-shell nanoparticle powder samples was dispersed in about 5 mL of ethanol and sonicated for about 15 min which avoids aggregation of the particles and makes a good dispersion. After that, about two to three drops of the suspension was placed on a carbon coated copper grid with the help of a micropipette and the grids were dried under air for overnight. In the sample chamber of TEM, high vacuum of 1×10^{-9} Torr was created using a turbo molecular pump and an ion getter pump. Then, the sample grids were inserted into the sample holder and the electron beam was focused on the sample by adjusting Z-height of the sample specimen. Finally, images of the samples were seen on a fluorescent screen which were recorded using a charge coupled device (CCD) detector. To record a SAED pattern, the objective aperture was removed and SAD aperture was inserted. Then, the electron beam was focused on image of the back focal plane of the objective lens. The role of SAD aperture is to limit the sample volume and intensity of the electron beam that contributes to the diffraction pattern.

2.6. X-ray Photoelectron Spectroscopy (XPS)

XPS is an important technique which gives information about the surface composition, depth profiling, empirical formula, and electronic state of the metal. It is a surface sensitive technique and it requires ultrahigh vacuum of about 10^{-9} Torr [8]. The basic principle involved in XPS is photoelectric effect discovered by Albert Einstein in 1905 and it was successfully demonstrated by Kai Siegbahn and his group in 1961 [8]. Two types of X-ray sources are used; they are Mg K_α (1253.6 eV) and Al K_α (1486.6 eV). The X-ray source hits the solid sample surface and emits the core electrons with characteristic binding energy corresponding to a particular element. The number of electrons emitted and their kinetic energy in the depth of 1-10 nm from the surface are analyzed using a cylindrical mirror analyzer.

In the present study, the oxidation state of silver and surface composition of ZnO@Ag core-shell nanoparticles (Chapter-4) were studied using a VG Microtech ESCA (XPS) 3000 spectrometer with Al K_α X-ray source. The sample preparation for XPS was as follows. First, a few milligrams of sample powder was sprinkled on a carbon tape and introduced into a low vacuum chamber which was in contact with the environment. Once ultrahigh vacuum was attained in the second chamber, the sample was introduced into the ultrahigh vacuum chamber. After that, any contaminated gases present on sample surface was removed by bombardment with argon ions (Ar^+). Then, the survey spectrum of the sample was recorded and the peaks of various elements were analyzed. The binding energy values give information about the

oxidation state of the metal and the intensity gives information regarding the surface composition.

2.7. Zeta Potential Measurements

Zeta potential gives information about surface charge of core-shell nanoparticles. It helps in choosing appropriate shell material to coat on a particular core based on the surface charge. Zeta potential works on the principle of laser Doppler micro-electrophoresis. When an electric field is applied to a colloidal solution, the sol particles move with a velocity according to their Zeta potential. The velocity is calculated using phase analysis light scattering [9]. In the present study, surface charge of SiO_2, $NiCo_2O_4$ nanoparticles, and SiO_2@Ni-Co mixed metal oxide core-shell nanorattles (Chapter-5) were analyzed using a Malvern Zetasizer (Nanoseries, Nano ZS-90). The instrumental input parameters were given using Malvern Zetasizer (version 7.03) software. To measure the zeta potential, about 0.1 milligram of each sample powder was dispersed in 10 mL of Millipore® water and sonicated for about 5 min. A few milliliter of the obtained colloid solution was injected into a capillary cell using a syringe and the cell was introduced into the sample chamber. The Zeta potential measurements were then carried out using the standard operating procedure.

2.8. Surface Area Measurements (BET)

Surface area analysis provides information about specific surface area, pore size and pore volume of the materials. Mostly nitrogen gas is used as the adsorbate and the adsorption or desorption of nitrogen gas on the surface of a material is measured as a function of relative pressure P/P_o [10]. Brunauer-Emmett-Teller (BET) method is the mostly commonly used method to measure the specific surface area of the materials whereas Barrett–Joyner–Halenda (BJH) method is used for the determination of pore volume and pore size of the materials [2].

In the present study, the specific surface area of different shaped Cu_2O polyhedral microcrystals and Cu_2O@Ag polyhedral core-shell nanoparticles (Chapter-4), SiO_2, Co_3O_4, and SiO_2@Co_3O_4 core-shell nanorattles (Chapter-5), $NiCo_2O_4$ and SiO_2@Ni-Co mixed metal oxide core-shell nanorattles (Chapter-5) were analyzed using Nova 2200e Quantachrome instrument and nitrogen gas was used as the adsorbate. All the measurements were carried out at 77 K *via* nitrogen gas adsorption. For the surface area measurements, about 100 mg of the sample powder was weighed in a glass bulb which was degassed under vacuum at 150 ^oC for about 2 hours. After that, the sample bulbs were attached to the measurement stations and the

input parameters were given using Quantachrome™ NOVA Win software. Surface area of the materials was calculated using BET multi-point method and the formula is as follows.

$$S_t = \frac{W_m N A_{cs}}{M} \quad (3)$$

where S_t is total surface area, W_m is the weight of monolayer of adsorbate, N is Avogadro's number, A_{cs} is cross sectional area of adsorbate molecule (N_2), and M is molar mass of the adsorbate.

The specific surface area of the materials was calculated using the following equation.

$$S = S_t / w \quad (4)$$

where w is weight of the sample.

2.9. UV-Visible Spectroscopy

The basic principle involved in UV-Visible spectroscopy is the absorption of UV or visible light of electromagnetic radiation (200-800 nm) by molecules which causes excitation of electrons [11]. UV-Visible diffuse reflectance spectroscopy (DRS) provides information about band gap of semiconductor nanoparticles. In the case of solid samples, when a beam of light hits the surface of sample, it undergoes reflection in various directions which is measured as reflectance [12]. In the present study, diffuse reflectance spectra of all the synthesized samples were carried out in the reflectance mode and the slit width used was 5 nm with a time constant of 0.1 seconds. The wavelength range used was 300-700 nm for SiO_2@CdS and ZnO@CdS core-shell nanoparticles (Chapter-3), 350-550 nm for ZnO@Ag core-shell nanoparticles (Chpater-4), 360-800 nm for SiO_2@Co_3O_4 core-shell nanorattles and 280-800 nm for SiO_2@Ni-Co mixed metal oxide core-shell nanorattles (Chpater-5) and the DRS measurements of all these samples were carried out on a Shimadzu UV-2450 UV-Vis spectrophotometer attached with a diffuse reflectance accessory. The diffuse reflectance spectra of Cu_2O@Ag polyhedral core-shell nanoparticles were recorded on a Varian Carry 5000 UV-VIS-NIR spectrophotometer in the wavelength range of 350-650 nm (Chapter-4). The sample preparation for the DRS measurements is as follows. About 40 mg of the sample powder was mixed thoroughly with about 4 g of $BaSO_4$ using a mortar and pestle. Before running measurements on the samples, baseline correction was carried out using $BaSO_4$ as the reference material. The obtained percentage of reflectance was converted to absorbance unit using Kubelka-Munk equation which is expressed as follows.

$$F(R_\infty) = \frac{(1-R_\infty)^2}{2R_\infty} = \frac{AC}{S} = \frac{K}{S} \quad (5)$$

where $F(R_\infty)$ is remission or Kubelka-Munk function, R_∞ is the percentage of reflectance of an infinitely thick sample, A is the absorbance, C is the concentration of absorbing species, S is the scattering coefficient, and K is the absorption coefficient [12]. The band gap of core-shell nanoparticle samples was estimated from $(\alpha h\nu)^2$ versus $h\nu$ plots.

In the case of liquid samples, absorbance was measured using UV-Visible spectroscopy at ambient conditions. In the present study, photodegradation of methylene blue, peroxidase activity of 3,3',5,'5'-tetramethyl benzidine (TMB), adsorption of mixture of rhodamine B and methylene blue in aqueous solutions, and reduction of 4-nitro phenol and methylene blue in aqueous solutions (Chapter-6) were studied using a Shimadzu UV-2450 UV-Visible spectrophotometer. All the measurements were carried out using quartz cuvettes in the absorbance mode and the slit width used was 5 nm with a time constant of 0.1 seconds. Initially, by keeping both the reference and sample cuvettes in their compartments with the solvent, baseline correction was made. After that, the sample solution was placed in one cuvette and other one was filled with the solvent and the absorbance spectra in the wavelength range of 200-800 nm were recorded.

2.10. Photoluminescence Spectroscopy (PL)

Photoluminescence spectroscopy provides information about band edge emission and surface defect states present in semiconductor nanoparticles. The absorption of either UV or visible light by a semiconductor promotes the excitation of electrons from valence band to conduction band. The electrons return back to the valence band *via* radiative or non-radiative recombinations [8]. The emitted emission depends on different singlet or triplet excited states and based on that photoluminescence is divided into several types. They are fluorescence, phosphorescence, cathodoluminescence, and electroluminescence [8, 12]. The mostly used term to indicate photoluminescence is either fluorescence or phosphorescence.

In the present study, photoluminescence spectra of the samples were carried out using Shimadzu RF 5301-PC fluorescence spectrophotometer. The instrumental parameters were as follows. All the spectra were recorded in emission mode. Both the excitation and emission slit widths were kept as 5 nm, and Xenon lamp was used as the source. The PL spectra were recorded in the wavelength range of 400-700 nm for SiO_2@CdS core-shell nanoparticles and the excitation wavelength was 380 nm (Chapter-3), 350-700 nm for ZnO@CdS core-shell

nanoparticles (Chapter-3) and 350-600 nm for ZnO@Ag core-shell nanoparticles (Chapter-4) and in both the cases (ZnO@CdS and ZnO@Ag), the excitation wavelength used was 325 nm. The sample preparation for the PL measurements was as follows. About 5 mg of the sample powder was dispersed in about 5 mL of methanol and sonicated for about 10 min to obtain a uniform suspension. Then, the PL measurements were carried out using the prepared suspensions.

References

1. Cullity B. D., Stock S. R., 'Elements of X-Ray Diffraction', *Addison-Wesley Publishing Company, Inc., Massachusetts* (1956).

2. Chaudhuri R. G., Paria S., 'Core/shell nanoparticles: Classes, properties, synthesis mechanisms, characterization, and applications', *Chemical Reviews*, **112**, 2373–2433 (2012).

3. Patterson A. L., 'The Scherrer formula for X-ray particle-size determination', *Physical Review*, **56**, 978-982 (1939).

4. Silverstein R. M., Webster F. X., 'Spectrometric identification of organic compounds', 6th edition, *John Wiley & Sons, New Jersey* (2005).

5. Kalska-Szostko B., Wykowska U., Satula D., Zambrzycka E. 'Stability of core-shell magnetite nanoparticles', *Colloids and Surfaces, B: Biointerfaces*, **113**, 295-301 (2014).

6. Jeffery G. H., Bassett J., Mendham J., Denney R. C., 'Textbook of quantitative chemical analysis', 5th edition, *John Wiley & Sons, Inc., New York* (1989).

7. Pradeep T., 'Nano: The essentials, understanding nanoscience and nanotechnology', *Tata McGraw-Hill, New Delhi* (2007).

8. Patnaik P., 'Dean's analytical chemistry handbook', 2nd edition, *McGraw-Hill Handbooks, United States of America* (2004).

9. http://www.malvern.com/en/products/product-range/zetasizer-range/zetasizer-nano-range/zetasizer-nano-zs90/

10. Gawande M. B., Goswami A., Asefa T., Guo H., Biradar A. V, Peng D.-L., Zboril R., Varma R. S., 'Core-shell nanoparticles: Synthesis and applications in catalysis and electrocatalysis', *Chemical Society Reviews*, **44**, 7540–7590 (2015).

11. Harvey D., 'Modern analytical chemistry', *The McGraw Hill Companies, Inc., United States of America* (2000).

12. Kortum G., 'Reflectance spectroscopy. Principles, methods, applications', *Springer-Verlag-New York Inc.* (1969).

Chapter-3

Synthesis of SiO_2@CdS (Type-I) and ZnO@CdS (Type-II) Core-Shell Nanoparticles *via* a Novel Thermal Decomposition Approach

3.1 Synthesis of SiO_2@CdS (Type-I) Core-Shell Nanoparticles *via* a Novel Thermal Decomposition Approach

3.1.1 Introduction

Over the past decade, scientists have been devoting their efforts to make advanced heteronanostructures which can be useful in multi-functional applications. Among them, core-shell nanoparticles have attracted significant attention due to their versatile physicochemical properties and various functional applications [1–4]. The physicochemical properties of core-shell nanoparticles are strongly dependent on size of the core, the shell and the ratio of core to shell nanoparticles [5]. Core-shell nanoparticles have been used in various interdisciplinary fields such as material science, chemistry, physics, electronics, biology, etc [1–3,5–7]. These materials show improved properties and activity as compared to their counter parts which is attributed to synergistic interaction between the constituents at the interface. Due to their improved activity, core-shell nanoparticles have been used in different applications such as photocatalysis, adsorption, data storage, supercapacitors, solar cells, drug delivery, bio-imaging, tumor therapy, etc [2,3,8–12].

Among the core-shell nanoparticles, optoelectronic core-shell nanoparticles have great impact in various applications such as photocatalysis, water splitting, energy storage devices, surface enhanced Raman scattering (SERS) substrates, solar cells, and LEDs' [13–17]. Various optoelectronic core-shell nanoparticles have been reported and some examples are Au@Ag [18], Au@Pd [19], SnO_2@ZnO@SiO_2 [20], $CuInS_2$@ZnS [21], Au@polystyrene [22], ZnTe@ZnS [23], CdSe@CdS [24], ZnO@In_2S_3 [25], etc. The TEM images of Au@polystyrene and ZnO@In_2S_3 core-shell nanoparticles are shown in Figure 3.1.1.

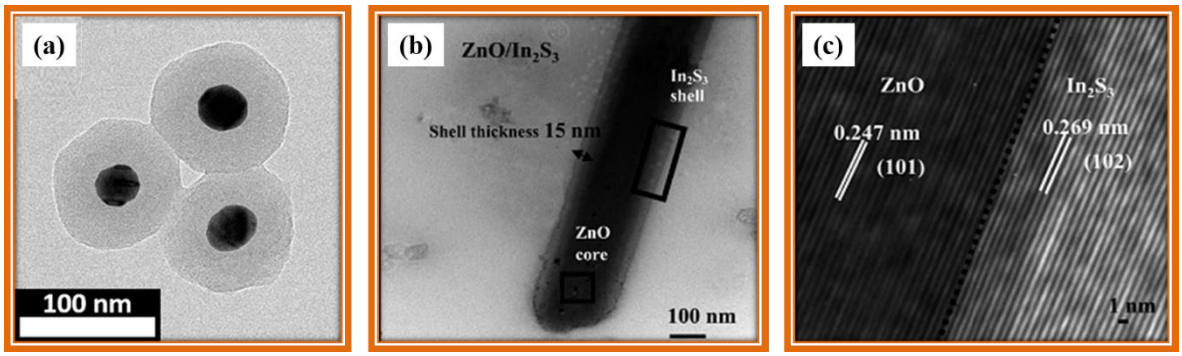

Fig. 3.1.1: (a) TEM image of Au@polystyrene core-shell nanoparticles [22], and **(b, c)** TEM and HRTEM images of ZnO@In_2S_3 core-shell nanoparticles [25].

Now-a-days, metal sulfide nanoparticles such as CdS, ZnS, CoS, Bi_2S_3, SnS_2, etc., have attracted great attention of scientists due to their unique optoelectronic properties. They have potential applications in photocatalysis, fuel cells, drug delivery, solar cells, and sensing [26–31]. The metal sulfide nanoparticles have some disadvantages such as less stability, tendency to aggregate and it is difficult to separate them from a reaction medium. To overcome these drawbacks, metal sulfide nanoparticles have been incorporated in polymer matrices or other inorganic materials [32,33]. Cadmium sulfide (CdS) is a well-known II-IV group n-type semiconductor with a direct bulk band gap of 2.42 eV. Cadmium sulfide nanoparticles have applications in areas such as light emitting diodes, photovoltaic devices, water splitting, sensors and biology [34]. CdS nanoparticles have a tendency to aggregate with the formation of bigger particles. To avoid aggregation of CdS nanoparticles, silica has been chosen as the core material. Silica exists in polymorphic forms such as quartz, tridymite or cristobalite along with an amorphous form [35]. Silica exists as SiO_4 in quartz and the four oxygen atoms are located at each apex of a tetrahedron and silicon atom exists at the center. Silica is a well-known inert, optically transparent material which reduces bulk conductivity with increase in suspension stability [5]. Silica is used in various industrial applications such as ceramics, glass, semiconductors, metallurgy, and photovoltaic cells. In many applications, silica has been used as an adsorbent as well as a catalyst support [35].

A lot of reports are available on core-shell materials in which semiconductors act as the core and silica acts as the shell. Examples are CdS@SiO_2 [36], CdTe@SiO_2 [37], CdSe@SiO_2 [38], CdTe@CdS@SiO_2 [39], PbS@SiO_2 [40], $Zn_xCd_{1-x}Se$@SiO_2 [41], ZnO@SiO_2 [42], and Fe_2O_3@SiO_2 [43]. In these core-shell materials, the core materials have been synthesized using methods such as hydrothermal, reverse microemulsion, radio frequency magnetron co-sputtering, precipitation, chemical vapor deposition, and polyol mediated reaction [36–43]. The shell (SiO_2) was synthesized using either StÖber's method or reverse micelle method. Only a few reports are available in which silica acts as the core and metals or semiconductors act as the shell. Examples are SiO_2@M (M = Au, Pd, Pt) [44], SiO_2@CdS [45], SiO_2@CdSe [46], SiO_2@TiO_2 [47], and SiO_2@ZnO [48]. In these core-shell materials, the core (SiO_2) has been synthesized using StÖber's method and the shell materials have been synthesized using methods such as reduction, successive ionic layer adsorption and reaction (SILAR), sonochemical method, layer by layer self-assembly, and thermal decomposition [44–48]. In addition, core-shell systems such as SiO_2@CdTe@SiO_2, SiO_2@Ag@SiO_2@TiO_2 have also

been reported [49,50]. The TEM images of some of the above mentioned core-shell nanoparticles are given in Figure 3.1.2.

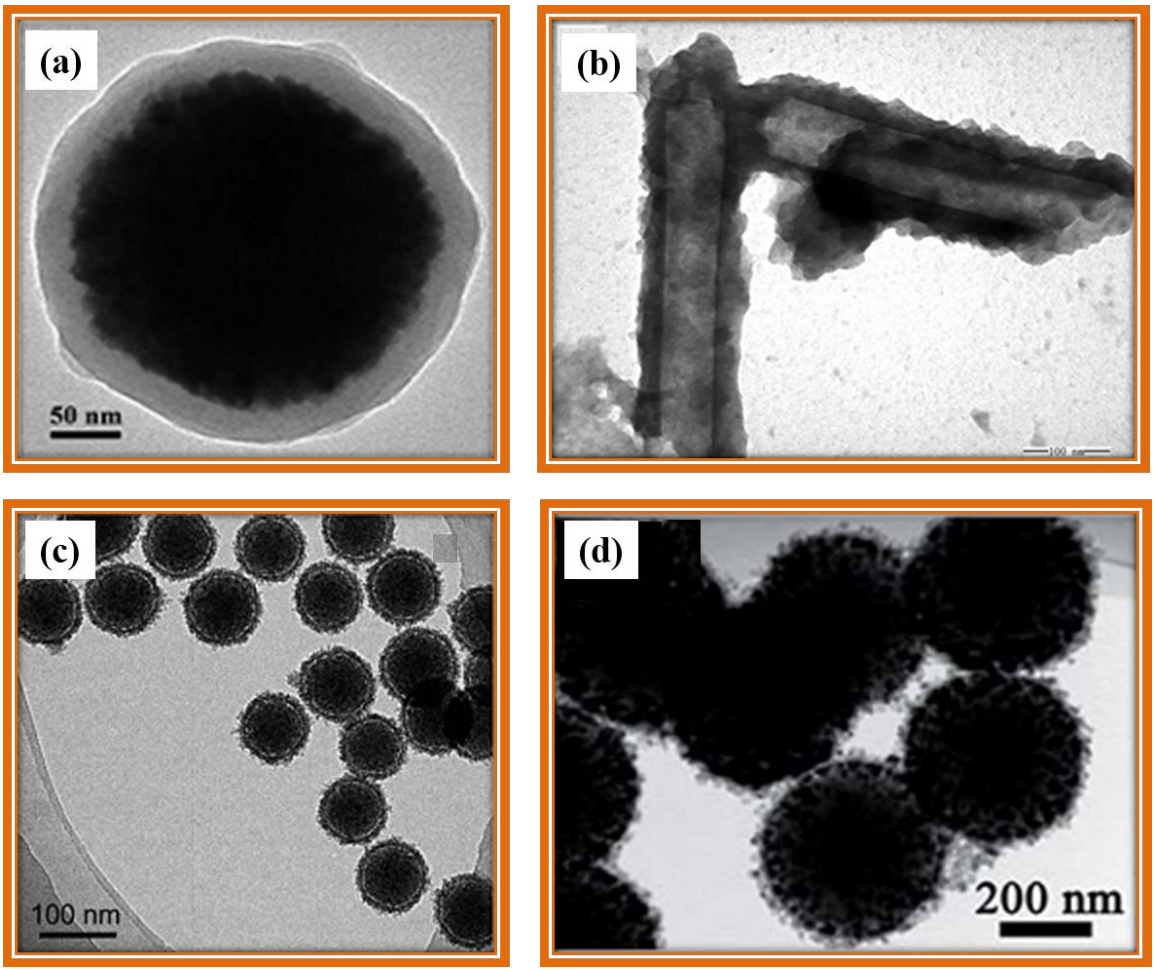

Fig. 3.1.2: TEM images of **(a)** PbS@SiO_2 core-shell nanoparticles [40], **(b)** ZnO@SiO_2 core-shell nanorods [42], **(c)** SiO_2@TiO_2 core-shell nanoparticles [47], and **(d)** SiO_2@Ag@SiO_2@TiO_2 core-multishell nanoparticles [50].

SiO_2@CdS core-shell nanoparticles come under type-I core-shell nanoparticles (section 3.1) and type-I core-shell nanoparticles have important applications in various fields. The optical properties of type-I core-shell nanoparticles have been discussed in Chapter-1 (Section 1.5.1.1). Synthesis of SiO_2@CdS core-shell nanoparticles have been reported by different synthetic methods such as successive ionic layer adsorption reaction (SILAR) [45], layer-by-layer self-assembly [51,52], sonochemcial deposition [53,54], solution route [55], reverse microemulsion [56], chemical coordination [57], and sol-gel method [58]. A brief description of the reported methods for the synthesis of SiO_2@CdS core-shell nanoparticles are given below.

Successive ionic layer adsorption and reaction [45]: In this method, SiO_2 microspheres are synthesized using StÖber process. Initially, SiO_2 beads are immersed in an aqueous solution of cadmium sulfate for about 5 min and washed thoroughly for several times with distilled water. After that, the Cd^{2+} adsorbed SiO_2 microspheres are immersed in an aqueous solution of sodium sulfide and kept for about 5 min and washed for several times to obtain the CdS deposited SiO_2 microspheres. The amount of CdS nanoparticles on the SiO_2 microspheres is controlled by varying the number of SILAR cycles.

Layer-by-layer self-assembly [51]: In this method, mesoporous SiO_2 microspheres are prepared by modified StÖber process and hexadecylamine is used as a template. To expand the pore size, the mesoporous SiO_2 microspheres are soaked in a mixture of LiCl, NaCl, and KNO_3 solution and sonicated for several hours and the obtained product is calcined at 300 ^oC for 3 h. To deposit Cd^{2+} ions on the mesoporous SiO_2 microspheres, certain amount of $Cd(NO_3)_2$ is added to an aqueous suspension containing the mesoporous SiO_2 microspheres and stirred at room temperature for 24 h. Then, polyelectrolytes such as poly(allylamine hydrochloride) or poly(styrene sulfonate) are deposited by layer-by-layer self-assembly on the Cd^{2+} deposited mesoporous SiO_2 microspheres. After this, thioacetamide solution is mixed with the obtained product and sonicated for several minutes to coat CdS nanoparticles on the polyelectrolyte deposited mesoporous SiO_2 microspheres. Finally, hollow mesoporous SiO_2 microspheres decorated with CdS nanoparticles are obtained by etching with hydrofluoric acid. A schematic illustration of CdS nanoparticles deposition on mesoporous SiO_2 microspheres *via* layer-by-layer self-assembly is shown in Figure 3.1.3.

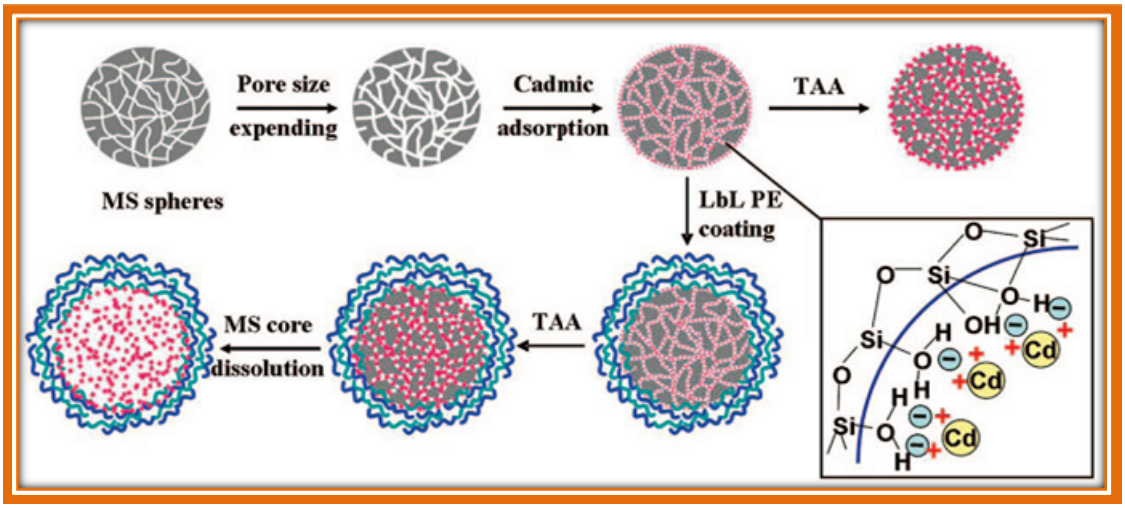

Fig. 3.1.3: Schematic illustration of CdS nanoparticles deposition on mesoporous SiO_2 microspheres *via* layer-by-layer self-assembly [51].

Sonochemcial deposition [54]: In this method, silica microspheres are prepared by StÖber process and calcined at 750 ^{o}C for 6 h. To deposit CdS nanoparticles on the SiO_2 spheres, 100 mg of SiO_2 microspheres are mixed with certain amounts of cadmium sulfate and thiourea in an aqueous solution. The reaction contents are sonicated using high intense ultrasonicator for three hours at 80 ^{o}C.

Solution route [55]: In this method, SiO_2 microspheres are synthesized using StÖber process and the surface of SiO_2 microspheres is modified using 3-aminopropyltrimethoxysilane (APS). CdS nanoparticles are synthesized by mixing cadmium acetate and thioglycerol in ethanol and then sodium sulfide is added drop wise and stirred for 6 h. The surface functionalized SiO_2 microspheres and CdS nanoparticles are mixed in ethanol and stirred at room temperature for several hours to obtain CdS deposited SiO_2 microspheres.

Reverse microemulsion [56]: In this method, SiO_2 spheres are synthesized using a reverse microemulsion method. A quaternary mixture of cyclohexane, water, hexanol, and Triton-101 or poly(oxyethy1ene) nonylphenyl ether (Igepal CO520) are mixed with 10 mL of tetraethyl orthosilicate and stirred at room temperature for 24 h. To deposit CdS shell on the SiO_2 microspheres, initially, a microemulsion is prepared using a mixture of cyclohexane, water, hexanol, and Triton-101. Then, required amounts of cadmium nitrate and ammonium sulfide are dissolved in the microemulsion mixture. After that, a specific amount of SiO_2 microspheres are mixed with the microemulsion mixture and stirred at room temperature for several hours.

Chemical coordination [57]: In this method, SiO_2 microspheres are synthesized using StÖber process and calcined at 700 ^{o}C for 4 h. Then, certain amounts of diethylamine or n-hexylmethylamine along with CS_2 are mixed with an ethanolic solution of cadmium hydroxide and stirred for 2 h to obtain cadmium alkyldithiocarbamate. About 250 mg of SiO_2 microspheres are then mixed with the cadmium alkyldithiocarbamate complex in acetone and then ethylenediamine is added drop wise. The contents are stirred under N_2 flow at room temperature to deposit CdS shell on the SiO_2 microspheres.

Sol-gel method [58]: Initially, tetraethyl orthosilicate, water, ethanol and nitric acid are added in a round bottom flask and stirred at room temperature for about half an hour. Then, ethanolic solutions of cadmium nitrate and thiourea are added and stirred for 30 min. After that, a few milliliters of water is added and the stirring is continued for about one hour. The obtained

mixture is transferred into a Teflon lined stainless steel container and gelatinized at 40 ^{o}C. The obtained alcogel is aged at 40 ^{o}C for four days and finally annealed at 150 ^{o}C for 2 h.

The TEM images of SiO_2@CdS core-shell nanoparticles, prepared by some of the above mentioned methods, are shown in Figure 3.1.4.

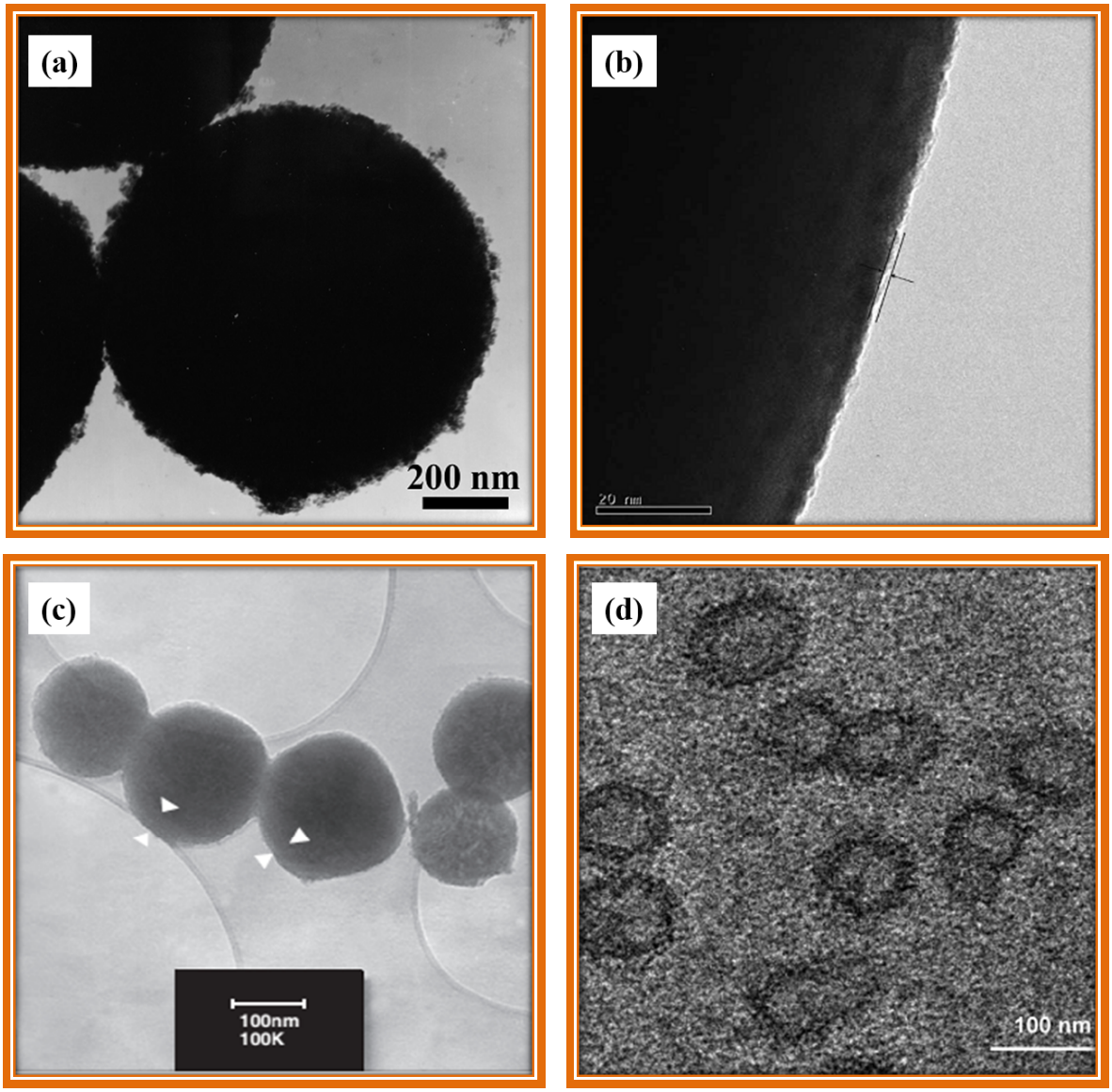

Fig. 3.1.4: TEM images of SiO_2@CdS core-shell nanoparticles prepared by **(a, b)** layer-by-layer self-assembly [51,52], **(c)** sonochemcial deposition [53], and **(d)** solution route [55].

The reported methods for the synthesis of SiO_2@CdS core-shell nanoparticles have several disadvantages. For example, the SILAR technique produces only decorated CdS nanoparticles with aggregation on the silica microspheres [45]. Sonochemical deposition and solution routes require surface modification of SiO_2 microspheres to deposit the CdS shell [53,55]. Layer-by-

layer self-assembly and chemical coordination methods require separate coupling agents to anchor CdS nanoparticles on the SiO_2 microspheres [51,57]. The reverse microemulsion method is expensive and requires longer time [56]. The sol-gel method also requires longer time [58].

In the present study, StÖber's process was chosen for the preparation of silica microspheres. StÖber's process is simple and one can have control on size distribution and achieving monodispersity is possible on nano to micro-meter scale. The thermal decomposition approach has been used to prepare the SiO_2@CdS core-shell nanoparticles for the first time.

3.1.2 Experimental details

Tetraethyl orthosilicate (98%, ACROS®), ethanol (99.9%, AR), ammonia solution (25%, Rankem, AR), cadmium acetate (99%, Himedia, AR), thiourea (99%, Rankem, LR), and ethylene glycol (99%, Rankem, LR) were used as received and methanol (99%, SD Fine) was distilled before further use. The synthesis of SiO_2@CdS core-shell nanoparticles involves two steps and the details are as follows.

3.1.2.1 Synthesis of SiO_2 microspheres

The schematic illustration of the synthesis of SiO_2 microspheres is shown in Scheme 3.1.1. Silica microspheres were synthesized according to StÖber process [59]. In a typical synthesis, about 88 mL of ethanol and 12 mL of ammonia solution were mixed in a 250 mL beaker. Then, about 3.7 mL of tetraethyl orthosilicate (TEOS) was added drop wise under vigorous stirring and then, the contents were kept under constant stirring for 24 h at room temperature. The obtained white precipitate was centrifuged at 3000 rpm for about 15 min, washed several times with ethanol and kept for drying in an oven at 70 ^oC for overnight. As prepared SiO_2 microspheres were calcined at 500 ^oC for 3 h to obtain the activated SiO_2 microspheres.

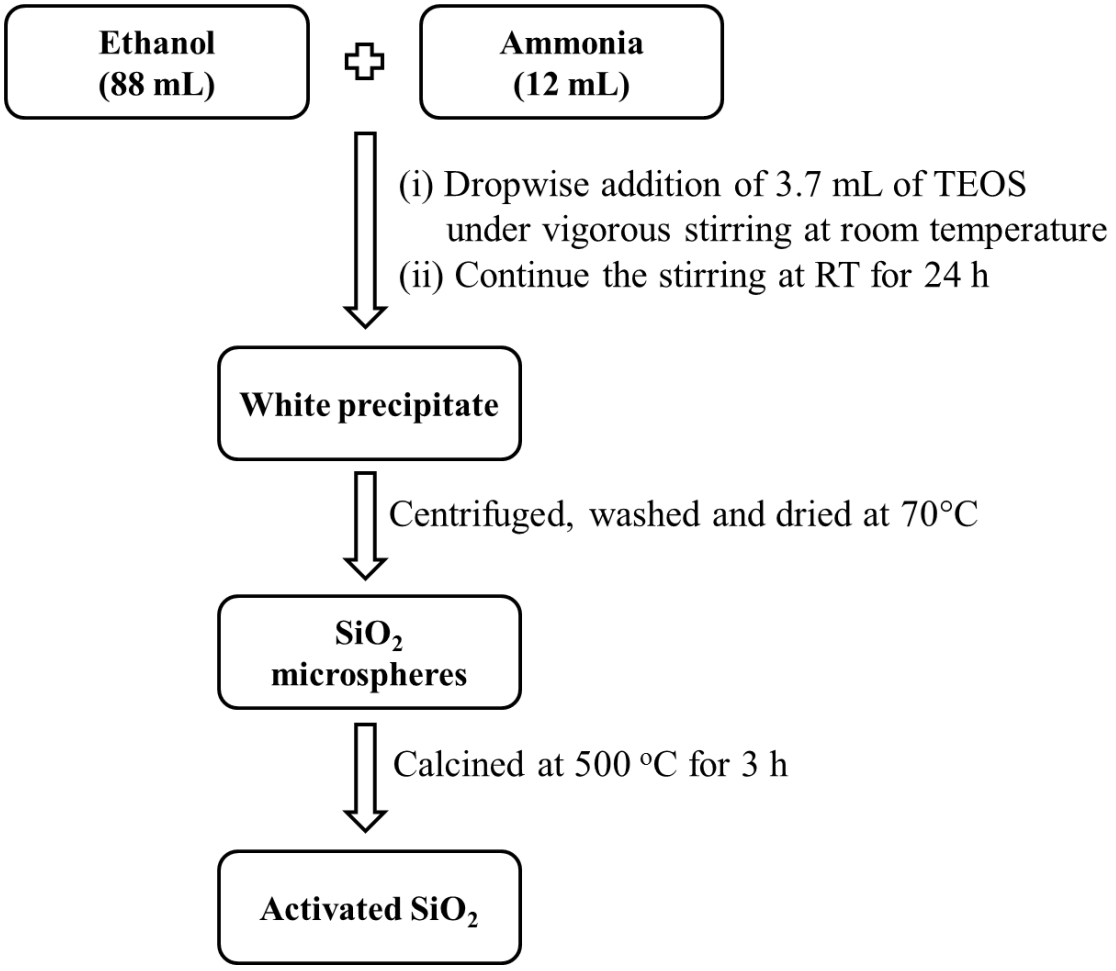

Scheme 3.1.1: Synthesis of SiO_2 microspheres using StÖber process.

3.1.2.2 Synthesis of SiO_2@CdS core-shell nanoparticles

The schematic representation of synthesis of SiO_2@CdS core-shell nanoparticles is given in Scheme 3.1.2. The deposition of cadmium sulfide nanoparticles on the silica microspheres was carried out by the thermal decomposition of cadmium acetate and thiourea in ethylene glycol. The synthetic procedure is as follows. Two different silica samples (unactivated silica and activated silica (at 500 °C, 3 h, air)) were used for the synthesis of SiO_2@CdS core-shell nanoparticles. In a typical synthesis, 0.5 mM of silica powder was mixed with different molar ratios of cadmium acetate and thiourea (Table 3.1.1) in a 50 mL round bottom flask. Then, about 20 mL of ethylene glycol was added and sonicated for 3 min. The contents were refluxed at 180 °C for 1 h in air. The yellow colored slurry obtained was allowed to cool to room temperature. Then, about 25 mL of methanol was added. The obtained precipitate was centrifuged at 3000 rpm for 3 min, washed with methanol and dried under vacuum. The

nomenclature and various synthetic conditions employed for the preparation of SiO_2@CdS core-shell nanoparticles are given in Table 3.1.1.

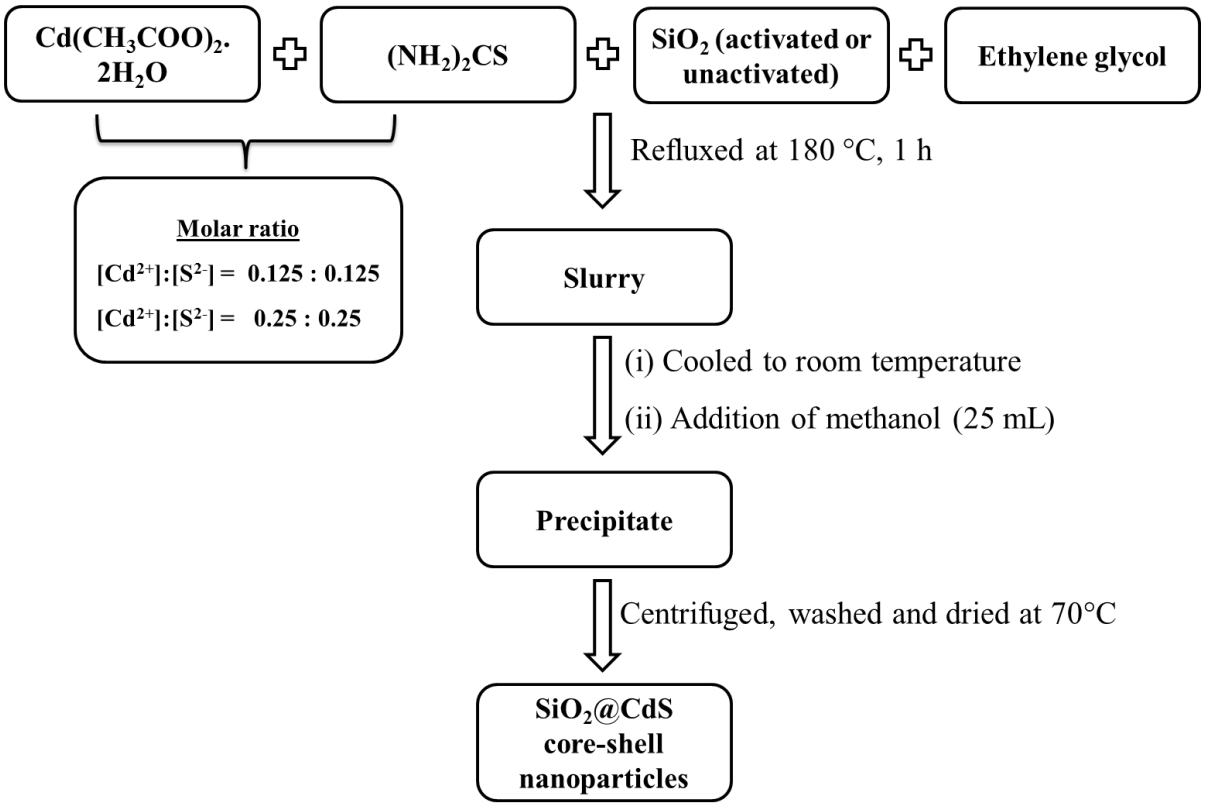

Scheme 3.1.2: Synthesis of SiO_2@CdS core-shell nanoparticles *via* thermal decomposition approach.

Table 3.1.1: Nomenclature and concentration of reagents used during the preparation of SiO_2@CdS core-shell nanoparticles.

Sl. no	Sample ID	Type of silica used	Amount of silica (mM)	$[Cd(CH_3COO)_2.2H_2O]$ (mM)	$[(NH_2)_2CS]$ (mM)
1	S1	Unactivated	0.5	0.125	0.125
2	S2	Unactivated	0.5	0.25	0.25
3	S3	Activated	0.5	0.125	0.125
4	S4	Activated	0.5	0.25	0.25

The synthesized SiO_2@CdS core-shell nanoparticles were characterized using X-ray diffraction (PXRD), Fourier transform infrared spectroscopy (FT-IR), field emission scanning electron microscopy (FE-SEM) and transmission electron microscopy (TEM). The optical properties of SiO_2@CdS core-shell nanoparticles were studied using UV-Visible diffuse

reflectance spectroscopy (DRS) and photoluminescence spectroscopy (PL). More details on the experimental techniques have been discussed in Chpater-2.

3.1.3 Results and discussion

3.1.3.1 XRD analysis

The XRD patterns of pure silica, cadmium sulfide, and SiO_2@CdS core-shell nanoparticles, prepared using unactivated and activated silica, are shown in Figure 3.1.5. Pure silica is amorphous. The SiO_2@CdS core-shell nanoparticles (S1-S4) show peaks due to cadmium sulfide (JCPDS file no: 75-1546). The XRD patterns show three prominent broad peaks due to cadmium sulfide which could be indexed to (111), (220) and (311) reflections of cubic CdS. Two minor peaks observed between 70° and 85° could be indexed to (331) and (422) planes of CdS. The crystallite size of cadmium sulfide was calculated using Debye-Scherrer formula using (111) reflection of CdS at $2\theta = 26^{o}$. The CdS in the core-shell nanoparticles possess a crystallite size of about 2 nm and pure cadmium sulfide exhibits a crystallite size of about 6 nm.

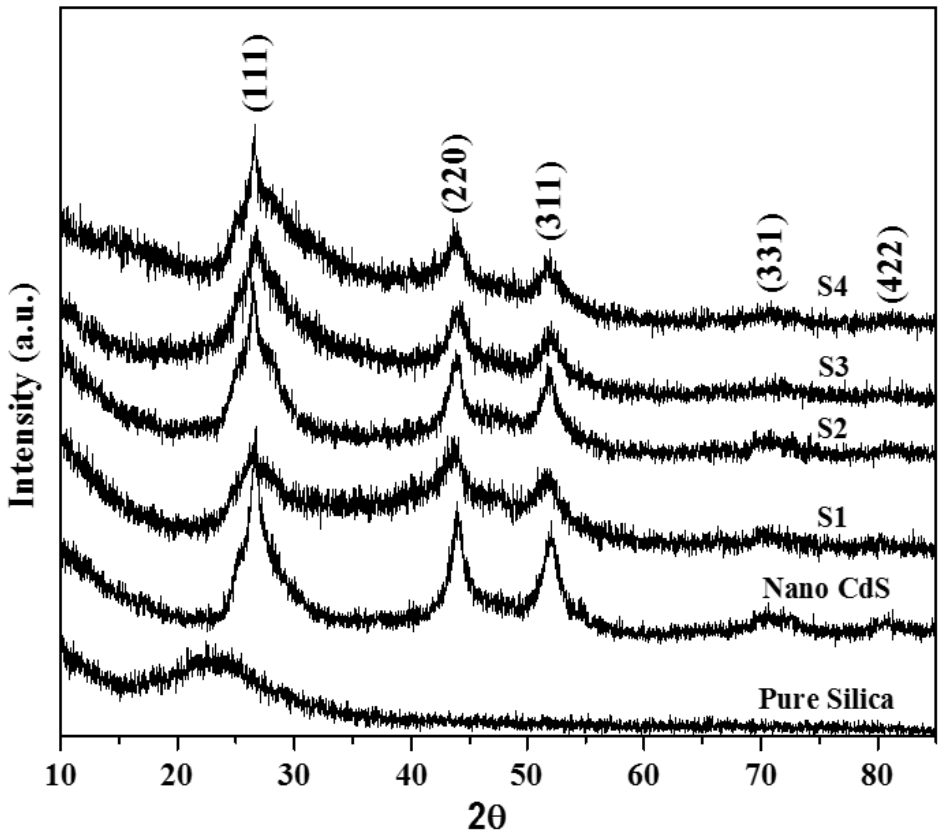

Fig. 3.1.5: XRD patterns of silica, cadmium sulfide, and SiO_2@CdS core-shell nanoparticles (S1 to S4).

3.1.3.2 FT-IR spectral studies

FT-IR spectra of as prepared silica, activated silica, pure cadmium sulfide nanoparticles and SiO_2@CdS core-shell nanoparticles are shown in Figure 3.1.6. Silica and SiO_2@CdS core-shell nanoparticles show a broad band at about 3400 cm^{-1} due to hydroxyl stretching and a band at 1650 cm^{-1} due to hydroxyl bending. The bands at 1100 and 800 cm^{-1} are attributed to asymmetric and symmetric stretching of Si–O–Si bond. The band at about 475 cm^{-1} is due to Si–O–Si bending vibration. The band at 950 cm^{-1} in the spectrum of as prepared silica is due to Si–OH group and this band is absent in the spectra of activated silica and the core-shell nanoparticles prepared using activated silica (S3 and S4). This indicates the absence of surface hydroxyl groups in these samples [60,61].

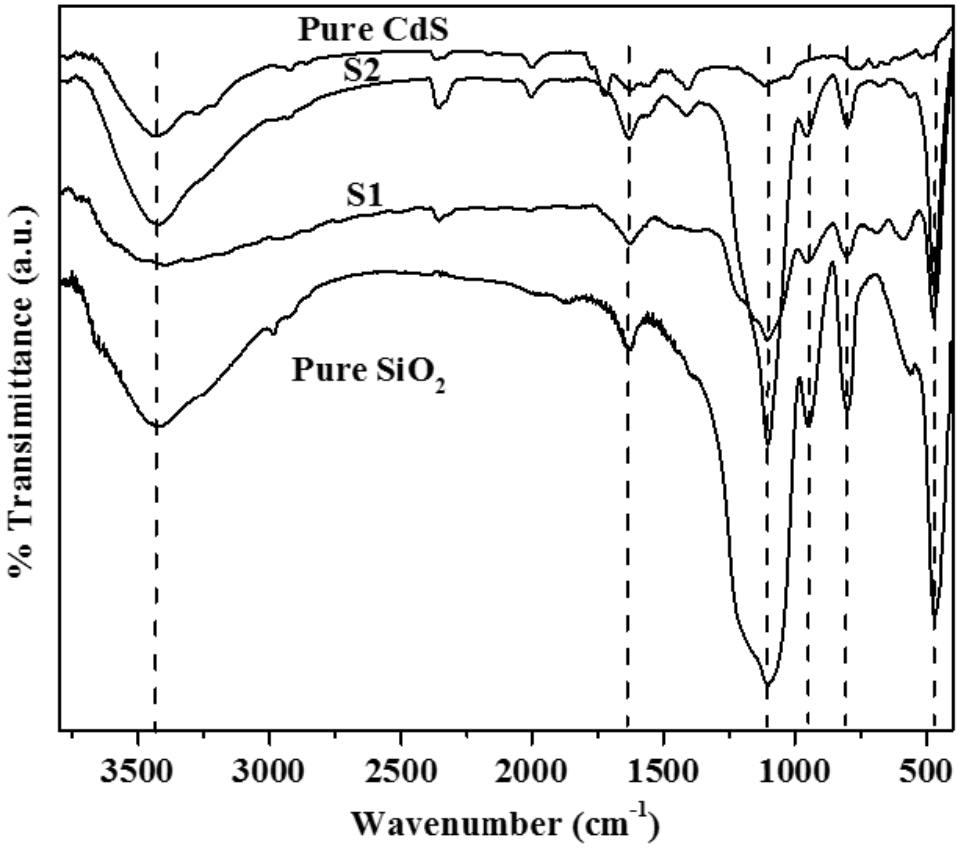

(a)

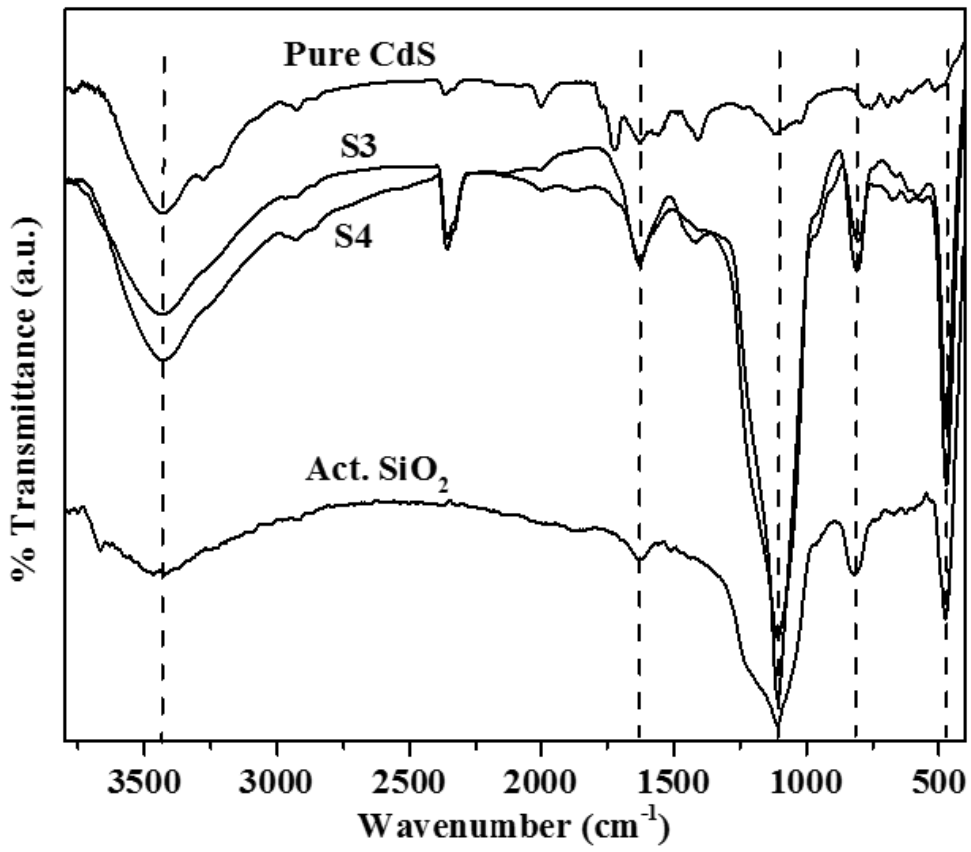

(b)

Fig. 3.1.6: FT-IR spectra of **(a)** as prepared silica, pure CdS nanoparticles and SiO_2@CdS core-shell nanoparticles prepared using unactivated silica (S1 and S2), and **(b)** activated silica, pure CdS, and SiO_2@CdS core-shell nanoparticles prepared using activated silica (S3 and S4).

3.1.3.3 FE-SEM studies

The FE-SEM images of pure silica, cadmium sulfide and SiO_2@CdS core-shell nanoparticles, prepared using unactivated and activated silica (S1 to S4) are shown in Figure 3.1.7. Pure silica shows spherical particles (diameter = 300 ± 20 nm) and pure cadmium sulfide shows agglomerated small particles. The SiO_2@CdS samples, prepared using unactivated silica (S1 and S2), show uniform deposition of cadmium sulfide nanoparticles on silica. In sample S1, prepared using low concentration of cadmium acetate and thiourea ($[Cd^{2+}]$:$[S^{2-}]$ = 0.125:0.125), uniform deposition with thinner shell of CdS is observed. Sample S2 shows thicker shell of CdS on the silica spheres attributed to the formation of bigger CdS nanoparticles compared to sample S1. In samples S1 and S2, the uniform deposition of CdS is attributed to strong interaction between the cadmium ions (Cd^{2+}) and the surface silanol groups (vicinal and geminal) of silica. In comparison to S1 and S2, the SiO_2@CdS samples prepared using

activated silica (S3 and S4) show the deposition of cadmium sulfide nanoparticles on silica but a few extra uncoated particles of cadmium sulfide nanoparticles are also noticed. This is due to lack of presence of surface hydroxyl groups on the surface of activated silica. In the core-shell nanoparticle samples S3 and S4, the interaction between cadmium ions and the silanol groups is weak due to the absence of vicinal silanol groups on the surface of activated silica. Out of all the SiO_2@CdS samples, S1 shows the uniform deposition of cadmium sulfide nanoparticles on the silica spheres.

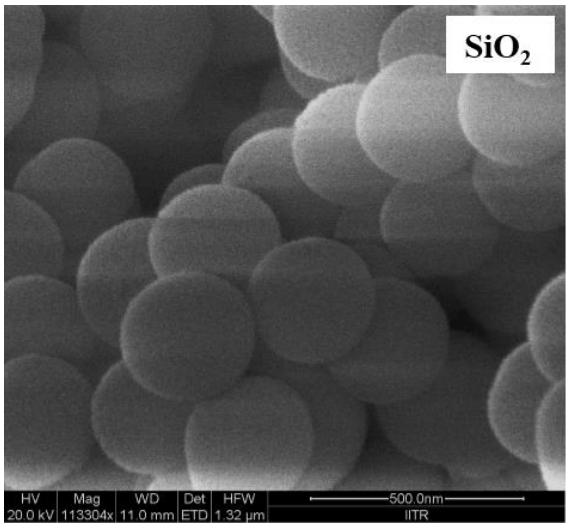

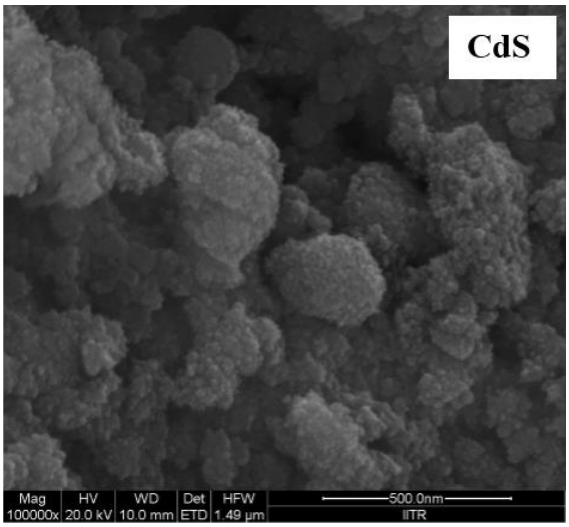

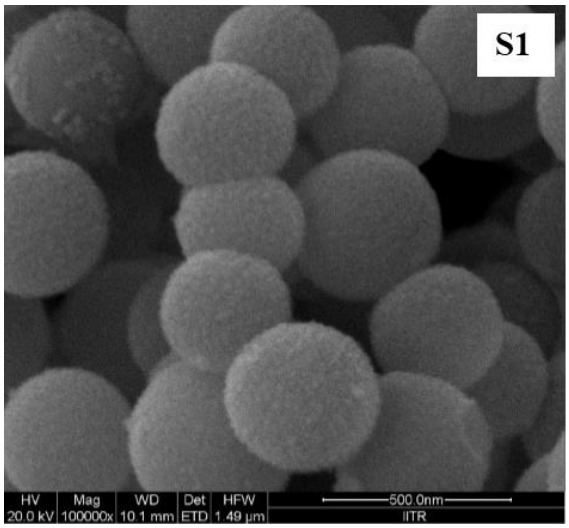

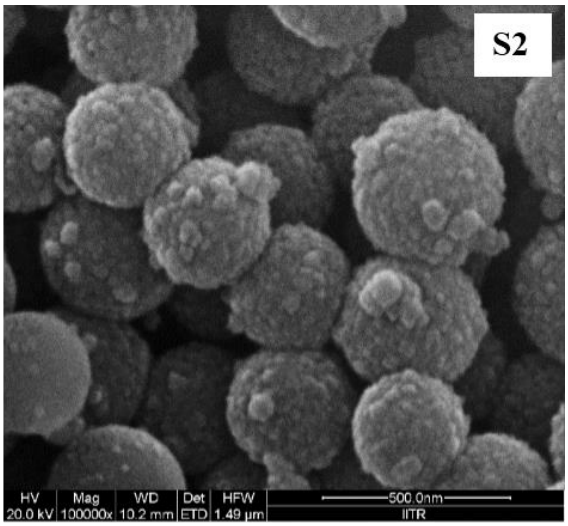

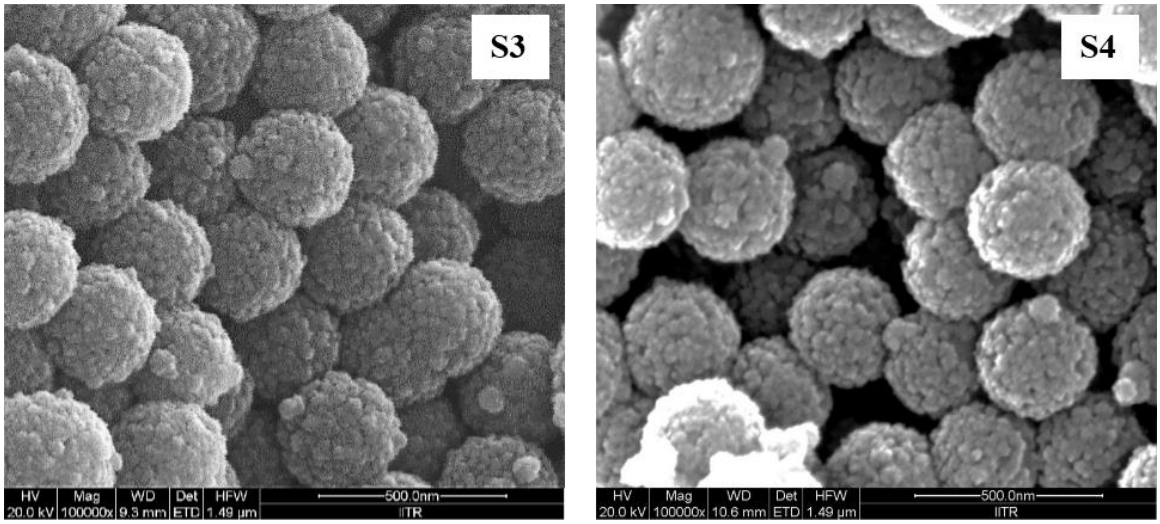

Fig. 3.1.7: FE-SEM images of SiO_2 microspheres, CdS nanoparticles and SiO_2@CdS core-shell nanoparticles prepared using unactivated silica (S1 and S2) and activated silica (S3 and S4).

3.1.3.4 SEM-EDX analysis

The amount of cadmium, sulfur, silicon and oxygen present in the SiO_2@CdS core-shell nanoparticles was analyzed using EDX analysis. The EDX results (Figure 3.1.8) indicate uniform distribution of cadmium and sulfur in all the samples. The atomic percent of oxygen in the SiO_2@CdS core-shell nanoparticles varies from 0.7 to 2.

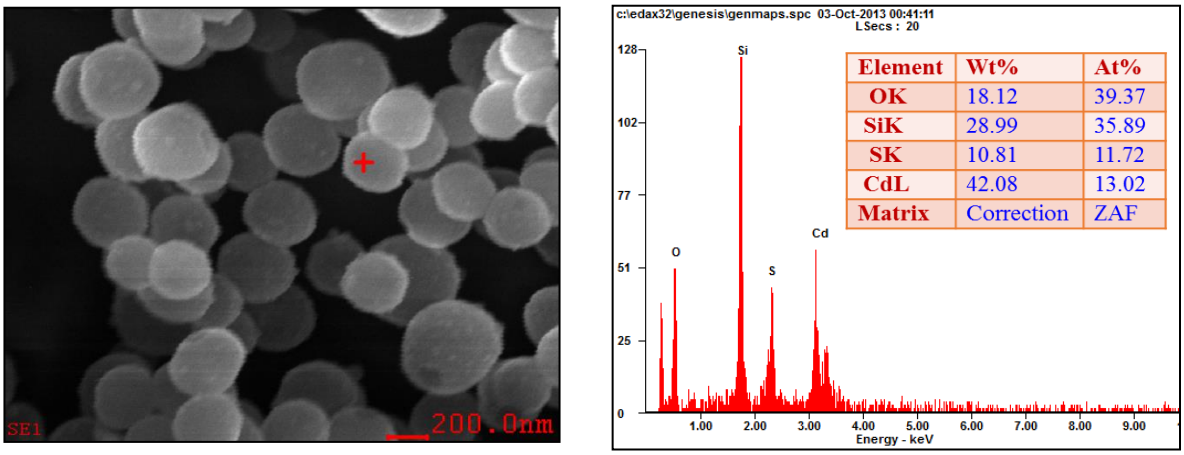

(a)

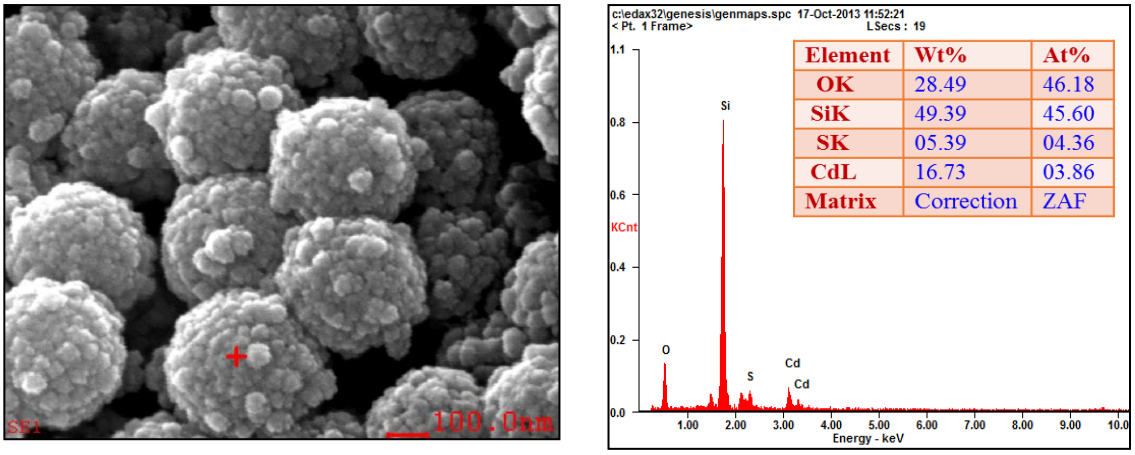

(b)

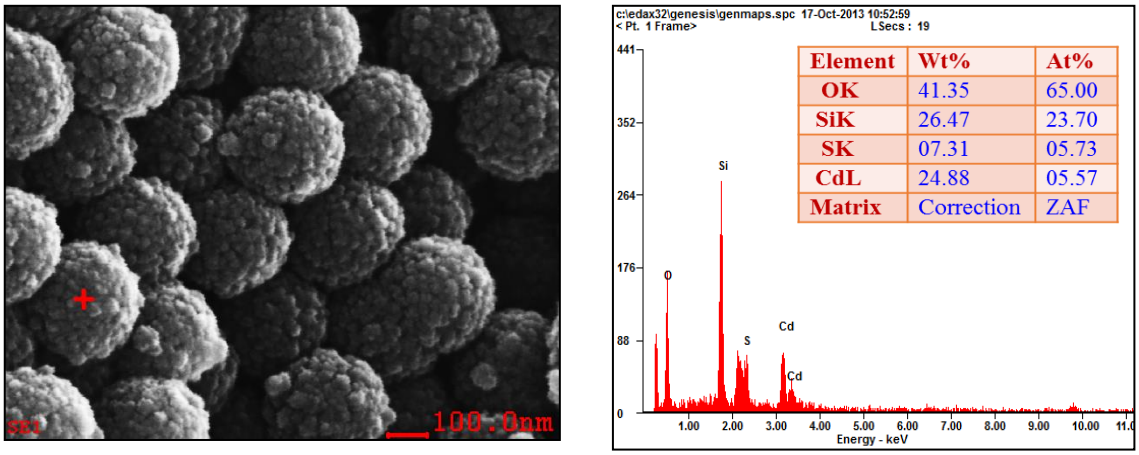

(c)

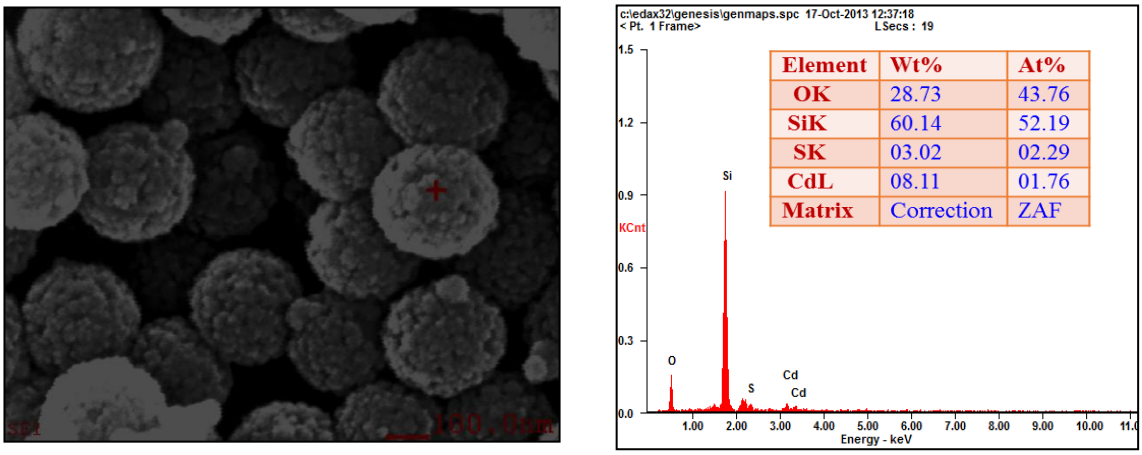

(d)

Fig. 3.1.8: EDX patterns of SiO_2@CdS core-shell nanoparticles prepared using (**a, b**) unactivated silica sample S1 and S2, and (**c, d**) activated silica sample S3 and S4.

The effects of temperature, thermal decomposition time and sonication on the deposition of CdS nanoparticles on silica were investigated using the synthetic conditions for SiO_2@CdS

sample S1. It was observed that 150 ^{o}C is not sufficient for the good deposition of cadmium sulfide nanoparticles on silica, as observed by the SEM studies (Figure 3.1.9a) which show uncoated cadmium sulfide nanoparticles. On the other hand, uniform deposition of cadmium sulfide nanoparticles over silica is observed at 180 ^{o}C. Sonication was found to play an important role in uniform dispersion of the reactants (cadmium acetate and thiourea) and sonication was carried out before start of the reaction. Two thermal decomposition reactions were tried, one with sonication for 3 min and another without sonication. Sonication leads to good deposition of CdS nanoparticles but in the absence of sonication, uncoated CdS particles are observed (Figure 3.1.9b).

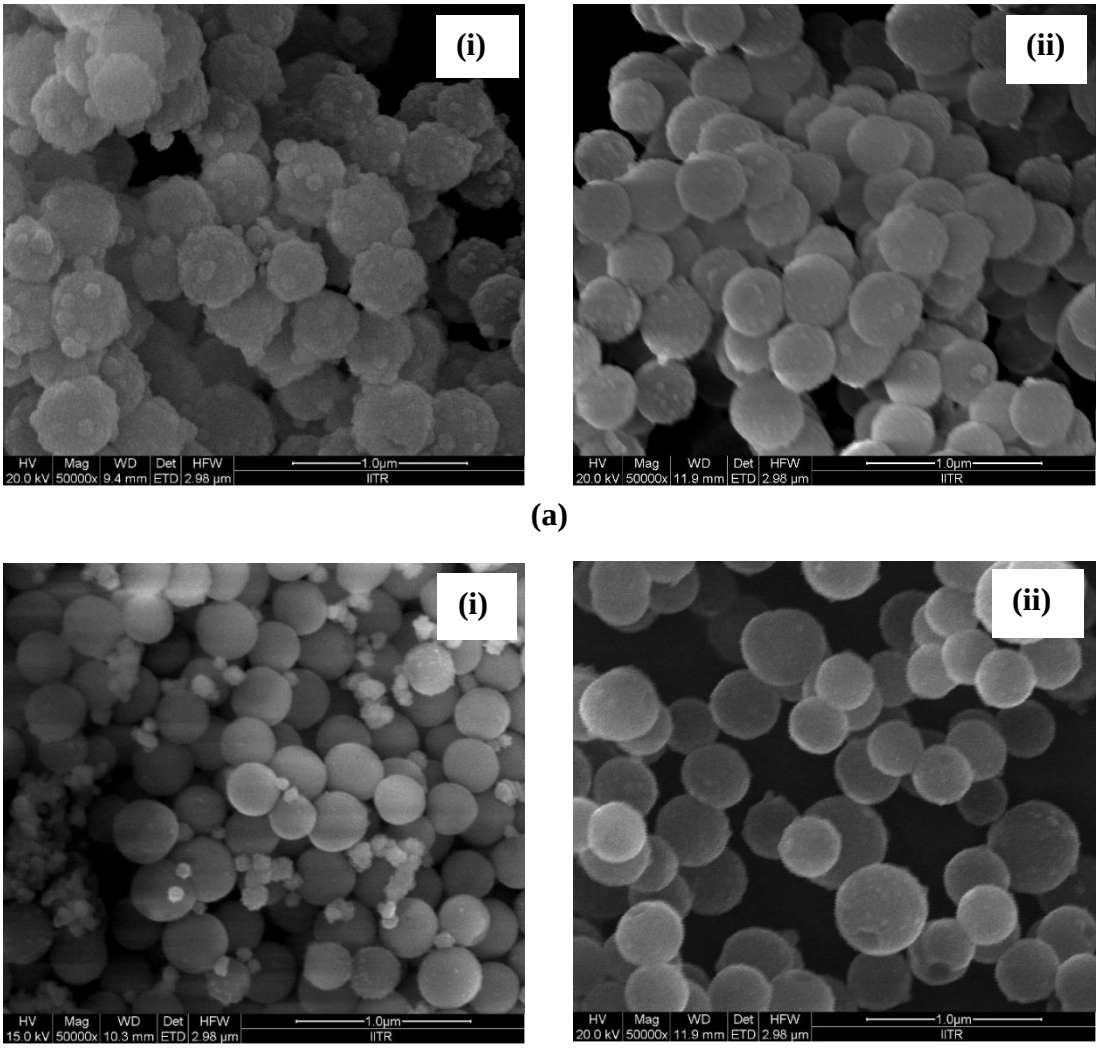

Fig. 3.1.9: FE-SEM images of SiO_2@CdS core-shell nanoparticles demonstrating the effect of temperature **(a)** (i) 150 ^{o}C and (ii) 180 ^{o}C and the effect of sonication time **(b)** (i) without sonication and (ii) with sonication.

To study the effect of time on CdS coating on the SiO_2 spheres, the synthesis was carried out at 180 ^oC for different time periods (30 min, 60 min and 90 min). In 30 min, lack of deposition and some uncoated cadmium sulfide nanoparticles are observed (Figure 3.1.10a). At 90 min, agglomerated cadmium sulfide nanoparticles on silica are observed (Figure 3.1.10c). But in the case of 60 min, uniform deposition of CdS with no uncoated CdS nanoparticles is observed (Figure 3.1.10b).

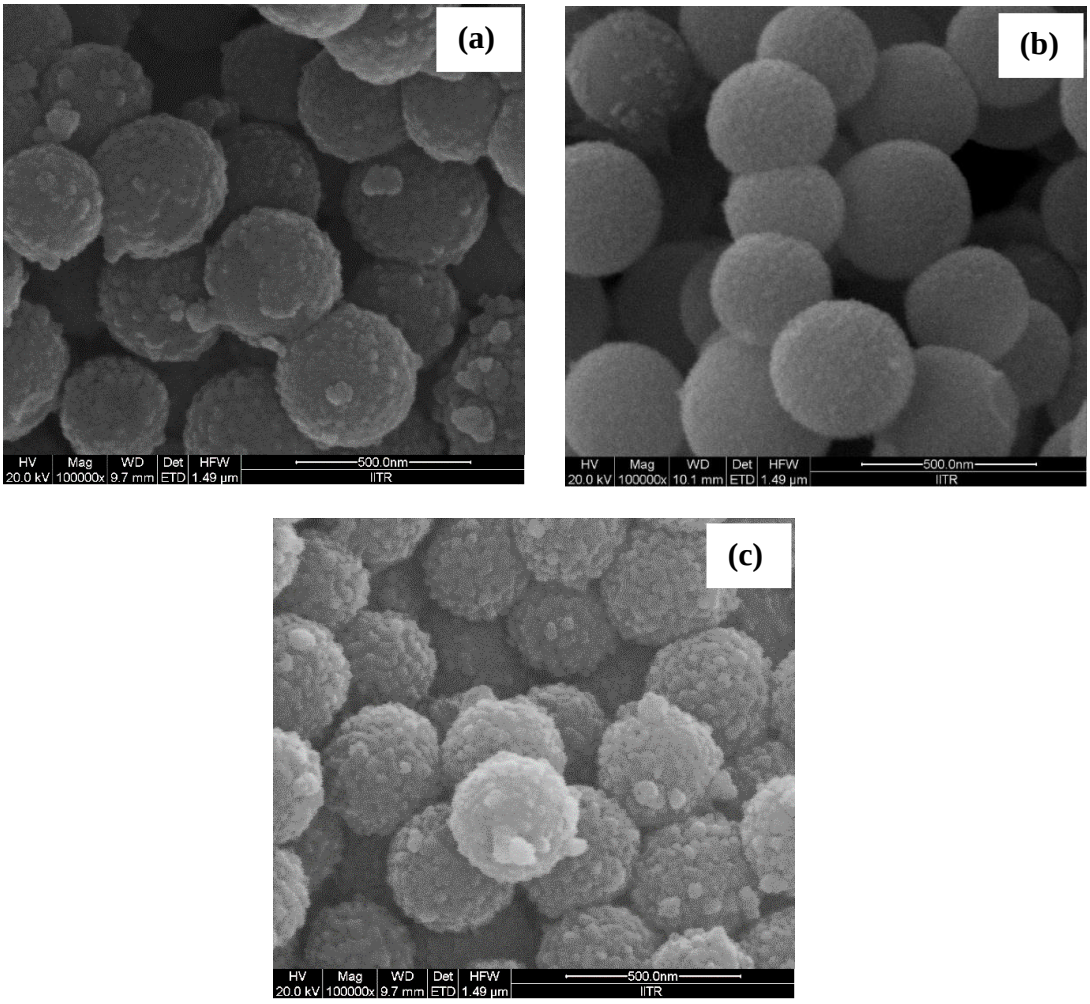

Fig. 3.1.10: FE-SEM images of SiO_2@CdS core-shell nanoparticles (sample S1) prepared at different thermal decomposition timings; **(a)** 30 min, **(b)** 60 min and **(c)** 90 min at 180 ^oC.

3.1.3.5 TEM studies

The TEM images of SiO_2@CdS core-shell nanoparticles are shown in Figure 3.1.11. Silica shows spherical morphology and cadmium sulfide shows agglomerated nanoparticles. The diameter of the silica spheres is 300 ± 20 nm. Sample S1 which was prepared using unactivated silica shows uniform CdS shell over the silica spheres; the shell thickness is 25 ± 3 nm. Sample

S2 shows a CdS shell thickness of 70 ± 10 nm. The increment in the shell thickness is due to higher concentration of precursors (cadmium acetate and thiourea) used during the synthesis. The SiO_2@CdS samples S3 and S4, prepared using activated silica, show cadmium sulfide nanoparticles on the surface of silica but they also show some uncoated cadmium sulfide particles. The poor deposition is attributed to lack of surface silanol groups on the surface of activated silica. The SAED patterns show three rings corresponding to (111), (220) and (311) reflections of CdS. The ring patterns also indicate polycrystalline nature of CdS nanoparticles on the surface of SiO_2 microspheres.

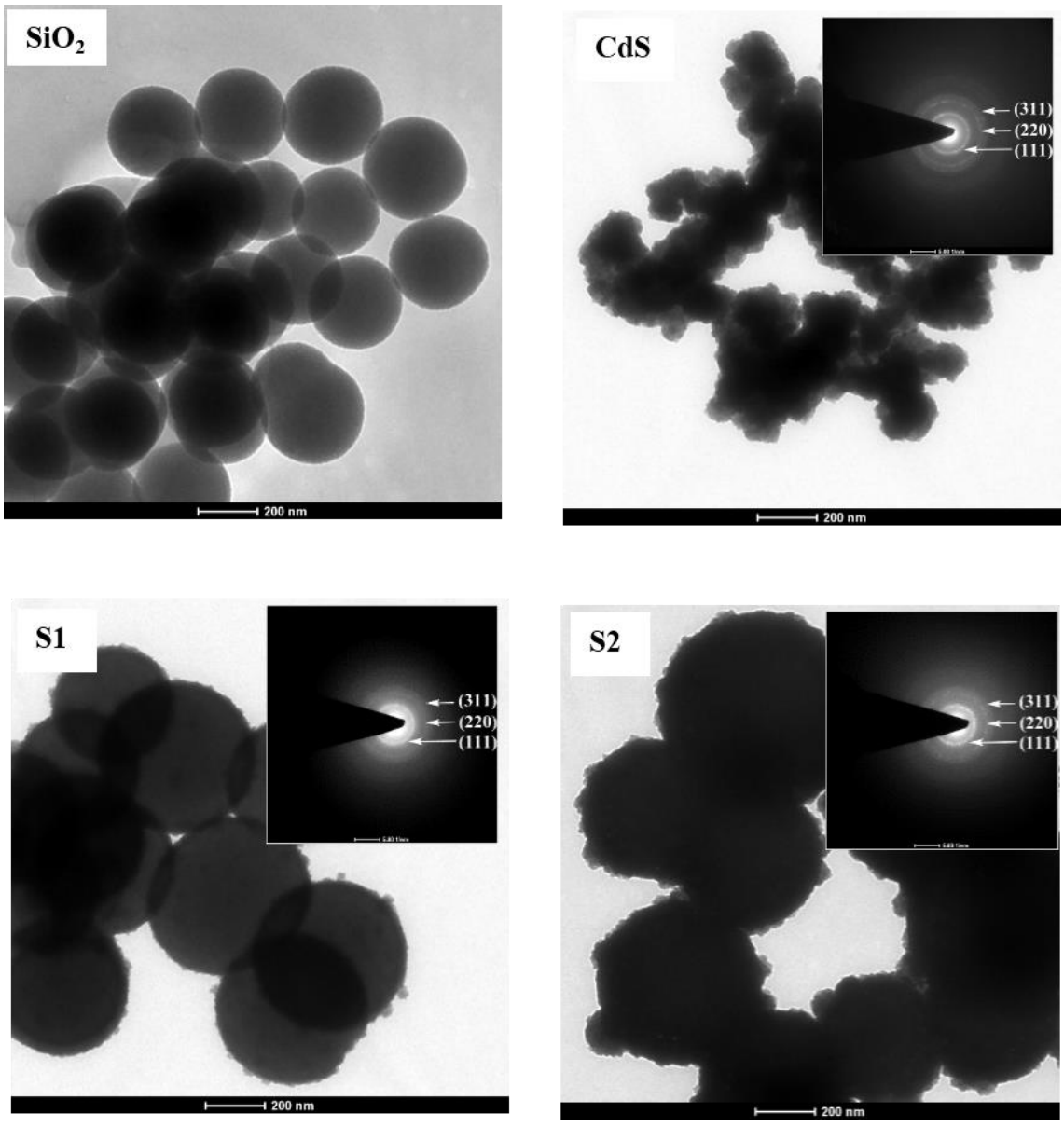

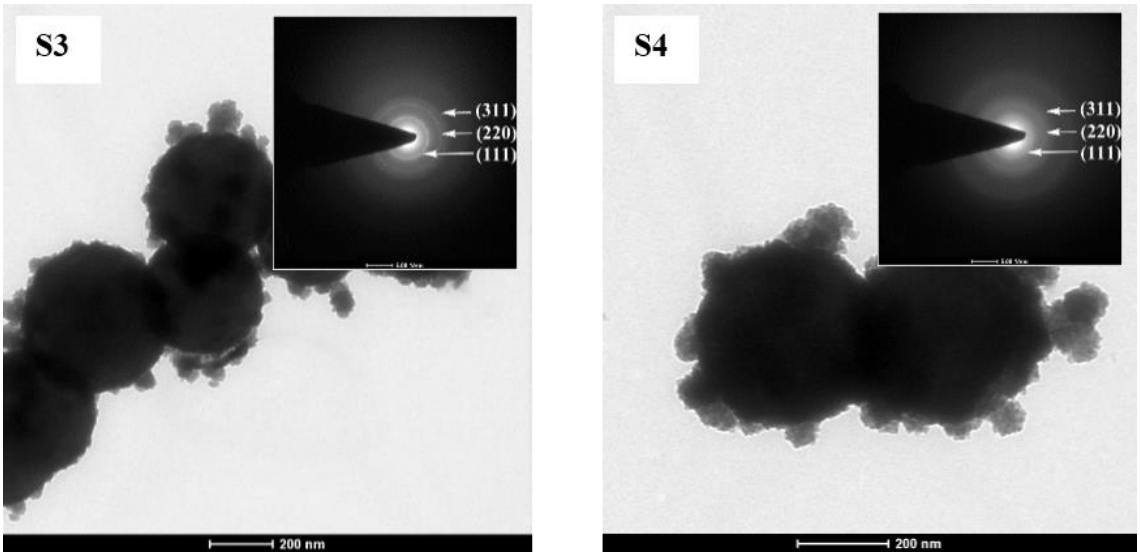

Fig. 3.1.11: TEM images of SiO_2 microspheres, CdS nanoparticles and SiO_2@CdS core-shell nanoparticles prepared using unactivated silica (S1 and S2) and activated silica (S3 and S4).

A detailed structural investigation of cadmium sulfide nanoparticles on the silica was carried out by HRTEM studies. The HRTEM images (Figure 3.1.12) clearly indicate the crystalline nature of cadmium sulfide nanoparticles with a lattice spacing of about 0.36 nm corresponding to (111) plane of cubic cadmium sulfide.

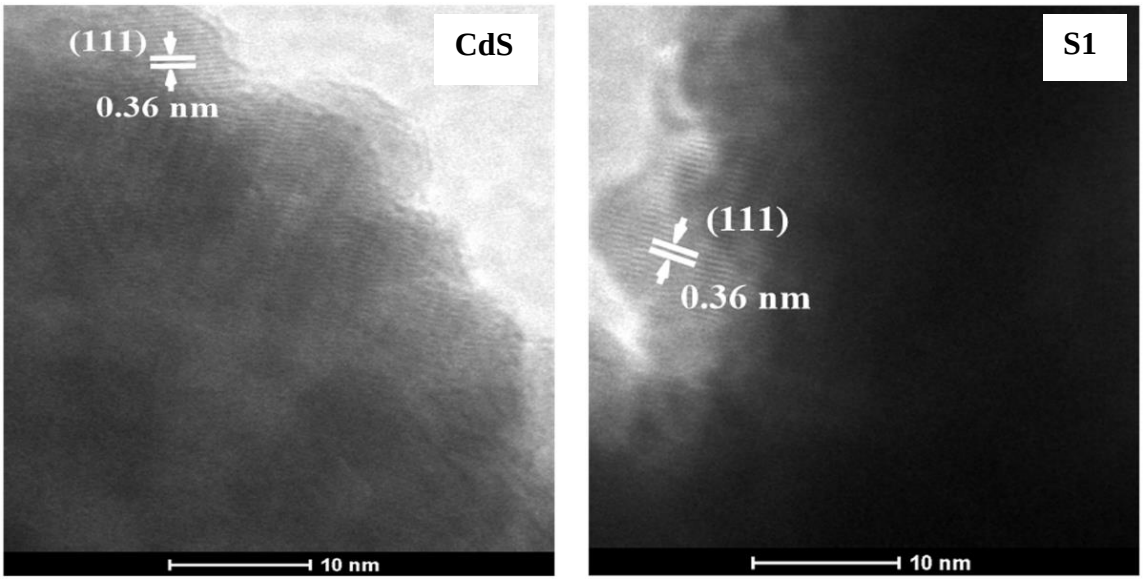

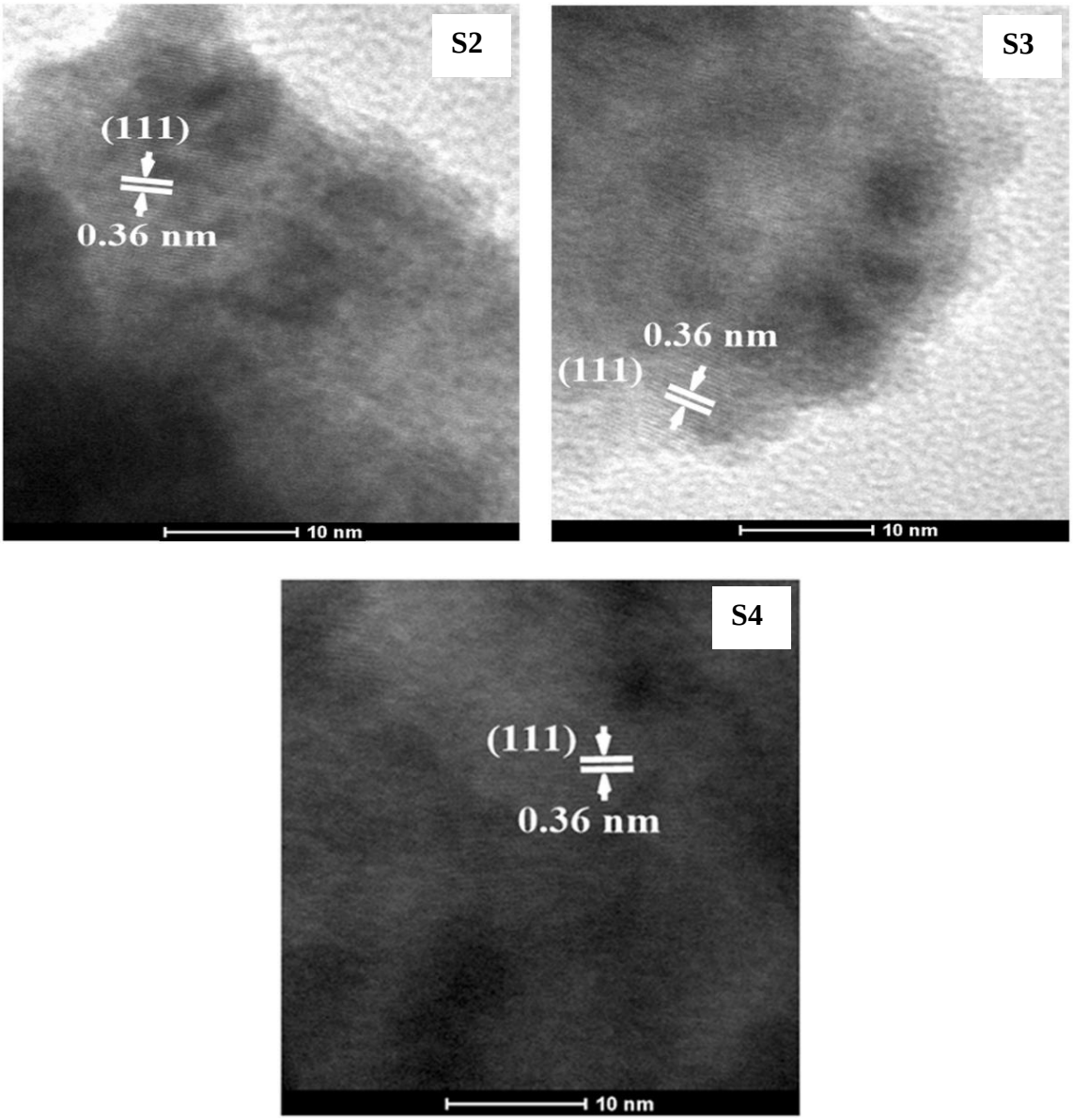

Fig. 3.1.12: HRTEM images of CdS nanoparticles and SiO_2@CdS core-shell nanoparticles prepared using unactivated silica (S1 and S2) and activated silica (S3 and S4).

The optical properties of SiO_2@CdS core-shell nanoparticles were studied using UV-Visible diffuse reflectance spectroscopy (DRS) and photoluminescence spectroscopy (PL) and the results are discussed below.

3.1.3.6 UV-Visible diffuse reflectance spectroscopy (DRS)

The DRS results for the SiO_2@CdS core-shell nanoparticles are shown in Figure 3.1.13a. The band gap of pure cadmium sulfide nanoparticles and the SiO_2@CdS core-shell nanoparticles were estimated from DRS results using the equation proposed by Tauc et al [62]. The band gap values for pure cadmium sulfide and SiO_2@CdS core-shell nanoparticles were estimated by

plotting $(\alpha h\nu)^2$ versus $h\nu$ (Figure 3.1.13b). Pure cadmium sulfide nanoparticles possess a band gap of about 2.55 eV which is higher than the bulk band gap of CdS (2.42 eV) [63]. In the present study, the SiO_2@CdS core-shell nanoparticles show band gap absorption between 2.56 and 2.60 eV. The SiO_2@CdS core-shell nanoparticles show a blue shift in the band gap absorption by about 0.18 eV with respect to bulk CdS and the observed increase in the band gap depends on the particle size of CdS.

The particle size of CdS in the SiO_2@CdS core-shell nanoparticles was calculated using Brus equation which is expressed as follows [64]:

$$\Delta E_g = E_g^{nano} - E_g^{bulk} = \frac{\hbar^2 \pi^2}{2R^2}\left(\frac{1}{m_e^*} + \frac{1}{m_h^*}\right) - \frac{1.86e^2}{\epsilon R} \qquad (1)$$

Where ΔE_g is the shift in the band gap with respect to the bulk E_g, R is the radius of CdS nanoparticle, m_e^* is the effective mass of electron (0.19 m_o), m_h^* is the effective mass of hole (0.80 m_0), m_o is the mass of electron ($9.11 \times 10^{-28}\ g$), ϵ is the relative permittivity of CdS (5.7), e is the charge of an electron ($1.6 \times 10^{-19}\ C$ or $1\ eV$) and h is the Plank's constant ($6.62 \times 10^{-34}\ J$ S or $4.13 \times 10^{-15}\ eV$).

The band gap values and calculated particle size of pure CdS and the CdS in SiO_2@CdS core-shell nanoparticles are given in Table 3.1.2. The SiO_2@CdS core-shell nanoparticles exhibit particle size less than the Bohr radius of bulk CdS and this is the reason for the increase in the band gap of CdS in the SiO_2@CdS core-shell nanoparticles. The Bohr radius (a_B) for bulk CdS is 2.5 nm [65]. The small size of cadmium sulfide nanoparticles on the surface of silica limits the volume occupied by the electron-hole pairs [56].

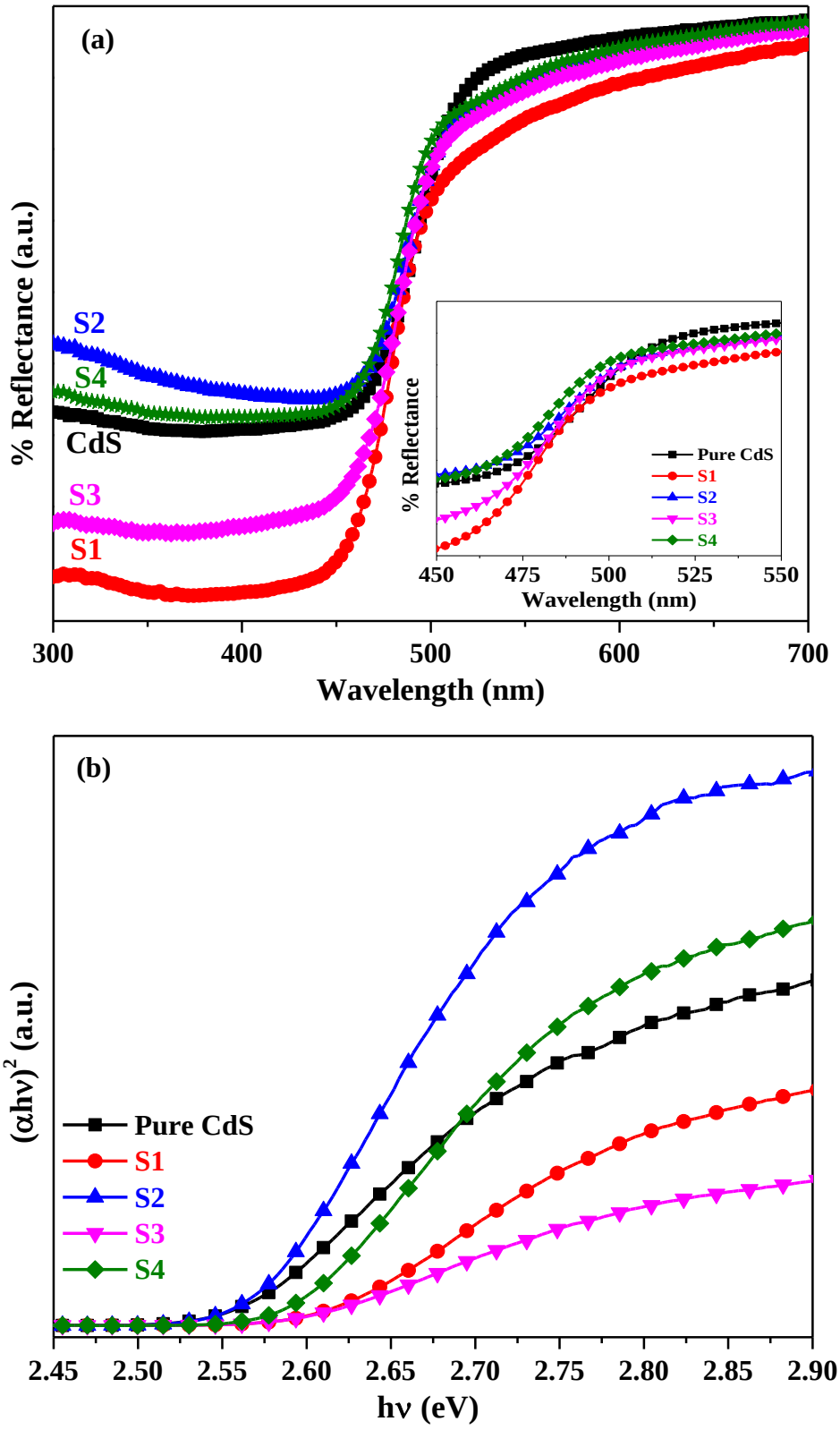

Fig. 3.1.13: (a) DRS spectra for SiO_2@CdS core-shell nanoparticles (inset shows the enlarged portion) and **(b)** estimation of band gap of CdS and SiO_2@CdS samples using the Tauc plots.

Table 3.1.2: Band gap and estimated particle size of CdS in SiO_2@CdS core-shell nanoparticles.

Sample name	Band gap (eV)	Estimated particle size (nm)
Bulk CdS	2.42	-
Nano CdS	2.55	2.15
S1	2.60	1.83
S2	2.56	2.10
S3	2.58	1.95
S4	2.58	1.95

3.1.3.7 Photoluminescence spectroscopy (PL)

The PL spectra of cadmium sulfide nanoparticles and the SiO_2@CdS core-shell nanoparticles are shown in Figure 3.1.14. Pure cadmium sulfide nanoparticles show an emission band at about 540 nm attributed to surface trap states and no band is observed due to near band edge emission [66]. The surface trap state emission in cadmium sulfide nanoparticles is due to recombination of electrons trapped in the sulfur vacancies with holes in the valence band. The SiO_2@CdS core-shell nanoparticles S1, S2, S3 and S4 show emission bands at about 510, 520, 505 and 510 nm, respectively. These emission bands are attributed to near band edge emission of cadmium sulfide nanoparticles [67]. All the SiO_2@CdS samples show a very weak shoulder band at about 560 nm and this is attributed to surface trap states. The SiO_2@CdS core-shell nanoparticles show about 20 nm red shift of the surface trap state emission compared to pure cadmium sulfide nanoparticles. The PL results also show enhancement in the intensity of near band edge emission of CdS due to immobilization of CdS nanoparticles on the surface of silica and also by reducing the surface trap states in the SiO_2@CdS core-shell nanoparticles [52,68].

Rafati et al. and Hebalkar et al. have reported the band gap of CdS in SiO_2@CdS core-shell nanoparticles as 3.7 and 3.0 eV, respectively [53,55]. The reported band gap of CdS in these samples lies near to UV region which restricts its use in visible light. Kang et al. have reported the band gap of CdS in SiO_2@CdS core-shell nanoparticles as 2.8 eV [52]. In the present study, the synthesized SiO_2@CdS core-shell nanoparticles exhibit the band gap of CdS as 2.6 eV. Compared to the previous reports, the SiO_2@CdS core-shell nanoparticles reported in the present study can be useful in the visible region of the solar spectrum. Kang et al. have reported

the photoluminescence of CdS in SiO_2@CdS core-shell nanoparticles at 468 nm attributed to band edge emission and at 663 nm attributed to surface defects [52]. Li et al. have reported the photoluminescence of CdS in SiO_2@CdS core-shell nanoparticles at 383 nm attributed to band edge emission and at 486 nm attributed to surface defects [51]. Dhas et al. have reported the photoluminescence of CdS in SiO_2@CdS core-shell nanoparticles at 500 nm related to band edge emission and at 570 nm related to surface trap states [54]. In the present study, the SiO_2@CdS nanoparticles show emission due to band edge at 510 nm and a weak shoulder emission at 560 nm due to surface defects. The observed photoluminescence spectral results compare with those reported by Dhas et al [54]. The SiO_2@CdS core-shell nanoparticles show a red shift (about 20 nm) of surface defect emission with respect to pure CdS. This indicates the synergistic interaction between CdS and SiO_2. The presence of weak emission with reduced intensity in the SiO_2@CdS core-shell nanoparticles indicates the presence of less number of defects in the core-shell nanoparticles. Semiconductor materials with fewer defects have good efficiency compared to those with more defects and they can be useful in different applications such as photodegradation of organic pollutants in industrial waste, environmental remediation, etc.

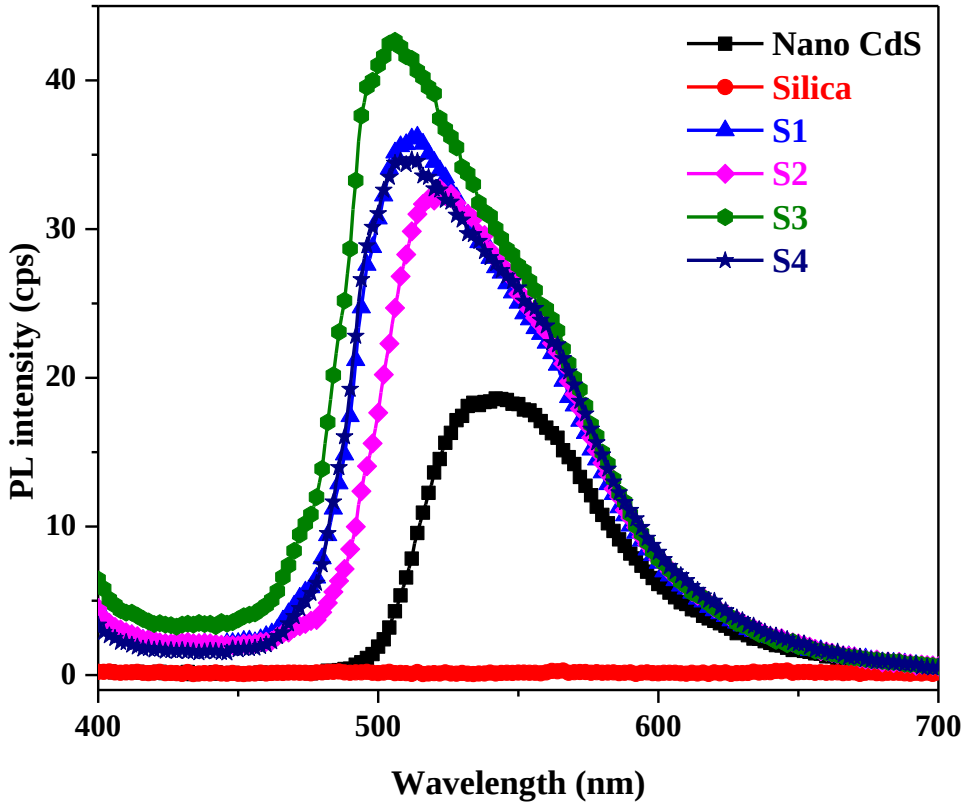

Fig. 3.1.14: Photoluminescence spectra for silica, pure CdS and SiO_2@CdS core-shell nanoparticles (S1 to S4).

3.1.4 Proposed mechanism of formation of SiO_2@CdS core-shell nanoparticles

The possible mechanism of formation of SiO_2@CdS core-shell nanoparticles is shown in Scheme 3.1.3. Silica has a number of hydroxyl groups on the surface. The silanol groups readily react with hydroxyl groups of ethylene glycol and form silica-ethylene glycol complex ($SiO_2(EG)_2$) with the loss of water molecules [69–71]. Cadmium acetate reacts with the silica-ethylene glycol complex with the formation of ionic bond between the hydroxyl groups of silica and the cadmium ions. Thiourea reacts with the water present in the ethylene glycol and also the water of crystallization present in cadmium acetate, releasing H_2S, gradually. The released hydrogen sulfide reacts with the cadmium ions of the complex leading to the nucleation of small CdS particles on silica [69,72]. The small cadmium sulfide nanoparticles undergo further growth and form a uniform shell over the silica core.

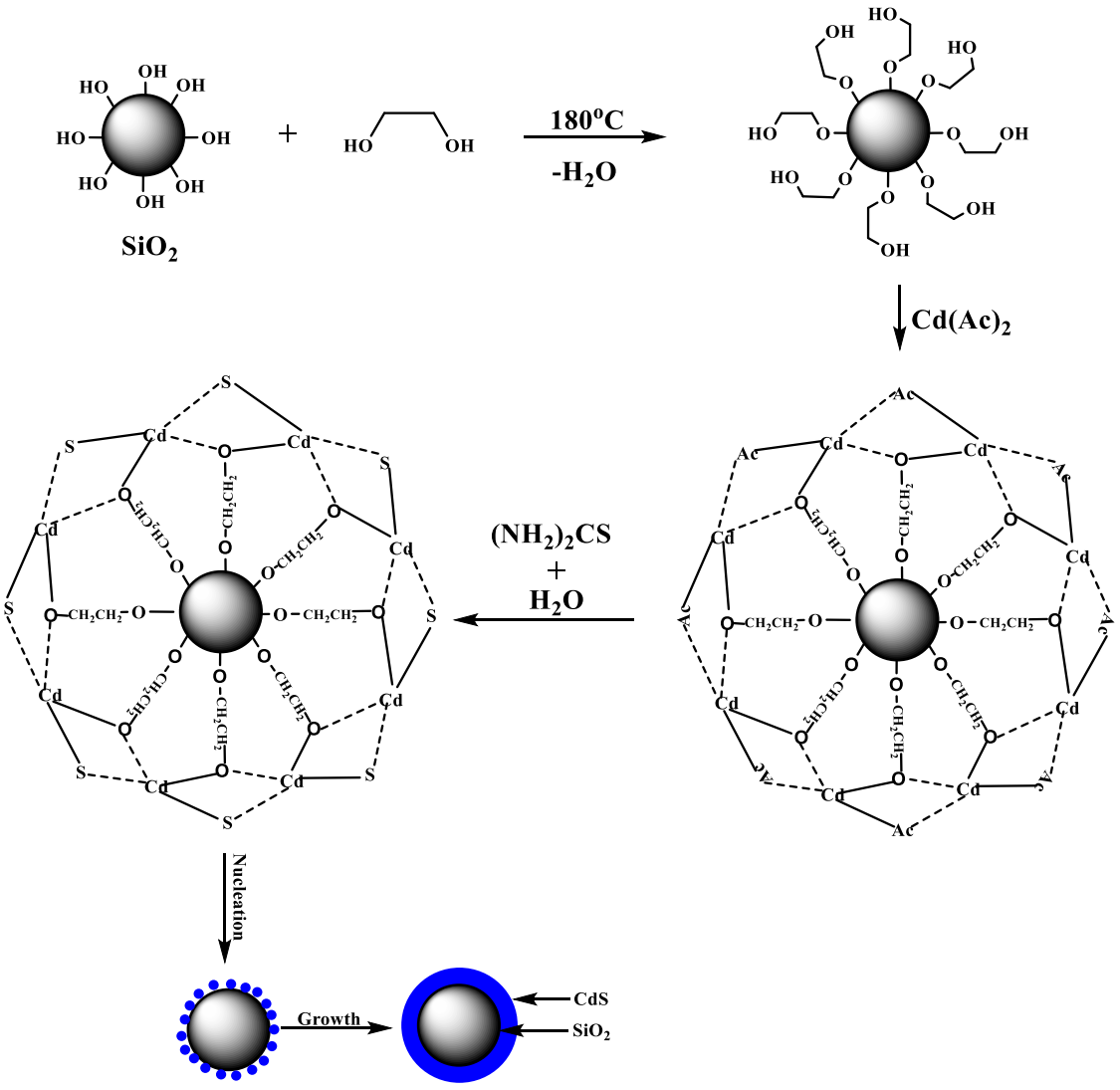

Scheme 3.1.3: Possible mechanism for the formation of SiO_2@CdS core-shell nanoparticles.

3.1.5 Conclusions

SiO_2@CdS core-shell nanoparticles with different shell thickness have been successfully synthesized by a thermal decomposition approach. Uniform deposition of cadmium sulfide nanoparticles over unactivated silica spheres is possible at 180 ^oC. TEM / SEM images clearly show the uniform deposition of cadmium sulfide nanoparticles on unactivated silica microspheres. SAED / HRTEM studies confirm the crystalline nature of cubic cadmium sulfide nanoparticles on the surface of silica. DRS results show an increase in the band gap of CdS and a blue shift is observed in the SiO_2@CdS core-shell nanoparticles compared to pure CdS nanoparticles due to quantum size effect. PL results show enhancement in the intensity of near band edge emission of CdS due to immobilization of CdS nanoparticles on the surface of silica and also by reducing the surface trap states in the SiO_2@CdS core-shell nanoparticles. Compared to all the reported methods, the present method is superior, facile and has several advantages. There is no need for surface functionalization of silica core and uniform CdS shell with different thicknesses on silica can be achieved in 60 min. The chemicals used in the preparation are inexpensive and no inert atmosphere is required. This method can be extended to prepare other core-shell nanomaterials with type-I band alignment.

3.2 Synthesis of ZnO@CdS (Type-II) Core-Shell Nanoparticles *via* a Novel Thermal Decomposition Approach

3.2.1 Introduction

A number of researchers have made tremendous effort to use semiconductors in photocatalysis, water splitting, environmental remediation, solar cells, and sensors[73–80]. Metal oxide semiconductors such as ZnO [81,82], TiO_2 [83,84], and α-Fe_2O_3 [85,86] have been used as efficient photocatalysts. Among the metal oxide semiconductors, ZnO is the most widely used one and it is an intrinsic semiconductor with a band gap of about 3.38 eV, and high exciton binding energy (60 meV) [87]. ZnO mainly exists in two forms. They are hexagonal wurzite and cubic zinc blende structure. The most stable structure of ZnO is hexagonal wurzite with lattice parameters a = 3.25 Å and c = 5.21 Å [88]. In hexagonal wurzite structure of ZnO, both the Zn^{2+} cations and O^{2-} anions are in tetrahedral coordination which results in non-central symmetrical structure. This type of symmetry leads to piezoelectricity and pyroelectricity in ZnO [88]. The crystal structures of ZnO (hexagonal wurzite and cubic zinc blend) are shown in Figure 3.2.1.

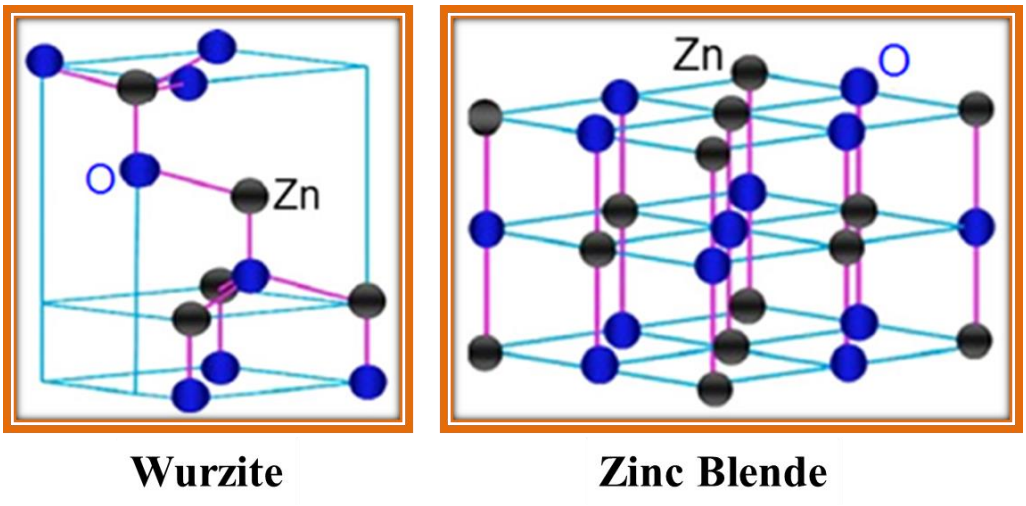

Fig. 3.2.1: A schematic representation of wurzite and zinc blende crystal structures of ZnO [88].

In the past few years, a lot of effort has been made by researchers for the synthesis of ZnO nanoparticles with different morphologies and sizes. The SEM and TEM images of various morphologies of ZnO are shown in Figure 3.2.2. One dimensional nanostructures (e.g. nanowires, nanorods, nanoneedles, nanotubes, columns, and helices) play an important role in many applications because they possess high surface to volume ratio with short diffusion length

[88–93]. The one dimensional nanostructures provide a direct pathway for charge transport since they possess large junction area which imparts low reflectance [94]. Also, these materials reduce the recombination of excitons and thus show high energy conversion efficiency.

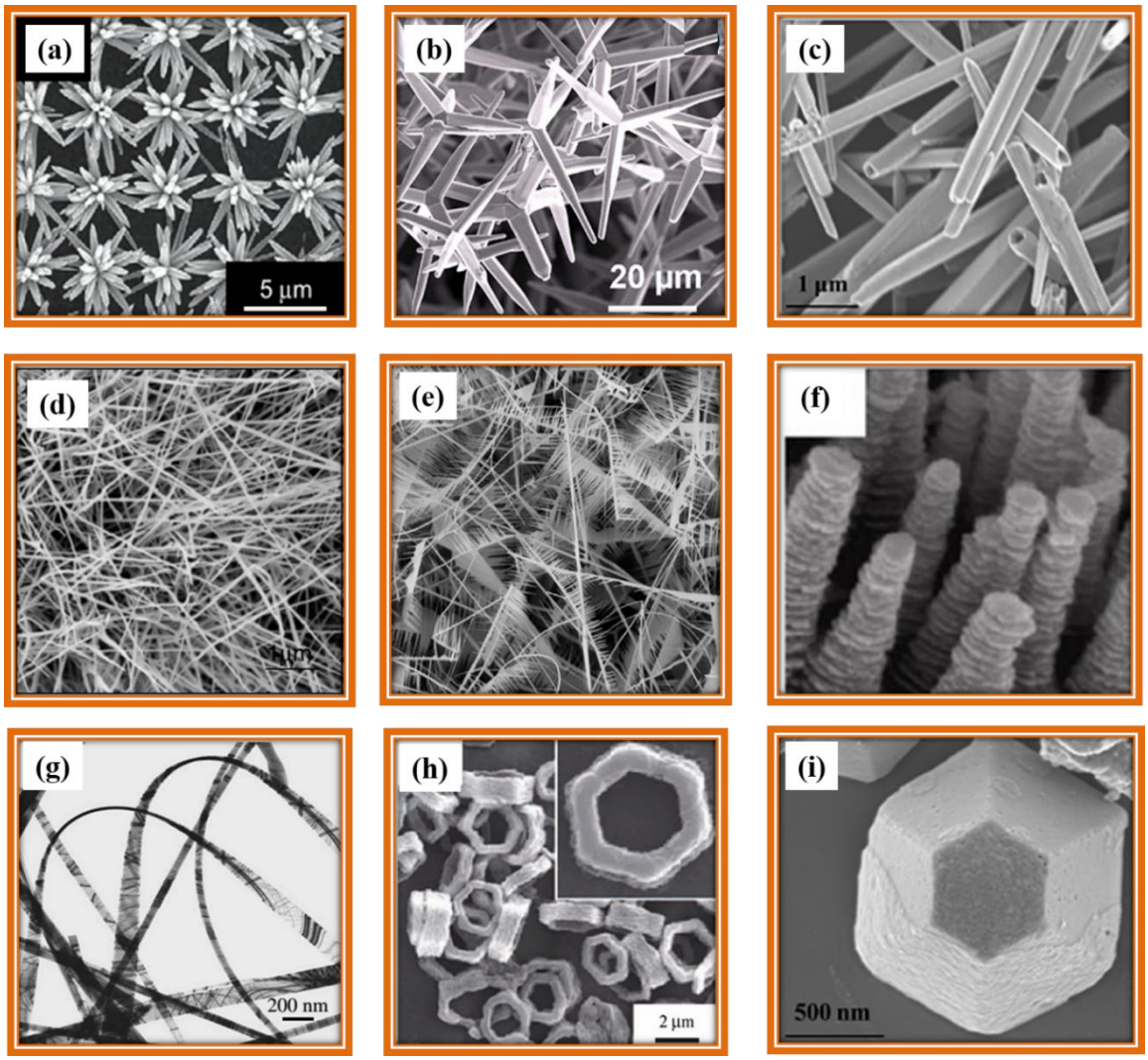

Figure 3.2.2: Various morphologies of ZnO; **(a)** flower-like, **(b)** tetrapod, **(c)** tube, **(d)** wire, **(e)** comb-like, **(f)** columnar nanoplates, **(g)** belt-like, **(h)** hexagonal ring, and **(i)** cone-like [88–92].

Since ZnO has a wide band gap, its use is restricted to the UV region. To enable the use of semiconductors in the visible region, the wide band gap semiconductors have been coupled with semiconductors with narrow band gap such as CdS, ZnS, PbS, ZnSe, and CdSe [95–101]. The coupling of wide band gap semiconductor with a narrow band gap semiconductor can lead to type-II structures. The condition to form a type-II structure is that both the valence and conduction bands of the wide band gap semiconductor should be either lower or higher than those of the narrow band gap semiconductor. They have potential applications in areas such as

nonlinear optics, photovoltaics, photodetectors, cell imaging, etc [102–105]. The TEM and HRTEM images of ZnO coupled with ZnS and ZnSe are shown in Figure 3.2.3.

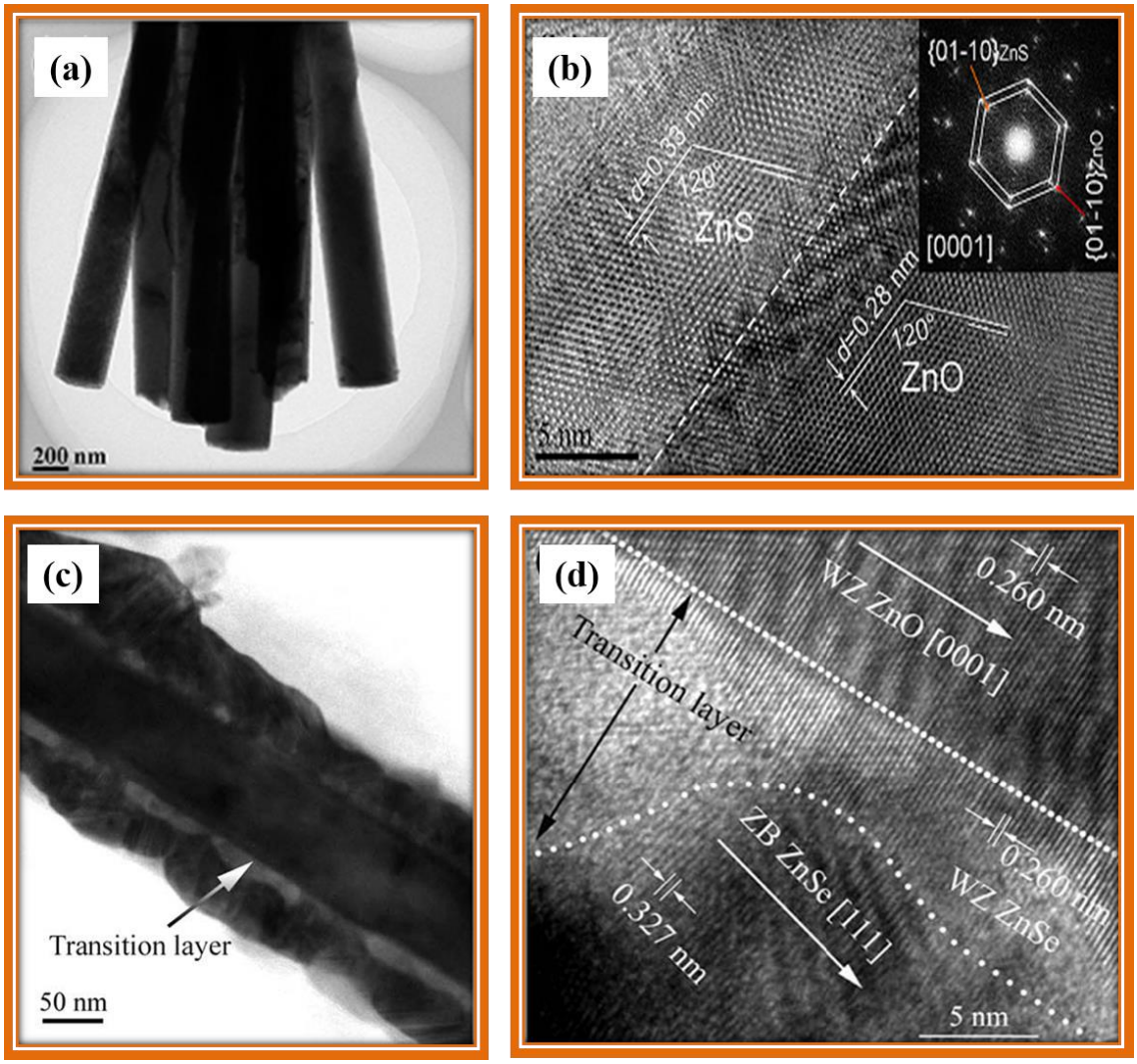

Fig. 3.2.3: TEM and HRTEM images of **(a, b)** ZnO coupled with ZnS [97] and **(c, d)** ZnO coupled with ZnSe [98].

Among the narrow band gap semiconductors, CdS is an excellent choice since it has a band gap of about 2.42 eV and the conduction band edge of CdS (− 4.1 eV) is slightly higher than that of ZnO (− 4.3 eV) [106]. Also, ZnO and CdS have nearly the same lattice constants. These characteristics have enabled achieving good efficiency in different applications like photocatalysis, solar cells, etc [87,106].

Different synthetic routes have been reported in the literature for the synthesis of ZnO@CdS core-shell nanoparticles. They include solution route [87], successive ionic layer adsorption and reaction [106,107], chemical bath deposition [75,94,108], sonochemical synthesis [109–

111], hydrothermal synthesis [112], electro deposition [113], sol-gel method [114], and photodeposition [115]. A brief description of the reported methods for the synthesis of ZnO@CdS core-shell nanoparticles are given below.

Solution route [87]: In this method, ZnO nanorod arrays are synthesized by heating zinc acetate at 300 ^{o}C for 12 h in air. Then, certain amount of ZnO nanorod arrays are dispersed in an aqueous solution containing different amounts of citric acid and stirred at 40 ^{o}C for 2 h to obtain functionalized ZnO nanorods. After that, cadmium chloride solution is added drop wise to the aqueous solution containing the functionalized ZnO nanorods and stirred for about 2 h. This is followed by drop wise addition of sodium sulfide solution and the stirring is continued for further 1 h to obtain CdS deposited ZnO nanorods. A schematic illustration of ZnO@CdS core-shell nanorod arrays, synthesized using the solution route, is shown in Figure 3.2.4.

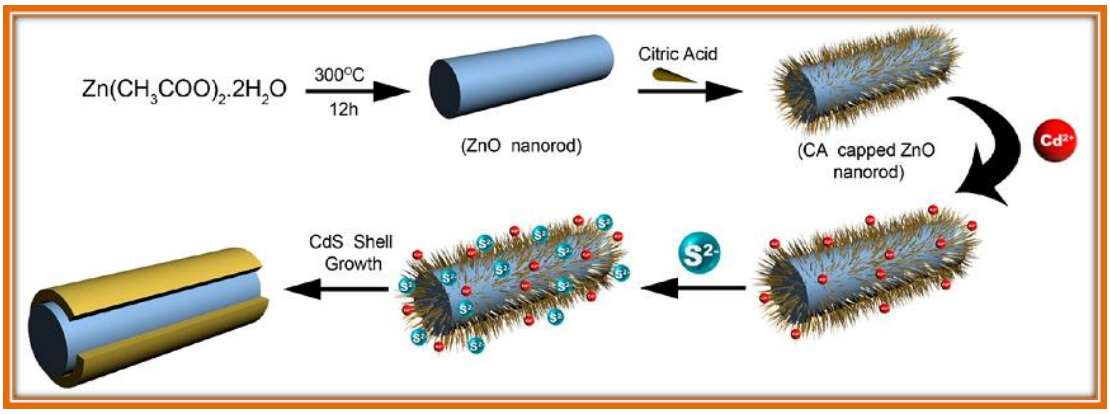

Fig. 3.2.4: Schematic illustration of the synthesis of ZnO@CdS core-shell nanorod arrays using solution route [87].

Successive ionic layer adsorption and reaction [107]: In this method, ZnO nanorods are deposited on indium tin oxide (ITO) glass *via* hydrothermal method. The obtained ZnO nanorods are immersed in cadmium nitrate aqueous solution for 30 s and rinsed thoroughly with water. Then, the Cd^{2+} adsorbed ZnO nanorods are immersed in aqueous sodium sulfide solution for 30 s and rinsed several times with water. The thickness of CdS shell on the ZnO nanorods is controlled by varying the number of SILAR cycles.

Chemical bath deposition [108]: In this method, ZnO nanowires are grown on silicon substrate *via* hydrothermal method. The obtained ZnO nanowires are annealed at 400 ^{o}C for 1 h in air. Then, the ZnO nanowires are immersed in a mixture of cadmium sulfate, thiourea and ammonium hydroxide and the reaction contents are heated at 60 ^{o}C for a period of 100-200 min.

Sonochemcial synthesis [111]: In sonochemical method, zinc nitrate is dissolved in an aqueous solution and then polyethyleneglycol (PEG-20000) and tetraethylamine (TEA) are added. Before ultrasonic irradiation, the oxygen present in the reaction mixture is removed by purging high purity argon gas for several minutes. Then, the reaction contents are irradiated with high intensity ultrasound for 2 h at room temperature which results in the production of ZnO nanospheres. A mixture of cadmium chloride and thiourea are added to an ethanol suspension of ZnO nanospheres. The reaction contents are irradiated for about 30 min to produce CdS deposited ZnO nanospheres.

Hydrothermal synthesis [112]: ZnO nanorods are prepared using the sonochemcial route. To deposit CdS shell on the ZnO nanorods, certain amount of ZnO nanorods is suspended in an aqueous solution and then cadmium nitrate is added and the pH is maintained at 8 by adding ammonia solution. After that, required amount of thiourea is added to the above mixture and oxygen is removed from the reaction mixture by purging high purity argon gas and the stirring is continued for 1 h. Finally, a few milliliters of mercaptoethanol are added. The reaction contents are transferred into a Teflon lined autoclave and are heated at 150 ^{o}C for 24 h.

Electro deposition [113]: In this method, ZnO nanorods are obtained by mixing zinc nitrate, ammonium acetate and bis(hexamethylene)triamine in aqueous solution followed by stirring for half an hour. The obtained ZnO nanorods are calcined at 350 ^{o}C for 1 h. The obtained ZnO nanorods are used as working electrode which is dipped in a mixture of aqueous solutions of cadmium nitrate and thiourea at 90 ^{o}C. A current density of 0.5 $mAcm^{-2}$ is applied to deposit CdS nanoparticles on the ZnO nanorods.

Sol-gel method [114]: In this method, zinc acetate is dissolved in a mixture of 2-propanol and diethanolamine and stirred for 2 h. A mixture of cadmium nitrate and thiourea is dissolved in 2-propanol and stirred for 2 h. After that, both the solutions are mixed and stirred for a few hours and the obtained sol is evaporated to get a gel. The gel is dried in an oven to get CdS coated ZnO.

Photodeposition method [115]: First, ZnO nanoparticles are prepared by a solution route. Then, certain amount of ZnO nanoparticles, S_8, and cadmium nitrate are mixed in a mixture of ethanol and water. Before the photodeposition, the suspension is purged with nitrogen gas for 2 h under dark to eliminate oxygen. Then, the reaction contents are irradiated with a 300 W xenon lamp for about 3 h to obtain CdS deposited ZnO nanoparticles.

The TEM images of ZnO@CdS core-shell nanoparticles, prepared by solution route and successive ionic layer adsorption and reaction (SILAR), are shown in Figure 3.2.5.

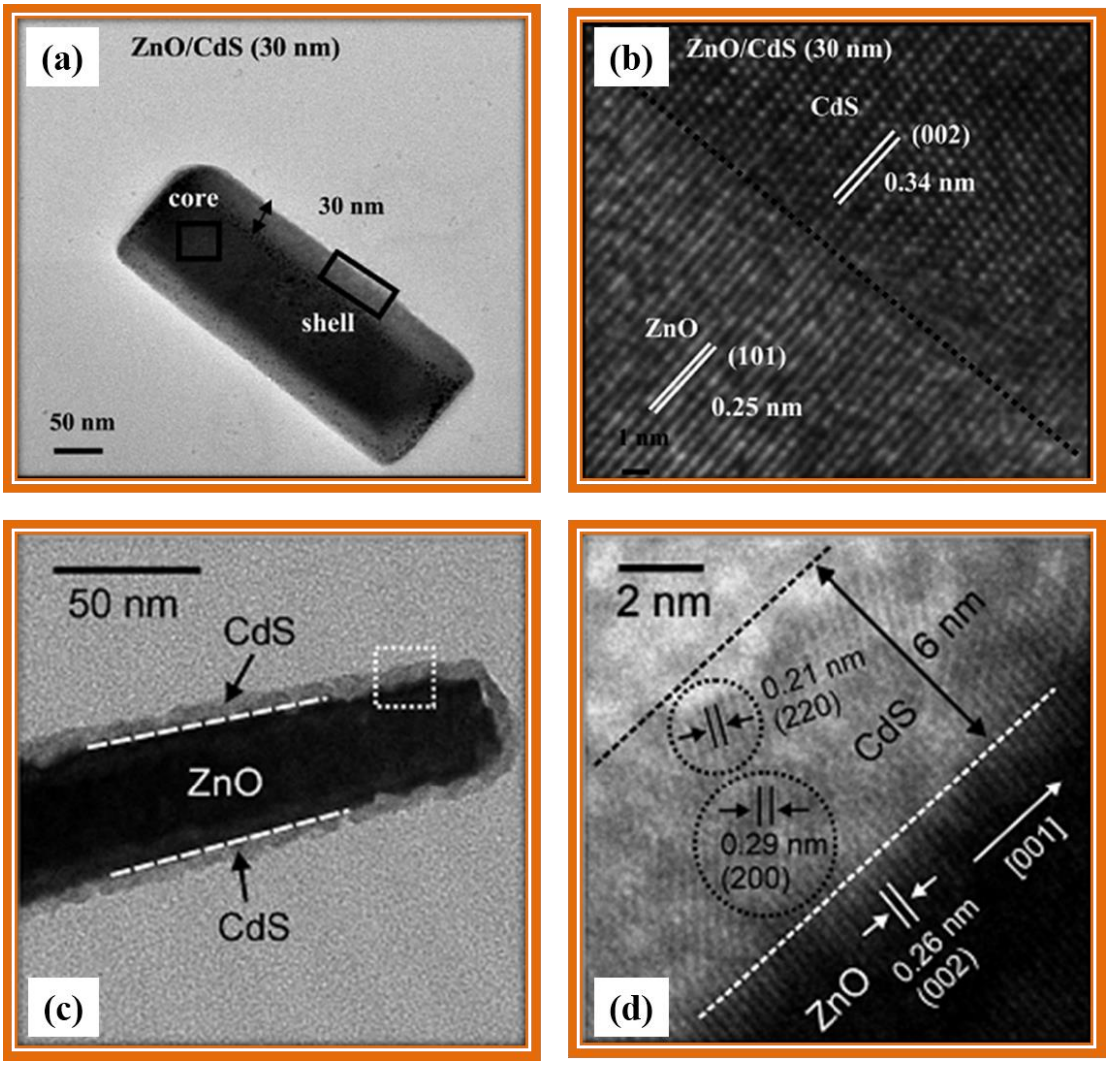

Figure 3.2.5: TEM and HRTEM images of ZnO@CdS core-shell nanoparticles synthesized *via* **(a, b)** solution route [87] and **(c, d)** successive ionic layer adsorption and reaction [107].

In the present study, ZnO@CdS core-shell nanoparticles have been successfully synthesized by a simple, economical and novel thermal decomposition approach. The CdS shell thickness in the ZnO@CdS nanoparticles could be controlled by varying the concentrations of precursors used during the thermal decomposition.

3.2.2 Experimental details

Zinc nitrate (99%, Himedia, AR), urea (99.5%, Rankem, AR), citric acid (99%, Himedia, LR), cadmium acetate (99%, Himedia, AR), thiourea (99%, Rankem, LR), and ethylene glycol (99%, Rankem, LR) were used as received and methanol (99%, SD Fine) was distilled before

further use. The ZnO@CdS core-shell heteronanostructures were synthesized in three steps and the detailed procedure is as follows.

3.2.2.1 Synthesis of ZnO hexagonal nanorods

The schematic representation of synthesis of hexagonal ZnO nanorods is given in Scheme 3.2.1. The ZnO hexagonal nanorods were synthesized by homogeneous precipitation method as reported in the literature with some modifications [116]. The concentration of reagents used were 0.05 M zinc nitrate and 0.25 M urea in a mixture of ethylene glycol and water (1:1 vol %). In a typical synthesis, 100 mL of 0.05 M zinc nitrate solution was mixed with 100 mL of 0.25 M urea solution and the contents were stirred at 90 ^{o}C. After completion of 5 h, a white precipitate was obtained. The contents were cooled to room temperature, filtered, washed with water and allowed to dry in an oven at 70 ^{o}C for 12 h.

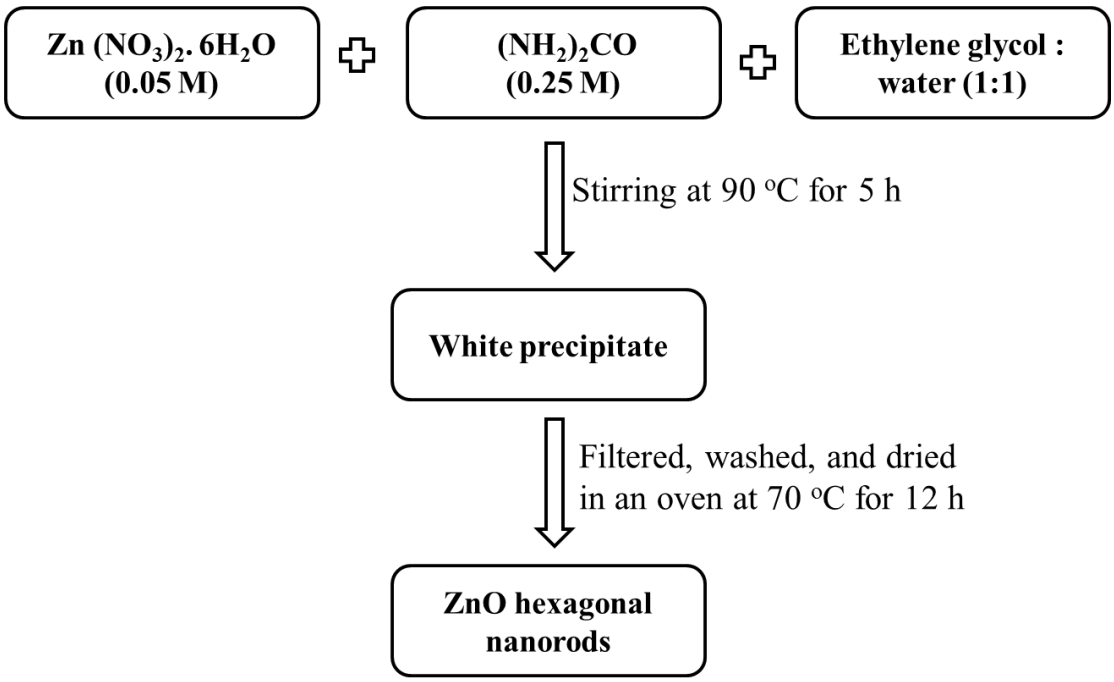

Scheme 3.2.1: Schematic representation of synthesis of ZnO hexagonal nanorods.

3.2.2.2 Surface modification of ZnO nanorods

The schematic representation of surface functionalization of hexagonal ZnO nanorods with citric acid is given in Scheme 3.2.2. Surface modification of ZnO hexagonal nanorods was carried out using citric acid as the surface modifying agent. Citric acid was chosen since it has been successfully used as the surface modifying agent for ZnO [87,117]. About 1 mM of ZnO powder (0.0873 g) was dispersed in 50 mL of distilled water and then 5 mg of citric acid was

added. At higher amount of citric acid (i.e. > 5 mg), it was found that the ZnO nanorods begin to dissolve. The contents were stirred at room temperature for 4 h, filtered, washed and dried in the oven at 70 ^{o}C.

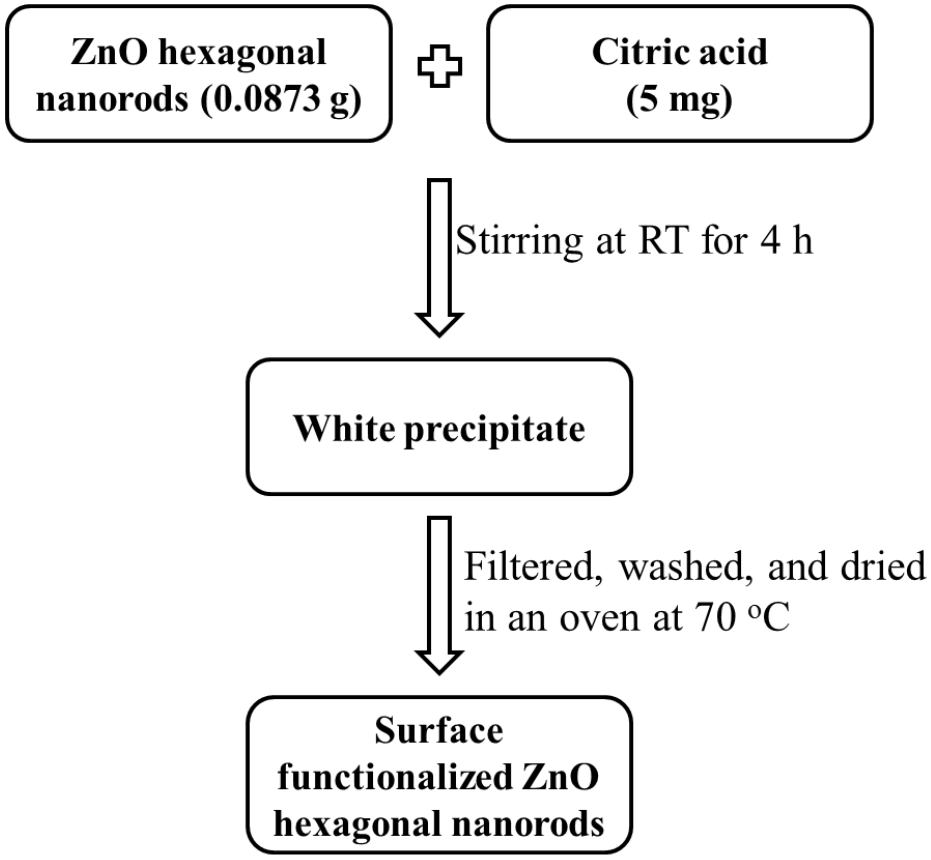

Scheme 3.2.2: Schematic representation of surface functionalization of ZnO hexagonal nanorods using citric acid.

3.2.2.3 Synthesis of ZnO@CdS core-shell nanoparticles

The schematic representation of experimental setup and the procedure for the deposition of CdS shell on the ZnO hexagonal nanorods is given in Scheme 3.2.3. In a typical synthesis, about 50 mg of the surface modified ZnO hexagonal nanorods was mixed with different molar ratios of cadmium acetate and thiourea (Table 3.2.1) in 10 mL of ethylene glycol. The contents were sonicated for 3 min to achieve good dispersion, and heated at 180 ^{o}C for 1 h. During the reaction, the color of the contents changed to yellow which indicates the formation of CdS. After completion of the reaction, the contents were cooled to room temperature and 25 mL of methanol was added to get a precipitate. The obtained precipitate was centrifuged, washed with methanol and dried under vacuum to get the ZnO@CdS powder samples. The nomenclature of various ZnO@CdS samples, prepared in the present study, is given in Table 3.2.1.

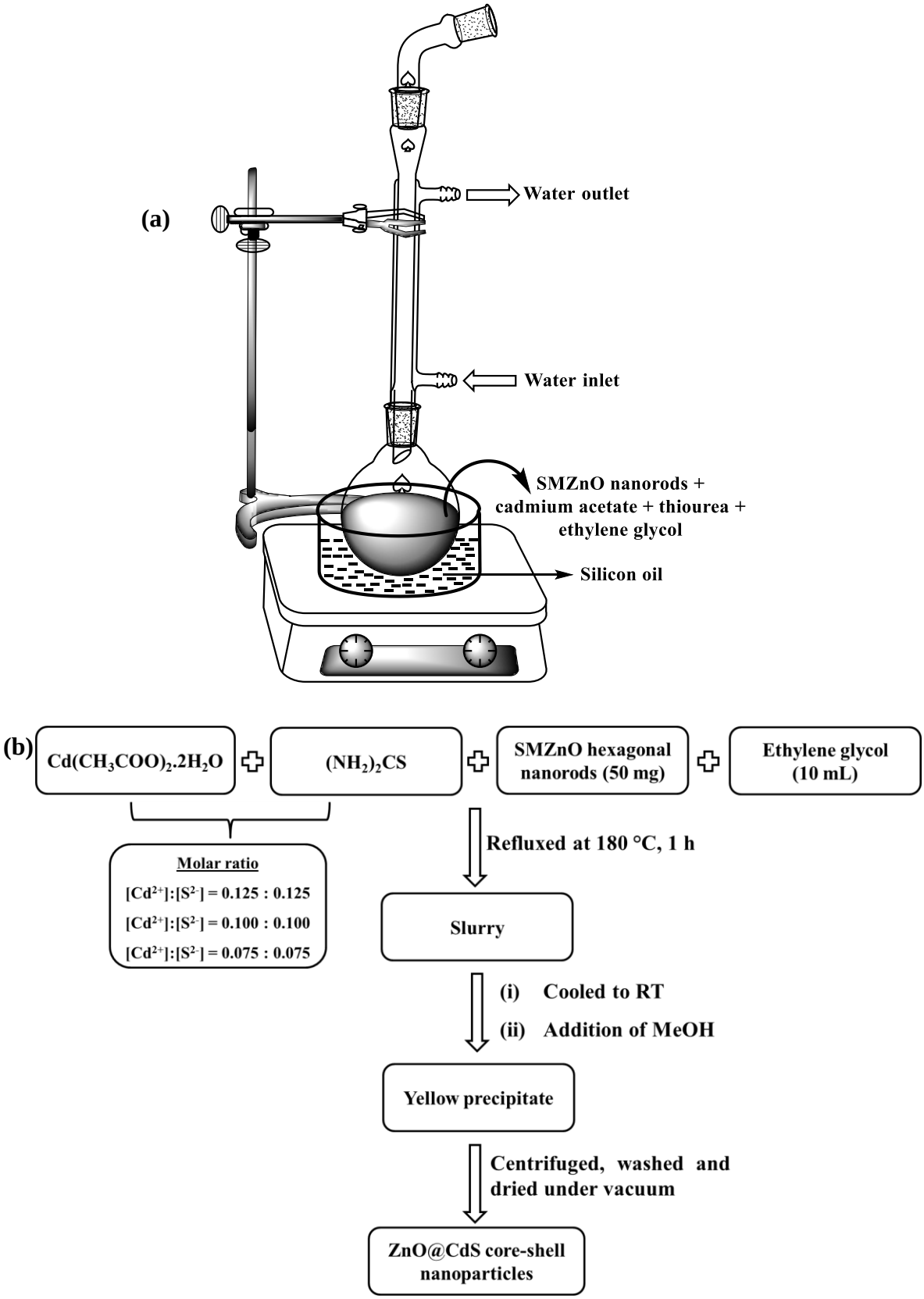

Scheme 3.2.3: Schematic representation of **(a)** experimental setup, and **(b)** procedure for the synthesis of ZnO@CdS core-shell nanoparticles.

Table 3.2.1: Concentration of reagents used during the synthesis of ZnO@CdS core-shell nanoparticles. The nomenclature for the samples is also given.

Sample ID	Amount of surface modified ZnO (mg)	$[Cd(CH_3COO)_2.2H_2O]$ (mM)	$[(NH_2)_2CS]$ (mM)
ZC1	50	0.075	0.075
ZC2	50	0.100	0.100
ZC3	50	0.125	0.125

The synthesized ZnO@CdS core-shell nanoparticles were characterized using PXRD, FT-IR, TGA, FE-SEM, EDX, and TEM. The optical properties were studied using DRS and PL spectroscopy. More details on the experimental techniques have been discussed in Chapter-2.

3.2.3 Results and discussion

3.2.3.1 XRD analysis

The XRD patterns of pure ZnO, surface modified ZnO, pure CdS and ZnO@CdS core-shell nanoparticles (ZC1, ZC2 and ZC3) are shown in Figure 3.2.6. Pure ZnO and surface modified ZnO show reflections due to only ZnO (JCPDS file No: 36-1451). The observed reflections at 31.75^o, 34.41^o, 36.25^o, 47.54^o, 56.55^o, 62.82^o, 67.92^o and 69.17^o are attributed to (100), (002), (101), (102), (110), (103), (112) and (201) planes of ZnO, respectively. The intense peak at 2θ = 36.25^o confirms the preferred orientation of ZnO facet along the (101) plane. Pure CdS shows reflections at 26.44^o, 43.80^o and 52.00^o corresponding to (111), (220) and (311) planes of cubic CdS (JCPDS file no: 75-1546). In the XRD patterns of ZnO@CdS core-shell nanoparticles, reflections due to both ZnO and CdS are observed. The XRD peaks due to CdS in the core-shell heteronanostructures are less intense and broad and they are shown in the inset of Figure 3.2.6. The crystallite size of ZnO and CdS in the ZnO@CdS samples was calculated using Debye Scherrer equation using the XRD peaks at 2θ = 36.25^o for ZnO (*(101)*) and at 2θ = 26.44^o for CdS (*(111)*). The crystallite size of pure ZnO is higher (50 nm) compared to that in the ZnO@CdS core-shell heteronanostructures (36-45 nm). The crystallite size of ZnO decreases after the formation of CdS shell on the ZnO. It was difficult to calculate the crystallite size of CdS in the ZnO@CdS samples due to less intense and broad XRD peaks of CdS. This suggests the presence of small CdS nanoparticles in the ZnO@CdS samples.

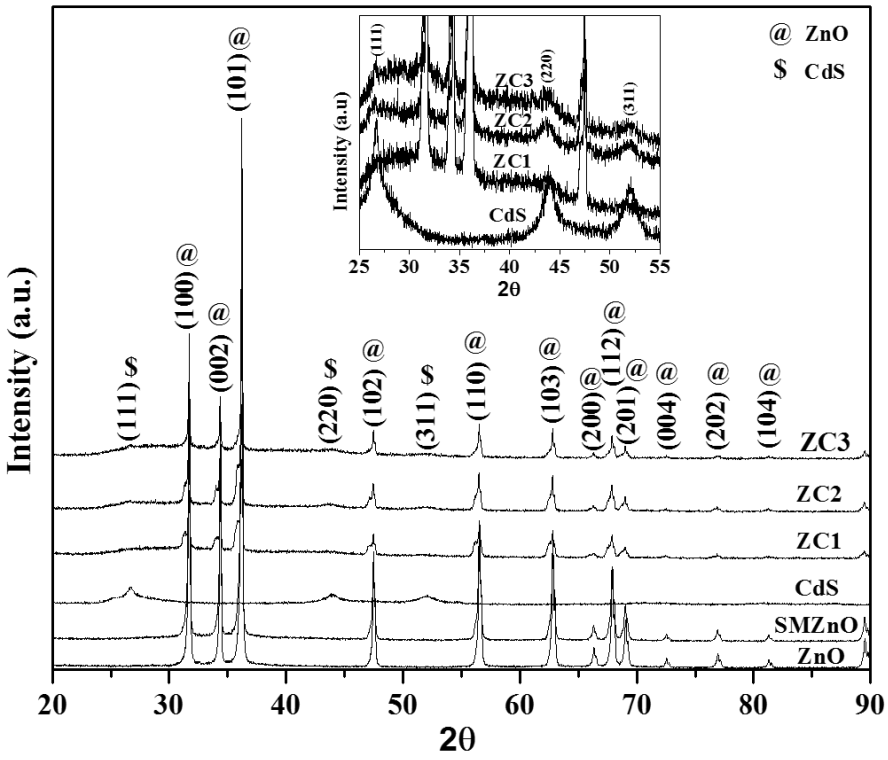

Fig. 3.2.6: XRD patterns for pure ZnO, surface modified ZnO, CdS and ZnO@CdS core-shell nanoparticles (ZC1, ZC2 and ZC3). The inset shows peaks due to CdS.

3.2.3.2 FT-IR analysis

FT-IR spectra of pure ZnO, surface modified ZnO, pure CdS and ZnO@CdS core-shell nanoparticles (ZC1, ZC2 and ZC3) are shown in Figure 3.2.7 and the assignments are given in Table 3.2.2. All the samples show IR bands at 3435 and 1630 cm^{-1} attributed to stretching and bending modes of hydroxyl groups of water molecules physisorbed on the surface of ZnO [118]. They show a weak band at 2922 cm^{-1} and another band at 1120 cm^{-1} attributed to asymmetrical stretching of $–CH_2$ group and symmetrical stretching of C–OH due to ethylene glycol molecules, respectively [119,120]. All the samples show a band corresponding to Zn–O vibration at about 570 cm^{-1} [116,121]. In ZnO, the band at 1382 cm^{-1} is attributed to symmetrical stretching of carbonate groups [116]. Surface modified ZnO shows a band at 1397 cm^{-1} attributed to symmetrical stretching of COO^- due to citrate ions used during the surface modification of ZnO [120]. Pure CdS shows a band at 649 cm^{-1} attributed to Cd–S stretching [122]. Pure CdS and the ZnO@CdS core-shell nanoparticles (ZC1, ZC2 and ZC3) show bands at 1403, 1397, 1395 and 1395 cm^{-1}, respectively, which are attributed to symmetrical stretching of COO^- group [120].

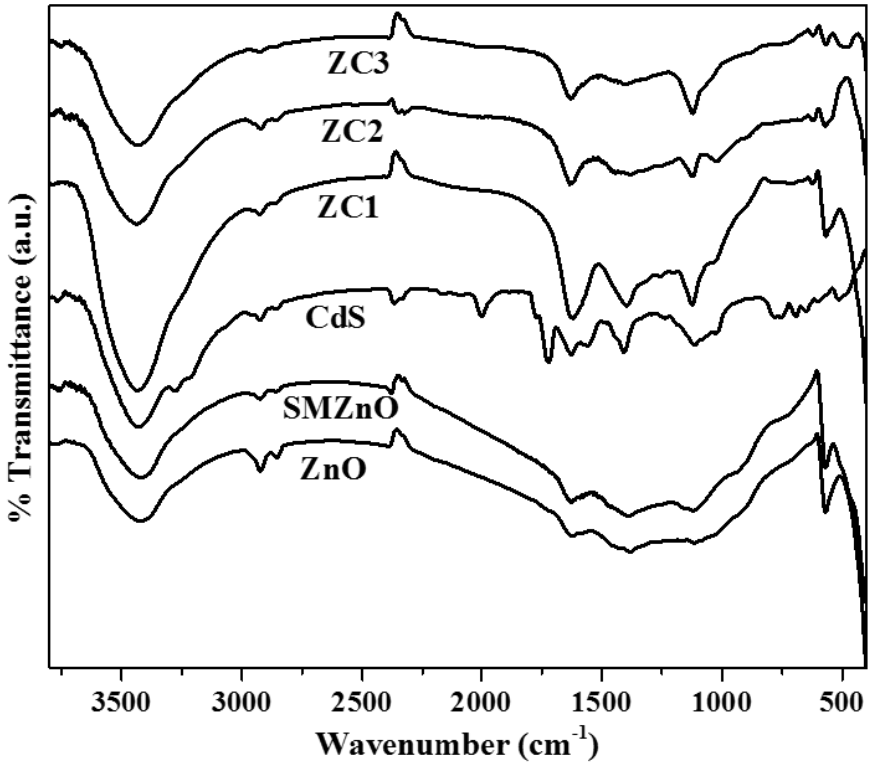

Fig. 3.2.7: FT-IR spectra of pure ZnO, surface modified ZnO, CdS and ZnO@CdS core-shell nanoparticles (ZC1, ZC2 and ZC3).

Table 3.2.2: FT-IR band assignments for ZnO, surface modified ZnO, CdS and ZnO@CdS core-shell nanoparticles (ZC1, ZC2 and ZC3).

Band position (cm^{-1})						Assignment
ZnO	**SMZnO**	**CdS**	**ZC1**	**ZC2**	**ZC3**	
3430	3430	3435	3430	3430	3430	$\nu_{sym}(-OH)$
2922	2922	2922	2922	2922	2922	$\nu_{sym}(-CH_2)$
-	-	1725	-	-	-	$\nu_{sym}(C{=}O)$
1628	1628	1628	1628	1628	1628	$\delta\,(-OH)$
-	1397	1403	1397	1395	1395	$\nu_{sym}(COO^-)$
1382	-	-	-	-	-	$\nu_{sym}(NO_3^-)$
1118	1118	1120	1118	1118	1118	$\nu_{sym}(C{-}OH)$
-	-	649	-	-	-	$\nu_{sym}(Cd{-}S)$
570	570	-	570	570	570	$\nu_{sym}(Zn{-}O)$

3.2.3.3 TGA analysis

TGA analysis was carried out for pure ZnO hexagonal nanorods and surface functionalized ZnO hexagonal nanorods and the TGA patterns are shown in Figure 3.2.8. Pure ZnO shows a weight loss of 1.8 % and surface modified ZnO shows a weight loss of 2.5 % in the region 35-800 ^{o}C. This indicates the presence of more organic content in the surface modified ZnO compared to pure ZnO [123,124].

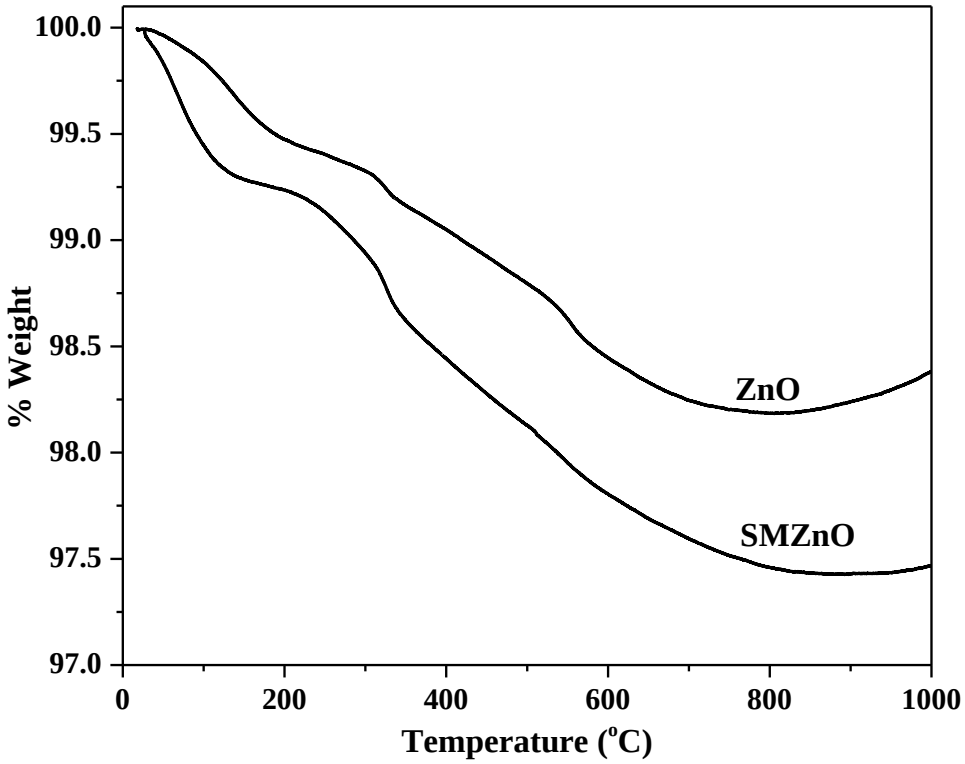

Figure 3.2.8: TGA patterns of pure ZnO and surface functionalized ZnO hexagonal nanorods.

3.2.3.4 FE-SEM studies

The FE-SEM images of pure ZnO, CdS and ZnO@CdS samples are shown in Figure 3.2.9. Pure ZnO shows rods with hexagonal facets and smooth surface. The length of ZnO rods is about 2 μm and the diameter is 250 ± 20 nm. Pure CdS shows agglomerated small particles. In the ZnO@CdS samples, the surface of ZnO is rough which indicates the deposition of CdS on ZnO and the diameter of the ZnO nanorods (250 nm) increases in the ZnO@CdS samples (ZC1, ZC2 and ZC3) to about 290, 330 and 370 nm, respectively.

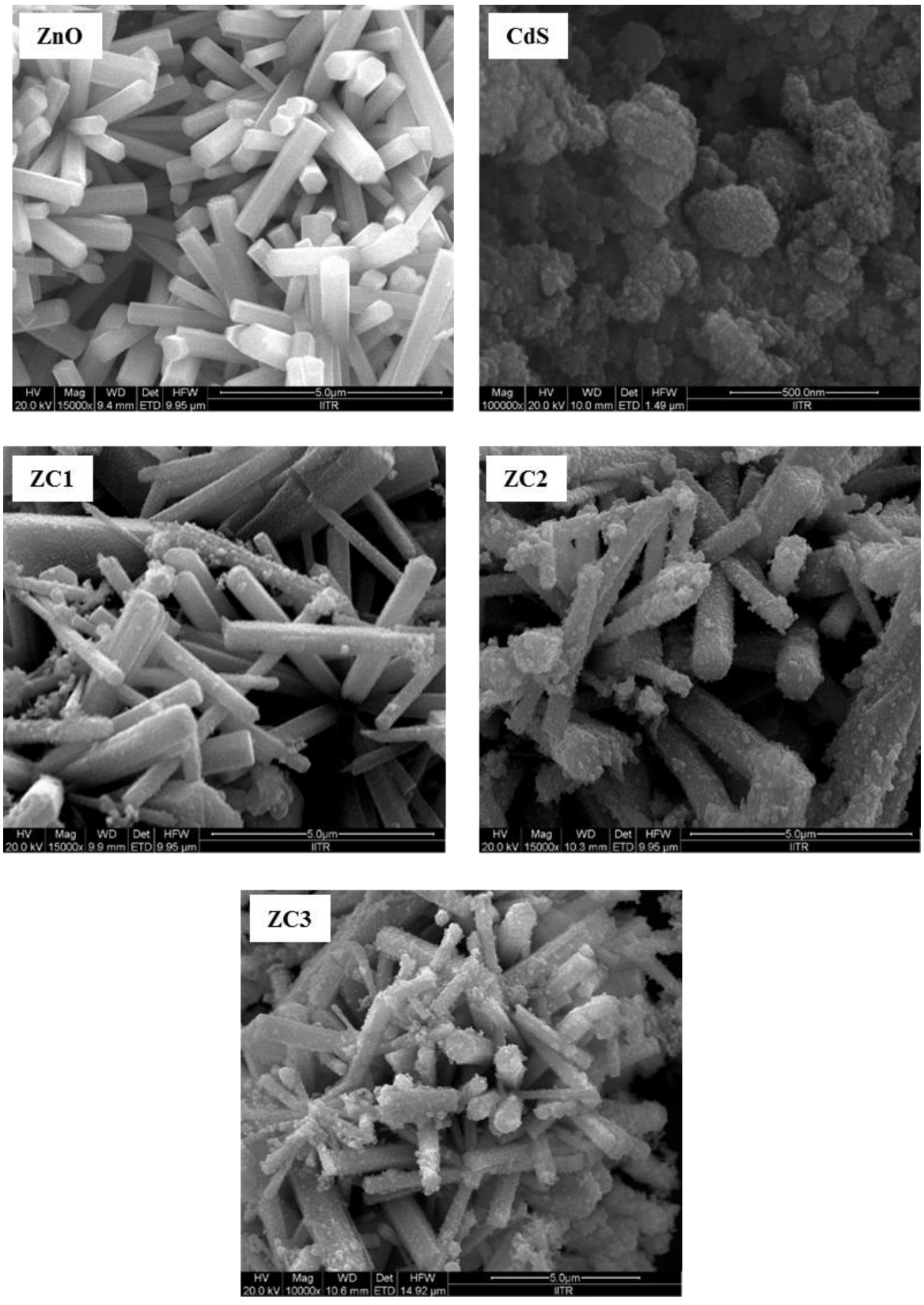

Fig. 3.2.9: FE-SEM images of pure ZnO, CdS and ZnO@CdS core-shell nanoparticles (ZC1, ZC2 and ZC3).

3.2.3.5 EDX analysis

The elemental composition of ZnO@CdS core-shell nanoparticles was analyzed using EDX analysis (Figure 3.2.10). The elemental composition along with standard deviation (cadmium and sulfur) from the data measured at different spots on the samples is given in Table 3.2.3. All the samples show the presence of cadmium and sulfur on the surface of ZnO nanorods. An increase in the weight percent of cadmium and sulfur is observed according to the concentrations of CdS precursors (cadmium acetate and thiourea) used during the synthesis ($[Cd^{2+}]:[S^{2-}]$ = 0.075:0.075, 0.100:0.100 and 0.125:.125).

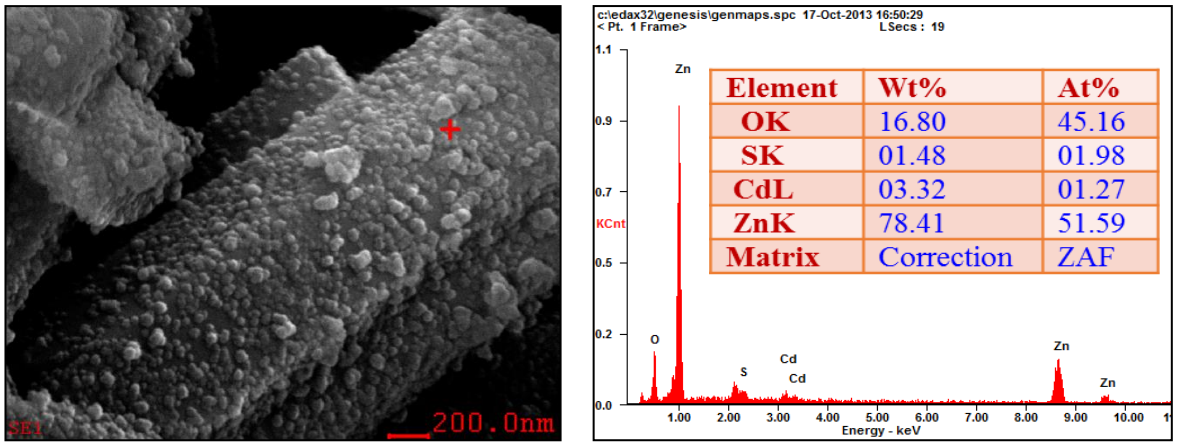

(a)

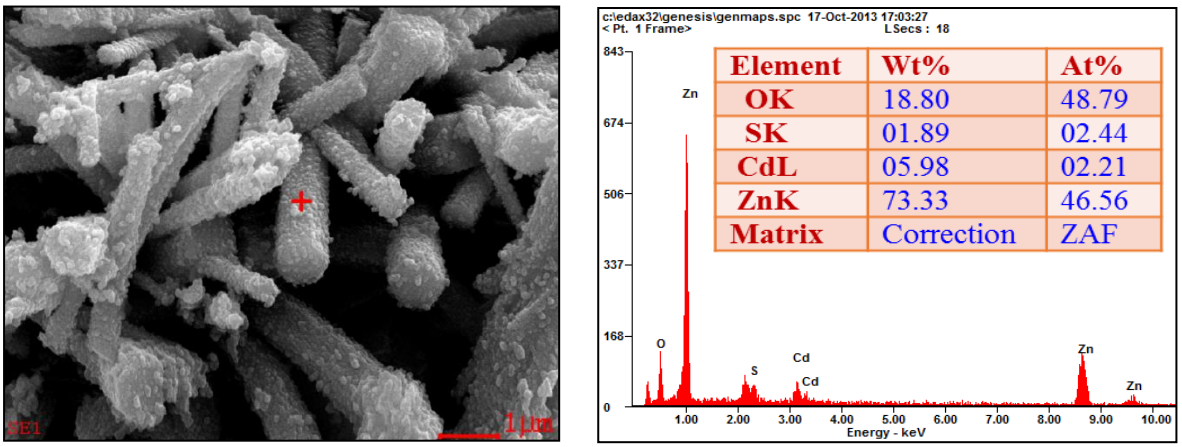

(b)

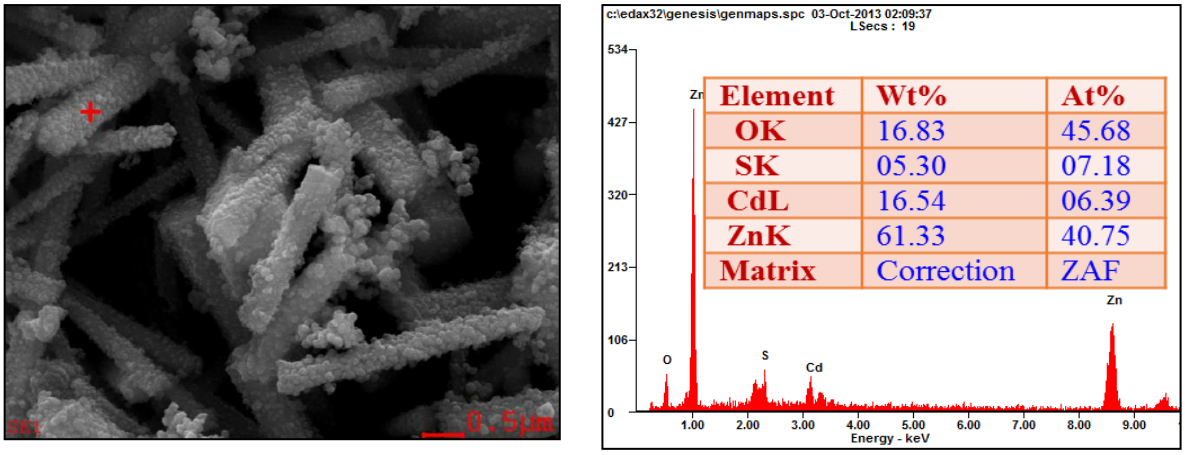

(c)

Fig. 3.2.10: EDX analysis patterns of ZnO@CdS core-shell nanoparticles; **(a)** ZC1, **(b)** ZC2, and **(c)** ZC3.

Table 3.2.3 Elemental composition along with standard deviation of cadmium and sulfur in the ZnO@CdS core-shell nanoparticles.

Sample name	Weight percent of cadmium	Weight percent of sulfur
ZC1	3.3±0.2	1.5±0.2
ZC2	6.1±0.3	1.8±0.1
ZC3	16.4±0.3	5.3±0.2

The effects of reaction temperature, thermal decomposition time and surface modification of ZnO nanorods on the quality of CdS coating in the ZnO@CdS core-shell nanoparticles were studied and the results are discussed below.

Since sample ZC3 shows more uniform deposition of CdS on ZnO compared to the other samples (ZC1 and ZC2) as evidenced by the SEM results, the thermal decomposition reactions were carried out for this sample at 150 ^{o}C and 180 ^{o}C while the heating time was fixed (1 h). The sample prepared at 150 ^{o}C shows poor deposition of CdS on ZnO (Figure 3.2.11a). In the case of 180 ^{o}C, the ZnO@CdS sample clearly shows good deposition of CdS. Two CdS deposition reactions were carried out using (i) surface unmodified ZnO nanorods and (ii) with surface modified ZnO nanorods at 180 ^{o}C for 1 h. In the case of surface unmodified ZnO, poor deposition of CdS and extra CdS particles are observed in the ZnO@CdS core-shell

nanoparticles (Figure 3.2.11b). In the case of surface functionalized ZnO, uniform deposition of CdS nanoparticles on the surface of ZnO nanorods is observed.

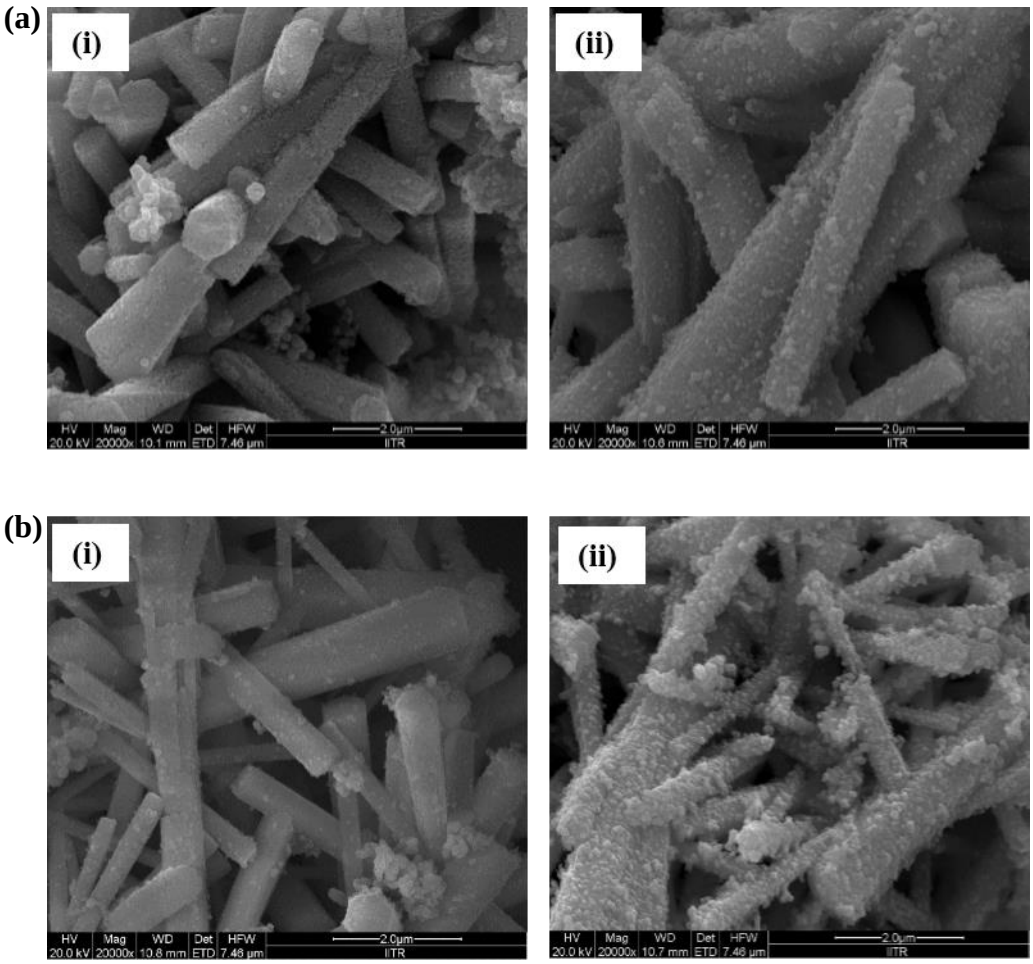

Fig. 3.2.11: FE-SEM images of ZnO@CdS samples: **(a)** prepared at different temperatures **(i)** 150 ^{o}C and **(ii)** 180 ^{o}C, and **(b)** ZnO@CdS samples prepared using **(i)** surface unmodified ZnO nanorods and **(ii)** surface modified ZnO nanorods.

To understand the effect of thermal decomposition time on the deposition of CdS shell on the ZnO nanorods, the reactions were carried out for sample ZC3 at 180 ^{o}C for different times, e.g. 30 min, 60 min and 90 min. Deposition of CdS shell is observed in all the cases but in the case of 30 min and 90 min, extra CdS particles are observed in the ZnO@CdS core-shell nanoparticles (Figures 3.2.12 (i) and (iii)). In the case of 60 min, uniform CdS shell on the ZnO nanorods with no extra CdS particles is observed (Figure 3.2.12 (ii)).

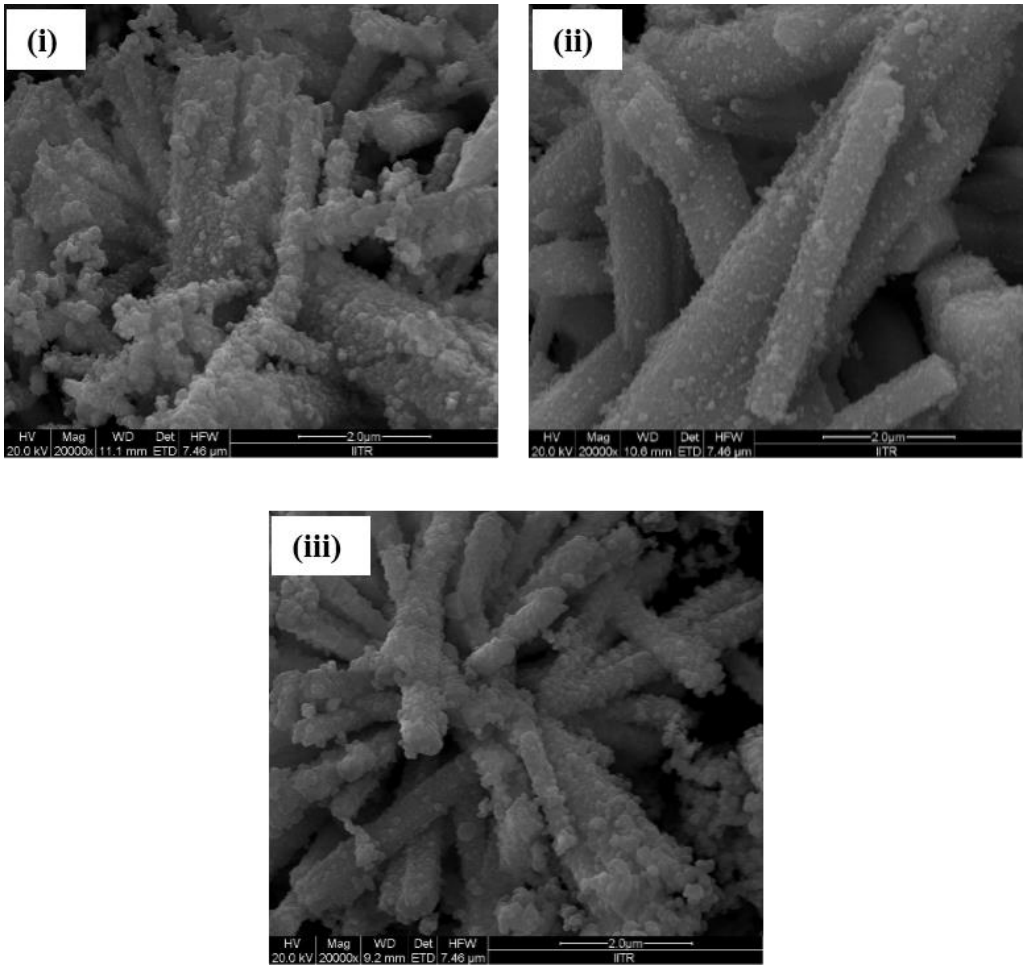

Fig. 3.2.12: FE-SEM images of ZnO@CdS samples prepared at different thermal decomposition times: **(i)** 30 min, **(ii)** 60 min and **(iii)** 90 min.

3.2.3.6 TEM studies

The TEM, and SAED images of pure ZnO, CdS and ZnO@CdS core-shell nanoparticles (ZC1, ZC2 and ZC3) are shown in Figure 3.2.13. Pure ZnO nanorods show very smooth surface and the length of ZnO nanorods is about 2 μm and diameter is about 200 nm. Pure CdS nanoparticles show aggregated particles. The ZnO@CdS samples show clearly the deposition of CdS shell on the ZnO nanorods. Compared to samples ZC1 and ZC2, sample ZC3 shows uniform CdS shell on the ZnO nanorods. The SAED patterns for pure ZnO, CdS and ZnO@CdS core-shell nanoparticles are shown as insets in the corresponding TEM images (Figure 3.2.13). The SAED pattern of a single ZnO nanorod shows a set of diffraction spots due to hexagonal structure and this confirms the single crystalline nature of the nanorods. The distance between two adjacent spots was measured as 0.27 nm which is attributed to (002) plane of hexagonal ZnO [125,126]. The SAED pattern of pure CdS shows a ring confirming

the polycrystalline nature of CdS and the rings are attributed to (311), (220) and (111) planes of cubic CdS [95]. The SAED patterns for ZnO@CdS samples ZC1 and ZC2 show both spots and ring patterns due to ZnO and CdS but sample ZC3 shows only a ring pattern due to CdS which suggests thicker CdS shell on the ZnO nanorods.

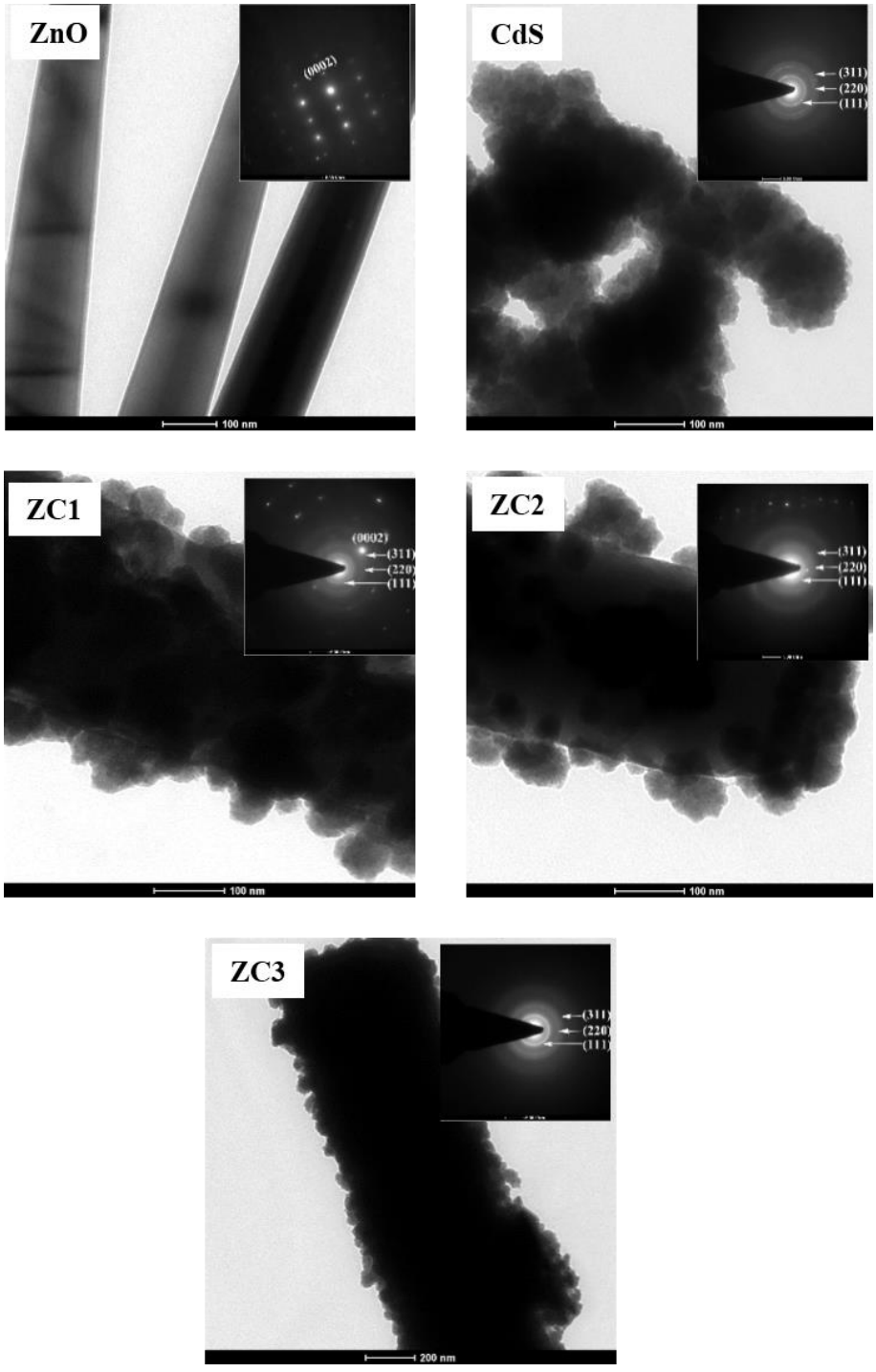

Fig. 3.2.13: TEM images of ZnO nanorods, CdS nanoparticles and ZnO@CdS core-shell nanoparticles (ZC1, ZC2 and ZC3) and the insets show the corresponding SAED patterns.

3.2.3.7 HRTEM studies

The HRTEM images of ZnO@CdS samples (Figure 3.2.14) show clearly the crystalline interface between the ZnO core and the CdS shell. A crystalline interface facilitates the injection of photo excited electrons from the CdS shell to the ZnO nanorods [106]. The thickness of CdS shell in the ZnO@CdS core-shell nanoparticles was estimated from the images and the thickness values for the samples ZC1, ZC2 and ZC3 are about 20 nm, 33 nm and 45 nm, respectively. The CdS shell thickness increases with increasing concentration of CdS precursors ($[Cd^{2+}]$:$[S^{2-}]$ = 0.075:0.075, 0.100:0.100 and 0.125:0.125) used during the synthesis. From the HRTEM images, lattice spacing was calculated for the CdS shell as 0.36 nm which corresponds to (111) plane of cubic CdS. This indicates that the growth of CdS shell on the ZnO nanorods is along the (111) direction.

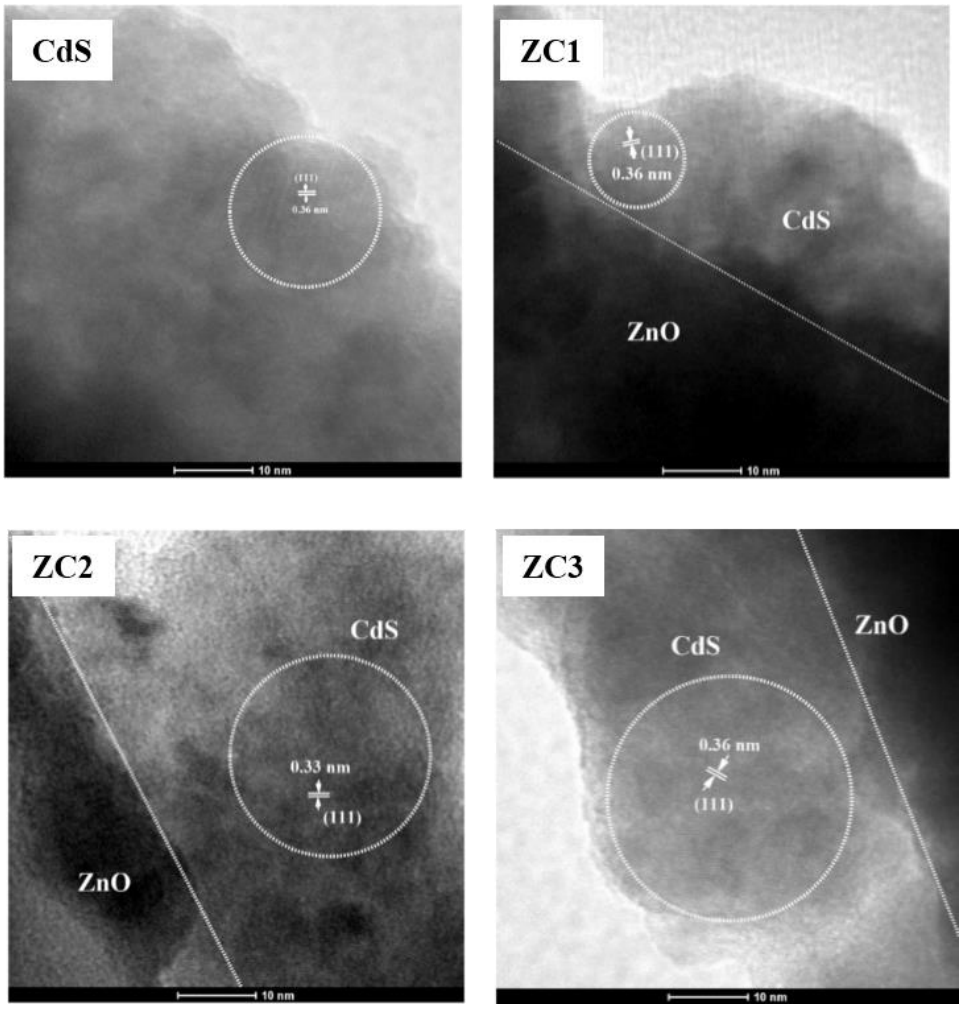

Figure 3.2.14: HRTEM images of CdS nanoparticles and the ZnO@CdS core-shell nanoparticles (ZC1, ZC2 and ZC3).

3.2.3.8 UV-Visible diffuse reflectance spectroscopy (DRS)

The DRS spectra of ZnO@CdS core-shell nanoparticles are shown in Figure 3.2.15. The band gap values of pure ZnO, CdS and the ZnO@CdS core-shell nanoparticles were calculated using the Tauc equation [94,127] and the Tauc plots were obtained by plotting $(\alpha h\nu)^2$ versus $h\nu$. Pure ZnO and CdS have direct bulk band gap values of 3.38 and 2.42 eV, respectively [63,109]. In the present study, pure ZnO nanorods possess a band gap of 3.31 eV and this is in good agreement with the reported band gap for hexagonal ZnO nanorods [106,128]. No quantum confinement effect is observed in the case of ZnO nanorods as their diameter (250 nm) is much larger than the Bohr exciton radius for ZnO (a_B = 1.8 nm) [106,128]. Pure CdS nanoparticles exhibit a band gap of 2.53 eV with a blue shift of about 0.1 eV with respect to bulk CdS which is attributed to quantum size effect [56]. The ZnO@CdS core-shell nanoparticles show band gap of about 3.25 eV for ZnO core and between 2.61 and 2.66 eV for the CdS shell. The ZnO in the ZnO@CdS core-shell nanoparticles show about 0.13 eV red shift with respect to bulk ZnO (E_g = 3.38 eV) and the CdS in the ZnO@CdS samples show about 0.24 eV blue shift with respect to bulk CdS. The blue shift in the band gap of CdS is attributed to quantum size effect due to the presence of small CdS nanoparticles on the ZnO nanorods; small size limits the volume occupied by the electron-hole pairs [56]. In the DRS spectra of ZnO@CdS core-shell nanoparticles, the intensity of ZnO band gap absorption decreases and the intensity of CdS band gap absorption increases. This also indicates the formation of CdS shell on the ZnO nanorods.

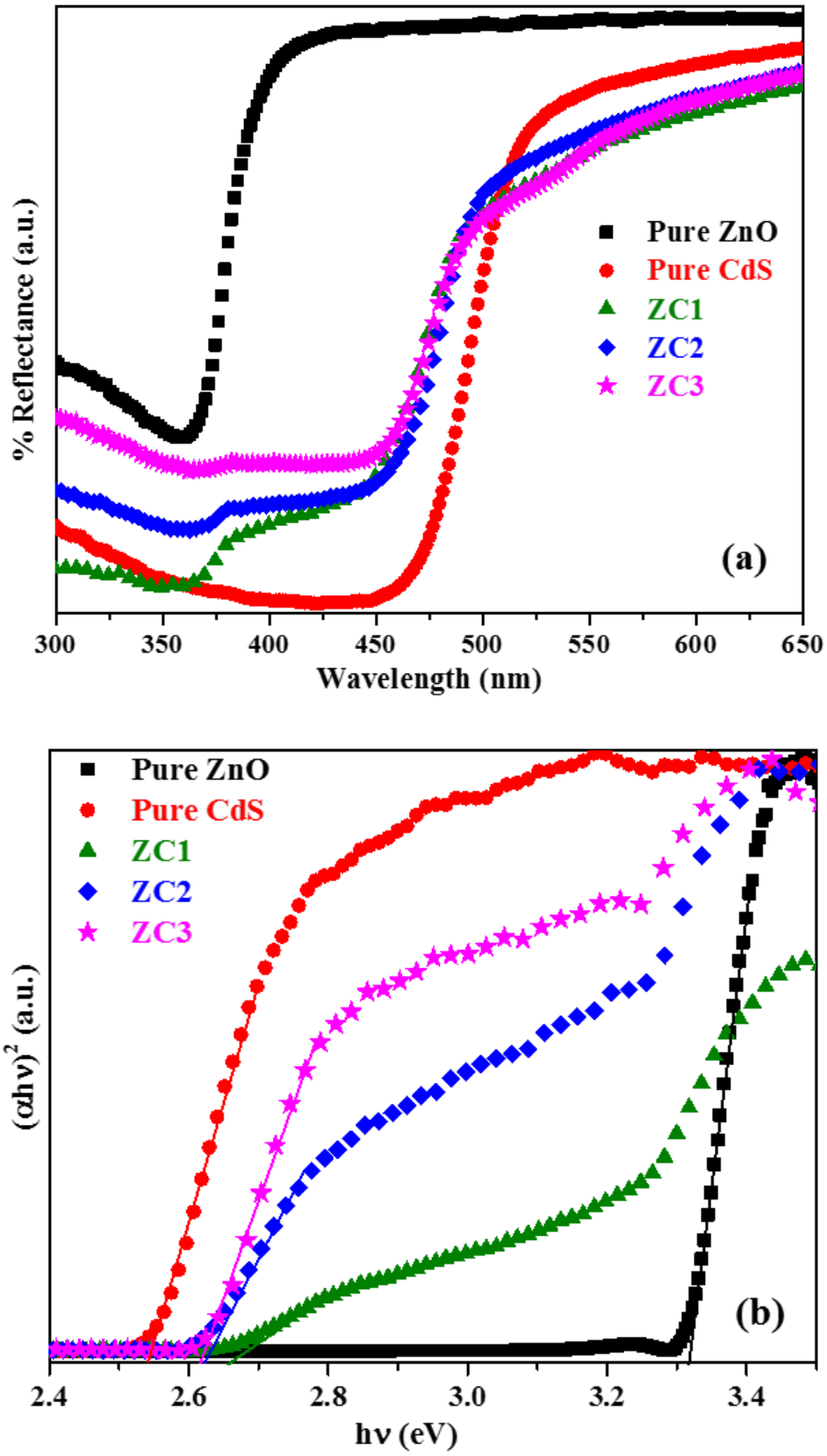

Figure 3.2.15 (a) UV-Visible diffuse reflectance spectra and **(b)** Tauc plots for ZnO@CdS core-shell nanoparticles (ZC1, ZC2 and ZC3).

The particle size of CdS nanoparticles on the ZnO nanorods was calculated using the Brus equation [64]. For CdS, m_e^* = 0.19 m_o, m_h^* = 0.80 m_o, m_o = 9.11 × 10^{-28} g and ε = 5.7. The calculated band gap and particle size values for CdS are given in Table 3.2.4. The calculated particle size of CdS nanoparticles using the Brus equation is smaller than the Bohr radius of CdS (2.5 nm). The blue shift of the band gap absorption of CdS in the ZnO@CdS core-shell nanoparticles is attributed to quantum size effect [56].

Table 3.2.4 Band gap and calculated particle size values of CdS in ZnO@CdS core-shell nanoparticles (ZC1, ZC2 and ZC3).

Sample name	Band gap (eV)		Calculated Particle size of CdS from E_g
	ZnO	CdS	
Pure ZnO	3.31	-	-
Pure CdS	-	2.53	2.15
ZC1	3.26	2.66	1.58
ZC2	3.26	2.62	1.73
ZC3	3.25	2.61	1.77

3.2.3.9 Photoluminescence spectroscopy (PL)

The room temperature PL spectra of pure ZnO, CdS and ZnO@CdS core-shell nanoparticles are shown in Figure 3.2.16. Pure ZnO nanorods exhibit emission bands at 383, 452, 469, 485 and 494 nm and the observed spectrum is in good agreement with results reported for ZnO nanorods [125,129]. The strong UV emission band centered at 383 nm is attributed to excitonic recombination corresponding to the near band edge emission of ZnO [95]. The emission band in the blue region at about 452 nm is associated with the electronic transition between excitonic level and interstitial oxygen (O_i). The emission band in the blue-green region at 469 nm is attributed to the electron transition between a shallow donor (Zn_i) and a deep acceptor (V_{Zn}) [130]. The two emission bands in the green region (485 and 494 nm) are attributed to stoichiometry related defects and these are generally attributed to zinc vacancies as well as interstitial zinc and structural defects [129,131]. Pure CdS shows a broad emission band between 450 and 630 nm which is attributed to surface defects associated with cadmium and sulfur vacancies [66].

In the case of PL spectra of ZnO@CdS core-shell nanoparticles (ZC1, ZC2 and ZC3), the luminescence in the UV region has vanished. They show luminescence in the visible range

between 450 and 630 nm. The emission bands in the ZnO@CdS core-shell nanoparticles are attributed to the following transitions: (i) from conduction band to deep acceptor levels (O_i or O_{Zn}), (ii) from deep donor levels ($V_O Zn_i$) to valence band, and (iii) from shallow donor levels (Zn_i) to shallow acceptor levels (V_{Zn} and O_i) [87,125,132]. The emission intensity related to defect states in the visible region, in the case of ZnO@CdS samples, is relatively lower compared to pure ZnO. In the ZnO@CdS core-shell nanoparticles, the CdS nanoparticles (shell) act as the sulfur dopant, which reduces defect emission from the surface of ZnO nanorods [94]. The absence of luminescence in the UV region and reduced intensity in the visible region in the ZnO@CdS samples is attributed to the synergistic interaction between ZnO core and CdS shell. In the case of ZnO@CdS core-shell nanoparticles, the emission maximum (495 nm) is blue shifted by about 40 nm compared to pure CdS nanoparticles (535 nm). This is again the evidence for electron transfer from CdS shell to the ZnO core on excitation.

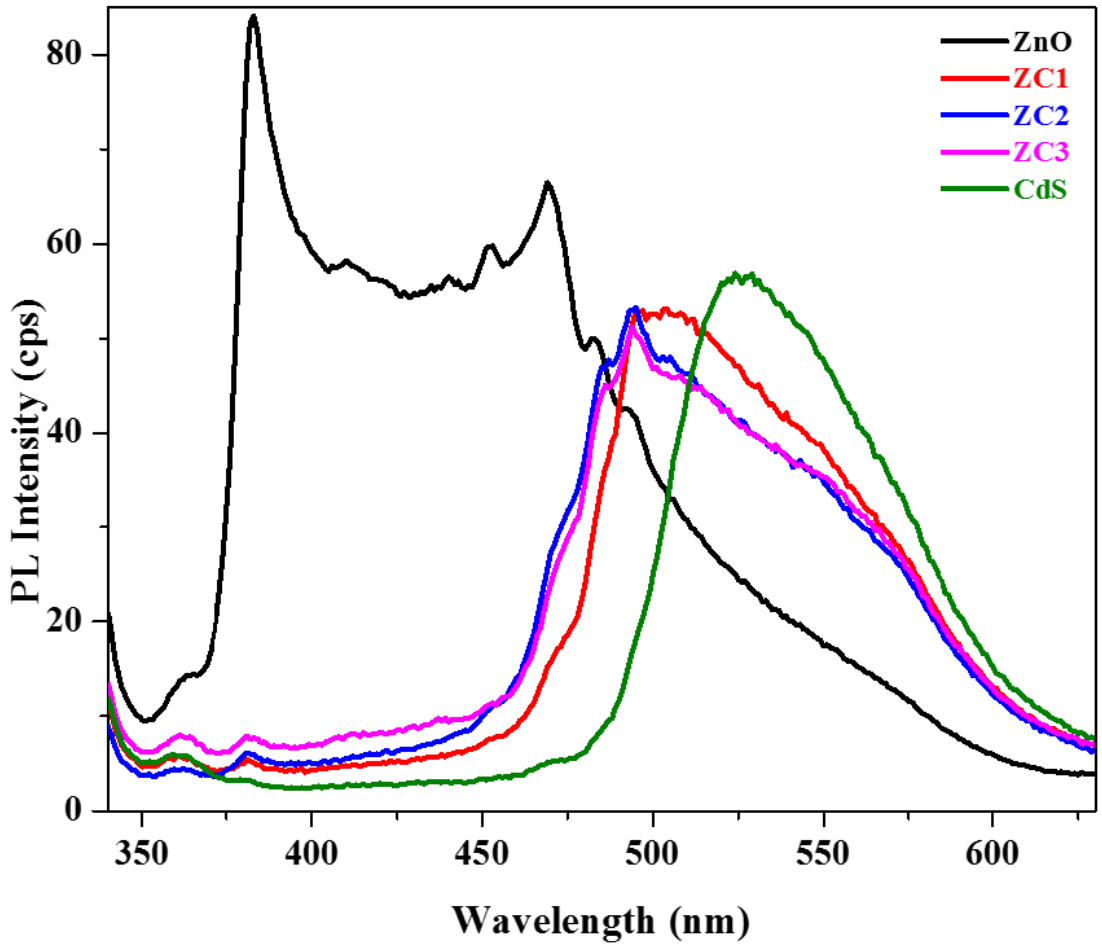

Figure 3.2.16: Photoluminescence spectra of ZnO nanorods, CdS nanoparticles and ZnO@CdS core-shell nanoparticles (ZC1, ZC2 and ZC3).

The band alignment of ZnO core with the CdS shell in ZnO@CdS is shown in Scheme 3.2.4. The excitons are generated in the CdS shell on visible light excitation and the photo generated electrons in the conduction band of CdS migrate to that of ZnO. This is because the conduction band of CdS is higher than that of ZnO [87]. The photogenerated holes in the valence band of ZnO migrate to that of CdS. The interfacial charge transfer lowers the direct transition probability from the conducting band to valence band and reduces the emission intensity related to defect states [133] and the same is observed in the present study.

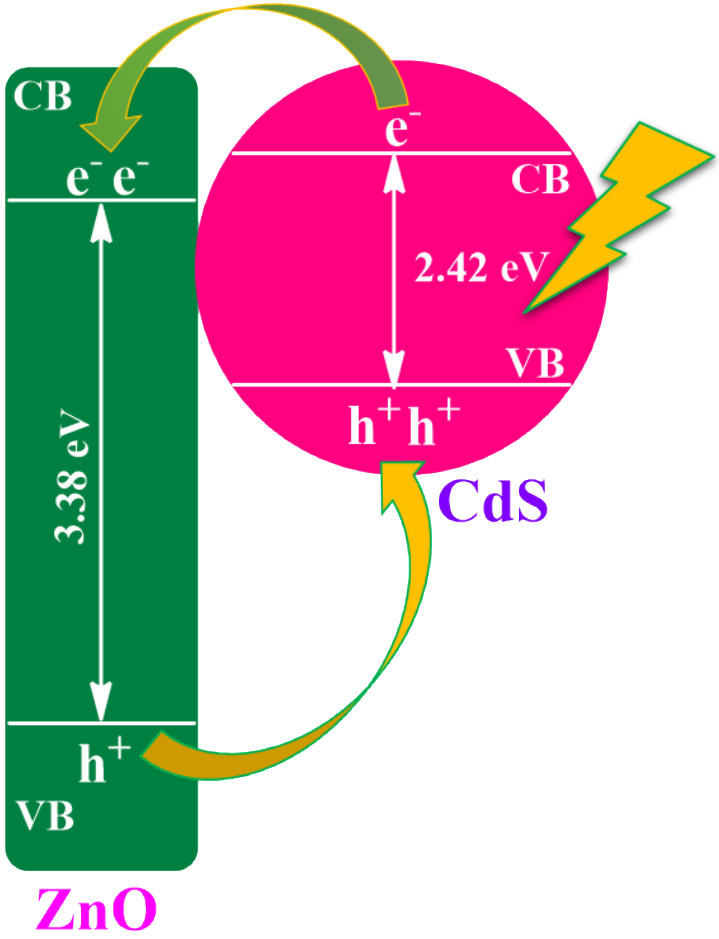

Scheme 3.2.4: Band alignment of ZnO (core) with CdS (shell) in the ZnO@CdS core-shell nanoparticles.

3.2.4 Proposed mechanism for the formation of ZnO@CdS core-shell nanoparticles

The proposed mechanism for the formation of ZnO@CdS core-shell nanoparticles is shown in Scheme 3.2.5. On surface modification of ZnO nanorods with citric acid, the citrate groups adsorb on the surface of hexagonal ZnO nanorods [87]. Cadmium acetate and thiourea form a complex $[Cd(Tu)_2]^{2+}$ in ethylene glycol which prevents the release of a large amount of S^{2-} ions

in the solution [134]. The cadmium ions in the complex ($[Cd(Tu)_2]^{2+}$) form an ionic bond with the citrate groups present on the surface of ZnO nanorods. When the temperature is increased about to 180 ^oC, the complex undergoes decomposition leading to the formation of uniform nanocrystalline CdS shell on the surface of ZnO nanorods [134–136]. In the case of 30 min and 90 min, the amount of CdS seems to be higher compared to that at 60 min due to non-uniform deposition of CdS on the surface of ZnO at these timings. In the case of 30 min, very few CdS nuclei are generated in the solution and the growth of CdS is faster. Hence, the CdS nanoparticles deposit irregularly on the surface of ZnO which leads to agglomeration. As the reaction time is increased to 60 min, stable CdS nuclei are formed in large numbers. This leads to decrease in the concentration of CdS precursors in the solution with a uniform deposition of CdS. In the case of 90 min, further growth of CdS occurs, which results in agglomeration.

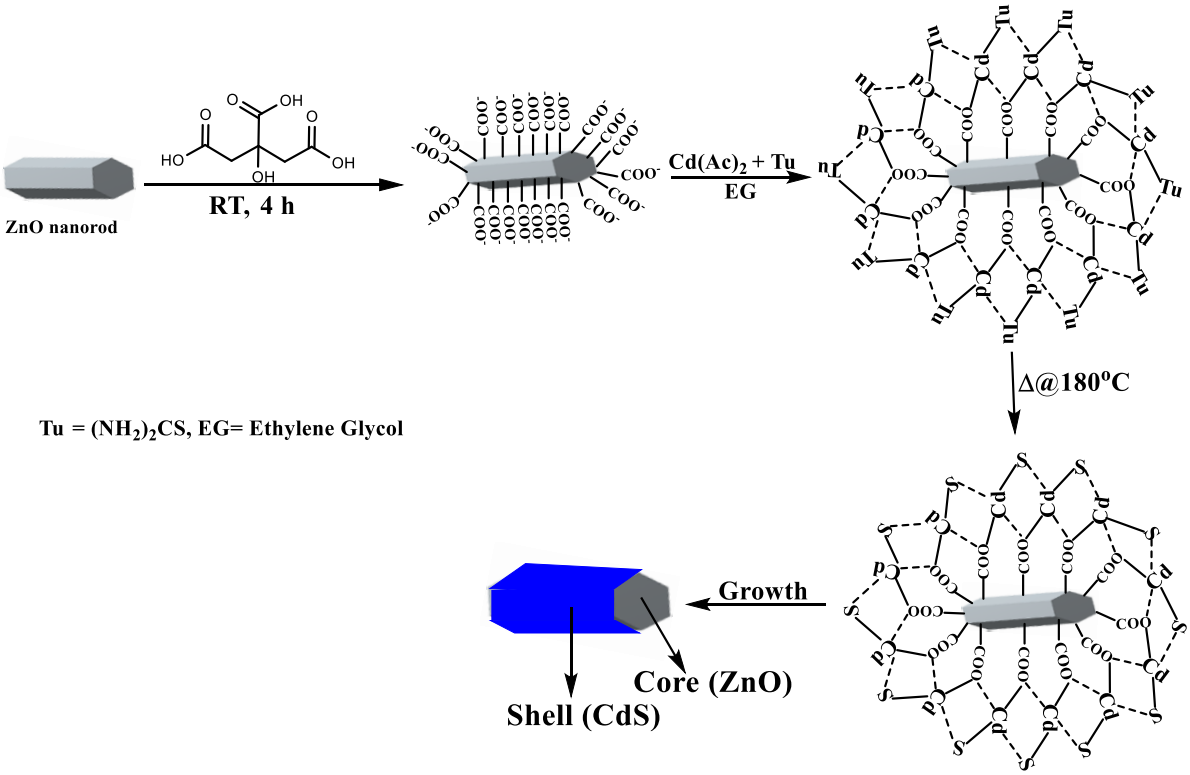

Scheme 3.2.5: Proposed mechanism for the formation of ZnO@CdS core-shell nanoparticles.

3.2.5 Conclusions

ZnO@CdS core-shell nanoparticles with different CdS shell thickness (20 nm to 45 nm) have been successfully synthesized by a novel thermal decomposition approach. XRD results indicate the presence of both ZnO and CdS in all the ZnO@CdS core-shell nanoparticles. Uniform deposition of cadmium sulfide nanoparticles on the surface modified ZnO nanorods

is possible at 180 ^{o}C. Surface modification of ZnO nanorods is necessary for the uniform deposition of CdS on the ZnO nanorods. TEM/SEM images clearly show the uniform deposition of cadmium sulfide nanoparticles on the surface functionalized ZnO nanorods. SAED/HRTEM studies confirm the crystalline nature of hexagonal ZnO nanorods and cubic cadmium sulfide nanoparticles. DRS results show red shift of the band gap of ZnO and blue shift of the band gap of CdS in the ZnO@CdS core-shell nanoparticles compared to pure ZnO and CdS nanoparticles. The blue shift in the band gap of CdS shell is attributed to quantum size effect. Photoluminescence spectroscopy results show disappearance of UV emission band and reduction in the intensity of visible emission in the ZnO@CdS core-shell nanoparticles. These observations are explained on the basis of synergistic interaction between ZnO and CdS in the ZnO@CdS core-shell nanoparticles.

References

1. Yang D., Pang X., He Y., Wang Y., Chen G., Wang W., Lin Z., 'Precisely size-tunable magnetic/plasmonic core/shell nanoparticles with controlled optical properties', *Angewandte Chemie International Edition*, **54**, 12091–12096 (2015).

2. Yuan C., Cao H., Zhu S., Hua H., Hou L., 'Core–shell ZnO/$ZnFe_2O_4$@C mesoporous nanospheres with enhanced lithium storage properties towards high-performance Li-ion batteries', *Journal of Materials Chemistry A*, **3**, 20389–20398 (2015).

3. Li Y., Tang J., He L., Liu Y., Liu Y., Chen C., Tang Z., 'Core-shell upconversion nanoparticle@metal-organic framework nanoprobes for luminescent/magnetic dual-mode targeted imaging', *Advanced Materials*, **27**, 4075–4080 (2015).

4. Zaiats G., Shapiro A., Yanover D., Kauffmann Y., Sashchiuk A., Lifshitz E., 'Optical and electronic properties of nonconcentric PbSe/CdSe colloidal quantum dots', *The Journal of Physical Chemistry Letters*, **6**, 2444–2448 (2015).

5. Chaudhuri R. G., Paria S., 'Core/shell nanoparticles: Classes, properties, synthesis mechanisms, characterization, and applications', *Chemical Reviews*, **112**, 2373–2433 (2012).

6. Huang L., Zhu P., Li G., Lu D., Sun R., Wong C., 'Core–shell SiO_2@RGO hybrids for epoxy composites with low percolation threshold and enhanced thermo-mechanical properties', *Journal of Materials Chemistry A*, **2**, 18246–18255 (2014).

7. Shinde S., El-Schich Z., Malakpour A., Wan W., Dizeyi N., Mohammadi R., Rurack K., Wingren A. G., Sellergren B., 'Sialic acid imprinted fluorescent core-shell particles for selective labeling of cell surface glycans', *Journal of the American Chemical Society*, **137**, 13908–13912 (2015).

8. Ha E., Lee L. Y. S., Man H. W., Tsang S. C. E., Wong K. Y., 'Morphology-controlled synthesis of Au/Cu_2FeSnS_4 core-shell nanostructures for plasmon-enhanced photocatalytic hydrogen generation', *ACS Applied Materials and Interfaces*, **7**, 9072–9077 (2015).

9. Wang W., Jiao T., Zhang Q., Luo X., Hu J., Chen Y., Peng Q., Yan X., Li B., 'Hydrothermal synthesis of hierarchical core–shell manganese oxide nanocomposites as efficient dye adsorbents for wastewater treatment', *RSC Advances*, **5**, 56279–56285

(2015).

10. Dai Q., Frommer J., Berman D., Virwani K., Davis B., Cheng J. Y., Nelson A., 'High-throughput directed self-asssembly of core-shell ferrimagnetic nanoparticle arrays', *Langmuir*, **29**, 7472–7477 (2013).

11. Choi H., Song J. H., Jang J., Mai X. D., Kim S., Jeong S., 'High performance of PbSe/PbS core/shell quantum dot heterojunction solar cells: Short circuit current enhancement without the loss of open circuit voltage by shell thickness control', *Nanoscale*, **7**, 17473–17481 (2015).

12. Kashyap S., Jayakannan M., 'Super LCST thermo-responsive nanoparticle assembly for ATP binding through the Hofmeister effect', *Journal of Materials Chemistry B*, **3**, 1957–1967 (2015).

13. Mazumdar S., Bhattacharyya A. J., 'One-pot synthesis of a TiO_2–CdS nano-heterostructure assembly with enhanced photocatalytic activity', *RSC Advances*, **5**, 34942–34948 (2015).

14. Xia C., Alshareef H. N., 'Self-templating scheme for the synthesis of nanostructured transition-metal chalcogenide electrodes for capacitive energy storage', *Chemistry of Materials*, **27**, 4661–4668 (2015).

15. Wang C., Li P., Wang J., Rong Z., Pang Y., Xu J., Dong P., Xiao R., Wang S., 'Polyethylenimine-interlayered core–shell–satellite 3D magnetic microspheres as versatile SERS substrates', *Nanoscale*, **7**, 18694–18707 (2015).

16. Sahasrabudhe A., Bhattacharyya S., 'Dual sensitization strategy for high-performance core/shell/quasi-shell quantum dot solar cells', *Chemistry of Materials*, **27**, 4848–4859 (2015).

17. Park S. H., Hong A., Kim J. H., Yang H., Lee K., Jang H. S., 'Highly bright yellow-green-emitting $CuInS_2$ colloidal quantum dots with core/shell/shell architecture for white light-emitting diodes', *ACS Applied Materials and Interfaces*, **7**, 6764–6771 (2015).

18. Yuan P., Ma R., Gao N., Garai M., Xu Q. H., 'Plasmon coupling-enhanced two-photon photoluminescence of Au@Ag core–shell nanoparticles and applications in the nuclease assay', *Nanoscale*, **7**, 10233–10239 (2015).

19. Chiu C. Y., Chen C. K., Chang C. W., Jeng U. S., Tan C. S., Yang C. W., Chen L. J., Yen T. J., Huang M. H., 'Surfactant-directed fabrication of supercrystals from the assembly of polyhedral Au-Pd core-shell nanocrystals and their electrical and optical properties', *Journal of the American Chemical Society*, **137**, 2265–2275 (2015).

20. Selvi N., Sankar S., Dinakaran K., 'Interfacial effect on the structural and optical properties of pure SnO_2 and dual shells ($ZnO;SiO_2$) coated SnO_2 core-shell nanospheres for optoelectronic applications', *Superlattices and Microstructures*, **76**, 277–287 (2014).

21. Hua J., Cheng H., Yuan X., Zhang Y., Liu M., Meng X., Li H., Zhao J., 'Photoluminescence quenching and electron transfer in $CuInS_2$/ZnS core/shell quantum dot and FePt nanoparticle blend films', *RSC Advances*, **5**, 30981–30988 (2015).

22. Kim T., Kang H., Jeong S., Kang D. J., Lee C., Lee C., Seo M., Lee J., Kim B. J., 'Au@polymer core−shell nanoparticles for simultaneously enhancing efficiency and ambient stability of organic optoelectronic devices', *ACS Applied Materials and Interfaces*, **6**, 16956–16965 (2014).

23. Lincheneau C., Amelia M., Oszajca M., Boccia A., D'Orazi F., Madrigale M., Zanoni R., Mazzaro R., Ortolani L., Morandi V., Silvi S., Szaciłowski K., Credi A., 'Synthesis and properties of ZnTe and ZnTe/ZnS core/shell semiconductor nanocrystals', *Journal of Materials Chemistry C*, **2**, 2877–2886 (2014).

24. Cirillo M., Aubert T., Gomes R., Deun R. V., Emplit P., Biermann A., Lange H., Thomsen C., Brainis E., Hens Z., ''Flash' synthesis of CdSe/CdS core-shell quantum dots', *Chemistry of Materials*, **26**, 1154–1160 (2014).

25. Khanchandani S., Kundu S., Patra A., Ganguli A. K., 'Band gap tuning of ZnO/In_2S_3 core/shell nanorod arrays for enhanced visible-light-driven photocatalysis', *The Journal of Physical Chemistry C*, **117**, 5558–5567 (2013).

26. Luo J. Y., Chen L. L., Liang X. H., Zhao Q. W., Li H., 'Anodic deposition-assisted photoelectrocatalytic degradation of bisphenol A at a cadmium sulfide modified electrode based on visible light-driven fuel cells', *Electrochimica Acta*, **186**, 420–426 (2015).

27. Kumari V., Chatterjee N., Das S., Bhunia S., Saha K. D., Bhaumik A., 'Self-assembled ZnS nanospheres with nanoscale porosity as an efficient carrier for the delivery of

doxorubicin', *RSC Advances*, **5**, 92499–92505 (2015).

28. Congiu M., Albano L. G. S., Decker F., Graeff C. F. O., 'Single precursor route to efficient cobalt sulphide counter electrodes for dye sensitized solar cells', *Electrochimica Acta*, **151**, 517–524 (2015).

29. Cabrita J. F., Ferreira V. C., Monteiro O. C., 'Titanate nanofibers sensitized with nanocrystalline Bi_2S_3 as new electrocatalytic materials for ascorbic acid sensor applications', *Electrochimica Acta*, **135**, 121–127 (2014).

30. Jana M. K., Rajendra H. B., Bhattacharyya A. J., Biswas K., 'Green ionothermal synthesis of hierarchical nanostructures of SnS_2 and their Li-ion storage properties', *CrystEngComm*, **16**, 3994–4000 (2014).

31. Luo M., Liu Y., Hu J., Li J., Liu J., Richards R. M., 'General strategy for one-pot synthesis of metal sulfide hollow spheres with enhanced photocatalytic activity', *Applied Catalysis B: Environmental*, **125**, 180–188 (2012).

32. Varga A., Endrődi B., Hornok V., Visy C., Janáky C., 'Controlled photocatalytic deposition of CdS nanoparticles on poly(3-hexylthiophene) nanofibers: A versatile approach to obtain organic/inorganic hybrid semiconductor assemblies', *The Journal of Physical Chemistry C*, **119**, 28020–28027 (2015).

33. Chen B., Li R., Ma G., Gou X., Zhu Y., Xia Y., 'Cobalt sulfide/N,S codoped porous carbon core–shell nanocomposites as superior bifunctional electrocatalysts for oxygen reduction and evolution reactions', *Nanoscale*, **7**, 20674–20684 (2015).

34. Hullavarad N. V, Hullavarad S. S., Karulkar P. C., 'Cadmium sulphide (CdS) nanotechnology: Synthesis and applications.', *Journal of Nanoscience and Nanotechnology*, **8**, 3272–3299 (2008).

35. Jankiewicz B. J., Jamiola D., Choma J., Jaroniec M., 'Silica–metal core–shell nanostructures', *Advances in Colloid and Interface Science*, **170**, 28–47 (2012).

36. Guo Q., Zhou Y., Nie W., Chen P., Song L., 'Synthesis of highly monodispersed CdS/SiO_2 core-shell nanoparticles and their photocatalytic activities', *Journal of Nanoscience and Nanotechnology*, **15**, 2364–2370 (2015).

37. Jing L., Yang C., Qiao R., Niu M., Du M., Wang D., Gao M., 'Highly fluorescent $CdTe@SiO_2$ particles prepared *via* reverse microemulsion method', *Chemistry of*

Materials, **22**, 420–427 (2010).

38. Ye Y., Ma Y., Yue S., Dai L., Meng H., Li Z., Tong L., Qin G., 'Lasing of CdSe/SiO_2 nanocables synthesized by the facile chemical vapor deposition method', *Nanoscale*, **3**, 3072–3075 (2011).

39. Song J., Dai Z., Guo W., Li Y., Wang W., Li N., Wei J., 'Preparation of CdTe/CdS/SiO_2 core/multishell structured composite nanoparticles', *Journal of Nanoscience and Nanotechnology*, **13**, 6924–6927 (2013).

40. Li C. G., Bai T. Y., Li T., Li F. F., Dong W. J., Shi Z., Feng S. H., 'A facile approach for transferring PbS colloidal photonic structures into alkanol solutions and composite solid films', *European Journal of Inorganic Chemistry*, **2012**, 1204–1209 (2012).

41. Ge J. P., Xu S., Zhuang J., Wang X., Peng Q., Li Y. D., 'Synthesis of CdSe, ZnSe, and $Zn_xCd_{1-x}Se$ nanocrystals and their silica sheathed core/shell structures', *Inorganic Chemistry*, **45**, 4922–4927 (2006).

42. Xue C. H., Yin W., Zhang P., Zhang J., Ji P. T., Jia S. T., 'UV-durable superhydrophobic textiles with UV-shielding properties by introduction of ZnO/SiO_2 core/shell nanorods on PET fibers and hydrophobization', *Colloids and Surfaces A: Physicochemical and Engineering Aspects*, **427**, 7–12 (2013).

43. Ding H., Zhang Y., Wang S., Xu J., Xu S. C., Li G., 'Fe_3O_4@SiO_2 core/shell nanoparticles: The silica coating regulations with a single core for different core sizes and shell thicknesses', *Chemistry of Materials*, **24**, 4572–4580 (2012).

44. Zhang X., Ye S., Zhang X., Wu L., 'Optical properties of SiO_2@M (M = Au, Pd, Pt) core–shell nanoparticles: Material dependence and damping mechanisms', *Journal of Materials Chemistry C*, **3**, 2282–2290 (2015).

45. Lee S. H., Ryu J., Nam D. H., Park C. B., 'Photoenzymatic synthesis through sustainable NADH regeneration by SiO_2-supported quantum dots', *Chemical Communications*, **47**, 4643–4645 (2011).

46. Wang Y., Zou B., Li G., Zhou S., 'A facile method to synthesize hierarchical SiO_2@CdSe and CdSe hollow spheres', *Materials Letters*, **65**, 1601–1604 (2011).

47. Luo Y., Zhang J., Sun A., Chu C., Zhou S., Guo J., Chen T., Xu G., 'Electric field induced structural color changes of SiO_2@TiO_2 core–shell colloidal suspensions',

Journal of Materials Chemistry C, **2**, 1990–1994 (2014).

48. Jeong B., Kim D. H., Park E. J., Jeong M. G., Kim K. D., Seo H. O., Kim Y. D., Uhm S., 'ZnO shell on mesoporous silica by atomic layer deposition: Removal of organic dye in water by an adsorbent and its photocatalytic regeneration', *Applied Surface Science*, **307**, 468–474 (2014).

49. Zhu Y., Li Z., Chen M., Cooper H. M., Xu Z. P., 'Tuning core–shell SiO_2@CdTe@SiO_2 fluorescent nanoparticles for cell labeling', *Journal of Materials Chemistry B*, **1**, 2315–2323 (2013).

50. Zhou J., Ren F., Zhang S., Wu W., Xiao X., Liu Y., Jiang C., 'SiO_2–Ag–SiO_2–TiO_2 multi-shell structures: Plasmon enhanced photocatalysts with wide-spectral-response', *Journal of Materials Chemistry A*, **1**, 13128–13138 (2013).

51. Li Y., Zhu Y., Yang X., Li C., 'Mesoporous silica spheres as microreactors for performing CdS nanocrystal synthesis', *Crystal Growth and Design*, **8**, 4494–4498 (2008).

52. Kang S., Yang Y., Xu Z., Mu J., 'Effect of the spherical silica surface on the photoluminescence of the loaded CdS nanoparticles', *Journal of Dispersion Science and Technology*, **29**, 521–524 (2008).

53. Rafati A. A., Borujeni A. A., Najafi M., Hajian A., 'Synthesis and characterization of supported silica nano hollow spheres with CdS quantum dots', *Journal of Molecular Liquids*, **174**, 124–128 (2012).

54. Dhas N. A., Gedanken A., 'A sonochemical approach to the surface synthesis of cadmium sulfide nanoparticles on submicron silica', *Applied Physics Letters*, **72**, 2514–2516 (1998).

55. Hebalkar N., Kharrazi S., Ethiraj A., Urban J., Fink R., Kulkarni S. K., 'Structural and optical investigations of SiO_2-CdS core-shell particles.', *Journal of Colloid and Interface Science*, **278**, 107–114 (2004).

56. Chang S. Y., Liu L., Asher S. A., 'Preparation and processing of monodisperse colloidal silica-cadmium sulfide nanocomposites', *Journal of the American Chemical Society*, **346**, 6739–6744 (1994).

57. Monteiro O. C., Esteves A. C. C., Trindade T., 'The synthesis of SiO_2@CdS

nanocomposites using single-molecule precursors', *Chemistry of Materials*, **14**, 2900–2904 (2002).

58. Mu J., Xu L., Wei Q., 'Influence of CdS nanoparticles on the photoluminescence of silica xerogel', *Journal of Dispersion Science and Technology*, **27**, 171–173 (2006).

59. Stöber W., Fink A., Bohn E., 'Controlled growth of monodisperse silica spheres in the micron size range', *Journal of Colloid and Interface Science*, **26**, 62–69 (1968).

60. Dembski S., Milde M., Dyrba M., Schweizer S., Gellermann C., Klockenbring T., 'Effect of pH on the synthesis and properties of luminescent SiO_2/calcium phosphate: Eu^{3+} core-shell nanoparticles', *Langmuir*, **27**, 14025–14032 (2011).

61. Kishore P. N. R., Jeevanandam P., 'A novel thermal decomposition approach for the synthesis of silica-iron oxide core-shell nanoparticles', *Journal of Alloys and Compounds*, **522**, 51–62 (2012).

62. Tauc J., Grigorovic R., Vancu A., 'Optical properties and electronic structure of amorphous germanium', *Physica Status Solidi*, **15**, 627–637 (1966).

63. Fan D., Thomas P. J., O'Brien P., 'Deposition of CdS and ZnS thin films at the water/toluene interface', *Journal of Materials Chemistry*, **17**, 1381–1386 (2007).

64. Brus L., 'Electronic wave functions in semiconductor clusters: Experiment and theory', *The Journal of Physical Chemistry*, **90**, 2555–2560 (1986).

65. Zeiri L., Patla I., Acharya S., Golan Y., Efrima S., 'Raman spectroscopy of ultranarrow CdS nanostructures', *The Journal of Physical Chemistry C*, **111**, 11843–11848 (2007).

66. Xiao Q., Xiao C., 'Surface-defect-states photoluminescence in CdS nanocrystals prepared by one-step aqueous synthesis method', *Applied Surface Science*, **255**, 7111–7114 (2009).

67. Kotov N. A., Meldrum F. C., Wu C., Fendler J. H., 'Monoparticulate layer and Langmuir-Blodgett-type multiparticulate layers of size-quantized cadmium sulfide clusters: A colloid-chemical approach to superlattice construction', *The Journal of Physical Chemistry*, **98**, 2735–2738 (1994).

68. Hullavarad N. V., Hullavarad S. S., 'Optical properties of organic and inorganic capped CdS nanoparticles and the effects of X-ray irradiation on organic capped CdS

nanoparticles', *Journal of Vacuum Science and Technology A: Vacuum, Surfaces, and Films*, **26**, 1050–1057 (2008).

69. Cheng H., Tamaki R., Laine R. M., Babonneau F., Chujo Y., Treadwell D. R., 'Neutral alkoxysilanes from silica', *Journal of the American Chemical Society*, **122**, 10063–10072 (2000).

70. Khushalani D., Ozin G. A., Kuperman A., 'Glycometallate surfactants. Part 1: Non-aqueous synthesis of mesoporous silica', *Journal of Materials Chemistry*, **9**, 1483–1489 (1999).

71. Blohowiak K. Y., Treadwell D. R., Mueller B. L., Hoppe M. L., Jouppi S., Kansal P., Chew K. W., Scotto C. L. S., Babonneau F., Kampf J., Laine R. M., 'SiO_2 as a starting material for the synthesis of pentacoordinate silicon complexes .1', *Chemistry of Materials*, **6**, 2177–2192 (1994).

72. Li Y., Huang F., Zhang Q., Gu Z., 'Solvothermal synthesis of nanocrystalline cadmium sulfide', *Journal of Materials Science*, **5**, 5933–5937 (2000).

73. Xiao F. X., Miao J., Liu B., 'Layer-by-layer self-assembly of CdS quantum dots/graphene nanosheets hybrid films for photoelectrochemical and photocatalytic applications', *Journal of the American Chemical Society*, **136**, 1559–1569 (2014).

74. Latthe S. S., An S., Jin S., Yoon S. S., 'High energy electron beam irradiated TiO_2 photoanodes for improved water splitting', *Journal of Materials Chemistry A*, **1**, 13567–13575 (2013).

75. Li C., Ahmed T., Ma M., Edvinsson T., Zhu J., 'A facile approach to ZnO/CdS nanoarrays and their photocatalytic and photoelectrochemical properties', *Applied Catalysis B: Environmental*, **138-139**, 175–183 (2013).

76. Li L., Salvador P. A., Rohrer G. S., 'Photocatalysts with internal electric fields.', *Nanoscale*, **6**, 24–42 (2014).

77. Galoppini E., Rochford J., Chen H., Saraf G., Lu Y., Hagfeldt A., Boschloo G., 'Fast electron transport in metal organic vapor deposition grown dye-sensitized ZnO nanorod solar cells', *The Journal of Physical Chemistry B*, **110**, 16159–16161 (2006).

78. Kadir R. A., Li Z., Sadek A. Z., Rani R. A., Zoolfakar A. S., Field M. R., Ou J. Z., Chrimes A. F., Kalantar-Zadeh K., 'Electrospun granular hollow SnO_2 nanofibers

hydrogen gas sensors operating at low temperatures', *The Journal of Physical Chemistry C*, **118**, 3129–3139 (2014).

79. Krishna K. S., Vivekanandan G., Ravinder D., Eswaramoorthy M., 'ZnO: A versatile template to obtain unusual morphologies of silica, gold and carbon nanostructures', *Chemical Communications*, **46**, 2989–2991 (2010).

80. Mazumdar S., Bhattacharyya A. J., 'Shape effect on electronic and photovoltaic properties of CdS nanocrystals', *Journal of Nanoscience and Nanotechnology*, **12**, 6308–6314 (2012).

81. Becker J., Raghupathi K. R., St. Pierre J., Zhao D., Koodali R. T., 'Tuning of the crystallite and particle sizes of ZnO nanocrystalline materials in solvothermal synthesis and their photocatalytic activity for dye degradation', *The Journal of Physical Chemistry C*, **115**, 13844–13850 (2011).

82. Ashokkumar M., Muthukumaran S., 'Microstructure, optical and FTIR studies of Ni, Cu co-doped ZnO nanoparticles by co-precipitation method', *Optical Materials*, **37**, 671–678 (2014).

83. Ren L., Li Y., Hou J., Zhao X., Pan C., 'Preparation and enhanced photocatalytic activity of TiO_2 nanocrystals with internal pores', *ACS Applied Materials and Interfaces*, **6**, 1608–1615 (2014).

84. Mazumdar S., Roy K., Srihari V., Umapathy S., Bhattacharyya A. J., 'Probing ultrafast photoinduced electron transfer to TiO_2 from CdS nanocrystals of varying crystallographic phase content', *The Journal of Physical Chemistry C*, **119**, 17466–17473 (2015).

85. Mansour A. M., 'Photocatalytic degradation of methylene blue with hematite nanoparticles synthesized by thermal decomposition of fluoroquinolones oxalato–iron(III) complexes', *RSC Advances*, **5**, 62052–62061 (2015).

86. Theerthagiri J., Senthil R. A., Priya A., Madhavan J., Michael R. J. V., Ashokkumar M., 'Photocatalytic and photoelectrochemical studies of visible-light active α-Fe_2O_3–gC_3N_4 nanocomposites', *RSC Advances*, **4**, 38222–38229 (2014).

87. Khanchandani S., Kundu S., Patra A., Ganguli A. K., 'Shell thickness dependent photocatalytic properties of ZnO/CdS core-shell nanorods', *The Journal of Physical*

Chemistry C, **116**, 23653–23662 (2012).

88. Modi G., 'Zinc oxide tetrapod: A morphology with multifunctional applications', *Advances in Natural Sciences: Nanoscience and Nanotechnology*, **6**, 033002/1–8 (2015).

89. Kim Y. J., Yoo J., Kwon B. H., Hong Y. J., Lee C. H., Yi G. C., 'Position-controlled ZnO nanoflower arrays grown on glass substrates for electron emitter application', *Nanotechnology*, **19**, 315202/1–5 (2008).

90. Xu S., Wang Z. L., 'One-dimensional ZnO nanostructures: Solution growth and functional properties', *Nano Research*, **4**, 1013–1098 (2011).

91. Xu L., Hu Y. L., Pelligra C., Chen C. H., Jin L., Huang H., Sithambaram S., Aindow M., Joesten R., Suib S. L., 'ZnO with different morphologies synthesized by solvothermal methods for enhanced photocatalytic activity', *Chemistry of Materials*, **21**, 2875–2885 (2009).

92. Wang Z. L., 'Zinc oxide nanostructures: Growth, properties and applications', *Journal of Physics: Condensed Matter*, **16**, R829–R858 (2004).

93. Giri P. K., Bhattacharyya S., Chetia B., Kumari S., Singh D. K., Iyer P. K., 'High-yield chemical synthesis of hexagonal ZnO nanoparticles and nanorods with excellent optical properties', *Journal of Nanoscience and Nanotechnology*, **12**, 201–206 (2011).

94. Misra M., Kapur P., Ghanshyam C., Singla M. L., 'ZnO@CdS core-shell thin film: fabrication and enhancement of exciton life time by CdS nanoparticle', *Journal of Materials Science: Materials in Electronics*, **24**, 3800–3804 (2013).

95. Xu F., Lu Y., Xie Y., Liu Y., 'Synthesis and photoluminescence of assembly-controlled ZnO architectures by aqueous chemical growth', *The Journal of Physical Chemistry C*, **113**, 1052–1059 (2009).

96. Zhu Y. F., Zhou G. H., Ding H. Y., Liu A. H., Lin Y. B., Dong Y. W., 'Synthesis and characterization of highly-ordered ZnO/PbS core/shell heterostructures', *Superlattices and Microstructures*, **50**, 549–556 (2011).

97. Huang X., Wang M., Willinger M., Shao L., Su D. S., Meng X., 'Assembly of three-dimensional hetero-epitaxial ZnO/ZnS core/shell nanorod and single crystalline hollow ZnS nanotoube arrays', *ACS Nano*, **6**, 7333–7339 (2012).

98. Wu Z., Zhang Y., Zheng J., Lin X., Chen X., Huang B., Wang H., Huang K., Li S., Kang J., 'An all-inorganic type-II heterojunction array with nearly full solar spectral response based on ZnO/ZnSe core/shell nanowires', *Journal of Materials Chemistry*, **21**, 6020–6026 (2011).

99. Tena-Zaera R., Katty A., Bastide S., Lévy-Clément C., 'Annealing effects on the physical properties of electrodeposited ZnO/CdSe core-shell nanowire arrays', *Chemistry of Materials*, **19**, 1626–1632 (2007).

100. Mittal M., Sapra S., 'Narrowing the size distribution of CdTe nanocrystals using digestive ripening', *Pramana-Journal of Physics*, **84**, 1049–1054 (2015).

101. Yanover D., Čapek R. K., Rubin-Brusilovski A., Vaxenburg R., Grumbach N., Maikov G. I., Solomeshch O., Sashchiuk A., Lifshitz E., 'Small-sized PbSe/PbS core/shell colloidal quantum dots', *Chemistry of Materials*, **24**, 4417–4423 (2012).

102. Liu Y., Zhang C., Zhang H., Wang R., Hua Z., Wang X., Zhang J., Xiao M., 'Broadband optical non-linearity induced by charge-transfer excitons in type-II CdSe/ZnTe nanocrystals', *Advanced Materials*, **25**, 4397–4402 (2013).

103. Wang K., Rai S. C., Marmon J., Chen J., Yao K., Wozny S., Cao B., Yan Y., Zhang Y., Zhou W., 'Nearly lattice matched all wurtzite CdSe/ZnTe type II core-shell nanowires with epitaxial interfaces for photovoltaics', *Nanoscale*, **6**, 3679–3685 (2014).

104. Huang X., Yu Y. Q., Xia J., Fan H., Wang L., Willinger M. G., Yang X. P., Jiang Y., Zhang T. R., Meng X. M., 'Ultraviolet photodetectors with high photosensitivity based on type-II ZnS/SnO_2 core/shell heterostructured ribbons', *Nanoscale*, **7**, 5311–5319 (2015).

105. Chen X., Li L., Lai Y., Yan J., Tang Y., Wang X., 'Microwave-assisted synthesis of glutathione-capped CdTe/CdSe near-infrared quantum dots for cell imaging', *International Journal of Molecular Sciences*, **16**, 11500–11508 (2015).

106. Guerguerian G., Elhordoy F., Pereyra C. J., Marotti R. E., Martín F., Leinen D., Ramos-Barrado J. R., Dalchiele E. A., 'ZnO nanorod/CdS nanocrystal core/shell-type heterostructures for solar cell applications', *Nanotechnology*, **22**, 505401/1–9 (2011).

107. Cui Q., Liu C., Wu F., Yue W., Qiu Z., Zhang H., Gao F., Shen W., Wang M., 'Performance improvement in polymer/ZnO nanoarray hybrid solar cells by formation

of ZnO/CdS-core/shell heterostructures', *The Journal of Physical Chemistry C*, **117**, 5626–5637 (2013).

108. Tak Y., Kim H., Lee D., Yong K., 'Type-II CdS nanoparticle-ZnO nanowire heterostructure arrays fabricated by a solution process: Enhanced photocatalytic activity', *Chemical Communications*, 4585–4587 (2008).

109. Gao T., Li Q., Wang T., 'Sonochemical synthesis, optical properties, and electrical properties of core/shell-type ZnO nanorod/CdS nanoparticle composites', *Chemistry of Materials*, **17**, 887–892 (2005).

110. Zhai J., Wang D., Peng L., Lin Y., Li X., Xie T., 'Visible-light-induced photoelectric gas sensing to formaldehyde based on CdS nanoparticles/ZnO heterostructures', *Sensors and Actuators B: Chemical*, **147**, 234–240 (2010).

111. Geng J., Jia X. D., Zhu J. J., 'Sonochemical selective synthesis of ZnO/CdS core/shell nanostructures and their optical properties', *CrystEngComm*, **13**, 193–198 (2011).

112. Mukhopadhyay S., Mondal I., Pal U., Devi P. S., 'Fabrication of hierarchical ZnO/CdS heterostructured nanocomposites for enhanced hydrogen evolution from solar water splitting', *Physical Chemistry Chemical Physics*, **17**, 20407–20415 (2015).

113. Li H., Yao C., Meng L., Sun H., Huang J., Gong Q., 'Photoelectrochemical performance of hydrogenated ZnO/CdS core-shell nanorod arrays', *Electrochimica Acta*, **108**, 45–50 (2013).

114. Panda S. K., Chakrabarti S., Satpati B., Satyam P. V, Chaudhuri S., 'Optical and microstructural characterization of CdS–ZnO nanocomposite thin films prepared by sol–gel technique', *Journal of Physics D: Applied Physics*, **37**, 628–633 (2004).

115. Zhao H., Dong Y., Jiang P., Wang G., Miao H., Wu R., Kong L., Zhang J., Zhang C., 'Light-assisted preparation of a ZnO/CdS nanocomposite for enhanced photocatalytic H_2 evolution: An insight into importance of in situ generated ZnS', *ACS Sustainable Chemistry and Engineering*, **3**, 969–977 (2015).

116. Bitenc M., Zorica C. O., 'Synthesis and characterization of crystalline hexagonal bipods of zinc oxide', *Materials Research Bulletin*, **44**, 381–387 (2009).

117. Bishop L. M., Yeager J. C., Chen X., Wheeler J. N., Torelli M. D., Benson M. C., Burke S. D., Pedersen J. A., Hamers R. J., 'A citric acid-derived ligand for modular

functionalization of metal oxide surfaces *via* 'click' chemistry', *Langmuir*, **28**, 1322–1329 (2012).

118. Wahab R., Kim Y. S., Lee K., Shin H. S., 'Fabrication and growth mechanism of hexagonal zinc oxide nanorods *via* solution process', *Journal of Materials Science*, **45**, 2967–2973 (2010).

119. Wang Y., Sun X., Li H., 'Synthesis, characterization and room temperature photoluminescence properties of briers-like ZnO nanoarchitectures', *Materials Science and Engineering B*, **167**, 177–181 (2010).

120. Mudunkotuwa I. A., Grassian V. H., 'Citric acid adsorption on TiO_2 nanoparticles in aqueous suspensions at acidic and circumneutral pH: Surface coverage, surface speciation, and its impact on nanoparticle-nanoparticle interactions', *Journal of the American Chemical Society*, **132**, 14986–14994 (2010).

121. Rahman Q. I., Ahmad M., Misra S. K., Lohani M. B., 'Hexagonal ZnO nanorods assembled flowers for photocatalytic dye degradation: Growth, structural and optical properties', *Superlattices and Microstructures*, **64**, 495–506 (2013).

122. Yang G., Yang B., Xiao T., Yan Z., 'One-step solvothermal synthesis of hierarchically porous nanostructured CdS/TiO_2 heterojunction with higher visible light photocatalytic activity', *Applied Surface Science*, **283**, 402–410 (2013).

123. Feng Y., Feng N., Wei Y., Zhang G., 'An in situ gelatin-assisted hydrothermal synthesis of ZnO–reduced graphene oxide composites with enhanced photocatalytic performance under ultraviolet and visible light', *RSC Advances*, **4**, 7933–7943 (2014).

124. Singh J., Im J., Whitten J. E., Soares J. W., Steeves D. M., 'Encapsulation of zinc oxide nanorods and nanoparticles', *Langmuir*, **25**, 9947–9953 (2009).

125. Zhong K., Xia J., Li H. H., Liang C. L., Liu P., Tong Y. X., 'Morphology evolution of one-dimensional-based ZnO nanostructures synthesized *via* electrochemical corrosion', *The Journal of Physical Chemistry C*, **113**, 15514–15523 (2009).

126. Hu J., Fan Y., Pei Y., Qiao M., Fan K., Zhang X., Zong B., 'Shape effect of ZnO crystals as cocatalyst in combined reforming- hydrogenolysis of glycerol', *ACS Catalysis*, **3**, 2280–2287 (2013).

127. Li L., Liu X., Zhang Y., Salvador P. A., Rohrer G. S., 'Heterostructured

(Ba,Sr)TiO_3/TiO_2 core/shell photocatalysts: Influence of processing and structure on hydrogen production', *International Journal of Hydrogen Energy*, **38**, 6948–6959 (2013).

128. Özgür Ü., Alivov Y. I., Liu C., Teke A., Reshchikov M. A., Doğan S., Avrutin V., Cho S. J., Morkǫ H., 'A comprehensive review of ZnO materials and devices', *Journal of Applied Physics*, **98**, 1–103 (2005).

129. Chong X., Li L., Yan X., Hu D., Li H., Wang Y., 'Synthesis, characterization and room temperature photoluminescence properties of Al doped ZnO nanorods', *Physica E: Low-dimensional Systems and Nanostructures*, **44**, 1399–1405 (2012).

130. Behera D., Acharya B. S., 'Nano-star formation in Al-doped ZnO thin film deposited by dip-dry method and its characterization using atomic force microscopy, electron probe microscopy, photoluminescence and laser Raman spectroscopy', *Journal of Luminescence*, **128**, 1577–1586 (2008).

131. Wu Y. L., Tok A. I. Y., Boey F. Y. C., Zeng X. T., Zhang X. H., 'Surface modification of ZnO nanocrystals', *Applied Surface Science*, **253**, 5473–5479 (2007).

132. Villani M., Calestani D., Lazzarini L., Zanotti L., Mosca R., Zappettini A., 'Extended functionality of ZnO nanotetrapods by solution-based coupling with CdS nanoparticles', *Journal of Materials Chemistry*, **22**, 5694–5699 (2012).

133. Fang F., Zhao D. X., Li B. H., Zhang Z. Z., Zhang J. Y., Shen D. Z., 'The enhancement of ZnO nanowalls photoconductivity induced by CdS nanoparticle modification', *Applied Physics Letters*, **93**, 233115/1–3 (2008).

134. Khatamian M., Saket Oskoui M., Haghighi M., 'Photocatalytic hydrogen generation over CdS–metalosilicate composites under visible light irradiation', *New Journal of Chemistry*, **38**, 1684–1693 (2014).

135. Yu S. H., Yang J., Han Z. H., Zhou Y., Yang R. Y., Qian Y. T., Zhang Y. H., 'Controllable synthesis of nanocrystalline CdS with different morphologies and particle sizes by a novel solvothermal process', *Journal of Materials Chemistry*, **9**, 1283–1287 (1999).

136. Murugan A. V., Sonawane R. S., Kale B. B., Apte S. K., Kulkarni A. V., 'Microwave – solvothermal synthesis of nanocrystalline cadmium sulfide', *Materials Chemistry and Physics*, **71**, 98–102 (2001).

Chapter-4

Synthesis of ZnO@Ag and Cu_2O@Ag Core-Shell Nanoparticles *via* a Novel Thermal Decomposition Approach

4.1 Synthesis of ZnO@Ag Core-Shell Heteronanostructures *via* a Novel Thermal Decomposition Approach

4.1.1 Introduction

In recent years, various heteronanostructures such as semiconductor-semiconductor, metal-semiconductor, and carbon-semiconductors have attracted the attention of scientists due to their improved optical and electronic properties and they have been used in multi-functional applications such as catalysis, sensors, and optoelectronics [1–6]. Among them, metal-semiconductor heteronanostructures have great importance and they exhibit better and tunable physicochemical properties [7–9]. Metal-semiconductor heteronanostructures have been extensively used as photocatalysts and these heterostructures enhance the photocatalytic efficiency by reducing the electron-hole pair recombination. The photogenerated electrons in the conduction band of the semiconductor transfer to the metal which enables lower recombination rate of the photogenerated excitons. The metal acts as an electron sink due to the Schottky barrier at the metal-semiconductor interface [7–9].

In the metal-semiconductor heteronanostructures, metal nanoparticles are used either as the core or the shell material. A number of reports are available where metal acts as the core and semiconductor acts as the shell material. Examples are Ag@AgX (X = Cl, Br) [10], Ag/Au@CdSe [11–13], Au@MO_2 (M = Sn, Ti) [14,15], Au@Fe_2O_3 [16], Au@MS (M = Cd, Pb, Zn) [17], M@ZnO (M = Au, Zn) [18,19], M@In_2O_3 (M = Au, In) [20,21], Zn@ZnSe [22], Si@WO_3 [23], Ge@Si($GeSi)_n$, and Si@$(GeSi)_n$ [24]. Various authors have reported metal-semiconductor heteronanostructures where semiconductor acts as the core and metal acts as the shell. Examples are CdSe@M (M = Au, Pd, Pt) [25], FePt@Au [26], GaAs@M (M = Al, Ga, Si) [27–29], GaP@Si [30], MnSi@Si [31], SnO_2@Te [32], WO_3@Ag [33], and ZnO@M (M = Ag, Au, Pt, Si) [34–36]. In addition to these metal-semiconductor heteronanostructures, bimetallic core or shell nanomaterials coupled with semiconductor nanoparticles have also been reported. Examples are AuCo@g-C_3N_4 [37], AuNi@ZnO [38], Co@$CoPt_3$ [39], and α-Fe_2O_3@Ag/AgCl [40]. The TEM and HRTEM images of Au@Ag_2S and Au@PbS core-shell nanoparticles are shown in Figure 4.1.1 and the TEM and HRTEM images of GaAs@Si and GaP@Si core-shell nanoparticles are shown in Figure 4.1.2.

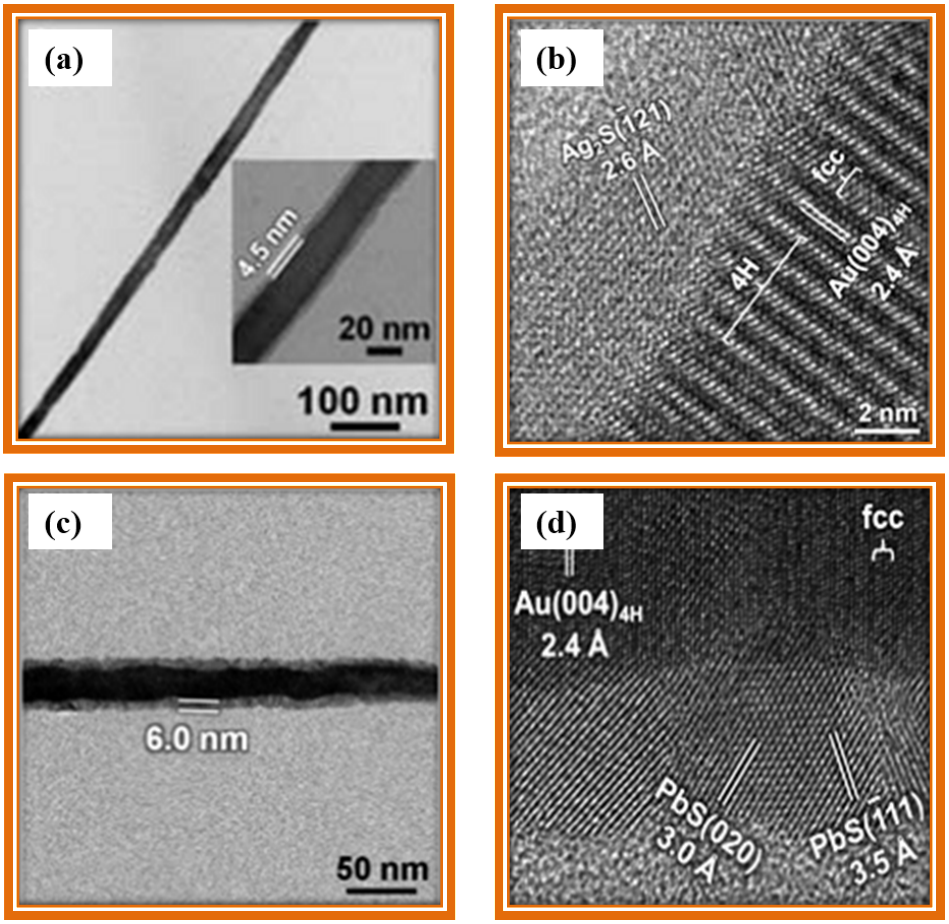

Fig. 4.1.1: TEM and HRTEM images of **(a, b)** Au@Ag_2S and **(c, d)** Au@PbS core-shell nanoparticles [17]. Here Au is the core material.

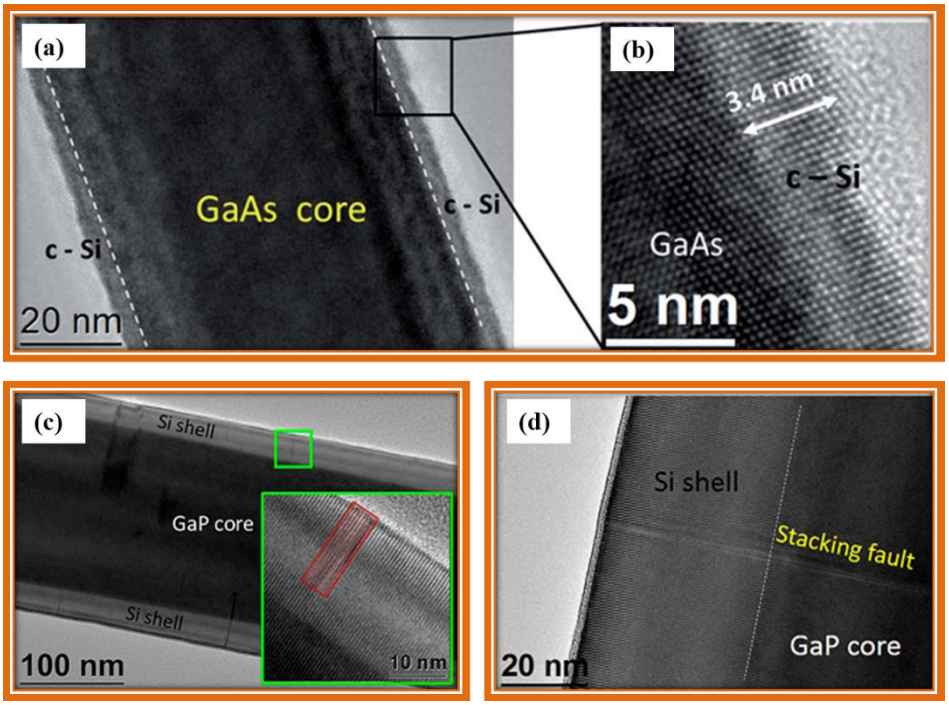

Fig. 4.1.2: TEM and HRTEM images of **(a, b)** GaAs@Si [29] and **(c, d)** GaP@Si [30] core-shell nanoparticles. Here Si is the shell material.

Among the noble metals, silver is the most sought after metal due to its good chemical stability, low-cost and high efficiency [41,42]. Silver has been used as the core or shell in silver based heterostructures. A schematic representation of silver based core-shell heterostructures is shown in Figure 4.1.3.

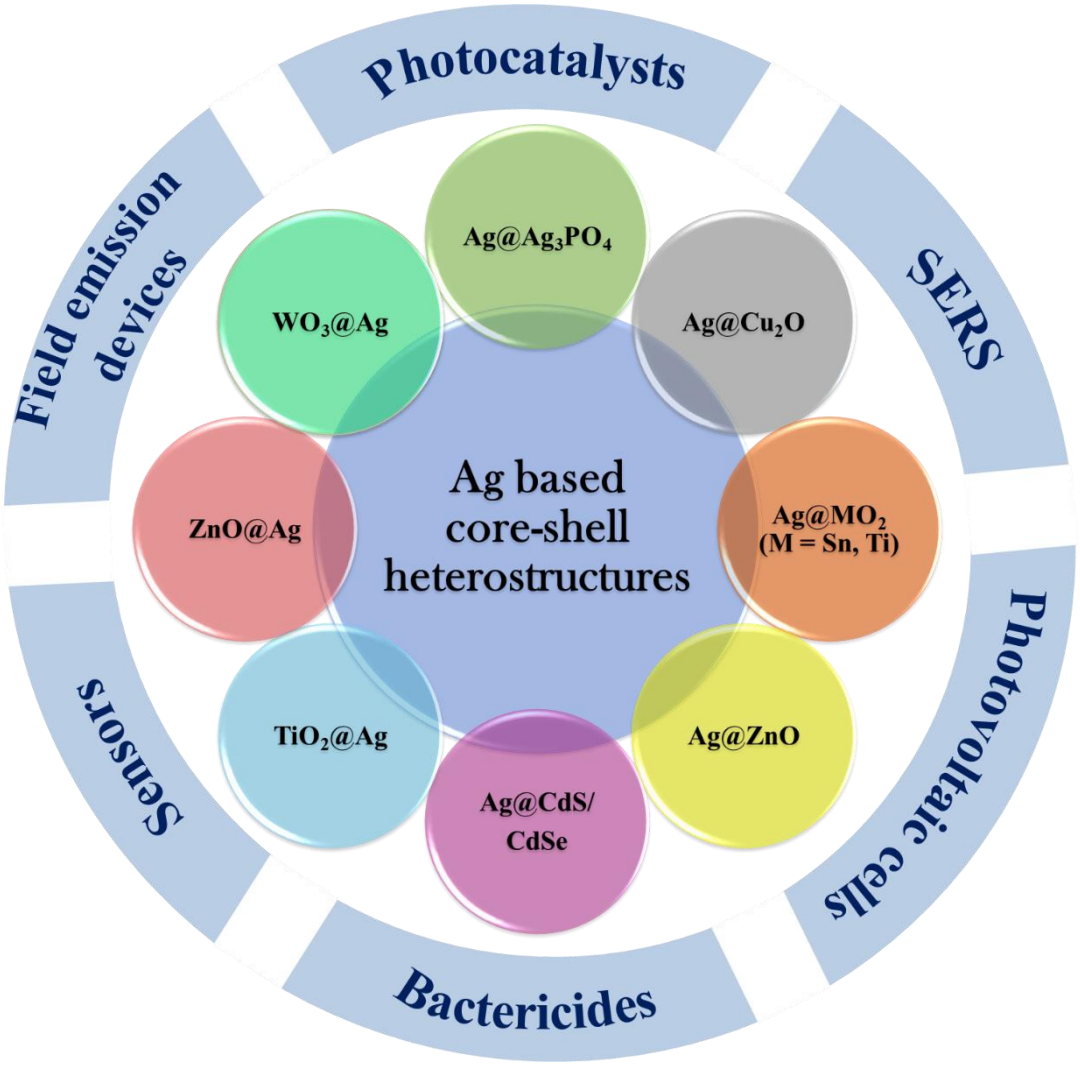

Fig. 4.1.3: Schematic representation of silver based core-shell heterostructures and the various applications [4,7–9].

Among the silver based core-shell heteronanostructures, ZnO@Ag core-shell heteronanostructures have much attracted immense attention. On coupling silver nanoparticles with ZnO, the photocatalytic activity and light harvesting efficiency of ZnO are enhanced under visible light by improving the charge separation at the interface. Moreover, the surface plasmon resonance absorption of silver nanoparticles creates a local electric field which enhances the photocatalytic activity.

Different chemical and physical methods have been reported for the synthesis of ZnO@Ag core-shell heteronanostructures. The chemical methods include electrodeposition [43], hydrothermal/solvothermal [44,45], water-in-oil microemulsion [45], seed mediated particle growth [46,47], sol-gel [48], wet-chemical method [49], photodeposition [50], sonochemcial [51], chemical methodology [52], and dip-redox method [53]. The physical methods include electron beam evaporation [54], laser ablation [55], and microwave assisted route [56]. A brief description of some of the methods for the deposition of silver nanoparticles on ZnO nanorods are discussed below.

Solvothermal [44]: In this method, appropriate amounts of zinc acetate and silver acetate are placed in a Teflon lined stainless steel container and then 30 mL of ethanolic NaOH solution is added drop wise to the above contents with stirring. After that, the reaction contents are heated at 160 ^{o}C for 24 h.

Water-in-oil microemulsion [45]: In this method, first Triton X-100 solution is prepared in a mixture of cyclohexane and hexanol. Then, certain amount of zinc nitrate is taken in the Triton X-100 solution and after that, ammonium hydroxide solution is added and kept for overnight to get ZnO solution. To this certain amount of $AgNO_3$ dissolved in Triton X-100 is added followed by addition of $NaBH_4$ to deposit Ag nanoparticles on ZnO.

Seed mediated particle growth [46]: In this method, first ZnO microspheres are synthesized by a two-step thermal decomposition approach. Then, certain amount of ZnO microspheres are dispersed in an ethanolic solution of $SnCl_2.H_2O$ and stirred for half an hour. The Sn^{2+} deposited ZnO microspheres are dispersed in an ethanolic solution of $Ag(NH_3)_2^+$ and stirred for 1 h. During the stirring, silver ions are reduced by Sn^{2+} ions and silver seeds are formed on the ZnO microspheres. The silver seeded ZnO microspheres are redispersed into an aqueous $AgNO_3$ solution and heated to 80 ^{o}C. To grow the silver nanoparticles on the ZnO microspheres, sodium citrate is added at 80 ^{o}C and the stirring is continued for about 1 h.

Photodeposition [50]: In this method, ZnO nanorods are deposited on a glass substrate using chemical solution deposition. The ZnO nanorods are dispersed in $AgNO_3$ solution to adsorb Ag^+ ions on the ZnO nanorods. Then, the film is irradiated with a 20 W low-pressure mercury lamp (λ = 254 nm, 1.9 mW/cm^2) for 20 min to deposit Ag

nanoparticles on the ZnO nanorods. A schematic representation of Ag deposition on the ZnO nanorods is shown in Figure 4.1.4.

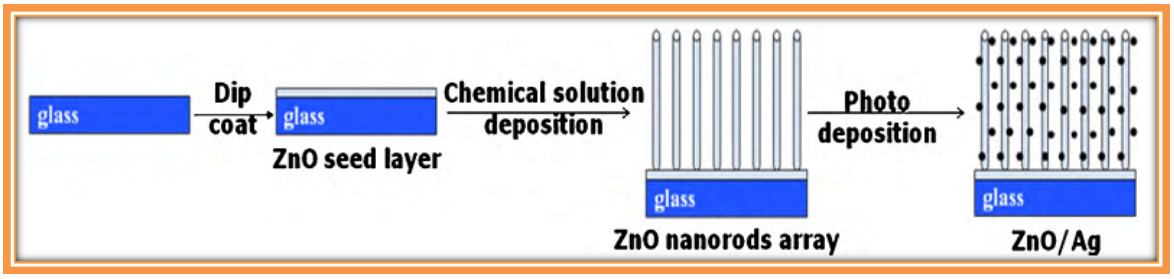

Fig. 4.1.4: Schematic representation of silver deposition on ZnO nanorods using photodeposition [50].

Sonochemical route [51]: First, ZnO nanorods are prepared using hydrothermal method. The ZnO nanorods are dispersed in $Ag(NH_3)_2^+$ solution and stirred at room temperature for about 30 min. Then, formaldehyde solution is added drop wise to the reaction mixture and then the reaction contents are irradiated using a high intense ultrasonicator at room temperature for 1 h to deposit Ag nanoparticles on the ZnO nanorods.

Chemical method [52]: First, ZnO nanorods are prepared by hydrothermal process. The ZnO nanords are dispersed in an aqueous solution and sonicated for about half an hour. After this, certain amount of CTAB is added, heated to 40 ^oC under constant stirring and cooled down to room temperature gradually. Then, $AgNO_3$ aqueous solution is added to the above solution at room temperature and stirred for 1 h. To reduce the Ag^+ ions, an aqueous solution of $NaBH_4$ is added and stirred for further 1 h.

Dip-redox process [53]: ZnO nanords are first synthesized *via* hydrothermal process. The surface of ZnO nanorods is modified with polydopamine *via in situ* polymerization. Then, the surface modified ZnO nanorods are dipped in $AgNO_3$ solution at room temperature for 2 h followed by drying in vacuum for 24 h. The samples are annealed at 500 ^oC for 3 h under argon flow to deposit Ag nanoparticles on the ZnO nanorods.

Laser ablation [55]: ZnO nanorods are first prepared using hydrothermal method. Ag nanoparticles are then prepared by laser ablation. High purity plates of Ag with thickness of 1 mm are irradiated with Q-switched Nd:YAG pulsed laser (λ = 532 nm) for 20 min. Then, the obtained Ag nanoparticles and ZnO nanorods are mixed in an aqueous solution

and irradiated for about one and half hour to deposit silver nanoparticles on the ZnO nanorods.

The TEM and HRTEM images of ZnO@Ag heterostructures, prepared using solvothermal and reduction methods, are shown in Figure 4.1.5.

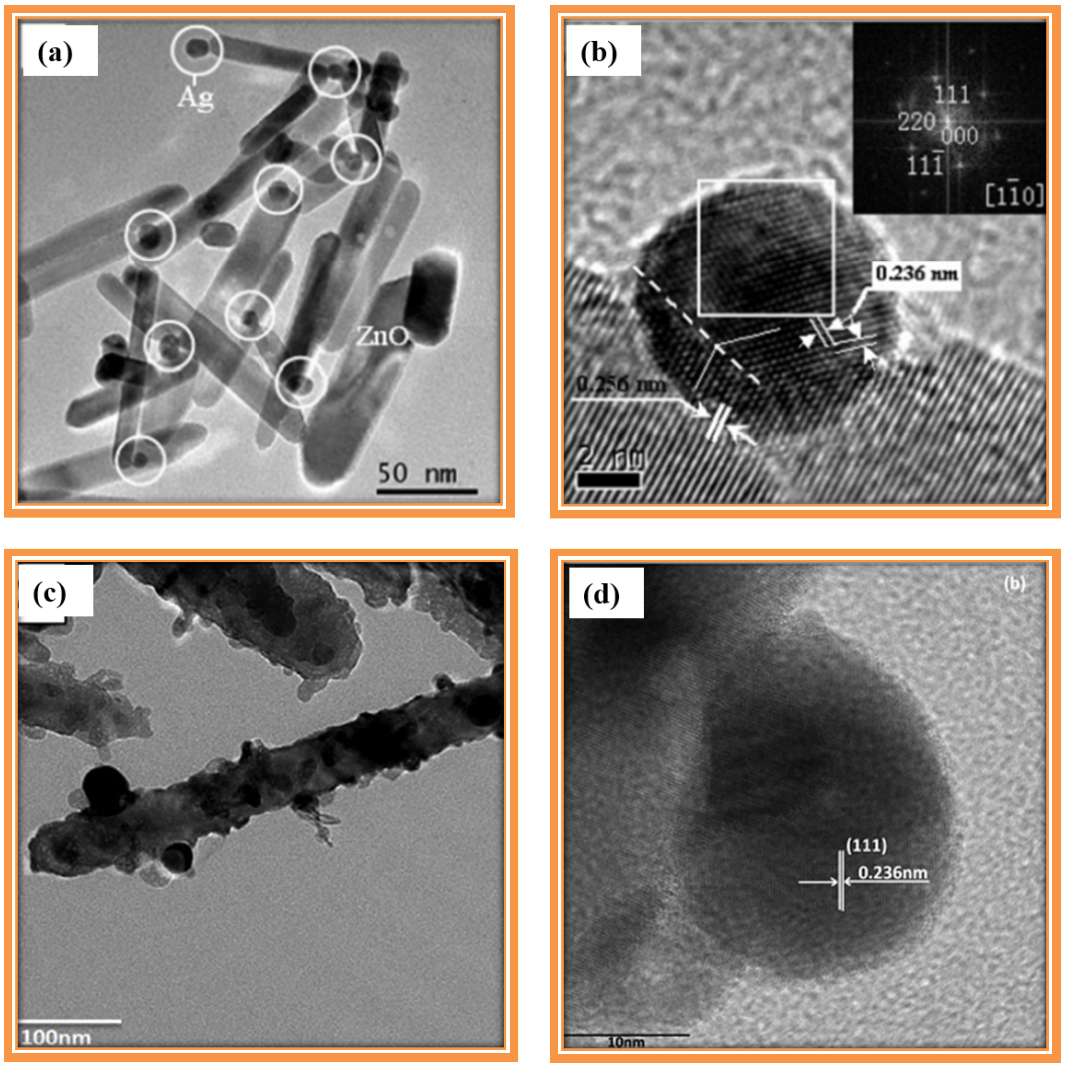

Fig. 4.1.5: TEM and HRTEM images of ZnO@Ag core-shell heterostructures prepared using **(a, b)** solvothermal method [44] and **(c, d)** chemical reduction method [52]. Inset in Figure 4.1.5b shows the FFT pattern of Ag in the ZnO@Ag core-shell heterostructures.

The preparation of ZnO@Ag heteronanostructures with uniformly deposited silver nanoparticles on ZnO nanorods without free silver particles is still a challenge due to self-nucleation of silver nanoparticles during the deposition of silver on ZnO. In the present study, a facile, economical, and simple thermal decomposition approach for the

synthesis of ZnO@Ag heteronanostructures has been reported. The particle size of silver nanoparticles on the ZnO nanorods could be controlled simply by varying the concentration of silver acetate during the thermal decomposition.

4.1.2 Experimental details

Zinc nitrate (99%, SRL, AR), urea (99.5%, Rankem, AR), ethylene glycol (99%, Rankem, LR), silver acetate (98%, Loba Chemie), diphenyl ether (99%, Sigma-Aldrich) were used as received without further purification. Methanol was received from SD Fine Chemicals and was used after distillation. More details on the synthetic procedure for the preparation of ZnO@Ag core-shell heteronanostructures are discussed below.

4.1.2.1 Synthesis of ZnO nanorods

ZnO nanorods were synthesized using homogeneous precipitation method [57,58]. The details on synthesis of ZnO nanorods have been given in Chapter-3.

4.1.2.2 Synthesis of ZnO@Ag core-shell heteronanostructures

The schematic representation of synthesis of ZnO@Ag core-shell heteronanostructures is given in Scheme 4.1.1. About 50 mg of ZnO nanorods was mixed with different amounts of silver acetate (0.10, 0.15 and 0.25 mmol) in 10 mL of diphenyl ether and the contents were sonicated for about 3 min to achieve good dispersion. The contents were refluxed at about 220 ^{o}C for 1 h in air. After completion of the reaction, the obtained slurry was cooled to room temperature and then 25 mL of methanol was added. The obtained precipitate was centrifuged, washed with methanol several times and dried in an oven for overnight. The obtained silver deposited ZnO samples were labelled as A1, A2, and A3 corresponding to 0.10, 0.15, and 0.25 mmol concentration of silver acetate, respectively.

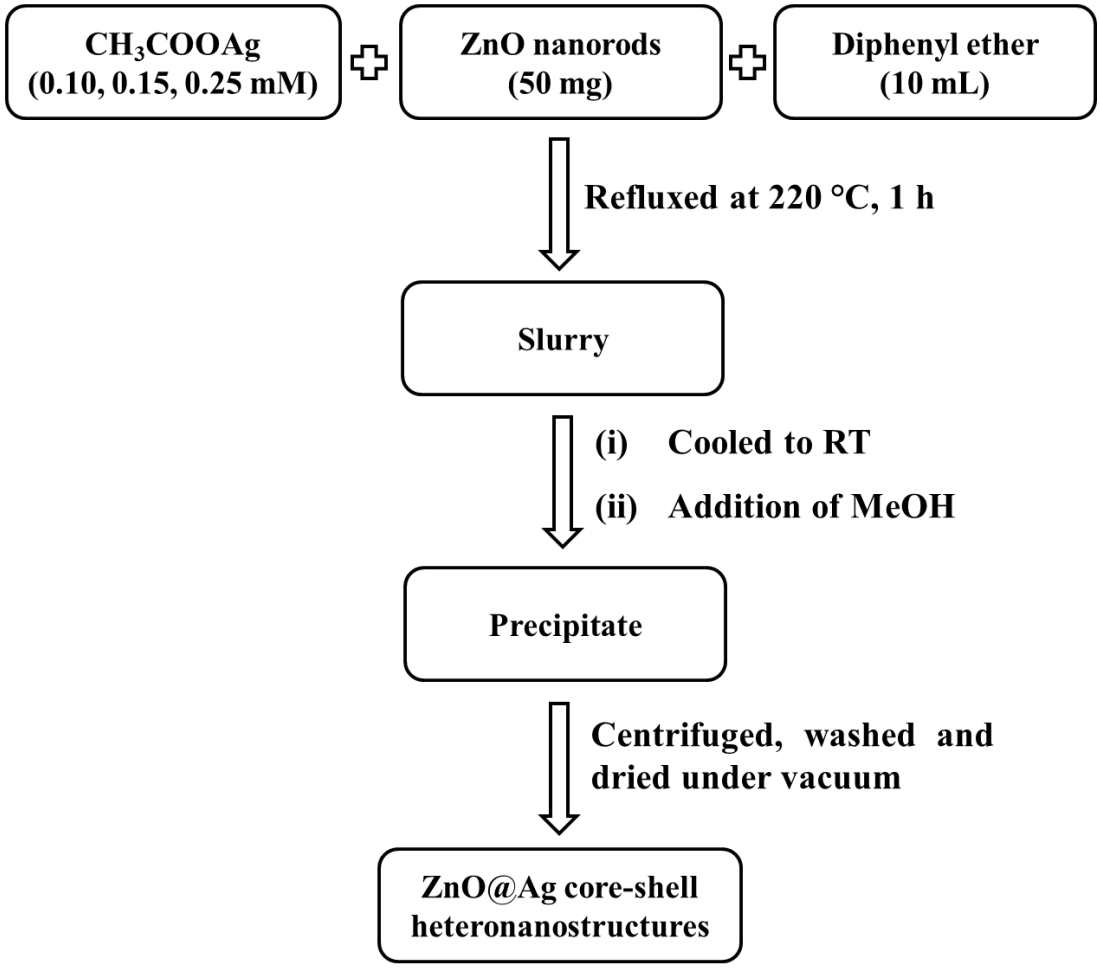

Scheme 4.1.1: Schematic representation of synthesis of ZnO@Ag core-shell heteronanostructures *via* thermal decomposition approach.

The synthesized ZnO@Ag core-shell heteronanostructures were characterized by PXRD, FE-SEM, SEM-EDX, TEM and XPS. The optical properties were studied using DRS and PL spectroscopies. More details on the experimental techniques have been discussed in Chapter-2.

4.1.3 Results and discussion

4.1.3.1 XRD analysis

The XRD patterns of pure ZnO and ZnO@Ag core-shell heteronanostructures (A1, A2 and A3) are shown in Figure 4.1.6. Pure ZnO shows diffraction peaks at 2θ values of 31.61°, 34.41°, 36.24°, 47.61°, 56.59°, 62.87°, 66.31°, 67.94°, 69.06°, 72.54°, 76.96°, and 81.31° attributed to (100), (002), (101), (102), (110), (103), (200), (112), (201), (004), (202), and (104) planes of wurzite ZnO (JCPDS file no. 36-1451), respectively. All the

as prepared ZnO@Ag samples show two set of diffraction peaks. The diffraction peaks marked with "#" indicate peaks due to wurzite ZnO. The peaks marked with "*" at 2θ values of 38.12°, 44.32°, 64.46°, 77.47°, and 81.53° correspond to (111), (200), (220), (311), and (222) planes of face centered cubic silver (JCPDS file no. 04-0783), respectively. The crystallite size of ZnO and silver in all the ZnO@Ag samples was calculated using Debye-Scherrer formula using the XRD peaks at 2θ = 36.24° and 38.12°, respectively. The crystallite size of pure ZnO is about 50 nm. In the ZnO@Ag samples, the crystallite size of silver nanoparticles was found to be 24 nm, 26 nm, and 31 nm and the crystallite size of ZnO was 48 nm, 42 nm and 35 nm for the samples A1, A2, and A3, respectively. In the ZnO@Ag samples, the decrease in the crystallite size of the ZnO compared to pure ZnO is attributed to the deposition of silver nanoparticles on its surface.

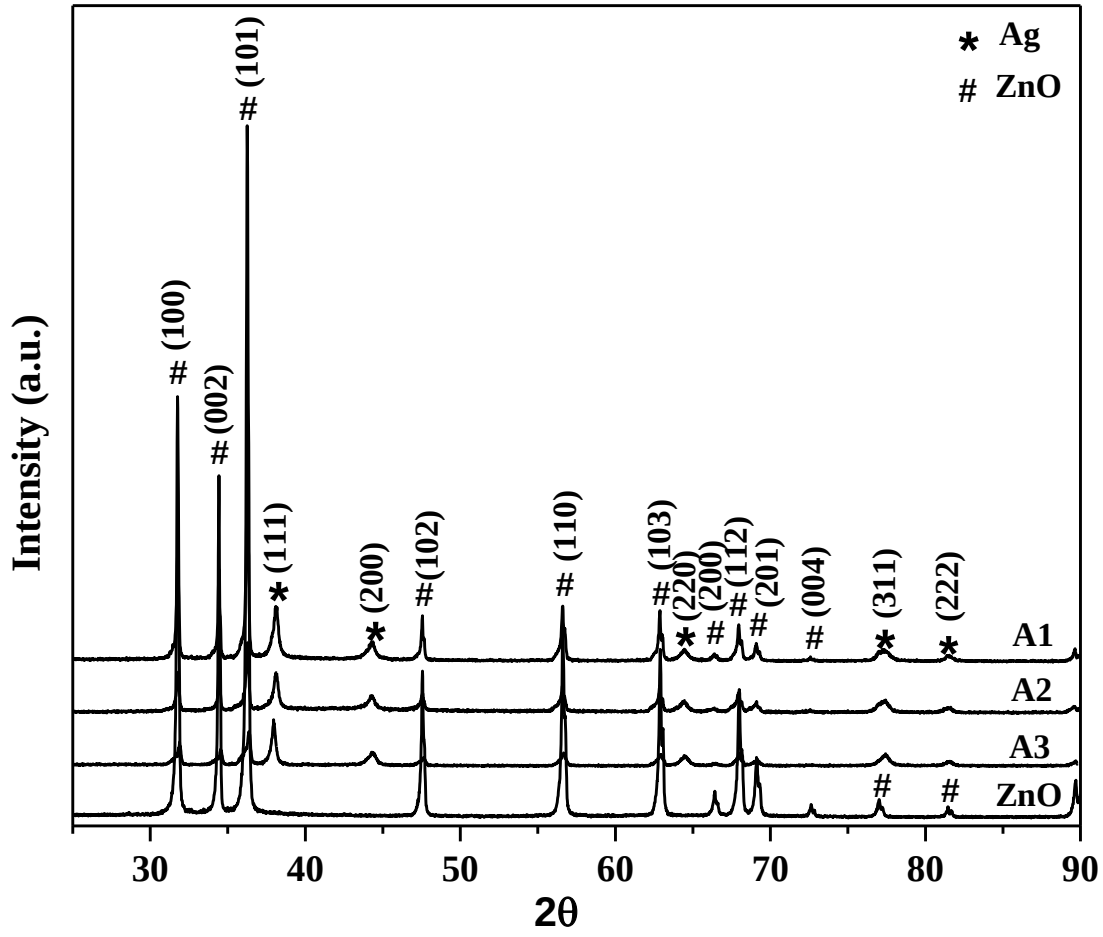

Fig. 4.1.6: XRD patterns of ZnO and ZnO@Ag core-shell heteronanostructures (A1, A2 and A3).

4.1.3.2 FE-SEM studies

The morphological studies were first carried out using FE-SEM analysis and the FE-SEM images of pure ZnO nanorods and the ZnO@Ag core-shell heteronanostructures (A1, A2, and A3) are shown in Figure 4.1.7. The length and diameter of pure ZnO nanorods were found to be about 2.5 ± 0.4 μm and 260 ± 20 nm, respectively. The FE-SEM images of ZnO@Ag samples (A1 to A3) show clearly the deposition of silver on the ZnO nanorods. The particle size values of silver in the ZnO@Ag heteronanostructures are 53.5 ± 15.7 nm, 62.3 ± 14.2 nm, and 70.2 ± 16.4 nm for samples A1, A2, and A3, respectively. As the concentration of silver increases from sample A1 to A3, the particle size of silver also increases.

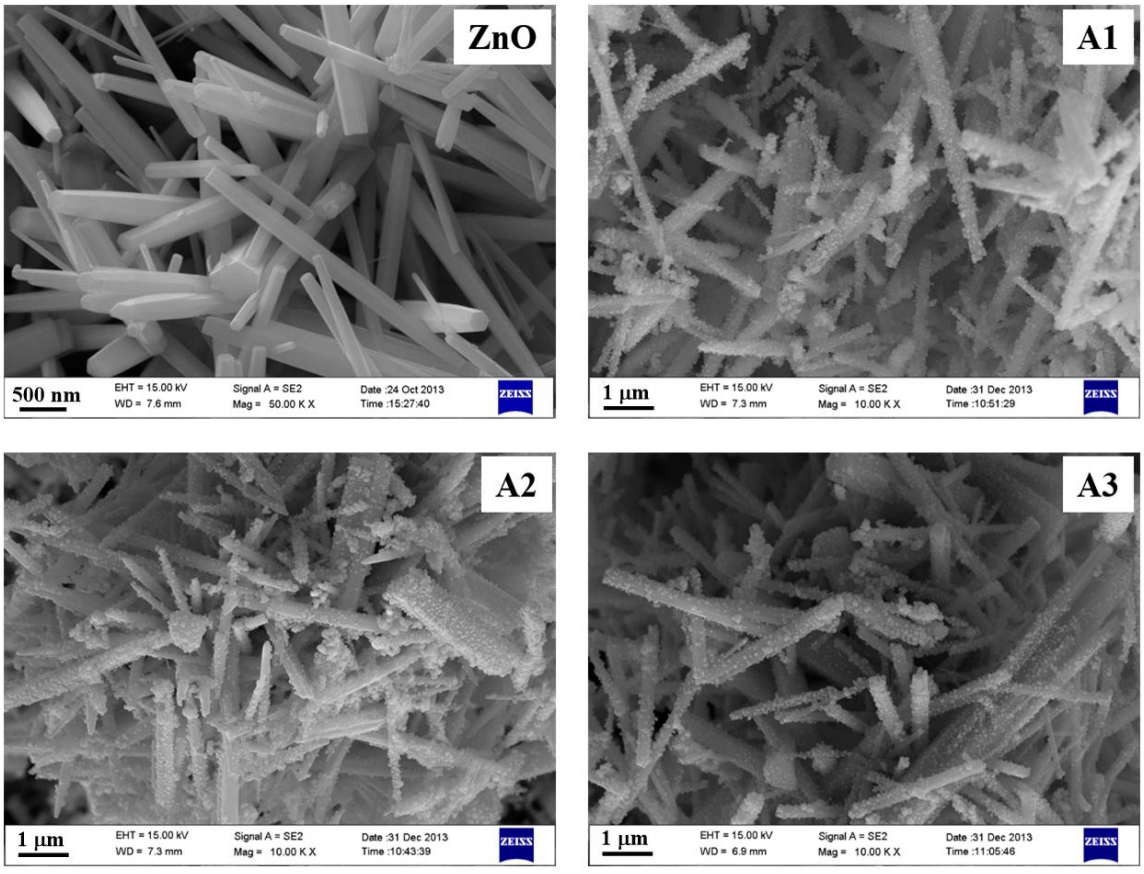

Fig. 4.1.7: FE-SEM images of ZnO nanorods and ZnO@Ag core-shell heteronanostructures (A1, A2 and A3).

4.1.3.3 SEM-EDX analysis

The elemental composition of ZnO@Ag core-shell heteronanostructures was estimated using energy dispersive X-ray analysis and the results are shown in Figure 4.1.8. The

EDXA results of ZnO@Ag core-shell heteronanostructures show the presence of zinc, oxygen, and silver in all the samples (A1, A2 and A3). The weight percent of silver in the ZnO@Ag core-shell heteronanostructures was found to be 20.4 ± 2.3, 25.4 ± 1.9, and 26.6 ± 3.7 for the samples A1, A2 and A3, respectively.

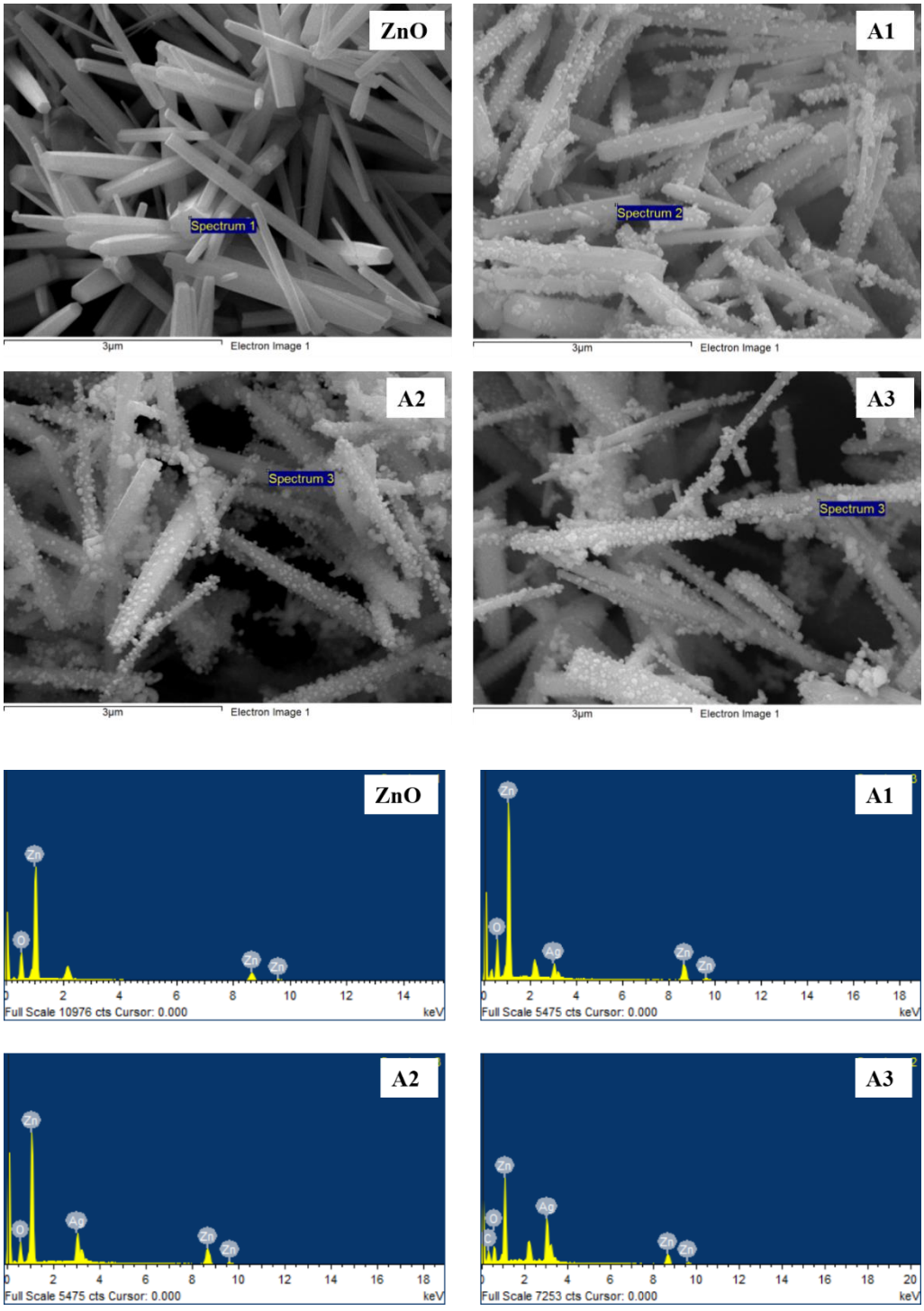

Fig. 4.1.8: SEM-EDX of ZnO nanorods and ZnO@Ag core-shell heteronanostructures (A1, A2 and A3).

4.1.3.4 TEM studies

To understand the ZnO@Ag core-shell heteronanostructures better, TEM analysis was carried out for pure ZnO and ZnO@Ag core-shell heteronanostructures and the TEM images are shown in Figure 4.1.9. The length of pure ZnO nanorods is about 2.5 ± 0.15 μm and the diameter is about 200 ± 20 nm. In the TEM images of ZnO@Ag core-shell heteronanostructures (A1, A2 and A3), one can clearly see adhered silver nanoparticles on the surface of ZnO nanorods; no free silver nanoparticles are found in the TEM images. The particle size distribution of silver nanoparticles on the ZnO nanorods are shown as insets in the corresponding TEM images. The mean diameter of silver nanoparticles on ZnO nanorods was found to be 52.8 ± 14.1 nm, 60.7 ± 16.7 nm, and 68.4 ± 8.8 nm for samples A1, A2, and A3, respectively. The broad size distribution of silver nanoparticles on ZnO nanorods is attributed to site-selective positioning of silver on ZnO nanorods prompted *via* a small lattice mismatch between silver and ZnO at the respective crystallographic plane [56]. The nucleation of silver takes place on energetically favoured (101) plane of ZnO nanorods and then the silver clusters are formed at different positions on the ZnO nanorods. The SAED patterns of pure ZnO and ZnO@Ag samples are shown in Figure 4.1.10. Pure ZnO nanorods show a set of diffraction spots in the SAED patterns due to hexagonal wurzite structure which indicates single crystalline nature of the ZnO nanorods. The distance between the two consecutive spots in the SAED pattern of pure ZnO was found to be 0.263 nm which is attributed to (002) plane of hexagonal ZnO which suggests the preferential growth of ZnO nanorods along (001) direction [59]. The SAED patterns of ZnO@Ag heteronanostructures show spot patterns due to ZnO and ring patterns due to cubic silver.

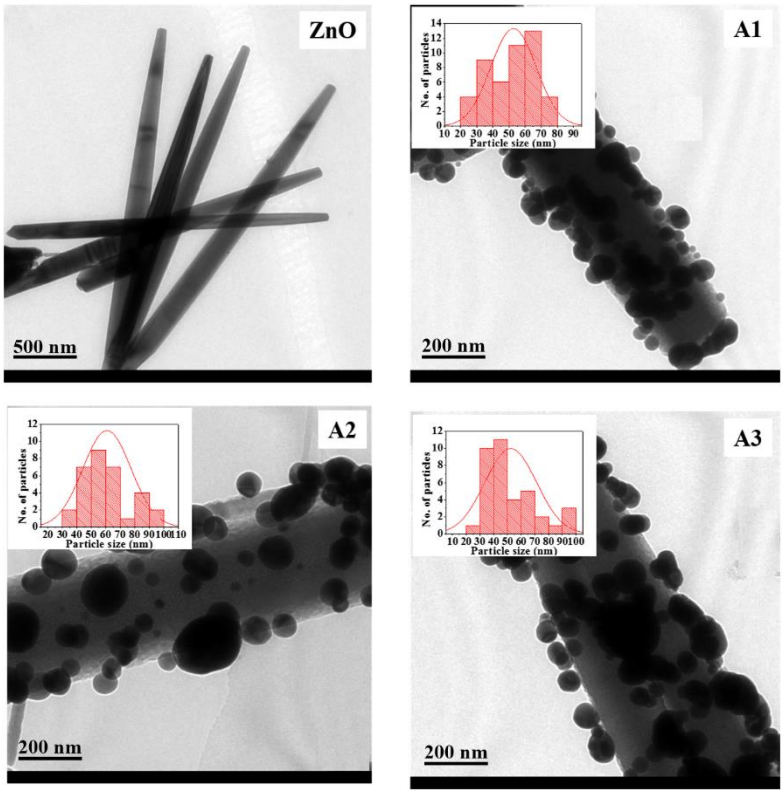

Fig. 4.1.9 TEM images of ZnO and ZnO@Ag core-shell heteronanostructures (A1, A2 and A3).

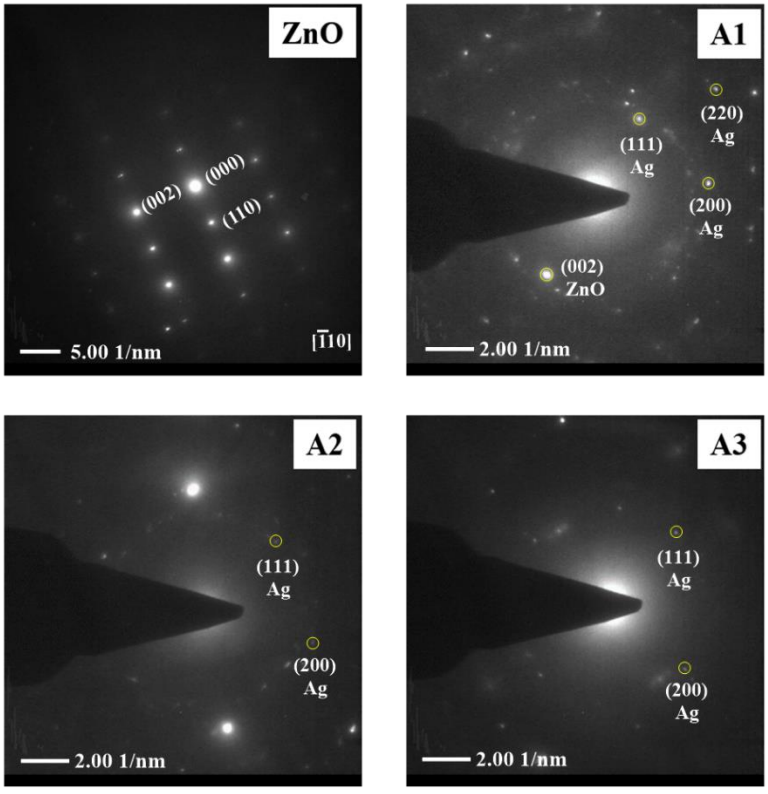

Fig. 4.1.10 SAED patterns of ZnO and ZnO@Ag core-shell heteronanostructures (A1, A2 and A3).

4.1.3.5 XPS studies

In order to understand if the silver deposited on the ZnO surface is in metallic form or not and also the surface composition of ZnO@Ag sample, XPS analysis was carried out and the results are shown in Figure 4.1.11. The XPS results for ZnO@Ag (A1) indicate the presence of Zn, O, and Ag. The Zn $2p_{3/2}$ spectrum (Figure 4.1.11b) shows a peak centered at about 1021.3 eV. This is attributed to the presence of Zn^{2+} on the sample surface [44]. The O1s spectrum (Figure 4.1.11c) is asymmetric and the spectrum was deconvoluted. The deconvolution results suggest that there are two kind of oxygen species; the peak with binding energy of about 530.5 eV is due to lattice oxygen of ZnO and the XPS peak at about 532.1 eV is due to the oxygen of surface hydroxyls [43]. The Ag 3d spectrum (Figure 4.1.11d) shows two peaks with binding energies 367.4 eV (Ag $3d_{5/2}$) and 373.4 eV (Ag $3d_{3/2}$) with a splitting of 6 eV. The observed binding energies and the doublet splitting indicate the presence of metallic silver in the ZnO@Ag sample [60]. The ratio of Zn to Ag in ZnO@Ag sample (A1) was found to be 2.46.

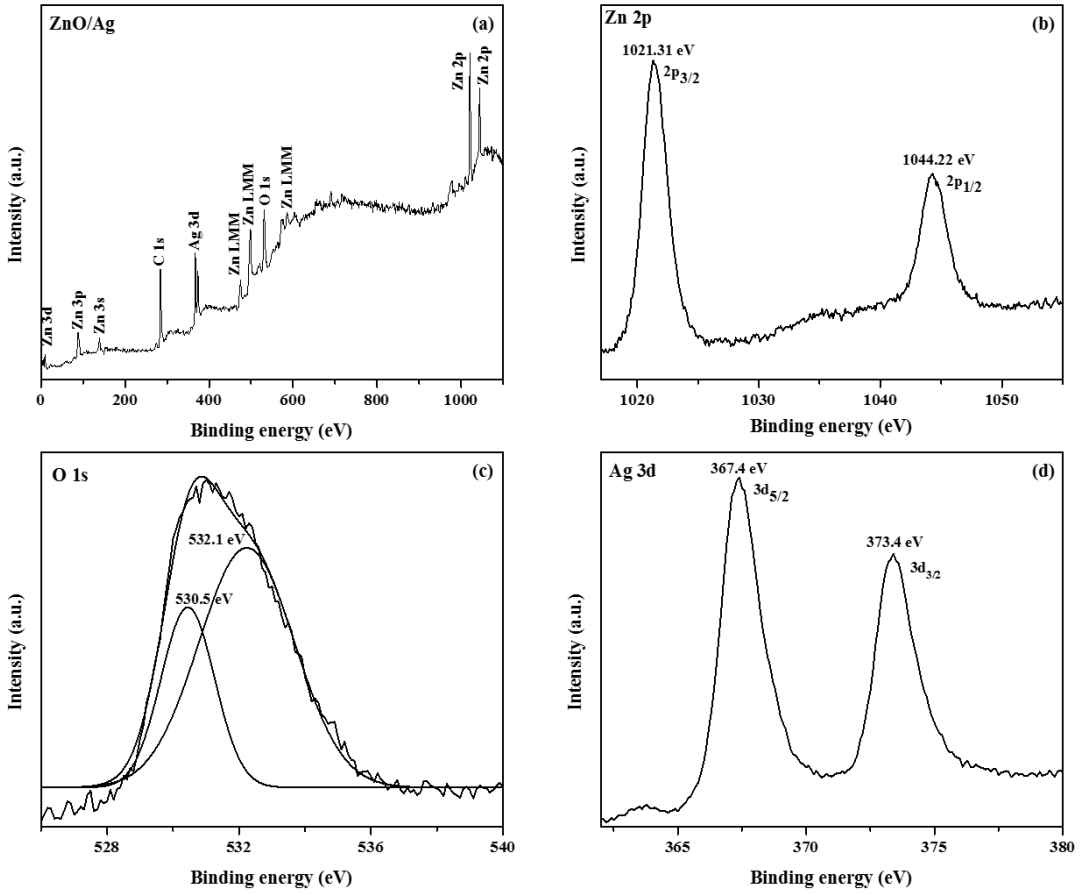

Fig. 4.1.111: (a) XPS survey spectra of ZnO@Ag sample A1, and **(b-d)** high resolution XPS spectra of Zn 2p, O 1s, and Ag 3d, respectively.

The optical properties of pure ZnO nanorods and ZnO@Ag core-shell heteronanostructures (A1, A2, and A3) were investigated using UV-Visible diffuse reflectance spectroscopy (DRS) and photoluminescence (PL) spectroscopy.

4.1.3.6 UV-Visible diffuse reflectance spectroscopy (DRS) studies

The DRS spectra of pristine ZnO nanorods, and ZnO@Ag core-shell heteronanostructures are shown in Figure 4.1.12. The bulk band gap of pure ZnO is 3.38 eV [61] and pristine ZnO nanorods possess band gap absorption at 373 nm (3.33 eV). Quantum confinement effect is not observed in the case of ZnO nanorods due to their large diameter (about 250 nm) which is much higher than the Bohr radius of ZnO (a_B = 1.8 nm). Pure Ag nanoparticles show surface plasmon resonance absorption at about 405 nm (inset in Figure 4.1.12). The DRS spectra of ZnO@Ag core-shell heteronanostructures show two prominent absorption bands in the UV-Visible region. The band at 370 nm is due to the band gap absorption of ZnO and the band at about 400 nm is due to the surface plasmon resonance of silver nanoparticles present in the ZnO@Ag core-shell heteronanostructures.

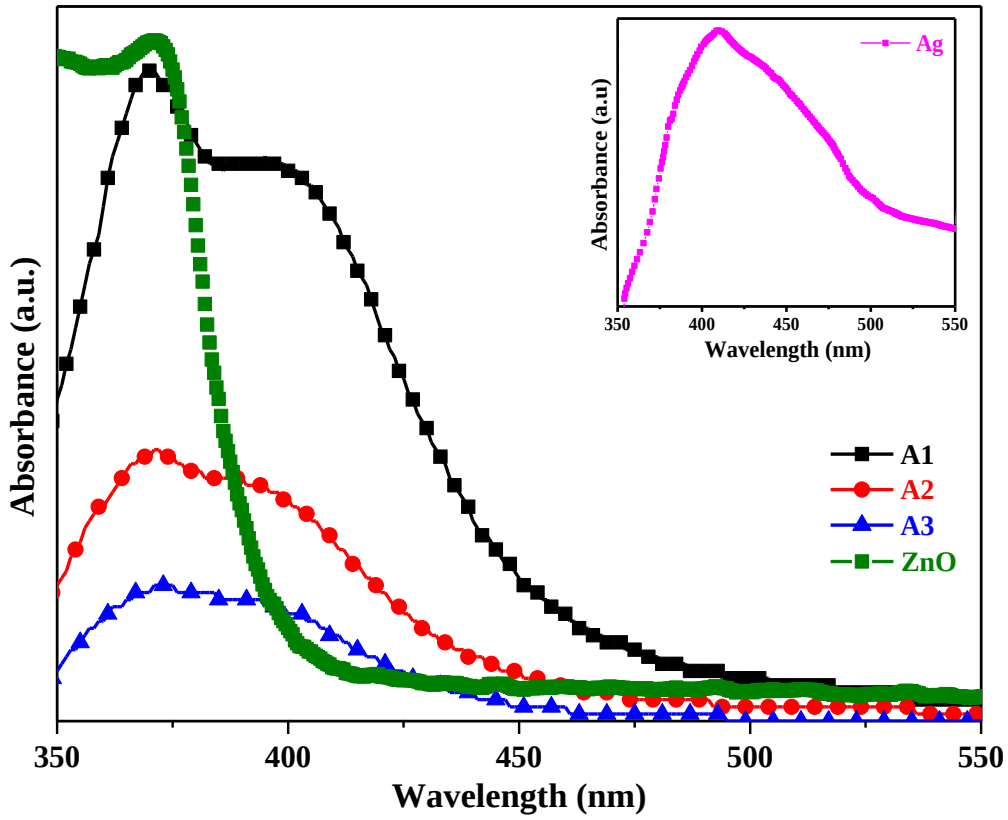

Fig. 4.1.12 UV-Visible diffuse reflectance spectra of ZnO nanorods and ZnO@Ag core-shell heteronanostructures. The UV-Vis spectrum of Ag nanoparticles is shown as inset.

4.1.3.7 Photoluminescence spectroscopy (PL) studies

The room temperature photoluminescence (PL) spectra of pristine ZnO nanorods, pure Ag nanoparticles, and ZnO@Ag core-shell heteronanostructures (A1, A2 and A3) are shown in Figure 4.1.13. The PL spectrum of pristine ZnO nanorods show emission bands at 380, 412, 435, 466, 485 and 494 nm. The emission bands at 380 and 412 nm are attributed to band edge free exciton recombination of ZnO [56,62]. The multiple peaks in this region are due to the formation of different shallow levels inside the band gap due to the presence of interstitial zinc atoms [56,63]. The strong emission in the blue region at about 435 nm is attributed to the electronic transition between the excitonic level and the interstitial oxygen (O_i). The emission in the blue-green region (at 466 nm) is attributed to the electronic transition between a deep acceptor (V_{Zn}) and a shallow donor (Zn_i). The emission bands in the green region (at 485 and 494 nm) are attributed to zinc vacancies, interstitial zinc and structural defects [57]. Pure Ag nanoparticles show a strong emission band at 357 nm and a broad emission between 400 and 600 nm. The strong emission band at 357 nm is attributed to radiative recombination of occupied electrons from the *sp* band with holes in the valence *d* band [64]. The broad emission between 400 and 600 nm is due to radiative decay of the surface plasmon resonance (SPR) excitation in the Ag nanoparticles [65].

The PL spectra of ZnO@Ag core-shell heteronanostructures exhibit similar emission bands as that of pure ZnO nanorods and pure Ag nanoparticles with noticeable intensity reduction. The reduction in intensity, observed in the PL spectra of ZnO@Ag core-shell heteronanostructures as compared to pure ZnO nanorods, is attributed to an efficient interfacial charge transfer from the ZnO nanorods to the silver nanoparticles; silver acts as an electron sink which traps the electrons from ZnO and hinder the recombination of photogenerated excitons in ZnO [46]. In the case of ZnO@Ag core-shell heteronanostructures, sample A1 exhibits lower PL emission intensity compared to the other ZnO@Ag samples and the PL intensity order is A1 < A2 < A3. The recombination of electron-hole pairs depends on the amount of silver nanoparticles present on the surface of ZnO nanorods. From A1 to A3, the amount of silver nanoparticles on the surface of ZnO nanorods increases and the extent of recombination of electron-hole pairs increases and accordingly, the PL intensity also increases in the same order. When sufficient amount of silver metal sites are present on the surface of ZnO nanorods (e.g.

sample A1), these metal sites trap the electrons effectively and this leads to an increase in the charge separation of photogenerated electron and hole pairs on the surface of ZnO nanorods [66].

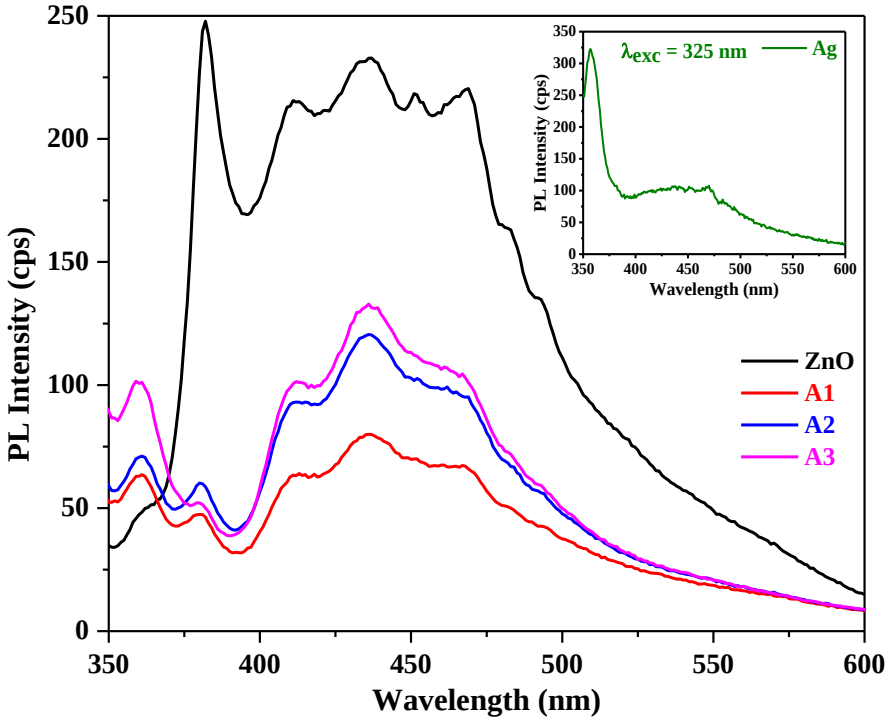

Fig. 4.1.13: Photoluminescence (PL) spectra of ZnO nanorods and ZnO@Ag core-shell heteronanostructures. The PL spectrum of Ag nanoparticles is shown as inset.

4.1.4 Proposed mechanism of formation of ZnO@Ag core-shell heteronanostructures

The possible mechanism for the formation of ZnO@Ag core-shell heteronanostructures is described in Scheme 4.1.2. In the first step, silver acetate decomposes to produce silver ions and acetate ions at 220 ^{o}C. At elevated temperatures, the thermal energy is sufficient to drive the silver ions (Ag^{+}) to the surface of the ZnO nanorods. In the second step, the acetate ions transfer electrons to the silver ions with the formation of silver nanoparticles on the surface of ZnO nanorods with the release of CO_2 and H_2 [67]. The reducing environment (H_2) leads to more decomposition of silver acetate.

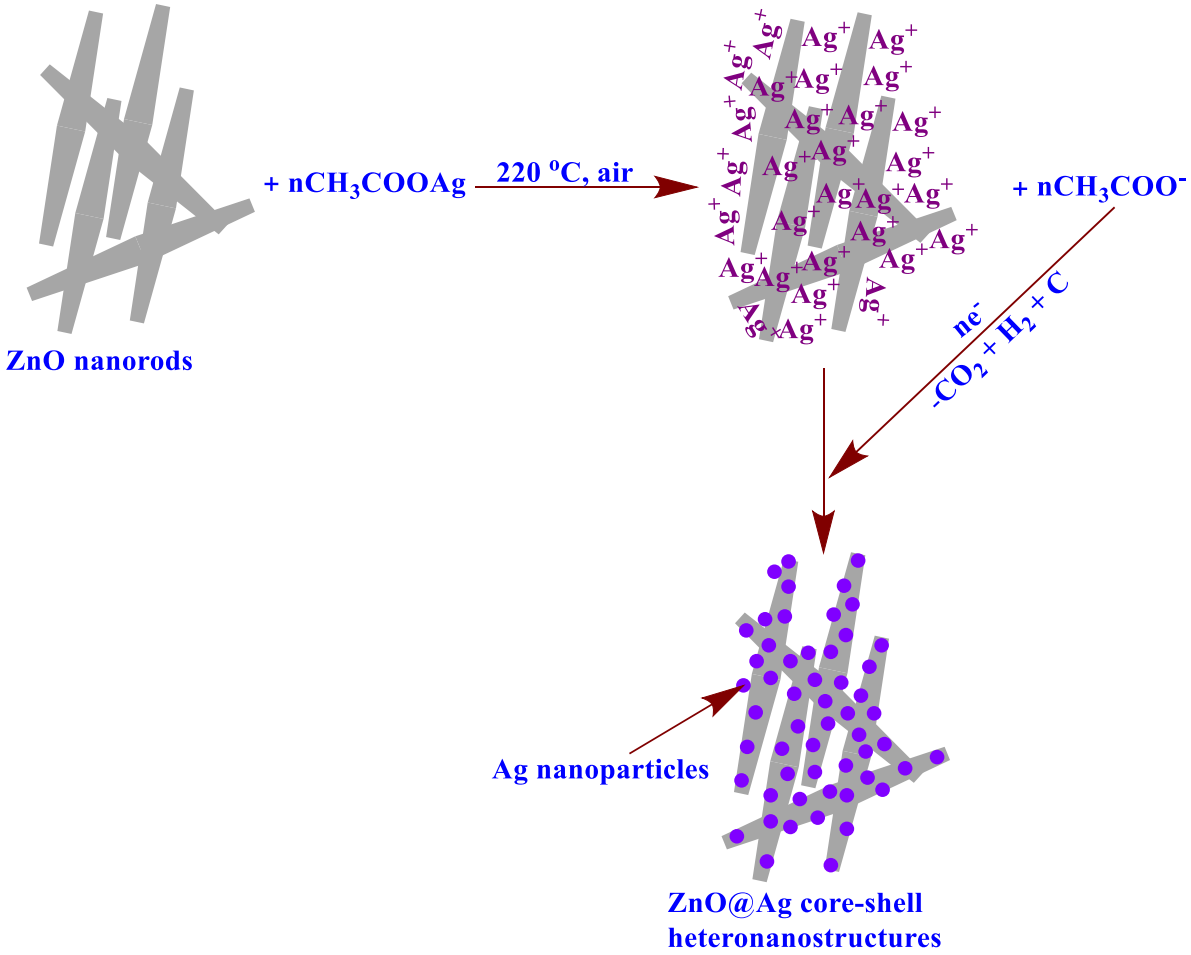

Scheme 4.1.2: The proposed mechanism for the formation of ZnO@Ag core-shell heteronanostructures.

To understand the silver deposition on the surface of ZnO nanorods better, thermal decomposition reactions were carried out at different temperatures (180, 200 and 220 °C) and the ZnO@Ag samples were analyzed using FE-SEM. At 220 °C, uniform deposition of silver nanoparticles on ZnO nanorods is noticed as compared to the reaction carried out at 180 °C (Figure 4.1.14). The ZnO@Ag sample prepared at 180 °C shows adherence of a few silver nanoparticles on the surface of ZnO nanorods. The ZnO@Ag sample prepared at 200 °C shows the deposition of silver nanoparticles on ZnO nanorods but some of the ZnO nanorods are uncoated and free silver nanoparticles are also observed. The thermal decomposition carried out at 220 °C leads to good adherence of silver nanoparticles on the surface of ZnO nanorods and the SEM image does not show any free silver nanoparticles. The better deposition of silver nanoparticles on ZnO at 220 °C is attributed to higher rate of reduction of silver acetate at elevated temperatures [68,69].

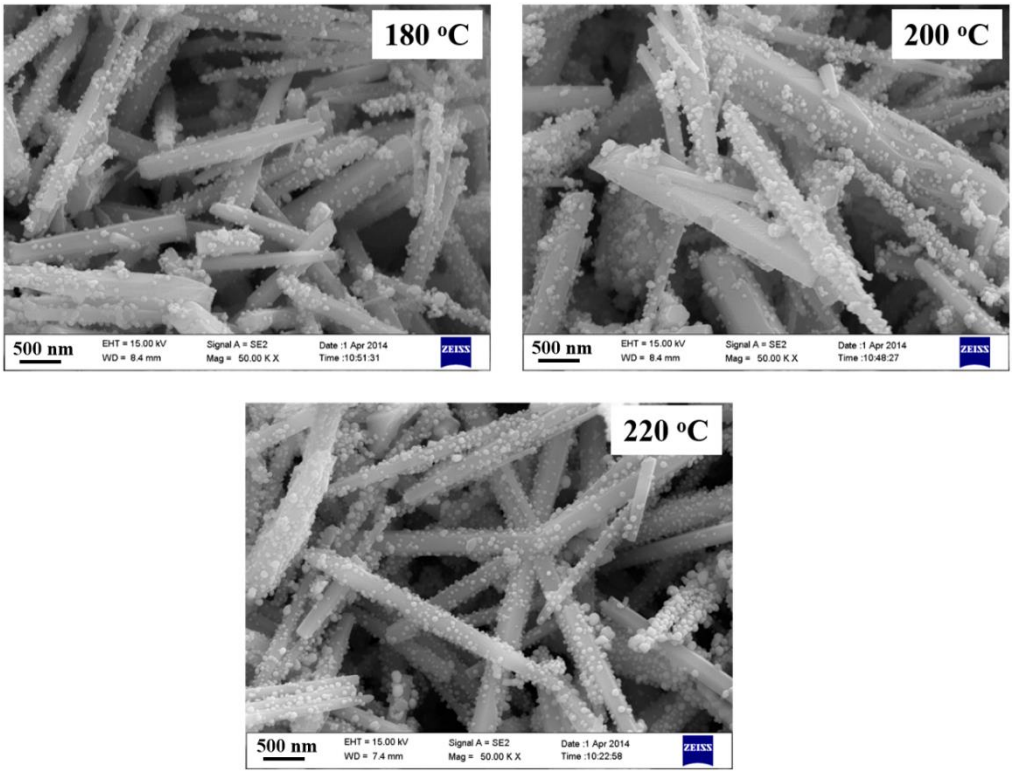

Fig. 4.1.14 FE-SEM images of ZnO@Ag samples prepared at different thermal decomposition temperatures.

The quality of silver coating on the ZnO nanorods was also studied by varying the thermal decomposition time (at 220 ^{o}C) from 30 min to 90 min and the SEM results are shown in Figure 4.1.15. In the case of 30 min, the average particle size of silver nanoparticles present on ZnO is 66.2 ± 17.3 nm. When the reaction time is increased to 60 min, the average particle size of silver nanoparticles decreases to 53.5 ± 15.7 nm. When the thermal decomposition time is further increased to 90 min, an increase in the average particle size of silver (83.3 ± 19.2 nm) is observed. At lower thermal decomposition time, i.e. 30 min, only less amount of silver nuclei nucleates from the solution and during the growth stage, these fewer nuclei grow rapidly as the concentration of silver ions per silver nuclei in the solution is high and this results in an increase in the average particle size of silver [68,69]. At 60 min, nucleation takes place rapidly compared to that at 30 min thereby resulting in a decrease in the concentration of silver in the solution. This leads to decrease in the particle size of silver at 60 min as compared to that at 30 min. When the thermal decomposition time is increased to 90 min, further growth of silver nuclei occurs resulting in an increase in the average particle size of silver nanoparticles.

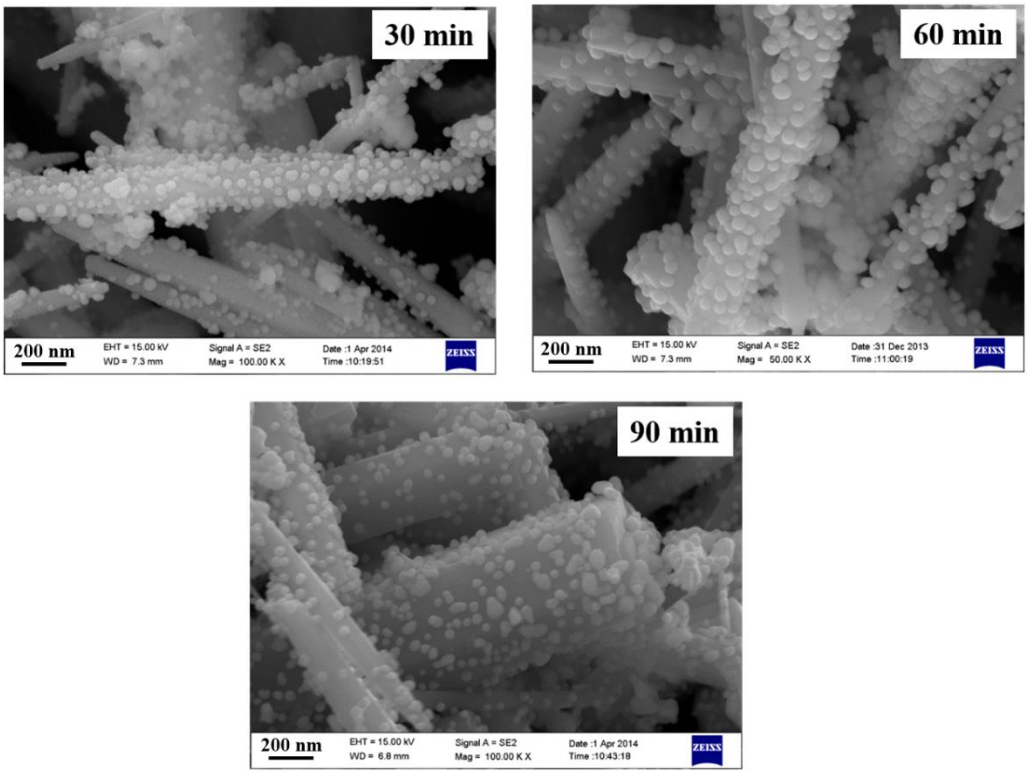

Fig. 4.1.15 FE-SEM images of ZnO@Ag samples prepared at different thermal decomposition times.

These results conclude that the thermal decomposition time of 60 min and temperature of 220 ^{o}C leads to uniform deposition of silver nanoparticles on the surface of ZnO nanorods.

4.1.5 Conclusions

ZnO@Ag core-shell heteronanostructures have been successfully synthesized through a cost effective, facile and simple thermal decomposition approach. XRD results indicate the presence of both ZnO and Ag in all the ZnO@Ag core-shell heteronanostructures (A1, A2 and A3). Better deposition of silver nanoparticles on surface of ZnO nanorods is possible at 220 ^{o}C. SEM and TEM images show the deposition of Ag nanoparticles on ZnO nanorods. SAED studies confirm the crystalline nature of ZnO and ZnO@Ag core-shell heteronanostructures. DRS results show the absorption bands of both ZnO and Ag nanoparticles in the ZnO@Ag samples. PL results of ZnO@Ag samples show emission bands with reduced intensity as compared to pure ZnO which is attributed to effective charge separation at the interface of ZnO and Ag nanoparticles. The reported synthetic method can be extended to prepare other metal-semiconductor heteronanostructured materials for various functional applications.

4.2 Synthesis of Cu_2O@Ag Polyhedral Core-Shell Nanoparticles *via* a Novel Thermal Decomposition Approach

4.2.1 Introduction

In the past few decades, semiconductor nanoparticles have attracted considerable attention of the scientists because of their potential applications in multidisciplinary fields. Among the metal oxide semiconductors, Cu_2O is an important visible light active semiconductor and its performance strongly depends on size, morphology, and composition [70–73]. Cu_2O is a non-stoichiometric p-type semiconductor with a direct band gap of 2.17 eV [74]. It possesses cuprite structure in which oxygen forms body centered cubic lattice while copper goes to half of the tetrahedral sites. Various morphologies of Cu_2O have been reported and they are polyhedra, branched structures, solid/hollow spheres, and hierarchical structures [75–78]. Cu_2O polyhedral crystals with different shapes (cubes, truncated cubes, rhombicuboctahedrons, cuboctahedrons, truncated octahedrons, octahedrons, etc.) have been reported which are composed of low index facets such as {100}, {110} and {111} [71,76]. A schematic representation of crystal structure and polyhedral morphologies of Cu_2O are shown in Figure 4.2.1.

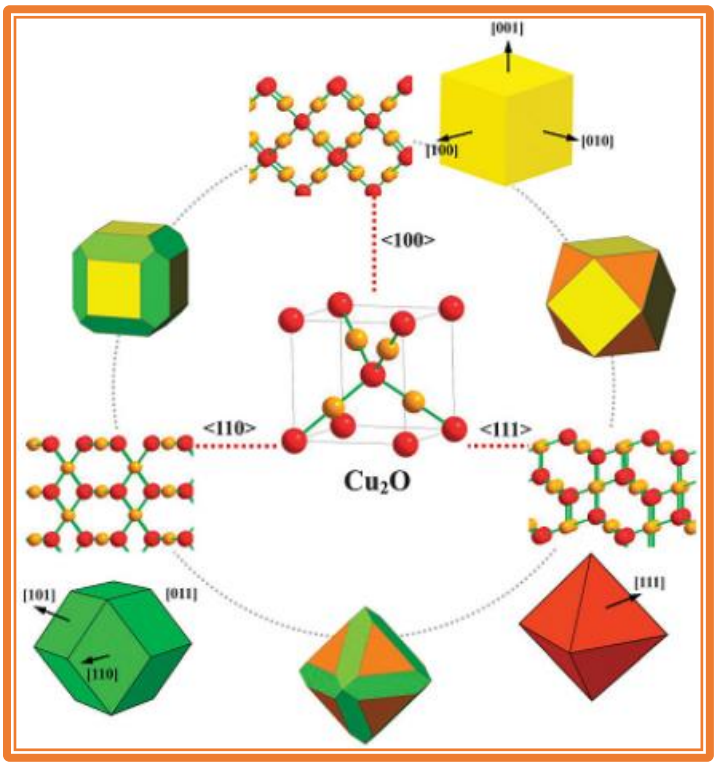

Fig. 4.2.1: Crystal structure and various polyhedral morphologies of Cu_2O with low index facets [75].

In addition to Cu_2O polyhedra with low index facets, Cu_2O polyhedra with high index facets have also been reported. SEM images of various polyhedral microcrystals of Cu_2O composed of low and high index facets are shown in Figure 4.2.2.

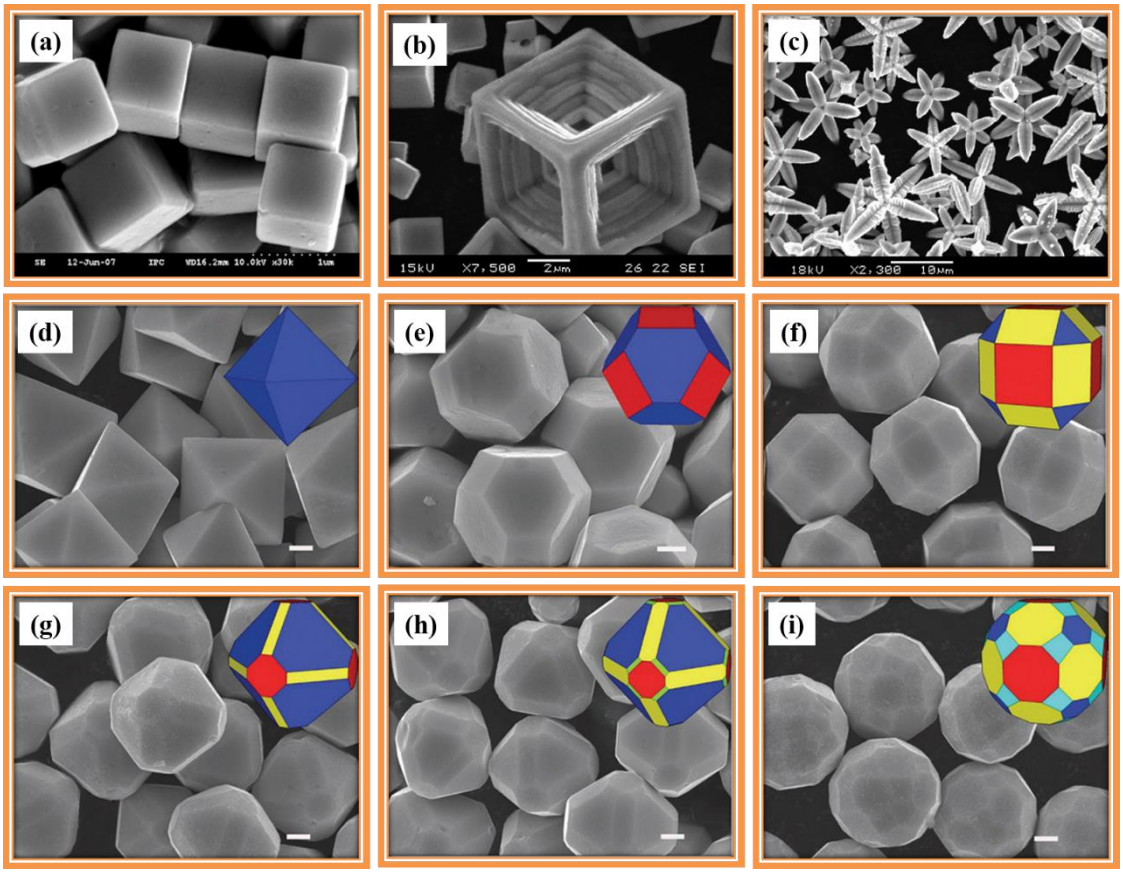

Fig. 4.2.2: SEM images of various polyhedral Cu_2O microcrystals with low and high index facets; **(a)** cube, **(b)** hopper cube, **(c)** 6-pod branched structure, **(d)** octahedra, **(e)** cuboctahedra, **(f)** rhombicuboctahedra, **(g)** 26-facet octahedra, **(h)** 50-facet polyhedra with high index {211} facets, and **(i)** 50-facet polyhedra with high index {522} facets [76,79,80].

Cu_2O has been used in various applications such as photocatalysis [81], water splitting [82], solar energy conversion [83], sensors [84], antibacterial agents [85], carbon monoxide (CO) oxidation [86], lithium-ion batteries [87], switching memories [88], bio-medicine [89], chemiluminescence [90], and chemical templates [91]. To improve its performance in various applications, Cu_2O has been coupled with different metals and semiconductors to produce heterostructures. These heterostructures show improved physicochemical properties as well as enhanced performance in multifunctional

applications [70,92] A schematic representation of Cu_2O based core-shell heterostructures along with their applications is shown in Figure 4.1.3.

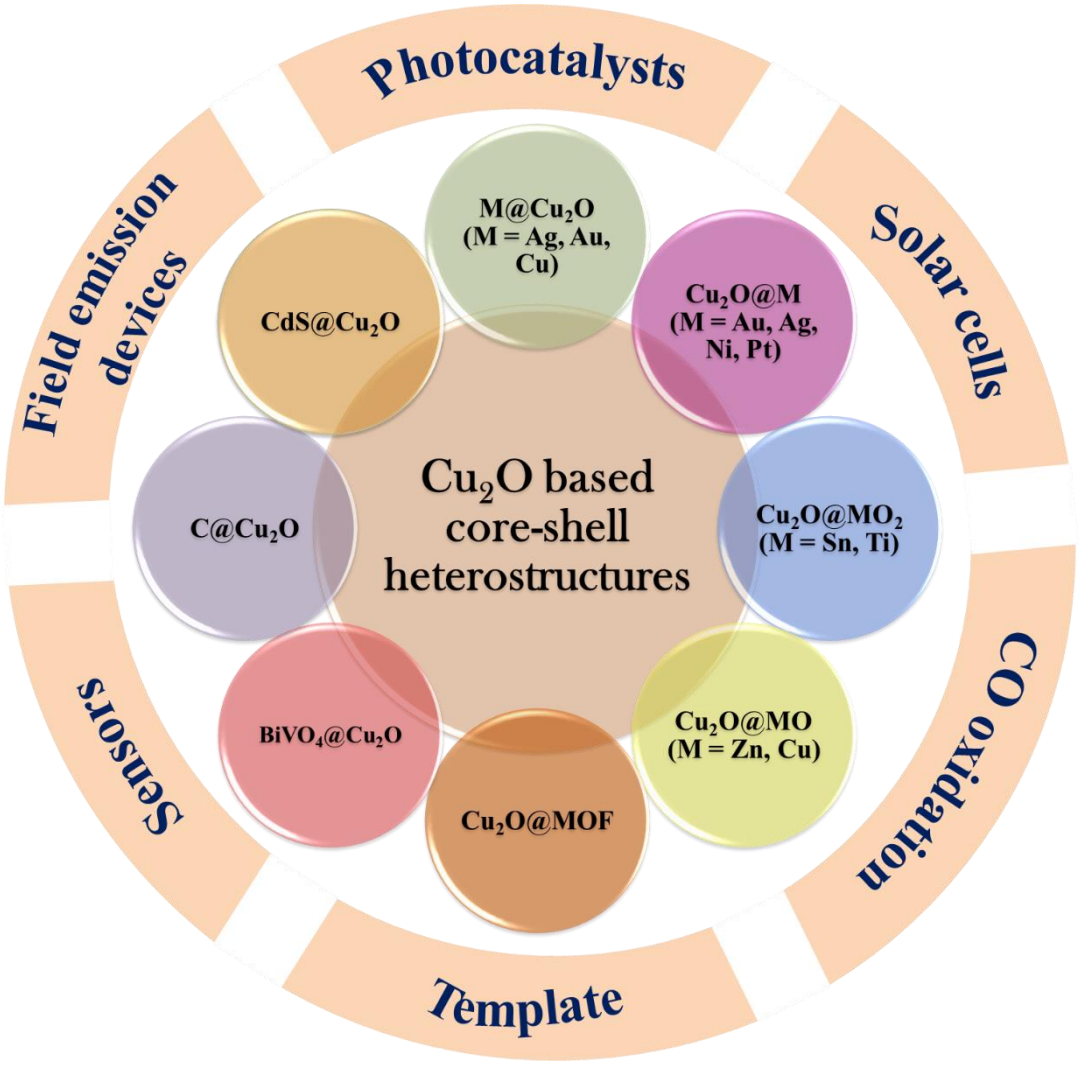

Fig. 4.2.3: Schematic representation of Cu_2O based core-shell heterostructures and their applications [70,71].

Among the Cu_2O based core-shell heterostructures, Cu_2O@Ag polyhedral core-shell nanoparticles are of significant interest due to their improved optoelectronic properties as well as their applications in various fields such as catalysis, surface enhanced Raman scattering and bactericides [93–101]. Coating metal or semiconductor nanoparticles on Cu_2O with different shapes helps in tuning their optical properties and catalytic activity. The catalytic activity of different shaped Cu_2O heterostructures is dissimilar and it is dependent on band alignment, facet surface energy and reactivity of exposed facets at the interface [102]. The synthesis of Cu_2O@Ag core-shell nanoparticles has been reported using various methods such as photocatalytic method [93], one-pot room

temperature method [94], successive one-pot route [95], electron beam irradiation [96], *in situ* solution route [97], wet-chemical reduction [98], galvanic displacement [99], hydrothermal method [100], and photodeposition [101]. A brief description of reported synthetic methods for the synthesis of Cu_2O@Ag polyhedral heteronanostructures is given below.

Photocatalytic method [93]: First, Cu_2O octahedral nanocrystals are synthesized *via* reduction route. Then, the Cu_2O octahedral nanocrystals are dispersed in 50 mL of distilled water and sonicated for a few minutes at 30 ^oC. This suspension is irradiated with 500 W iodine tungsten lamp and then certain amount of $AgNO_3$ solution is added. The contents are irradiated for another 20 min to deposit Ag shell on the Cu_2O octahedral nanocrystals.

One-pot room temperature method [94]: In this method, certain amount of copper acetate is dissolved in distilled water and then required amount of $N_2H_4.H_2O$ solution is added and stirred for 30 min to get Cu_2O microspheres. After this, $AgNO_3$ solution is added drop wise to the Cu_2O mother solution and stirred for another 30 min to deposit Ag on the Cu_2O microspheres.

Successive one-pot route [95]: Copper sulfate is dissolved in distilled water and then a aqueous solution containing sodium citrate and sodium carbonate is added. After some time, polyvinylpyrrolidone is added to the above solution and then a few mL of glucose solution is added drop wise. The contents are heated to 80 ^oC and kept for 15 min and then exposed to air for 14 days at room temperature. After 14 days, certain amount of $AgNO_3$ is added to the above solution and stirred for 20 min to deposit Ag on the Cu_2O cuboctahedron microcrystals. A schematic illustration of Cu_2O@Ag polyhedral core-shell microcrystals using the one-pot solution route is shown in Figure 4.2.4.

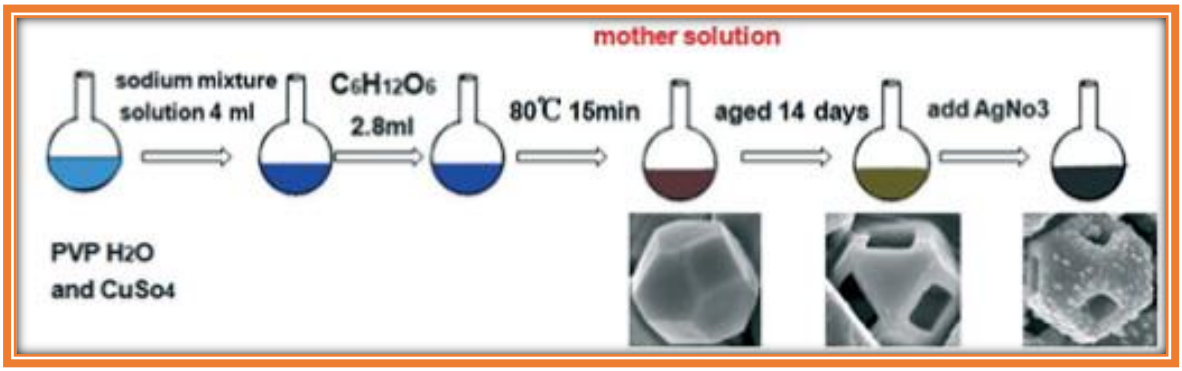

Fig. 4.2.4: Schematic illustration of synthesis of Cu_2O@Ag polyhedral core-shell microcrystals using a one-pot solution route [95].

Electron beam irradiation [96]: In this method, certain amount of $AgNO_3$ is dissolved in a mixture of water, polyvinyl alcohol, and isopropanol. To this mixture, required amount of $CuSO_4.5H_2O$ is added and pH of the solution is maintained at 8 using ammonium hydroxide solution. Then, the reaction contents are transferred into a plastic bag and irradiated using an accelerator at the absorbed dose of 280 kGy.

Wet-chemical reduction [98]: Initially, Cu_2O nanocubes are synthesized *via* solution route. Certain amounts of $CuCl_2$ and NaOH are dissolved in distilled water under magnetic stirring. Then, ascorbic acid is added and the contents are stirred at room temperature for 15 min. The obtained Cu_2O nanocubes are redispersed in an aqueous solution and then $AgNO_3$ and HNO_3 are added to it. The contents are then stirred at room temperature for 2 h.

Galvanic displacement [99]: Branched Cu_2O crystals are deposited on ITO substrate *via* electrodeposition. The obtained branched Cu_2O crystals are immersed in a solution of $AgNO_3$ and 5-sulfosalicylic acid for a certain period of time to deposit Ag nanoparticles on the Cu_2O microcrystals. A schematic illustration of deposition of Ag nanoparticles on branched Cu_2O microcrystals *via* galvanic displacement is shown in Figure 4.2.5.

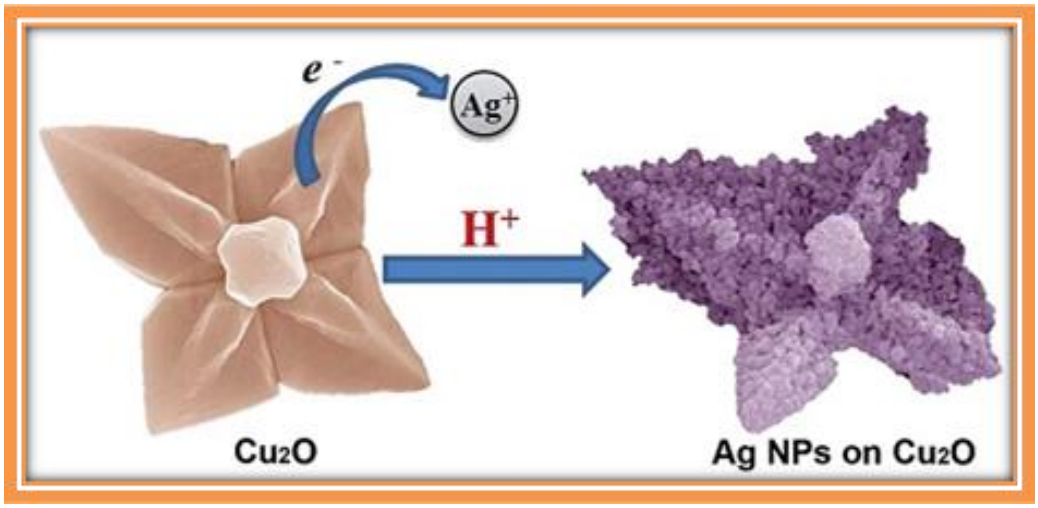

Fig. 4.2.5: Schematic illustration of deposition of Ag nanoparticles on branched Cu_2O microcrystals *via* galvanic displacement [99].

Hydrothermal method [100]: Before the deposition of Ag nanoparticles, Cu foil is cleaned with HCl and then washed with ethanol and water mixture. After that, $AgNO_3$ solution is prepared by dissolving in water and transferred to a Teflon lined stainless steel autoclave. Then, the cleaned Cu foil is dipped into the autoclave and the contents are heated in the oven at 120 ^oC for 12 h.

The TEM and HRTEM images of Cu_2O@Ag core-shell heteronanostructures, synthesized using one-pot room temperature method and successive one-pot route, are shown in Figure 4.2.5.

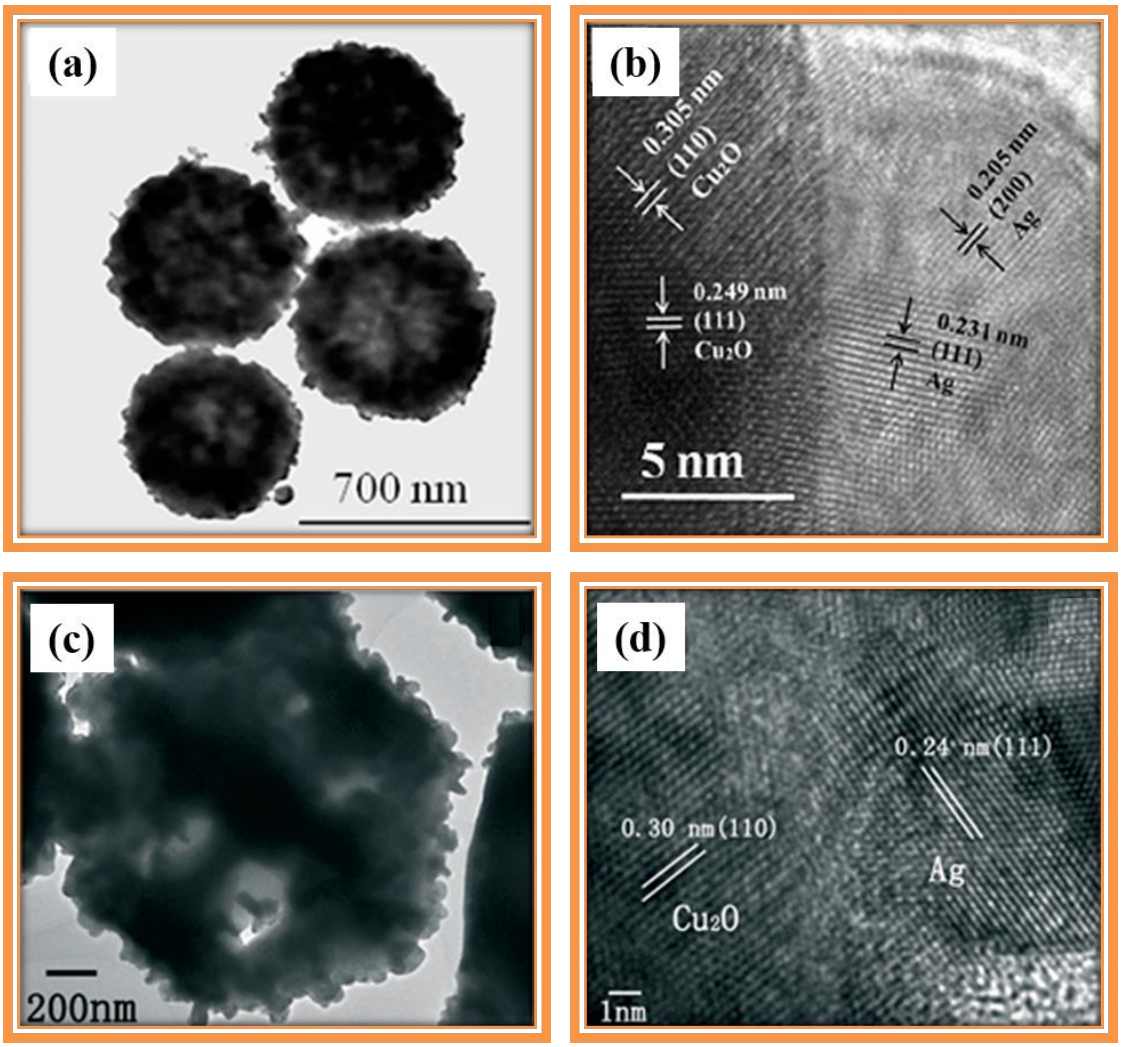

Fig. 4.2.6: TEM and HRTEM images of Cu_2O@Ag core-shell nanoparticles synthesized *via* **(a, b)** one-pot room temperature method [94] and **(c, d)** successive one-pot route [95].

In the present study, Ag nanoparticles have been successfully deposited on Cu_2O with rhombicuboctahedron, cuboctahedron, truncated octahedron and octahedron morphologies *via* a novel, facile, and economical thermal decomposition approach.

4.2.2 Experimental details

Copper (II) chloride dihydrate (99 %, Merck), diethylene glycol (98.5 %, SD Fine Chemicals Limited), poly(vinylpyrrolidone) (PVP, M_w = 10000, Sigma-Aldrich), sodium hydroxide (98 %, SD Fine Chemicals Limited), L-ascorbic acid (99.7 %, Rankem), silver acetate (98 %

Loba Chemie), diphenyl ether (99 %, Sigma-Aldrich) and ethanol were used as received. Methanol was received from SD Fine Chemicals Limited and was distilled before further use. The procedure for the synthesis of Cu_2O@Ag polyhedral core-shell nanoparticles with different shapes is as follows.

4.2.2.1 Synthesis of Cu_2O polyhedral microcrystals

Cu_2O polyhedral microcrystals were synthesized according to a reported method with some modifications [79]. A schematic representation of synthesis of Cu_2O polyhedral microcrystals is shown in Scheme 4.2.1. A summary on the synthetic conditions employed and the obtained morphologies for Cu_2O are given in Table 4.2.1. For the synthesis of rhombicuboctahedron Cu_2O, copper chloride (0.85 g, 0.05 M) was dissolved in 100 mL of water in a beaker and for the synthesis of Cu_2O cuboctahedron, the same amount of copper chloride was dissolved in a mixture of 73 mL water and 27 mL diethylene glycol. For the synthesis of truncated octahedron and octahedron shaped Cu_2O microcrystals, copper chloride (0.05 M) was dissolved in the mixture of 73 mL water and 27 mL diethylene glycol along with polyvinylpyrrolidone (1.11 g (10 mM) or 2.22 g (20 mM)). In all the cases, once the reaction temperature reached 55 ^oC, under constant stirring, 50 mL of 2 M sodium hydroxide solution was added drop wise in about 30 min, followed by the addition of 50 mL of 0.6 M ascorbic acid solution in water drop wise in about 30 min. Finally, the contents were aged for 3 h at 55 ^oC and the obtained products were centrifuged, washed with ethanol several times and dried under vacuum. The obtained Cu_2O powder samples with rhombicuboctahedron, cuboctahedron, truncated octahedron, and octahedron morphologies were designated as C1, C2, C3 and C4, respectively.

Table 4.2.1: Summary of synthetic conditions employed and morphologies obtained for Cu_2O microcrystals.

Sample code	$CuCl_2.2H_2O$ (g)	Amount of reagents	Morphology of Cu_2O
		H_2O (mL): DEG (mL): PVP (mM)	
C1	0.85	100: 0: 0	Rhombicuboctahedron
C2	0.85	73: 27: 0	Cuboctahedron
C3	0.85	73: 27: 10	Truncated octahedron
C4	0.85	73: 27: 20	Octahedron

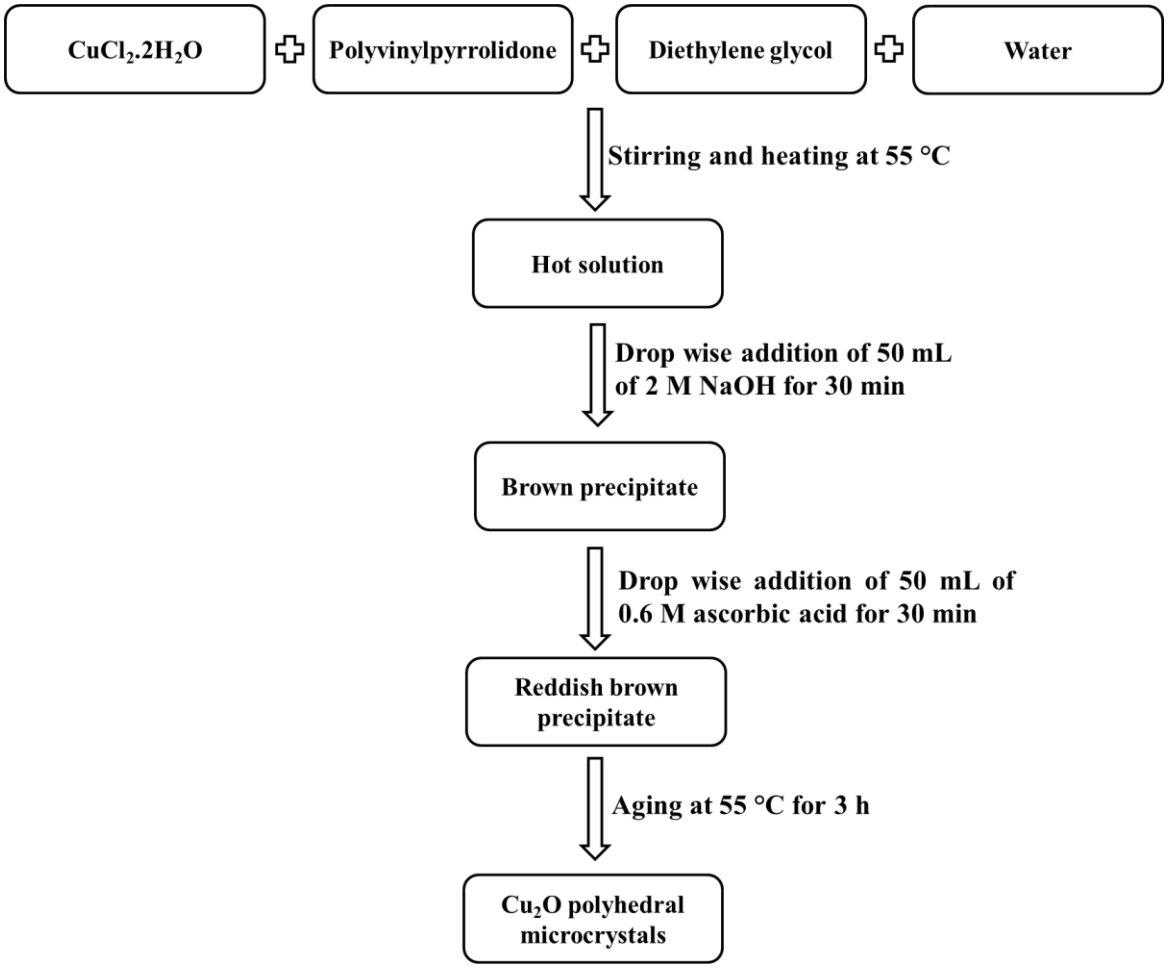

Scheme 4.2.1: Schematic representation of synthesis of Cu_2O polyhedral microcrystals.

4.2.2.2 Synthesis of Cu_2O@Ag polyhedral core-shell nanoparticles

The schematic representation of synthesis of Cu_2O@Ag polyhedral core-shell nanoparticles is shown in Scheme 4.2.2. About 50 mg of each Cu_2O powder samples (C1, C2, C3, and C4) with various morphologies was mixed with silver acetate (0.075 mmol) in 10 mL of diphenyl ether in a round bottom flask and sonicated for about 3 min to get a uniform dispersion. Then, the contents were first refluxed at 220 ^oC for 30 min, followed by heating at 150 ^oC for 30 min. After completion of the reaction, the contents were allowed to cool to room temperature and then about 25 mL of methanol was added to get a precipitate. Finally, the precipitate was centrifuged, washed with methanol several times and dried under vacuum. The obtained Cu_2O@Ag powder samples were labelled as C1A, C2A, C3A and C4A corresponding to rhombicuboctahedron, cuboctahedron, truncated octahedron, and octahedron morphologies of Cu_2O microcrystals, respectively. Pure silver nanoparticles were also synthesized using the same procedure as discussed above but in the absence of Cu_2O microcrystals. Ag

nanoparticles stabilized by polyvinylpyrrolidone (PVP) were also synthesized by a polyol process [103]. In a typical synthesis, 0.075 mM silver nitrate was dispersed in 20 mL of ethylene glycol along with 75 mg of polyvinylpyrrolidone (PVP 10 K) and refluxed at 160 ^{o}C for 1 h to get polyvinylpyrrolidone stabilized Ag nanoparticles.

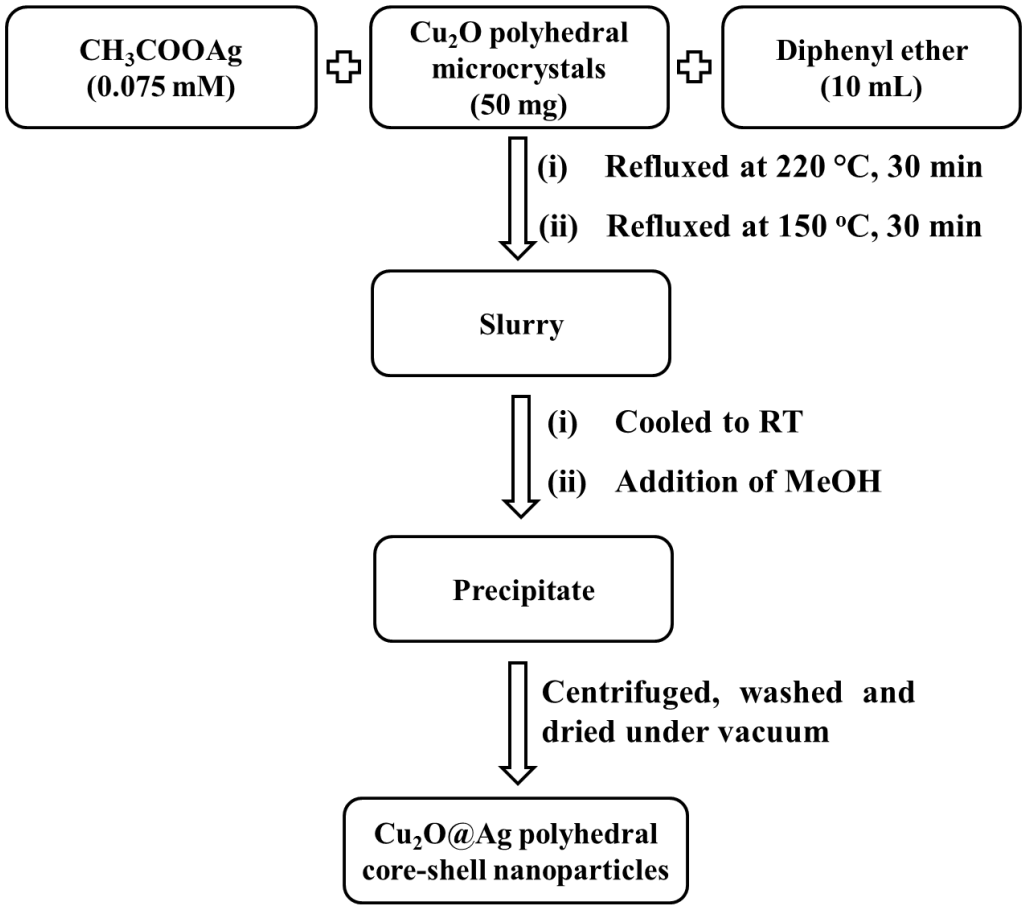

Scheme 4.2.2: Schematic representation of synthesis of Cu_2O@Ag polyhedral core-shell nanoparticles.

The synthesized Cu_2O@Ag polyhedral core-shell nanoparticles were characterized using PXRD, FT-IR, TGA, FE-SEM, SEM-EDX, TEM and BET analysis. The optical properties were studied using DRS spectroscopy. More details on the experimental techniques have been discussed in Chapter-2.

4.2.3 Results and discussion

4.2.3.1 XRD analysis

The XRD patterns of pure Cu_2O samples are shown in Figure 4.2.7. Pure Cu_2O samples (C1 to C4) show reflections at 2θ values 29.65^{o}, 36.52^{o}, 42.42^{o}, 61.54^{o}, 73.72^{o}, and

77.61° corresponding to (110), (111), (200), (220), (311), and (222) planes of cubic Cu_2O (JCPDS no. 77-0199), respectively. The ratio of intensity of (111) to (200) planes ($I_{(111)}/I_{(200)}$) increases gradually with the shape evolution of Cu_2O from rhombicuboctahedron through cuboctahedron, truncated octahedron and finally to octahedron. The shape evolution of Cu_2O is attributed to progressive shrinkage of {100} facet and enlargement of {111} facet [79].

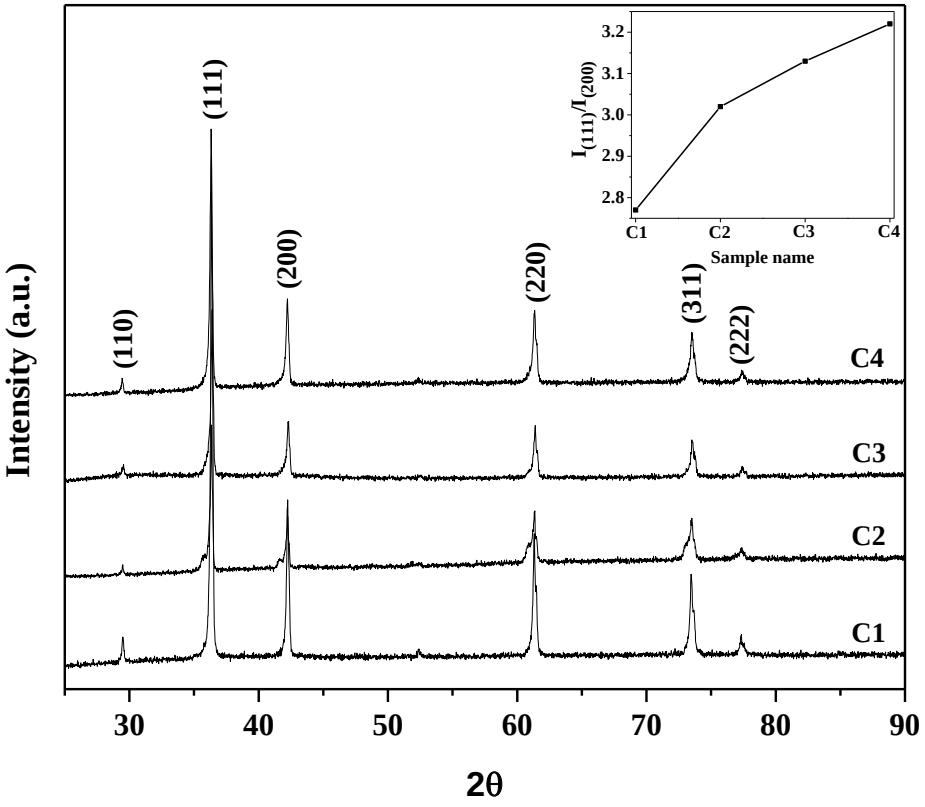

Fig. 4.2.7: XRD patterns of Cu_2O polyhedral microcrystals (C1, C2, C3, and C4). Inset shows the $I_{(111)}/I_{(200)}$ ratio for different Cu_2O microcrystals.

The XRD patterns of Cu_2O@Ag samples are shown in Figure 4.2.8. The XRD patterns of Cu_2O@Ag samples (C1A to C4A) show two sets of peaks. The XRD peaks marked with "*" are the reflections due to cubic Cu_2O and the diffraction peaks marked with "#" at the 2θ values 38.12°, 44.27°, and 64.43° correspond to (111), (200), and (220) planes of cubic silver (JCPDS no. 04-0783), respectively. In the Cu_2O@Ag samples, the diffraction peaks due to silver are broader as compared to that of Cu_2O indicating the presence of nanosized silver particles. The crystallite size of silver in the Cu_2O@Ag samples was calculated using Debye-Scherrer formula using the (111) reflection and it was found to be 23, 30, 27, and 21 nm for the samples C1A, C2A, C3A and C4A, respectively.

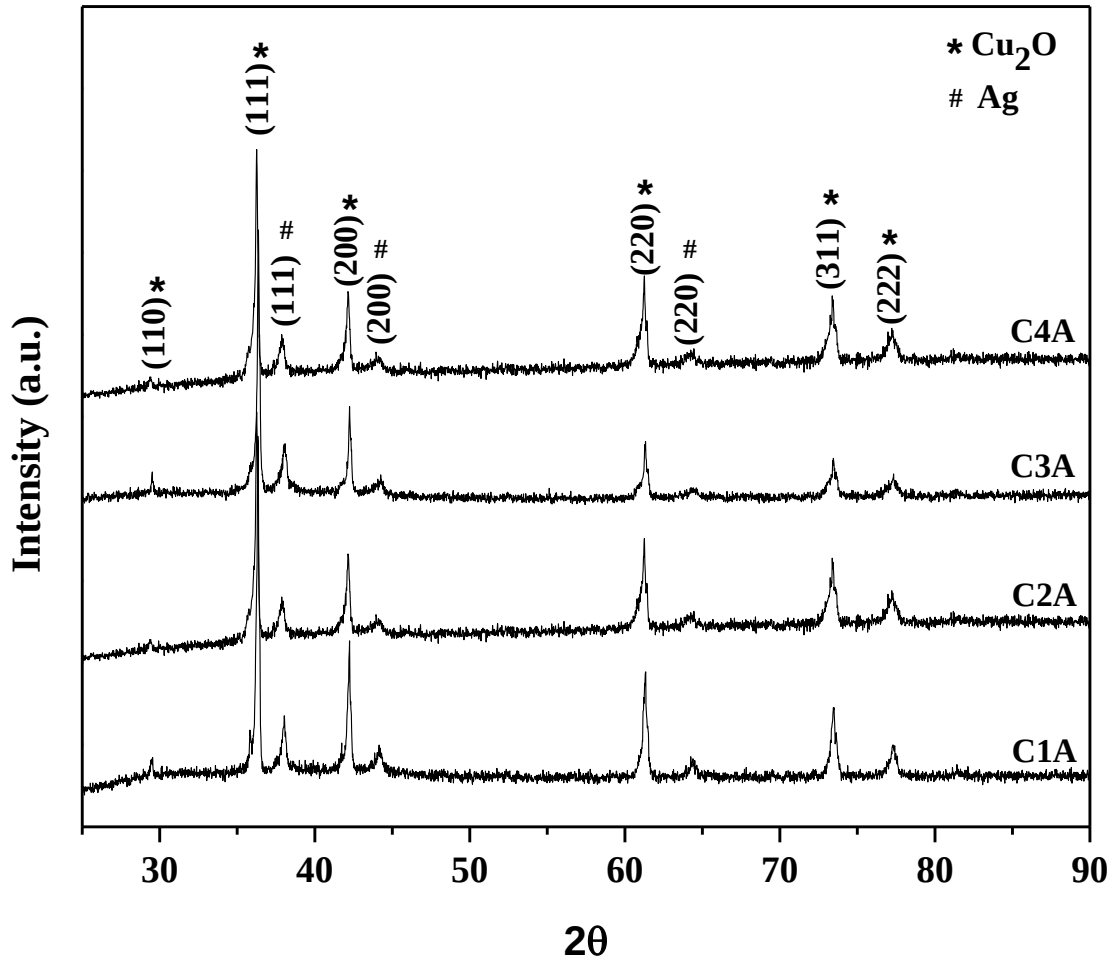

Fig. 4.2.8: XRD patterns of Cu_2O@Ag polyhedral core-shell nanoparticles (C1A, C2A, C3A and C4A).

4.2.3.2 FT-IR spectral studies

The FT-IR spectra of pure Cu_2O samples (C1 to C4) are shown in Figure 4.2.9. All the samples show IR bands at about 3440 and 1620 cm^{-1} attributed to stretching and bending modes of physisorbed water molecules [57]. The bands at 1386, 1268, and 1130 cm^{-1} are attributed to symmetric deformation of C-H, symmetric stretching vibration of C-O-C, and symmetric stretching vibration of C-OH due to surface adsorbed ascorbic acid, respectively [57,77]. All the samples show a prominent IR band at about 625 cm^{-1} attributed to Cu(I)-O stretching [77].

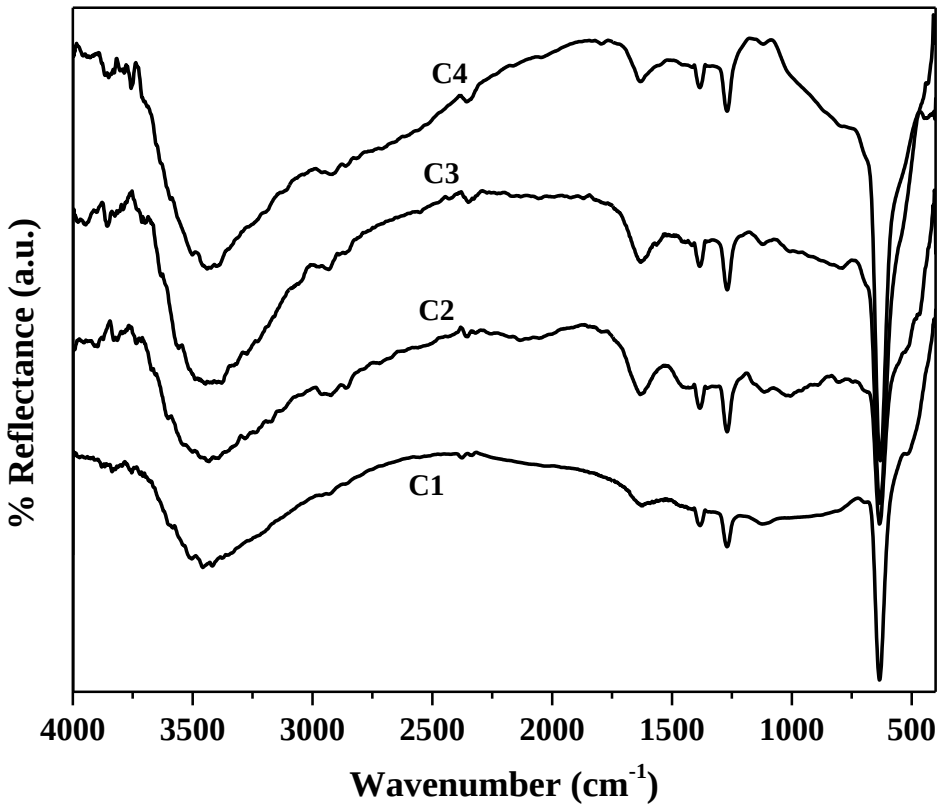

Fig. 4.2.9: FT-IR spectra of polyhedral Cu_2O microcrystals (C1, C2, C3, and C4).

4.2.3.3 TGA analysis

The TGA patterns of pure Cu_2O samples (C1 to C4) are shown in Figure 4.2.10. The TGA patterns of all the Cu_2O samples (C1 to C4) show a minor weight loss (<1.5 %) from 30 ^oC to 200 ^oC attributed to the loss of moisture. The samples show 9.4, 9.2, 9.1, and 8.7 % increase in weight in the temperature range 290-530 ^oC attributed to the oxidation of Cu_2O to CuO [104]. A close look at the TGA results indicate different oxidation onset temperatures for Cu_2O with different shapes. The oxidation starts at 290 ^oC for rhombicuboctahedron (C1), 300 ^oC for cuboctahedron (C2), 320 ^oC for truncated octahedron (C3), and at 345 ^oC for octahedron (C4). The oxidation is completed at about 460, 460, 490 and 530 ^oC for the samples C1, C2, C3, and C4, respectively. The order of oxidation temperature in pure Cu_2O samples follows the order of facet stability; {111} > {110} > {100} [71]. Sample C4 with octahedron morphology possesses higher number of {111} facets compared to the other morphologies which leads to higher stability compared to the other Cu_2O samples. The higher oxidation temperature of Cu_2O@Ag sample C4 indicates that octahedron is more stable than the other morphologies of Cu_2O.

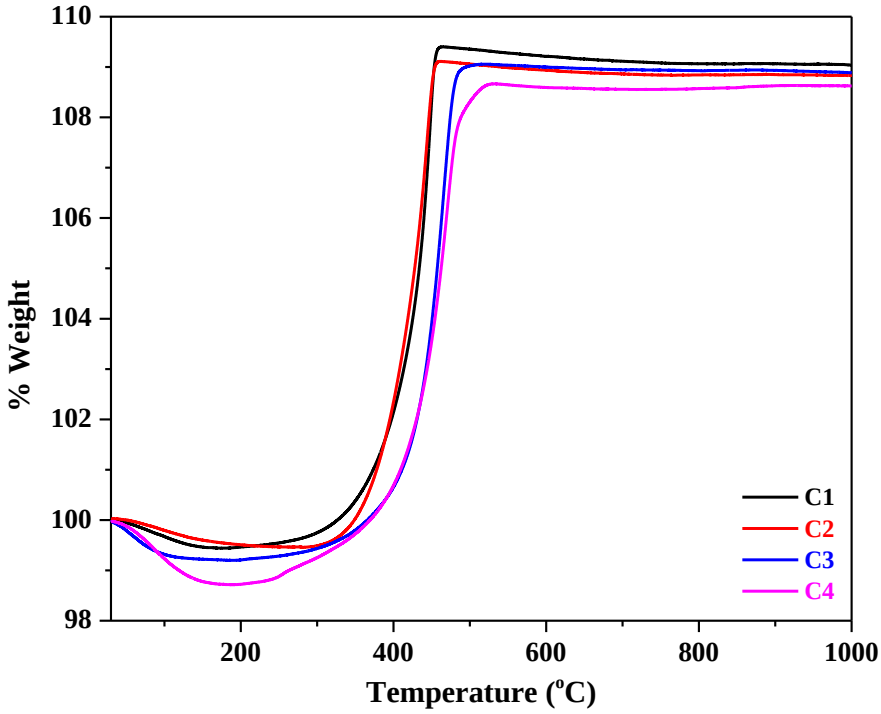

Fig. 4.2.10: TGA patterns of polyhedral Cu_2O microcrystals (C1, C2, C3, and C4).

4.2.3.4 FE-SEM studies

The Cu_2O samples with various morphologies were studied using field emission scanning electron microscopy and the SEM images are shown in Figure 4.2.11. It is known that varying the concentration of surfactants/organic additives, during the synthesis, produce particles with variable sizes and shapes [79]. In the present study, diethylene glycol and polyvinylpyrrolidone (PVP) play an important role *via* face selective adsorption in determining final shapes of the Cu_2O microcrystals. In the absence of diethylene glycol and PVP, Cu_2O rhombicuboctahedrons are produced (Fig. 4.2.11 (C1)). The rhombicuboctahedrons consist of three pairs of {100} facets, four pairs of {111} facets and six pairs of {110} facets. The mean diameter of the rhombicuboctahedron is 1.8 μm and the mean edge length is 0.73 μm. The addition of diethylene glycol during the synthesis of Cu_2O leads to vanishing of {110} facets resulting in the formation of cuboctahedron (Fig. 4.2.11 (C2)) with four pairs of {111} facets and three pairs of {100} facets. The mean diameter of cuboctahedron is 1.4 μm and the mean edge length is 0.56 μm. PVP is known to preferentially adsorb on the {111} planes of the Cu_2O crystals and the amount of PVP, added during the synthesis, controls the evolution of different morphologies [79]. The use of 10 mM PVP along with diethylene glycol (27 mL) results in

lowering the surface energy of {111} plane. This leads to shrinkage of {100} and enlargement of {111} planes producing truncated octahedron (Fig. 4.2.11 (C3)) exposing four pairs of {111} facets and three pairs of {100} facets [79]. The mean diameter is 1.2 μm and the mean edge length is 0.17 μm. Increased amount of PVP (20 mM) along with diethylene glycol (27 mL) results in further lowering of surface energy of the {111} plane with the evolution of octahedron (Fig. 4.2.11 (C4)) exposing four pairs of {111} facets. The mean diameter of the octahedron is 1 μm. From the SEM results, it is observed that the edge length of Cu_2O microcrystals decreases on going from rhombicuboctahedron to truncated octahedron.

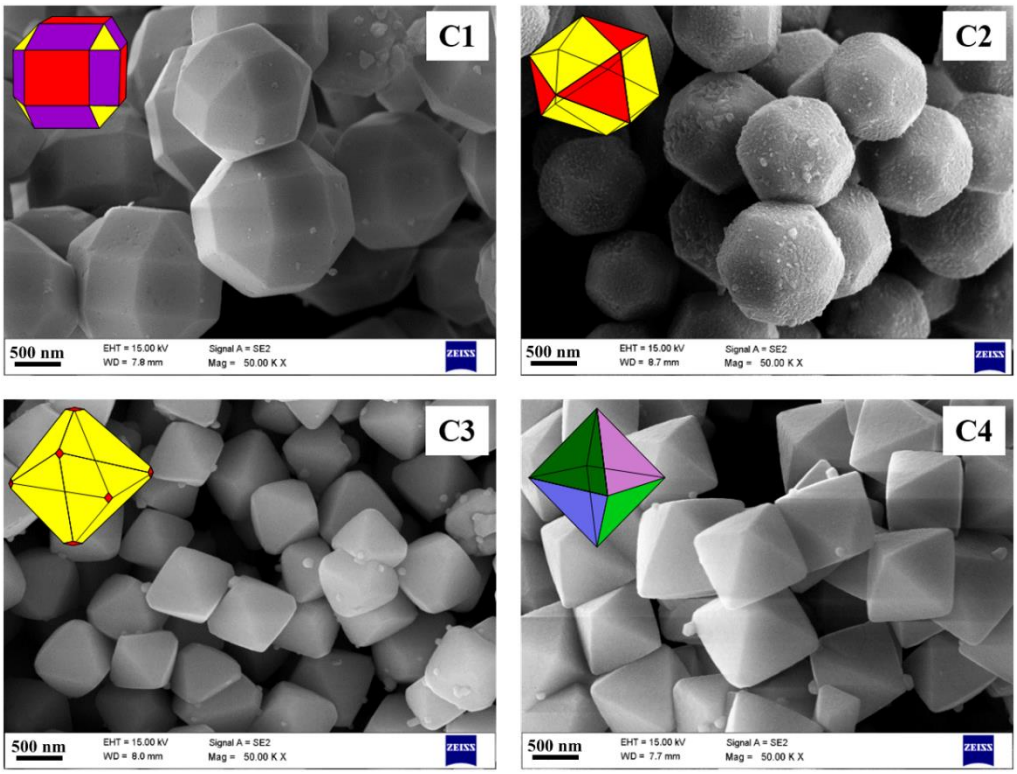

Fig.4.2.11: FE-SEM images of Cu_2O microcrystals with different shapes (C1, C2, C3, and C4).

The SEM images of silver deposited Cu_2O polyhedral microcrystals (C1A, C2A, C3A and C4A) are shown in Figure 4.2.12. The SEM images show the deposition of silver nanoparticles on the surface of Cu_2O polyhedral microcrystals. The Cu_2O@Ag polyhedral core-shell nanoparticles possess the same shapes as that of the Cu_2O microcrystals. The mean diameter of the Cu_2O@Ag samples is 1.9, 1.6, 1.4, and 1.1 μm for the samples C1A, C2A, C3A, and C4A, respectively. The diameter of Cu_2O@ Ag samples is higher than that of the Cu_2O microcrystals due to the deposition of silver nanoparticles on the surface of Cu_2O microcrystals. It was unable to estimate the edge length due to thick deposition of silver

nanoparticles on the surface of Cu_2O polyhedral microcrystals. In the Cu_2O@Ag polyhedral core-shell nanoparticles (C1A, C2A, C3A, and C4A), the mean particle size of silver nanoparticles is 54.2 ± 6.7, 70.8 ± 6.3, 65.2 ± 3.8, and 50.9 ± 2.6 nm, respectively.

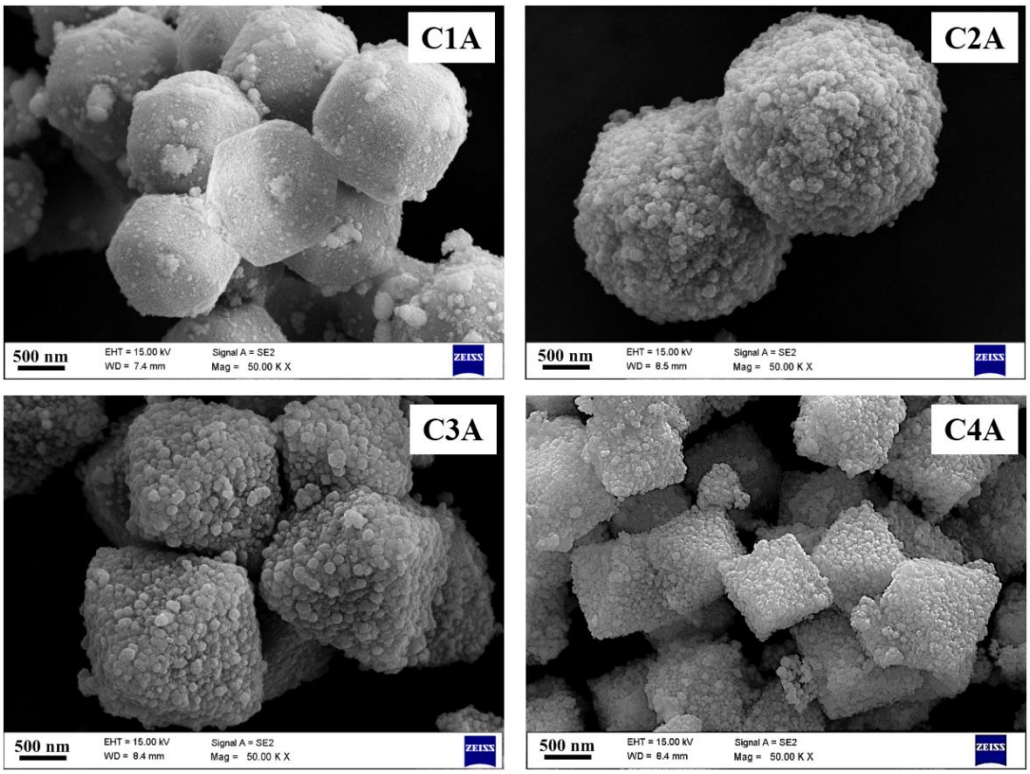

Fig. 4.2.12: FE-SEM images of Cu_2O@Ag polyhedral core-shell nanoparticles (C1A, C2A, C3A, and C4A).

4.2.3.5 SEM-EDX analysis

In the case of pure Cu_2O polyhedral microcrystals, the atomic ratio of copper to oxygen was estimated and it was found to be 2:1 as expected. The SEM-EDX analysis results for pure Cu_2O polyhedral microcrystals are shown in Figure 4.2.13.

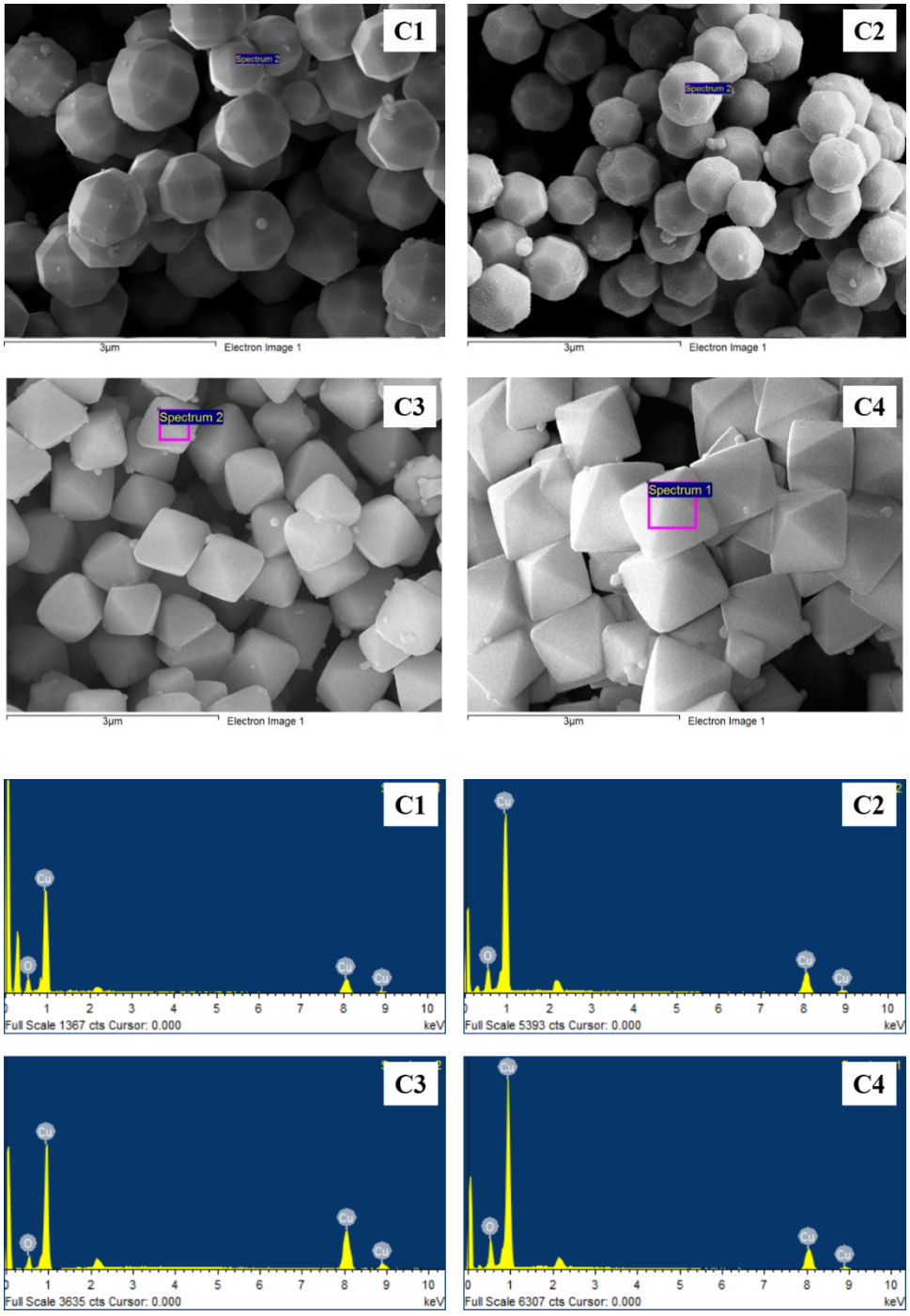

Fig. 4.2.13: SEM-EDX of Cu_2O polyhedral microcrystals (C1, C2, C3 and C4).

The EDX spectra of Cu_2O@Ag polyhedral core-shell nanoparticles are shown in Figure 4.2.14. The EDX spectra confirm the presence of copper, oxygen, and silver in all the Cu_2O@Ag core-shell nanoparticles. The weight percent of silver (by analyzing at different spots on the surface of Cu_2O@Ag samples) was 10.1 ± 0.9, 12.9 ± 1.4, 9.8 ± 0.8, and 5.1 ± 0.3, for the samples C1A, C2A, C3A, and C4A, respectively.

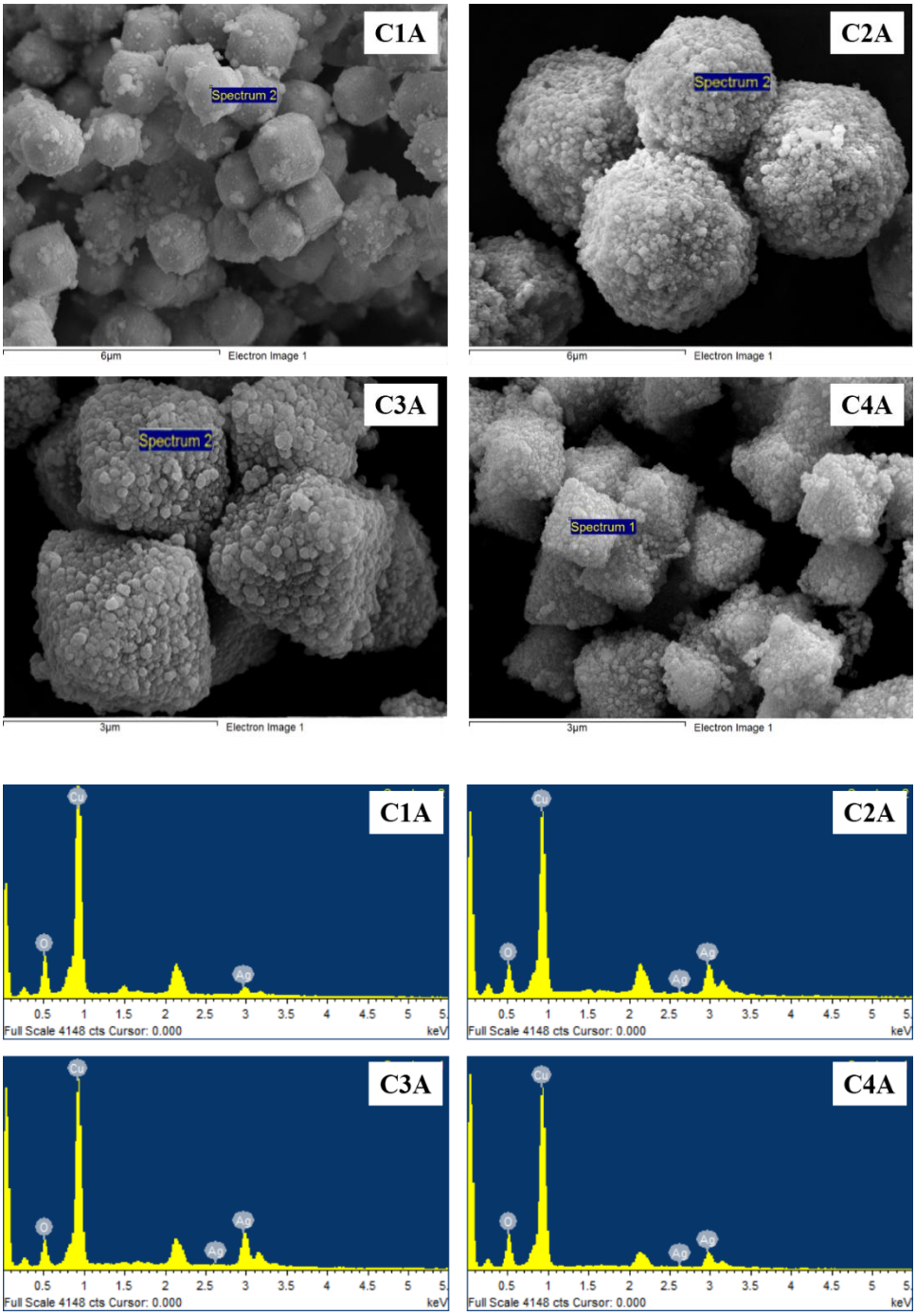

Fig. 4.2.14: SEM-EDX of Cu_2O@Ag polyhedral core-shell nanoparticles (C1A, C2A, C3A and C4A).

The nucleation and growth rates of silver nanoparticles on different facets of Cu_2O decide the particle size as well as the weight percent of silver [68]. Zhang et al. have theoretically predicted that Cu_2O with {111} facet is thermodynamically more favorable, as compared to the other facets, for exchange of surface atoms with silver atoms [79] and the order is {111} > {110} > {100}. Silver embryo is easily formed on

the {111} facet during nucleation as compared to the other facets. During the growth stage, the small silver embryos grow and form silver shell on the Cu_2O with smaller silver particle size. Thus, the Cu_2O@Ag sample with octahedron morphology (C4A) possesses smaller silver nanoparticles compared to other morphologies of Cu_2O@Ag samples. The weight percent of silver in the Cu_2O@Ag polyhedral core-shell nanoparticles follows the order C2A > C1A > C3A >C4A.

To understand the nature of deposition of silver nanoparticles on the Cu_2O polyhedral microcrystals better, the nucleation time (N_t), the growth time (G_t) and the concentration of silver acetate were varied during the synthesis of Cu_2O@Ag samples. The thermal decomposition reactions were carried out using the Cu_2O samples C1, C2, C3, and C4 with 0.075 mM silver acetate at 220 ^oC for 15 mins followed by growth of 15 mins at 150 ^oC and the corresponding SEM images of the products obtained are shown in Figure 4.2.15. Under these conditions, the SEM images show incomplete deposition of silver nanoparticles on the surface of Cu_2O microcrystals with broad particle size distribution (120-180 nm) along with some free silver nanoparticles.

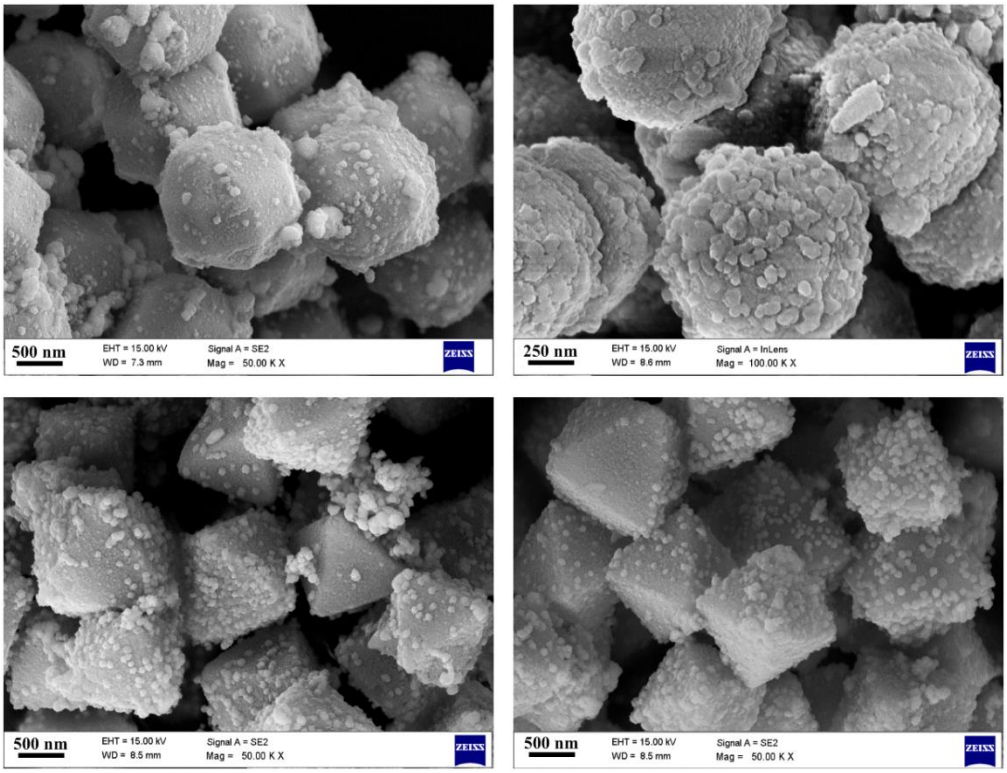

Fig. 4.2.15: FE-SEM images of Cu_2O@Ag polyhedral core-shell nanoparticles prepared at nucleation time (N_t) and growth time (G_t) of 15 mins, and [CH_3COOAg] = 0.075 mM.

Another synthesis was carried out by lowering the concentration of silver acetate from 0.075 mM to 0.05 mM while keeping the nucleation time (N_t) as 30 min at 220 ^oC and the growth time (G_t) as 30 min at 150 ^oC and the corresponding SEM images of the products are shown in Figure 4.2.16. On decreasing the concentration of silver acetate from 0.075 mM to 0.05 mM, the SEM images show deposition of silver nanoparticles on the edges, vertices and facets of Cu_2O. In both the cases (decreasing the nucleation time (N_t), and growth time (G_t) from 30 mins to 15 mins as well as lowering the concentration of silver acetate from 0.075 mM to 0.05 mM), complete coverage of silver nanoparticles on the Cu_2O microcrystals is not observed.

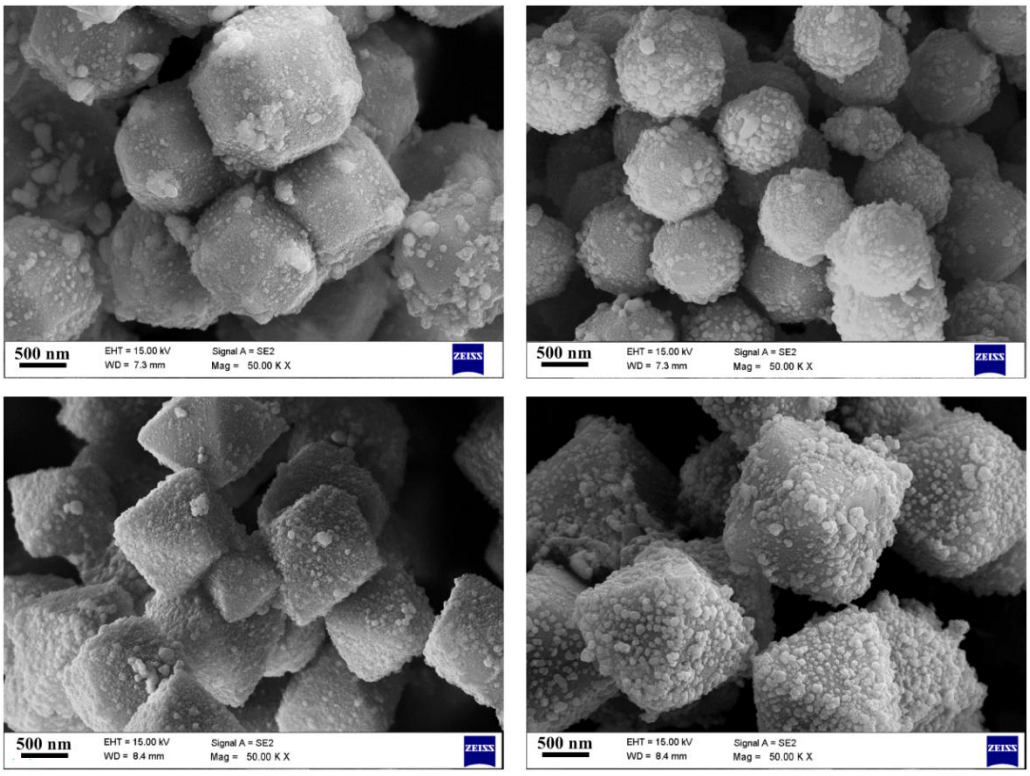

Fig. 4.2.16: FE-SEM images of Cu_2O@Ag polyhedral core-shell nanoparticle samples prepared using 0.05 mM silver acetate, and nucleation time (N_t) and growth time (G_t) of 30 min.

4.2.3.6 TEM studies

For understanding the deposition of silver nanoparticles on the Cu_2O microcrystals better, TEM analysis was carried out for the Cu_2O@Ag samples (C1A to C4A) and the corresponding TEM images are shown in Figure 4.2.17. All the Cu_2O@Ag samples clearly show thick deposition of silver nanoparticles on the surface of the Cu_2O

microcrystals. No free silver nanoparticles are observed in the TEM images. The particle diameter of the Cu_2O@Ag polyhedral core-shell nanoparticles is 2.1, 1.6, 1.4, and 1.2 μm for the samples C1A, C2A, C3A, and C4A, respectively. The mean particle size of silver nanoparticles is 53.5 ± 5.9, 67.3 ± 6.2, 63.4 ± 3.7, and 49.4 ± 4.1 nm for the samples C1A, C2A, C3A, and C4A, respectively. The observed size of silver nanoparticles on Cu_2O, from the TEM studies, is comparable with that observed from SEM studies.

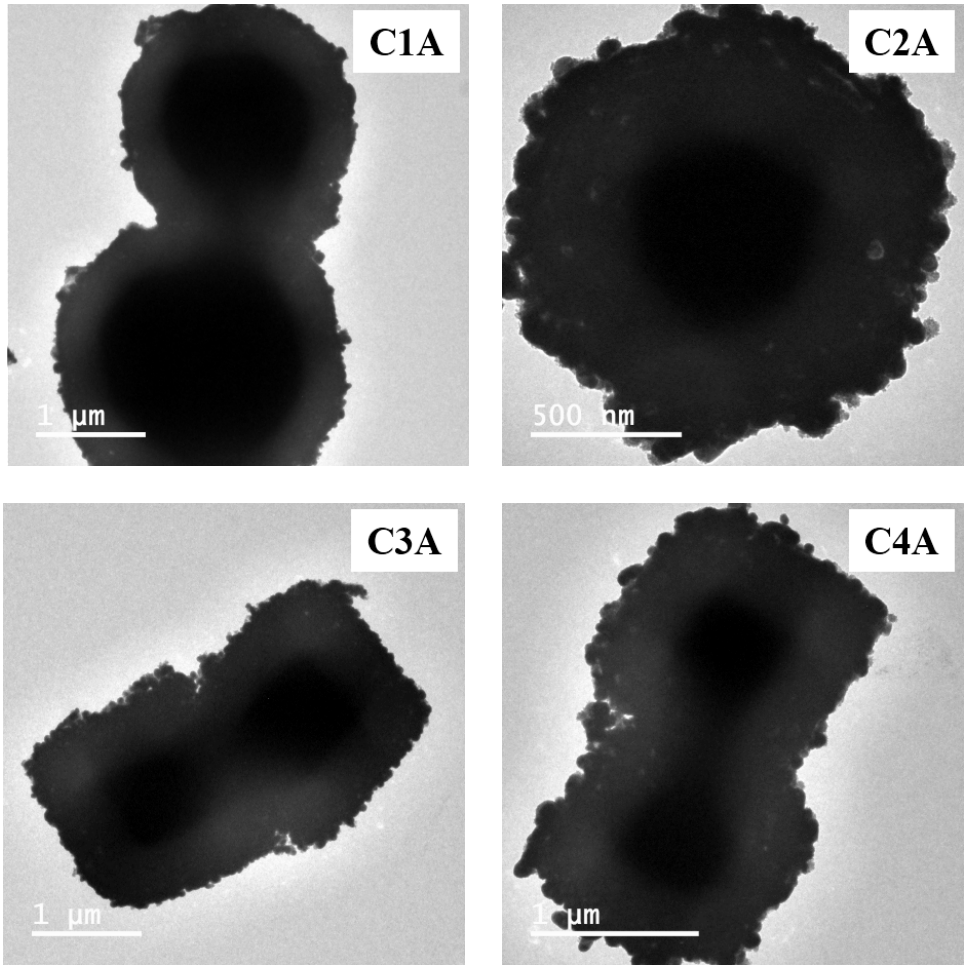

Fig. 4.2.17: TEM images of Cu_2O@Ag polyhedral core-shell nanoparticles (C1A, C2A, C3A, and C4A). The samples were prepared by refluxing conditions at 220 ^oC, 30 min followed by refluxing at 150 ^oC, 30 min and [CH_3COOAg] = 0.075 mM.

Selected area electron diffraction (SAED) patterns of the Cu_2O@Ag polyhedral core-shell nanoparticles are shown in Figure 4.2.18. The SAED patterns of Cu_2O@Ag samples show rings corresponding to (111), (200), (220), (222), and (420) planes of silver which indicate poly-crystalline nature of silver nanoparticles on the surface of

Cu_2O microcrystals. No diffraction due to Cu_2O was observed which proves the formation of thick silver shell on the surface of Cu_2O microcrystals.

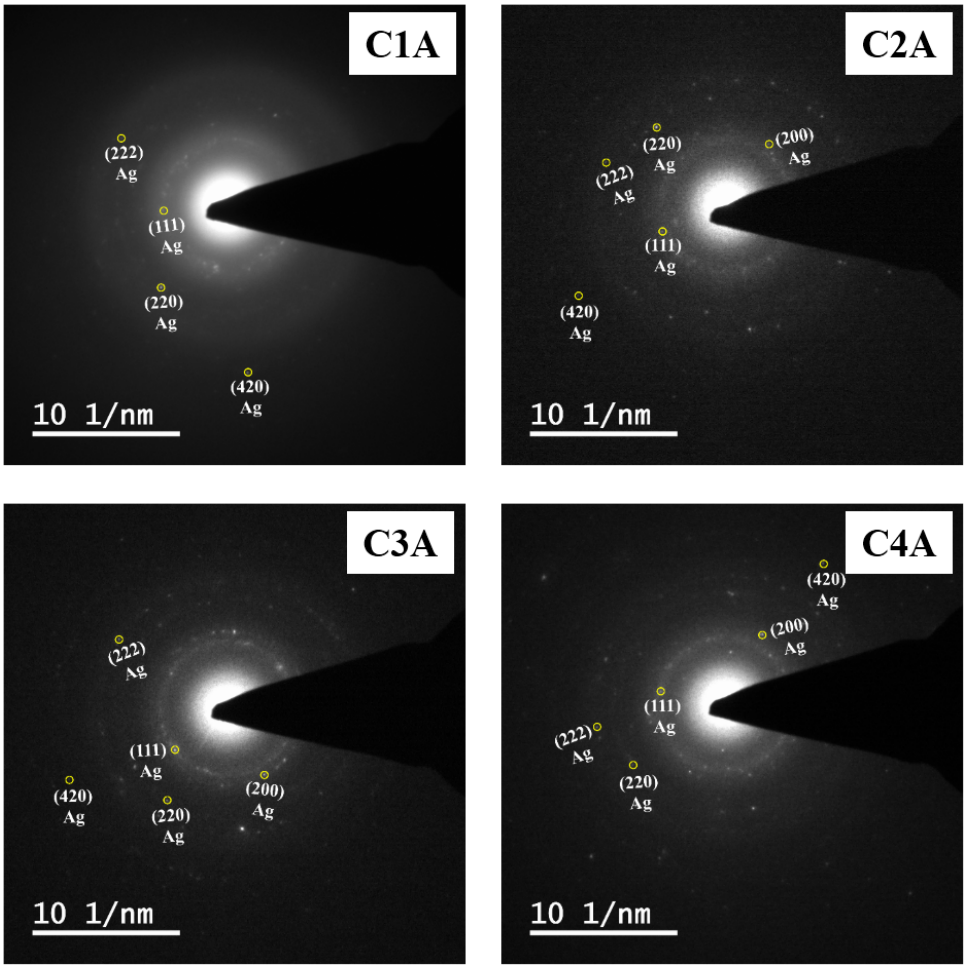

Fig. 4.2.18: SAED patterns of Cu_2O@Ag polyhedral core-shell nanoparticles (C1A, C2A, C3A, and C4A).

4.2.3.7 BET surface area analysis

The surface area of pure Cu_2O microcrystals and the Cu_2O@Ag polyhedral core-shell nanoparticles were measured using Brunauer-Emmett-Teller (BET) method. The values of crystallite size, particle size, and surface area of pure Cu_2O microcrystals and Cu_2O@Ag polyhedral core-shell nanoparticles are summarized in Table 4.2.2. Pure Cu_2O microcrystals C1, C2, C3, and C4 possess surface area of 14.3, 12.2, 15.1, and 16.2 m^2/g, respectively. The surface area of Cu_2O@Ag polyhedral core-shell nanoparticles is 15.9, 14.4, 19.0, and 22.2 m^2/g for the samples C1A, C2A, C3A, and C4A, respectively. The Cu_2O@Ag polyhedral core-shell nanoparticles possess marginally higher surface area compared to pure Cu_2O microcrystals.

Table 4.2.2: Crystallite size, particle size, and surface area of Cu_2O and Cu_2O@Ag polyhedral core-shell nanoparticles.

Sample code	Crystallite size of Ag from XRD (nm)	Diameter of Cu_2O and Cu_2O@Ag particles (μm)		Particle size of Ag (nm)		Wt.% of Ag (From EDX)	Surface area (m^2/g)
		SEM	TEM	SEM	TEM		
C1	-	1.8	-	-	-	-	14.3
C2	-	1.4	-	-	-	-	12.2
C3	-	1.2	-	-	-	-	15.1
C4	-	1.0	-	-	-	-	16.2
C1A	23	1.9	2.1	54.2 ± 6.7	53.5 ± 5.9	10.1 ± 0.9	15.9
C2A	30	1.6	1.6	70.8 ± 6.3	67.3 ± 6.2	12.9 ± 1.4	14.4
C3A	27	1.4	1.4	65.2 ± 3.8	63.4 ± 3.7	9.8 ± 0.8	19.0
C4A	21	1.1	1.2	50.9 ± 2.6	49.4 ± 4.1	5.1 ± 0.3	22.2

4.2.3.8 UV-Visible diffuse reflectance spectroscopy (DRS)

The optical properties of pure Cu_2O microcrystals with various morphologies (C1 to C4) and Cu_2O@Ag polyhedral core-shell nanoparticles (C1A to C4A) were studied using UV-Visible diffuse reflectance spectroscopy. The DRS spectra of bare Cu_2O and Cu_2O@Ag polyhedral core-shell nanoparticles are shown in Figure 4.2.19 and Figure 4.2.20, respectively. Pure Cu_2O samples show band gap absorption at 579, 576, 572, and 568 nm for the samples C1, C2, C3, and C4, respectively [102]. Pure silver nanoparticles show an absorption band at about 420 nm attributed to surface plasmon resonance [93]. The Cu_2O@Ag polyhedral core-shell nanoparticles (C1A to C4A) show two sets of absorption bands. The absorption bands at 580, 577, 574, and 571 nm are attributed to band gap absorption of Cu_2O and the absorption at about 415 nm is attributed to surface plasmon resonance (SPR) of the silver nanoparticles present on the surface of Cu_2O microcrystals [93]. The Cu_2O@Ag polyhedral core-shell nanoparticles do not show red shift of SPR band compared to pure Ag nanoparticles. The shift of SPR band due to metal aggregates depend on several factors such as particle size within the aggregate, interparticle distance, electron density, dielectric constant of the medium, degree of aggregation and orientation of the individual particles within the aggregate [105]. When the interparticle spacing between the nanoparticles within the aggregate increases, dipole-dipole interaction becomes weaker and no shift in SPR band of metal is observed [105]. In the case of Cu_2O@Ag polyhedral core-shell nanoparticles, it is

proposed that the interparticle spacing between the Ag nanoparticles within the aggregate is increased which weakens the dipole-dipole interactions and hence no red shift in SPR band of Ag nanoparticles is observed. Various authors have reported the UV-visible DRS spectra for Cu_2O@Ag core-shell nanoparticles up to 800 nm [93,94] and any important spectral feature for Ag nanoparticles beyond 650 nm has not been observed.

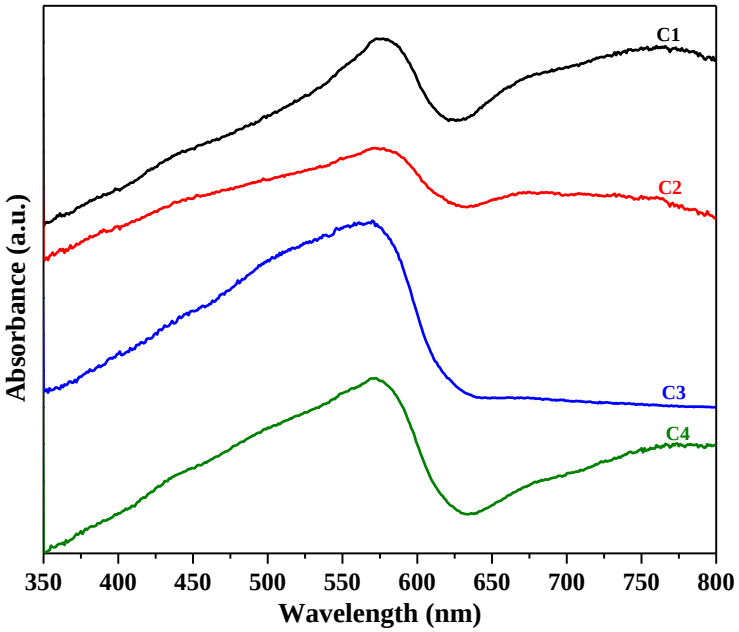

Fig. 4.2.19: DRS spectra of Cu_2O polyhedral microcrystals (C1, C2, C3, and C4).

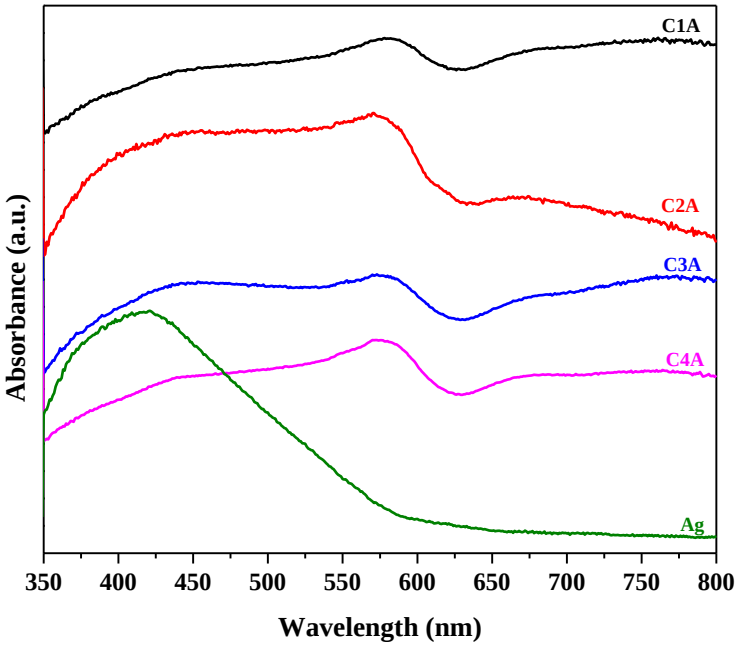

Fig. 4.2.20: DRS spectra of Cu_2O@Ag polyhedral core-shell nanoparticles (C1A, C2A, C3A, and C4A) along with the spectrum of silver nanoparticles.

4.2.4 Proposed mechanism of formation of Cu_2O@Ag polyhedral core-shell nanoparticles

The mechanism of formation of Cu_2O@Ag polyhedral core-shell nanoparticles is described in Scheme 4.2.3. The nature of silver coating and the particle size of silver are dependent primarily on three factors; nucleation temperature (N_T), nucleation time (N_t), and the difference between the nucleation temperature (N_T) and the growth temperature (G_T), $\Delta T = N_T - G_T$. In the case of pure silver nanoparticles, nucleation temperature (N_T) of 200-220 ^oC and growth temperature (G_T) of 150 ^oC produce narrow sized silver nanoparticles [68]. At shorter nucleation time (N_t), the size of silver embryos would be large and longer nucleation time (N_t) leads to dissolution of initially formed silver embryos producing stable smaller silver embryo. With further increase in the nucleation time (N_t), the stable smaller silver embryos grow further resulting in an increase in the size of silver [68,98]. In the present study, the deposition of silver nanoparticles on the surface of Cu_2O occurs in two steps. Initially, silver acetate decomposes at 220 ^oC and produces silver ions and acetate ions in the solution [106]. At elevated temperatures (e.g. ~ 220 ^oC), the silver ions and acetate ions possess high thermal energy and the silver ions present in the solution preferentially adsorb on different planes of the Cu_2O microcrystals. The acetate ions in the solution provide electrons to the silver ions leading to the formation of silver embryos on the surface of Cu_2O microcrystals with the release of CO_2 and H_2 [68,106]. In the second step, when the reaction temperature is decreased to growth temperature (G_T), i.e. 150 ^oC, the silver embryos on the surface of Cu_2O dissolve in the growth medium due to sufficient ΔT (in this case, 70 ^oC). During the growth process, Ostwald's ripening occurs, which controls the coating and the particle size of silver nanoparticles on the surface of Cu_2O microcrystals [68,98].

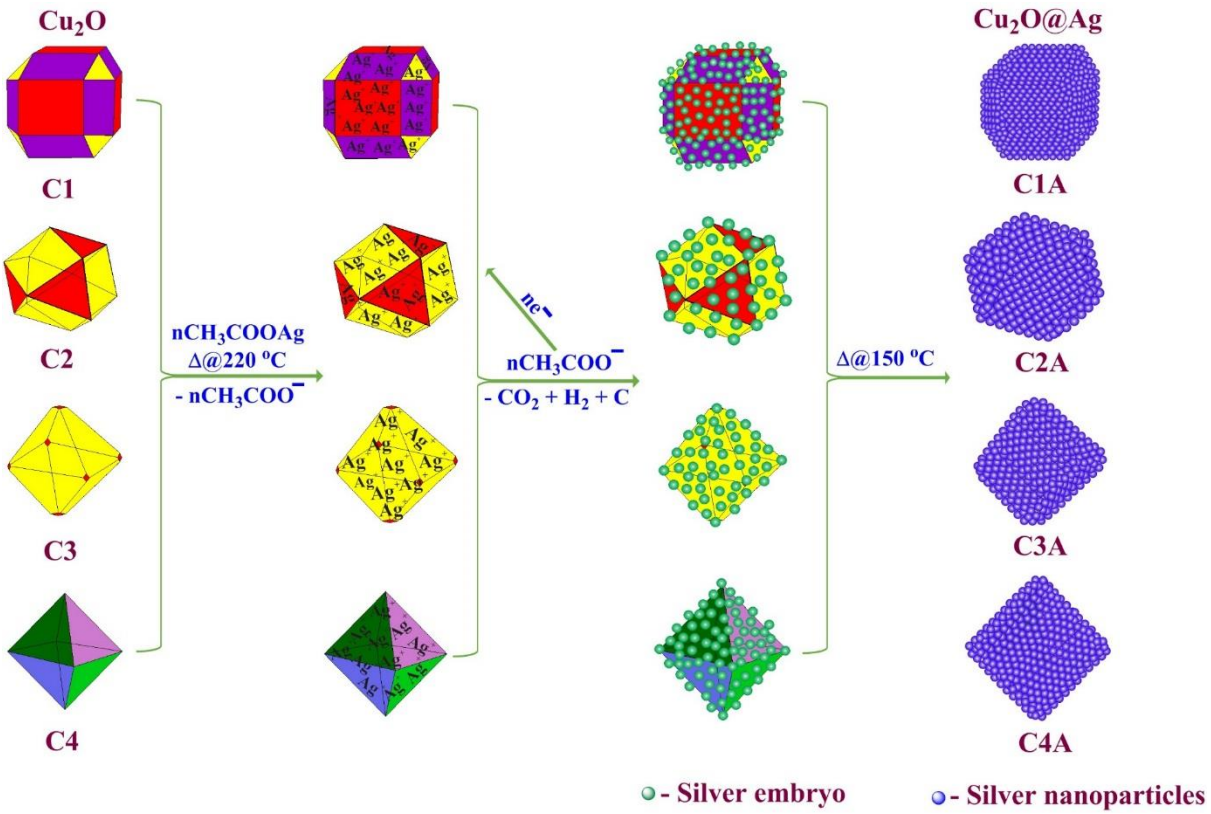

Scheme 4.2.3: Proposed mechanism for the formation of Cu_2O@Ag polyhedral core-shell nanoparticles.

4.2.5 Conclusions

A facile, economical and an efficient thermal decomposition approach has been demonstrated for the preparation of Cu_2O@Ag polyhedral core-shell nanoparticles with different morphologies. XRD results indicate the presence of Cu_2O and Ag in all the Cu_2O@Ag samples. SEM and TEM results confirm the deposition of Ag on Cu_2O microcrystals with various polyhedral morphologies. The nature of coating and particle size of silver nanoparticles on the surface of Cu_2O microcrystals were successfully controlled by optimizing the thermal decomposition conditions. DRS spectra show the bands due to Cu_2O and Ag in the Cu_2O@Ag samples. The current synthetic approach can be extended to prepare other metal-semiconductor core-shell materials for various functional applications.

References

1. Liu H., Feng Y., Chen D., Li C., Cui P., Yang J., 'Noble metal-based composite nanomaterials fabricated *via* solution-based approaches', *Journal of Materials Chemistry A,* **3**, 3182–3223 (2015).

2. Wang H., Zhang L., Chen Z., Hu J., Li S., Wang Z., Liu J., Wang X., 'Semiconductor heterojunction photocatalysts: Design, construction, and photocatalytic performances', *Chemical Society Reviews,* **43**, 5234–5244 (2014).

3. Qu Y., Duan X., 'Progress, challenge and perspective of heterogeneous photocatalysts', *Chemical Society Reviews,* **42**, 2568–2580 (2013).

4. Wang P., Huang B., Dai Y., Whangbo M. H., 'Plasmonic photocatalysts: Harvesting visible light with noble metal nanoparticles', *Physical Chemistry Chemical Physics,* **14**, 9813–9825 (2012).

5. Das S. K., Bhattacharyya A. J., 'Electrochemical performance of mixed crystallographic phase nanotubes and nanosheets of titania and titania-carbon/silver composites for lithium-ion batteries', *Materials Chemistry and Physics,* **130**, 569–576 (2011).

6. Khan M. R., Chuan T. W., Yousuf A., Chowdhury M. N. K., Cheng C. K., 'Schottky barrier and surface plasmonic resonance phenomena towards the photocatalytic reaction: Study of their mechanisms to enhance photocatalytic activity', *Catalysis Science and Technology,* **5**, 2522–2531 (2015).

7. Li J., Wu N., 'Semiconductor-based photocatalysts and photoelectrochemical cells for solar fuel generation: A review', *Catalysis Science and Technology,* **5**, 1360–1384 (2015).

8. Kochuveedu S. T., Jang Y. H., Kim D. H., 'A study on the mechanism for the interaction of light with noble metal-metal oxide semiconductor nanostructures for various photophysical applications', *Chemical Society Reviews,* **42**, 8467–8493 (2013).

9. Yang P., Jia C., He H., Chen L., Matras-Postolek K., 'Preparation and characteristics of molecularly homogeneous Ag/AgCl nano-heterostructures *via* a two-step synthesis', *RSC Advances,* **5**, 17210–17215 (2015).

10. Okasha A., Mohamed M. B., Negm S., Talaat H., 'Weak exciton–plasmon and exciton–phonon coupling in chemically synthesized Ag/CdSe metal/semiconductor hybrid

nanocomposite', *Physica E,* **44**, 2094–2098 (2012).

11. Haldar K. K., Sinha G., Lahtinen J., Patra A., 'Hybrid colloidal Au-CdSe pentapod heterostructures synthesis and their photocatalytic properties', *ACS Applied Materials and Interfaces,* **4**, 6266–6272 (2012).

12. Soni U., Tripathy P., Sapra S., 'Photocatalysis from fluorescence-quenched CdSe/Au nanoheterostructures: A size-dependent study', *The Journal of Physical Chemistry Letters,* **5**, 1909–1916 (2014).

13. Lee S. H., Rusakova I., Hoffman D. M., Jacobson A. J., Lee T. R., 'Monodisperse SnO_2-coated gold nanoparticles are markedly more stable than analogous SiO_2-coated gold nanoparticles', *ACS Applied Materials and Interfaces,* **5**, 2479–2484 (2013).

14. Zheng D., Pang X., Wang M., He Y., Lin C., Lin Z., 'Unconventional route to hairy plasmonic/semiconductor core/shell nanoparticles with precisely controlled dimensions and their use in solar energy conversion', *Chemistry of Materials,* **27**, 5271–5278 (2015).

15. Dani R. K., Wang H., Bossmann S. H., Wysin G., Chikan V., 'Faraday rotation enhancement of gold coated Fe_2O_3 nanoparticles: Comparison of experiment and theory', *The Journal of Chemical Physics,* **135**, 224502/1–9 (2011).

16. Fan Z., Zhang X., Yang J., Wu X. J., Liu Z., Huang W., Zhang H., 'Synthesis of 4H/fcc-Au@metal sulfide core–shell nanoribbons', *Journal of the American Chemical Society,* **137**, 10910–10913 (2015).

17. Wu F., Tian L., Kanjolia R., Singamaneni S., Banerjee P., 'Plasmonic metal-to-semiconductor switching in Au nanorod-ZnO nanocomposite films', *ACS Applied Materials and Interfaces,* **5**, 7693–7697 (2013).

18. Zeng H., Cai W., Cao B., Hu J., Li Y., Liu P., 'Surface optical phonon Raman scattering in Zn/ZnO core-shell structured nanoparticles', *Applied Physics Letters,* **88**, 181905/1–3 (2006).

19. Li X., Liu J., Guo H., Zhou X., Wang C., Sun P., Hu X., Lu G., 'Au@In_2O_3 core-shell composites: A metal-semiconductor heterostructure for gas sensing applications', *RSC Advances,* **5**, 545–551 (2015).

20. Lei Y., Chim W., 'Highly ordered arrays of metal/semiconductor core-shell

nanoparticles with tunable nanostructures and photoluminescence', *Journal of the American Chemical Society*, **127**, 1487–1492 (2005).

21. Wang S., Xiao C., Shi X., Cui G., Yao B., Wang P., Tian T., Zhang M., 'Electrodeposition and characterization of a bamboo-like ZnSe/Zn heterostructure ordered array', *RSC Advances*, **3**, 12861–12866 (2013).

22. Chong S. K., Dee C. F., Rahman S. A., 'Single reactor deposition of silicon/tungsten oxide core–shell heterostructure nanowires with controllable structure and optical properties', *RSC Advances*, **5**, 2346–2353 (2015).

23. Ben-Ishai M., Patolsky F., 'A route to high-quality crystalline coaxial core/multishell Ge@Si(GeSi) and Si@(GeSi) nanowire heterostructures', *Advanced Materials*, **22**, 902–906 (2010).

24. Naskar S., Schlosser A., Miethe J. F., Steinbach F., Feldhoff A., Bigall N. C., 'Site-selective noble metal growth on CdSe nanoplatelets', *Chemistry of Materials*, **27**, 3159–3166 (2015).

25. Zhang Y., Wang Q., Ashall B., Zerulla D., Lee G. U., 'Magnetic-plasmonic dual modulated FePt-Au ternary heterostructured nanorods as a promising nano-bioprobe', *Advanced Materials*, **24**, 2485–2490 (2012).

26. Mokkapati S., Saxena D., Jiang N., Parkinson P., Wong-Leung J., Gao Q., Tan H. H., Jagadish C., 'Polarization tunable, multicolor emission from core-shell photonic III-V semiconductor nanowires', *Nano Letters*, **12**, 6428–6431 (2012).

27. Karlina L. B., Vlasov A. S., Ber B. Y., Kazanthev D. Y., Marukhina E. P., 'Surfactant effects on GaAs-Ge heterostructures', *Journal of Crystal Growth*, **380**, 138–142 (2013).

28. Conesa-Boj S., Dunand S., Russo-Averchi E., Heiss M., Ruffer D., Wyrsch N., Ballif C., Fontcuberta i Morral A., 'Hybrid axial and radial Si-GaAs heterostructures in nanowires', *Nanoscale*, **5**, 9633–9639 (2013).

29. Conesa-Boj S., Hauge H. I. T., Verheijen M. A., Assali S., Li A., Bakkers E. P. A. M., Fontcuberta i Morral A., 'Cracking the Si shell growth in hexagonal GaP-Si core–shell nanowires', *Nano Letters*, **15**, 2974–2979 (2015).

30. Hsieh Y. H., Chiu C. H., Huang C. W., Chen J. Y., Lin W. J., Wu W. W., 'Dynamic observation on the growth behaviors in manganese silicide/silicon nanowire

heterostructures', *Nanoscale*, **7**, 1776–1781 (2015).

31. Her Y., Yeh B., Huang S., 'Vapor-solid growth of p-Te/n-SnO_2 hierarchical heterostructures and their enhanced room-temperature gas sensing properties', *ACS Applied Materials and Interfaces*, **6**, 9150–9159 (2014).

32. Xi G., Ye J., Ma Q., Su N., Bai H., Wang C., 'In situ growth of metal particles on 3D urchin-like WO_3 nanostructures.', *Journal of the American Chemical Society*, **134**, 6508–6511 (2012).

33. Wu Z., Xue Y., Wang H., Wu Y., Yu H., 'ZnO nanorods/Pt and ZnO nanorods/Ag heteronanostructure arrays with enhanced photocatalytic degradation of dyes', *RSC Advances*, **4**, 59009–59016 (2014).

34. Thiyagarajan P., Ahn H. J., Lee J. S., Yoon J. C., Jang J. H., 'Hierarchical metal/semiconductor nanostructure for efficient water splitting', *Small*, **9**, 2341–2347 (2013).

35. Huang J., Chen F., Zhang Q., Zhan Y., Ma D., Xu K., Zhao Y., '3D Silver nanoparticles decorated zinc oxide/silicon heterostructured nanomace arrays as high-performance surface enhanced Raman scattering substrates', *ACS Applied Materials and Interfaces*, **7**, 5725–5735 (2015).

36. Guo L., Cai Y., Ge J., Zhang Y., Gong L., Li X., Wang K., Ren Q., Su J., Chen J., 'Multifunctional Au−Co@CN nanocatalyst for highly efficient hydrolysis of ammonia borane', *ACS Catalysis*, **5**, 388–392 (2015).

37. Chen Y., Zeng D., Cortie M. B., Dowd A., Guo H., Wang J., Peng D. L., 'Seed-induced growth of flower-like Au-Ni-ZnO metal-semiconductor hybrid nanocrystals for photocatalytic applications', *Small*, **11**, 1460–1469 (2015).

38. Su Y., Tang J., Yang H., Cheng Z., 'Multifunctional multisegmented Co/$CoPt_3$ heterostructure nanowires', *Nanoscale*, **5**, 9709–9713 (2013).

39. Liu J., Wu W., Tian Q., Yang S., Sun L., Xiao X., Ren F., Jiang C., Roy V. A. L., 'Tube-like α-Fe_2O_3@Ag/AgCl heterostructure: Controllable synthesis and enhanced plasmonic photocatalytic activity', *RSC Advances*, **5**, 61239–61248 (2015).

40. Lu Y., Liu G. L., Lee L. P., 'High-density silver nanoparticle film with temperature-controllable interparticle spacing for a tunable surface enhanced Raman scattering

substrate', *Nano Letters*, **5**, 5–9 (2005).

41. Merga G., Cass L. C., Chipman D. M., Meisel D., 'Probing silver nanoparticles during catalytic H_2 evolution', *Journal of the American Chemical Society*, **130**, 7067–7076 (2008).

42. Kandjani A. E., Sabri Y. M., Mohammad-Taheri M., Bansal V., Bhargava S. K., 'Detect, remove and reuse: A new paradigm in sensing and removal of Hg (II) from wastewater *via* SERS-active ZnO/Ag nanoarrays', *Environmental Science and Technology*, **49**, 1578–1584 (2015).

43. Lu W., Gao S., Wang J., 'One-pot synthesis of Ag/ZnO self-assembled 3D hollow microspheres with enhanced photocatalytic performance', *The Journal of Physical Chemistry C*, **112**, 16792–16800 (2008).

44. Zheng Y., Zheng L., Zhan Y., Lin X., Zheng Q., Wei K., 'Ag/ZnO heterostructure nanocrystals: Synthesis, characterization, and photocatalysis', *Inorganic Chemistry*, **46**, 6980–6986 (2007).

45. Satter S. S., Hoque M., Rahman M. M., Mollah M. Y. A., Abu Bin Hasan Susan M., 'An approach towards the synthesis and characterization of ZnO@Ag core@shell nanoparticles in water-in-oil microemulsion', *RSC Advances*, **4**, 20612–20615 (2014).

46. Guo X. H., Ma J. Q., Ge H. G., 'Preparation, characterization, and photocatalytic performance of pear-shaped ZnO/Ag core-shell submicrospheres', *Journal of Physics and Chemistry of Solids*, **74**, 784–788 (2013).

47. Li J., Yan J., Liu C., Dong L., Lv H., Sun W., Xing S., 'Manipulation on ZnO heterostructures: From binary ZnO–Ag to ternary ZnO–Ag–polypyrrole', *CrystEngComm*, **16**, 10943–10948 (2014).

48. Ivanova T., Harizanova A., Koutzarova T., Vertruyen B., 'Sol–gel nanocrystalline ZnO:Ag films: Structural and optical properties', *Superlattices and Microstructures*, **70**, 1–6 (2014).

49. Hou X., 'ZnO/Ag heterostructured nanoassemblies: Wet-chemical preparation and improved visible-light photocatalytic performance', *Materials Letters*, **139**, 201–204 (2015).

50. Ren C., Yang B., Wu M., Xu J., Fu Z., lv Y., Guo T., Zhao Y., Zhu C., 'Synthesis of

Ag/ZnO nanorods array with enhanced photocatalytic performance', *Journal of Hazardous Materials*, **182**, 123–129 (2010).

51. Li F., Liu X., Qin Q., Wu J., Li Z., Huang X., 'Sonochemical synthesis and characterization of ZnO nanorod/Ag nanoparticle composites', *Crystal Research and Technology*, **44**, 1249–1254 (2009).

52. Khan M., Wei C., Chen M., Tao J., Huang N., Qi Z., Li L., 'CTAB-mediated synthesis and characterization of ZnO/Ag core–shell nanocomposites', *Journal of Alloys and Compounds*, **612**, 306–314 (2014).

53. Wei Y., Kong J., Yang L., Ke L., Tan H. R., Liu H., Huang Y., Sun X. W., Lu X., Du H., 'Polydopamine-assisted decoration of ZnO nanorods with Ag nanoparticles: an improved photoelectrochemical anode', *Journal of Materials Chemistry A*, **1**, 5045–5052 (2013).

54. Wei Y., Ke L., Kong J., Liu H., Jiao Z., Lu X., Du H., Sun X. W., 'Enhanced photoelectrochemical water-splitting effect with a bent ZnO nanorod photoanode decorated with Ag nanoparticles', *Nanotechnology*, **23**, 235401/1–8 (2012).

55. Zamiri R., Zakaria A., Jorfi R., Zamiri G., Mojdehi M. S., Ahangar H. A., Zak A. K., 'Laser assisted fabrication of ZnO/Ag and ZnO/Au core/shell nanocomposites', *Applied Physics A: Materials Science and Processing*, **111**, 487–493 (2013).

56. Bhattacharyya S., Gedanken A., 'Microwave-assisted insertion of silver nanoparticles into 3-D mesoporous zinc oxide nanocomposites and nanorods', *The Journal of Physical Chemistry C*, **112**, 659–665 (2008).

57. Kandula S., Jeevanandam P., 'Visible-light-induced photodegradation of methylene blue using ZnO/CdS heteronanostructures synthesized through a novel thermal decomposition approach', *Journal of Nanoparticle Research*, **16**, 2452/1–18 (2014).

58. Bitenc M., Zorica C. O., 'Synthesis and characterization of crystalline hexagonal bipods of zinc oxide', *Materials Research Bulletin*, **44**, 381–387 (2009).

59. Zhong K., Xia J., Li H. H., Liang C. L., Liu P., Tong Y. X., 'Morphology evolution of one-dimensional-based ZnO nanostructures synthesized *via* electrochemical corrosion', *The Journal of Physical Chemistry C*, **113**, 15514–15523 (2009).

60. Chen C., Zheng Y., Zhan Y., Lin X., Zheng Q., Wei K., 'Enhanced Raman scattering

and photocatalytic activity of Ag/ZnO heterojunction nanocrystals', *Dalton Transactions*, **40**, 9566–9570 (2011).

61. Djurišić A. B., Chen X., Leung Y. H., Ng A. M. C., 'ZnO nanostructures: Growth, properties and applications', *Journal of Materials Chemistry*, **22**, 6526–6535 (2012).

62. Warule S. S., Chaudhari N. S., Khare R. T., Ambekar J. D., Kale B. B., More M. A., 'Single step hydrothermal approach for devising hierarchical Ag–ZnO heterostructures with significant enhancement in field emission performance', *CrystEngComm*, **15**, 7475–7483 (2013).

63. Ischenko V., Polarz S., Grote D., Stavarache V., Fink K., Driess M., 'Zinc oxide nanoparticles with defects', *Advanced Functional Materials*, **15**, 1945–1954 (2005).

64. Desarkar H. S., Kumbhakar P., Mitra A. K., 'Synthesis of silver hollow nanoparticles and observation of photoluminescence emission properties', *Journal of Luminescence*, **134**, 1–7 (2013).

65. Yeshchenko O. A., Dmitruk I. M., Alexeenko A. A., Losytskyy M. Y., Kotko A. V., Pinchuk A. O., 'Size-dependent surface-plasmon-enhanced photoluminescence from silver nanoparticles embedded in silica', *Physical Review B: Condensed Matter and Materials Physics*, **79**, 235438/1–8 (2009).

66. Wu Z., Xu C., Wu Y., Yu H., Tao Y., Wan H., Gao F., 'ZnO nanorods/Ag nanoparticles heterostructures with tunable Ag contents: A facile solution-phase synthesis and applications in photocatalysis', *CrystEngComm*, **15**, 5994–6002 (2013).

67. Sahoo P. K., Kamal S. S. K., Shankar B., Sreedhar B., Durai L., 'Facile chemical synthesis of nano-silver powders for printable electronics applications', *Journal of Experimental Nanoscience*, **7**, 520–528 (2012).

68. Chandni, Andhariya N., Pandey O., Chudasama B., 'A growth kinetic study of ultrafine monodispersed silver nanoparticles', *RSC Advances*, **3**, 1127–1136 (2013).

69. Sun Y., 'Controlled synthesis of colloidal silver nanoparticles in organic solutions: Empirical rules for nucleation engineering', *Chemical Society Reviews*, **42**, 2497–2511 (2013).

70. Sun S., 'Recent advances in hybrid Cu_2O-based heterogeneous nanostructures', *Nanoscale*, **7**, 10850–10882 (2015).

71. Huang M. H., Rej S., Hsu S. C., 'Facet-dependent properties of polyhedral nanocrystals', *Chemical Communications*, **50**, 1634–1644 (2014).

72. Zoolfakar A. S., Rani R. A., Morfa A. J., O'Mullane A. P., Kalantar-Zadeh K., 'Nanostructured copper oxide semiconductors: A perspective on materials, synthesis methods and applications', *Journal of Materials Chemistry C*, **2**, 5247–5270 (2014).

73. Filipič G., Cvelbar U., 'Copper oxide nanowires: A review of growth', *Nanotechnology*, **23**, 194001/1–16 (2012).

74. Kuo C. H., Huang M. H., 'Morphologically controlled synthesis of Cu_2O nanocrystals and their properties', *Nano Today*, **5**, 106–116 (2010).

75. Chen K., Sun C., Xue D., 'Morphology engineering of high performance binary oxide electrodes', *Physical Chemistry Chemical Physics*, **17**, 732–750 (2015).

76. Chen K., Sun C., Song S., Xue D., 'Polymorphic crystallization of Cu_2O compound', *CrystEngComm*, **16**, 5257–5267 (2014).

77. Yao K. X., Yin X. M., Wang T. H., Zeng H. C., 'Synthesis, self-assembly, disassembly, and reassembly of two types of Cu_2O nanocrystals unifaceted with {001} or {110} planes', *Journal of the American Chemical Society*, **132**, 6131–6144 (2010).

78. Xu H., Wang W., 'Template synthesis of multishelled Cu_2O hollow spheres with a single-crystalline shell wall', *Angewandte Chemie International Edition*, **46**, 1489–1492 (2007).

79. Zhang D. F., Zhang H., Guo L., Zheng K., Han X. D., Zhang Z., 'Delicate control of crystallographic facet-oriented Cu_2O nanocrystals and the correlated adsorption ability', *Journal of Materials Chemistry*, **19**, 5220–5225 (2009).

80. Sun S., Song X., Sun Y., Deng D., Yang Z., 'The crystal-facet-dependent effect of polyhedral Cu_2O microcrystals on photocatalytic activity', *Catalysis Science and Technology*, **2**, 925–930 (2012).

81. Barreca D., Carraro G., Gombac V., Gasparotto A., Maccato C., Fornasiero P., Tondello E., 'Supported metal oxide nanosystems for hydrogen photogeneration: Quo vadis?', *Advanced Functional Materials*, **21**, 2611–2623 (2011).

82. Kwon Y., Soon A., Han H., Lee H., 'Shape effects of cuprous oxide particles on stability

in water and photocatalytic water splitting', *Journal of Materials Chemistry A*, **3**, 156–162 (2015).

83. Wick R., Tilley S. D., 'Photovoltaic and photoelectrochemical solar energy conversion with Cu_2O', *The Journal of Physical Chemistry C*, **119**, 26243–26257 (2015).

84. Zhang H., Zhu Q., Zhang Y., Wang Y., Zhao L., Yu B., 'One-pot synthesis and hierarchical assembly of hollow Cu_2O microspheres with nanocrystals-composed porous multishell and their gas-sensing properties', *Advanced Functional Materials*, **17**, 2766–2771 (2007).

85. Pang H., Gao F., Lu Q., 'Morphology effect on antibacterial activity of cuprous oxide', *Chemical Communications*, 1076–1078 (2009).

86. Wang X., Liu C., Zheng B., Jiang Y., Zhang L., Xie Z., Zheng L., 'Controlled synthesis of concave Cu_2O microcrystals enclosed by {hhl} high-index facets and enhanced catalytic activity', *Journal of Materials Chemistry A*, **1**, 282–287 (2013).

87. Kang W., Liu F., Su Y., Wang D., Shen Q., 'The catanionic surfactant-assisted syntheses of 26-faceted and hexapod-shaped Cu_2O and their electrochemical performances', *CrystEngComm*, **13**, 4174–4180 (2011).

88. Chen A., Haddad S., Wu Y. C., Fang T. N., Kaza S., Lan Z., 'Erasing characteristics of Cu_2O metal-insulator-metal resistive switching memory', *Applied Physics Letters*, **92**, 013503/1–3 (2008).

89. Wongrakpanich A., Mudunkotuwa I. A., Geary S. M., Morris A. S., Mapuskar K. A., Spitz D. R., Grassian V. H., Salem A. K., 'Size-dependent cytotoxicity of copper oxide nanoparticles in lung epithelial cells', *Environmental Science: Nano*, (2016). doi:10.1039/C5EN00271K

90. Kaviyarasan K., Anandan S., Mangalaraja R. V., Sivasankar T., Ashokkumar M., 'Sonochemical synthesis of Cu_2O nanocubes for enhanced chemiluminescence applications', *Ultrasonics Sonochemistry*, **29**, 388–393 (2016).

91. Nai J., Wang S., Bai Y., Guo L., 'Amorphous $Ni(OH)_2$ nanoboxes: Fast fabrication and enhanced sensing for glucose', *Small*, **9**, 3147–3152 (2013).

92. Huang M. H., Rej S., Chiu C. Y., 'Facet-dependent optical properties revealed through investigation of polyhedral Au-Cu_2O and bimetallic core-shell nanocrystals', *Small*, **11**,

2716–2726 (2015).

93. Wang Z., Zhao S., Zhu S., Sun Y., Fang M., 'Photocatalytic synthesis of M/Cu_2O (M = Ag, Au) heterogeneous nanocrystals and their photocatalytic properties', *CrystEngComm*, **13**, 2262–2267 (2011).

94. Zhang W., Yang X., Zhu Q., Wang K., Lu J., Chen M., Yang Z., 'One-pot room temperature synthesis of Cu_2O/Ag composite nanospheres with enhanced visible-light-driven photocatalytic performance', *Industrial and Engineering Chemistry Research*, **53**, 16316–16323 (2014).

95. Yang L., Lv J., Sui Y., Fu W., Zhou X., Ma J., Su S., Zhang W., Lv P., Wu D., Mu Y., Yang H., 'Fabrication of Cu_2O/Ag composite nanoframes as surface-enhanced Raman scattering substrates in a successive one-pot procedure', *CrystEngComm*, **16**, 2298–2304 (2014).

96. Lin X., Zhou R., Zhang J., Fei S., 'A novel one-step electron beam irradiation method for synthesis of Ag/Cu_2O nanocomposites', *Applied Surface Science*, **256**, 889–893 (2009).

97. Yang L., Lv J., Sui Y., Fu W., Zhou X., Ma J., 'Ag-Cu_2O composite microstructures with tunable Ag contents: Synthesis and surface-enhanced (resonance) Raman scattering (SE(R)RS) properties', *RSC Advances*, **4**, 17249–17254 (2014).

98. Wang J., Cui F., Chu S., Jin X., Pu J., Wang Z., 'In situ growth of noble-metal nanoparticles on Cu_2O nanocubes for surface-enhanced Raman scattering detection', *ChemPlusChem*, **79**, 684–689 (2014).

99. Jin W., Xu P., Xiong L., Jing Q., Zhang B., Sun K., Han X., 'SERS-active silver nanoparticle assemblies on branched Cu_2O crystals through controlled galvanic replacement', *RSC Advances*, **4**, 53543–53546 (2014).

100. Ji R., Sun W., Chu Y., 'One-step hydrothermal synthesis of Ag/Cu_2O heterogeneous nanostructures over Cu foil and their SERS applications', *RSC Advances*, **4**, 6055–6059 (2014).

101. Ma J., Guo S., Guo X., Ge H., 'Preparation, characterization and antibacterial activity of core–shell Cu_2O@Ag composites', *Surface and Coatings Technology*, **272**, 268–272 (2015).

102. Liu L., Yang W., Sun W., Li Q., Shang J. K., 'Creation of $Cu_2O@TiO_2$ composite photocatalysts with p-n heterojunctions formed on exposed Cu_2O facets, their energy band alignment study, and their enhanced photocatalytic activity under illumination with visible light', *ACS Applied Materials and Interfaces*, **7**, 1465–1476 (2015).

103. Tang Y., He W., Wang S., Tao Z., Cheng L., 'New insight into the size-controlled synthesis of silver nanoparticles and its superiority in room temperature sintering', *CrystEngComm*, **16**, 4431–4440 (2014).

104. Zhang Z., Che H., Gao J., Wang Y., She X., Sun J., Gunawan P., Zhong Z., Su F., 'Shape-controlled synthesis of Cu_2O microparticles and their catalytic performances in the Rochow reaction', *Catalysis Science and Technology*, **2**, 1207–1212 (2012).

105. Ghosh S. K., Pal T., 'Interparticle coupling effect on the surface plasmon resonance of gold nanoparticles: From theory to applications', *Chemical Reviews*, **107**, 4797–4862 (2007).

106. Kandula S., Jeevanandam P., 'Sun-light-driven photocatalytic activity by ZnO/Ag heteronanostructures synthesized *via* a facile thermal decomposition approach', *RSC Advances*, **5**, 76150–76159 (2015).

Chapter-5

Synthesis of SiO_2@Co_3O_4 and SiO_2@Ni-Co Mixed Metal Oxide Core-Shell Nanorattles *via* Homogeneous Precipitation Method

5.1 Synthesis of SiO_2@Co_3O_4 Core-Shell Nanorattles *via* Homogeneous Precipitation Method

5.1.1 Introduction

In recent years, research is focused on core-shell nanoparticles with yolk-shell or nanorattle morphology. Nanorattles refer to hollow shells with solid cores with interstitial hollow space between core and the shell [1,2]. As compared to core-shell nanoparticles, nanorattles have advantages of having both hollow and core-shell structures together. They possess enhanced surface area [3], and provide more active sites on core surface due to unblocking of the surface [4]. The porous shell has access to active sites from inner and outer sides [5], and the void space is able to accommodate guest molecules like drugs and vesicles [6]. Nanorattles exhibit interesting characteristics which are useful in diverse areas such as catalysis [7], sensors [8], gas storage [9], energy storage [10], adsorbents [11], microwave absorbers [12], dye-sensitized solar cells [13], switches [14], and bio-medicine [15,16]. A schematic representation of different types of core-shell nanorattles and their various applications is shown in Figure 5.1.1.

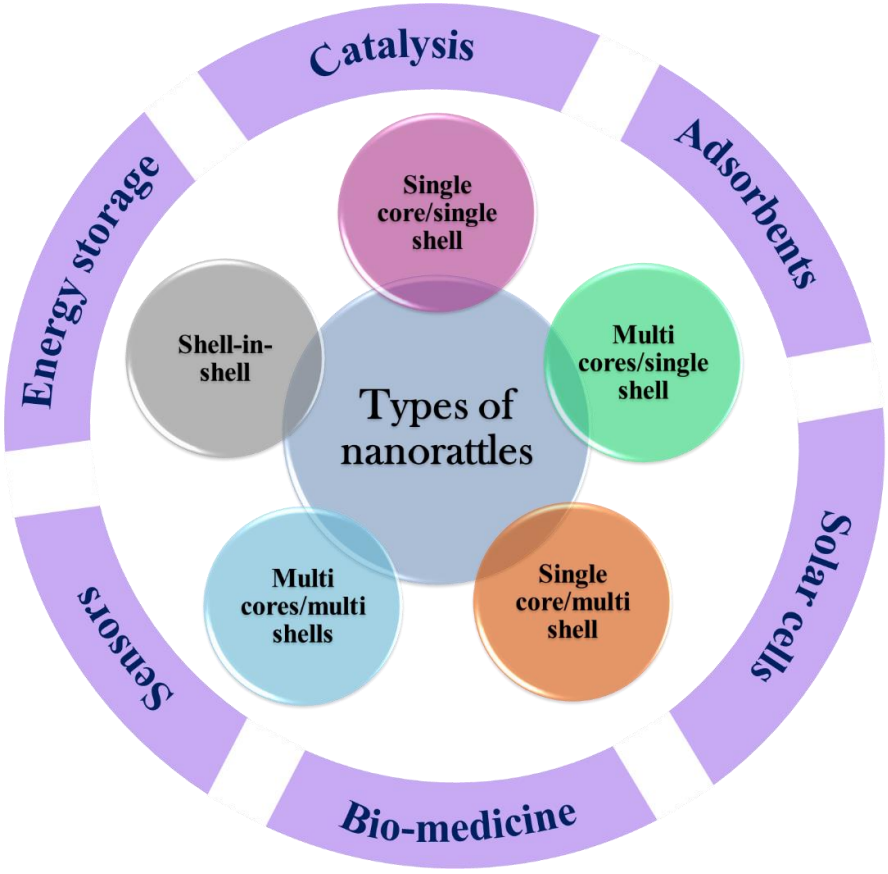

Fig.5.1.1: Types of nanorattles and various applications [7-13].

In the last decade, noble metals, metal oxides, metal sulfides and metal nitrides with nanorattle morphology have been reported by several authors. In the case of metal oxides, SiO_2 [17], CeO_2 [18], Fe_2O_3 [19], SnO_2 [20], TiO_2 [21], and V_2O_5 [22] nanorattles have been well studied. The TEM images of various metal oxide nanorattles are shown in Figure 5.1.2.

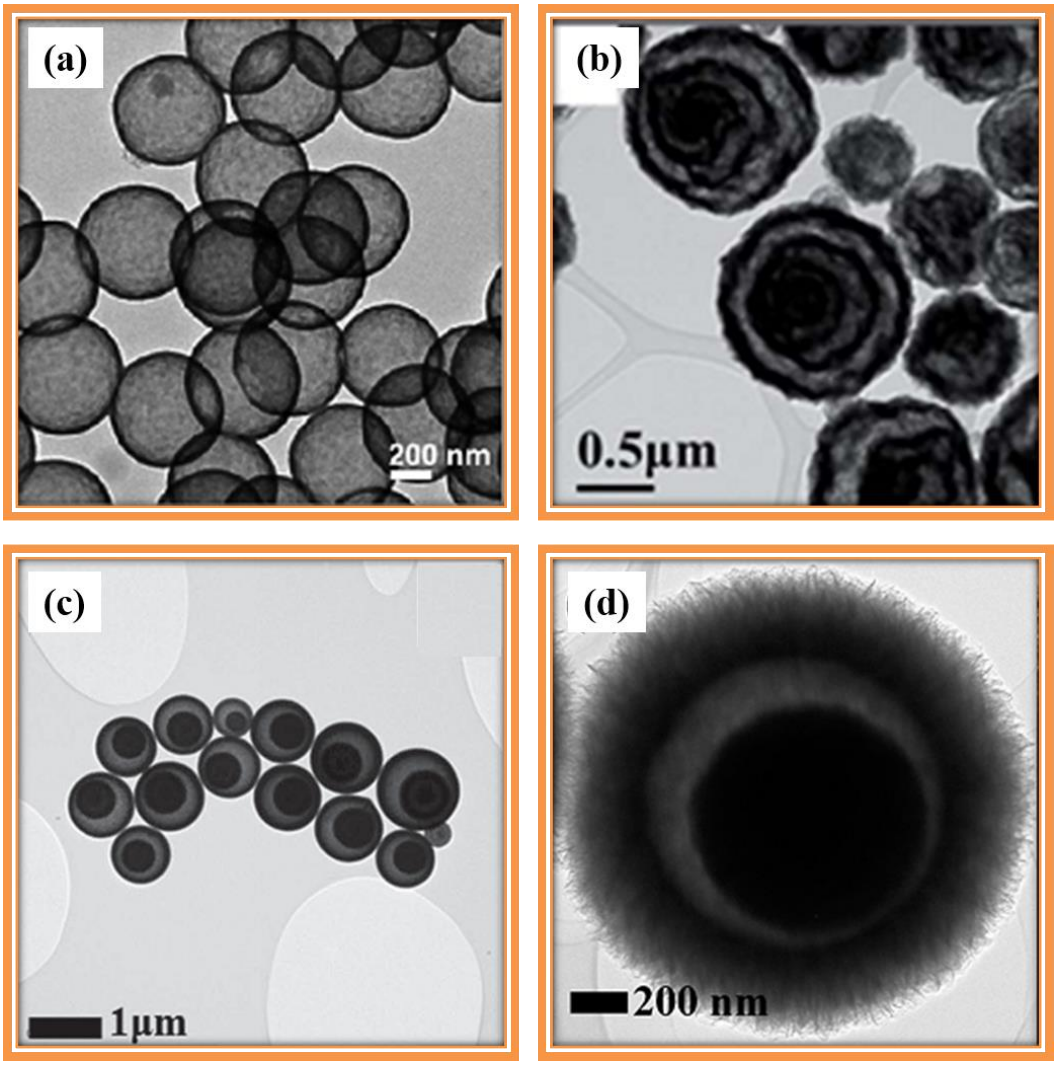

Fig.5.1.2: TEM images of different metal oxide nanorattles; **(a)** SiO_2 [17], **(b)** Fe_2O_3 with multi-shells [19], **(c)** SnO_2 [20], and **(d)** TiO_2 [21].

Mostly, noble metals have been explored as effective catalysts for organic conversions. But, in most of the cases, during the catalysis, noble metals undergo either leaching or aggregation [1,2]. To avoid these problems, noble metals have been incorporated into mesoporous shells such as SiO_2, CeO_2, TiO_2, ZrO_2, and carbon. Various reports are available on metal@metal oxide nanorattles where noble metals act as the core and metal oxides act as the shell. Examples are $Au@Al_2O_3$ [23], $Au@SiO_2$ [24], $Pd@CeO_2$

[25], and Pt@TiO_2 [26]. Reports are available on metal oxide@metal oxide and metal sulfide@metal oxide nanorattles where either metal oxide or metal sulfide acts as the core and a metal oxide acts as the shell. Examples are α-Fe_2O_3@SnO_2 [27], Fe_3O_4@SnO_2 [28], Fe_3O_4@TiO_2 [29], ZnO@Mn_3O_4 [30], and SnS_2@TiO_2 [31]. Carbon has been used as a shell and various metal@carbon and metal oxide@carbon nanorattles have also been reported. Examples are Au@C [32], Si@C [33], Fe_3O_4@C [34], SnSb@C [35], and SnO_2@C [36]. TEM images of some of the above mentioned nanorattles are shown in Figure 5.1.3.

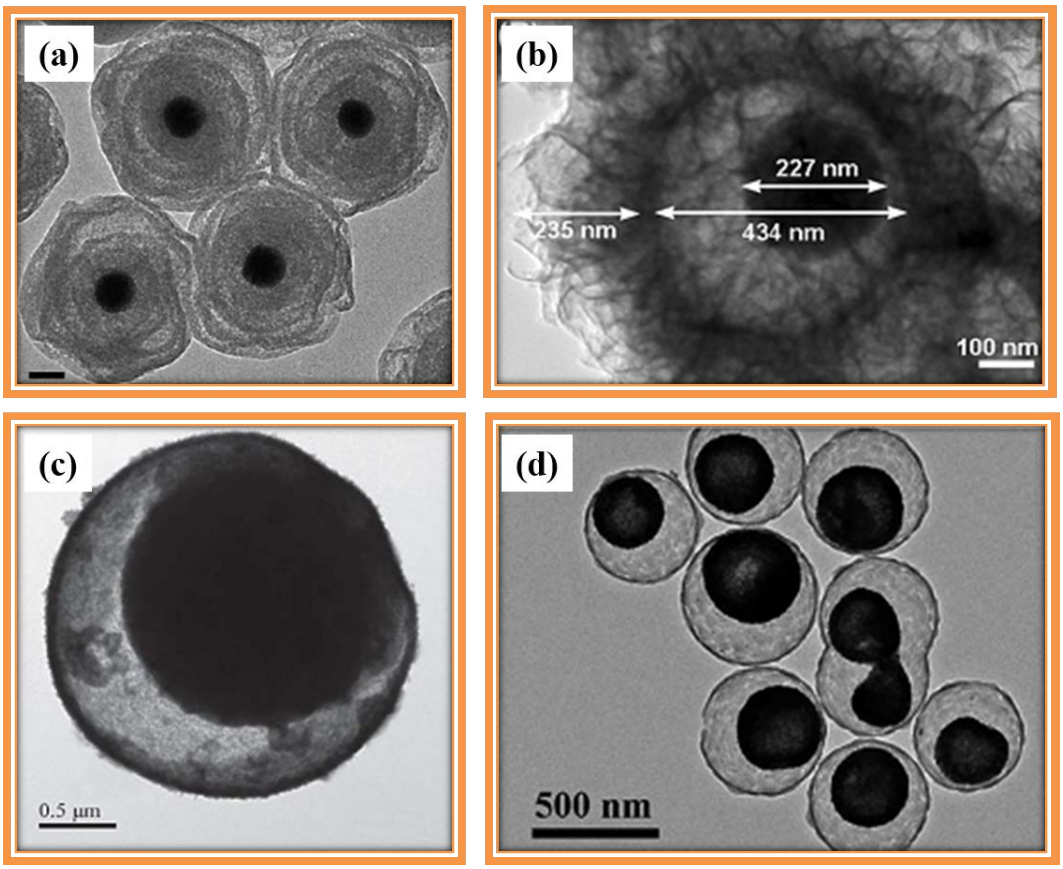

Fig.5.1.3: TEM images of **(a)** Au@SiO_2 nano-matryoshka [24], **(b)** Fe_3O_4@TiO_2 [29], **(c)** SnS_2@TiO_2 [31], and **(d)** SnO_2@C [36] nanorattles.

Among the metal oxides, SiO_2 has been used as the core or as the shell material. Very few reports are available where silica is used as the core. Examples are SiO_2@C [37], SiO_2@TiO_2 [38], and SiO_2@PSDVB@PAN [39]. Most of the authors have reported SiO_2 as the shell and a metal or metal oxide as the core. Some of the examples are Ag@SiO_2 [40], Au@SiO_2 [41], Pt@SiO_2 [42], Ru@SiO_2 [43], Ni@SiO_2 [44],

Fe_2O_3@SiO_2 [45], Fe_3O_4@SiO_2 [46], ZnO@SiO_2 [47], etc. TEM images of some of the above mentioned nanorattles are shown in Figure 5.1.4.

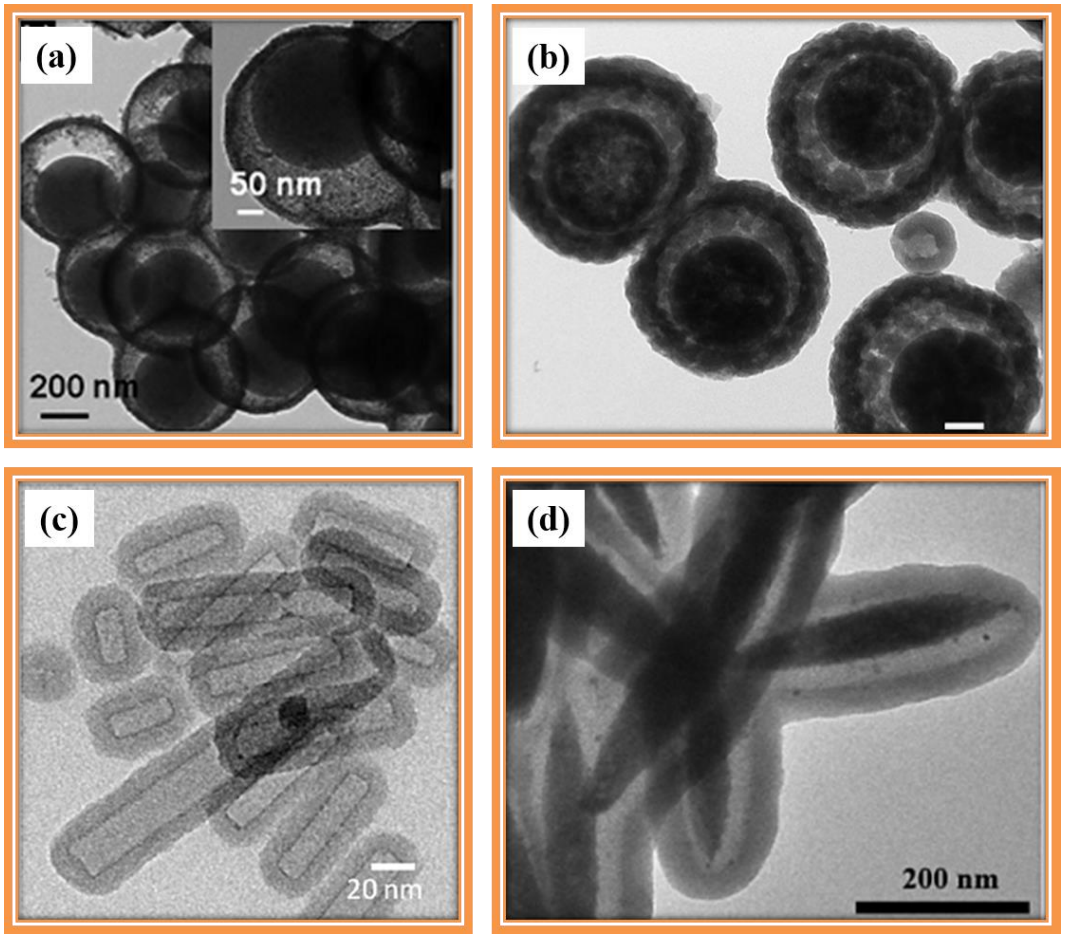

Fig.5.1.4: TEM images of **(a)** SiO_2@TiO_2 [38], **(b)** Ru@SiO_2 [43], **(c)** Ni@SiO_2 [44], and **(d)** Fe_2O_3@SiO_2 [45] nanorattles.

Co_3O_4 is an important p-type antiferromagnetic semiconductor with a normal spinel structure [48]. It is used in various applications such as anode materials in lithium ion rechargeable batteries [49], sensors [50], electrochemical devices [51], supercapacitors [52], water oxidation [53], and heterogeneous catalysis [54]. Especially, the electrochemcial properties of Co_3O_4 strongly depend on morphology and structure. Various morphologies of Co_3O_4 have been reported and they are nanowires [55], nanoneedles [56], nanobelts [57], nanoplatelets [58], and multishells [59]. In the case of nanorattles, Co_3O_4 has been used as either as the core or shell. Examples are Co_3O_4 multishells [59], Pd loaded Co_3O_4 multishells [60], Co_3O_4@SiO_2 [61], and Fe_3O_4@Co_3O_4 [62] nanorattles. TEM images of Co_3O_4 based nanorattles are shown in Figure 5.1.5.

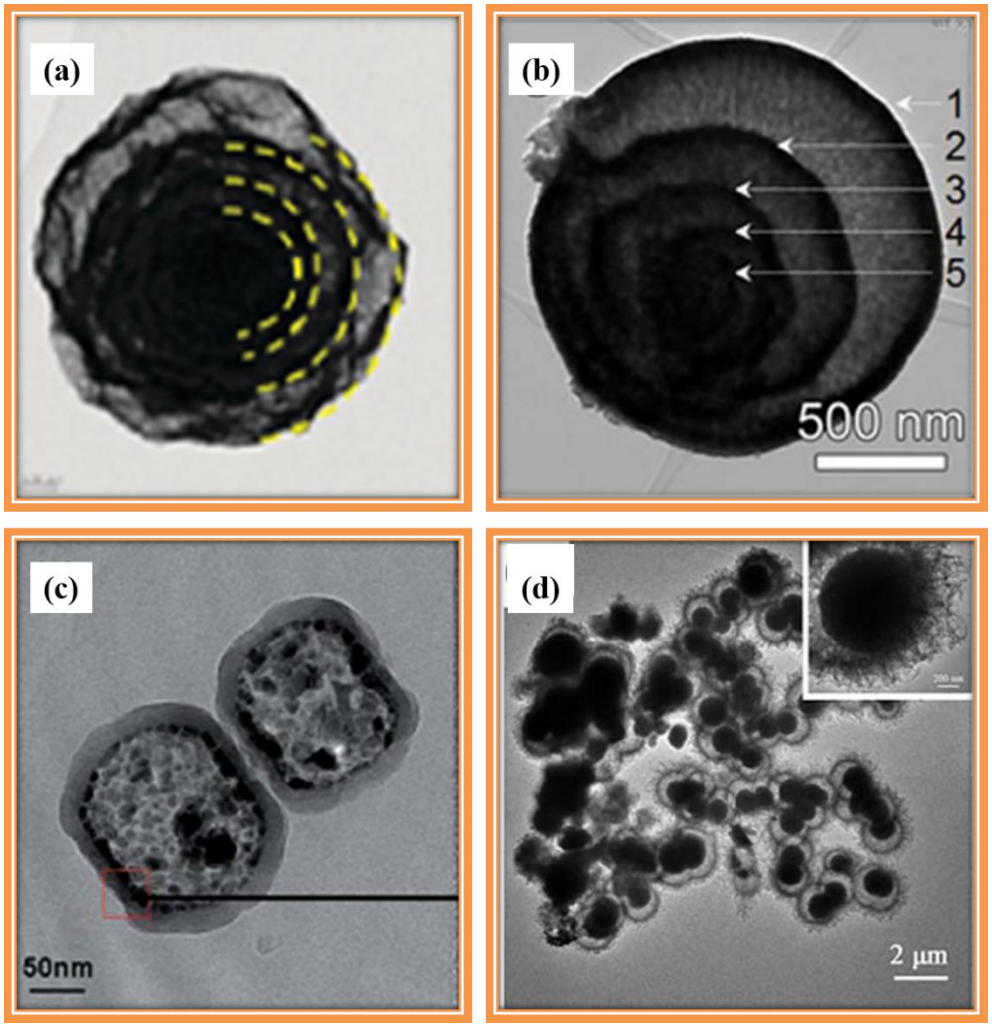

Fig.5.1.5: TEM images of **(a)** Co_3O_4 multishells [59], **(b)** Pd loaded Co_3O_4 multishells [60], **(c)** Co_3O_4@SiO_2 [61], and **(d)** Fe_3O_4@Co_3O_4 [62] nanorattles.

Several methods have been reported for the synthesis of nanorattles and they include hydrothermal synthesis [18], spray pyrolysis [19], template-route [34], selective etching [41], annealing [43], ship in bottle [63], galvanic replacement [64], Kirkendall reaction [65], and Ostwald ripening [66]. Some of the methods for the synthesis of nanorattles are discussed briefly below.

Hydrothermal synthesis [18]: This method is used to synthesize either the core or the shell or both the materials. In this approach, metal salts are mixed in water or in an organic solvent and stirred for some time. After uniform mixing, the reactants are transferred to a Teflon lined stainless steel autoclave and heated to elevated temperatures for a certain period of time to get the nanorattles. In some cases, the obtained products are calcined to get the nanorattles. Examples are CeO_2 [18], α-Fe_2O_3@SnO_2 [27], Fe_3O_4@TiO_2 [29], and SnS_2@TiO_2 [31].

Spray pyrolysis [19]: In this approach, a metal salt is reduced by a reducing agent at high temperature in an aqueous droplet. Then, the excess reducing agent forms the shell on the periphery of the hot droplet. In most of the cases, sodium citrate and glucose are used as the reducing agents. Once the shell is completely carbonized, removal of water soluble products occurs resulting in the formation of void space. Examples are Fe_2O_3 [19], SnO_2 [20], and ZnO@Mn_3O_4 [30]. A schematic representation of synthesis of Fe_2O_3 nanorattles with multiple shells by spray pyrolysis is shown in Figure 5.1.6.

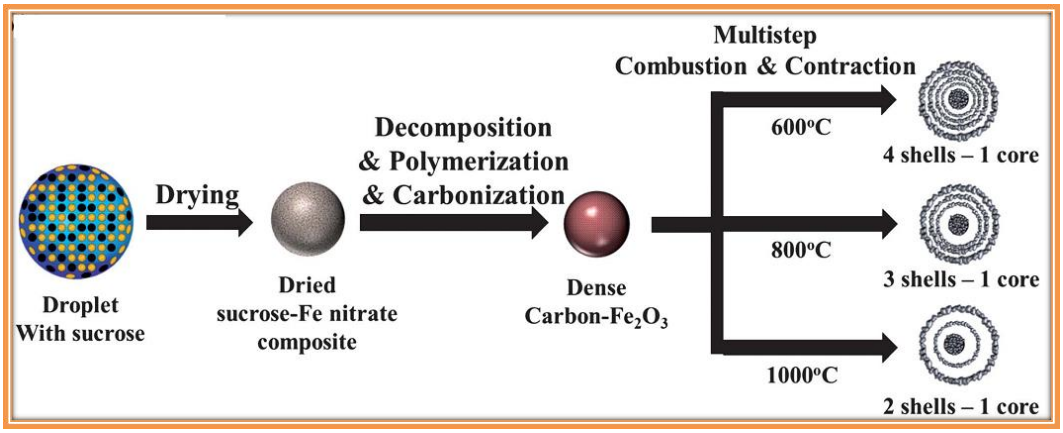

Fig.5.1.6: Schematic representation of synthesis of Fe_2O_3 nanorattles with multiple shells by spray pyrolysis method [19].

Template approach [34]*:* This is the most commonly used approach to synthesize nanorattles. In this approach, first the core material is coated with one or more shell materials and then the middle layer is selectively removed by calcination or etching. The sacrificial layer is other than the core or the shell of interest. In some of the cases, either the core or inner portion of the shell is removed partially. Examples are SnO_2@C [36], SiO_2@TiO_2 [38], and Au@SiO_2 [41].

Ship in a bottle approach [63]: This is an advanced synthetic approach to encapsulate core materials with shells. In this approach, first hollow shells are prepared and then core precursors are introduced into a solution containing the hollow shells. The core material is developed in a shell *via* self-assembly or chemical reactions. Metal, metal oxides, drugs, and polymers are easily encapsulated using this approach. Examples are Au@Pt/Pd [63], and Au@SiO_2 [67].

Galvanic displacement [64]: This strategy is mostly used to synthesize metal alloy nanorattles with different sizes, shapes and morphologies. The basic principle involved

in this method is electrode potential difference between the core and the shell metals; one of the metals acts as the cathode and the other one acts as the anode. The metal with low standard reduction potential acts as sacrificial core and that with high standard potential acts as the shell. The ions of one metal react with other zero valent metal, and galvanic displacement occurs spontaneously in the aqueous solution. Examples are Au@Pt [64], and Ag@Cu [68]. A schematic representation of synthesis of Au@Pt yolk-shell by galvanic displacement is shown in Figure 5.1.7.

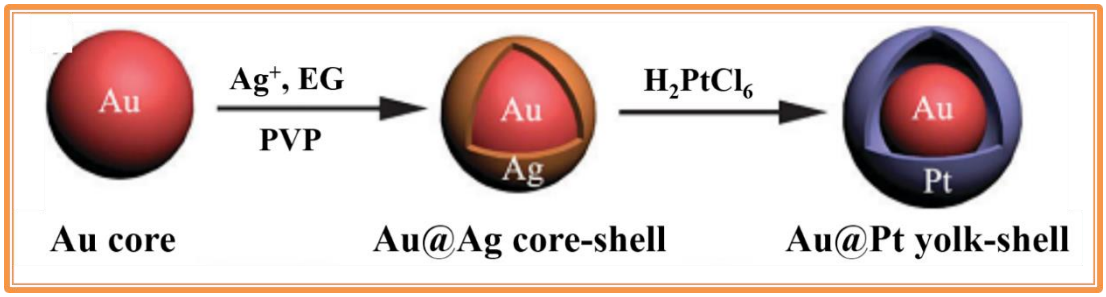

Fig.5.1.7: Schematic representation of synthesis of Ag@Pt yolk-shell using galvanic displacement [64].

Kirkendall reaction [65]: The basic principle involved in this method is diffusion of metal ions at the interface. Diffusion occurs *via* vacancies or ions with different mobilities. The movement of vacancies is from material with low diffusion coefficient to that with high diffusion coefficient. The excess vacancies undergo condensation at the interface and produce void space *via* faster diffusion. Examples are Au@Fe_2O_3 [65], and FePt@CoS_2 [69].

Ostwald ripening [66]: Ostwald ripening is a template-free approach. In Ostwald ripening, smaller crystals with higher solubility dissolve and form larger crystals by minimizing the surface energy. This is a physical phenomenon. During ripening, a void space is generated between the core and the shell. When the core is composed of small nanoparticles and located at the central part of the nanorattle, the process is called as symmetric Ostwald ripening and when the core is located asymmetrically in the nanorattle, the process is termed as asymmetric Ostwald ripening. Examples are Co_3O_4 [59], and Fe_3O_4@Co_3O_4 [62].

In the present study, SiO_2@Co_3O_4 core-shell nanorattles with uniform Co_3O_4 porous shell over the silica core have been successfully synthesized using a self-template route

by the calcination of SiO_2@α-$Co(OH)_2$ at 500 ºC. The shell thickness is controlled by varying the concentration of precursors during the synthesis.

5.1.2 Experimental details

Tetraethyl orthosilicate (98%, ACROS®), ethanol (99.9%, AR), ammonia solution (25%, Rankem, AR), cobaltous nitrate hexahydrate (98%, Rankem, LR), and urea (99.5%, Rankem, AR) were used as received without further purification. The synthesis of SiO_2@Co_3O_4 core-shell nanorattles involves two steps and the details on synthesis is as follows.

5.1.2.1 Synthesis of SiO_2 microspheres

SiO_2 microspheres were synthesized according to StÖber process [70]. The details on the synthesis of SiO_2 microspheres have been discussed in Chapter-3 (Section 3.1.2.1).

5.1.2.2 Synthesis of SiO_2@Co_3O_4 core-shell nanorattles

A schematic representation of the synthesis of SiO_2@Co_3O_4 core-shell nanorattles is shown in Scheme 5.1.1. About 100 mg each of silica microspheres was dispersed in 100 mL of aqueous cobaltous nitrate solution with different concentrations (5 mM, 10 mM and 15 mM) in a 250 mL beaker and sonicated for 3 min. After uniform dispersion of the silica spheres, 5 g of urea was added. The contents were heated at 85 ºC and stirred for 6 h. During the reaction, the colour of the contents changed from pink to violet indicating the formation of α-cobalt hydroxide. After 6 h, the contents were allowed to cool to room temperature, filtered using Whatman® filter paper, washed with Millipore® water several times and dried in an oven for overnight. The obtained products were calcined in a muffle furnace (Nabertherm®) at 500 ºC for 3 hours (heating rate = 2^o min^{-1}), under air, to get the SiO_2@Co_3O_4 core-shell nanorattles. The obtained SiO_2@Co_3O_4 samples were labelled as S1, S2, and S3, corresponding to 5 mM, 10 mM and 15 mM concentrations of cobaltous nitrate used during the preparation of SiO_2@α-$Co(OH)_2$ samples (P1, P2 and P3 corresponding to 5 mM, 10 mM and 15 mM), respectively.

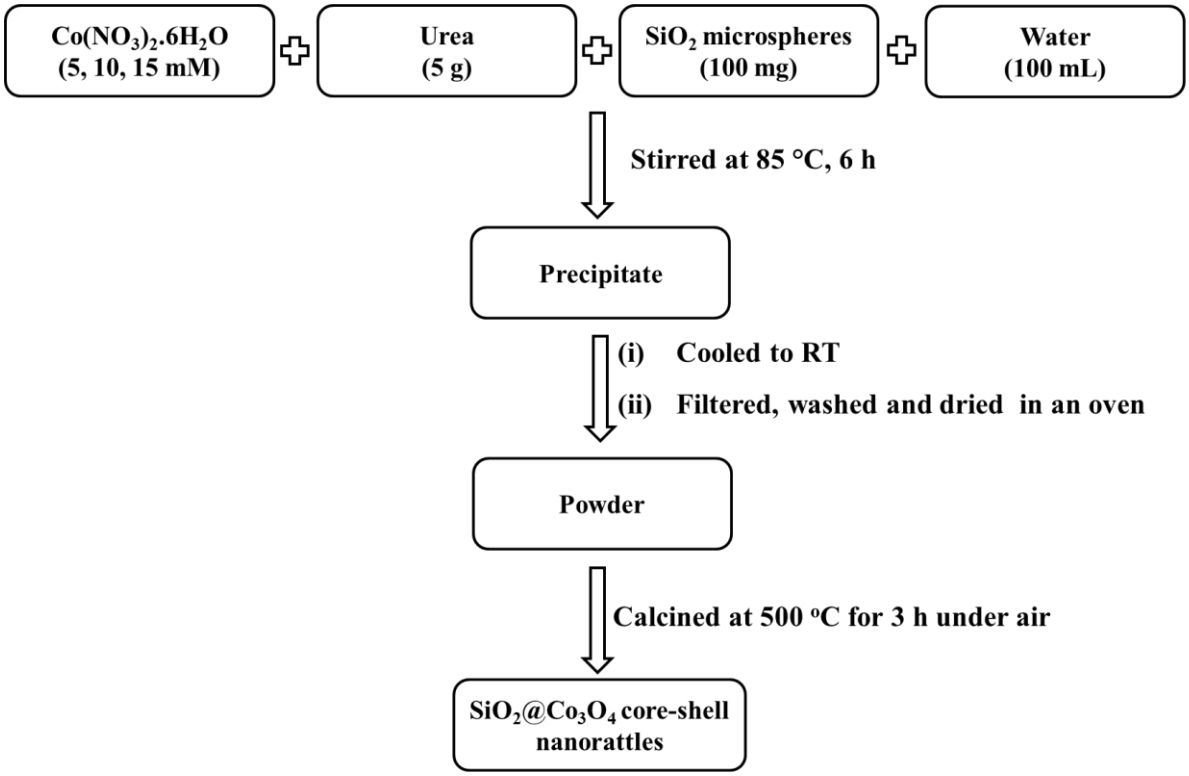

Scheme 5.1.1: Schematic representation of procedure for the synthesis of $SiO_2@Co_3O_4$ core-shell nanorattles.

The synthesized $SiO_2@Co_3O_4$ core-shell nanorattles were characterized using PXRD, FT-IR, TGA, FE-SEM, EDX, TEM and BET analysis. The optical properties were studied using DRS spectroscopy. More details on the experimental techniques have been discussed in Chapter-2.

5.1.3 Results and discussion

5.1.3.1 XRD analysis

The XRD patterns of as prepared SiO_2, α-$Co(OH)_2$, and $SiO_2@\alpha$-$Co(OH)_2$ are shown in Figure 5.1.8. Silica is amorphous. The XRD patterns of α-$Co(OH)_2$, and $SiO_2@\alpha$-$Co(OH)_2$ show raising background which is attributed to X-ray fluorescence since Cu-K_α was used as the X-ray source during the measurements. α-$Co(OH)_2$ shows reflections at 12.18°, 24.37°, 33.11°, 38.08°, 45.98°, 52.05°, and 59.71° which are attributed to (003), (006), (012), (015), (018), (100), and (110) crystal planes (JCPDS file no: 46-0605), respectively [71,72]. The first two planes in the XRD pattern of α-$Co(OH)_2$ are related to d-spacing between the intercalated layers ($d_{(003)} = 2d_{(006)}$) [73]. The XRD patterns of $SiO_2@\alpha$-$Co(OH)_2$ samples show broad peaks due to (003), (006), and (110) planes of α-$Co(OH)_2$ with low crystallinity [74,75]. The

interplanar spacings of α-$Co(OH)_2$ and SiO_2@α-$Co(OH)_2$ samples was calculated using the (003) plane and the value is *ca.* 7.2 Å.

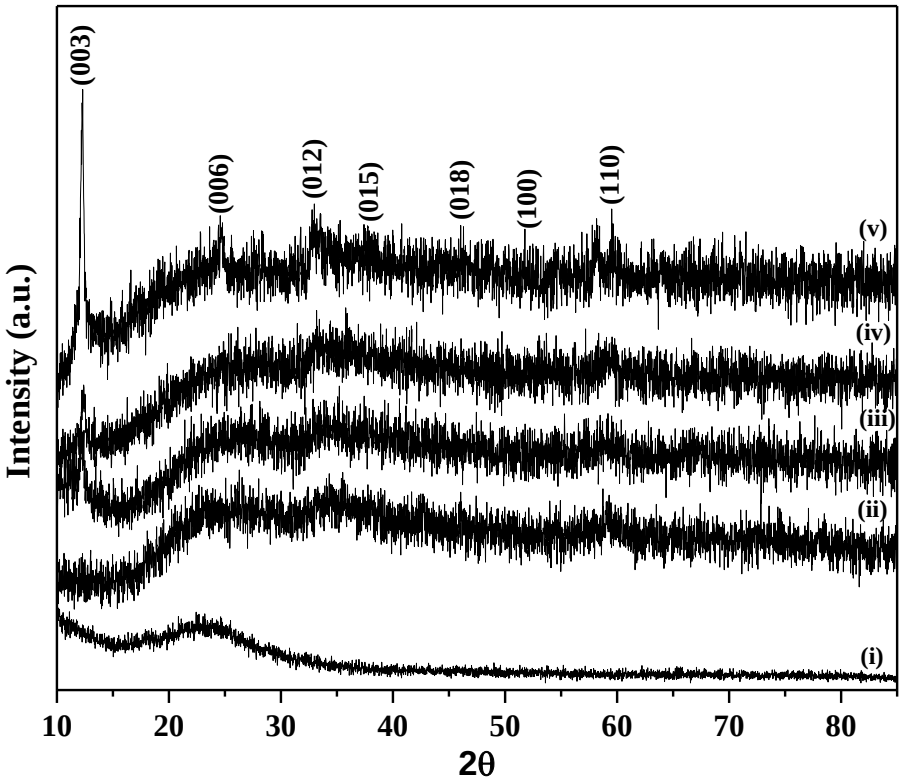

Fig. 5.1.8: XRD patterns of **(i)** as prepared SiO_2, **(ii-iv)** SiO_2@α-$Co(OH)_2$ samples (P1, P2 and P3), and **(v)** α-$Co(OH)_2$.

The XRD patterns of SiO_2, Co_3O_4 and SiO_2@Co_3O_4 samples (S1, S2, and S3) after calcination at 500 ^oC are shown in Figure 5.1.9. Pure Co_3O_4 shows reflections at 19.09^o, 31.26^o, 36.89^o, 38.47^o, 44.77^o, 59.19^o, 65.27^o, 74.26^o, and 78.80^o corresponding to (111), (220), (311), (222), (400), (511), (440), (620), and (622) planes of cubic Co_3O_4 (JCPDS file no. 42-1467), respectively. Since the major component in the core-shell nanorattles is SiO_2 which is amorphous, the XRD patterns for SiO_2@α-$Co(OH)_2$ (Fig. 5.1.8) as well as SiO_2@Co_3O_4 core-shell nanorattles (obtained on calcination) indicate poorly crystallinity. The XRD patterns for α-$Co(OH)_2$ (Figure 5.1.8 (v)) and pure Co_3O_4 (Figure 5.1.9 (v)), however, show that these samples are more crystalline compared to the other samples. Calcination does not improve the crystallinity since it only converts α-$Co(OH)_2$ present on SiO_2 to Co_3O_4 and Co_3O_4 exists as small nanoparticles (as evidenced by the TEM results).

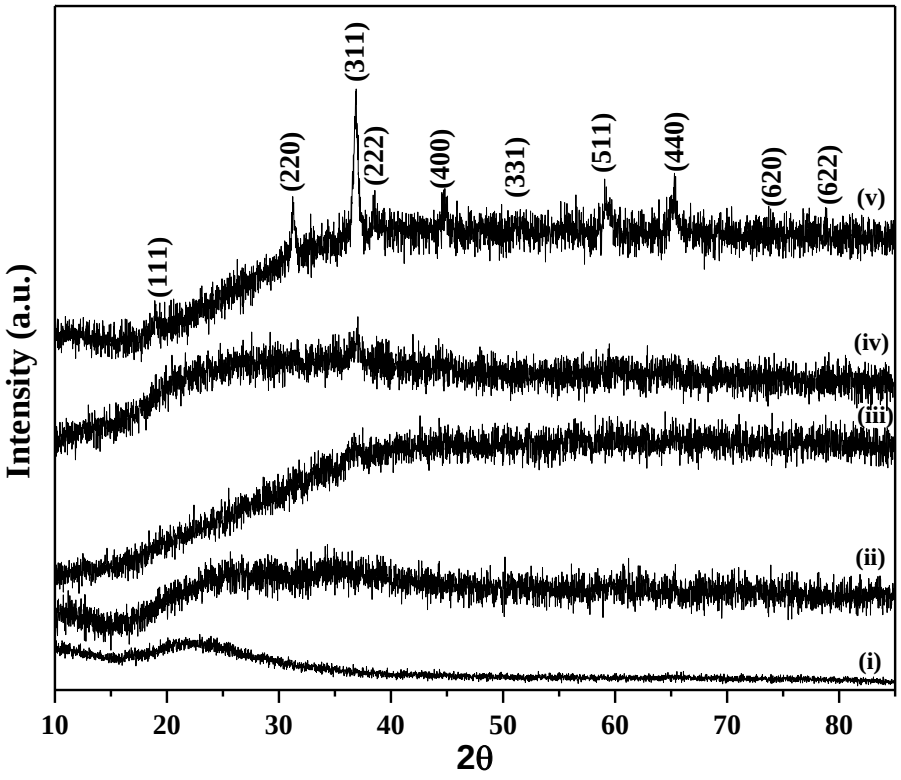

Fig. 5.1.9: XRD patterns of **(i)** SiO_2, **(ii-iv)** $SiO_2@Co_3O_4$ (S1, S2, and S3), and **(v)** Co_3O_4. All the samples were calcined at 500 ^oC.

5.1.3.2 FT-IR spectral studies

FT-IR spectra were recorded for as prepared SiO_2, α-$Co(OH)_2$, and SiO_2@α-$Co(OH)_2$ samples (P1, P2 and P3) (Figure 5.1.10a). The IR spectra for calcined SiO_2, Co_3O_4, and $SiO_2@Co_3O_4$ (S1, S2, and S3) samples are shown in Figure 5.1.10b. All the samples show two bands at about 3430 and 1630 cm^{-1} assigned to stretching and bending vibrations of –OH groups of physisorbed water molecules. All the samples except α-$Co(OH)_2$ and Co_3O_4 show bands at about 1100, 800, and 475 cm^{-1} attributed to asymmetric, symmetric stretching, and bending vibration modes of Si–O–Si. Pure SiO_2 shows a characteristic band at 950 cm^{-1} due to Si–OH group [70]. The SiO_2@α-$Co(OH)_2$ samples and α-$Co(OH)_2$ show IR bands at 2235 and 1387 cm^{-1}, attributed to stretching frequencies of NCO^-, and NO_3^-, respectively. This indicates the presence of NCO^-, and NO_3^- in between the layers [73,76]. All the samples except SiO_2 show a band at 1023 cm^{-1} attributed to the deformation mode of –OH group [77]. The α-$Co(OH)_2$ and SiO_2@α-$Co(OH)_2$ samples show a band at about 660 cm^{-1} attributed to Co–OH vibration. Pure Co_3O_4 shows two characteristic bands attributed to Co(II)–O stretching

when Co^{2+} ions are in tetrahedral coordination and Co(III)–O stretching when Co^{3+} ions are in octahedral coordination [76]; SiO_2@Co_3O_4 (S1) shows IR bands at 667 and 560 cm^{-1}, sample S2 shows bands at 667 and 576 cm^{-1}, and sample S3 shows bands at 664 and 568 cm^{-1}. In summary, FT-IR results show evidence for the presence of NCO^-, and NO_3^- ions in α-$Co(OH)_2$, and SiO_2@α-$Co(OH)_2$ and the presence of Co_3O_4 in the SiO_2@Co_3O_4 samples.

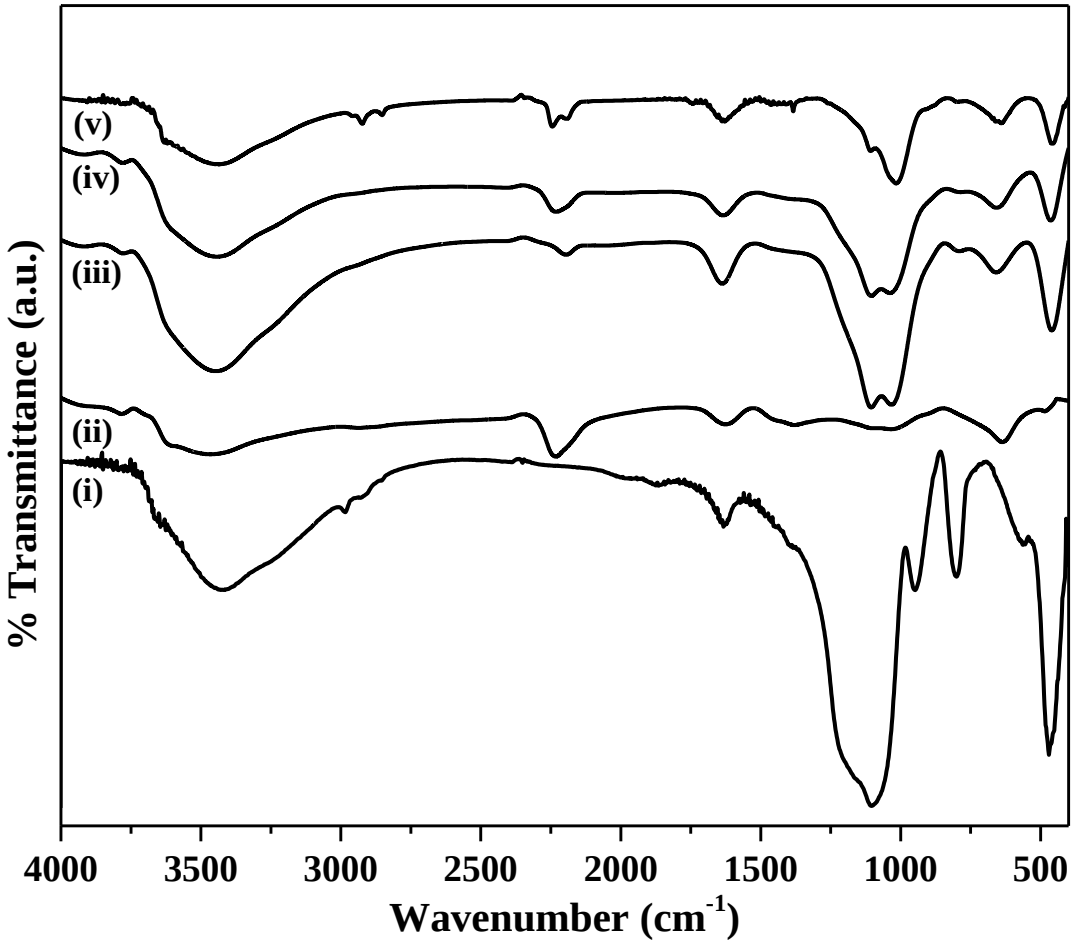

(a)

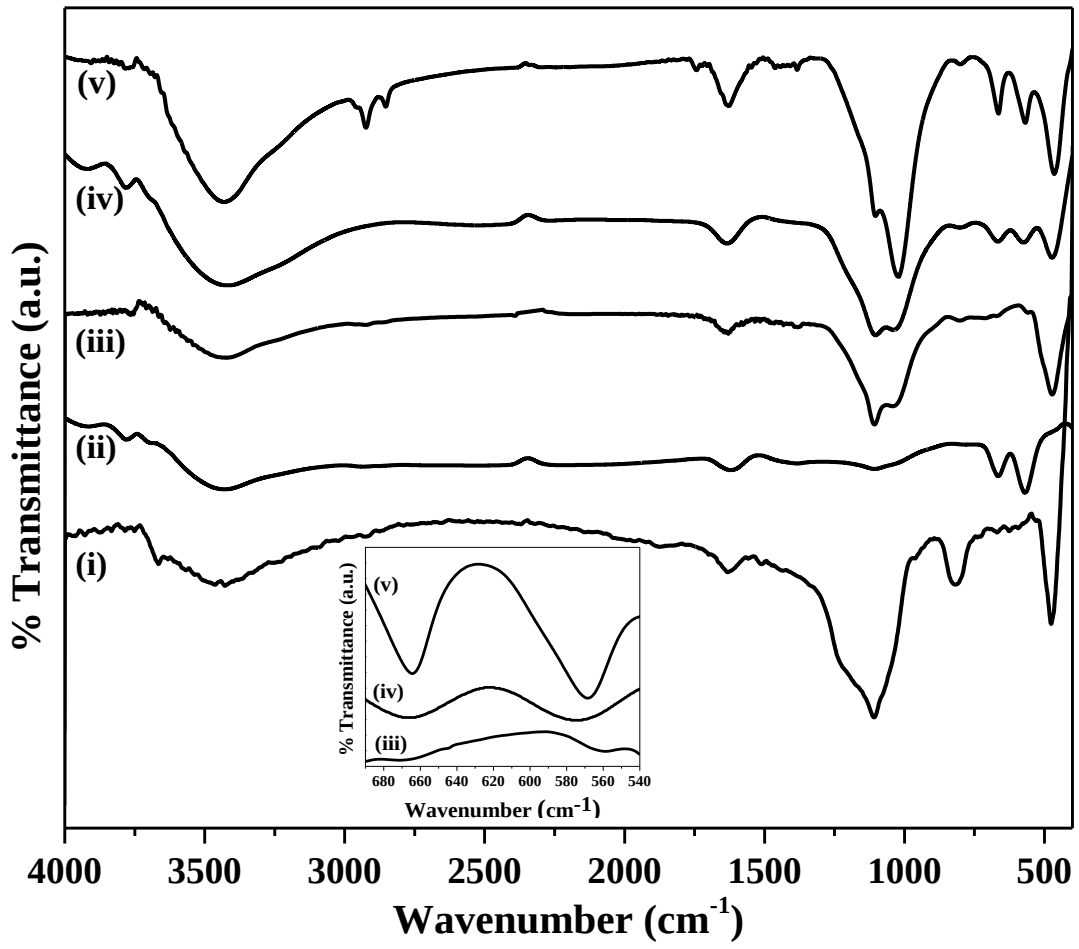

(b)

Fig. 5.1.10 (a) FT-IR spectra of **(i)** as prepared SiO_2, **(ii)** α-$Co(OH)_2$, and **(iii-v)** SiO_2@α-$Co(OH)_2$ samples (P1, P2 and P3) and **(b)** FT-IR spectra of **(i)** SiO_2, **(ii)** Co_3O_4, and **(iii-v)** SiO_2@Co_3O_4 (S1, S2, and S3) samples after calcination at 500 ^oC. The inset shows the magnified view of IR bands for SiO_2@Co_3O_4 samples (S1, S2, and S3).

5.1.3.3 TGA analysis

The thermogravimetric analysis (TGA) patterns of as prepared SiO_2, α-$Co(OH)_2$, and SiO_2@α-$Co(OH)_2$ samples are shown in Figure 5.1.11. The as prepared SiO_2 shows a total weight loss of 12.5 % upto 1000 ^oC with two weight loss steps. The first step from 35 ^oC to 170 ^oC (weight loss = 5 %) is attributed to the loss of physisorbed water molecules. The second weight loss from 350 ^oC to 660 ^oC (wt. loss ~ 7.5 %) is attributed to the dehydroxylation of surface hydroxyl groups [78]. The α-$Co(OH)_2$ shows a total weight loss of about 35 % upto 1000 ^oC in three steps. The weight loss upto 150 ^oC (~ 2.5 %) is related to the loss of physisorbed water molecules. The major weight loss (~

28.3 %) observed between 220 and 400 ^{o}C is attributed to the loss of intercalated water molecules, anions, and dehydroxylation of α-$Co(OH)_2$ accompanied by its conversion to spinel Co_3O_4 [79]. Another weight loss (~ 4.2 %) between 940 and 985 ^{o}C is associated with the thermal decomposition of Co_3O_4 to CoO [80]. The SiO_2@α-$Co(OH)_2$ samples (P1, P2 and P3) show weight loss features due to both SiO_2 and α-$Co(OH)_2$ and the overall weight loss values are 25.5 %, 25.2 % and 19.5 %, respectively. The SiO_2@α-$Co(OH)_2$ samples (P1 and P2) show major weight loss (~ 12.5 %) between 30 and 150 ^{o}C, while SiO_2@α-$Co(OH)_2$ sample (P3) shows a weight loss of about 4.5 % in the same temperature range. Sample P3 (SiO_2@α-$Co(OH)_2$ prepared using 15 mmol cobalt nitrate) shows different weight loss features compared to P1 and P2 (SiO_2@α-$Co(OH)_2$ samples, prepared using 5 mmol and 10 mmol cobalt nitrate, respectively). It was found from SEM studies (see Figure 5.1.12e) that sample P3 before calcination consists of SiO_2@α-$Co(OH)_2$ as well as free α-$Co(OH)_2$ particles. Sample P3 (SiO_2@α-$Co(OH)_2$) shows less weight loss below 150 ^{o}C (~ 4.5 %) similar to α-$Co(OH)_2$ (~ 2.5 %). The low weight loss below 150 ^{o}C in these samples (α-$Co(OH)_2$ and P3) is attributed to strong interaction between the surface hydroxyl groups which delay the dehydroxylation process [81,82]. The low weight loss at temperature below 150 ^{o}C leads to an overall low weight loss in P3. TGA results indicate that the complete formation of spinel Co_3O_4 occurs at about 500 ^{o}C by the loss of intercalated water molecules, anions and dehydroxylation of surface hydroxyl groups of α-$Co(OH)_2$.

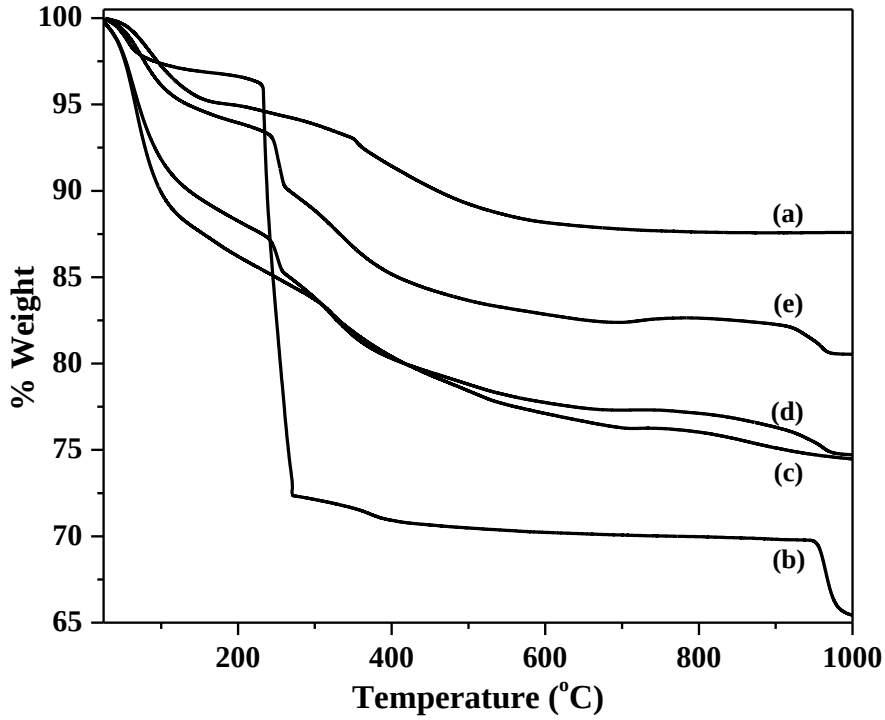

Fig. 5.1.11: TGA patterns of **(a)** as prepared SiO_2, **(b)** α-$Co(OH)_2$, and **(c-e)** SiO_2@α-$Co(OH)_2$ samples (P1, P2 and P3).

5.1.3.4 FE-SEM studies

Morphological studies of the synthesized samples were first investigated using FE-SEM. The FE-SEM images of SiO_2, α-$Co(OH)_2$, and SiO_2@α-$Co(OH)_2$ samples (P1, P2 and P3, before calcination) are shown in Figure 5.1.12 (a-e). Pure silica shows uniform spherical particles and the diameter of the spheres is 300 ± 20 nm; the average diameter of particles and errors were calculated using about ten particles. α-$Co(OH)_2$ consists of sheets and clusters. The SiO_2@α-$Co(OH)_2$ (P1 and P2) show that the silica spheres are completely covered with α-$Co(OH)_2$ sheets (petals) to form flower-like morphology. But in the case of SiO_2@α-$Co(OH)_2$ sample (P3), the SiO_2 spheres are covered with α-$Co(OH)_2$ sheets and some uncoated particles of α-$Co(OH)_2$ can also be noticed.

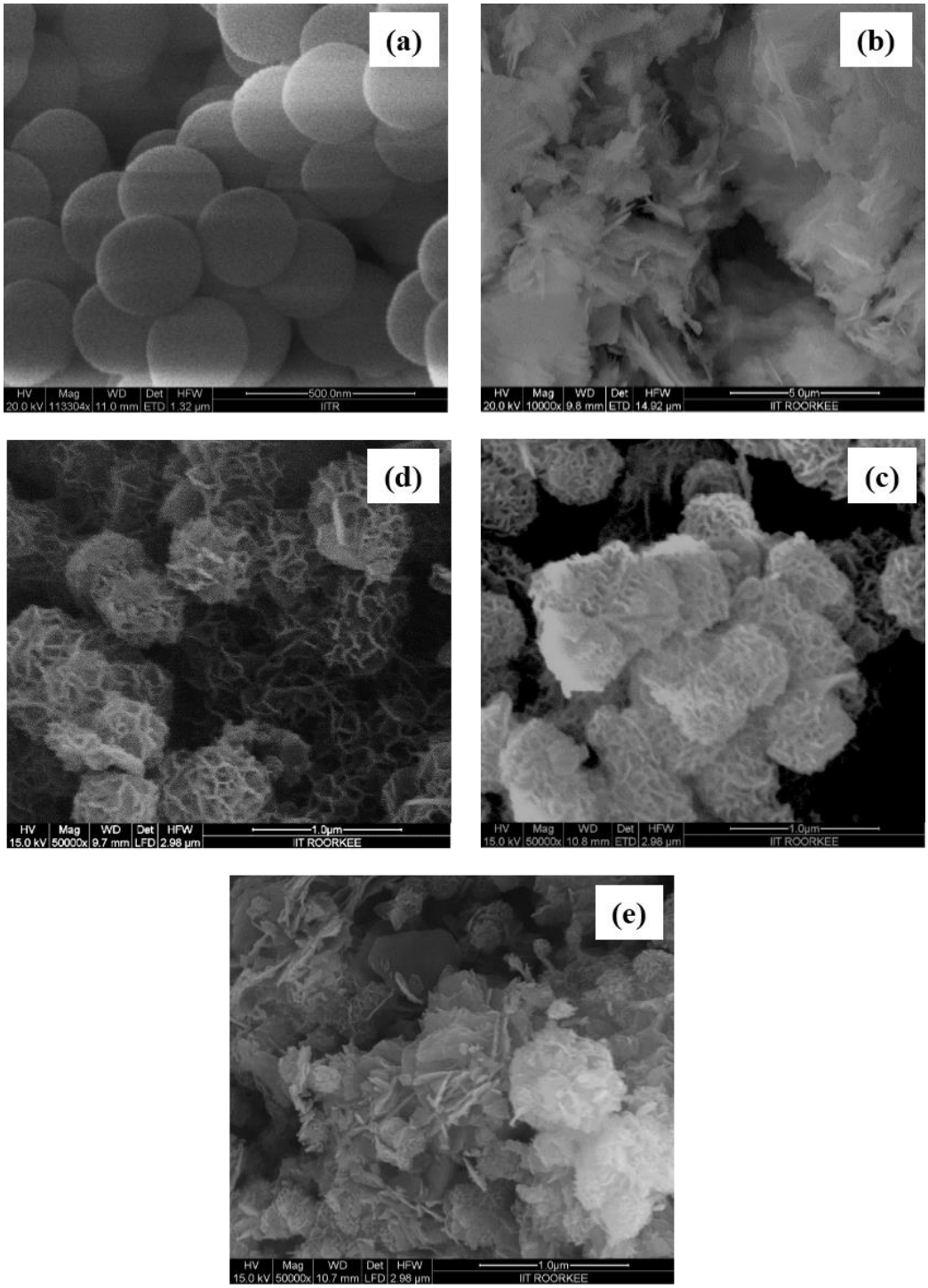

Fig. 5.1.12: FE-SEM images of **(a)** as prepared SiO_2 **(b)** α-$Co(OH)_2$, and (**c-e)** SiO_2@α-$Co(OH)_2$ samples (P1, P2 and P3).

The FE-SEM images of Co_3O_4 and SiO_2@Co_3O_4 samples (i.e. after calcination) are shown in Figure 5.1.13 (a-d). Pure Co_3O_4 shows particles with petals-like morphology. The SiO_2@Co_3O_4 samples (S1 and S2) show uniform shell of Co_3O_4 over the silica core but sample S3 shows coating of Co_3O_4 shell on the SiO_2 spheres with some extra

uncoated particulates of Co_3O_4. Based on UV-Vis transmittance measurements, it was found that the dispersion of the core-shell particles in water is stable for at least 6 h. It was also found that the powder obtained after drying the particles can be redispersed effectively.

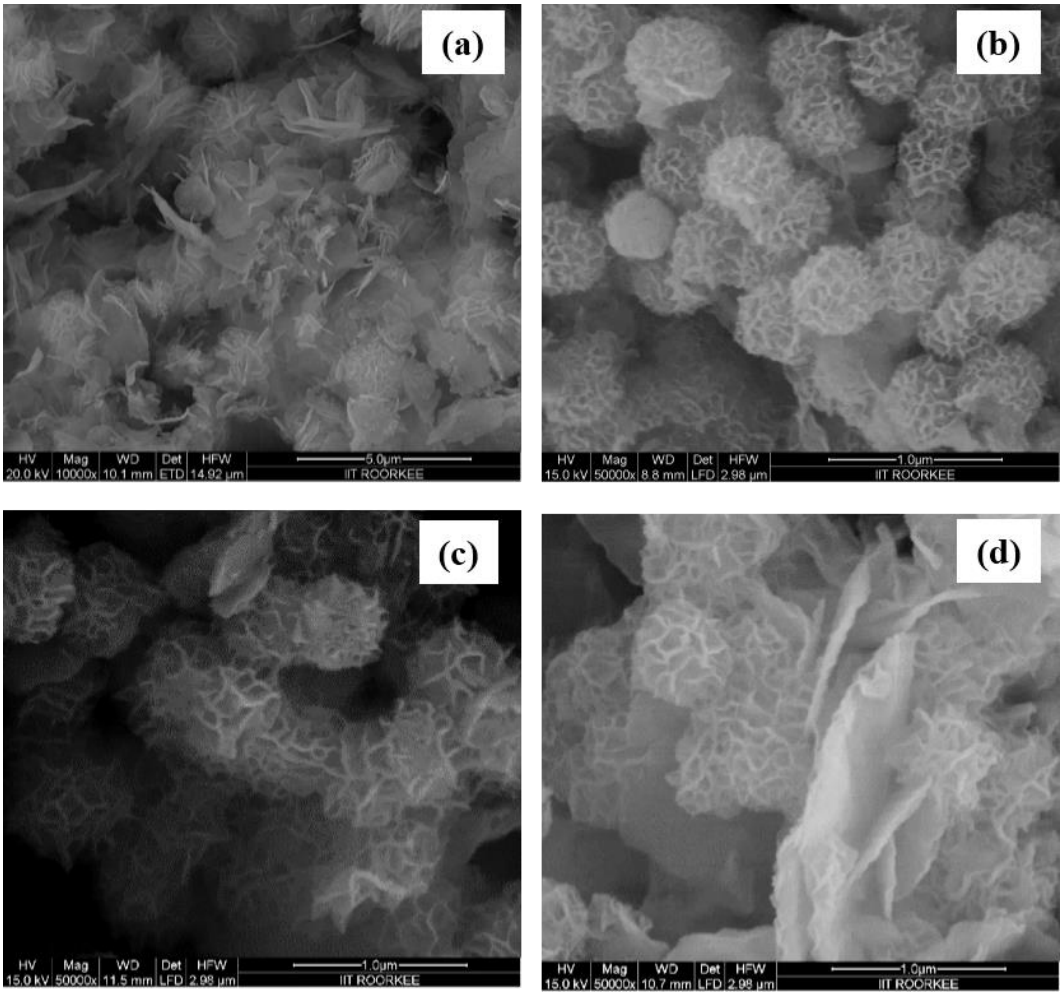

Fig. 5.1.13: FE-SEM images of **(a)** Co_3O_4, and **(b-d)** $SiO_2@Co_3O_4$ samples (S1, S2, and S3). All the samples were calcined at 500 ^oC.

5.1.3.5 SEM-EDX analysis

The elemental composition of the $SiO_2@\alpha$-$Co(OH)_2$ samples (P1, P2 and P3) and $SiO_2@Co_3O_4$ core-shell nanorattles (S1, S2, and S3) was determined using EDX analysis (Table 5.1.1) and EDX spectra of $SiO_2@\alpha$-$Co(OH)_2$ core-shell nanorattles are shown in Figure 5.1.14 and EDX spectra of $SiO_2@Co_3O_4$ core-shell nanorattles are shown in Figure 5.1.15. The EDX results confirm the presence of silicon, oxygen and cobalt in the $SiO_2@Co_3O_4$ core-shell nanorattles as well as the $SiO_2@\alpha$-$Co(OH)_2$ samples. Increase in the weight percent of cobalt in the core-shell samples is observed

according to the concentration of cobaltous nitrate used during the synthesis of SiO_2@α-$Co(OH)_2$ samples (5 mM, 10 mM, and 15 mM).

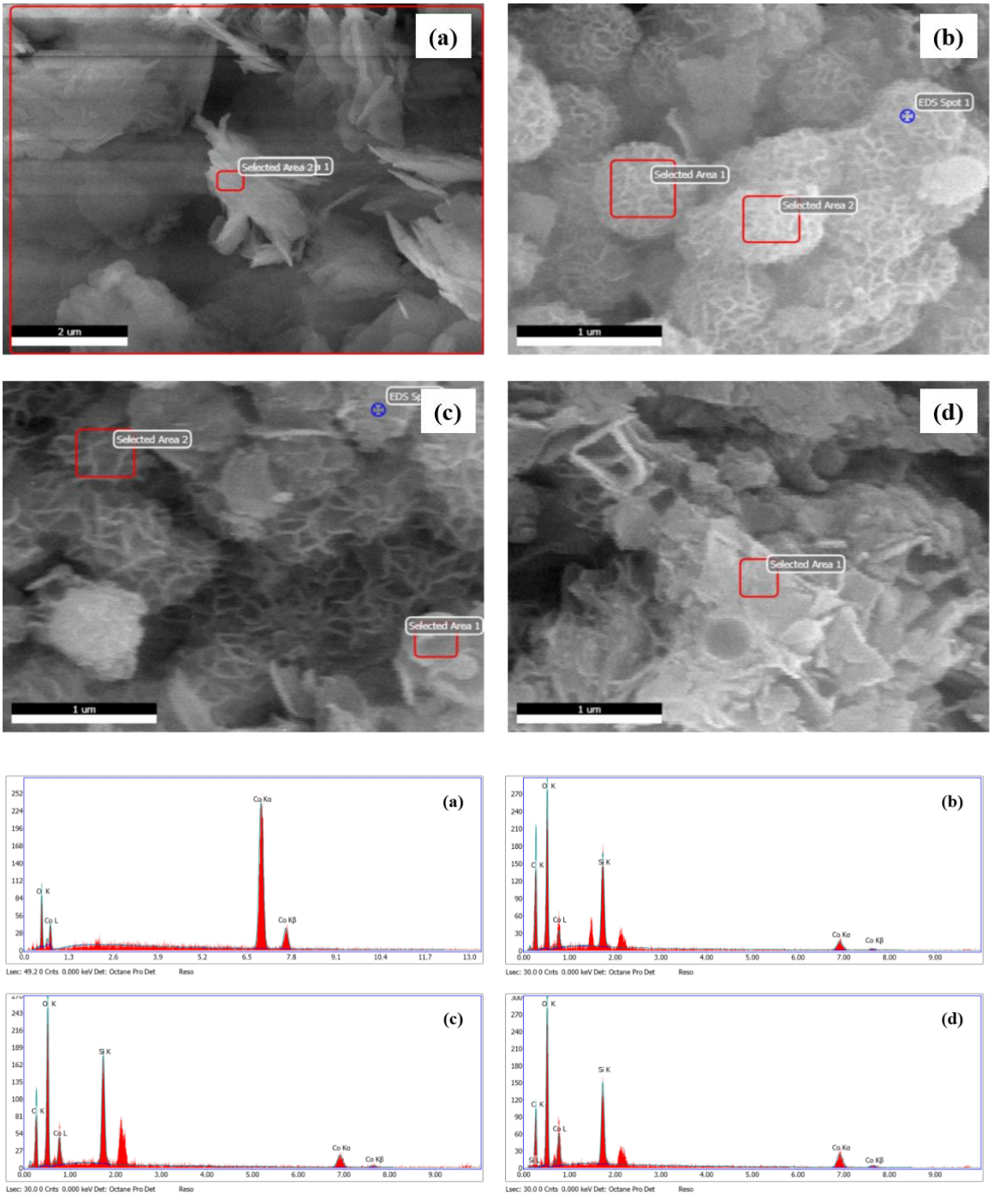

Fig. 5.1.14: EDX spectra of **(a)** α-$Co(OH)_2$ and **(b-d)** SiO_2@α-$Co(OH)_2$ core-shell nanorattles (P1, P2 and P3).

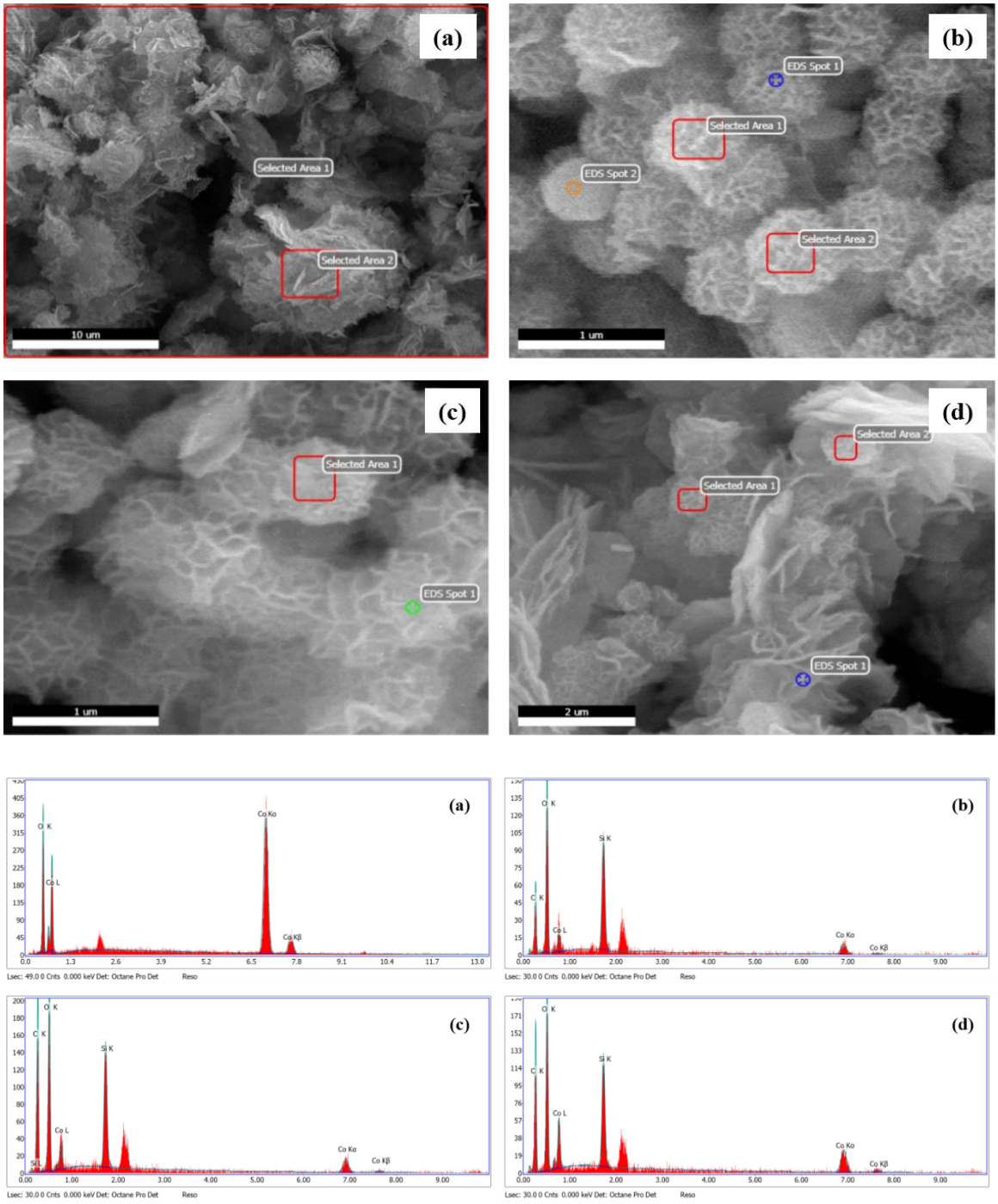

Fig. 5.1.15: EDX spectra of **(a)** Co_3O_4 and **(b-d)** $SiO_2@Co_3O_4$ core-shell nanorattles (S1, S2 and S3).

Table 5.1.1: Elemental composition (Wt. %) of silicon, cobalt, and oxygen in the SiO_2@α-$Co(OH)_2$ samples (P1, P2 and P3) and the SiO_2@Co_3O_4 core-shell nanorattles (S1, S2 and S3).

Sample name	Weight percent		
	Si	Co	O
SiO_2	28.0 ± 1.4	-	32.5 ± 3.5
α–$Co(OH)_2$	-	93.4 ± 1.5	6.6 ± 1.5
SiO_2@α-$Co(OH)_2$ (P1)*	15.2 ± 1.9	17.6 ± 3.1	37.4 ± 2.3
SiO_2@α-$Co(OH)_2$ (P2)*	13.4 ± 0.2	21.2 ± 2.6	35.1 ± 1.2
SiO_2@α-$Co(OH)_2$ (P3)*	10.9 ± 0.5	23.6 ± 1.5	38.9 ± 1.3
Co_3O_4	-	83.6 ± 0.7	16.4 ± 0.3
SiO_2@Co_3O_4 (S1)	11.1 ± 0.6	14.0 ± 0.5	37.9 ± 0.7
SiO_2@Co_3O_4 (S2)	11.4 ± 0.2	16.0 ± 1.0	34.8 ± 0.1
SiO_2@Co_3O_4 (S3)	9.7 ± 1.1	27.9 ± 0.3	30.3 ± 0.2

*The concentrations of $Co(NO_3)_2.6H_2O$ used during the preparation of SiO_2@α-$Co(OH)_2$ samples P1, P2 and P3 were 5 mM, 10 mM and 15 mM, respectively.

5.1.3.6 TEM studies

The TEM images of SiO_2, Co_3O_4 and SiO_2@Co_3O_4 core-shell samples (S1 and S2) are shown in Figure 5.1.16. TEM analysis was not carried out for the SiO_2@Co_3O_4 sample S3 since the SEM analysis on this sample indicated the presence of uncoated α-$Co(OH)_2$ particles in the SiO_2@ α-$Co(OH)_2$ sample (see Figure 5.1.12e). SiO_2 shows uniform spherical particles with a diameter of 300 ± 10 nm. The TEM image indicates the nanosized nature of Co_3O_4 particles (13.7 ± 2.1 nm). The TEM images for the SiO_2@Co_3O_4 samples (S1 and S2) show the core-shell morphology with a void space between the SiO_2 core and the Co_3O_4 shell. These type of structures are referred to as "nanorattles" [83,84]. In addition to the nanorattle morphology, the SiO_2@Co_3O_4 samples show porous hair-like morphology for the Co_3O_4 shell. The measured shell thickness values are 37 ± 3 nm, 63 ± 8 nm, for S1 and S2, respectively. The estimated void space between the core and the shell lies between 40 and 45 nm and 64 and 72 nm for the SiO_2@Co_3O_4 samples S1 and S2, respectively. The thickness of hair-like structure of the Co_3O_4 shell is 27 ± 3 nm and 45 ± 5 nm for the samples S1 and S2, respectively.

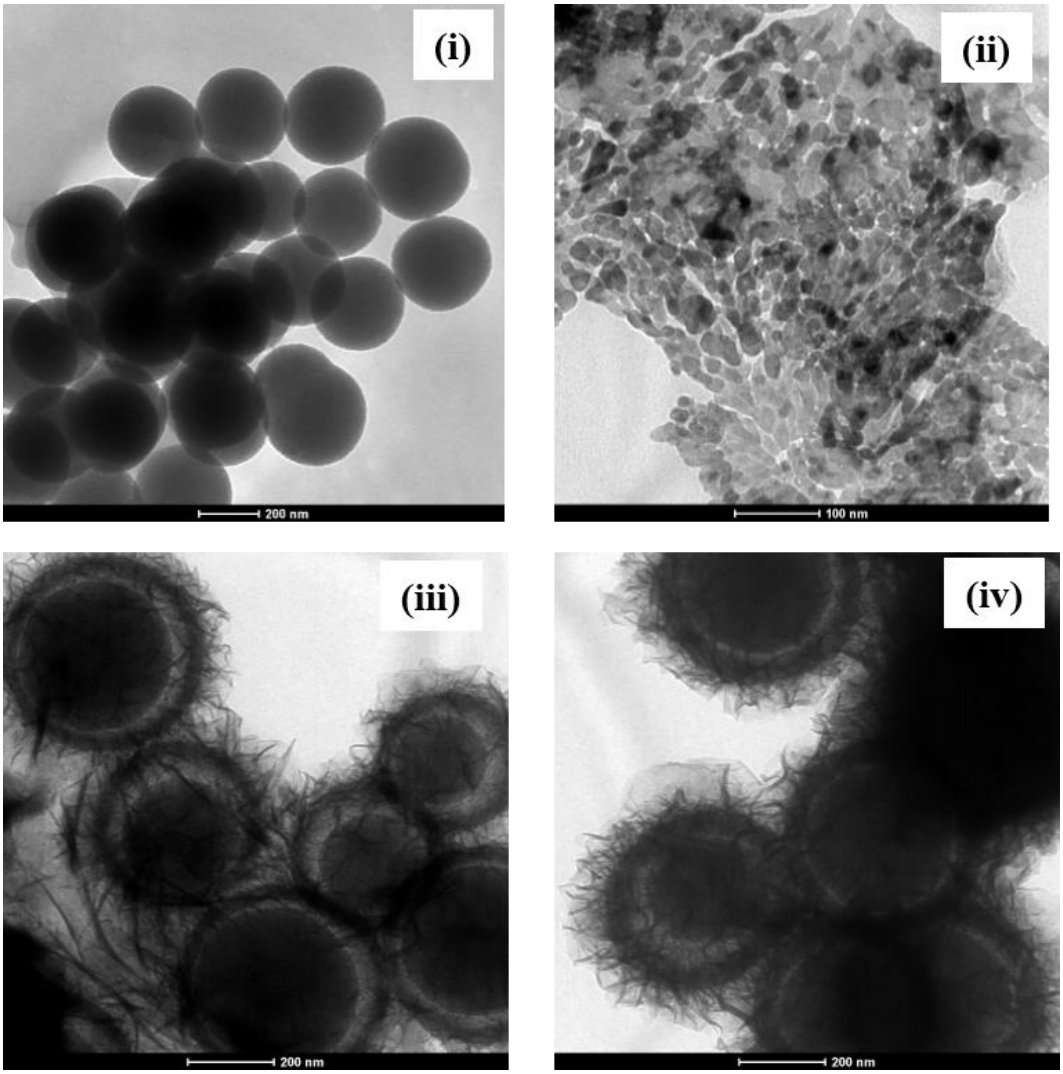

Fig. 5.1.16: TEM images of **(i)** SiO_2, **(ii)** Co_3O_4, and **(iii and iv)** $SiO_2@Co_3O_4$ samples (S1, and S2). The images are obtained for all the samples after calcination at 500 ^oC.

The SAED patterns of pure Co_3O_4 and $SiO_2@Co_3O_4$ core-shell nanorattles (S1 and S2) are shown in Figure 5.1.17. The SAED patterns show spots/rings indicating polycrystalline nature of the samples. The SAED patterns could be indexed to (111), (220), (311), (400), (511), and (440) planes of cubic Co_3O_4. Pure Co_3O_4 exhibits stronger electron diffraction compared to the $SiO_2@Co_3O_4$ nanorattles (S1 and S2). The less crystalline nature of $SiO_2@Co_3O_4$ samples compared to pure Co_3O_4 suggests that the Co_3O_4 (shell) particles formed on the silica are smaller in size.

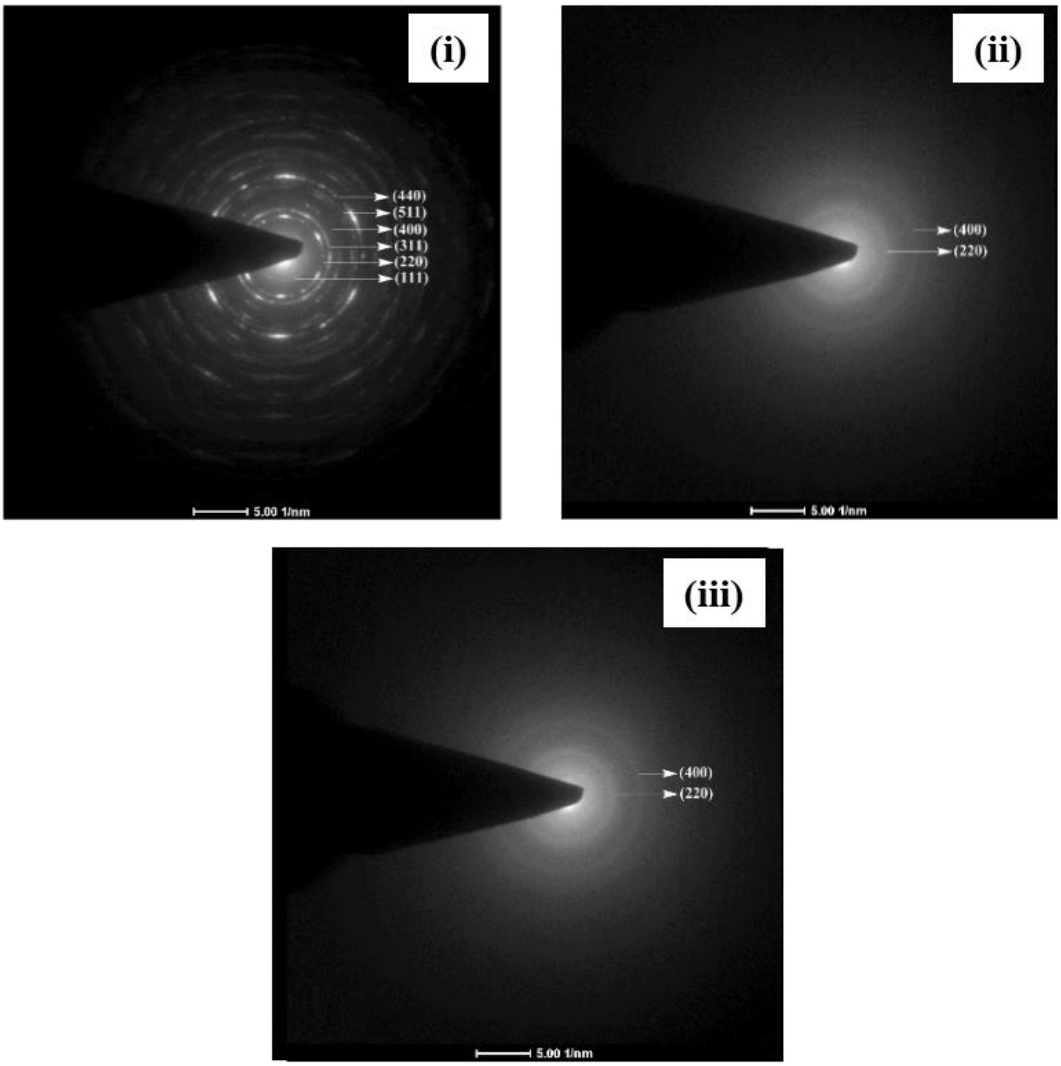

Fig. 5.1.17: SAED patterns of **(i)** Co_3O_4, and **(ii and iii)** $SiO_2@Co_3O_4$ core-shell nanorattles (S1, and S2).

5.1.3.7 BET surface area analysis

The specific surface area of pure SiO_2, Co_3O_4 and the $SiO_2@Co_3O_4$ nanorattles (S1 and S2) were measured using Brunauer-Emmett-Teller (BET) measurements using nitrogen gas physisorption. Pure SiO_2 and Co_3O_4 possess surface area of 34.2 and 46.5 m^2/g, respectively. The $SiO_2@Co_3O_4$ nanorattles (S1 and S2) possess surface area of about 279 m^2/g and 268 m^2/g, respectively. The higher surface area of $SiO_2@Co_3O_4$ core-shell nanorattles (S1 and S2) compared to pure Co_3O_4 and SiO_2 is attributed to the nanorattle morphology of $SiO_2@Co_3O_4$ (S1 and S2). The nanorattles consist of porous shell along with interior void space between the core and the shell.

5.1.3.8 UV-Visible diffuse reflectance spectroscopy (DRS) studies

The optical properties of pure Co_3O_4 and $SiO_2@Co_3O_4$ nanorattles (S1 and S2) were studied using UV-Vis diffuse reflectance spectroscopy (Figures 5.1.18a and 5.1.18b). All the samples exhibit two broad bands in the region 420-450 and 700-750 nm. Co_3O_4 shows absorption bands at 745 and 450 nm while $SiO_2@Co_3O_4$ samples (S1 and S2) show absorption bands at about 705 and 425 nm. The band at 745 nm in pure Co_3O_4 and 705 nm in $SiO_2@Co_3O_4$ samples (S1 and S2) are due to $O^{2-} \rightarrow Co^{3+}$ charge transfer transition and the band at 450 nm in pure Co_3O_4 and 425 nm in $SiO_2@Co_3O_4$ samples (S1 and S2) are due to $O^{2-} \rightarrow Co^{2+}$ charge transfer transition [53,85]. Both the $SiO_2@Co_3O_4$ samples (S1 and S2) show blue shift of about 40 nm with respect to the 745 nm band in pure Co_3O_4 and 25 nm with respect to the 450 nm band in pure Co_3O_4. The blue shift in the case of $SiO_2@Co_3O_4$ samples (S1 and S2) is attributed to quantum confinement effect and smaller particle size of Co_3O_4 [53,85]. Co_3O_4 is a p-type semiconductor and the band gap energies are calculated using the Tauc equation which can be expressed as $\alpha h\nu = k\,(h\nu - E_g)^n$, where E_g represents the band gap, $h\nu$ is the photon energy, k is the constant, α is the Kubelka-Munk function and n is dependent on the type of transition involved. In the present case, n = 1/2 gives the best fit for $(\alpha h\nu)^{1/n}$ versus $h\nu$ plots suggesting direct allowed transition in Co_3O_4. The calculated band gap energy (E_g) values for Co_3O_4 is 1.70 and 2.43 eV and for the $SiO_2@Co_3O_4$ samples, the values were 1.72 and 2.52 eV (S1) and 1.74 and 2.57 eV (S2). The band gap values for bulk Co_3O_4 are 1.48 and 2.19 eV [86]. The obtained band gap values for $SiO_2@Co_3O_4$ samples (S1 and S2) are in good agreement with the previously reported values for Co_3O_4 nanoparticles [53,87].

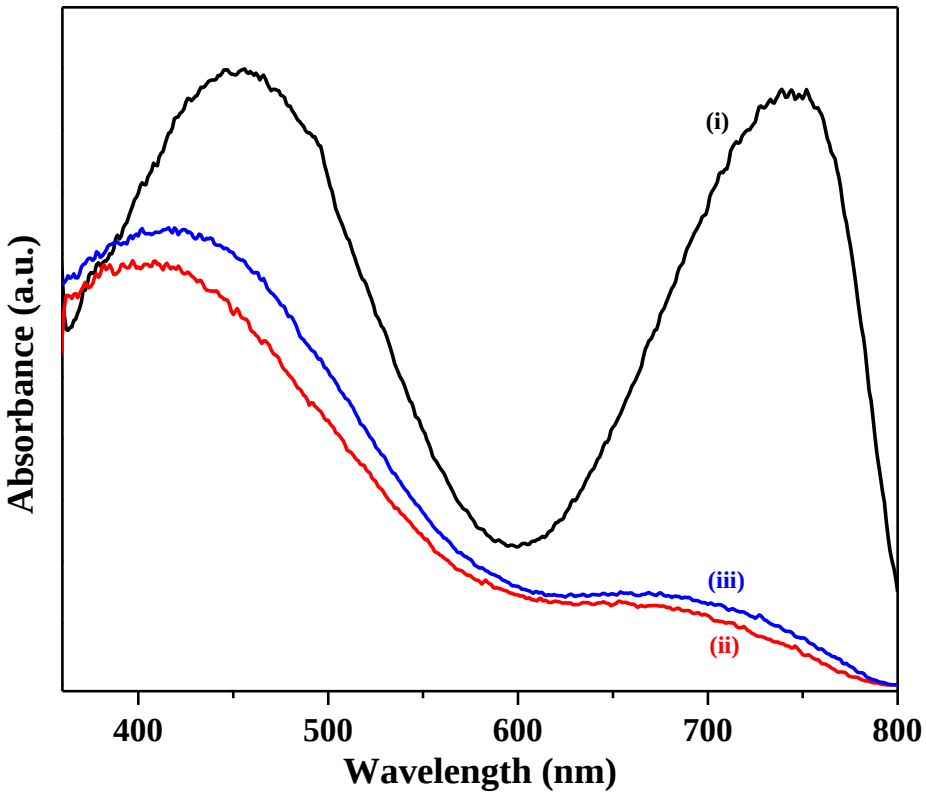

(a)

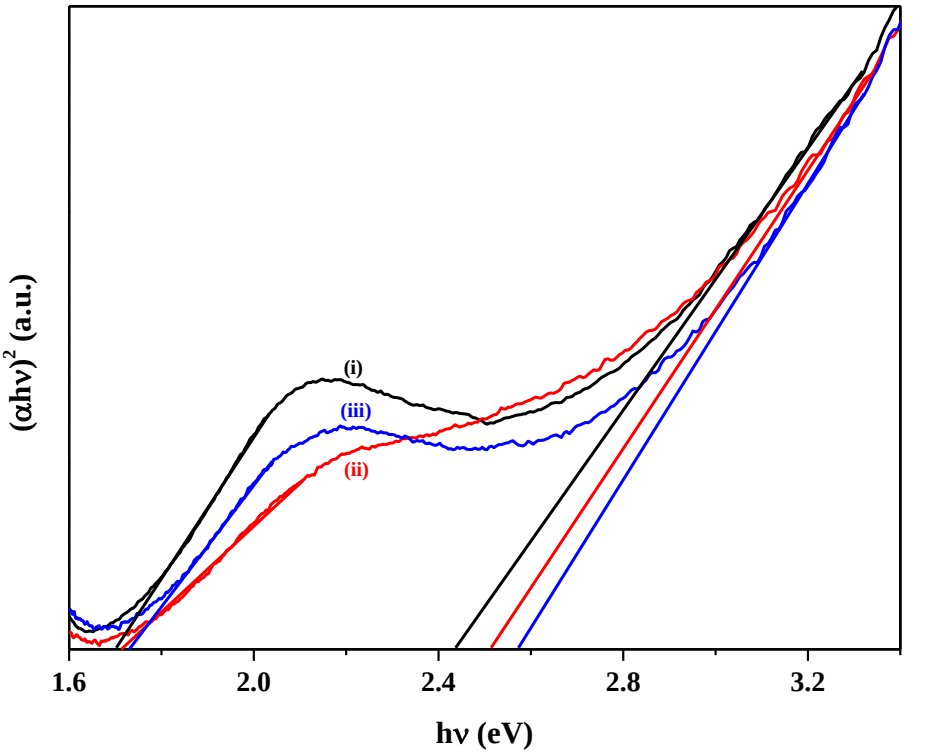

(b)

Fig. 5.1.18: (a) UV-Visible DRS spectra of **(i)** Co_3O_4, and **(ii and iii)** $SiO_2@Co_3O_4$ core-shell nanorattles (S1 and S2) and **(b)** Tauc plots of **(i)** Co_3O_4, and **(ii and iii)** $SiO_2@Co_3O_4$ core-shell nanorattles (S1 and S2).

5.1.4 Proposed mechanism for the formation of SiO_2@Co_3O_4 core-shell nanorattles

For the formation of Co_3O_4 shell on the SiO_2 core, the following mechanism is proposed based on the experimental results (Scheme 5.1.2). It is proposed that an adsorption-nucleation-coalescence-anisotropic growth-self-assembly occurs [88,89]. At first, Co^{2+} ions from the solution are adsorbed on the surface of SiO_2 through electrostatic interaction. Urea decomposes to produce NH_3 and CO_2 and the released NH_3 readily reacts with the available Co^{2+} ions on the surface of SiO_2 to form a complex (i.e. $Co(NH_3)_y$; $y \leq 2$) which reduces the concentration of free Co^{2+} ions in the solution. After attaining the optimum temperature (e.g. 85 ^oC), OH^- ions are steadily produced through the hydrolysis of urea, which is favourable for nucleation and formation of α-$Co(OH)_2$ on the surface of SiO_2 spheres based on the coalescence mechanism. The α-$Co(OH)_2$ further undergoes Ostwald ripening to produce flower-like hierarchical α-$Co(OH)_2$ on the surface of SiO_2 [89].

Yan et al. and Yuan et al. have explained the formation of hierarchical 3D metal hydroxide flower-like structures based on thermodynamics [88,89]. If one considers a single nanoplatelet of α-$Co(OH)_2$, the surface energy is very high. In order to reduce the overall surface energy, the formed ultrathin α-$Co(OH)_2$ nanoplatelets tend to aggregate which decreases the surface energy by reducing the unsatisfied bonds at the exposed areas. The formed thinner plates self-assemble spontaneously based on the coalescence mechanism to produce thicker plates. The pH would decrease and Ostwald ripening would dominate leading to flower-like hierarchical α-$Co(OH)_2$ on the surface of SiO_2. In the final step, calcination of SiO_2@α-$Co(OH)_2$ in air at 500 ^oC for 3 h leads to the formation of SiO_2@Co_3O_4 core-shell nanorattles through self-template route retaining its 3D hierarchical flower-like morphology.

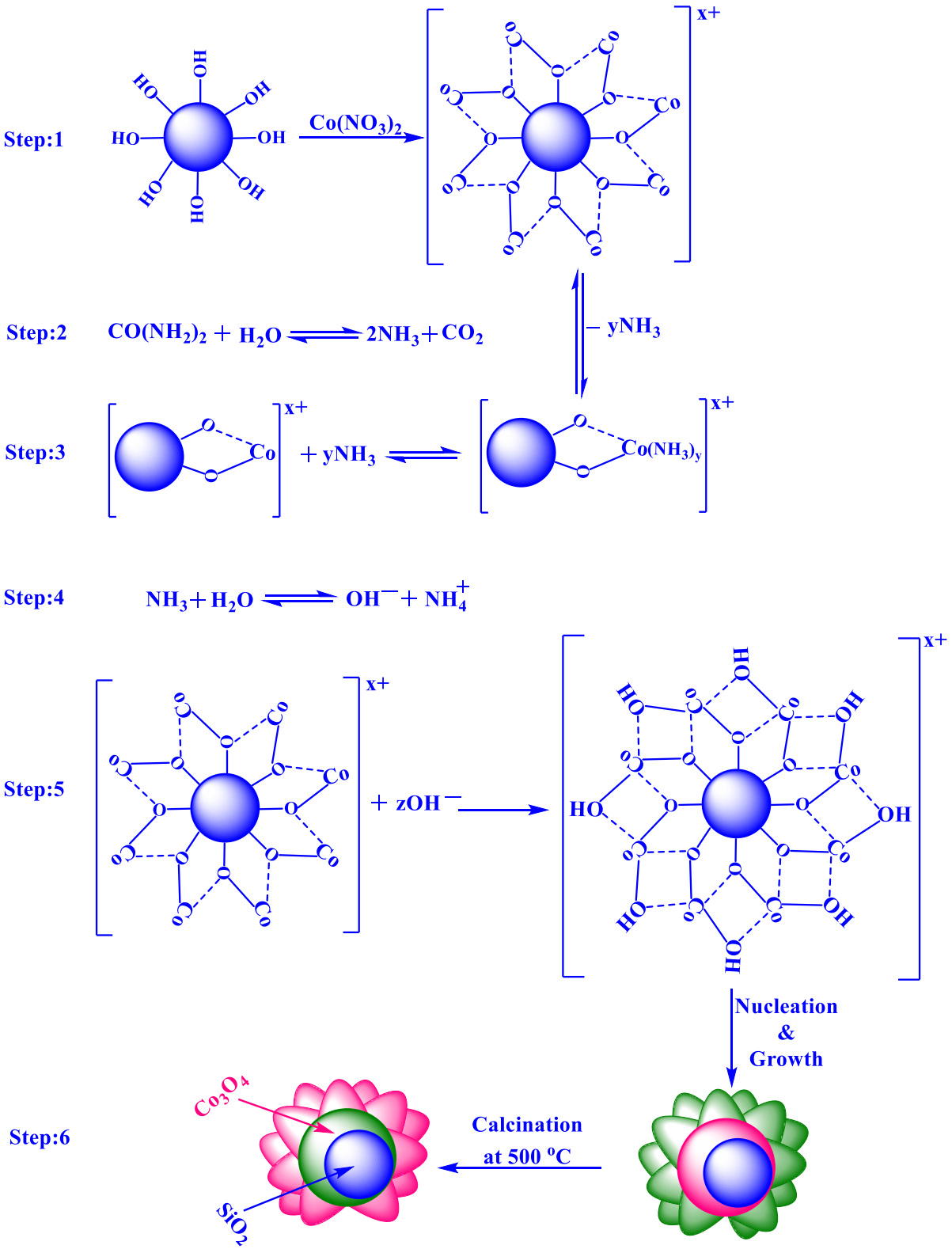

Scheme 5.1.2: Proposed mechanism for the formation of SiO_2@Co_3O_4 core-shell nanorattles.

To understand the mechanism of formation of nanorattle structures further, time dependent TEM analysis (Figure 5.1.19) was performed at different time intervals for

SiO_2@α-$Co(OH)_2$ (P1) (e.g. 2 h, 4 h and 6h) and SiO_2@Co_3O_4 (S1) (e.g. 1 h and 3 h). An overview image for the formation of SiO_2@Co_3O_4 core-shell nanorattles is shown in Scheme 5.1.3.

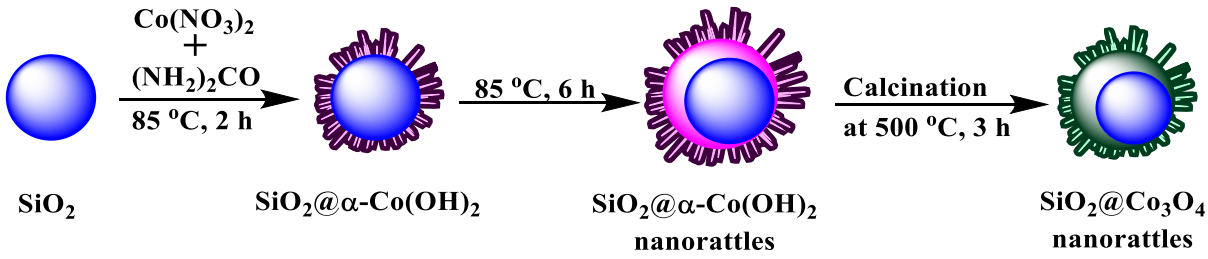

Scheme 5.1.3: An overview image for the formation of SiO_2@Co_3O_4 core-shell nanorattles.

Initially (e.g. 2 h), α-$Co(OH)_2$ nanoparticles are formed around the SiO_2 spheres (Figure 5.1.19a). The crystallites of α-$Co(OH)_2$ present on SiO_2 are loosely packed and the crystallites located at the outermost surface act as the nucleation seeds for the recrystallization process. As the reaction proceeds from 2 h to 4 h, inside-out Ostwald ripening process dominates which starts the hollowing process by dissolving the smaller crystallites of α-$Co(OH)_2$ present in the interior region. At 6 h, the outer α-$Co(OH)_2$ crystallites become larger which creates an interstitial space with the formation of a compact shell. Calcination of SiO_2@α-$Co(OH)_2$ at 500 °C leads to the formation of SiO_2@Co_3O_4 core-shell nanorattles with the retention of core-shell nanorattles morphology (Figure 5.1.19b). The TEM images show the shrinkage of silica core as well as the Co_3O_4 shell.

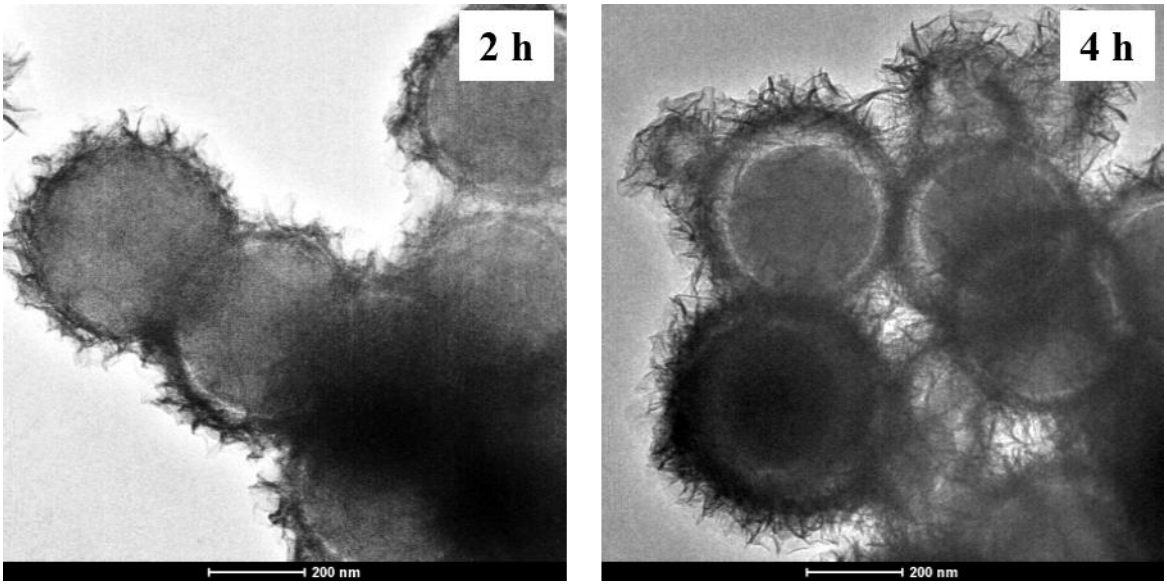

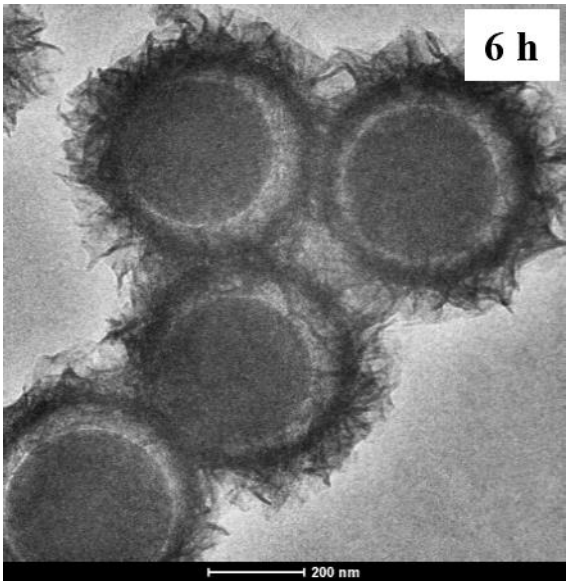

(a)

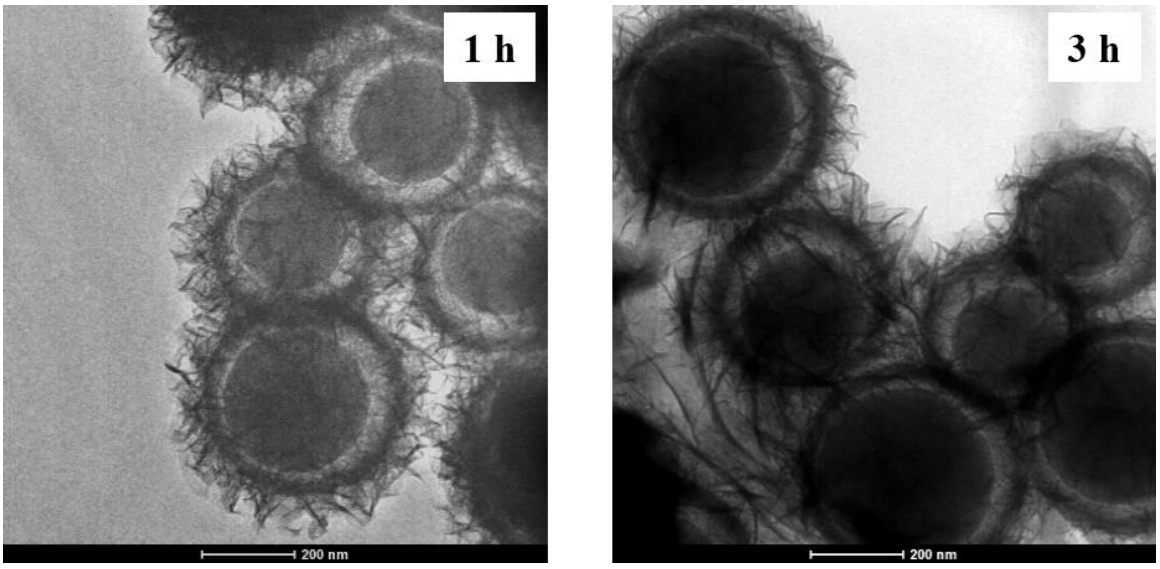

(b)

Fig. 5.1.19: (a) TEM images of SiO_2@α-$Co(OH)_2$ sample (P1) synthesized at 2 h, 4 h and 6 h and **(b)** TEM images of SiO_2@Co_3O_4 obtained on calcination of SiO_2@α-$Co(OH)_2$ (P1) at 500 ^oC for 1 h and 3 h.

The size of inner core (SiO_2) and shell (Co_3O_4) particles exhibits a rather larger polydispersity compared to pure SiO_2 and Co_3O_4 particles. This is explained as follows. It can be noted from TEM studies that the formation of an interface between SiO_2 core and α-$Co(OH)_2$ shell occurs within 2 h. After 4 h, formation of core-shell nanorattles with some extra particles of α-$Co(OH)_2$ occurs and core-shell nanorattles with compact

α-$Co(OH)_2$ shell are obtained after 6 h. When SiO_2@α-$Co(OH)_2$ core-shell nanorattles are calcined to get the SiO_2@Co_3O_4 core-shell nanorattles, polydispersion of silica core particles with slight shrinkage occurs. Intercalated water molecules and anions (NCO^-, and NO_3^-) present in α-$Co(OH)_2$ and surface hydroxyl groups in silica are lost during the conversion of SiO_2@α-$Co(OH)_2$ to SiO_2@Co_3O_4 core-shell nanorattles. The polydispersity of SiO_2 spheres and Co_3O_4 shell is attributed to different dehydroxylation rate of loss of surface hydroxyl groups and other species from silica (core) and α-$Co(OH)_2$ (shell).

5.1.5 Conclusions

A novel self-template method for the synthesis of SiO_2@Co_3O_4 core-shell nanorattles with different shell thickness has been reported. The shell thickness is controlled by varying the concentration of precursors during the synthesis. XRD results indicate the presence of Co_3O_4 in all the SiO_2@Co_3O_4 samples. SEM results show the deposition of Co_3O_4 on the SiO_2 microspheres. TEM results clearly show the nanorattle structures and void space between SiO_2 core and Co_3O_4 shell. SAED patterns indicate polycrystalline nature of Co_3O_4 shell on the surface of SiO_2. DRS results show absorption bands due to Co_3O_4 in all the SiO_2@Co_3O_4 samples. Compared to other preparation methods, this approach does not require any surface modification and the method is facile, and inexpensive. This method can be extended to prepare other metal oxide core-shell nanorattles for various functional applications.

5.2 Synthesis of SiO_2@Ni-Co Mixed Metal Oxide Core-Shell Nanorattles *via* Homogeneous Precipitation Method

5.2.1 Introduction

In recent years, binary transition metal oxides with spinel-like structures (e.g. AB_2O_4) have attracted considerable attention of scientists due to their tunable optical and electrical properties as well as wide range of applications in various fields such as water splitting [90], adsorption [91], sensors [92], gas storage [93], lithium ion batteries [94], and bio-medicine [95]. Various binary transition metal oxide nanorattles such as $NiCo_2O_4$ [94], $ZnCo_2O_4$ [96], $ZnFe_2O_4$ [97], $MnCo_2O_4$ [98], and $CoFe_2O_4$ [99] have been reported. TEM images of some binary metal oxide nanorattles are shown in Figure 5.2.1.

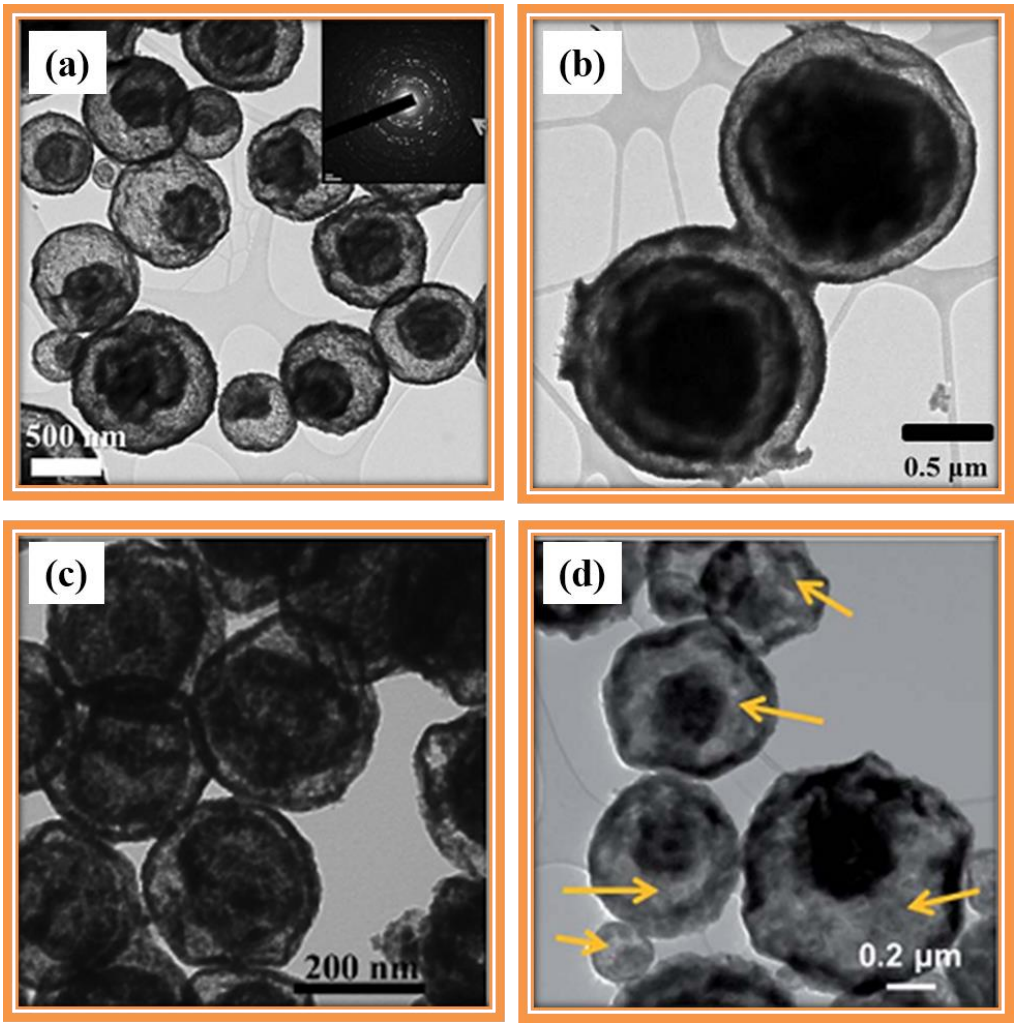

Fig.5.2.1: TEM images of various binary transition metal oxide nanorattles; **(a)** $ZnCo_2O_4$ [96], **(b)** $ZnFe_2O_4$ with double shell [97], **(c)** $MnCo_2O_4$ [98], and **(d)** $CoFe_2O_4$ [99].

In addition to binary transition metal oxides, tertiary, quaternary, and multi-transition mixed metal oxide nanorattles have also been reported. TEM images of some of multi-transition mixed metal oxide nanorattles are shown in Figure 5.2.2.

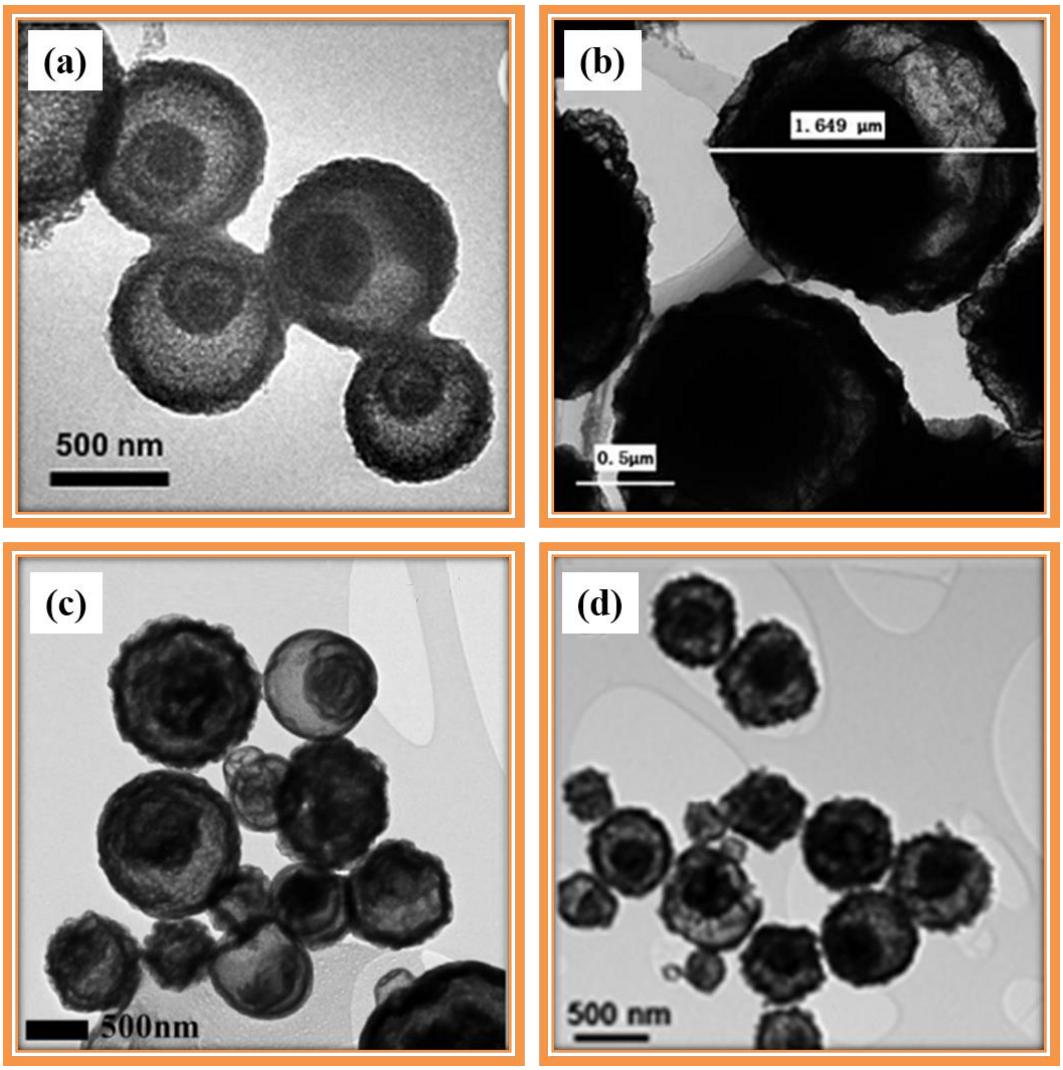

Fig.5.2.2: TEM images of various multi-transition metal oxide nanorattles; **(a)** $Mn_{0.75}Co_{0.25}Fe_2O_4$ [100], **(b)** $LiNi_{0.8}Co_{0.15}Al_{0.05}O_2$ [101], **(c)** TiO_2-Al_2O_3-ZrO_2-CeO_2- Y_2O_3 [102], and **(d)** AB_2O_4 (A = Cu, Zn, Ni, B = Co, Mn, Fe, Mo, Cr) [103].

Various mixed metal layered double hydroxides (LDH) such as $CoSn(OH)_6$ [104], MgFe-LDH [105], SiO_2@NiAl-LDH [106], and $M_1@M_2@M_1(OH)_2$ (M_1= Co, Ni, M_2 = Pt/Pd, Pt, Pd and Au) [107] have been reported by several authors. SEM, TEM and HRTEM images of some mixed metal layered double hydroxide nanorattles are shown in Figure 5.2.3.

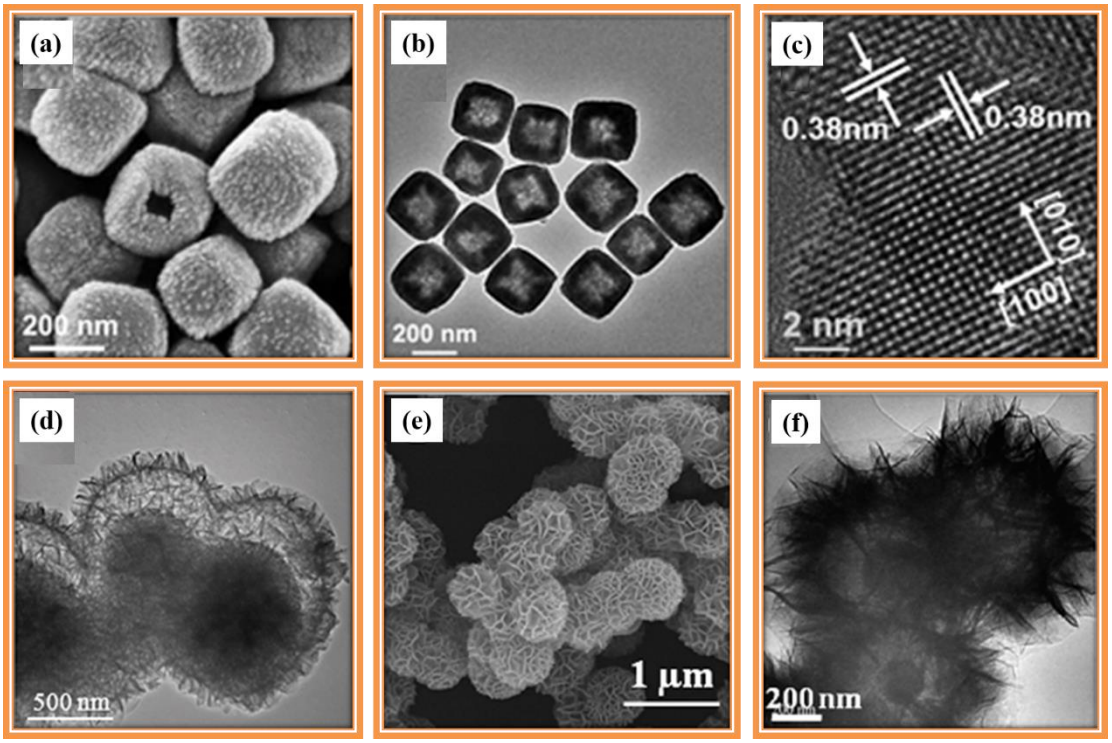

Fig.5.2.3: (a) SEM image of $CoSn(OH)_6$, **(b, c)** TEM and HRTEM images of $CoSn(OH)_6$ nanorattles [104], **(d)** TEM image of MgFe-LDH [105], and **(e, f)** SEM and TEM images of SiO_2@NiAl-LDH nanorattles [106].

Binary metal alloys have been used as the core or shell. Examples are Pd@M_xCu_{1-x} (M = Au, Pd and Pt) [108], AuAg@C [109], PtCu@Ru [110], and PdFe@SiO_2 [111]. Most of the authors have used Fe_3O_4 as the core and metal silicate as the shell because of their porous nature, good chemical and thermal stability. Some of the examples are Fe_3O_4@$CuSiO_3$ [84], Fe_3O_4@$MgSiO_3$ [91], Fe_3O_4@$NiSiO_3$ [112], and Fe_3O_4@$BaSiO_3$ [113]. Nanorattles with single core and multi shells have also been reported by several authors. Examples are CuO@CuO@CuO [114], α-Fe_2O_3@SiO_2@SiO_2 [115], α-Fe_2O_3@SiO_2@TiO_2 [116], Pd-SnO_2@Pd-SnO_2@Pd-SnO_2 [117], Fe_3O_4@SiO_2@Co_3O_4 [118], and Pd@TiO_2/ Pd@TiO_2 [119]. Some of the authors have reported, carbon as middle layer in the nanorattles. Examples are Fe_3O_4@C@TiO_2 [120] and Ag@C@mSiO_2 [121]. SiO_2 has been used as the core or shell material. Various reports are available where SiO_2 has been used as the shell and examples are Fe_xO_y/Pd@SiO_2 [122], Ni-yolk@Ni@SiO_2 [123], CdS-Au@SiO_2 [124]. Recently, Dong et al. have used SiO_2 as the core and $NiTiO_3$ as the shell [125]. TEM images of some of the above mentioned nanorattles are shown in Figure 5.2.4.

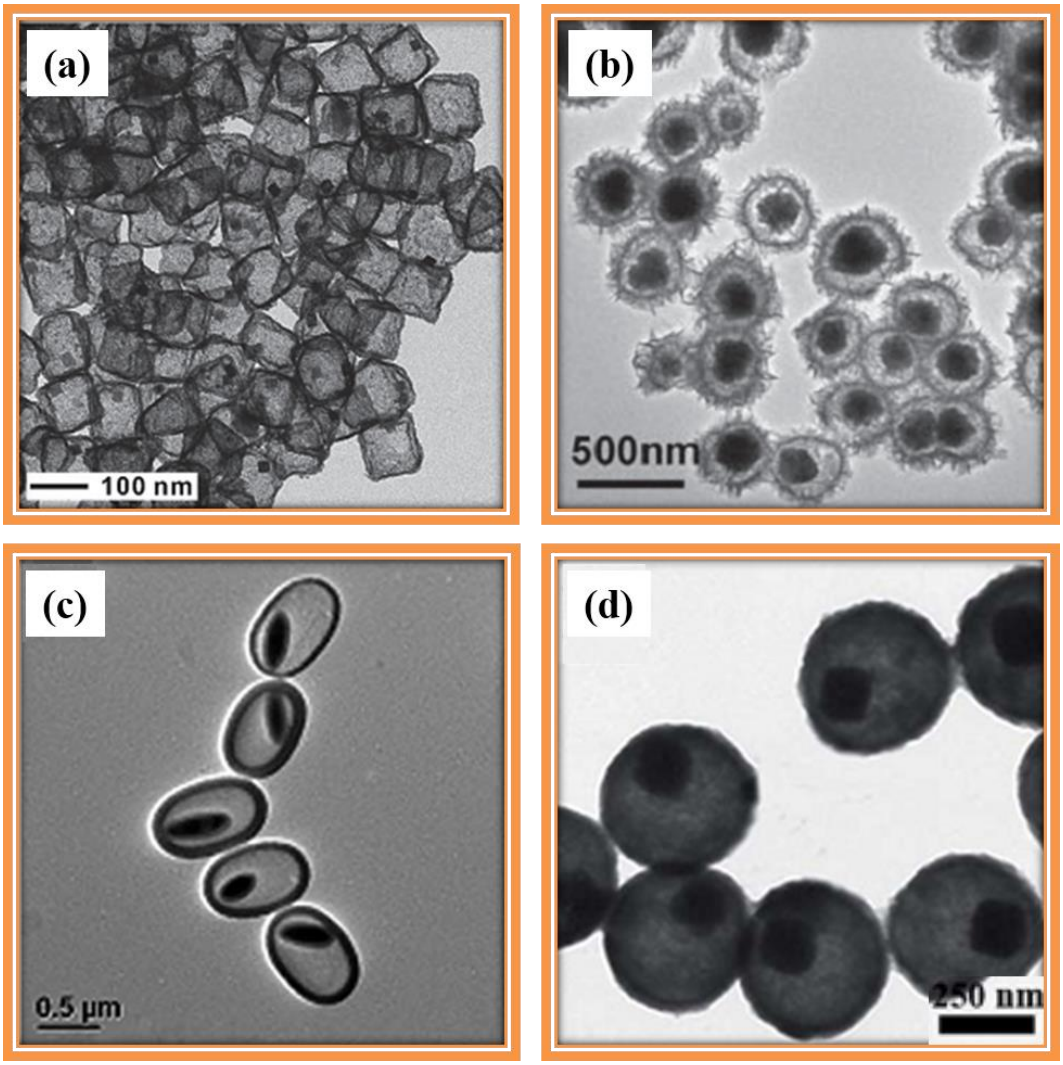

Fig.5.2.4: TEM images of **(a)** $Pd@Au_xCu_{1-x}$ [108], **(b)** $Fe_3O_4@NiSiO_3$ [112], **(c)** α-$Fe_2O_3@SiO_2@SiO_2$ [115], and **(d)** $Fe_3O_4@C@TiO_2$ [120] nanorattles.

Among the binary transition metal oxides, $NiCo_2O_4$ has been extensively studied. $NiCo_2O_4$ is a binary mixed metal oxide with spinel structure in which nickel ions occupy octahedral sites and cobalt ions randomly occupy both the octahedral and tetrahedral sites. $NiCo_2O_4$ has been used in various applications such as supercapacitors and methanol fuel cells because of its good electrical conductivity, availability, low cost, and eco-friendliness [94,126,127]. $NiCo_2O_4$ has also been used in lithium ion batteries [94], energy storage [126], electrocatalysis [127], radio frequency absorption [128], and photocatalytic splitting of water [129]. Hu et al. have reported the synthesis of $Co_3O_4@NiCo_2O_4$ core-shell nanorattles, where ZIF-8 has been used as a sacrificial template [130].

Various mixed metal layered double hydroxides or mixed metal oxide nanorattles have been synthesized using hydrothermal method, ultrasonic spray pyrolysis, thermal decomposition, and homogeneous precipitation. A brief description on the synthetic methods is given below.

Thermal decomposition [91]: In this approach, pre-prepared core material is mixed with shell precursors in a high boiling solvent. Then, the reaction contents are refluxed at elevated temperatures for several hours. Finally, the obtained products are calcined in the presence of air or an inert gas to get the nanorattles. $Mn_xCo_{1-x}Fe_2O_4$ nanorattles have been synthesized using this approach [91].

Ultrasonic spray pyrolysis [103]: In this method, a high frequency ultrasound is passed through precursor solutions to generate an aerosol, which is nebulized into micro-droplets. The generated micro-droplets are transferred to a furnace with the help of a carrier gas. In the furnace, the precursor molecules undergo decomposition by the loss of solvent. The decomposed reactants undergo diffusion. In the final step, the volatile components escape from the micro-droplets and produce the void space. The ultrasonic waves provide phase isolation of droplets from other droplets. Examples are $ZnCo_2O_4$ [96], TiO_2-Al_2O_3-ZrO_2-CeO_2-Y_2O_3 [102], AB_2O_4 (A = Cu, Zn, Ni, B = Co, Mn, Fe, Mo, Cr) [103], and CuO@CuO@CuO [114]. A schematic representation of synthesis of nanorattles using ultrasonic spray pyrolysis is shown in Figure 5.2.5.

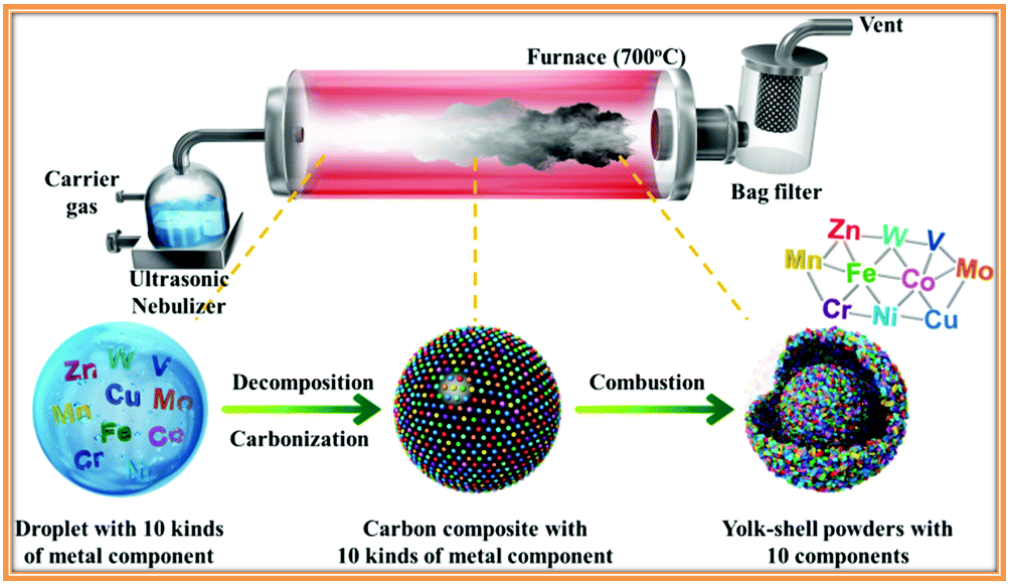

Fig.5.2.5: Schematic representation of the synthesis of mixed metal oxide nanorattles using ultrasonic spray pyrolysis [103].

Hydrothermal method [105]: In this method, two or more metal salts are mixed in an aqueous solution and stirred for a certain period of time. Then, the reaction contents are transferred to a Teflon lined stainless steel autoclave and heated inside an oven at relatively high temperature (e.g. 200 ^{o}C) to get mixed metal oxide nanorattles. Examples are $NiCo_2O_4$ [94], MgFe-layered double hydroxides [105], SiO_2@NiAl-layered double hydroxides [106], Co_3O_4@$NiCo_2O_4$ [130] and Au@$MSiO_3$ (M = Mg, Ni, Cu) [131].

Homogeneous precipitation [132]: This method comes under solution route and either core or shell materials are synthesized using this method. In this method, urea is generally used as a precipitating agent. Two or more metal salts such as metal nitrates, sulphates, or chlorides are mixed in an aqueous solution along with urea and the reaction contents are heated at 80-90 ^{o}C for several hours (e.g. 6 h) to get mixed metal layered double hydroxide nanorattles. Examples are MgAl-LDH [132], SiO_2@MgAl-LDH [133], CoNiAl-LDH [134], and NiCo-LDH [135].

In the present study, SiO_2@Ni-Co mixed metal oxide core-shell nanorattles have been successfully synthesized, for the first time, *via* a novel, economical, and facile self-template route. The composition of Ni-Co mixed metal oxides was controlled by varying the concentration of precursors during the synthesis.

5.2.2 Experimental details

Tetraethyl orthosilicate (98%, ACROS®), ethanol (99.9%), ammonia solution (25%, Rankem), cobaltous nitrate hexahydrate (98%, Rankem), nickel nitrate hexahydrate (98%, Rankem), and urea (99.5%, Rankem) were used as received without further purification.

5.2.2.1 Synthesis of SiO_2@Ni-Co mixed metal oxide core-shell nanorattles

A schematic representation of synthesis of SiO_2@Ni-Co mixed metal oxide core-shell nanorattles is shown in Scheme 5.2.1. The synthesis of SiO_2@Ni-Co mixed metal oxide core-shell nanorattles involves two steps. First, silica microspheres were synthesized according to StÖber process [70]. The details on the synthesis of SiO_2 microspheres have been discussed in Chapter-3 (Section 3.1.2.1).

In the second step, about 100 mg of silica microspheres was dispersed in 100 mL aqueous solution containing nickel nitrate and cobaltous nitrate with different molar ratios ($[Ni^{2+}]$: $[Co^{2+}]$ = 7:3, 5:5, 3:7; total concentration = 10 mmol) in a 250 mL beaker and sonicated for 3 min to get a uniform dispersion of the silica spheres. Then, 5 g of urea was added and the contents were continuously stirred at 85 ^oC for 6 h. After completion of the reaction, the contents were allowed to cool to room temperature, filtered using Whatman® filter paper, washed with Millipore® water for several times and dried in an oven for overnight. The obtained SiO_2@Ni-Co LDH samples were calcined in air inside a muffle furnace (Nabertherm®) at 500 ^oC for 3 h (heating rate = 2^o min^{-1}) to get the SiO_2@Ni-Co mixed metal oxide core-shell nanorattles. The SiO_2@Ni-Co LDH samples were labelled as PM1, PM2, and PM3, corresponding to Ni^{2+} to Co^{2+} ratios, 7:3, 5:5, and 3:7, respectively and the corresponding SiO_2@Ni-Co mixed metal oxide samples were labelled as M1, M2, and M3. For comparison, pure SiO_2@α-$Ni(OH)_2$, SiO_2@ α-$Co(OH)_2$, SiO_2@NiO and SiO_2@Co_3O_4 samples were also synthesized using the procedure similar to that used for the preparation of SiO_2@Ni-Co mixed metal oxides. The concentration of nickel nitrate and cobaltous nitrate solutions used was 10 mM each.

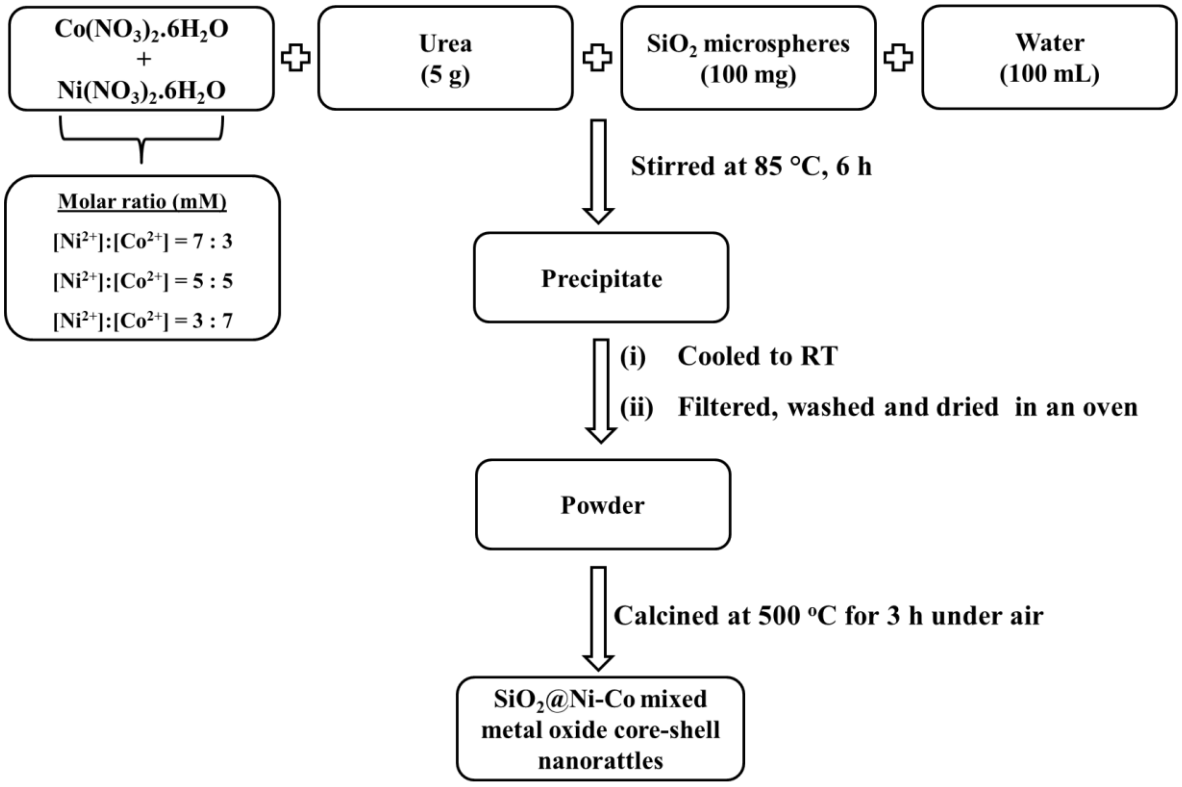

Scheme 5.2.1: Schematic representation of synthesis of SiO_2@Ni-Co mixed metal oxide core-shell nanorattles.

The synthesized SiO_2@Ni-Co mixed metal oxide core-shell nanorattles were characterized using a variety of analytical techniques such as PXRD, FT-IR, TGA, FE-SEM, EDX, TEM, Zeta potential, and BET surface area measurements. The optical properties were studied using UV-Visible DRS spectroscopy. More details on the experimental techniques have been discussed in Chapter-2.

5.2.3 Results and discussion

5.2.3.1 XRD analysis

The XRD patterns of SiO_2@Ni-Co LDH samples (PM1, PM2 and PM3) before calcination and that of pure Ni-Co LDH ([Ni^{2+}:Co^{2+} = 1:2)] are shown in Figure 5.2.6a. The XRD pattern of silica indicated amorphous nature. The XRD pattern of pure Ni-Co LDH ([Ni^{2+}:Co^{2+}] = 1:2) and SiO_2@Ni-Co LDH samples (PM1, PM2 and PM3) show four prominent peaks at 2θ values of 12.15º, 24.56º, 33.47º, and 59.48º which are attributed to (003), (006), (101), and (110) planes of α-$Co(OH)_2$ and α-$Ni(OH)_2$ [136]. Both α-$Co(OH)_2$ and α-$Ni(OH)_2$ have similar lattice constants, and their diffraction peaks are very close. The first two peaks (003 and 006) in the XRD patterns are related to d-spacing between the layers [134]. The broad XRD peaks with reduced intensity indicate less crystalline nature of the SiO_2@Ni-Co LDH samples. The interlayer d-spacing was estimated using the (003) plane and it was found to be ca. 7.28 Å. The XRD patterns of $NiCo_2O_4$ and SiO_2@Ni-Co mixed metal oxide samples (M1, M2 and M3) which were obtained after calcination of the corresponding LDHs at 500 ºC are shown in Figure 5.2.6b. Pure $NiCo_2O_4$ shows reflections at 19.21º, 31.12º, 36.75º, 43.82º, 59.02º, and 65.17º attributed to (111), (220), (311), (400), (511), and (440) planes of cubic $NiCo_2O_4$, respectively [137].

The SiO_2@Ni-Co mixed metal oxide samples show weak XRD peaks indicating the formation of nanosized mixed metal oxides on the surface of SiO_2. The XRD peaks are relatively stronger for M1 compared to that for M2 and M3 (Figure 5.2.6b). Sample M1 is nickel rich compared to M2 and M3 and it was prepared by the calcination of SiO_2@Ni-Co LDH sample PM1 at 500 ºC. Well-ordered LDH is formed in the case of samples prepared using higher Ni^{2+} concentration (Figure 5.2.6a) [138]. Incorporation of Co^{2+} ions with larger size (0.74 Å) into the lattice of LDH leads to its instability resulting in LDH samples with lower crystallinity (see the XRD patterns for PM2 and

PM3, Figure 5.2.6a). Since PM1 possesses well-ordered LDH structure compared to PM2, and PM3, the corresponding calcined sample M1 exhibits stronger XRD peaks (Figure 5.2.6b) compared to M2, and M3 [139]. The calculated crystallite size for pure $NiCo_2O_4$ nanoparticles is 4.6 nm and the crystallite size for $NiCo_2O_4$ in the SiO_2@Ni-Co mixed metal oxide samples could not be calculated.

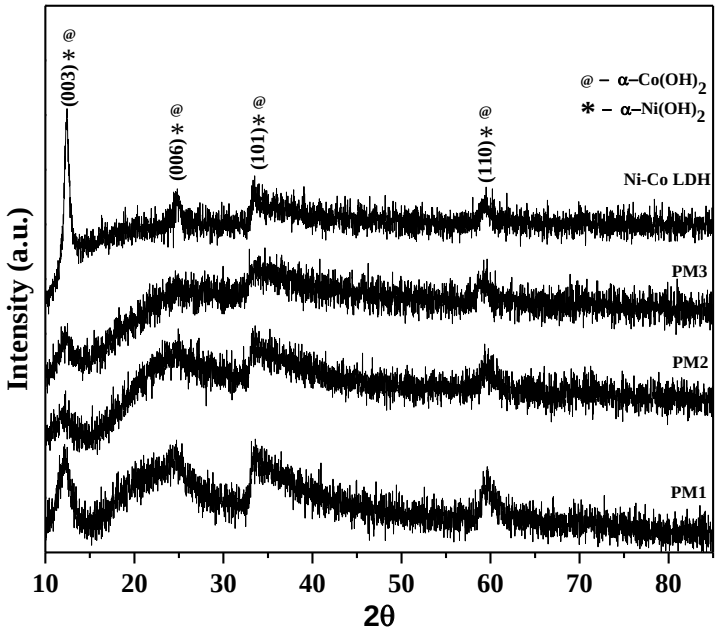

(a)

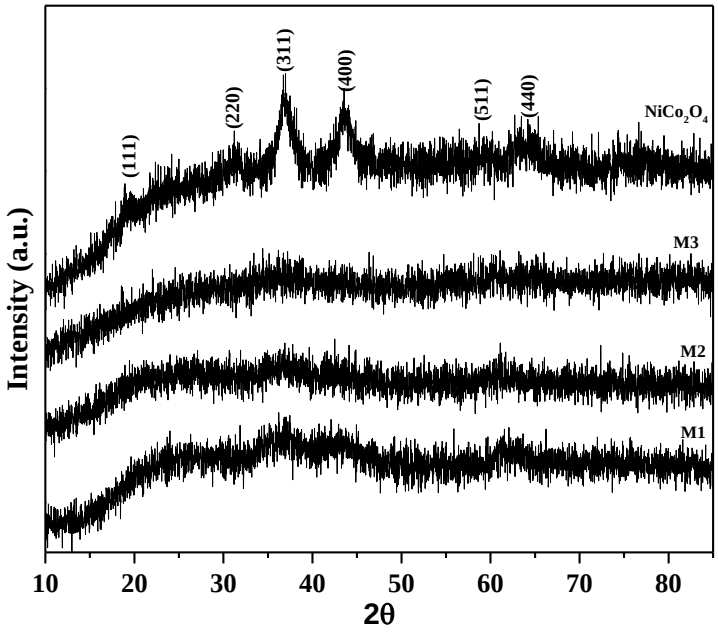

(b)

Fig. 5.2.6: (a) XRD patterns of SiO_2@Ni-Co LDH samples (PM1, PM2, and PM3), and Ni-Co LDH ($[Ni^{2+}:Co^{2+}] = 1:2$); **(b)** XRD patterns of SiO_2@Ni-Co mixed metal oxides (M1, M2, and M3), and $NiCo_2O_4$.

The XRD patterns of NiO, SiO_2@NiO, Co_3O_4, and SiO_2@Co_3O_4 samples are shown in Figure 5.2.7. The XRD patterns of SiO_2@NiO sample shows reflections due to only NiO whereas SiO_2@Co_3O_4 sample shows reflections due to Co_3O_4. The crystallite size values of pure NiO and Co_3O_4, estimated using Debye-Scherrer's equation, are *ca.* 7 nm and 21 nm, respectively. SiO_2@NiO and the SiO_2@Co_3O_4 samples show less intense XRD peaks compared to pure NiO and Co_3O_4 which indicates the formation of nano sized NiO and Co_3O_4 nanoparticles on SiO_2.

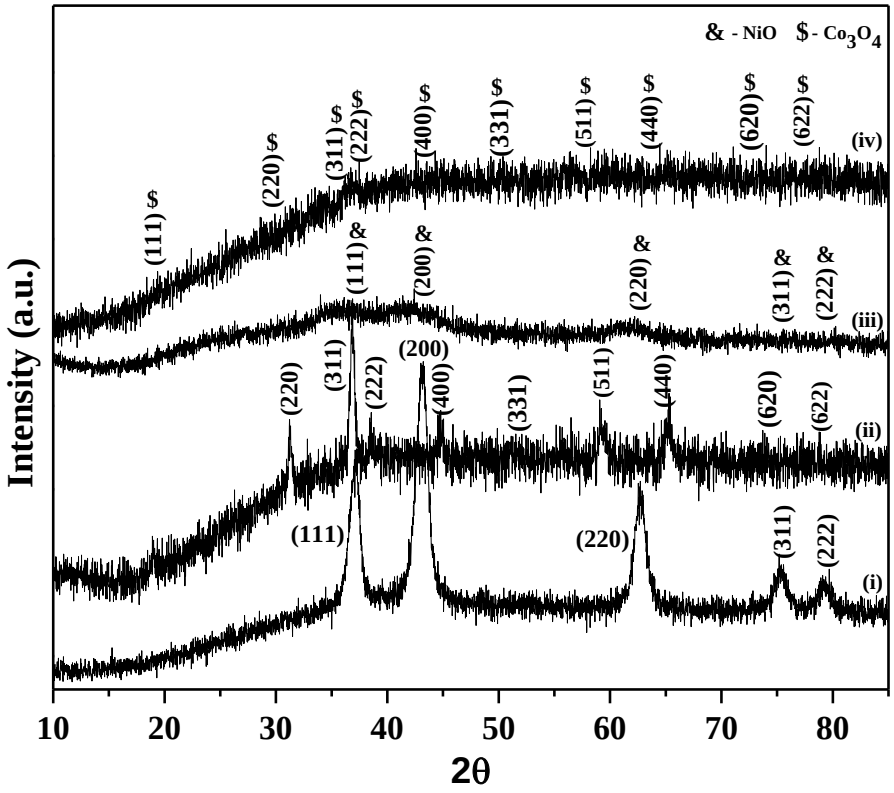

Fig. 5.2.7: XRD patterns of **(i)** NiO, **(ii)** Co_3O_4, **(iii)** SiO_2@NiO, and **(iv)** SiO_2@Co_3O_4 samples.

The XRD patterns of pure Ni-Co LDHs prepared using different Ni^{2+}:Co^{2+} ratios and the corresponding Ni-Co mixed metal oxides, which were obtained on calcination of the pure Ni-Co LDHs, are shown in Figure 5.2.8a and 5.2.8b, respectively. All the pure Ni-Co LDH samples show reflections attributed to both α-$Co(OH)_2$ and α-$Ni(OH)_2$. The XRD patterns of pure Ni-Co mixed metal oxide samples confirm the formation of mixed metal oxides. The mixed metal oxide prepared using [Ni^{2+}:Co^{2+}] = 7:3 shows (311) reflection due to cobalt oxide (JCPDS No. 42-1467) and (200) and (220) reflections due to nickel oxide (JCPDS No. 78-0423). In the case of mixed metal oxide prepared using [Ni^{2+}:Co^{2+}] = 5:5, the XRD pattern shows (111), (220) (311) (400) (511) and (440)

reflections due to nickel cobaltite (JCPDS No. 73-1702). The (200) reflection due to nickel oxide coincides with the (400) reflection of nickel cobaltite. In the case of the mixed metal oxide prepared using [Ni^{2+}:Co^{2+}] = 3:7, a mixture of nickel cobaltite and cobalt oxide is formed.

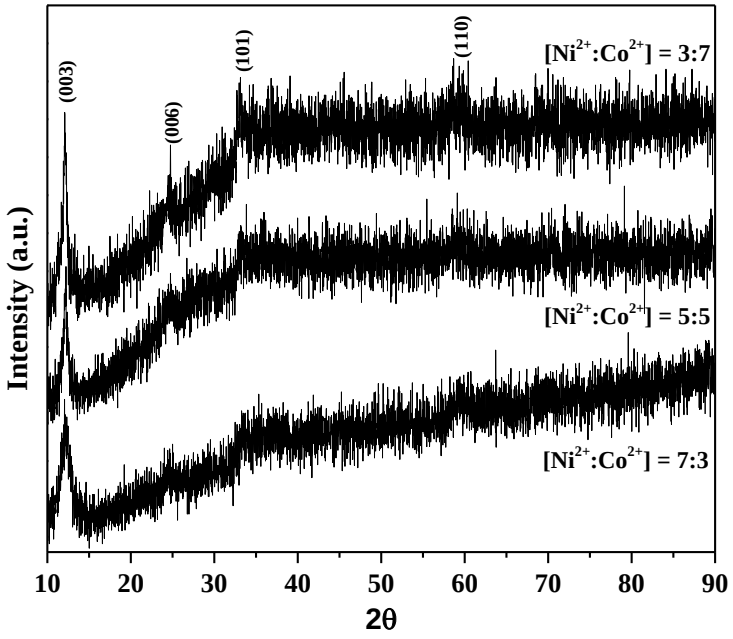

(a)

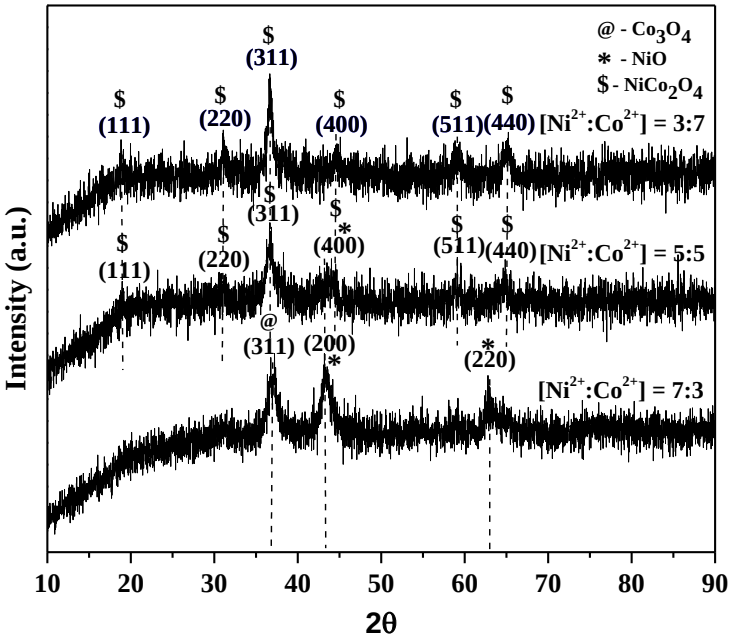

(b)

Fig. 5.2.8: (a) XRD patterns of pure Ni-Co LDH samples, and **(b)** pure Ni-Co mixed metal oxides which were obtained after calcination of the corresponding Ni-Co LDH samples at 500 ^{o}C in air.

5.2.3.2 FT-IR spectral studies

The FT-IR spectra of SiO_2, pure Ni-Co LDH [Ni^{2+}:Co^{2+} = 1:2] and SiO_2@Ni-Co LDH samples, before calcination and after calcination at 500 ^oC, were recorded (Figure 5.2.9). All the samples showed two IR bands at about 3438 and 1635 cm^{-1} attributed to stretching and bending vibrations of hydroxyl group of physisorbed water molecules. SiO_2, SiO_2@Ni-Co LDH samples and SiO_2@Ni-Co mixed metal oxide samples show three prominent IR bands at about 1108, 804, and 470 cm^{-1} attributed to asymmetric stretching, symmetric stretching, and bending modes of Si–O–Si bond. SiO_2 before calcination shows a band at 950 cm^{-1} which is characteristic band of Si–OH group [70]. The Ni-Co LDH ([Ni^{2+}:Co^{2+}] = 1:2) and all the SiO_2@Ni-Co LDH samples (PM1, PM2 and PM3) show IR bands at 2240 and 1383 cm^{-1} attributed to stretching vibrations of NCO^-, and NO_3^-, respectively which confirm the presence of NCO^-, and NO_3^- between the layers [128]. The Ni-Co LDH ([Ni^{2+}:Co^{2+}] = 1:2) and SiO_2@Ni-Co LDH samples also show a band at about 646 cm^{-1} attributed to the bending vibration of M–OH (M = Co, Ni). Pure $NiCo_2O_4$ show two characteristic IR bands at 660 and 561 cm^{-1} attributed to Co–O and Ni–O vibrations, respectively [127,140]. The SiO_2@Ni-Co mixed metal oxide samples (M1, M2 and M3) show IR bands at about 667 and 560 cm^{-1} attributed to metal-oxygen vibrations.

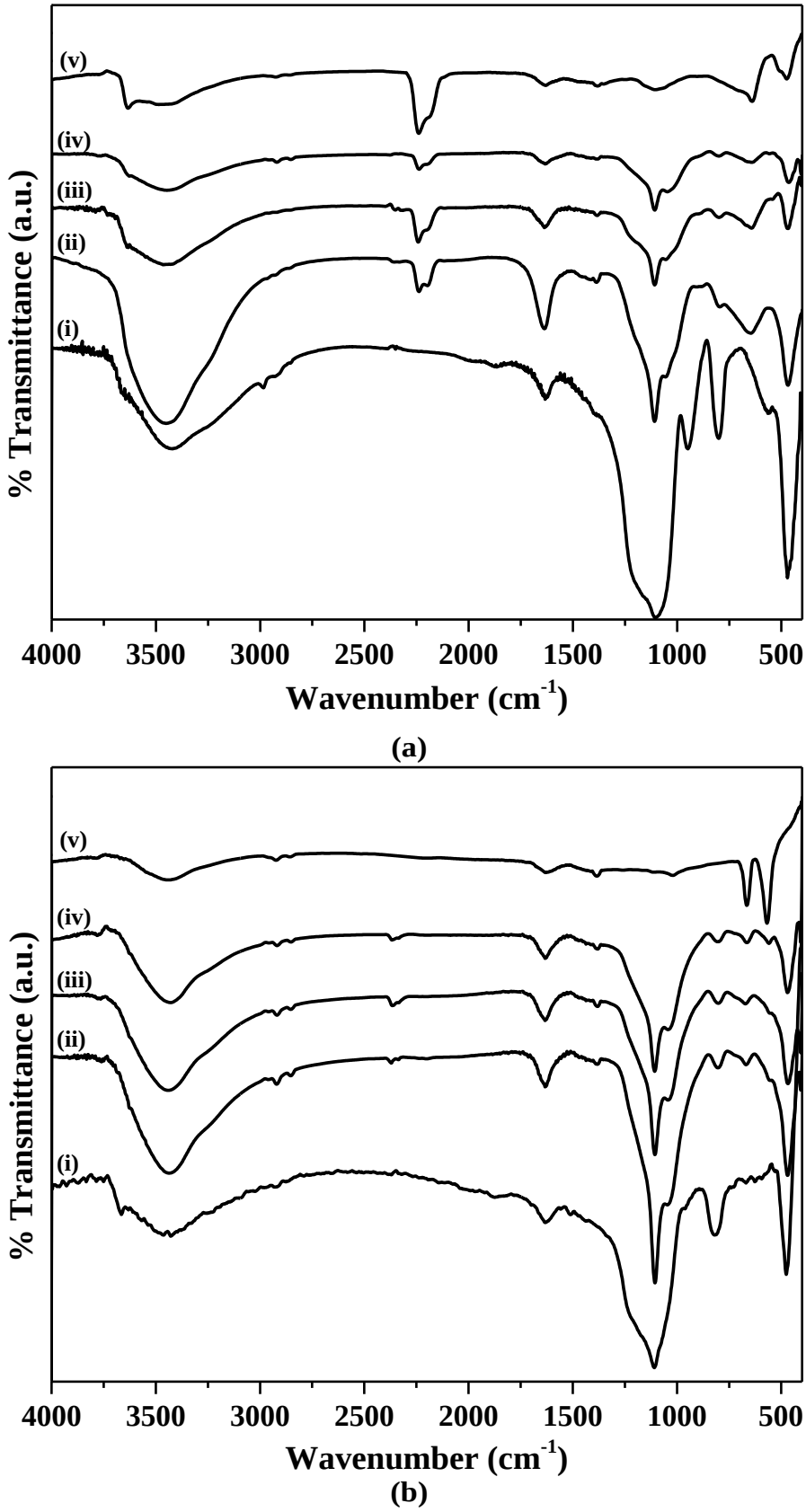

Fig. 5.2.9: (a) FT-IR spectra of **(i)** as prepared SiO_2, **(ii-iv)** SiO_2@Ni-Co LDH samples (PM1, PM2, and PM3), and **(v)** Ni-Co LDH (Ni^{2+}:Co^{2+} = 1:2); **(b)** FT-IR spectra of **(i)** SiO_2 after calcination, **(ii-iv)** SiO_2@Ni-Co mixed metal oxides (M1, M2, and M3), and **(v)** $NiCo_2O_4$.

5.2.3.3 TGA analysis

Thermogravimetric analysis of as prepared SiO_2, Ni-Co LDH ($[Ni^{2+}:Co^{2+}]$ = 1:2) and SiO_2@Ni-Co LDH samples before calcination are shown in Figure 5.2.10a. In pure silica, the first weight loss step observed between 35 ^oC and 170 ^oC (~5 % weight loss) is attributed to the loss of physisorbed water molecules [141,142]. The second weight loss observed between 350 ^oC and 660 ^oC (% wt. loss ~ 7.5 %) is attributed to the removal of surface hydroxyl groups [78]. SiO_2 shows a total weight loss of about 12.5 % up to 1000 ^oC. Pure Ni-Co LDH shows a total weight loss of about 33.1 % up to 1000 ^oC. The weight loss from room temperature to 140 ^oC (~ 2.5 %) is attributed to desorption of the physisorbed water molecules. The major weight loss (~ 28.1 %) observed between 140 ^oC and 300 ^oC is attributed to the loss of interlamellar water molecules and anions accompanied by the decomposition of Ni-Co LDH to form corresponding mixed metal oxides [143]. The third step shows a minor weight loss (~ 2.5 %) between 300 ^oC and 860 ^oC due to the decomposition of mixed metal oxides [136]. The SiO_2@Ni-Co LDH samples (PM1, PM2 and PM3) show weight loss due to both silica and Ni-Co LDH's and the overall weight loss values, up to 1000 ^oC, are 24.7 %, 21.7 % and 28.1 % for samples PM1, PM2, and PM3, respectively. All the SiO_2@Ni-Co LDH samples show an initial weight loss (8.8 to 10.0 %) at about 140 ^oC which is due to removal of the physisorbed water molecules. They show a major weight loss between 140 ^oC and 530 ^oC (~ 14.7 % for PM1, ~ 12.9 % for PM2, and ~ 18.1 % for PM3) which is attributed to the loss of interlayer water molecules and anions and also due to the conversion of Ni-Co LDHs to the corresponding mixed metal oxides [136].

α-$Ni(OH)_2$ looses its hydroxyl groups between 250-320 ^oC whereas α-$Co(OH)_2$ looses the hydroxyl groups between 220 and 300 ^oC [78,144]. The SiO_2@Ni-Co LDH samples exhibit different thermal decomposition behaviour which is an indication that the dehydroxylation and decomposition steps depend on the Ni/Co molar ratio which was used during the preparation of the LDHs. In the case of sample PM1 ($[Ni^{2+}:Co^{2+}]$ = 7:3), dehydroxylation starts at about 305 ^oC indicating that the major loss is due to the presence of higher α-$Ni(OH)_2$ content compared to α-$Co(OH)_2$. In sample PM2 ($[Ni^{2+}:Co^{2+}]$ = 5:5), dehydroxylation starts at about 290 ^oC which is lower than that of PM1. In the case of sample PM3 ($[Ni^{2+}:Co^{2+}]$ = 3:7), the loss due to dehydroxylation occurs in two steps. The first step is at 230-285 ^oC, due to the loss of hydroxyl groups

from the layers of α-$Co(OH)_2$. In the second step, the loss of hydroxyl groups from the layers of α-$Ni(OH)_2$ occurs at about 285-297 ^oC. Among all the SiO_2@Ni-Co LDH samples, PM3 exhibits the lowest dehydroxylation temperature as expected for Co-rich LDH samples. Based on the TGA results, the calcination temperature for SiO_2@Ni-Co LDH samples to obtain the SiO_2@Ni-Co mixed metal oxide was chosen as 500 ^oC. The TGA patterns of SiO_2@Ni-Co mixed metal oxide samples (M1, M2 and M3) are shown in Figure 5.2.10b. M1, M2 and M3 show an overall weight loss of 8.4 %, 10.1 % and 9.7 %, respectively. All the samples exhibit a weight loss of about 5 % in the temperature range 25 ^oC-180 ^oC due to the loss of physisorbed water molecules. The samples exhibit a weight loss of about 4-5 % in the temperature range 180 ^oC-1000 ^oC. The weight loss in the temperature range 800 ^oC-1000 ^oC is due to the decomposition of NiO, Co_3O_4, and $NiCo_2O_4$.

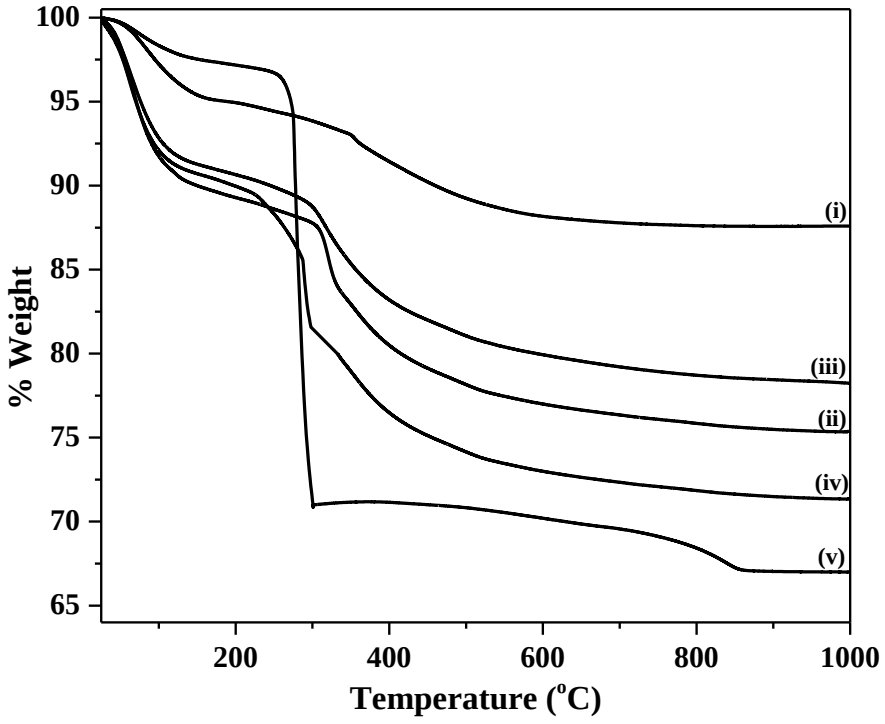

(a)

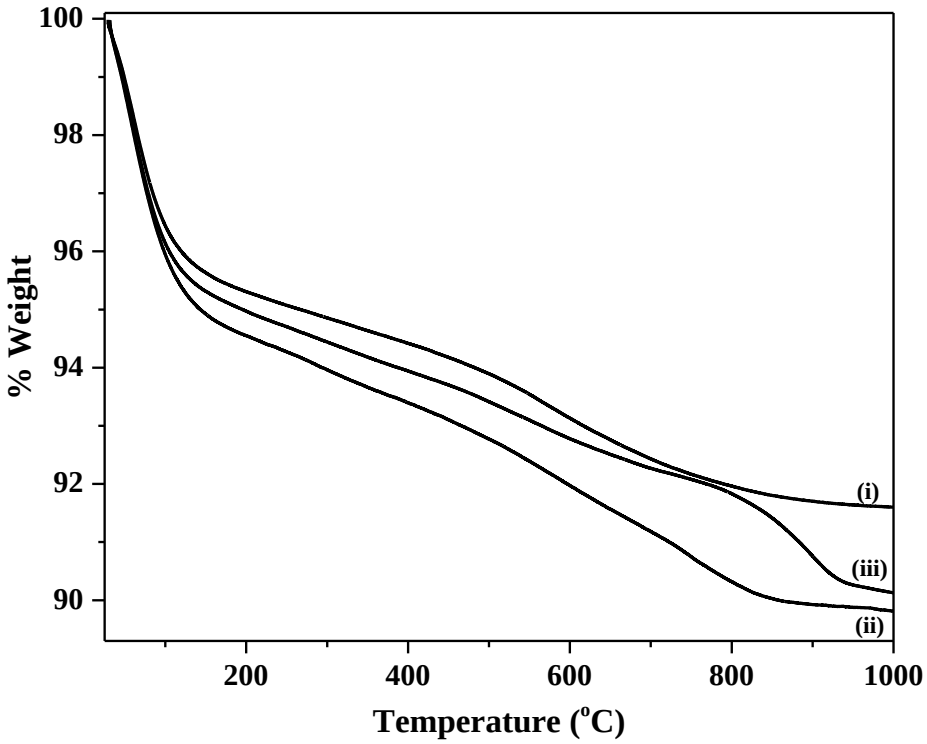

(b)

Fig. 5.2.10: TGA patterns of **(a) (i)** as prepared SiO_2, **(ii-iv)** SiO_2@Ni-Co LDH samples (PM1, PM2, and PM3), and **(v)** Ni-Co LDH (Ni^{2+}:Co^{2+} = 1:2) and **(b) (i-iii)** SiO_2@Ni-Co mixed metal oxide samples, M1, M2, and M3, respectively.

5.2.3.4 FE-SEM studies

The surface morphology of SiO_2, Ni-Co LDH ([Ni^{2+}:Co^{2+}] = 1:2), and SiO_2@Ni-Co LDH samples before calcination was investigated using FE-SEM analysis (Figure 5.2.11). SiO_2 shows well dispersed particles with uniform spherical morphology and diameter of the spheres lies in the range 250-320 nm. Pure Ni-Co LDH shows hierarchical flower-like morphology and these hierarchical structures are composed of thin plates. The FE-SEM images of SiO_2@Ni-Co LDH samples (PM1, PM2 and PM3) show hierarchical flower-like core-shell morphology. The images clearly indicate complete coverage of Ni-Co LDH sheets on the SiO_2 spheres.

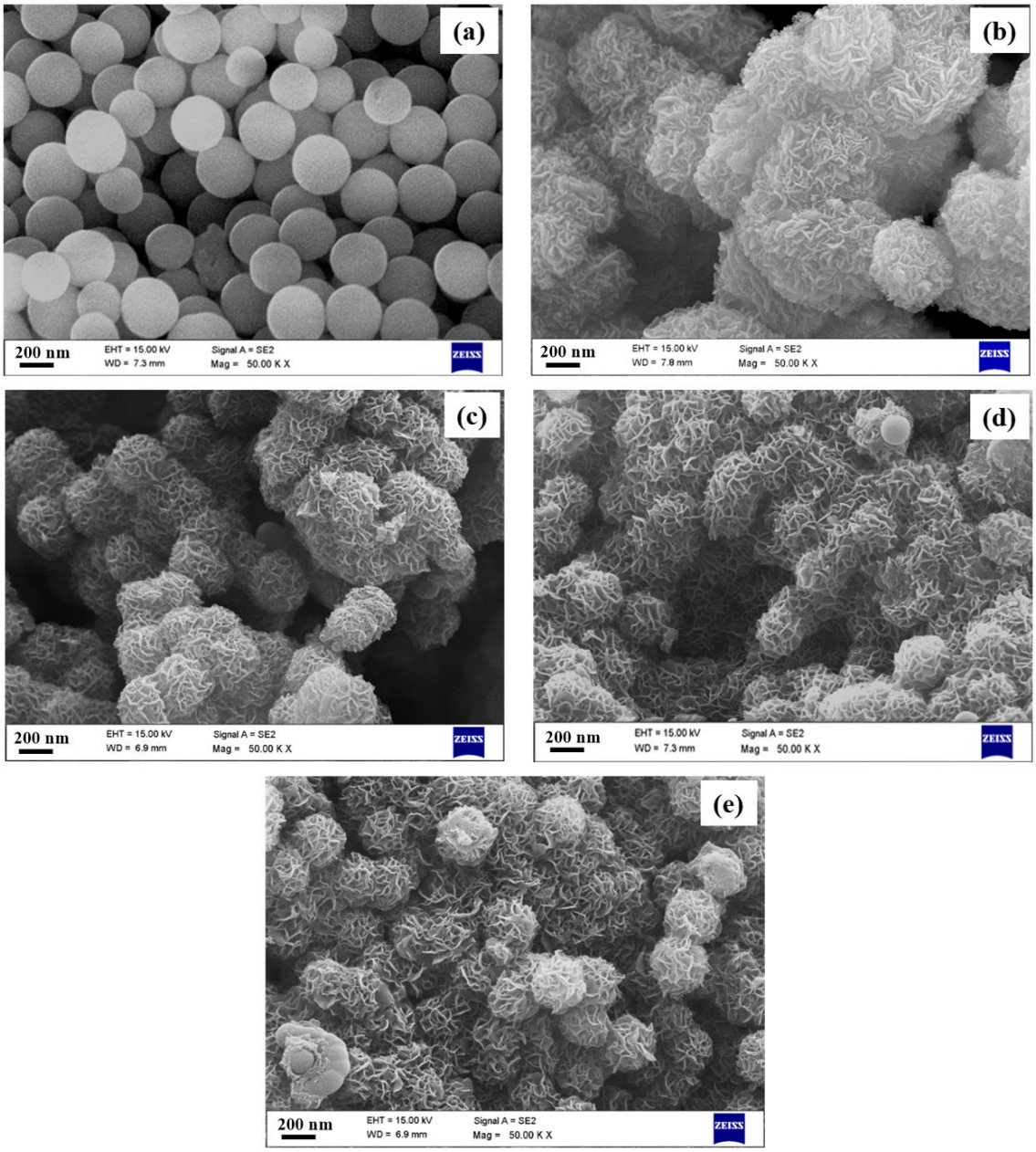

Fig. 5.2.11: FE-SEM images of **(a)** as prepared SiO_2, **(b)** Ni-Co LDH (Ni^{2+}:Co^{2+} = 1:2) and **(c-e)** SiO_2@Ni-Co LDH samples (PM1, PM2, and PM3).

The FE-SEM images of the $NiCo_2O_4$ and SiO_2@Ni-Co mixed metal oxide samples (M1, M2 and M3), which were obtained after the calcination of corresponding LDHs at 500 ^oC, are shown in Figure 5.2.12. All the samples retain their hierarchical flower-like morphology after calcination. α-$Ni(OH)_2$ and α-$Co(OH)_2$ showed petal-like morphology, and SiO_2@α-$Ni(OH)_2$ and SiO_2@α-$Co(OH)_2$ showed hierarchical flower-like core-shell morphology. Pure NiO and Co_3O_4 also showed petal-like morphology as that of α-$Ni(OH)_2$ and α-$Co(OH)_2$. The SEM images of SiO_2@NiO and SiO_2@Co_3O_4 showed core-shell morphology.

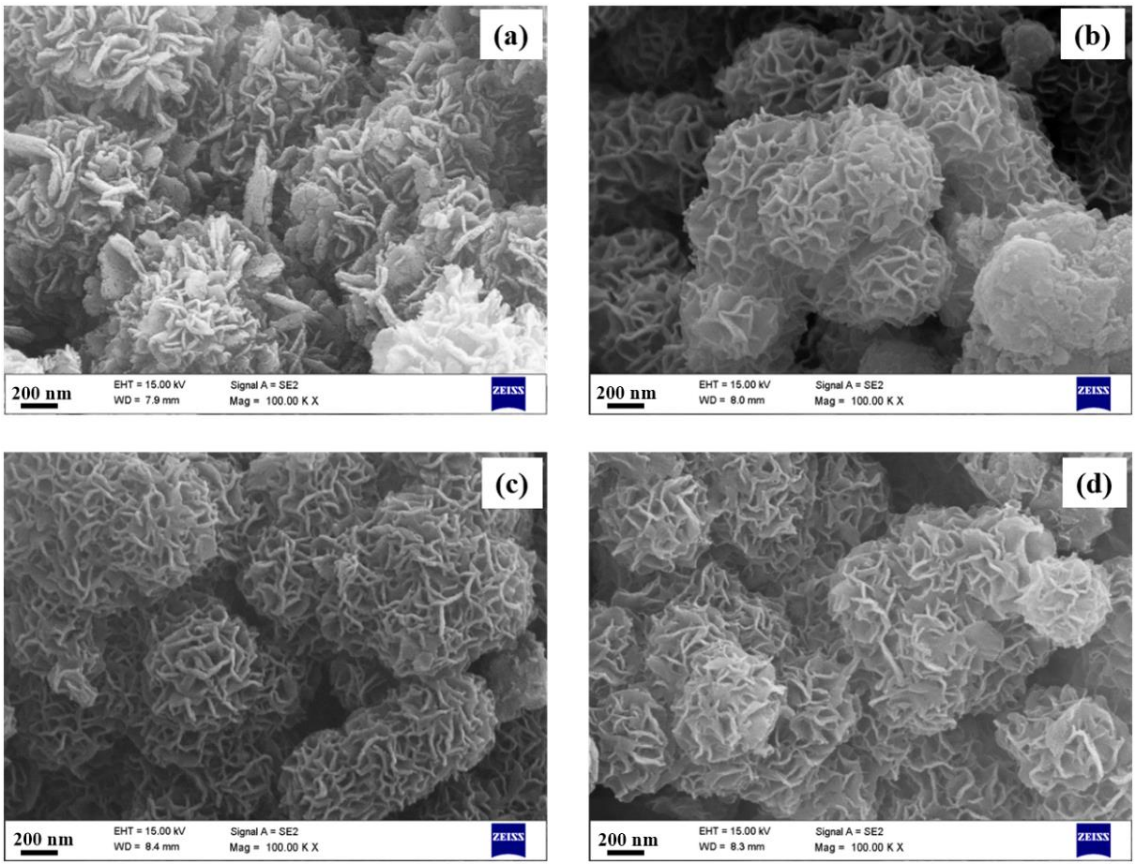

Fig. 5.2.12: FE-SEM images of **(a)** $NiCo_2O_4$ and **(b-d)** SiO_2@Ni-Co mixed metal oxide samples (M1, M2, and M3).

5.2.3.5 SEM-EDX analysis

The elemental composition of SiO_2@Ni-Co LDH samples (PM1, PM2 and PM3) and SiO_2@Ni-Co mixed metal oxide samples (M1, M2 and M3) was estimated using energy dispersive X-ray analysis (Table 5.2.1). EDX analysis confirms the presence of silicon, oxygen, nickel and cobalt in all the SiO_2@Ni-Co LDH samples (PM1, PM2 and PM3) as well as the SiO_2@Ni-Co mixed metal oxide samples (M1, M2 and M3). The SEM-EDX spectra of SiO_2@Ni-Co LDH samples (PM1, PM2 and PM3) are shown in Figure 5.2.13 and the SEM-EDX spectra of SiO_2@Ni-Co mixed metal oxide samples (M1, M2 and M3) are shown in Figure 5.2.14.

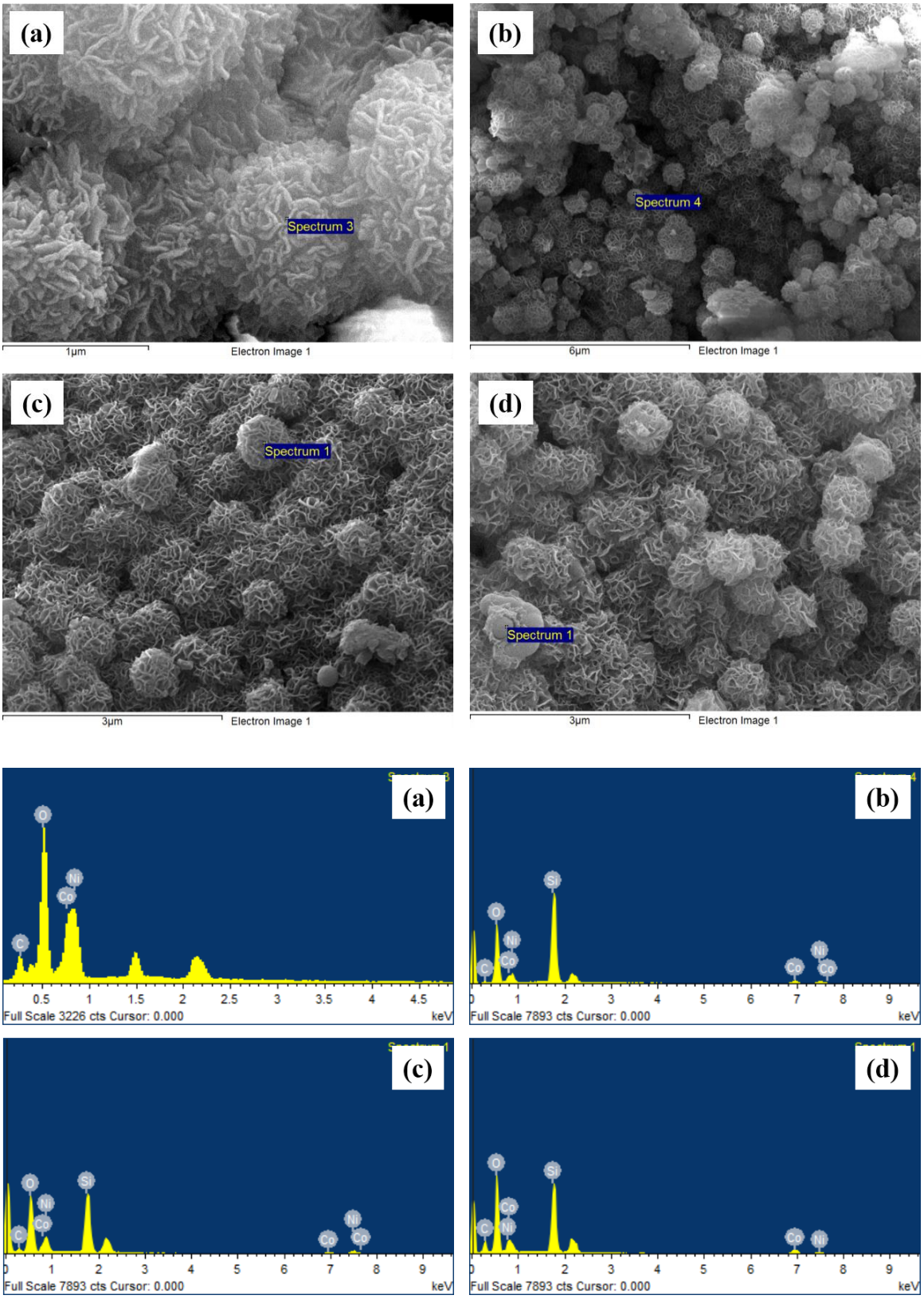

Fig. 5.2.13: SEM-EDX spectra of **(a)** Ni-Co LDH ([Ni^{2+}:Co^{2+}] = 1:2), and **(b-d)** SiO_2@Ni-Co LDH samples (PM1, PM2, and PM3).

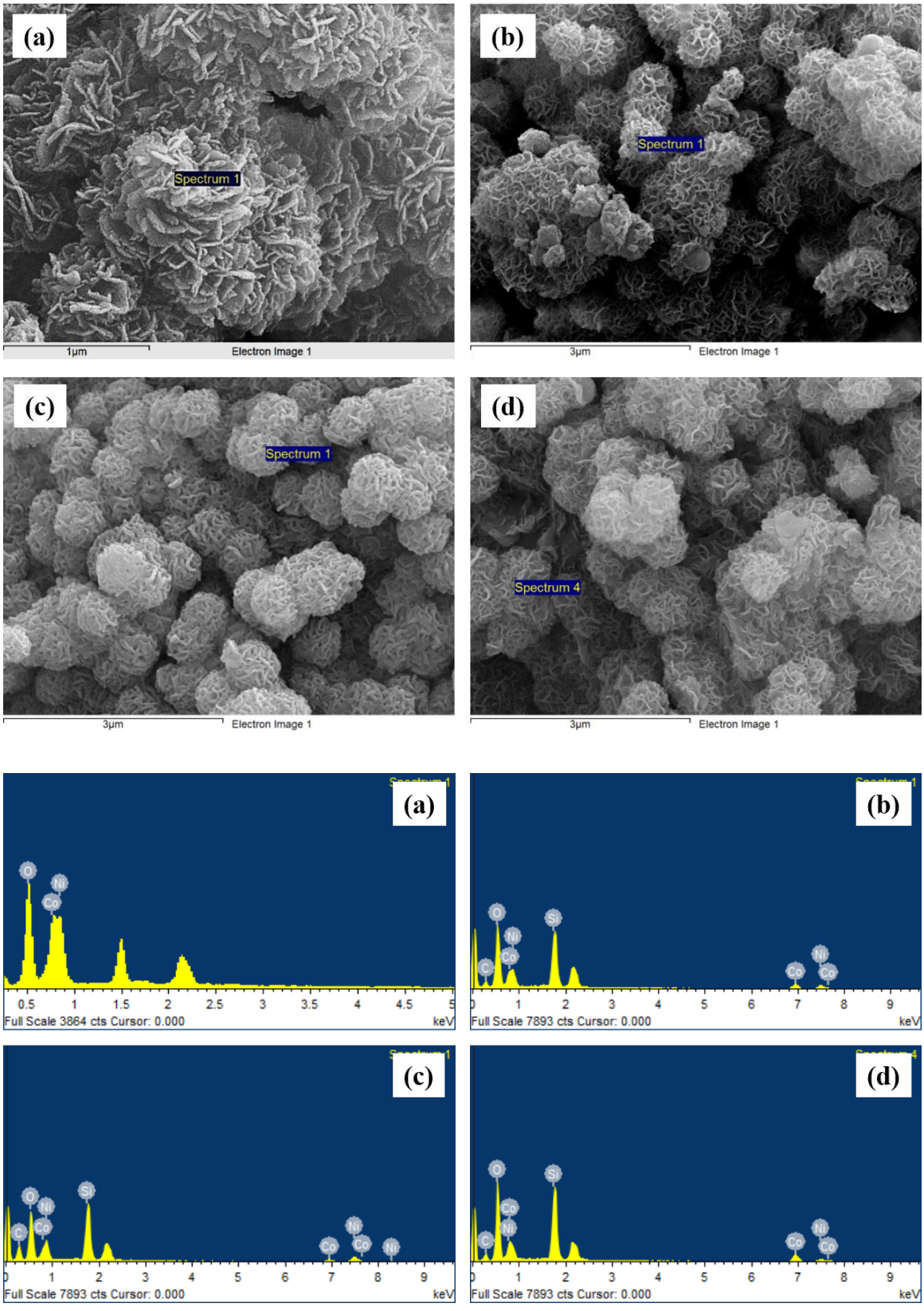

Fig. 5.2.14: SEM-EDX spectra of **(a)** $NiCo_2O_4$, and **(b-d)** SiO_2@Ni-Co mixed metal oxide samples (M1, M2, and M3).

Table 5.2.1: Elemental composition (At. %) of Si, Ni, Co, and O in SiO_2@Ni-Co LDH samples and SiO_2@Ni-Co mixed metal oxide (MMO) core-shell nanorattles.

Sample name	Atomic percent			
	Si	Ni	Co	O
SiO_2	28.0 ± 0.4	-	-	57.5 ± 0.4
Ni-Co LDH ($[Ni^{2+}:Co^{2+}]$ = 1:2)	-	9.1 ± 0.5	17.9 ± 0.3	54.5 ± 0.9
SiO_2@Ni-Co LDH (PM1)	17.7 ± 0.5	4.4 ± 0.2	1.4 ± 0.1	61.1 ± 0.8
SiO_2@Ni-Co LDH (PM2)	17.7 ± 0.8	4.5 ± 0.2	4.8 ± 0.3	56.2 ± 0.8
SiO_2@Ni-Co LDH (PM3)	16.3 ± 0.8	2.3 ± 0.1	4.5 ± 0.2	56.6 ± 0.3
$NiCo_2O_4$	-	8.7 ± 0.3	17.8 ± 0.4	35.7 ± 0.4
SiO_2@Ni-Co MMO (M1)	9.6 ± 0.8	4.6 ± 0.1	1.8 ± 0.1	43.8 ± 0.3
SiO_2@Ni-Co MMO (M2)	12.2 ± 0.9	3.3 ± 0.2	3.9 ± 0.2	54.2 ± 0.3
SiO_2@Ni-Co MMO (M3)	12.5 ± 0.3	2.3 ± 0.1	5.1 ± 0.2	55.3 ± 0.2

5.2.3.6 TEM studies

In order to understand the structural features further, TEM analysis was carried out for SiO_2, $NiCo_2O_4$ and SiO_2@Ni-Co mixed metal oxide samples (M1, M2 and M3) (Figure 5.2.15). Silica shows uniform spheres with a mean diameter of 310 ± 30 nm. Pure $NiCo_2O_4$ shows particles with sheet-like morphology. The TEM images of SiO_2@Ni-Co mixed metal oxide samples (M1, M2 and M3) show core-shell nanorattle morphology with void space between the SiO_2 core and the Ni-Co mixed metal oxide shell and the shell is composed of hair-like porous structure. The shell thickness was estimated from the TEM images and it is 39 ± 2, 55 ± 2, and 67 ± 3 nm, for samples M1, M2, and M3, respectively. The shell thickness of M3 is the largest and that of M1 the smallest. M1, M2 and M3 samples were prepared by the calcination of corresponding SiO_2@Ni-Co LDH samples with $[Ni^{2+}:Co^{2+}]$ ratios, 7:3 (PM1), 5:5 (PM2) and 3:7 (PM3), respectively. Thus, PM3 contains more α-$Co(OH)_2$ compared to α-$Ni(OH)_2$. The rate of dissolution-recrystallization of α-$Co(OH)_2$ and α-$Ni(OH)_2$ determines the thickness of the LDH shell on SiO_2 [145]. The solubility product of α-$Co(OH)_2$ is higher ($K_{sp} = 5.9 \times 10^{-15}$) compared to that of α-$Ni(OH)_2$ ($K_{sp} = 5.5 \times 10^{-16}$). This leads to more dissolution-recrystallization of α-$Co(OH)_2$ on SiO_2 in the case of PM3 ($[Ni^{2+}:Co^{2+}]$ = 3:7) compared to PM1 and PM2 leading to a thicker shell [146].

The order of shell thickness follows the order of concentration of Co^{2+} in the LDH (i.e. PM3>PM2>PM1). Calcination of a LDH precursor with thicker shell (PM3) leads to the corresponding SiO_2@Ni-Co mixed metal oxide (M3) with thicker shell. The void space was also estimated and the values are 80-85, 52-57, and 17-21 nm, for samples M1, M2, and M3, respectively. The thickness of porous hair-like structures of Ni-Co mixed metal oxides is 124 ± 5, 109 ± 3, and 100 ± 8 nm, for M1, M2, and M3, respectively. On-going from sample M1 to M3, increment in the shell thickness and decrement in the void space between the core and the shell can be noticed.

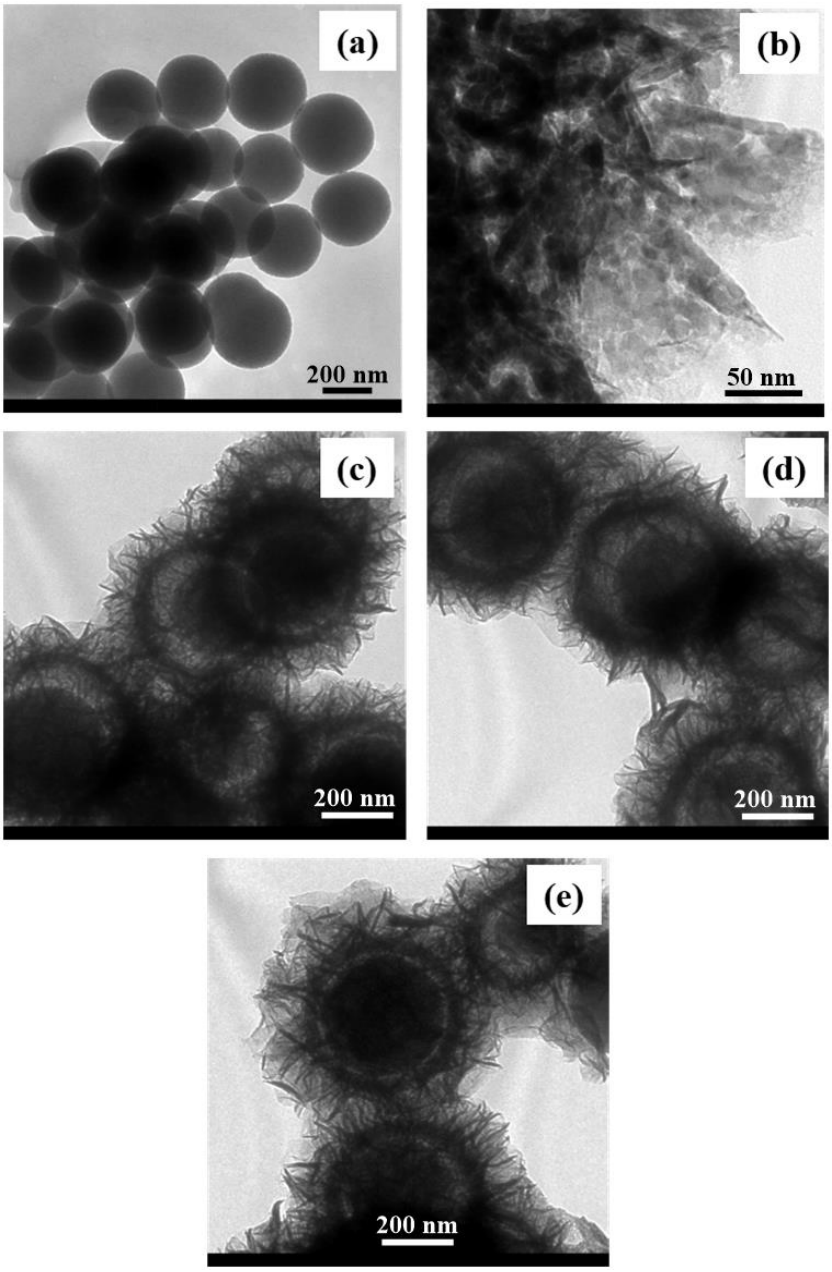

Fig. 5.2.15: TEM images of **(a)** SiO_2, **(b)** $NiCo_2O_4$ and **(c-e)** SiO_2@Ni-Co mixed metal oxide samples (M1, M2, and M3).

SAED patterns of pure $NiCo_2O_4$ and SiO_2@Ni-Co mixed metal oxide samples (M1, M2 and M3) are shown in Figure 5.2.16. The SAED pattern of pure $NiCo_2O_4$ shows spot pattern with well-defined rings while SiO_2@Ni-Co mixed metal oxide samples show ring patterns which suggest polycrystalline nature of the Ni-Co mixed metal oxides on the SiO_2 spheres. The SAED pattern of $NiCo_2O_4$ could be indexed to (220), (311), (400), (511), and (440) planes of cubic $NiCo_2O_4$. The SiO_2@Ni-Co mixed metal oxide (M1) shows (311) plane due to Co_3O_4 and (200) and (220) planes due to NiO. The SiO_2@Ni-Co mixed metal oxide (M2) shows (311) and (440) planes due to $NiCo_2O_4$ and (200) plane due to NiO. The SiO_2@Ni-Co mixed metal oxide (M3) shows (311) and (440) planes attributed to $Co_3O_4/NiCo_2O_4$ [147]. Pure $NiCo_2O_4$ shows stronger electron diffraction pattern compared to that of SiO_2@Ni-Co mixed metal oxides which indicate less crystalline nature of the Ni-Co mixed metal oxide nanoparticles on the SiO_2 spheres.

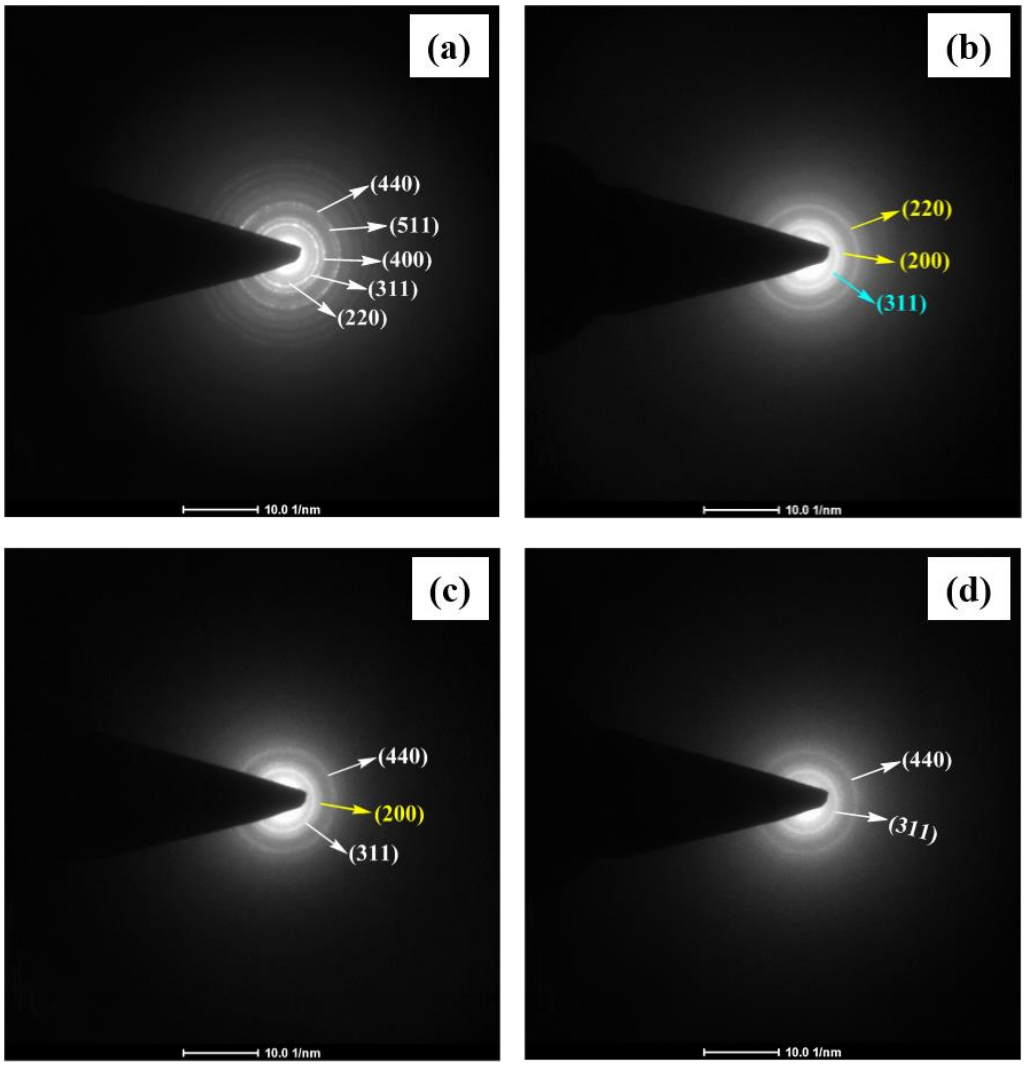

Fig. 5.2.16: SAED patterns of **(a)** $NiCo_2O_4$ and **(b-d)** SiO_2@Ni-Co mixed metal oxide samples (M1, M2, and M3, respectively).

5.2.3.7 BET surface area analysis

The specific surface area of SiO_2, $NiCo_2O_4$ and the SiO_2@Ni-Co mixed metal oxide samples (M1, M2, and M3) were determined using Brunauer-Emmett-Teller (BET) measurements using nitrogen physisorption. The surface area values of SiO_2 and $NiCo_2O_4$ are 34.2 and 95.4 m^2/g, respectively. The SiO_2@Ni-Co mixed metal oxide samples (M1, M2, and M3) possess surface area of about 234.5, 223.1, and 218.8 m^2/g, respectively. The higher surface area of SiO_2@Ni-Co mixed metal oxide samples is attributed to their nanorattle structure and also the porous hair-like structure of the shell on the surface of SiO_2 spheres.

5.2.3.8 UV-Visible diffuse reflectance spectroscopy (DRS) studies

The optical properties of pure Ni-Co mixed metal oxides, and the SiO_2@Ni-Co mixed metal oxide core-shell nanorattles (M1, M2 and M3) were studied using UV-Vis diffuse reflectance spectroscopy (DRS) and the DRS results are shown in Figure 5.2.17. The band gap energy of the samples was calculated using the equation, $E_g = 1240/\lambda\ (nm)$ [148]. In the structure of $NiCo_2O_4$, divalent Co^{2+} ($e_g^4 t_{2g}^3$) cations occupy the tetrahedral sites while the trivalent Co^{3+} (t_{2g}^6) and Ni^{3+} ($t_{2g}^6 e_g^1$) ions are located in the octahedral sites [149]. In the band structure of $NiCo_2O_4$, 2p orbitals of oxygen constitute the valence band and 3d orbitals of Ni or Co ions constitute the conduction band [150]. In $NiCo_2O_4$, two direct band gap transitions are possible, i.e. one transition from 2p orbital of oxygen to 3d-e_g of cobalt or nickel ions and the other from 2p orbital of oxygen to 3d-t_{2g} of cobalt or nickel ions [150].

The bulk band gap of NiO and Co_3O_4 are 3.9 eV and 2.19 eV, respectively. Pure mixed metal oxide sample prepared using [Ni^{2+}:Co^{2+}] = 7:3 shows a strong band gap absorption edge at about 360 nm (3.45 eV) due to NiO nanoparticles and another absorption band edge at about 575 nm (2.16 eV) attributed to Co_3O_4 nanoparticles. The red shift in the band gap absorption of NiO can be attributed to the presence of defects in the intergranular regions. The other pure mixed metal oxide samples ([Ni^{2+}:Co^{2+}] = 5:5 and 3:7) show absorption band edge at about 350 nm (3.54 eV) and 580 nm (2.14 eV) which are attributed to $O^{2-} \rightarrow Ni^{2+}$ and $O^{2-} \rightarrow Co^{3+}$ charge transfer transitions related to direct band gap of $NiCo_2O_4$. Pure $NiCo_2O_4$ shows absorption bands at 377 nm (3.32 eV) and 585 nm (2.12 eV). The band gap values of bulk $NiCo_2O_4$ are 1.97 and 3.40 eV [150].

The SiO_2@Ni-Co mixed metal oxide core-shell nanorattles (M1, M2, and M3) show absorption bands at 364 nm and 608 nm for M1, and 350 nm and 575 nm for M2 and M3. The SiO_2@Ni-Co mixed metal oxide (M1) possesses band gap energies of 2.04 and 3.41 eV due to Co_3O_4 nanoparticles and NiO nanoparticles, respectively. The SiO_2@Ni-Co mixed metal oxide samples (M2 and M3) possess band gap energies of 2.16 and 3.54 eV related to direct band gap transitions of $NiCo_2O_4$. Sample M1 exhibits red shift with respect to bulk NiO and samples M2 and M3 exhibit blue shift with respect to $NiCo_2O_4$. The red shift in sample M1 is attributed to the presence of defects in the intergranular region and blue shift in the band gap energies of samples M2 and M3 are attributed to quantum confinement effect and smaller particle size of $NiCo_2O_4$ [150,151].

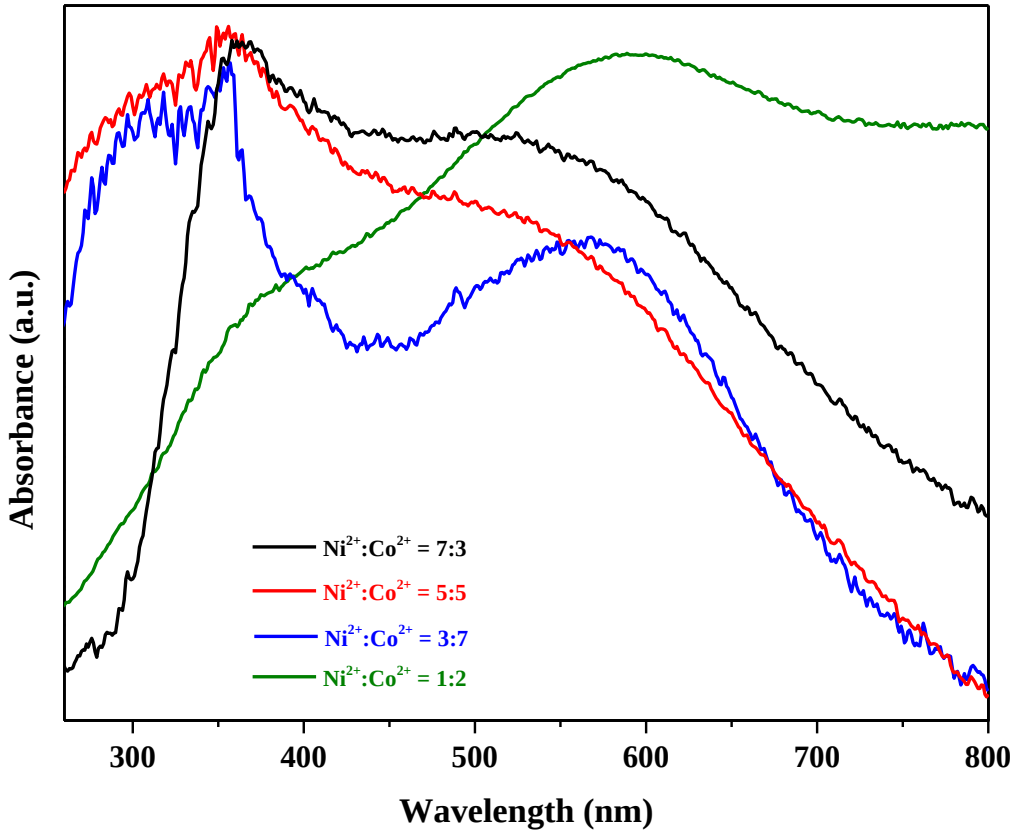

(a)

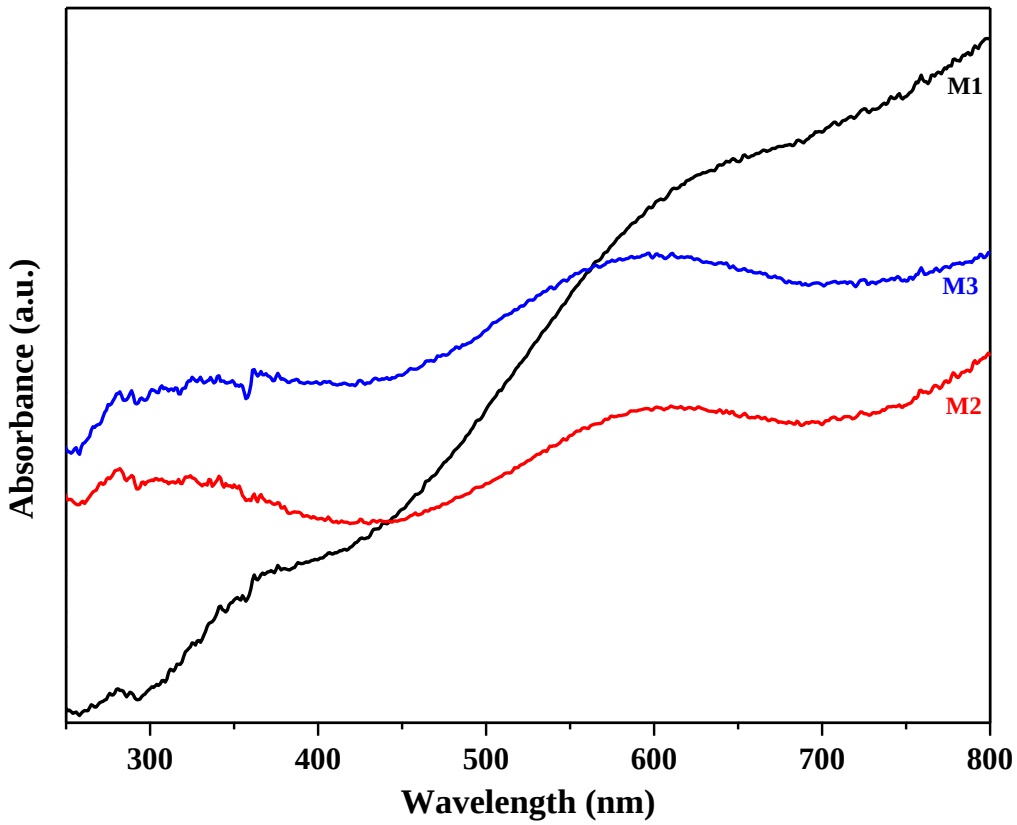

(b)

Fig. 5.2.17: UV-Visible DRS spectra of **(a)** pure Ni-Co mixed metal oxides and **(b)** SiO_2@Ni-Co mixed metal oxide core-shell nanorattles (M1, M2, and M3).

5.2.4 Proposed mechanism for the formation of SiO_2@Ni-Co mixed metal oxide core-shell nanorattles

For the formation of SiO_2@Ni-Co mixed metal oxide core-shell nanorattles, the following mechanism (Scheme 5.2.2), based on adsorption-nucleation-coalescence-anisotropic growth-self-assembly, is proposed [144]. Urea as a precipitating agent releases slowly OH^- ions due to its controlled hydrolysis [137]. In the aqueous solution, urea decomposes to produce NH_3 and CO_2. After attaining the optimum temperature (e.g. 85 ^oC), NH_3 readily undergoes hydrolysis and produces OH^- ions. In the aqueous solution, Co^{2+} and Ni^{2+} ions are able to adsorb on the surface of silica *via* electrostatic interaction. Then, the OH^- ions readily react with the available metal ions on the surface of silica and the nucleation and growth of Ni-Co LDH proceeds on the surface of SiO_2 based on the coalescence mechanism [126,137]. The formed Ni-Co LDH further undergoes Ostwald ripening to produce hierarchical flower-like Ni-Co LDH particles on the surface of SiO_2.

The single ultrathin nanoplatelet of Ni-Co LDH possesses high surface energy and, in order to minimize the overall surface energy, the formed ultrathin nanoplatelets of Ni-Co LDH undergo coalescence and self-assembly to produce thicker nanoplatelets of Ni-Co LDH. During this process, the pH of the solution decreases and Ostwald ripening would dominate leading to flower-like hierarchical Ni-Co LDH particles on the surface of SiO_2 [144]. In the final step, calcination of SiO_2@Ni-Co LDHs, in air at 500 ^oC, leads to the formation of SiO_2@Ni-Co mixed metal oxide core-shell nanorattles through self-template route while retaining their morphology as that of SiO_2@Ni-Co LDHs.

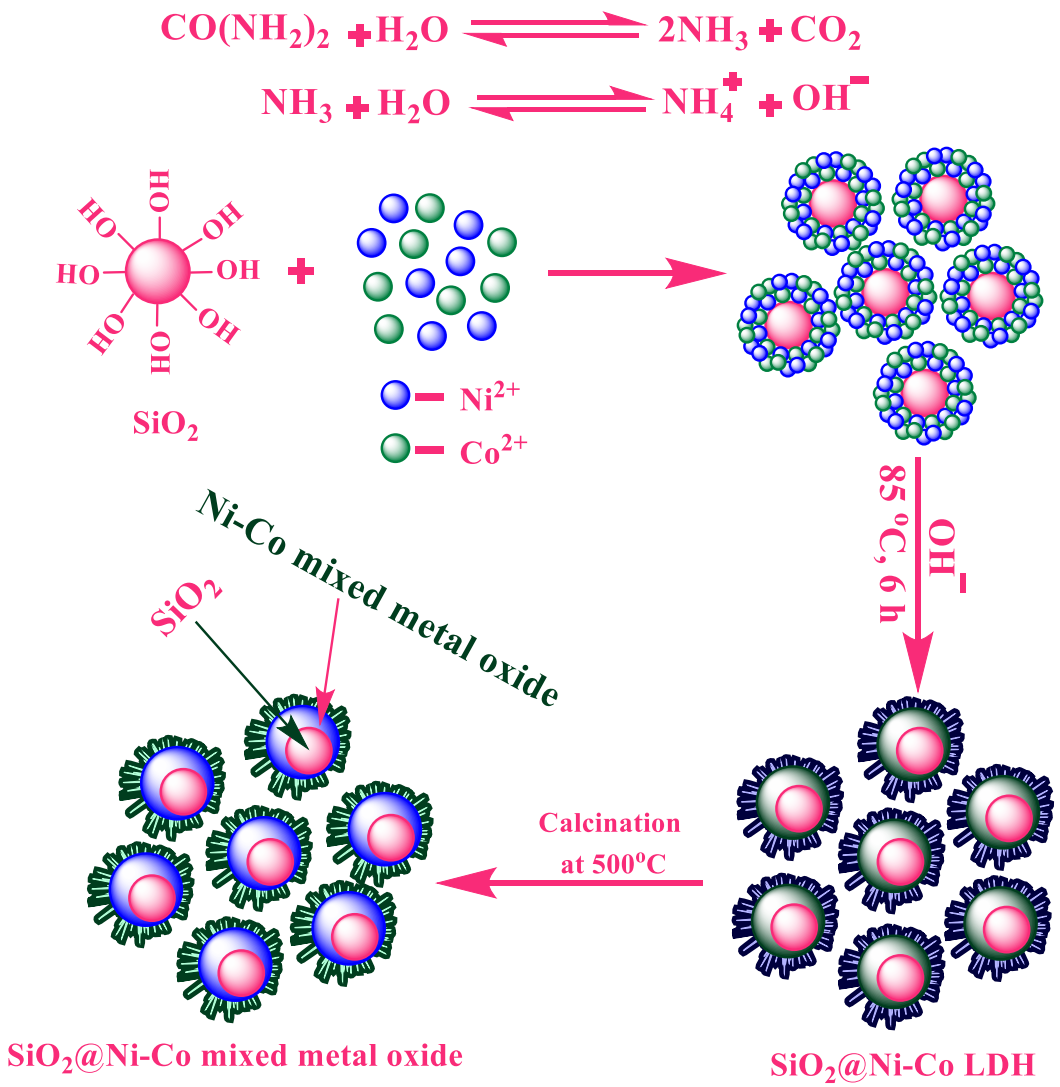

Scheme 5.2.2: Proposed mechanism for the formation of SiO_2@Ni-Co mixed metal oxide core-shell nanorattles.

To elucidate the formation mechanism of nanorattles further, time dependant TEM studies was carried out at different time intervals during the formation of SiO_2@Ni-Co

LDH (PM1) (e.g. 2 h, 4 h and 6 h) and SiO_2@Ni-Co mixed metal oxide (M1) (calcination temperature = 500 ^oC for 1 h and 3 h) (Figure 5.2.18). In the case of SiO_2@Ni-Co LDH, up to 2 h, a solid interface is formed between the SiO_2 core and the Ni-Co LDH shell leading to the formation of SiO_2@Ni-Co LDH core-shell structure (Figure 5.2.18a). As the reaction proceeds from 2 h to 4 h, the smaller crystallites of Ni-Co LDH located at the interior region starts dissolving and the hollowing process proceeds, which can be explained on the basis of inside-out Ostwald ripening. During this process, the loosely packed crystallites of Ni-Co LDH located at the outer region act as the nucleation sites for the recrystallization. After 4 h, dissolution of the interior crystallites of Ni-Co LDH is observed. At 6 h, the outer Ni-Co LDH crystallite becomes larger through recrystallization and forms the compact shell over the SiO_2 core which creates an interstitial space between the SiO_2 core and the Ni-Co LDH shell. Calcination of SiO_2@Ni-Co LDH at 500 ^oC for 1 h leads to the formation of SiO_2@Ni-Co mixed metal oxide core-shell nanorattles with the retention of core-shell nanorattles morphology. On further increase of calcination time to 3 h, creation of more interior space is observed (Figure 5.2.18b). During the calcination, shrinkage of SiO_2 core with creation of more interior space is observed. This is attributed to loss of surface hydroxyl groups present on SiO_2 as well as loss of intercalated water molecules and anions (NCO^-, and NO_3^-) present in Ni-Co LDH during the conversion of SiO_2@Ni-Co LDH to SiO_2@Ni-Co mixed metal oxide core-shell nanorattles.

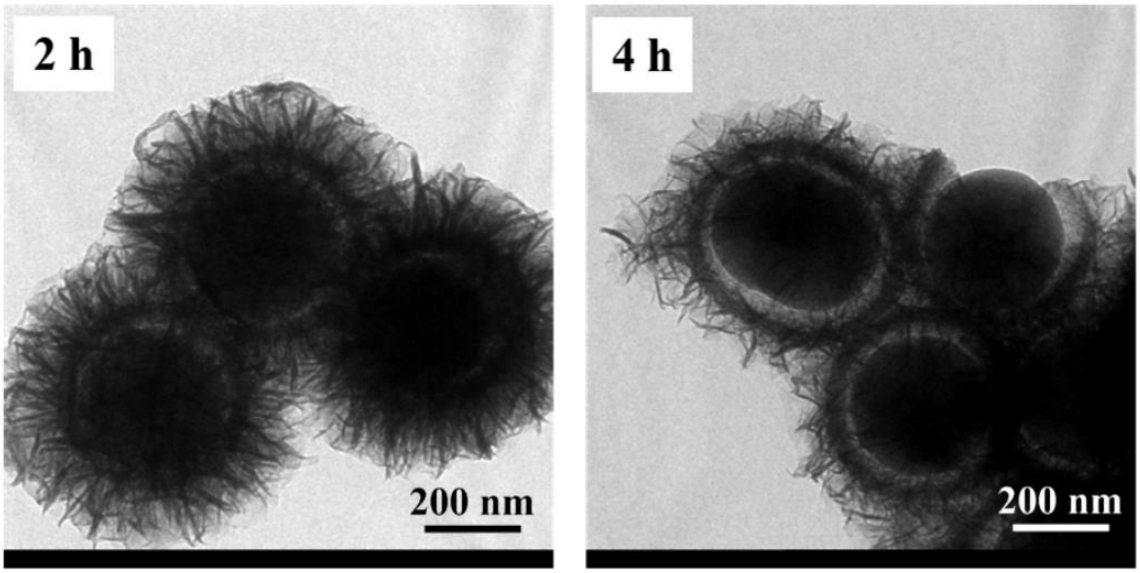

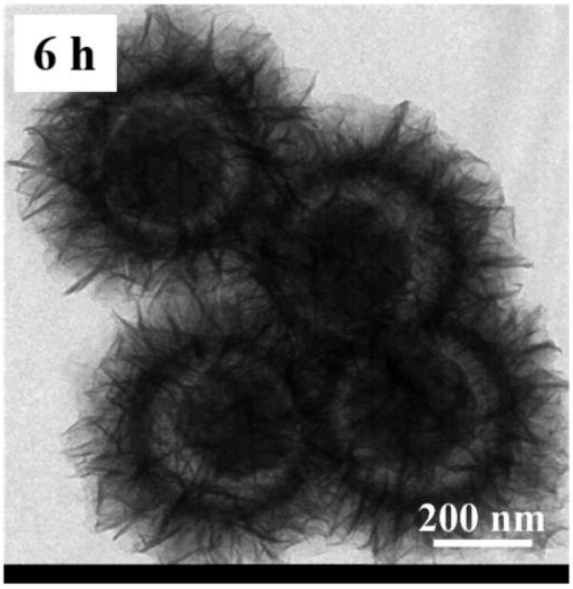

(a)

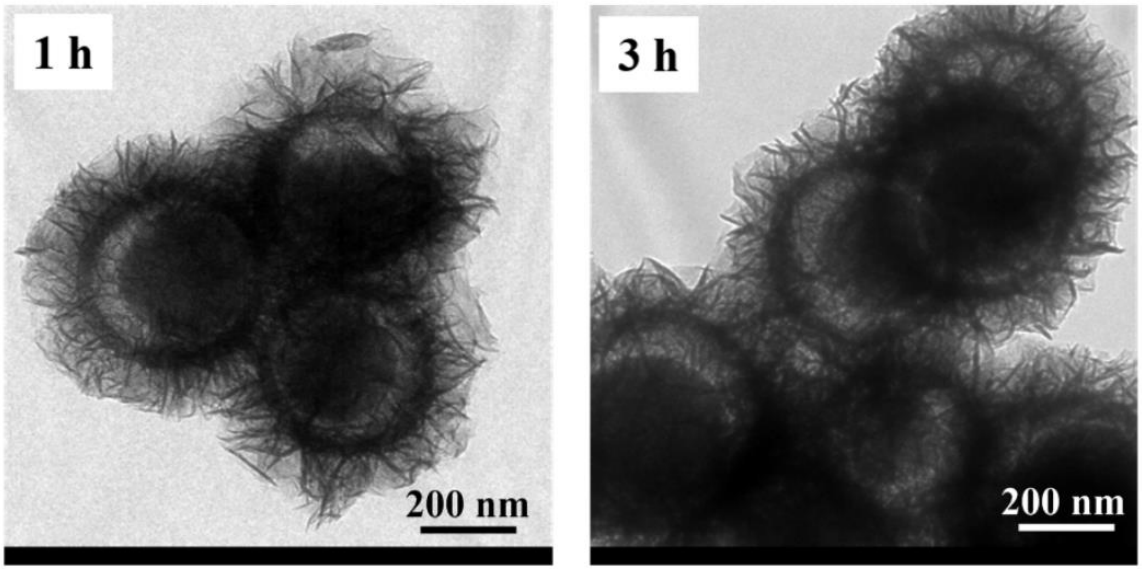

(b)

Fig. 5.2.18: (a) TEM images of SiO_2@Ni-Co LDH samples synthesized at 2 h, 4 h and 6 h and **(b)** SiO_2@Ni-Co mixed metal oxides obtained on calcination of SiO_2@Ni-Co LDH samples at 500 ^oC for 1 h and 3 h.

5.2.5 Conclusions

SiO_2@Ni-Co mixed metal oxide core-shell nanorattles have been successfully synthesized through a self-template route and the synthetic method is facile, and inexpensive. XRD results confirm the presence of Ni-Co mixed metal oxides (NiO, Co_3O_4, $NiCo_2O_4$) in the SiO_2@Ni-Co mixed metal oxide core-shell nanorattles. SEM results show the deposition of Ni-Co mixed metal oxides on the surface of SiO_2

microspheres. TEM images provide evidence for the formation of core-shell nanorattles. SAED patterns indicate polycrystalline nature of the Ni-Co mixed metal oxides. BET surface area results show higher surface area of SiO_2@Ni-Co mixed metal oxide samples due to the formation of nanorattles. DRS results show band gap absorptions of NiO, Co_3O_4 and $NiCo_2O_4$ in SiO_2@Ni-Co mixed metal oxide samples. The current method can be extended to prepare other mixed metal oxide core-shell nanorattles for various multi-functional applications.

References

1. Purbia R., Paria S., 'Yolk/shell nanoparticles: Classifications, synthesis, properties, and applications', *Nanoscale*, **7**, 19789–19873 (2015).

2. Liu J., Qiao S. Z., Chen J. S., Lou X. W., Xing X., Lu G. Q., 'Yolk/shell nanoparticles: New platforms for nanoreactors, drug delivery and lithium-ion batteries', *Chemical Communications*, **47**, 12578–12591 (2011).

3. Pang H., Cheng P., Yang H., Lu J., Guo C. X., Ning G., Li C. M., 'Template-free bottom-up synthesis of yolk-shell vanadium oxide as high performance cathode for lithium ion batteries', *Chemical Communications*, **49**, 1536–1538 (2013).

4. Galeano C., Güttel R., Paul M., Arnal P., Lu A. H., Schüth F., 'Yolk-shell gold nanoparticles as model materials for support-effect studies in heterogeneous catalysis: Au, @C and Au, @ZrO_2 for CO oxidation as an example', *Chemistry - A European Journal*, **17**, 8434–8439 (2011).

5. Mahmoud M. A., 'Plasmon resonance hybridization of gold nanospheres and palladium nanoshells combined in a rattle structure', *Journal of Physical Chemistry Letters*, **5**, 2594–2600 (2014).

6. Liu J., Qiao S. Z., Hartono S. B., Lu G. Q., 'Monodisperse yolk-shell nanoparticles with a hierarchical porous structure for delivery vehicles and nanoreactors', *Angewandte Chemie International Edition*, **49**, 4981–4985 (2010).

7. Xue W., Lifang C., Meng S., Feng L., Juncheng H., Richards R. M., 'Nanoscale gold intercalated into mesoporous silica as a highly active and robust catalyst', *Nanotechnology*, **23**, 294010/1–8 (2012).

8. Li X., Zhou X., Guo H., Wang C., Liu J., Sun P., Liu F., Lu G., 'Design of Au@ZnO yolk-shell nanospheres with enhanced gas sensing properties', *ACS Applied Materials and Interfaces*, **6**, 18661–18667 (2014).

9. Jayaramulu K., Datta K. K. R., Suresh M. V., Kumari G., Datta R., Narayana C., Eswaramoorthy M., Maji T. K., 'Honeycomb porous framework of zinc(II): Effective host for palladium nanoparticles for efficient three-component (A^3) coupling and

selective gas storage', *ChemPlusChem*, **77**, 743–747 (2012).

10. Liu C., Wang J., Li J., Luo R., Shen J., Sun X., Han W., Wang L., 'Controllable synthesis of functional hollow carbon nanostructures with dopamine as precursor for supercapacitors', *ACS Applied Materials and Interfaces*, **7**, 18609–18617 (2015).

11. Liu W., Liu Y., Yan X., Yong G., Xu Y., Liu S., 'One-pot synthesis of yolk–shell mesoporous carbon spheres with high magnetisation', *Journal of Materials Chemistry A*, **2**, 9600–9606 (2014).

12. Liu J., Cheng J., Che R., Xu J., Liu M., Liu Z., 'Synthesis and microwave absorption properties of yolk-shell microspheres with magnetic iron oxide cores and hierarchical copper silicate shells', *ACS Applied Materials and Interfaces*, **5**, 2503–2509 (2013).

13. Li Z. Q., Chen W. C., Guo F. L., Mo L. E., Hu L. H., Dai S. Y., 'Mesoporous TiO_2 yolk-shell microspheres for dye-sensitized solar cells with a high efficiency exceeding 11%', *Scientific Reports*, **5**, 14178 (2015).

14. Narasimha K., Jayakannan M., 'Pi-conjugated polymer anisotropic organogel nanofibrous assemblies for thermoresponsive photonic switches', *ACS Applied Materials and Interfaces*, **6**, 19385–19396 (2014).

15. Lin W. I., Lin C. Y., Lin Y. S., Wu S. H., Huang Y. R., Hung Y., Chang C., Mou C. Y., 'High payload Gd(III) encapsulated in hollow silica nanospheres for high resolution magnetic resonance imaging', *Journal of Materials Chemistry B*, **1**, 639–645 (2013).

16. Lehman S. E., Morris A. S., Mueller P. S., Salem A. K., Grassian V. H., Larsen S. C., 'Silica nanoparticle-generated ROS as a predictor of cellular toxicity: Mechanistic insights and safety by design', *Environmental Science: Nano*, **3**, 56–66 (2016).

17. Teng Z., Su X., Zheng Y., Sun J., Chen G., Tian C., Wang J., Li H., Zhao Y., Lu G., 'Mesoporous silica hollow spheres with ordered radial mesochannels by a spontaneous self-transformation approach', *Chemistry of Materials*, **25**, 98–105 (2013).

18. Fan C. M., Zhang L. F., Wang S. S., Wang D. H., Lu L. Q., Xu A. W., 'Novel CeO_2 yolk–shell structures loaded with tiny Au nanoparticles for superior catalytic reduction of p-nitrophenol', *Nanoscale*, **4**, 6835–6840 (2012).

19. Son M. Y., Hong Y. J., Lee J., Kang Y. C., 'One-pot synthesis of Fe_2O_3 yolk-shell particles with two, three, and four shells for application as an anode material in lithium-ion batteries', *Nanoscale*, **5**, 11592–11597 (2013).

20. Hong Y. J., Son M. Y., Kang Y. C., 'One-pot facile synthesis of double-shelled SnO_2 yolk-shell-structured powders by continuous process as anode materials for Li-ion batteries', *Advanced Materials*, **25**, 2279–2283 (2013).

21. Liu S., Xia J., Yu J., 'Amine-functionalized titanate nanosheet-assembled yolk@shell microspheres for efficient cocatalyst-free visible-light photocatalytic CO_2 reduction', *ACS Applied Materials and Interfaces*, **7**, 8166–8175 (2015).

22. Pan A., Wu H. Bin, Yu L., Lou X. W., 'Template-free synthesis of VO_2 hollow microspheres with various interiors and their conversion into V_2O_5 for lithium-ion batteries', *Angewandte Chemie International Edition*, **125**, 2226–2230 (2013).

23. Zhang W., Lin X. J., Sun Y. G., Bin D. S., Cao A. M., Wan L. J., 'Controlled formation of metal@Al_2O_3 yolk–shell nanostructures with improved thermal stability', *ACS Applied Materials and Interfaces*, **7**, 27031–27034 (2015).

24. Wong Y. J., Zhu L., Teo W. S., Tan Y. W., Yang Y., Wang C., Chen H., 'Revisiting the Stöber method: Inhomogeneity in silica shells', *Journal of the American Chemical Society*, **133**, 11422–11425 (2011).

25. Chen C., Fang X., Wu B., Huang L., Zheng N., 'A multi-yolk-shell structured nanocatalyst containing sub-10 nm Pd nanoparticles in porous CeO_2', *ChemCatChem*, **4**, 1578–1586 (2012).

26. Liang X., Li J., Joo J. B., Gutiérrez A., Tillekaratne A., Lee I., Yin Y., Zaera F., 'Diffusion through the shells of yolk-shell and core-shell nanostructures in the liquid phase', *Angewandte Chemie International Edition*, **51**, 8034–8036 (2012).

27. Chen J. S., Li C. M., Zhou W. W., Yan Q. Y., Archer L. A., Lou X. W., 'One-pot formation of SnO_2 hollow nanospheres and α-Fe_2O_3@SnO_2 nanorattles with large void space and their lithium storage properties', *Nanoscale*, **1**, 280–285 (2009).

28. Liu J., Cheng J., Che R., Xu J., Liu M., Liu Z., 'Double-shelled yolk−shell microspheres

with Fe_3O_4 cores and SnO_2 double shells as high-performance microwave absorbers', *The Journal of Physical Chemistry C*, **117**, 489–495 (2013).

29. Liu J., Xu J., Che R., Chen H., Liu M., Liu Z., 'Hierarchical Fe_3O_4@TiO_2 yolk-shell microspheres with enhanced microwave-absorption properties', *Chemistry - A European Journal*, **19**, 6746–6752 (2013).

30. Choi S. H., Kang Y. C., 'Using simple spray pyrolysis to prepare yolk-shell-structured ZnO-Mn_3O_4 systems with the optimum composition for superior electrochemical properties', *Chemistry - A European Journal*, **20**, 3014–3018 (2014).

31. Wang J., Li X., Li X., Zhu J., Li H., 'Mesoporous yolk-shell SnS_2-TiO_2 visible photocatalysts with enhanced activity and durability in Cr(VI) reduction', *Nanoscale*, **5**, 1876–1881 (2013).

32. Liu R., Qu F., Guo Y., Yao N., Priestley R. D., 'Au@carbon yolk–shell nanostructures *via* one-step core–shell–shell template', *Chemical Communications*, **50**, 478–480 (2014).

33. Ru Y., Evans D. G., Zhu H., Yang W., 'Facile fabrication of yolk-shell structured porous Si-C microspheres as effective anode materials for Li-ion batteries', *RSC Advances*, **4**, 71–75 (2014).

34. Fang X., Liu S., Zang J., Xu C., Zheng M. Sen, Dong Q. F., Sun D., Zheng N., 'Precisely controlled resorcinol–formaldehyde resin coating for fabricating core–shell, hollow, and yolk–shell carbon nanostructures', *Nanoscale*, **5**, 6908–6916 (2013).

35. Shiva K., Rajendra H. B., Bhattacharyya A. J., 'Electrospun SnSb crystalline nanoparticles inside porous carbon fibers as a high stability and rate capability anode for rechargeable batteries', *ChemPlusChem*, **80**, 516–521 (2015).

36. Wang J., Li W., Wang F., Xia Y., Asiri A. M., Zhao D., 'Controllable synthesis of SnO_2@C yolk-shell nanospheres as a high-performance anode material for lithium ion batteries', *Nanoscale*, **6**, 3217–3222 (2014).

37. Valle-Vigón P., Sevilla M., Fuertes A. B., 'Silica@carbon mesoporous nanorattle structures synthesised by means of a selective etching strategy', *Materials Letters*, **64**,

1587–1590 (2010).

38. Yoo J. B., Yoo H. J., Lim B. W., Lee K. H., Kim M. H., Kang D., Hur N. H., 'Controlled synthesis of monodisperse SiO_2-TiO_2 microspheres with a yolk-shell structure as effective photocatalysts', *ChemSusChem,* **5**, 2334–2340 (2012).

39. Liu H., Chen L., Liang Y., Fu R., Wu D., 'Multi-dimensional construction of a novel active yolk@conductive shell nanofiber web as a self-standing anode for high-performance lithium-ion batteries', *Nanoscale,* **7**, 19930–19934 (2015).

40. Liu C., Li J., Wang J., Qi J., Fan W., Shen J., Sun X., Han W., Wang L., 'Synthesis of Ag@SiO_2 yolk–shell nanoparticles for hydrogen peroxide detection', *RSC Advances,* **5**, 17372–17378 (2015).

41. Hu F., Zhang Y., Chen G., Li C., Wang Q., 'Double-walled Au nanocage/SiO_2 nanorattles: Integrating SERS imaging, drug delivery and photothermal therapy', *Small,* **11**, 985–993 (2015).

42. Peng J., Lan G., Guo M., Wei X., Li C., Yang Q., 'Fabrication of efficient hydrogenation nanoreactors by modifying the freedom of ultrasmall platinum nanoparticles within yolk-shell nanospheres', *Chemistry - A European Journal*, **21**, 10490–10496 (2015).

43. Li Q., Zhou T., Yang H., 'Encapsulation of Hoveyda–Grubbs^{2nd} catalyst within yolk–shell structured silica for olefin metathesis', *ACS Catalysis*, **5**, 2225–2231 (2015).

44. Dahlberg K. A., Schwank J. W., 'Synthesis of Ni@SiO_2 nanotube particles in a water-in-oil microemulsion template', *Chemistry of Materials*, **24**, 2635–2644 (2012).

45. Cui Z. M., Chen Z., Cao C. Y., Jiang L., Song W. G., 'A yolk-shell structured Fe_2O_3@mesoporous SiO_2 nanoreactor for enhanced activity as a Fenton catalyst in total oxidation of dyes', *Chemical Communications,* **49**, 2332–2334 (2013).

46. Zhang L., Wang T., Yang L., Liu C., Wang C., Liu H., Wang Y. A., Su Z., 'General route to multifunctional uniform yolk/mesoporous silica shell nanocapsules: A platform for simultaneous cancer-targeted imaging and magnetically guided drug delivery', *Chemistry - A European Journal,* **18**, 12512–12521 (2012).

47. He L., Li L., Zhang L., Xing S., Wang T., Li G., Wu X., Su Z., Wang C., 'ZIF-8

templated fabrication of rhombic dodecahedron-shaped ZnO@SiO_2, ZIF-8@SiO_2 yolk–shell and SiO_2 hollow nanoparticles', *CrystEngComm*, **16**, 6534–6537 (2014).

48. Ren L., Wang P., Han Y., Hu C., Wei B., 'Synthesis of $CoC_2O_4 \cdot 2H_2O$ nanorods and their thermal decomposition to Co_3O_4 nanoparticles', *Chemical Physics Letters*, **476**, 78–83 (2009).

49. Kim Y., Lee J. H., Cho S., Kwon Y., In I., Lee J., You N. H., Reichmanis E., Ko H., Lee K. T., Kwon H. K., Ko D. H., Yang H., Park B., 'Additive-free hollow-structured Co_3O_4 nanoparticle Li-ion battery: The origins of irreversible capacity loss', *ACS Nano*, **8**, 6701–6712 (2014).

50. Sun C., Rajasekhara S., Chen Y., Goodenough J. B., 'Facile synthesis of monodisperse porous Co_3O_4 microspheres with superior ethanol sensing properties', *Chemical Communications*, **47**, 12852–12854 (2011).

51. Wang X., Chen X., Gao L., Zheng H., Zhang Z., Qian Y., 'One-dimensional arrays of Co_3O_4 nanoparticles: Synthesis, characterization, and optical and electrochemical properties', *The Journal of Physical Chemistry B*, **108**, 16401–16404 (2004).

52. Deori K., Ujjain S. K., Sharma R. K., Deka S., 'Morphology controlled synthesis of nanoporous Co_3O_4 nanostructures and their charge storage characteristics in supercapacitors', *ACS Applied Materials and Interfaces*, **5**, 10665–10672 (2013).

53. Blakemore J. D., Gray H. B., Winkler J. R., Müller A. M., 'Co_3O_4 nanoparticles made by pulsed-laser ablation in liquids as high activity catalysts for water oxidation', *ACS Catalysis*, **3**, 2497–2500 (2013).

54. Kang N., Park J. H., Jin M., Park N., Lee S. M., Kim H. J., Kim J. M., Son S. U., 'Microporous organic network hollow spheres: Useful templates for nanoparticulate Co_3O_4 hollow oxidation catalysts', *Journal of the American Chemical Society*, **135**, 19115–19118 (2013).

55. Li Y., Tan B., Wu Y., 'Mesoporous Co_3O_4 nanowire arrays for lithium ion batteries with high capacity and rate capability', *Nano Letters*, **8**, 265–270 (2008).

56. Lou X. W., Deng D., Lee J. Y., Feng J., Archer L. A., 'Self-supported formation of

needlelike Co_3O_4 nanotubes and their application as lithium-ion battery electrodes', *Advanced Materials,* **20**, 258–262 (2008).

57. Wang Y., Xia H., Lu L., Lin J., 'Excellent performance in lithium-ion battery anodes: Rational synthesis of $Co(CO_3)_{0.5}(OH)_{0.11}H_2O$ nanobelt array and its conversion into mesoporous and single-crystal Co3O4', *ACS Nano,* **4**, 1425–1432 (2010).

58. Lu Y., Wang Y., Zou Y. Q., Jiao Z., Zhao B., He Y. Q., Wu M. H., 'Macroporous Co_3O_4 platelets with excellent rate capability as anodes for lithium ion batteries', *Electrochemistry Communications,* **12**, 101–105 (2010).

59. Son M. Y., Hong Y. J., Kang Y. C., 'Superior electrochemical properties of Co_3O_4 yolk-shell powders with a filled core and multishells prepared by a one-pot spray pyrolysis', *Chemical Communications,* **49**, 5678–5680 (2013).

60. Yoon J. W., Hong Y. J., Park G. D., Hwang S. J., Abdel-Hady F., Wazzan A. A., Kang Y. C., Lee J. H., 'Kilogram-scale synthesis of Pd-loaded quintuple-shelled Co_3O_4 microreactors and their application to ultrasensitive and ultraselective detection of methylbenzenes', *ACS Applied Materials and Interfaces,* **7**, 7717–7723 (2015).

61. Yan N., Chen Q., Wang F., Wang Y., Zhong H., Hu L., 'High catalytic activity for CO oxidation of Co_3O_4 nanoparticles in SiO_2 nanocapsules', *Journal of Materials Chemistry A,* **1**, 637–643 (2013).

62. Ye Y., Kuai L., Geng B., 'A template-free route to a Fe_3O_4–Co_3O_4 yolk–shell nanostructure as a noble-metal free electrocatalyst for ORR in alkaline media', *Journal of Materials Chemistry,* **22**, 19132–19138 (2012).

63. Xiao M., Zhao C., Chen H., Yang B., Wang J., ''Ship-in-a-Bottle' growth of noble metal nanostructures', *Advanced Functional Materials,* **22**, 4526–4532 (2012).

64. Kuai L., Wang S., Geng B., 'Gold-platinum yolk-shell structure: A facile galvanic displacement synthesis and highly active electrocatalytic properties for methanol oxidation with super CO-tolerance', *Chemical Communications,* **47**, 6093–6095 (2011).

65. Anderson B. D., Tracy J. B., 'Nanoparticle conversion chemistry: Kirkendall effect, galvanic exchange, and anion exchange', *Nanoscale,* **6**, 12195–12216 (2014).

66. Yec C. C., Zeng H. C., 'Synthesis of complex nanomaterials *via* Ostwald ripening', *Journal of Materials Chemistry A,* **2**, 4843–4861 (2014).

67. Goebl J., Yin Y., 'Ship in a bottle: In situ confined growth of complex yolk-shell catalysts', *ChemCatChem,* **5**, 1287–1288 (2013).

68. Xu S., Li H., Wang L., Yue Q., Sixiu S., Liu J., 'One-pot synthesis of Ag@Cu yolk–shell nanostructures and their application as non-enzymatic glucose biosensors', *CrystEngComm,* **16**, 9075–9082 (2014).

69. Gao J., Liang G., Cheung J. S., Pan Y., Kuang Y., Zhao F., Zhang B., Zhang X., Wu E. X., Xu B., 'Multifunctional yolk− shell nanoparticles: A potential MRI contrast and anticancer agent', *Journal of the American Chemical Society,* **130**, 11828–11833 (2008).

70. Kandula S., Jeevanandam P., 'Synthesis of SiOx@CdS core–shell nanoparticles by simple thermal decomposition approach and studies on their optical properties', *Journal of Alloys and Compounds,* **615**, 167–176 (2014).

71. Liu Z., Ma R., Osada M., Takada K., Sasaki T., 'Selective and controlled synthesis of α- and β-cobalt hydroxides in highly developed hexagonal platelets', *Journal of the American Chemical Society,* **127**, 13869–13874 (2005).

72. Chen W., Yang Y., Shao H., Fan J., 'Tunable electrochemical properties brought about by partial cation exchange in hydrotalcite-like Ni-Co/Co-Ni hydroxide nanosheets', *The Journal of Physical Chemistry C,* **112**, 17471–17477 (2008).

73. Cheng J. P., Liu L., Zhang J., Liu F., Zhang X. B., 'Influences of anion exchange and phase transformation on the supercapacitive properties of α-$Co(OH)_2$', *Journal of Electroanalytical Chemistry,* **722-723**, 23–31 (2014).

74. Wang Q., Liu S., Sun H., Lu Q., 'Synthesis and intrinsic peroxidase-like activity of sisal-like cobalt oxide architectures', *Industrial and Engineering Chemistry Research,* **53**, 7917–7922 (2014).

75. Oaki Y., Kajiyama S., Nishimura T., Kato T., 'Selective synthesis and thin-film formation of α-cobalt hydroxide through an approach inspired by biomineralization', *Journal of Materials Chemistry,* **18**, 4140–4142 (2008).

76. Kishore P. N. R., Jeevanandam P., 'Synthesis of cobalt oxide nanoparticles *via* homogeneous precipitation using different synthetic conditions', *Journal of Nanoscience and Nanotechnology*, **13**, 2908–2916 (2013).

77. Frost R. L., Wain D. L., Martens W. N., Reddy B. J., 'Vibrational spectroscopy of selected minerals of the rosasite group', *Spectrochimica Acta Part A: Molecular and Biomolecular Spectroscopy*, **66**, 1068–1074 (2007).

78. Bayal N., Jeevanandam P., 'Synthesis of SiO_2@NiO magnetic core–shell nanoparticles and their use as adsorbents for the removal of methylene blue', *Journal of Nanoparticle Research*, **15**, 2066/1–15 (2013).

79. Ghosh D., Giri S., Das C. K., 'Preparation of CTAB-assisted hexagonal platelet $Co(OH)_2$/graphene hybrid composite as efficient supercapacitor electrode material', *ACS Sustainable Chemistry and Engineering*, **1**, 1135–1142 (2013).

80. Xu Z., Chen Z., Ben Y., Shen J., 'Synthesis of hexagonal β-$Co(OH)_2$ nano-platelets with high catalytic activity *via* a low-temperature precipitation method', *Materials Letters*, **63**, 1210–1212 (2009).

81. Palmer S. J., Frost R. L., Nguyen T., 'Hydrotalcites and their role in coordination of anions in Bayer liquors: Anion binding in layered double hydroxides', *Coordination Chemistry Reviews*, **253**, 250–267 (2009).

82. Malherbe F., Besse J. P., 'Investigating the effects of guest–host interactions on the properties of anion-exchanged Mg–Al hydrotalcites', *Journal of Solid State Chemistry*, **155**, 332–341 (2000).

83. Yang P., Wang F., Luo X., Zhang Y., Guo J., Shi W., Wang C., 'Rational design of magnetic nanorattles as contrast agents for ultrasound/magnetic resonance dual-modality imaging', *ACS Applied Materials and Interfaces*, **6**, 12581–12587 (2014).

84. Xu J., Liu J., Che R., Liang C., Cao M., Li Y., Liu Z., 'Polarization enhancement of microwave absorption by increasing aspect ratio of ellipsoidal nanorattles with Fe_3O_4 cores and hierarchical $CuSiO_3$ shells', *Nanoscale*, **6**, 5782–5790 (2014).

85. Deori K., Deka S., 'Morphology oriented surfactant dependent CoO and reaction time

dependent Co_3O_4 nanocrystals from single synthesis method and their optical and magnetic properties', *CrystEngComm*, **15**, 8465–8474 (2013).

86. Farhadi S., Pourzare K., Bazgir S., 'Co_3O_4 nanoplates: Synthesis, characterization and study of optical and magnetic properties', *Journal of Alloys and Compounds*, **587**, 632–637 (2014).

87. Gulino A., Dapporto P., Rossi P., Fragala I., 'A Novel self-generating liquid MOCVD precursor for Co_3O_4 thin films', *Chemistry of Materials*, **15**, 3748–3752 (2003).

88. Yan J., Fan Z., Sun W., Ning G., Wei T., Zhang Q., Zhang R., Zhi L., Wei F., 'Advanced asymmetric supercapacitors based on $Ni(OH)_2$/graphene and porous graphene electrodes with high energy density', *Advanced Functional Materials*, **22**, 2632–2641 (2012).

89. Yuan C., Zhang X., Su L., Gao B., Shen L., 'Facile synthesis and self-assembly of hierarchical porous NiO nano/micro spherical superstructures for high performance supercapacitors', *Journal of Materials Chemistry*, **19**, 5772–5777 (2009).

90. Bie S., Zhu Y., Su J., Jin C., Liu S., Yang R., Wu J., 'One-pot fabrication of yolk–shell structured $La_{0.9}Sr_{0.1}CoO_3$ perovskite microspheres with enhanced catalytic activities for oxygen reduction and evolution reactions', *Journal of Materials Chemistry A*, **3**, 22448–22453 (2015).

91. Zeng M., Huang Y., Zhang S., Qin S., Li J., Xu J., 'Removal of uranium(VI) from aqueous solution by magnetic yolk–shell iron oxide@magnesium silicate microspheres', *RSC Advances*, **4**, 5021–5029 (2014).

92. Zhou X., Wang B., Sun H., Wang C., Sun P., Li X., Hu X., Lu G., 'Template-free synthesis of hierarchical $ZnFe_2O_4$ yolk–shell microspheres for high-sensitivity acetone sensors', *Nanoscale*, **8**, 5446–5453 (2016).

93. Jayaramulu K., Datta K. K. R., Shiva K., Bhattacharyya A. J., Eswaramoorthy M., Maji T. K., 'Controlled synthesis of tunable nanoporous carbons for gas storage and supercapacitor application', *Microporous and Mesoporous Materials*, **206**, 127–135 (2015).

94. Wang L., Zhuo L., Zhang C., Zhao F., 'Embedding $NiCo_2O_4$ nanoparticles into a

3DHPC assisted by CO_2-expanded ethanol: A potential lithium-ion battery anode with high performance', *ACS Applied Materials and Interfaces*, **6**, 10813–10820 (2014).

95. Lehman S. E., Mudunkotuwa I. A., Grassian V. H., Larsen S. C., 'Nano–bio interactions of porous and nonporous silica nanoparticles of varied surface chemistry: A structural, kinetic, and thermodynamic study of protein adsorption from RPMI culture medium', *Langmuir*, **32**, 731–742 (2016).

96. Choi S. H., Kang Y. C., 'Yolk-shell, hollow, and single-crystalline $ZnCo_2O_4$ powders: Preparation using a simple one-pot process and application in lithium-ion batteries', *ChemSusChem*, **6**, 2111–2116 (2013).

97. Won J. M., Choi S. H., Hong Y. J., Ko Y. N., Kang Y. C., 'Electrochemical properties of yolk-shell structured $ZnFe_2O_4$ powders prepared by a simple spray drying process as anode material for lithium-ion battery', *Scientific Reports*, **4**, 5857/1–5 (2014).

98. Li J., Wang J., Liang X., Zhang Z., Liu H., Qian Y., Xiong S., 'Hollow $MnCo_2O_4$ submicrospheres with multilevel interiors: From mesoporous spheres to yolk-in-double-shell structures', *ACS Applied Materials and Interfaces*, **6**, 24–30 (2014).

99. Ko Y. N., Park S. Bin, Lee J. H., Chan Kang Y., 'Comparison of the electrochemical properties of yolk–shell and dense structured $CoFe_2O_4$ powders prepared by a spray pyrolysis process', *RSC Advances*, **4**, 40188–40192 (2014).

100. Zhang Z., Ji Y., Li J., Tan Q., Zhong Z., Su F., 'Yolk bishell $Mn_xCo_{1-x}Fe_2O_4$ hollow microspheres and their embedded form in carbon for highly reversible lithium storage', *ACS Applied Materials and Interfaces*, **7**, 6300–6309 (2015).

101. Yang H., Liu P., Chen Q., Liu X., Lu Y., Xie S., Ni L., Wu X., Peng M., Chen Y., Tang Y., Chen Y., 'Fabrication and characteristics of high-capacity $LiNi_{0.8}Co_{0.15}Al_{0.05}O_2$ with monodisperse yolk–shell spherical precursors by a facile method', *RSC Advances*, **4**, 35522–35527 (2014).

102. Hong Y. J., Son M. Y., Park B. K., Kang Y. C., 'One-pot synthesis of yolk-shell materials with single, binary, ternary, quaternary, and quinary systems', *Small*, **9**, 2224–2227 (2013).

103. Choi S. H., Lee J. K., Kang Y. C., 'Controllable synthesis of yolk-shell-structured metal oxides with seven to ten components for finding materials with superior lithium storage properties', *Nanoscale*, **6**, 12421–12425 (2014).

104. Wang Z., Wang Z., Wu H., Lou X. W., 'Mesoporous single-crystal $CoSn(OH)_6$ hollow structures with multilevel interiors', *Scientific Reports*, **3**, 1391/1–8 (2013).

105. Shao M., Ning F., Zhao J., Wei M., Evans D. G., Duan X., 'Hierarchical layered double hydroxide microspheres with largely enhanced performance for ethanol electrooxidation', *Advanced Functional Materials*, **23**, 3513–3518 (2013).

106. Shao M., Ning F., Zhao Y., Zhao J., Wei M., Evans D. G., Duan X., 'Core-shell layered double hydroxide microspheres with tunable interior architecture for supercapacitors', *Chemistry of Materials*, **24**, 1192–1197 (2012).

107. Liu Y., Fang Z., Kuai L., Geng B., 'One-pot facile synthesis of reusable tremella-like $M_1@M_2@M_1(OH)_2$ (M_1 = Co, Ni, M_2 = Pt/Pd, Pt, Pd and Au) three layers core–shell nanostructures as highly efficient catalysts', *Nanoscale*, **6**, 9791–9797 (2014).

108. Xie S., Jin M., Tao J., Wang Y., Xie Z., Zhu Y., Xia Y., 'Synthesis and characterization of $Pd@M_xCu_{1-x}$ (M=Au, Pd, and Pt) nanocages with porous walls and a yolk-shell structure through galvanic replacement reactions', *Chemistry - A European Journal*, **18**, 14974–14980 (2012).

109. Manshina A. A., Grachova E. V, Povolotskiy A. V, Povolotckaia A. V, Petrov Y. V, Koshevoy I. O., Makarova A. A., Vyalikh D. V, Tunik S. P., 'Laser-induced transformation of supramolecular complexes: Approach to controlled formation of hybrid multi-yolk-shell Au-Ag@a-C:H nanostructures', *Scientific Reports*, **5**, 12027/1–11 (2015).

110. Park S., Yoon D., Baik H., Lee K., 'Synthesis of size-controlled PtCu@Ru nanorattles *via* Pt seed-assisted formation of size-controlled removable Cu template', *CrystEngComm*, **17**, 6852–6856 (2015).

111. Yang S., Cao C., Peng L., Huang P., Sun Y., Wei F., Song W., 'Spindle-shaped nanoscale yolk/shell magnetic stirring bars for heterogeneous catalysis in macro- and microscopic systems', *Chemical Communications*, **52**, 1575–1578 (2016).

112. Fang Q., Xuan S., Jiang W., Gong X., 'Yolk-like micro/nanoparticles with superparamagnetic iron oxide cores and hierarchical nickel silicate shells', *Advanced Functional Materials,* **21**, 1902–1909 (2011).

113. Liu J., Xu J., Che R., Chen H., Liu Z., Xia F., 'Hierarchical magnetic yolk–shell microspheres with mixed barium silicate and barium titanium oxide shells for microwave absorption enhancement', *Journal of Materials Chemistry*, **22**, 9277–9284 (2012).

114. Hong Y. J., Kang Y. C., 'Superior electrochemical performances of double-shelled CuO yolk–shell powders formed from spherical copper nitrate–polyvinylpyrrolidone composite powders', *RSC Advances,* **4**, 58231–58237 (2014).

115. Hu Y., Zheng X. T., Chen J. S., Zhou M., Li C. M., Lou X. W., 'Silica-based complex nanorattles as multifunctional carrier for anticancer drug', *Journal of Materials Chemistry,* **21**, 8052–8056 (2011).

116. Chen J. S., Chen C., Liu J., Xu R., Qiao S. Z., Lou X. W., 'Ellipsoidal hollow nanostructures assembled from anatase TiO_2 nanosheets as a magnetically separable photocatalyst', *Chemical Communications*, **47**, 2631–2633 (2011).

117. Hong Y. J., Yoon J. W., Lee J. H., Kang Y. C., 'One-pot synthesis of Pd-loaded SnO_2 yolk-shell nanostructures for ultraselective methyl benzene sensors', *Chemistry - A European Journal*, **20**, 2737–2741 (2014).

118. Wang M., Wei N., Fu W., Yan M., Long L., Yao Y., Yin G., Liao X., Huang Z., Chen X., 'An efficient and recyclable urchin-like yolk–shell Fe_3O_4@SiO_2@Co_3O_4 catalyst for photocatalytic water oxidation', *Catalysis Letters*, **145**, 1067–1071 (2015).

119. Liu B., Wang Q., Yu S., Jing P., Liu L., Xu G., Zhang J., 'Architecture engineering toward highly active palladium integrated titanium dioxide yolk-double-shell nanoreactor for catalytic applications', *Nanoscale,* **6**, 11887–11897 (2014).

120. Chen L., Li L., Wang T., Zhang L., Xing S., Wang C., Su Z., 'A novel strategy to fabricate multifunctional Fe_3O_4@C@TiO_2 yolk-shell structures as magnetically recyclable photocatalysts', *Nanoscale,* **6**, 6603–6608 (2014).

121. Yang T., Liu J., Zheng Y., Monteiro M. J., Qiao S. Z., 'Facile fabrication of core-shell-structured Ag@carbon and mesoporous yolk-shell-structured Ag@carbon@silica by an extended Stöber method', *Chemistry - A European Journal*, **19**, 6942–6945 (2013).

122. Yao T., Cui T., Fang X., Cui F., Wu J., 'Preparation of yolk–shell Fe_xO_y/Pd@mesoporous SiO_2 composites with high stability and their application in catalytic reduction of 4-nitrophenol', *Nanoscale*, **5**, 5896–5904 (2013).

123. Li Z., Mo L., Kathiraser Y., Kawi S., 'Yolk−satellite−shell structured Ni−yolk@Ni@SiO_2 nanocomposite: Superb catalyst toward methane CO_2 reforming reaction', *ACS Catalysis*, **4**, 1526–1536 (2014).

124. Huang C. M., Cheng S. H., Jeng U. S., Yang C. S., Lo L. W., 'Formation of CdSe/CdS/ZnS-Au/SiO_2 dual-yolk/shell nanostructures through a Trojan-type inside-out etching strategy', *Nano Research*, **5**, 654–666 (2012).

125. Dong W., Zhu Y., Huang H., Jiang L., Zhu H., Li C., Chen B., Shi Z., Wang G., 'A performance study of enhanced visible-light-driven photocatalysis and magnetical protein separation of multifunctional yolk–shell nanostructures', *Journal of Materials Chemistry A*, **1**, 10030–10036 (2013).

126. Shen L., Che Q., Li H., Zhang X., 'Mesoporous $NiCo_2O_4$ nanowire arrays grown on carbon textiles as binder-free flexible electrodes for energy storage', *Advanced Functional Materials*, **24**, 2630–2637 (2014).

127. Ding R., Qi L., Jia M., Wang H., 'Simple hydrothermal synthesis of mesoporous spinel $NiCo_2O_4$ nanoparticles and their catalytic behavior in CH_3OH electro-oxidation and H_2O_2 electro-reduction', *Catalysis Science and Technology*, **3**, 3207–3215 (2013).

128. Verma S., Joshi H. M., Jagadale T., Chawla A., Chandra R., Ogale S., 'Nearly monodispersed multifunctional $NiCo_2O_4$ spinel nanoparticles: Magnetism, infrared transparency, and radiofrequency absorption', *The Journal of Physical Chemistry C*, **112**, 15106–15112 (2008).

129. Lv X., Zhu Y., Jiang H., Yang X., Liu Y., Su Y., Huang J., Yao Y., Li C., 'Hollow mesoporous $NiCo_2O_4$ nanocages as efficient electrocatalysts for oxygen evolution reaction', *Dalton Transactions*, **44**, 4148–4154 (2015).

130. Hu H., Guan B., Xia B., Lou X. W., 'Designed formation of Co_3O_4/$NiCo_2O_4$ double-shelled nanocages with enhanced pseudocapacitive and electrocatalytic properties', *Journal of the American Chemical Society*, **137**, 5590–5595 (2015).

131. Dong K., Liu Z., Ren J., 'A general and eco-friendly self-etching route to prepare highly active and stable Au@metal silicate yolk-shell nanoreactors for catalytic reduction of 4-nitrophenol', *CrystEngComm*, **15**, 6329–6334 (2013).

132. Yang Y., Zhao X., Zhu Y., Zhang F., 'Transformation mechanism of magnesium and aluminum precursor solution into crystallites of layered double hydroxide', *Chemistry of Materials*, **24**, 81–87 (2012).

133. Chen C., Felton R., Buffet J. C., O'Hare D., 'Core–shell SiO_2@LDHs with tuneable size, composition and morphology', *Chemical Communications*, **51**, 3462–3465 (2015).

134. Su L., Hou T., Han W., 'Selective synthesis and capacitive characteristics of CoNiAl three-component layered double hydroxide platelets', *RSC Advances*, **3**, 19807–19811 (2013).

135. Ge Y., Kan K., Yang Y., Zhou L., Jing L., Shen P., Li L., Shi K., 'Highly mesoporous hierarchical nickel and cobalt double hydroxide composite: fabrication, characterization and ultrafast NO_x gas sensors at room temperature', *Journal of Materials Chemistry A*, **2**, 4961–4969 (2014).

136. Song J. M., Ni J. jing, Zhang J., Ling D., Niu H. L., Mao C. J., Zhang S. Y., Shen Y. H., 'A facile synthesis of graphene-like cobalt–nickel double hydroxide nanocomposites at room temperature and their excellent catalytic and adsorption properties', *Journal of Nanoparticle Research*, **16**, 2269/1–15 (2014).

137. Padmanathan N., Selladurai S., 'Controlled growth of spinel $NiCo_2O_4$ nanostructures on carbon cloth as a superior electrode for supercapacitors', *RSC Advances*, **4**, 8341–8349 (2014).

138. He L., Berntsen H., Ochoa-Fernandez E., Walmsley J. C., Blekkan E. A., Chen D., 'Co–Ni catalysts derived from hydrotalcite-like materials for hydrogen production by ethanol steam reforming', *Topics in Catalysis*, **52**, 206–217 (2009).

139. Salam M. A., Lwin Y., Sufian S., 'Synthesis of nano-structured Ni-Co-Al hydrotalcites and derived mixed oxides', *Advanced Materials Research*, **626**, 173–177 (2013).

140. Garg N., Basu M., Ganguli A. K., 'Nickel cobaltite nanostructures with enhanced supercapacitance activity', *The Journal of Physical Chemistry C*, **118**, 17332–17341 (2014).

141. Zhuravlev L. T., 'The surface chemistry of amorphous silica. Zhuravlev model', *Colloids and Surfaces A: Physicochemical and Engineering Aspects*, **173**, 1–38 (2000).

142. Cerveny S., Schwartz G. A., Otegui J., Colmenero J., Loichen J., Westermann S., 'Dielectric study of hydration water in silica nanoparticles', *The Journal of Physical Chemistry C*, **116**, 24340–24349 (2012).

143. Ding R., Qi L., Jia M., Wang H., 'Hierarchical porous $NiCo_2O_4$ nanomaterials with excellent cycling behavior for electrochemical capacitors *via* a hard-templating route', *Journal of Applied Electrochemistry*, **42**, 1033–1043 (2012).

144. Kandula S., Jeevanandam P., 'A facile synthetic approach for $SiO_2@Co_3O_4$ core–shell nanorattles with enhanced peroxidase-like activity', *RSC Advances*, **5**, 5295–5306 (2015).

145. Lei Y., Li J., Wang Y., Gu L., Chang Y., Yuan H., Xiao D., 'Rapid microwave-assisted green synthesis of 3D hierarchical flower-shaped $NiCo_2O_4$ microsphere for high-performance supercapacitor', *ACS Applied Materials and Interfaces*, **6**, 1773–1780 (2014).

146. Tang Y., Liu Y., Yu S., Guo W., Mu S., Wang H., Zhao Y., Hou L., Fan Y., Gao F., 'Template-free hydrothermal synthesis of nickel cobalt hydroxide nano flowers with high performance for asymmetric supercapacitor', *Electrochimica Acta*, **161**, 279–289 (2015).

147. Zhang G., Lou X. W., 'Controlled growth of $NiCo_2O_4$ nanorods and ultrathin nanosheets on carbon nanofibers for high-performance supercapacitors', *Scientific Reports*, **3**, 1470/1–6 (2013).

148. Jin X., Sun W., Chen C., Wei T., Cheng Y., Li P., Li Q., 'Efficiency enhancement *via*

tailoring energy level alignment induced by vanadium ion doping in organic/inorganic hybrid solar cells', *RSC Advances*, **4**, 46008–46015 (2014).

149. Marco J. F., Gancedo J. R., Gracia M., Gautier J. L., Rios E. I., Palmer H. M., Greaves C., Berry F. J., 'Cation distribution and magnetic structure of the ferrimagnetic spinel $NiCo_2O_4$', *Journal of Materials Chemistry*, **11**, 3087–3093 (2001).

150. Cui B., Lin H., Liu Y., Li J., Sun P., Zhao X., Liu C., 'Photophysical and photocatalytic properties of core-ring structured $NiCo_2O_4$ nanoplatelets', *The Journal of Physical Chemistry C*, **113**, 14083–14087 (2009).

151. Satoh N., Nakashima T., Kamikura K., Yamamoto K., 'Quantum size effect in TiO_2 nanoparticles prepared by finely controlled metal assembly on dendrimer templates', *Nature Nanotechnology*, **3**, 106–111 (2008).

Chapter-6

Applications of Core-Shell Nanoparticles / Nanorattles

Core-shell nanoparticles/nanorattles have potential applications in various fields such as catalysis [1–3], adsorption [4], peroxidase mimics [5], water splitting [6], supercapacitors [7], dye sensitized solar cells [8], energy storage [9], light emitting diodes [10], lithium ion batteries [11], sensors [12], gas storage [13], and bio-medicine [14]. In the present study, photocatalytic degradation of methylene blue (MB) using ZnO@CdS core-shell nanoparticles (Chapter-3) and ZnO@Ag core-shell heteronanostructures (Chapter-4), catalytic reduction of 4-nitrophenol (4-NP) and methylene blue using Cu_2O@Ag polyhedral core-shell nanoparticles (Chapter-4), peroxidase-like activity using SiO_2@Co_3O_4 core-shell nanorattles (Chapter-5), and adsorption of mixture of rhodamine B (RhB) and methylene blue using SiO_2@Ni-Co mixed metal oxide core-shell nanorattles (Chapter-5) have been demonstrated. An overview of various applications of synthesized core-shell nanoparticles/nanorattles is shown in Scheme 6.1.1.

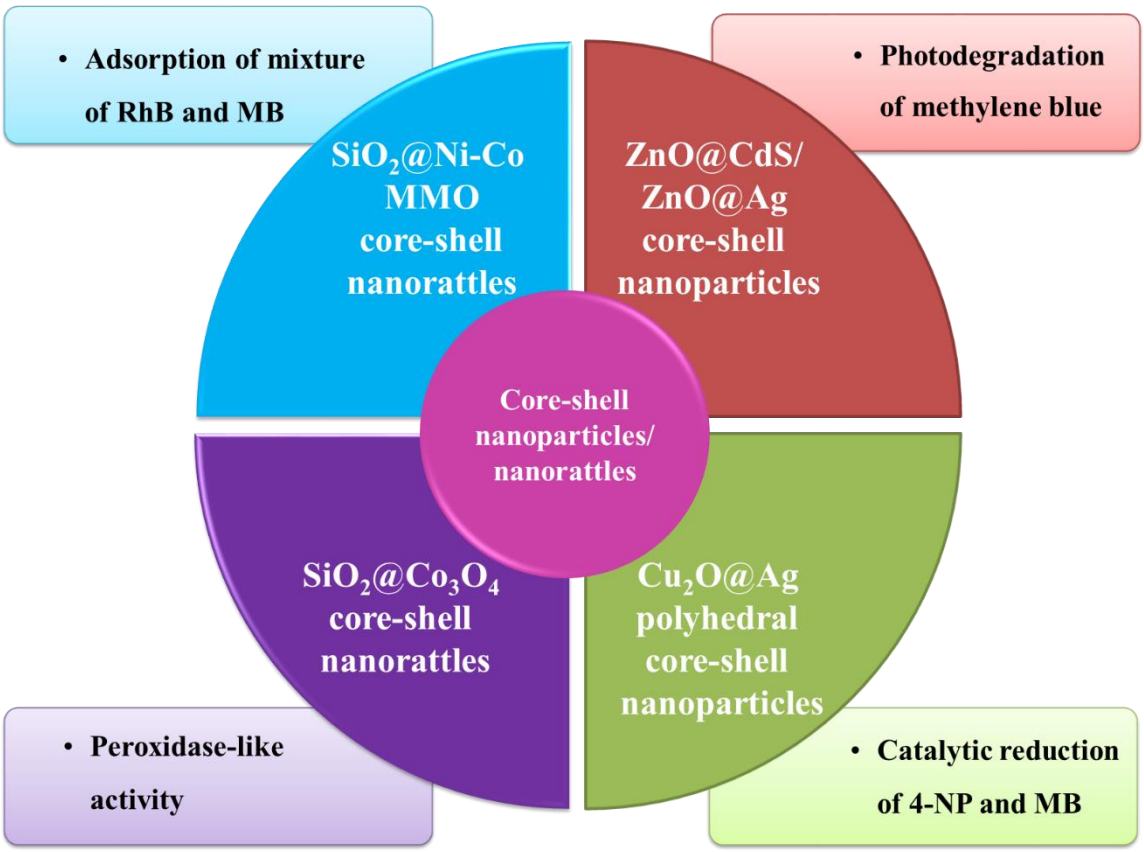

Scheme 6.1.1: Various applications of the synthesized core-shell nanoparticles/nanorattles explored in the present study.

The details on the catalytic experimental conditions and results on the above mentioned applications have been discussed in separate sections.

6.1 Photodegradation of methylene blue using ZnO@CdS core-shell nanoparticles and ZnO@Ag core-shell heteronanostructures

6.1.1 Introduction

Contamination of our water resources due to discharge of industrial effluents is one of the serious environmental issues. Textile, rubber, plastic, paper, cosmetics, leather, food, and mineral processing industries release often organic and inorganic wastes into the water sources leading to major environmental pollution [15,16]. The discharged industrial waste usually contains dyes (e.g. azo-aromatic dyes), which are non-degradable, toxic, carcinogenic, mutagenic, and tetratogenic. The industrial waste pose serious threat to aquatic life because of reduction in penetration of light which inhibits photosynthesis [17,18]. Removal of industrial waste is very important for the environmental safety. Semiconductors (e.g. ZnO, TiO_2, SnO_2, CdS, etc.) have been explored as effective photocatalysts and their band structure possesses a filled valence band (VB) and an empty conduction band (CB) [19–22]. Photocatalytic degradation of organic compounds usually involves the following steps: (i) when the energy of a photon is higher than or equal to the band gap of the semiconductor, electrons are excited from the VB to the CB with the creation of equal number of holes in the VB, (ii) the photogenerated excitons (electron-hole pairs) are trapped by dissolved oxygen in the aqueous solution resulting in the production of reactive oxidizing species (ROS), for example, $OH^{\bullet}$, and (iii) the ROS attacks and mineralize the adsorbed organic molecules. In a semiconductor, the photogenerated excitons easily undergo recombination which decreases the photocatalytic activity [18,20,21]. To overcome this limitation, semiconductor based heteronanostructures have been developed. Tak et al., Kanchandani et al., and Li et al. have demonstrated applications of ZnO@CdS core-shell nanoparticles in environmental remediation such as degradation of orange-II, rhodamine B and erichrome black T, respectively [22–24]. Lu et al., Zheng et al., Wu et al., and Shan et al. have used ZnO@Ag core-shell heteronanostructures as photocatalyst for the degradation of orange-II, methyl orange, rhodamine B, and rhodamine 6G, respectively [25–28]. Chen et al. and Lin et al. have used ZnO@Ag core-shell heteronanostructures as photocatalyst for the degradation of methyl orange, and rhodamine 6G, respectively [29,30]. Ren et al. and Sun et al. have used ZnO@Ag core-shell heteronanostructures as photocatalyst for the degradation of methylene blue [31,32].

In the present study, the synthesized ZnO@CdS core-shell nanoparticles and ZnO@Ag core-shell heteronanostructures were explored as photocatalysts for the degradation of methylene blue in aqueous solutions under sunlight irradiation.

6.1.2 Experimental details

The photocatalytic activity of synthesized ZnO@CdS core-shell nanoparticles and ZnO@Ag core-shell heteronanostructures was tested under sunlight irradiation and methylene blue was chosen as the model dye. The experimental procedure for the photodegradation of methylene blue using the ZnO@CdS core-shell nanoparticles and ZnO@Ag core-shell heteronanostructures is given in Scheme 6.1.2.

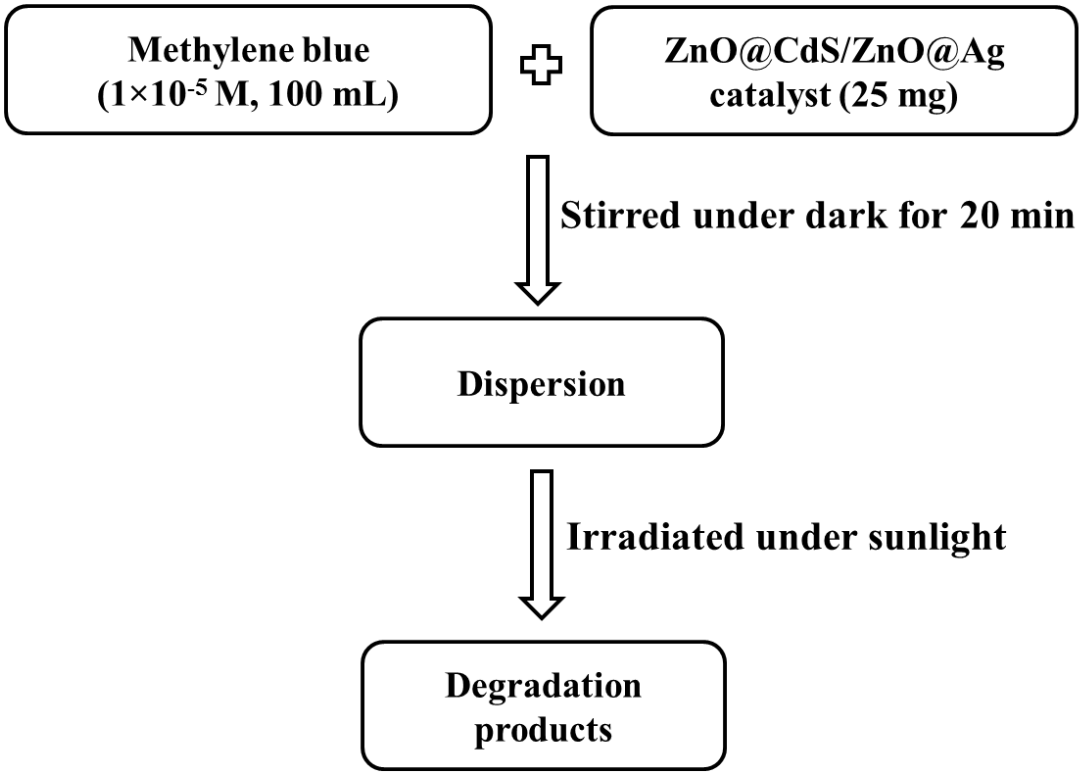

Scheme 6.1.2: Experimental procedure for the photodegradation of methylene blue using ZnO@CdS and ZnO@Ag as catalysts.

All the photocatalytic reactions using ZnO@CdS core-shell nanoparticles were carried out under direct sunlight between 12:00 noon and 14:00 pm at IIT Roorkee campus in the month of February 2014 when the solar intensity fluctuation was minimal. The intensity of sunlight at Roorkee (the latitude and longitude are $29^{o}52^{l}$ N and $77^{o}53^{l}$ E, respectively) in the month of February was 166 Watt/m^2 [33]. All the photocatalytic experiments using the ZnO@Ag core-shell heteronanostructures were carried out

between 11:30 am to 13:00 pm in the month of May 2015. The average sunlight intensity in the month of May 2015 was 245 Watt/m^2 [33]. In a typical photocatalytic experiment, about 25 mg of the photocatalyst (ZnO@CdS samples (ZC1, ZC2, and ZC3, see Table 3.2.1), ZnO@Ag samples (A1, A2 and A3, see Section 4.1.2.2), ZnO nanorods, CdS nanoparticles and silver nanoparticles) was dispersed in 100 mL of 1×10^{-5} M methylene blue aqueous solution in a beaker and stirred in dark for about 20 min to achieve adsorption-desorption equilibrium. After this, the beaker was kept under exposure of sunlight for about 90-120 min. During the photocatalytic experiments, about 5 mL each aliquot withdrawn at regular time intervals, centrifuged and the supernatant solutions were analyzed using UV-Visible spectroscopy. A blank reaction was also carried out without using any catalyst under similar experimental conditions. The percent degradation of methylene blue was estimated using the formula,

$$\% \text{ Degradation} = (1-C/C_o) \times 100 \qquad (1)$$

where C_o and C are the concentrations of methylene blue at adsorption equilibrium and at irradiation time 't', respectively.

To understand the mechanism of photodegradation of methylene blue better, and to prove the involvement of hydroxyl radicals in the photodegradation in the presence of ZnO@CdS and ZnO@Ag as the catalysts, terephthalic acid was used as a probe molecule [34,35]. In a typical experiment, 20 mg of the catalyst (ZnO@CdS (ZC3) or ZnO@Ag (A1)) was dispersed in 50 mL of an aqueous solution of terephthalic acid (5×10^{-4} M) containing sodium hydroxide (2×10^{-3} M). The contents were kept under sunlight for 2 h. During the irradiation, aliquots (5 mL each) were taken and analyzed by PL spectroscopy ($\lambda_{excitation}$= 315 nm) at regular intervals (10 min) after removing the solid residue by centrifuging.

6.1.3 Results and discussion

6.1.3.1 Photodegradation of methylene blue using ZnO@CdS core-shell nanoparticles

The kinetics of methylene blue degradation was studied using ZnO nanorods, CdS nanoparticles and ZnO@CdS samples (ZC1, ZC2 and ZC3) and the results are shown in Figure 6.1.1 (a-e).

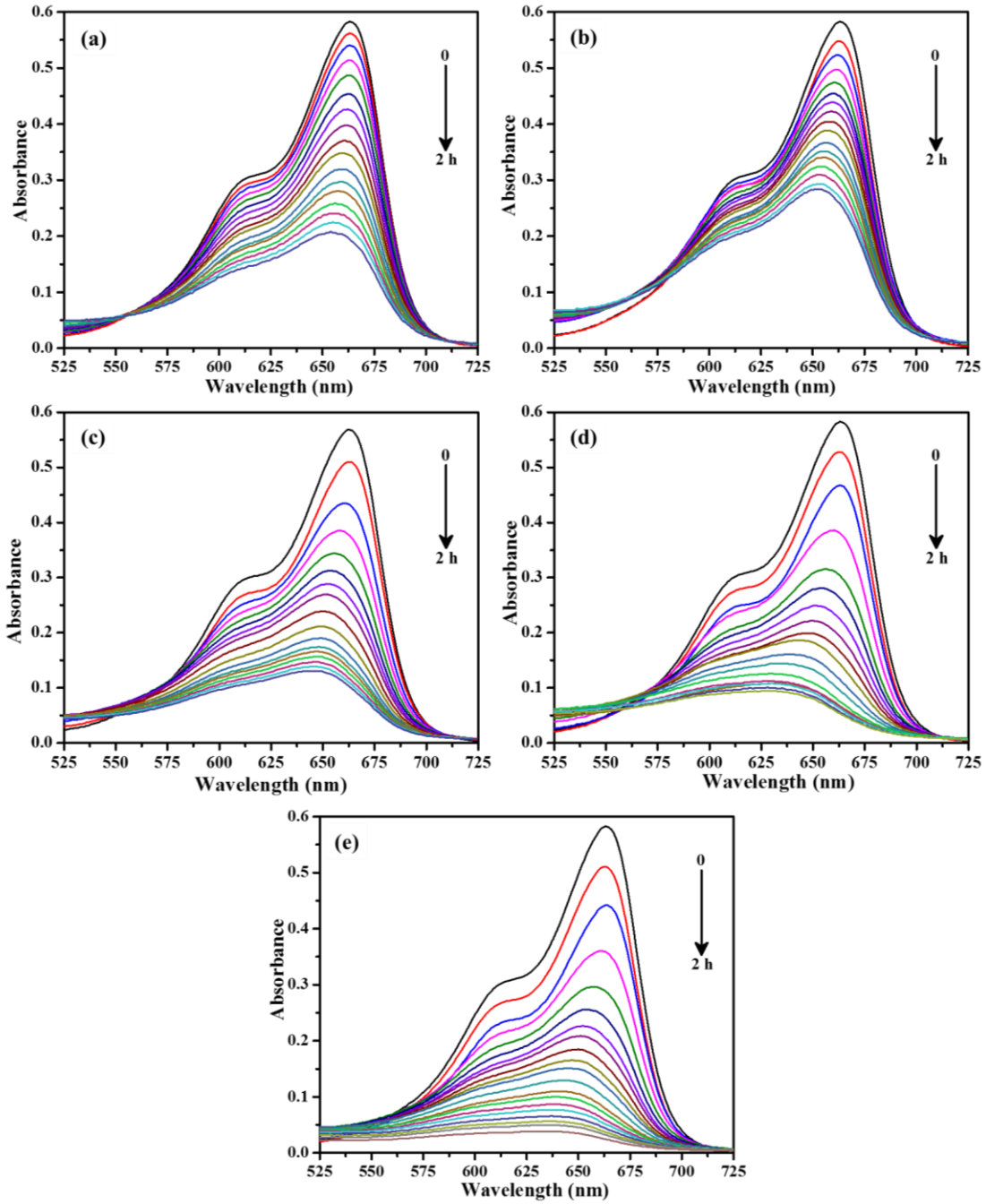

Fig. 6.1.1: Kinetics of photodegradation of methylene blue using **(a)** ZnO nanorods, **(b)** CdS nanoparticles, and **(c-e)** ZnO@CdS samples (ZC1, ZC2 and ZC3, respectively) as the catalysts. For more details on the samples, see Table 3.2.1.

The photodegradation of methylene blue follows pseudo-first-order kinetics which can be written as

$$\ln C_o/C_t = kt \qquad (2)$$

where C_o and C_t are the concentrations of methylene blue at time = 0 and time = t, respectively and k is the apparent pseudo-first-order rate constant. The ZnO@CdS samples show higher photocatalytic activity compared to pure ZnO nanorods and CdS nanoparticles (Figure 6.1.2a). The ZnO@CdS samples show linear relationship between $ln(C_o/C_t)$ and irradiation time (Figure 6.1.2b) which indicates that the photodegradation of methylene blue follows pseudo first order kinetics [36,37]. The apparent pseudo first order rate constant (k) for the degradation of methylene blue was calculated as 2.72×10^{-2}, 1.96×10^{-2}, 1.33×10^{-2}, 9.43×10^{-3}, and 6.58×10^{-3} min^{-1} for ZC3, ZC2, ZC1, ZnO, and CdS, respectively. Among all the samples, ZC3 shows the highest rate constant and the degradation efficiency follows the order: ZC3 > ZC2 > ZC1 > ZnO > CdS (Figure 6.1.2c).

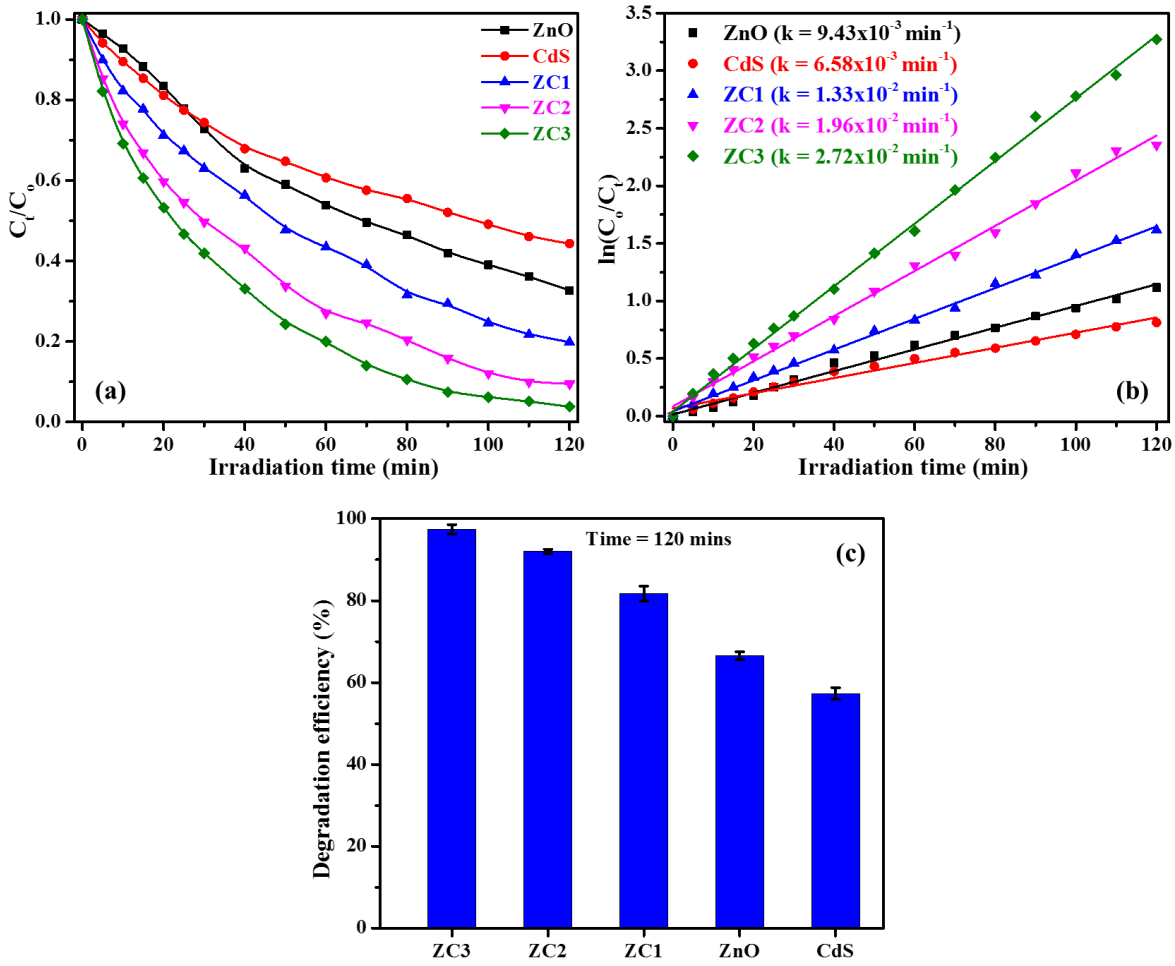

Fig. 6.1.2: (a) Comparison of photocatalytic performance of ZnO@CdS samples (ZC1, ZC2 and ZC3) with pure ZnO nanorods and CdS nanoparticles, **(b)** plots of $ln(C_o/C_t)$ versus irradiation time for various photocatalysts and **(c)** comparison of methylene blue degradation efficiencies of ZnO nanorods, CdS nanoparticles, and ZnO@CdS samples.

The higher photocatalytic efficiency of ZC3 is attributed to an efficient charge separation and good synergistic interaction between ZnO core and CdS shell in this sample. ZC3 consists of thicker shell of CdS compared to ZC1 and ZC2, and the increased photocatalytic efficiency of ZC3 is attributed to uniform coverage of CdS shell on the ZnO nanorods. The above results suggest that the synthesized ZnO@CdS core-shell nanoparticles can be used as good catalyst for the degradation of organic pollutants in aqueous solutions under sunlight.

6.1.3.1.1 Proposed mechanism for the photodegradation of methylene blue using ZnO@CdS core-shell nanoparticles

The possible mechanism for the photodegradation of methylene blue is given in Scheme 6.1.3. In type-II semiconductors such as ZnO@CdS, the photogenerated excitons are confined in the core and the shell. On illumination of ZnO@CdS samples under sunlight, the photogenerated electrons in the conduction band of CdS are transferred to that of ZnO which facilitates the charge separation of the electron-hole pairs before they recombine [38]. The conduction band of ZnO possesses more electrons and no free holes are available in the valence band of ZnO for the recombination. The holes remain in the valence band of CdS and they are not transferred to that of ZnO since the valence band of CdS is more cathodic than that of ZnO. The electrons in the conduction band of ZnO readily react with the dissolved oxygen in water and produce highly reactive superoxide radical anions ($O_2^{\bullet -}$). The electrons in the conduction band of ZnO also react with dissolved oxygen and H^+ ions present in the aqueous solution leading to the formation of hydroxy radicals ($OH^{\bullet}$). The active species such as holes (h^+) in the valance band of CdS, superoxide radical anions ($O_2^{\bullet -}$) and hydroxyl radicals ($OH^{\bullet}$) are responsible for the photodegradation of methylene blue [24,39,40].

$$ZnO@CdS + h\nu \rightarrow ZnO\ (e^-) + CdS\ (h^+)$$

$$ZnO\ (e^-) + O_2 \rightarrow O_2^{\bullet -} + ZnO$$

$$H_2O \rightleftharpoons H^+ + OH^-$$

$$2e^- + O_2 + 2H^+ \rightarrow H_2O_2$$

$$H_2O_2 \rightarrow 2OH^{\bullet}$$

$$MB + OH^{\bullet} + O_2^{\bullet -} + h^+ \rightarrow CO_2 + H_2O + SO_4^{2-} + NO_3^- + Cl^-$$

Scheme 6.1.3: Proposed mechanism for the photodegradation of methylene blue using ZnO@CdS core-shell nanoparticles as the catalyst.

6.1.3.2 Photodegradation of methylene blue using ZnO@Ag core-shell heteronanostructures

The photocatalytic activity of the ZnO@Ag core-shell heteronanostructures (A1, A2 and A3) was explored towards the photodegradation of methylene blue in an aqueous solution under sunlight and the kinetic results are shown in Figure 6.1.3. The results indicate that ZnO@Ag core-shell heteronanostructures possess higher photodegradation efficiency as compared to pristine ZnO nanorods and pure silver nanoparticles. Photodegradation of methylene blue in the absence of any catalyst under sunlight was also tested and the results indicated only a marginal degradation of methylene blue. The deposition of silver nanoparticles on the ZnO nanorods enhances the degradation of methylene blue. The degradation of methylene blue by the ZnO@Ag core-shell heteronanostructures follows pseudo-first-order kinetics as indicated by a linear relationship between $ln(C_o/C_t)$ and irradiation time. The apparent pseudo-first-order rate constant (k) was calculated from the slope of the plot between $ln(C_o/C_t)$ versus time 't'. The estimated apparent pseudo-first-order rate constant (k) values for the degradation of methylene blue are 0.041, 0.025, 0.024, 0.014, and 0.010 min^{-1} for the ZnO/Ag samples A1, A2, A3, pure ZnO nanorods and silver nanoparticles, respectively. The order of degradation efficiency of photocatalysts is A1 > A2 > A3 > ZnO > Ag. The higher degradation efficiency of ZnO@Ag core-shell heteronanostructures as compared to pristine ZnO and silver nanoparticles is due to the fact that the silver nanoparticles present on the surface of ZnO nanorods act as electron sink and provide sites for the accumulation of photogenerated electrons with an efficient charge separation of photogenerated electrons and holes.

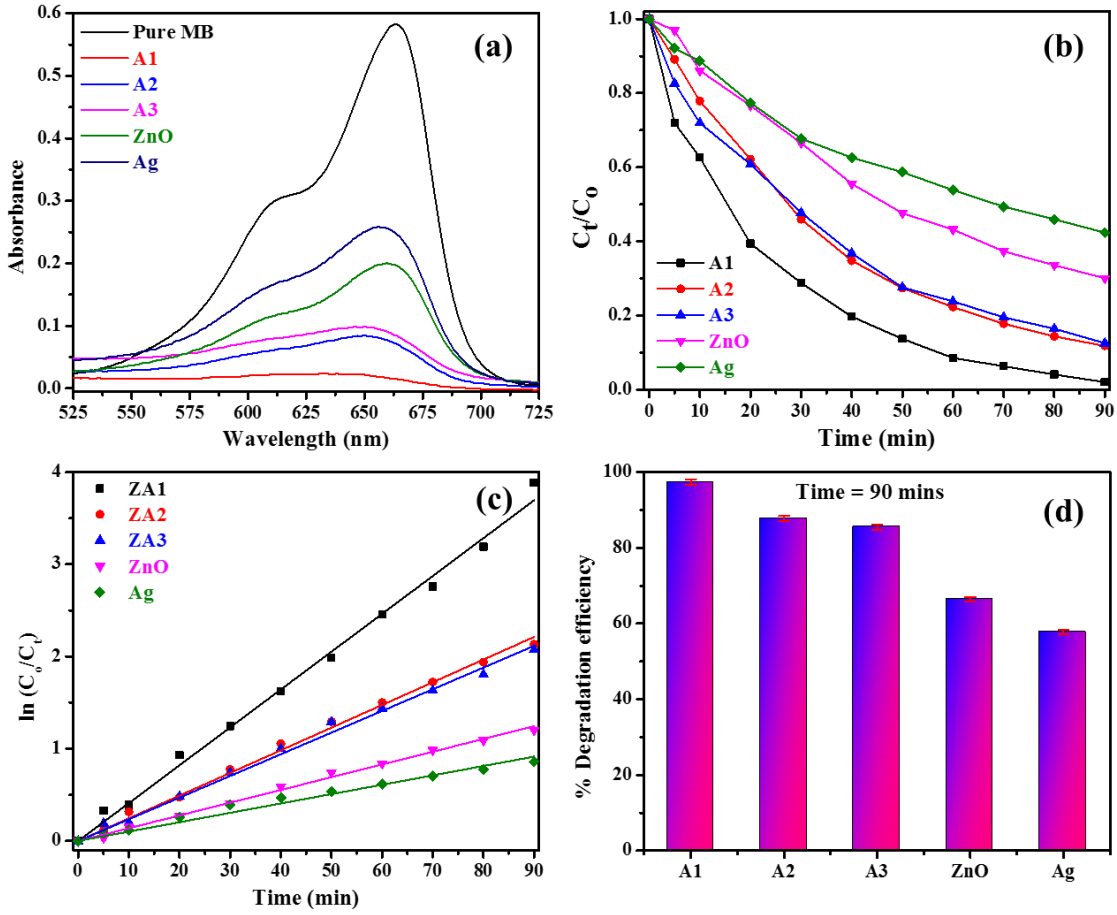

Fig. 6.1.3: (a) Photodegradation of methylene blue using ZnO nanorods, silver nanoparticles, and ZnO@Ag core-shell heteronanostructures (A1, A2, and A3), **(b)** comparison of kinetics of photocatalytic activity of ZnO@Ag core-shell heteronanostructures (A1, A2, and A3) with ZnO nanorods and silver nanoparticles, **(c)** plots between $ln(C_o/C_t)$ versus irradiation time using different photocatalysts, and **(d)** comparison of methylene blue degradation efficiency using ZnO nanorods, silver nanoparticles and ZnO@Ag core-shell heteronanostructures. For more details on the samples, see Section 4.1.2.2.

Li et al. have evaluated the photocatalytic activity of the ZnO@Ag samples using 12 mg of the catalyst in 40 mL of the methylene blue (10 ppm) aqueous solution, under visible light for 150 min with the first order rate constant (k) of 1.02×10^{-2} min^{-1} [41]. Ren et al. have investigated photocatalytic activity of ZnO@Ag films (1 cm × 2 cm) placed in 15 mL of methylene blue (2 mg/L) aqueous solution, irradiated in presence of UV light for about 90 min [29] and they found that the first order rate constant (k) was about 7.63×10^{-3} min^{-1}. Sun et al. have examined photocatalytic activity of ZnO@Ag samples using 50 mL of the methylene blue (20 mg/L) aqueous solution and 50 mg of the sample [32]. The aqueous solution was irradiated in the presence of UV light and they have reported

that complete degradation of methylene blue takes place in 2 h. Saravanan et al. have studied photocatalytic activity of ZnO@Ag samples using 500 mL of 3 × 10^{-5} M methylene blue aqueous solution [42]. The solution was irradiated under visible light for 2 h and they have reported a first order rate constant (*k*) of 3.66×10^{-4} min^{-1}. In the present study, 25 mg of ZnO@Ag sample was dispersed in 100 mL of 1×10^{-5} M methylene blue aqueous solution and the solution was irradiated under sunlight for about 90 min and the first order rate constant (*k*) is 4.10×10^{-2} min^{-1}. The synthesized ZnO@Ag heteronanostructures show higher rate constant (*k*) for the degradation of methylene blue as compared to the previous reports.

6.1.3.2.1 Proposed mechanism for the photodegradation of methylene blue using ZnO@Ag core-shell heteronanostructures

The proposed mechanism for the photodegradation of methylene blue by ZnO@Ag is shown in Scheme 6.1.4 [26,27]. On illumination with sunlight, electrons (e^-) in the valence band of ZnO are excited to the conduction band of ZnO which leaves the same amount of photogenerated holes (h^+) in the valence band. The energy of bottom of the conduction band of ZnO is higher than the Fermi energy of the ZnO@Ag core-shell heteronanostructures and the electrons in the conduction band of ZnO transfer to the silver nanoparticles. Silver acts as an electron sink which promotes interfacial charge-transfer and reduces the recombination of photogenerated electron-hole pairs. The electrons present on the surface of silver nanoparticles are trapped by dissolved oxygen in the aqueous solution and produce superoxide radical anions ($O_2^{\bullet -}$). The photogenerated holes in the valence band of ZnO are easily trapped by H_2O and OH^- and hydroxyl radicals ($OH^\bullet$) are produced. The active species such as holes (h^+), superoxide radical anions ($O_2^{\bullet -}$), and hydroxyl radicals ($OH^\bullet$) are responsible for the mineralization of methylene blue [26–28]. Pure Ag nanoparticles show considerable photocatalytic activity for the degradation of methylene blue and the suggested mechanism for the ability of naked silver nanoparticles in the photocatalytic degradation is as follows. On illumination with sun light, silver strongly absorbs the incident light through surface plasmon resonance (SPR) and the 5*sp* band electrons are excited to higher intraband energy levels [43]. The excited methylene blue dye molecules (MB*) inject their electrons to the 5*sp* band of silver nanoparticles *via* photosensitization. This reduces the concentration of holes in the 5*sp* band with reduction of recombination of excitons [44].

The electrons in the higher intraband energy levels are captured by oxygen with the formation of $O_2^{\bullet-}$ species on the surface of silver nanoparticles. The produced $O_2^{\bullet-}$ species react with H^+ and produce reactive species such as $HO_2^{\bullet}$ and $OH^{\bullet}$ which start the degradation of methylene blue [44]. The recombination rate of excitons is reduced by photosensitization.

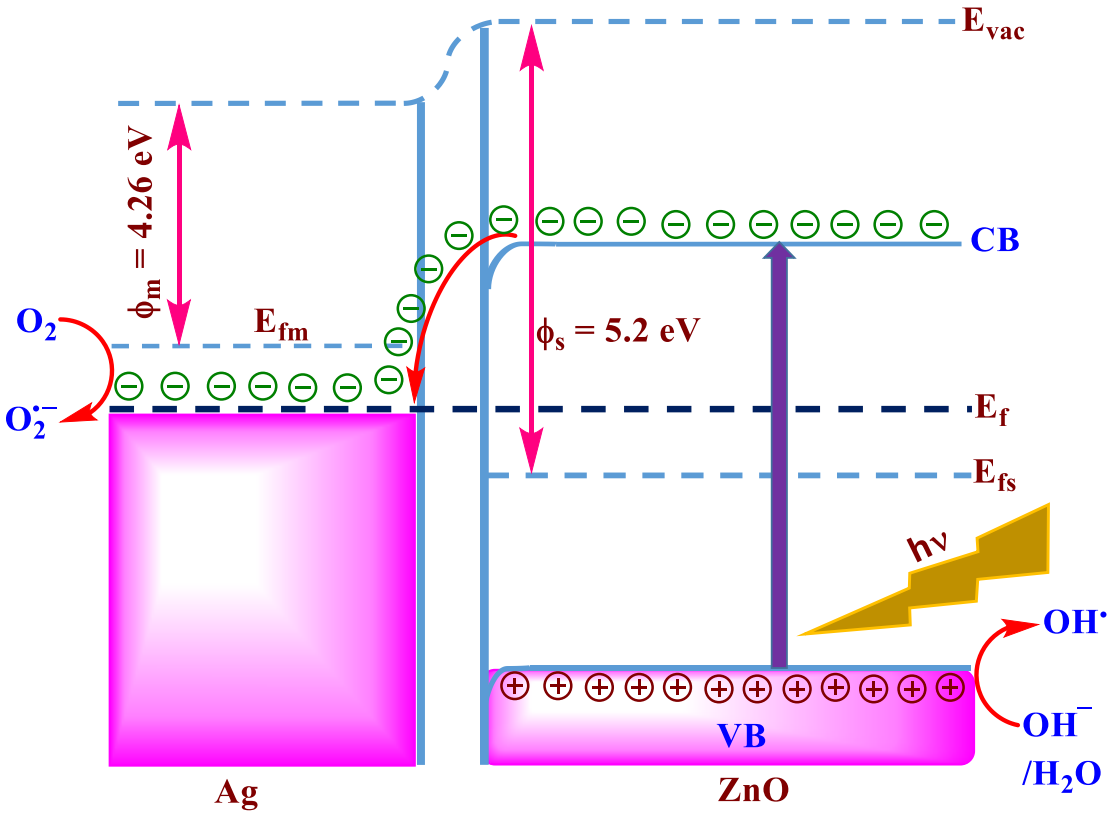

Scheme 6.1.4: Proposed band structure and photocatalytic mechanism using ZnO@Ag core-shell heteronanostructures as the catalyst [46,47].

$$ZnO + h\nu \rightarrow ZnO\ (e_{CB}^{-} + h_{VB}^{+})$$

$$Ag \rightarrow Ag^{+} + e^{-})$$

$$e^{-} + O_2 \rightarrow O_2^{\bullet-}$$

$$O_2^{\bullet-} + H^{+} \rightarrow HO_2^{\bullet}$$

$$HO_2^{\bullet} + HO_2^{\bullet} \rightarrow H_2O_2 + O_2$$

$$H_2O_2 + e^{-} \rightarrow OH^{\bullet} + OH^{-}$$

$$MB + OH^{\bullet} + O_2^{\bullet-} + h^{+} \rightarrow CO_2 + H_2O + SO_4^{2-} + NO_3^{-} + Cl^{-}$$

The enhanced photocatalytic activity of ZnO@Ag core-shell heteronanostructures as compared to pristine ZnO nanorods and silver nanoparticles can be explained based on the

photoluminescence results (see Chapter-4, Figure 4.1.13) and the relationship between photoluminescence properties and photocatalytic activity is of particular importance [26,29]. The observed photoluminescence intensity of the ZnO@Ag core-shell heteronanostructures is lower as compared to that of pristine ZnO nanorods. This indicates that the silver nanoparticles present on the ZnO nanorods reduce the recombination of electron-hole pairs on the surface of ZnO nanorods. Samples A2 and A3 possess larger silver nanoparticles as compared to sample A1. On illumination with sunlight, in these samples (A2 and A3), more accumulation of electrons on the silver nanoparticles occurs as compared to sample A1. The photogenerated holes in valence band of the ZnO are attracted to the electrons present in silver which enhances the recombination leading to lower catalytic activity in samples A2 and A3. Also, the larger silver nanoparticles present on A2 and A3 reduce the available surface on ZnO for light absorption thus lowering its photocatalytic activity. Sample A1 has the optimum amount/size of the silver nanoparticles on the ZnO nanorods as compared to samples A2 and A3 which leads to an effective separation of photogenerated electron-hole pairs.

6.1.3.3 Determination of hydroxyl radicals

Hydroxyl radicals play an important role in the degradation of organic pollutants. To prove the production of hydroxyl radicals on the surface of ZnO@CdS (ZC3) and ZnO@Ag (A1) under sun light illumination, terephthalic acid (TA) was chosen as the probe molecule [34,35]. On sun light irradiation, the hydroxyl radicals produced readily react with terephthalic acid and produce highly fluorescent 2-hydroxy terephthalic acid (TAOH), which exhibits an emission band at about 425 nm. The measured photoluminescence intensity of hydroxy terepthalic acid increases linearly with irradiation time. This suggests that the amount of hydroxyl radicals formed on the surface of photocatalysts is proportional to the irradiation time [45,46]. The determination of hydroxyl radicals on the surface of ZnO@CdS and ZnO@Ag samples under sunlight irradiation is shown in Figure 6.1.4.

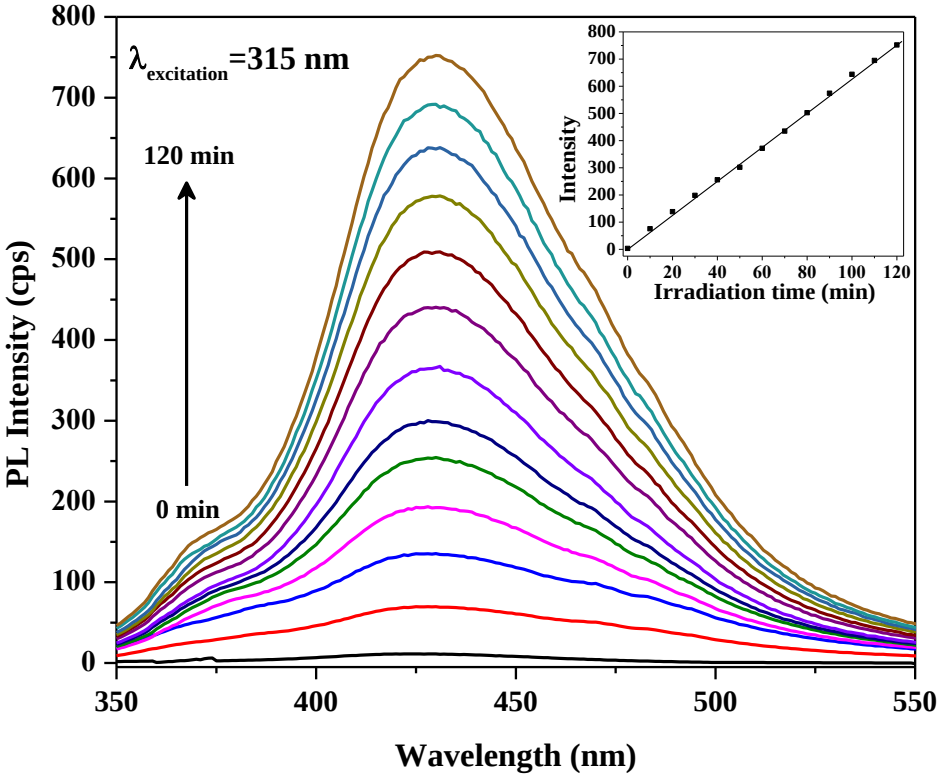

(a)

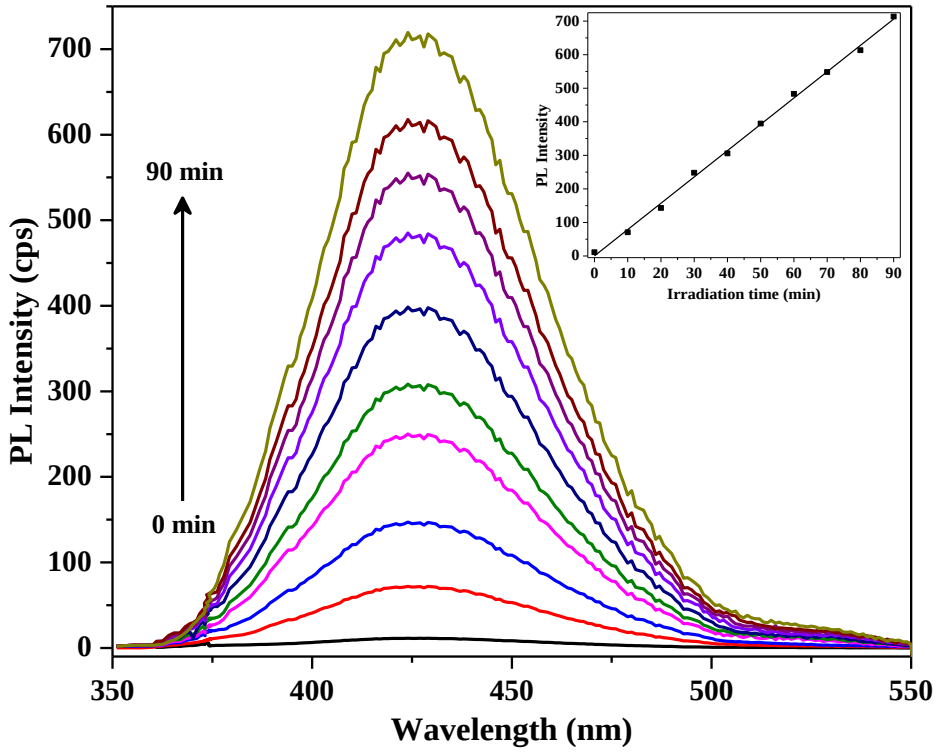

(b)

Fig. 6.1.4: Determination of hydroxyl radicals on the surface of **(a)** ZnO@CdS (ZC3) and **(b)** ZnO@Ag (A1) samples under sunlight irradiation using photoluminescence spectroscopy (λ_{exc} =315 nm). Insets show the plot of PL intensity versus irradiation time.

6.1.3.4 Reusability of ZnO@Ag core-shell heteronanostructures

The reusability of a photocatalyst explains stability and activity of the catalyst. One of the problems associated with ZnO as the photocatalyst is its lower photostability and it easily undergoes photoinduced dissolution [32]. The photocorrosion can be expressed as follows:

$$\mathrm{ZnO} + 2h^{+} \rightarrow Zn^{2+} + 1/2\, O_2$$

Holes in the valence band of ZnO migrate to the solid interface and react with the surface oxygen leading to the photocorrosion of ZnO. To test the photocatalytic stability (reusability) of the ZnO@Ag core-shell heteronanostructures, sample A1 (the best among the ZnO@Ag samples) was chosen and photocatalytic experiments were carried out up to 5 cycles (Figure 6.1.5). The efficiency of the sample A1 is reduced only by 3 % after five cycles indicating good stability and durability of the ZnO@Ag core-shell heteronanostructures. On the other hand, the photostability of pristine ZnO nanorods drastically decreases due to photocorrosion. These results demonstrate the role of silver nanoparticles present on the ZnO nanorods in improving photostability of the ZnO@Ag heteronanostructures as compared to pristine ZnO nanorods.

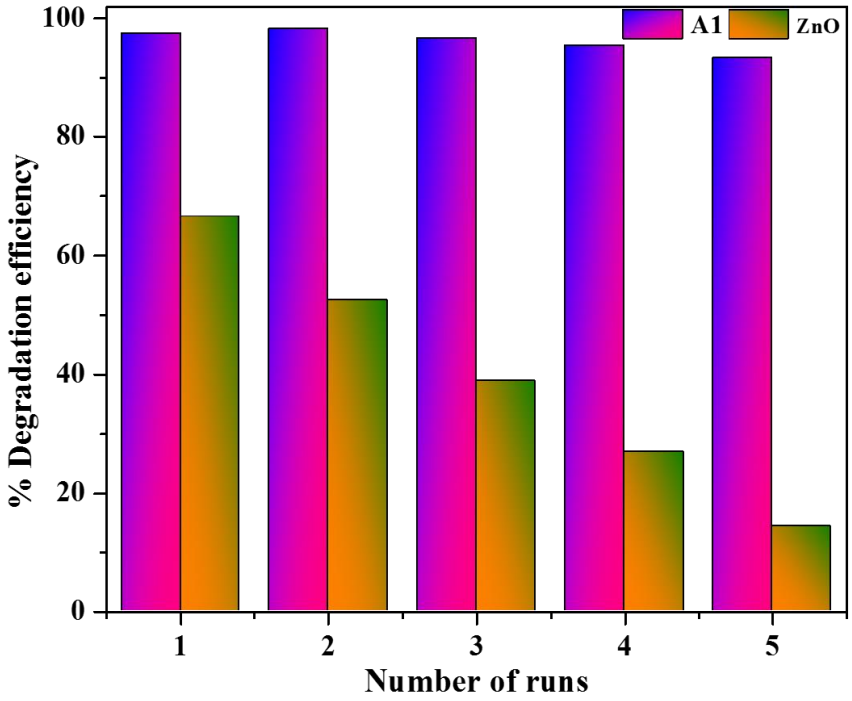

Fig. 6.1.5: The recyclability (photostability) of ZnO@Ag core-shell heteronanostructures (sample A1) and ZnO nanorods for the photodegradation of methylene blue.

6.2 Catalytic reduction of 4-nitrophenol and methylene blue using Cu_2O@Ag polyhedral core-shell nanoparticles

6.2.1 Introduction

Phenolic compounds such as nitrophenols, their derivatives, and organic dyes cause most of the water pollution which makes a serious threat to the environment and aquatic life [47–49]. 4-nitrophenol is toxic to the environment even at small amounts and degradation of 4-nitrophenol is very difficult due to its high stability and solubility in water [50]. The reduction product of 4-nitrophenol (i.e. 4-aminophenol) is less harmful to the environment compared to 4-nitrophenol and it is more biodegradable [51]. In addition, 4-aminophenol is used in various applications such as preparation of antipyretic and analgesic drugs, photographic developing, and anticorrosion lubricant [50]. The reduction of 4-nitrophenol to 4-aminophenol not only decreases the toxicity but also produces an important industrial intermediate. During the catalytic reduction, $NaBH_4$ reacts with water and produces hydrogen and sodium metaborate as the by-product which is less hazardous to the environment [52]. Pang et al. have been used Cu_2O@Au nanostructures as catalyst for the reduction of 4-nitrophenol [53]. Various other core-shell heteronanostructures such as C@Au, Au/α-Fe_2O_3@SiO_2, and SiO_2@Au yolk-shell nanoparticles have been used as the catalysts for the reduction of 4-nitrophenol [54–56]. Fe_3O_4@polydopamine-Ag core-shell microspheres, and Au@polypyrrole/Fe_3O_4 hollow capsules have been used as the catalysts for the reduction of methylene blue [57,58]. The reduction of 4-nitrophenol and methylene blue in aqueous solutions using Cu_2O@Ag polyhedral core-shell nanoparticles as the catalysts have not been reported yet. In the present study, the reduction of 4-nitrophenol to 4-aminophenol and methylene blue to leucomethylene blue were chosen as model reactions to evaluate catalytic activity of the Cu_2O@Ag polyhedral core-shell nanoparticles (C1A to C4A, Chapter 4.2).

6.2.2 Experimental details

6.2.2.1 Reduction of 4-nitrophenol to 4-aminophenol

The experimental procedure for the catalytic reduction of 4-nitrophenol and methylene blue using Cu_2O@Ag polyhedral core-shell nanoparticles is given in Scheme 6.2.1. In a typical catalytic experiment, 100 μL of 4-nitrophenol aqueous solution (5 mM) was

taken in a quartz cuvette. Then, freshly prepared 1 mL of $NaBH_4$ aqueous solution (0.02 M) and 2 mL of water were added. Finally, about 50 μg of the catalyst (Cu_2O polyhedral microcrystals, Ag nanoparticles, physical mixture of Cu_2O octahedrons with silver nanoparticles (wt. % of Ag = 5.1), PVP stabilized silver nanoparticles or Cu_2O@Ag polyhedral core-shell nanoparticles) was added. The reduction process was monitored *in situ* by UV-Vis spectroscopy using a Shimadzu UV-2450 UV-Visible spectrometer in the time course mode at room temperature in the wavelength range 200-800 nm.

6.2.2.2 Reduction of methylene blue to leucomethylene blue

About 3 mL of methylene blue aqueous solution (6×10^{-5} M) was taken in a quartz cuvette. Then, freshly prepared 0.3 mL of $NaBH_4$ aqueous solution (0.02 M) and 100 μg of the catalyst were added. The methylene blue reduction was monitored *in situ* using the UV-Visible spectrometer in the time course mode at room temperature in the wavelength range 200-800 nm.

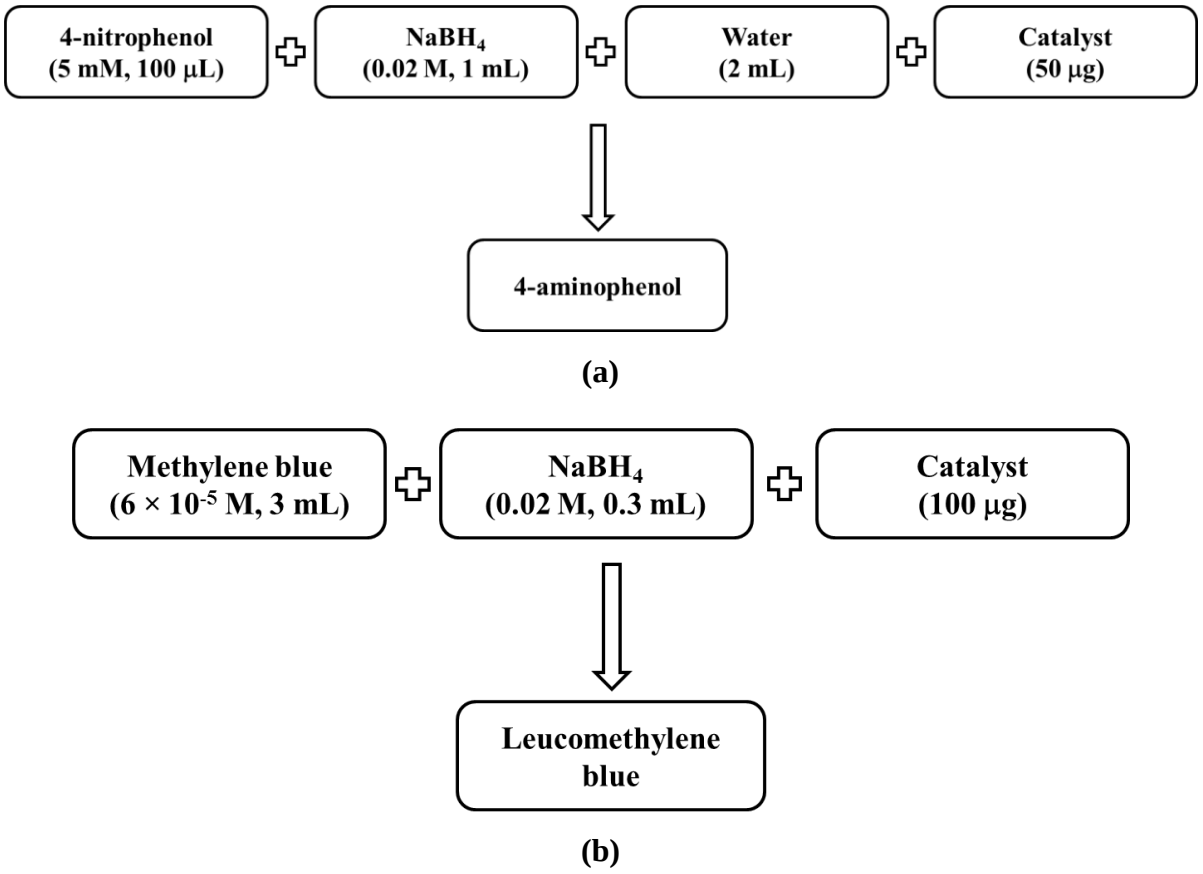

Scheme 6.2.1: Experimental procedure for the catalytic reduction of **(a)** 4-nitrophenol and **(b)** methylene blue.

6.2.3 Results and discussion

6.2.3.1 Catalytic reduction of 4-nitrophenol to 4-aminophenol

The reduction of 4-nitrophenol to 4-aminophenol in the presence of $NaBH_4$ over noble metal nanoparticles supported on various materials has been well studied [47,48,59]. The end product, i.e. 4-aminophenol is used in various applications [54]. An aqueous solution of 4-nitrophenol shows an UV-Visible absorbance band at 317 nm and upon the addition of freshly prepared $NaBH_4$, the absorbance maximum is red shifted to 400 nm due to the formation of 4-nitrophenolate ion [54,55]. In the present study, the reduction of 4-nitrophenol to 4-aminophenol was carried out using different Cu_2O@Ag polyhedral core-shell nanoparticles (C1A to C4A), pure Cu_2O microcrystals (C1 to C4), silver nanoparticles, physical mixture of Cu_2O octahedrons with silver nanoparticles (Ag wt. % = 5.1), and PVP stabilized silver nanoparticles. The UV-Visible spectral results indicating the reduction of 4-nitrophenol to 4-aminophenol using the Cu_2O@Ag polyhedral core-shell nanoparticles (C1A to C4A) as the catalysts in the presence of $NaBH_4$ are shown in Figure 6.2.1 (a-d). The UV-Visible spectral results for the reduction of 4-nitrophenol using Cu_2O microcrystals (C1 to C4), pure silver nanoparticles, physical mixture of Cu_2O (C4) and silver nanoparticles, and PVP stabilized silver nanoparticles are shown in Figure 6.2.2 (a-g). The spectral results show the disappearance of the band at 400 nm due to 4-nitrophenolate ion and the appearance of a new absorption band at 295 nm which confirms the formation of 4-AP [53].

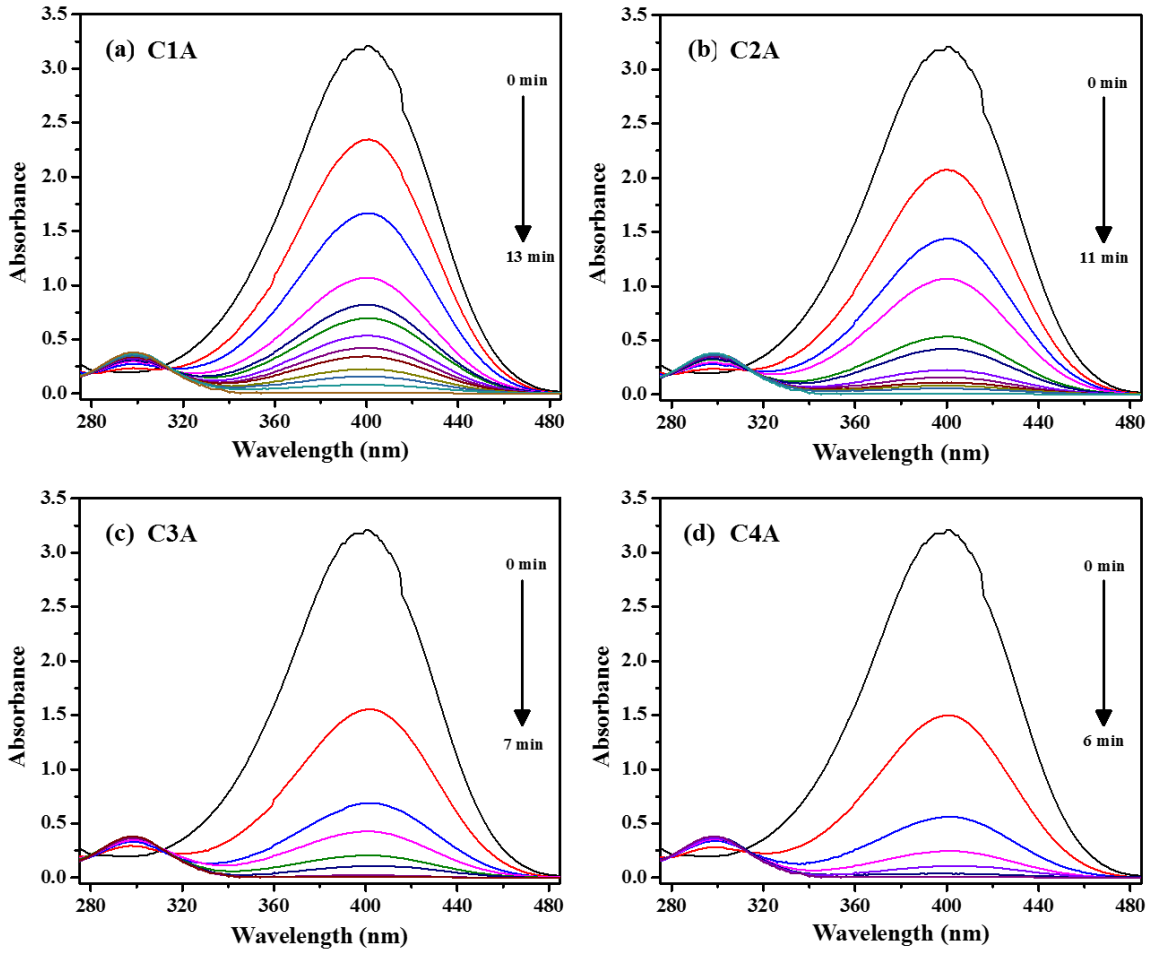

Fig. 6.2.1: (a-d) Catalytic reduction of 4-nitrophenol using Cu_2O@Ag polyhedral core-shell nanoparticles (C1A, C2A, C3A, and C4A). For more details on the samples, see Section 4.2.2.2.

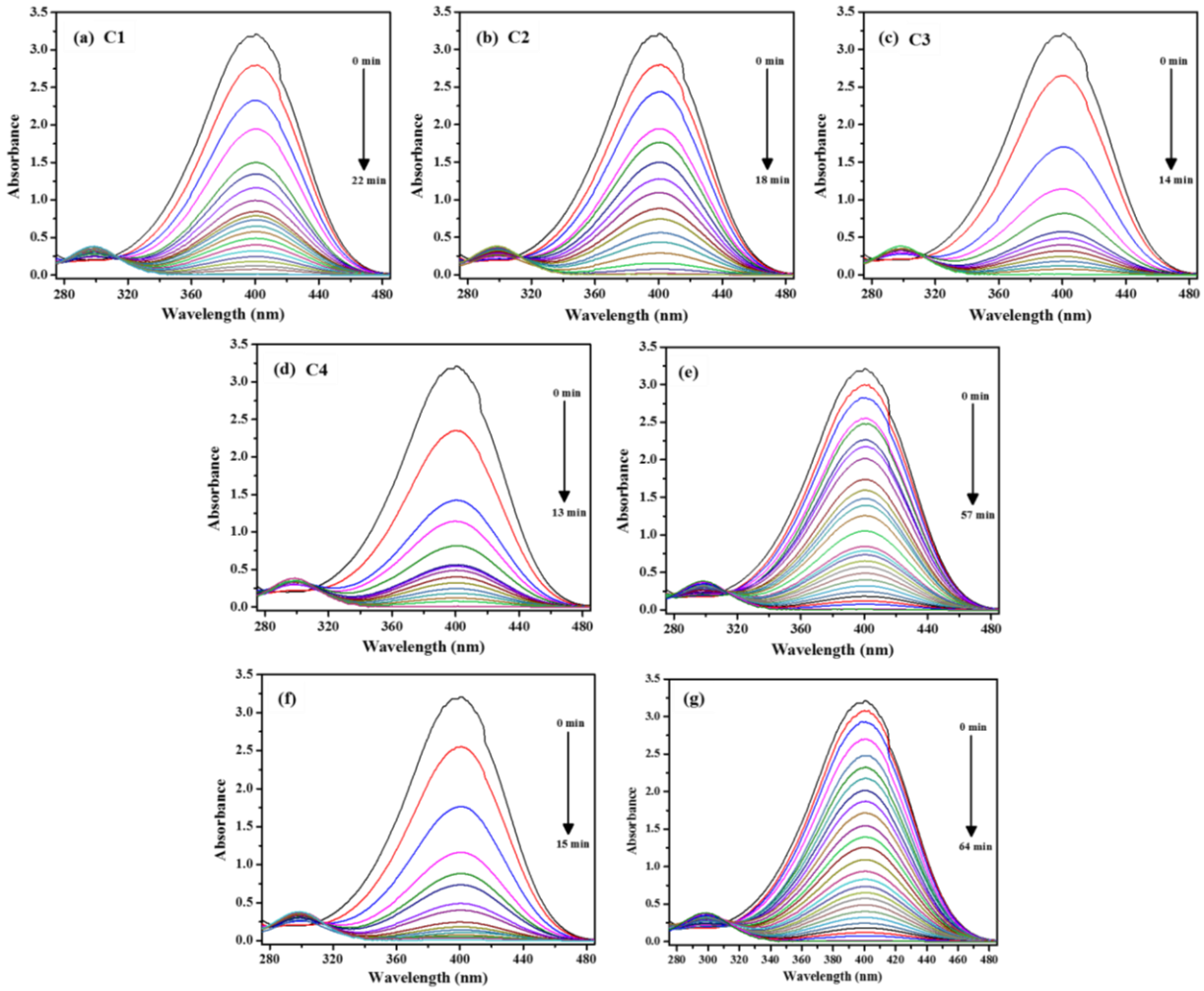

Fig. 6.2.2: (a-d) Catalytic reduction of 4-nitrophenol using pure Cu_2O microcrystals (C1, C2, C3, and C4), **(e)** silver nanoparticles, **(f)** physical mixture of Cu_2O (C4) and silver nanoparticles, and **(g)** PVP stabilized silver nanoparticles.

To understand the catalytic behavior better, kinetic studies for the reduction of 4-NP to 4-AP were carried out and the results are shown in Figure 6.2.3a using Cu_2O@Ag polyhedral core-shell nanoparticles (C1A to C4A) as the catalyst. The kinetics results for the reduction of 4-NP to 4-AP using pure Cu_2O microcrystals (C1 to C4), silver nanoparticles, physical mixture of Cu_2O (C4) and silver nanoparticles, and PVP stabilized silver nanoparticles as the catalysts are shown in Figure 6.2.3b. The Cu_2O@Ag polyhedral core-shell nanoparticles exhibit complete reduction of 4-NP to 4-AP within 6-13 min. Whereas pure Cu_2O microcrystals show the reduction in 13-22 min, pure silver nanoparticles in about 1 h, physical mixture exhibit the reduction in about 15 min, and PVP stabilized silver nanoparticles in about 64 min. The kinetic studies show that the reduction of 4-NP follows pseudo first order kinetics [54,60]. The

plots of $ln(C_o/C_t)$ versus time indicating linear relationship for all the Cu_2O@Ag polyhedral core-shell nanoparticles are shown in Figure 6.2.3c and for pure Cu_2O microcrystals, silver nanoparticles, physical mixture of Cu_2O (C4) and silver nanoparticles, and PVP stabilized silver nanoparticles, the plots are shown in Figure 6.2.3d. The apparent rate constant (k_{app}) calculated from the slope of the plots was found to be 5.28×10^{-3}, 7.26×10^{-3}, 1.14×10^{-2}, and 1.48×10^{-2} sec^{-1} for Cu_2O@Ag polyhedral core-shell nanoparticles C1A, C2A, C3A, and C4A, respectively. The k_{app} was 3.35×10^{-3}, 4.46×10^{-3}, 6.31×10^{-3}, 7.28×10^{-3}, 5.29×10^{-3}, 1.43×10^{-3}, 1.24×10^{-3} sec^{-1} for the pure Cu_2O microcrystals C1, C2, C3, C4, physical mixture of Cu_2O (C4) and silver nanoparticles, silver nanoparticles, and PVP stabilized silver nanoparticles, respectively. The Cu_2O@Ag polyhedral core-shell nanoparticles possess higher k_{app} indicating higher catalytic activity compared to pure Cu_2O microcrystals, silver nanoparticles, physical mixture of Cu_2O and silver nanoparticles, and PVP stabilized nanoparticles.

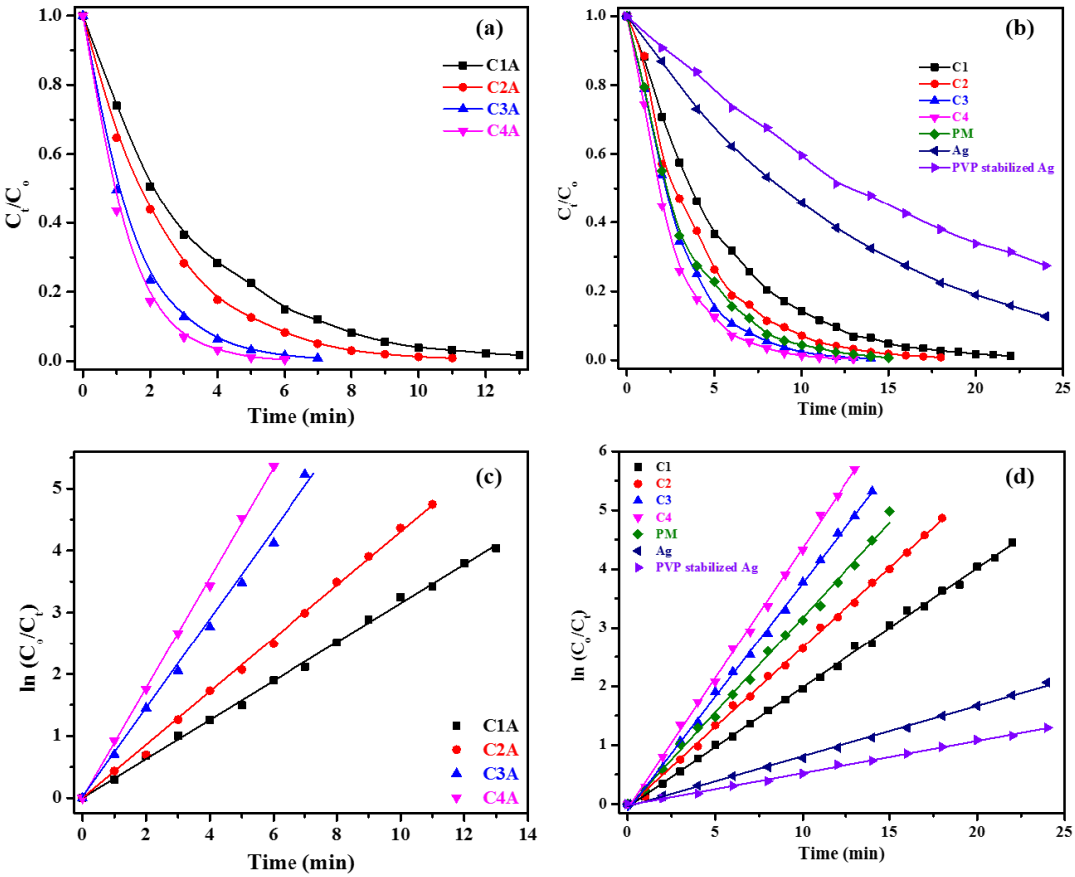

Fig. 6.2.3: Comparison of catalytic reduction of 4-nitrophenol using **(a)** various Cu_2O@Ag polyhedral core-shell nanoparticles (C1A, C2A, C3A, and C4A), **(b)** Cu_2O microcrystals (C1, C2, C3, and C4), silver nanoparticles, physical mixture of Cu_2O and silver nanoparticles, and

PVP stabilized silver nanoparticles, and **(c)** $ln(C_o/C_t)$ *vs.* time plots using different Cu_2O@Ag polyhedral core-shell nanoparticles (C1A, C2A, C3A, and C4A), **(d)** $ln(C_o/C_t)$ *vs.* time plots using different Cu_2O microcrystals (C1, C2, C3, and C4), silver nanoparticles, physical mixture of Cu_2O and silver nanoparticles, and PVP stabilized silver nanoparticles. The solid lines are the fits obtained using pseudo-first order kinetics model.

To compare catalytic activity of the catalysts, investigated in the present study, towards the reduction of 4-nitrophenol with the reported literature, the turnover frequency (TOF) and activity parameter (k_{act}) were calculated [47,48,54–56,59,60]. Turnover frequency (TOF) is defined as number of moles of 4-NP reduced per mole of silver per hour [56,61]. The TOF values were 49.2, 45.8, 94.8, and 211.5 h^{-1} for the Cu_2O@Ag polyhedral core-shell nanoparticles C1A, C2A, C3A, and C4A, respectively. k_{act} is defined as ratio of k_{app} to weight of the active sites of silver [48,55]. The amount of active silver sites was estimated from the weight percent of silver in Cu_2O@Ag polyhedral core-shell nanoparticles, as observed by the EDX analysis. The k_{act} was estimated to be 1.039×10^3, 1.125×10^3, 2.326×10^3, and 5.725×10^3 $s^{-1}g^{-1}$ for the Cu_2O@Ag polyhedral core-shell nanoparticles, C1A, C2A, C3A, and C4A, respectively. A comparison of TOF and k_{act} values for various noble metal nanoparticles supported on various materials as the catalysts with the values observed for the catalysts, investigated in the present study, is given in Table 6.2.1. As compared to the reported values, Cu_2O@Ag polyhedral core-shell nanoparticle sample C4A shows higher TOF and k_{act} values indicating better activity compared to the reported catalysts towards the reduction of 4-nitrophenol.

Table 6.2.1: Turnover frequency and k_{cat} values for the reduction of 4-nitrophenol using various catalysts along with that for Cu_2O@Ag samples.

Catalyst	Amount of catalyst (mg)	Metal loading (Wt. %)	Concentra-tion of 4-NP(M)	Time required for complete reduction (sec)	k_{app} (sec^{-1}) ($\times 10^{-2}$)	TOF (h^{-1})	k_{cat} ($s^{-1}g^{-1}$) ($\times 10^{3}$)	Reference
CNFs@Au	0.10	22.68	3.6×10^{-6}	300	0.542	-	0.0542	[54]
Au/α-Fe_2O_3@SiO_2@KCC-1	0.20	4.63	3.0×10^{-7}	370	1.450	-	1.5660	[55]
Ni@Au/KCC-1	0.30	9.10	3.0×10^{-7}	580	0.830	-	0.3070	[48]
Pd-Au@ MWCNT	0.02	46.70	2.0×10^{-7}	960	0.181	-	0.0205	[59]
Au@meso SiO_2	0.40	-	2.0×10^{-7}	900	-	38.0	-	[56]
TiO_2@Au	0.60	1.97	3.0×10^{-7}	960	0.406	58.8	-	[47]
TiO_2@GO@Au	0.04	63.80	7.4×10^{-5}	90	0.450	126.0	-	[60]
Ag(seed)-SiO_2 (*p*-TSA^-)	0.45	9.90	9.0×10^{-7}	600	0.248	186.0	-	[61]
Cu_2O@Ag (C1A)	0.05	10.12	5.0×10^{-7}	780	0.525	49.2	1.039	Present work
Cu_2O@Ag (C2A)	0.05	12.87	5.0×10^{-7}	660	0.726	45.8	1.1250	"
Cu_2O@Ag (C3A)	0.05	9.77	5.0×10^{-7}	420	1.14	94.8	2.3260	"
Cu_2O@Ag (C4A)	0.05	5.13	5.0×10^{-7}	360	1.46	211.5	5.7250	"
Physical mixture of Cu_2O (C4) and Ag nanoparticles	0.05	5.13	5.0×10^{-7}	900	0.529	84.4	2.0623	"
PVP stabilized Ag NPs	0.05	5.13	5.0×10^{-7}	3840	0.124	19.7	0.4829	"

6.2.3.2 Catalytic reduction of methylene blue to leucomethylene blue

The higher catalytic activity of Cu_2O@Ag polyhedral core-shell nanoparticles towards the reduction of 4-nitrophenol prompted an opportunity to investigate another catalytic reduction; the reduction of methylene blue to leucomethylene blue in the presence of $NaBH_4$ in an aqueous solution. An aqueous solution of methylene blue shows an UV-Visible absorption band at 655 nm and upon addition of the catalyst in the presence of $NaBH_4$, the absorbance approaches zero as a function of time due to the formation of colorless leucomethylene blue [57,61]. Figure 6.2.4 (a-d) show the reduction of methylene blue in an aqueous solution using Cu_2O@Ag polyhedral core-shell nanoparticles (C1A to C4A) as the catalyst in the presence of $NaBH_4$. The UV-Visible spectral results for the reduction of methylene blue using pure Cu_2O microcrystals (C1 to C4), silver nanoparticles, physical mixture of Cu_2O (C4) and silver nanoparticles, and PVP stabilized silver nanoparticles are shown in Figure 6.2.5 (a-g).

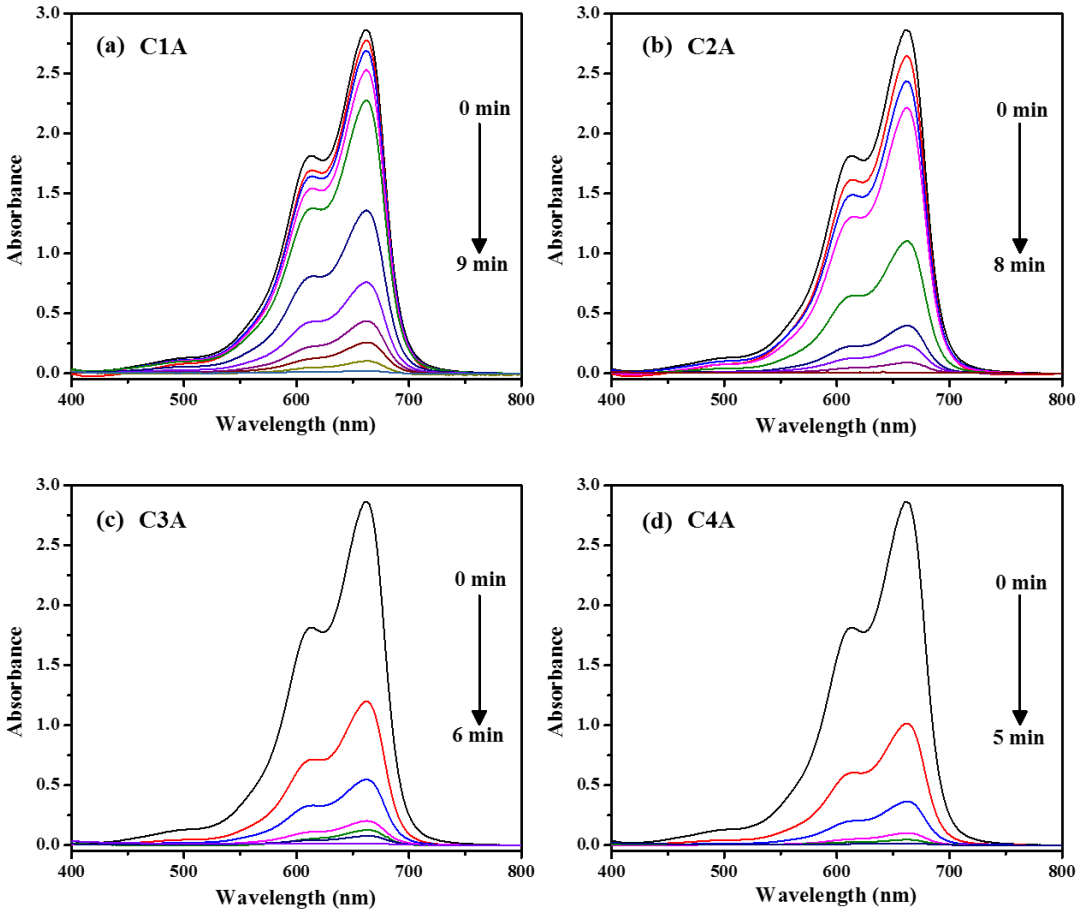

Fig. 6.2.4: (a-d) Catalytic reduction of methylene blue using Cu_2O@Ag polyhedral core-shell nanoparticles (C1A, C2A, C3A, and C4A).

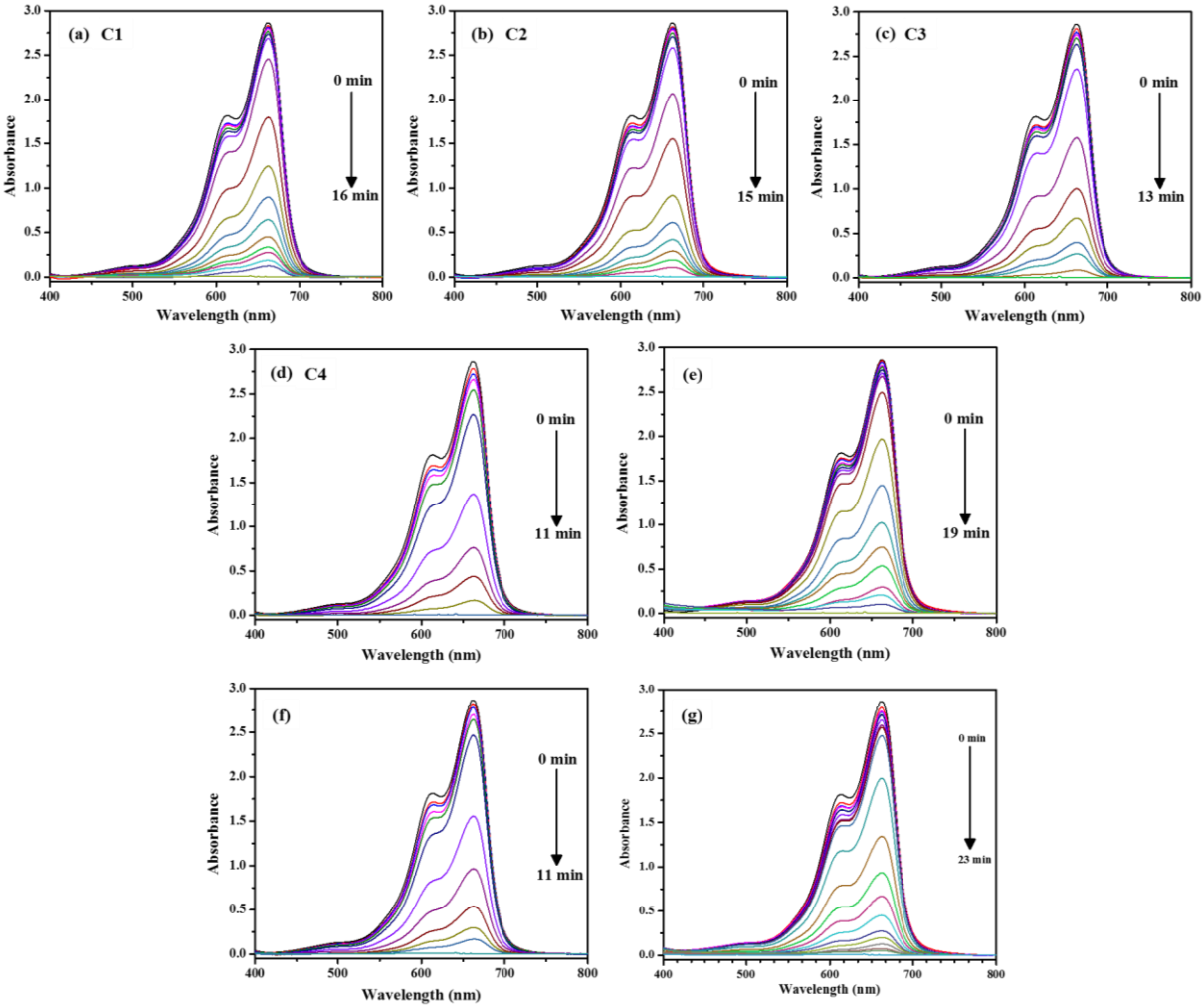

Fig. 6.2.5: (a-d) Catalytic reduction of methylene blue using Cu_2O microcrystals (C1, C2, C3, and C4), **(e)** silver nanoparticles, **(f)** physical mixture of Cu_2O (C4) and silver nanoparticles, and **(g)** PVP stabilized silver nanoparticles.

To understand the catalytic activity of Cu_2O@Ag polyhedral core-shell nanoparticles (C1A to C4A) towards the reduction of methylene blue, kinetic experiments were carried out and the results are shown in Figure 6.2.6a. No induction period is observed for the Cu_2O@Ag polyhedral core-shell nanoparticle samples C3A and C4A whereas an induction period is about 3-4 min is observed for the samples C1A and C2A. The kinetic results for the reduction of methylene blue using pure Cu_2O microcrystals (C1 to C4), silver nanoparticles, physical mixture of Cu_2O (C4) and silver nanoparticles, and PVP stabilized silver nanoparticles are shown in Figure 6.2.6b; induction period is observed in all the cases. The Cu_2O polyhedral microcrystals show an induction period of 5-7 min whereas silver nanoparticles and physical mixture of Cu_2O and silver nanoparticles show an induction period of about 8 min and 5 min, respectively. The PVP

stabilized silver nanoparticles show an induction period of about 12 min. The Cu_2O@Ag polyhedral core-shell nanoparticles exhibit complete reduction of methylene blue to leucomethylene blue within 5-9 min. Whereas, pure Cu_2O microcrystals exhibit the reduction in 11-16 min, pure silver nanoparticles show complete reduction in about 20 min, physical mixture of Cu_2O and silver nanoparticles completes the reduction in 15 min, and PVP stabilized silver nanoparticles show complete reduction in 23 mins. The observed results are in accordance with reported results on the catalytic reduction of methylene blue using Au@polypyrrole /Fe_3O_4 hollow capsules, and silver supported on silica spheres [58,62].

The plots between $ln(C_o/C_t)$ and time show linear relationship (Figure 6.2.6c) for the Cu_2O@Ag polyhedral core-shell nanoparticles (C1A to C4A) indicating that the reduction of methylene blue follows pseudo first order kinetics [61,63]. The k_{app}, calculated from the slope of the plots, was 1.36×10^{-2}, 1.48×10^{-2}, 1.54×10^{-2}, and 1.88×10^{-2} sec^{-1} for the Cu_2O@Ag polyhedral core-shell nanoparticles C1A, C2A, C3A, and C4A, respectively. The plots of $ln(C_o/C_t)$ versus time using pure Cu_2O microcrystals, silver nanoparticles, physical mixture of Cu_2O and silver nanoparticles and PVP stabilized silver nanoparticles as the catalysts are shown in Figure 6.2.6d. The k_{app} values for pure Cu_2O microcrystals (C1, C2, C3, and C4), physical mixture of Cu_2O and silver nanoparticles, silver nanoparticles, and PVP stabilized silver nanoparticles was 6.13×10^{-3}, 6.58×10^{-3}, 7.80×10^{-3}, 9.68×10^{-3}, 9.28×10^{-3}, 5.62×10^{-3}, and 5.21×10^{-3} sec^{-1}, respectively. The Cu_2O@Ag polyhedral core-shell nanoparticles show higher k_{app} than pure Cu_2O microcrystals, silver nanoparticles, the physical mixture of Cu_2O and silver nanoparticles, and PVP stabilized silver nanoparticles. The catalytic activity of Cu_2O@Ag polyhedral core-shell nanoparticles was compared with the reported literature values (Table 6.2.2). The higher k_{app} for Cu_2O@Ag sample C4A indicates higher catalytic activity towards the reduction of methylene blue compared to the reported catalysts.

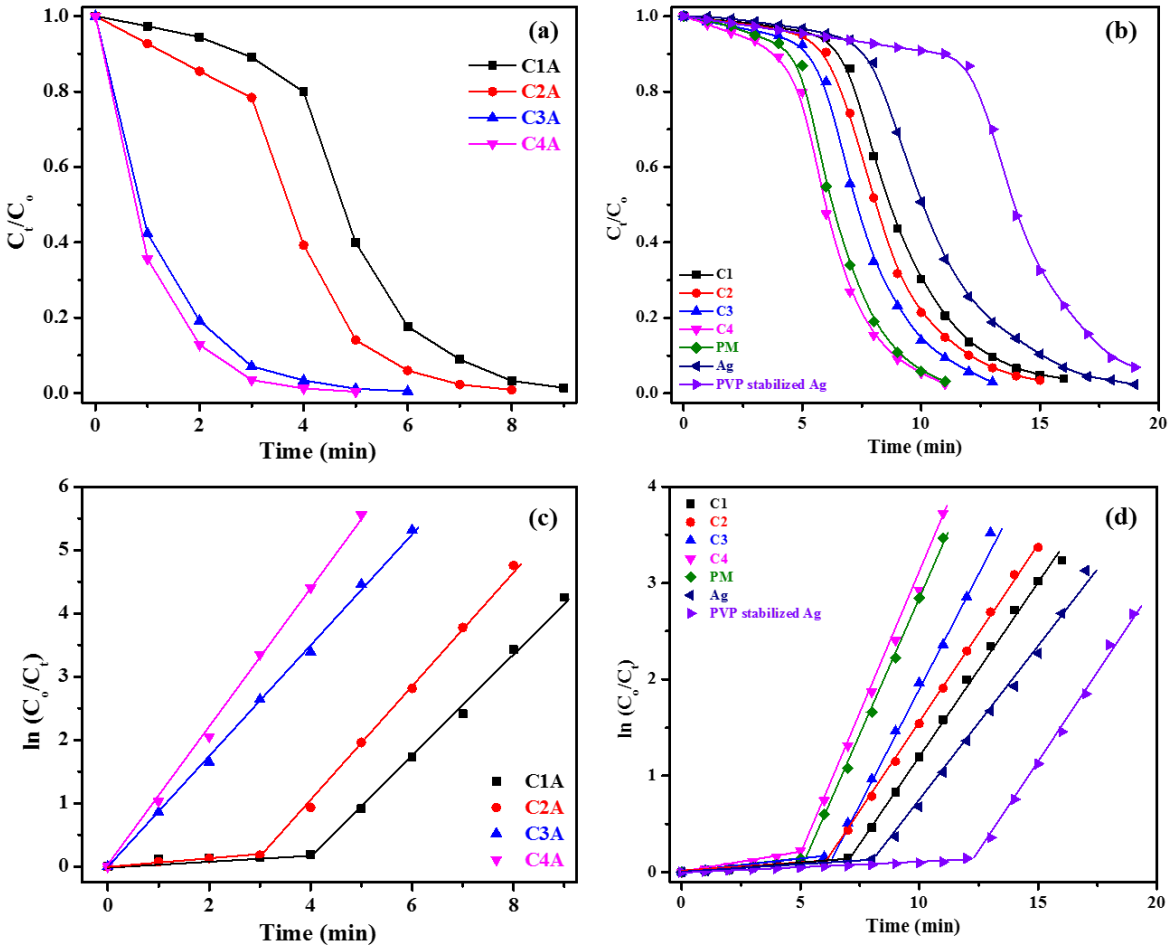

Fig. 6.2.6: Comparison of catalytic reduction of methylene blue using **(a)** Cu_2O@Ag polyhedral core-shell nanoparticles (C1A, C2A, C3A, and C4A), **(b)** Cu_2O microcrystals (C1, C2, C3, and C4), silver nanoparticles, physical mixture of Cu_2O and silver nanoparticles, and PVP stabilized silver nanoparticles, **(c)** $ln(C_o/C_t)$ *vs.* time plots using different Cu_2O@Ag polyhedral core-shell nanoparticles (C1A, C2A, C3A, and C4A), **(d)** $ln(C_o/C_t)$ vs. time plots using different Cu_2O microcrystals (C1, C2, C3, and C4), silver nanoparticles, physical mixture of Cu_2O and silver nanoparticles, and PVP stabilized silver nanoparticles. The solid lines are the fits using pseudo-first order kinetics model.

Table 6.2.2: Apparent rate constant (k_{app}) values for the reduction of methylene blue using various catalysts along with that for Cu_2O@Ag samples.

Catalyst	Concentration of MB (M)	Amount of catalyst (mg)	Required time for complete reduction (s)	k_{app} (s^{-1})	Reference
Fe_3O_4@PDA-Ag	1.3×10^{-4}	1.50	540	7.16×10^{-3}	[57]
Au@PPY@Fe_3O_4	7.5×10^{-5}	0.20	1200	4.43×10^{-3}	[58]
Ag(E)-SiO_2	5.0×10^{-4}	0.75	600	1.34×10^{-2}	[61]
Ag/Fe_3O_4@C	6.0×10^{-5}	1.50	240	1.71×10^{-2}	[63]
Cu_2O@Ag (C1A)	6.0×10^{-5}	0.10	540	1.36×10^{-2}	Present work
Cu_2O@Ag (C2A)	6.0×10^{-5}	0.10	480	1.48×10^{-2}	"
Cu_2O@Ag (C3A)	6.0×10^{-5}	0.10	360	1.54×10^{-2}	"
Cu_2O@Ag (C4A)	6.0×10^{-5}	0.10	300	1.88×10^{-2}	"
Physical mixture of Cu_2O (C4) and Ag nanoparticles	6.0×10^{-5}	0.10	660	9.28×10^{-3}	"
PVP stabilized Ag NPs	6.0×10^{-5}	0.10	1380	5.21×10^{-3}	"

6.2.4 Mechanism of reduction of 4-nitrophenol and methylene blue using Cu_2O@Ag polyhedral core-shell nanoparticles

The mechanism of catalytic reduction of 4-nitrophenol and methylene blue using Cu_2O@Ag polyhedral core-shell nanoparticles as the catalysts is shown in Scheme 6.2.2. The catalytic reduction reactions can be explained on the basis of two mechanisms; electrochemical mechanism and chemisorption [55,61]. In the electrochemical mechanism, the catalyst (Cu_2O@Ag polyhedral core-shell nanoparticles) acts as an electron relay for the oxidant as well as the reductant and the electron transfer is facilitated by the supported silver nanoparticles [61]. 4-nitrophenol and methylene blue act as electrophiles (electron acceptor) while BH_4^- acts as a nucleophile (electron donor) [61,64]. In the chemisorption mechanism, the nucleophile adsorbs on Cu_2O@Ag and the electrophile co-adsorbs simultaneously on the surface of supported silver nanoparticles. The nucleophile (i.e. BH_4^-) donates electrons to the electrophile (4-NP or MB) *via* the supported silver nanoparticles and the reduction proceeds [54,61]. The aqueous medium offers the required H^+ ions to complete the reduction of 4-NP to 4-AP (or MB to LMB) [65]. The higher catalytic activity of Cu_2O@Ag polyhedral core-shell nanoparticles as compared to pure Cu_2O microcrystals, and silver nanoparticles is explained as follows.

The electron relay in a catalytic reduction occurs on surface of the catalyst and the electron transfer ability depends on the particle size, stability as well as surface area of the catalyst [64,66]. The lower catalytic activity of pure Cu_2O microcrystals is attributed to low electron density as well as lower surface area as compared to that of Cu_2O@Ag polyhedral core-shell nanoparticles. In the catalytic reduction of rose bengal, methylene blue and eosin, Jiang et al. have attributed the lower catalytic activity and induction time of pure silver nanoparticles (as compared to supported silver nanoparticles) to the formation of silver aggregates in the aqueous solution which reduces the potential difference between the electrophiles and silver nanoparticles [64]. In the present study, it is proposed that aggregation of pure silver nanoparticles occurs in the aqueous solution. Due to aggregation, the particle size of Ag increases, which reduces the potential difference between the electrophile (4-NP or MB) and silver particles. This results in lower catalytic activity in both the reduction reactions [64,66]. The Cu_2O@Ag polyhedral core-shell nanoparticles possess marginally higher surface area compared to

Cu_2O microcrystals (see Chapter-4, Table 4.2.2) indicating the presence of higher number of reactive sites for the adsorption of electrophiles and nucleophiles. Further, the immobilization of silver nanoparticles on the surface prevents aggregation and increase in the stability of silver nanoparticles on the surface of Cu_2O microcrystals. The smaller silver nanoparticles present on Cu_2O@Ag polyhedral core-shell nanoparticles create a larger potential difference between them and the electrophile and fast electron transfer occurs [64,66]. Also, the electron density in the Cu_2O@Ag polyhedral core-shell nanoparticles is higher compared to pure Cu_2O microcrystals. The higher surface area and high electron density facilitates the electron transfer between 4-NP/MB and the supported silver nanoparticles which enables a fast reduction process [64,66]. Due to these reasons, either lower induction period or no induction period is observed in the case of reduction of MB where Cu_2O@Ag polyhedral core-shell nanoparticles are used as the catalysts. In the case of Cu_2O@Ag polyhedral core-shell nanoparticles, catalytic reduction occurs on the surface of Ag nanoparticles. The catalytic activity is primarily dependent on number of available active metal sites on the surface of catalyst. Depositing small amount of Ag nanoparticles on Cu_2O results in incomplete deposition of Ag nanoparticles on the Cu_2O polyhedral microcrystals. Growing thicker layer of Ag on Cu_2O leads to the formation of Cu_2O@Ag polyhedral core-shell particles which are more effective for the catalytic reduction because they provide more number of silver sites during the catalytic reduction as compared to partially covered Ag nanoparticles on the surface of Cu_2O.

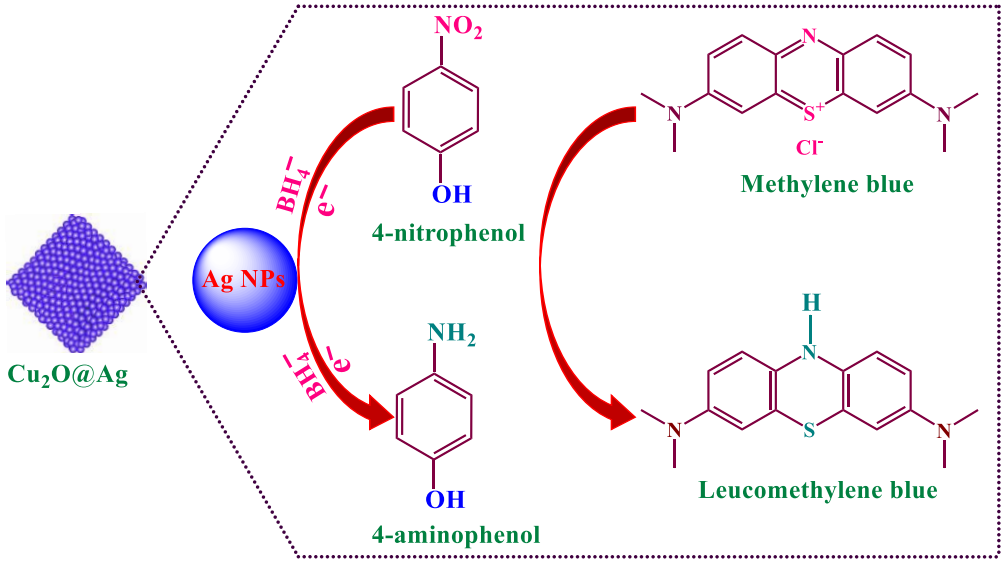

Scheme 6.2.2: Proposed mechanism for the catalytic reduction of 4-nitrophenol and methylene blue by Cu_2O@Ag polyhedral core-shell nanoparticles.

6.2.5 Reusability and stability of Cu_2O@Ag polyhedral core-shell nanoparticles

In the case of practical applications, reusability of the catalysts is very important [57,58,61]. The reusability studies for the best catalyst Cu_2O@Ag (C4A) was carried out upto five cycles. After the catalytic reduction, the catalyst was separated from the reaction flask through centrifugation and washed several times with water and the catalyst was reused for the next five cycles. The reusability of the catalyst was monitored using UV-Visible spectroscopy and the results are shown in Figure 6.2.7 (a, b). The corresponding percent reduction of 4-NP/MB using the catalyst up to five cycles are shown in Figure 6.2.7 (c, d). In the catalytic reduction of 4-NP and MB, about 2 % and 3 % decrease, respectively, in the catalytic activity is observed after five cycles which indicates higher stability and applicability of the Cu_2O@Ag polyhedral core-shell nanoparticles for practical applications.

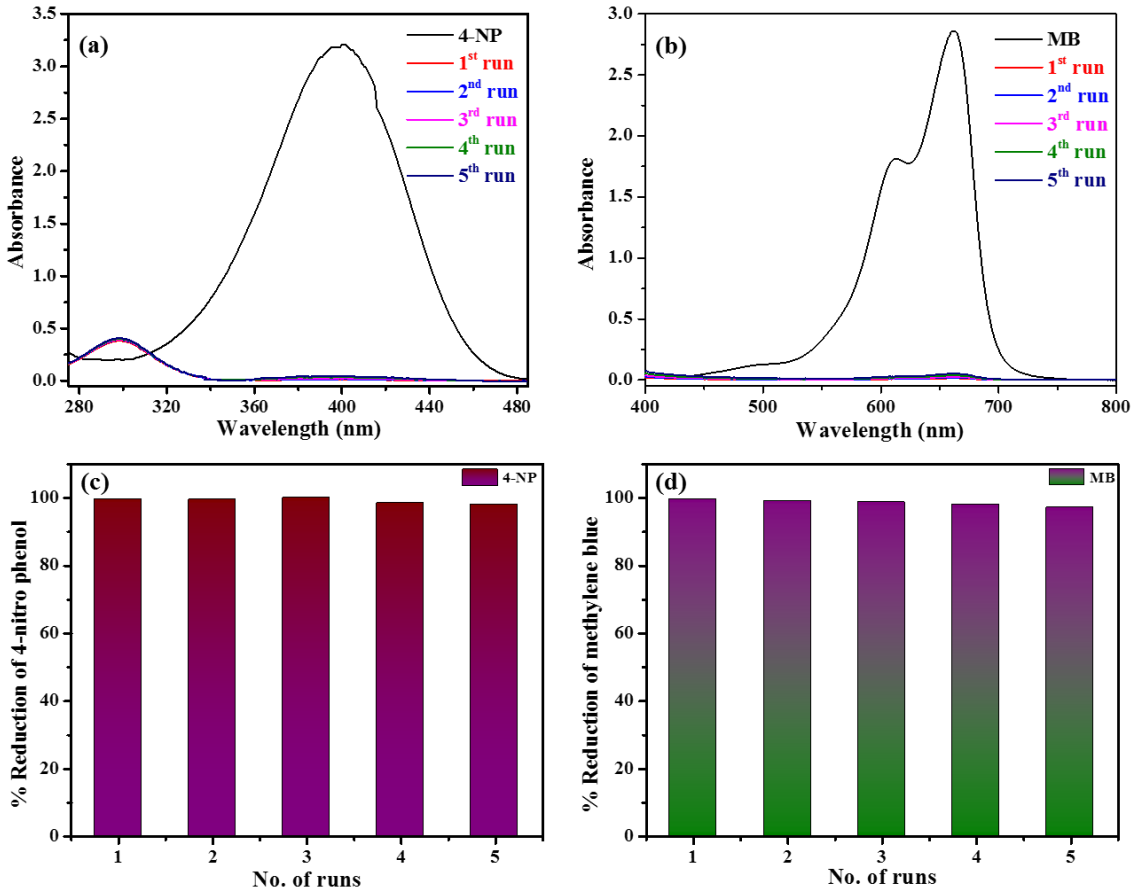

Fig. 6.2.7: (a, b) UV-Visible spectra indicating 4-nitrophenol and methylene blue reduction using Cu_2O@Ag polyhedral core-shell nanoparticle sample C4A up to five cycles, and **(c, d)** percent reduction of 4-nitrophenol and methylene blue using C4A up to five cycles.

6.3 Peroxidase-like activity of $SiO_2@Co_3O_4$ core-shell nanorattles

6.3.1 Introduction

In recent times, scientists are paying increasing attention towards the use of metal oxide nanoparticles in various biological applications due to their versatility, sensitivity, stability, etc [67–74]. Enzymes are typically proteins that catalyze bio-chemical reactions in cellular metabolic processes and they enhance rate of the reactions [75,76]. Horseradish peroxidase (HRP) is a natural peroxidase enzyme which is extracted from plants and it catalyzes decomposition of peroxides and oxidation of various substrates [77]. HRP is expensive, difficult to store, and it easily becomes inactive. Scientists have an immense interest to develop artificial enzymes (mimics) due to inherent drawbacks of the natural enzymes; they have a tendency to undergo denaturation under environmental conditions with low stability, and low redox activity [75,78]. Nanomaterials based enzyme mimics have the advantage of higher stability under harsh conditions, low cost, tunable catalytic activity and they can be potentially useful in different fields of biology.

Very less attention has been paid towards the use of metal oxide nanoparticles in biological applications. For example, Mu et al. have reported peroxidase-like activity for Co_3O_4 nanoparticles and, recently, they have also studied the effect of crystal plane of Co_3O_4 on the peroxidase-like activity [78,79]. Gao et al. have reported that Fe_3O_4 nanoparticles possess intrinsic peroxidase-like activity [80]. In addition to Fe_3O_4 and Co_3O_4 nanoparticles, other systems such as graphene supported Au-Pd bimetallic core-shell nanoparticles [81], Au nanoparticles on citrate-functionalized graphene sheets [82], Co-Al layered double hydroxides [83], porous platinum nanotubes [84], CuS-graphene nanosheets [85], and Fe_3O_4 nanoparticles loaded on graphene oxide-dispersed carbon nanotubes [86] have been explored for the intrinsic peroxidase-like activity. Peroxidase-like activity has also been demonstrated in Co_3O_4 nanoparticles coupled with carbon nitride nanotubes and reduced graphene oxide [87,88]. In the present study, the intrinsic peroxidase-like activity of $SiO_2@Co_3O_4$ core-shell nanorattles using 3,3’,5,5’-tetramethyl benzidine (TMB) as the substrate has been investigated.

6.3.2 Experimental details

To investigate the peroxidase-like redox catalytic activity of $SiO_2@Co_3O_4$ core-shell nanorattles (Chapter-5.1), the oxidation of 3,3’,5,5’-tetramethyl benzidine (TMB) was

examined in the presence of H_2O_2. The reaction was studied at room temperature in acetic acid-acetate buffer containing $SiO_2@Co_3O_4$ nanorattles as the catalyst. The experimental procedure for the peroxidase-like activity of $SiO_2@Co_3O_4$ core-shell nanorattles is given in Scheme 6.3.1.

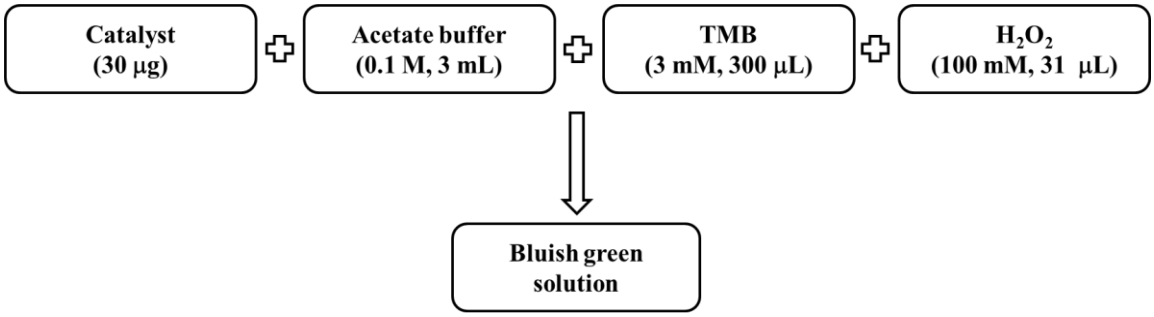

Scheme 6.3.1: Schematic representation of experimental procedure for studying peroxidase-like activity of $SiO_2@Co_3O_4$ core-shell nanorattles.

First, 30 μg of $SiO_2@Co_3O_4$ catalyst was dispersed in 3 mL of 0.1 M acetate buffer and sonicated for 3 min. Then, 300 μL of 3 mM DMSO solution of TMB and 31 μL of 30 % H_2O_2 (100 mM) were added. The absorbance values at λ_{max} = 652 nm were recorded upto 5 min in time course mode on a Shimadzu UV-2450 UV-Vis spectrophotometer. Kinetic studies were carried out using the same instrument. While keeping the TMB concentration constant, kinetic analysis was performed by varying amount of the $SiO_2@Co_3O_4$ catalyst (5-60 μg per 3 mL), pH (2-12), temperature (20-70 ^oC), and H_2O_2 concentration (5-200 mM). Kinetic studies were also carried out under the following conditions; 30 μg catalyst per 3 mL, pH = 5, temperature = 30 ^oC and TMB concentration = 0.015-0.4 mM while keeping H_2O_2 concentration as 100 mM. In another kinetic experiment, while keeping the concentration of TMB as 0.3 mM, the concentration of H_2O_2 was varied (20-200 mM). The apparent rate constant values (k_{app}) were evaluated from the absorbance data [77,78]. The Michaelis-Menten constant (K_m) and the maximal reaction velocity (V_{max}) were determined from the Lineweaver-Burk double reciprocal plots. The Michaelis-Menten equation can be expressed as

$$\frac{1}{\nu} = \left(\frac{K_m}{V_{max}}\right)\left(\frac{1}{[S]} + \frac{1}{[V_{max}]}\right) \qquad (3)$$

Where, ν is the initial velocity, K_m is the Michaelis-Menten constant, V_{max} is the maximal reaction velocity, and [S] is the concentration of the substrate (TMB).

6.3.3 Results and discussion

TMB is a colourless peroxidase substrate which is oxidized by H_2O_2 very slowly to form a blue coloured product. The oxidation of TMB was carried out using Co_3O_4 nanoparticles and SiO_2@Co_3O_4 core-shell nanorattles (S1, S2 and S3) as the catalysts in the presence of H_2O_2. The blue colored product formed as a result of the catalytic reaction was monitored by UV-Visible spectroscopy (λ_{max} = 652 nm). A blank reaction was also carried out with TMB and H_2O_2 in the absence of any catalyst. It was found that there is no peroxidase activity in absence of the catalyst which confirms the role of catalyst in the peroxidase-like activity towards TMB. Although, pure Co_3O_4 nanoparticles and SiO_2@Co_3O_4 core-shell nanorattles (S1, S2 and S3) produce blue coloured product on reaction with TMB in the presence of H_2O_2, the blue colour was more intense in the case of SiO_2@Co_3O_4 core-shell nanorattles (S1, S2 and S3) compared to pure Co_3O_4. The time dependent catalytic activity for Co_3O_4 nanoparticles and SiO_2@Co_3O_4 core-shell nanorattles towards TMB oxidation, as indicated by UV-Visible spectral results are shown in Figure 6.3.1a. The relative catalytic efficiency of various catalysts is shown in Figure 6.3.1b which follows the order: S2 > S3 > S1 > Co_3O_4 > SiO_2; the activity of sample S3 is lower compared to S2 but higher than that of S1.

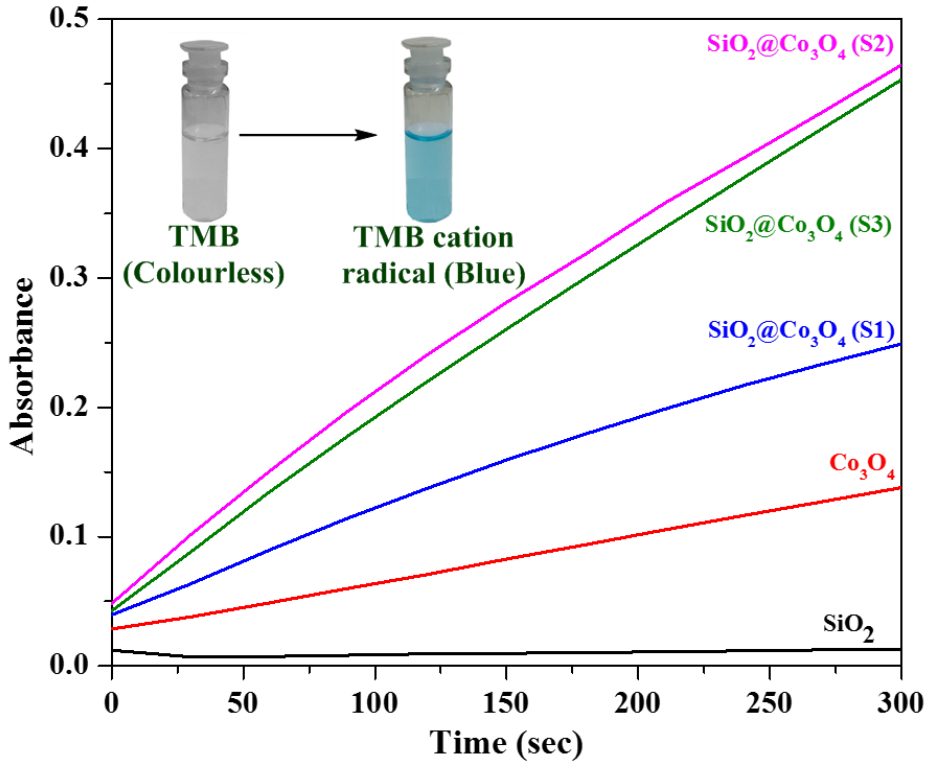

(a)

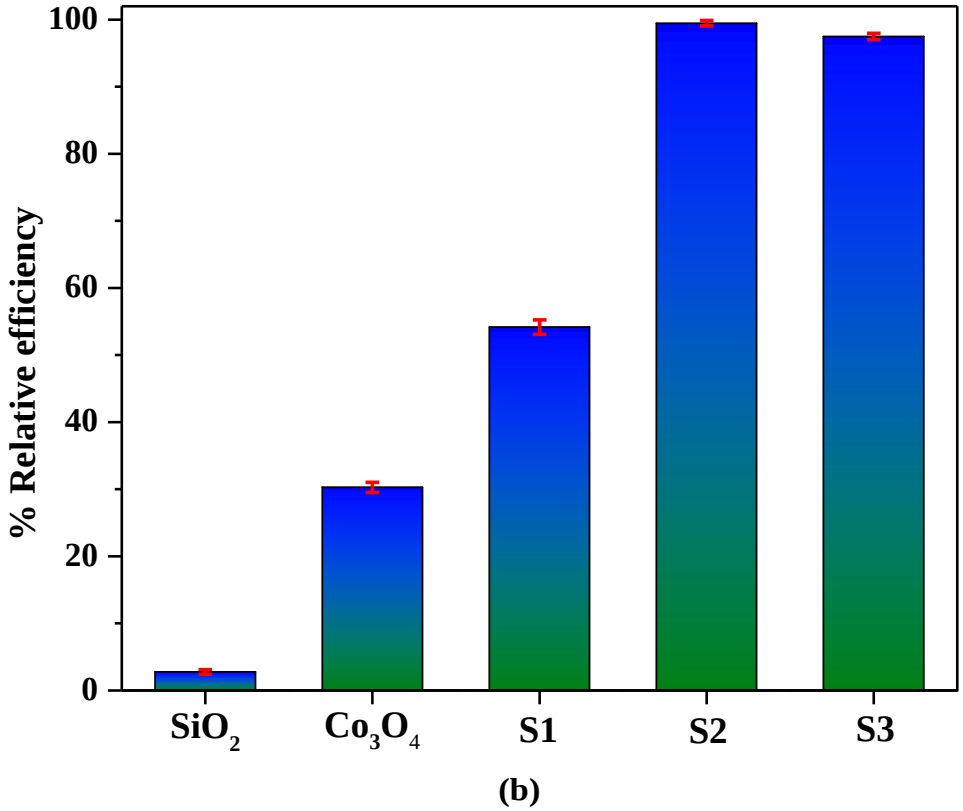

Fig. 6.3.1: (a) Time dependent UV-Visible spectral results indicating the peroxidase-like activity on TMB using SiO_2, Co_3O_4 nanoparticles, and SiO_2@Co_3O_4 core-shell nanorattles (S1, S2 and S3) as the catalyst (λ_{max} = 652 nm), **(b)** Comparison of peroxidase activity of SiO_2@Co_3O_4 core-shell nanorattles (S1, S2 and S3) with that of SiO_2 and Co_3O_4 nanoparticles. For more details on the samples, see Section 5.1.2.2.

6.3.3.1 Effect of physicochemical conditions on the peroxidase-like activity

Any catalytic reaction demands optimum conditions for maximum activity. In the present study, TMB and H_2O_2 were chosen as the reagents. Effort was made to understand the catalytic activity of SiO_2@Co_3O_4 core-shell nanorattles on varying conditions such as amount of the catalyst, temperature, and pH. The amount of catalyst (SiO_2@Co_3O_4, S2) was varied from 5 to 60 μg per 3 mL while keeping the pH at 5, temperature at 30 ^oC and the concentration of H_2O_2 at 100 mM. A linear relationship between amount of the catalyst and peroxidase activity was found (Figure 6.3.2a). The catalytic activity was tested by varying the pH from 2 to 12 and also by varying the temperature between 20 and 70 ^oC while keeping the amount of catalyst (SiO_2@Co_3O_4, S2) as 30 μg per 3 mL, and the concentration of TMB and H_2O_2 as 0.3 mM and 100 mM, respectively. From the results (Figures 6.3.2b and 6.3.2c), the optimized pH and

temperature are found as 5 and 30 ^{o}C, respectively. The effect of H_2O_2 concentration on the catalytic activity of $SiO_2@Co_3O_4$ (S2) was also studied. By increasing the H_2O_2 concentration, the peroxidase-like activity of $SiO_2@Co_3O_4$ core-shell nanorattles is steady even at higher H_2O_2 concentrations (Figure 6.3.2d). Previous reports have indicated that higher concentration of H_2O_2 leads to negative impact on the activity. At higher concentrations, H_2O_2 inhibits the catalytic activity of HRP due to its conversion from active form to an inactive form [78,89]. Leaching test was also performed to prove that the peroxidase-like activity of the catalysts does not result from leaching of the cobalt ions from the catalysts into the solution. To prove this, 30 μg of $SiO_2@Co_3O_4$ (S2) was incubated in 3 mL of acetate buffer solution (pH = 5) for 30 min, and then the $SiO_2@Co_3O_4$ sample was separated from the solution by centrifugation. The catalytic activity using the resultant solution (from the leaching experiment) was tested (3 mL of solution, 300 μL of 3 mM TMB, and 31 μL of 100 mM H_2O_2). The peroxidase activity using the leached solution was compared with that of $SiO_2@Co_3O_4$ sample (S2). Negligible absorbance was found as shown in Figure 6.3.2e when the leached solution was used as the catalyst. These results conclude that the peroxidase-like activity is only due to Co_3O_4 nanoparticles and not from the leached cobalt ions.

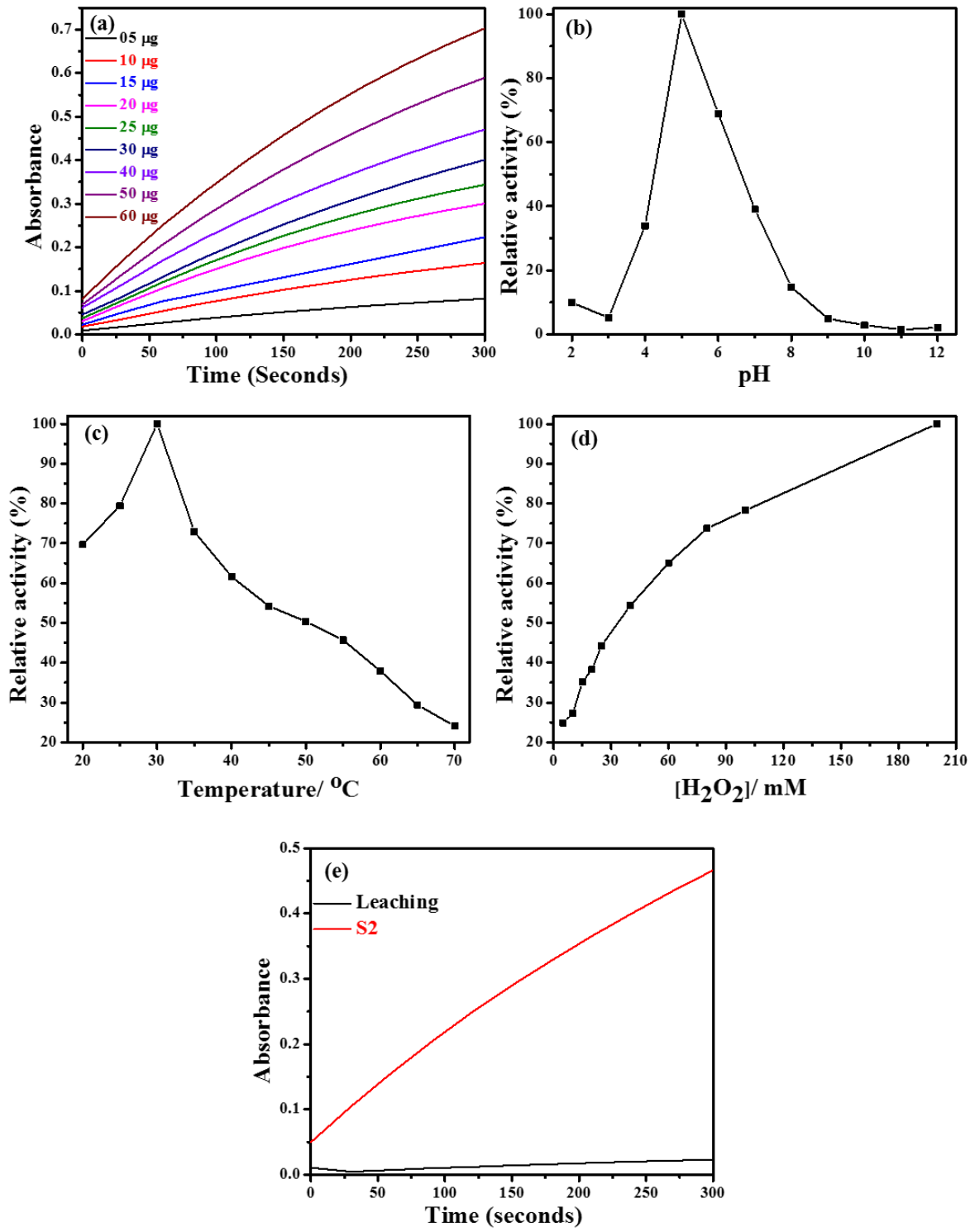

Fig. 6.3.2: The effect of physicochemical conditions on peroxidase-like activity of SiO_2@Co_3O_4 core-shell nanorattles (S2): **(a)** amount of catalyst, **(b)** pH, **(c)** temperature, **(d)** H_2O_2 concentration, and **(e)** the effect of leaching.

6.3.3.2 Kinetic studies of peroxidase-like activity using $SiO_2@Co_3O_4$ core-shell nanorattles

To understand the peroxidase-like activity of $SiO_2@Co_3O_4$ core-shell nanorattles better, steady state analysis was carried out by choosing TMB and H_2O_2 as the reactants. The kinetic analysis was carried out by varying the concentration of TMB while keeping the H_2O_2 concentration constant, and vice- versa (Figure 6.3.3). The steady state kinetic parameters (Michaelis constant, K_m and maximal reaction velocity, V_{max}) were estimated using the Lineweaver-Burk double reciprocal plots [77,87] which show linear relationship between 1/[V] and 1/[S], as shown in Figures 6.3.3c and 6.3.3d. The estimated kinetic parameters for the $SiO_2@Co_3O_4$ core-shell nanorattles (S2) were compared with the reported values for Co_3O_4 nanoparticles and HRP (Table 6.3.1).

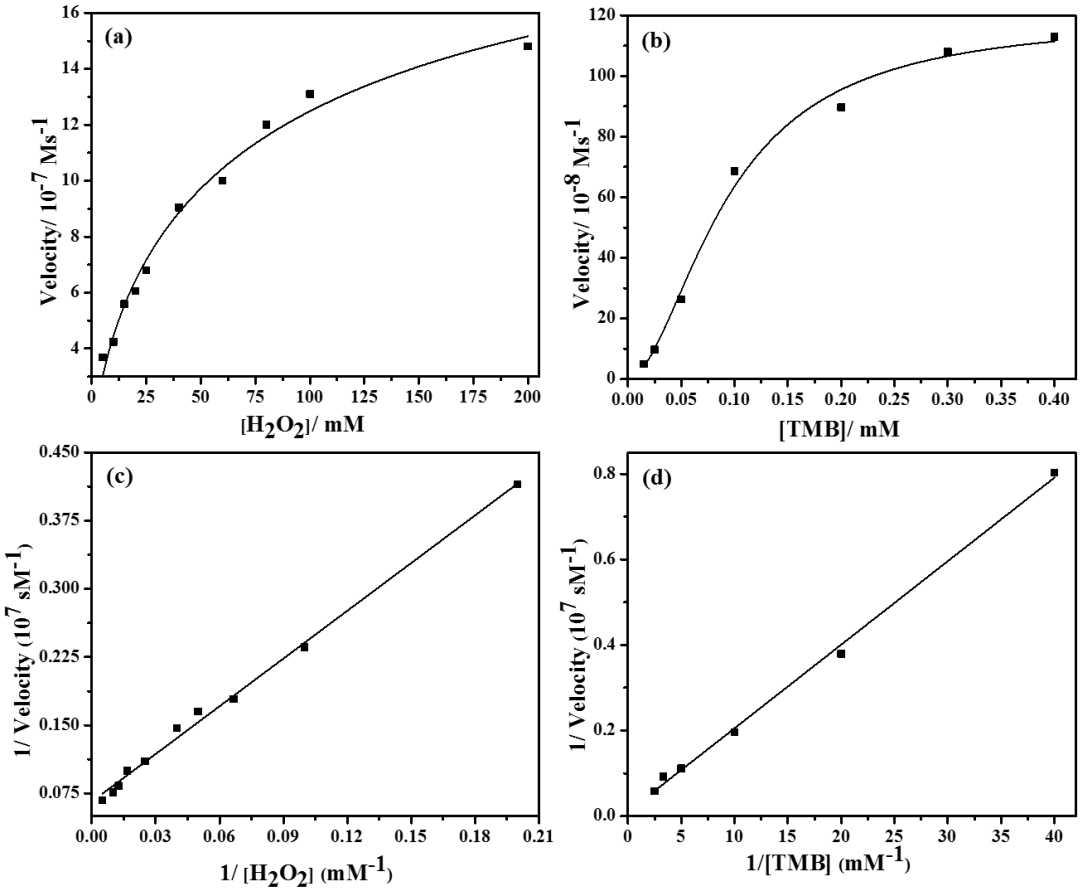

Fig. 6.3.3: Steady state kinetic analysis for $SiO_2@Co_3O_4$ core-shell nanorattles (S2) under various conditions: **(a)** [TMB] = 0.3 mM; [H_2O_2] = 20-200 mM, **(b)** [H_2O_2] = 100 mM; [TMB] = 0.015-0.4 mM, and **(c and d)** are the Lineweaver-Burk double reciprocal plots corresponding to conditions **(a)** and **(b)**. Other conditions: 30 μg catalyst per 3 mL of 0.1 M acetate buffer, pH = 5, and temperature = 30 ^oC.

The Michaelis constant (K_m), obtained from the slope of Lineweaver-Burk double reciprocal plot, is related to properties of the substrate, enzyme and the reaction conditions [77]. A smaller K_m value suggests higher affinity between the substrate and the enzyme. The K_m value for $SiO_2@Co_3O_4$ core-shell nanorattles (S2) is 0.087 for TMB and 25.2 for H_2O_2, respectively. The K_m values for TMB and H_2O_2 are comparable with that of Co_3O_4-carbon nitride nanotubes [87] (0.056 for TMB and 30.04 for H_2O_2) and Co_3O_4/reduced graphene oxide (0.19 for TMB and 24.04 for H_2O_2) [88]. The $SiO_2@Co_3O_4$ core-shell nanorattles (S2) exhibit five times higher affinity for TMB than HRP and almost two times lower affinity for TMB compared to pure Co_3O_4 nanoparticles. In the case of H_2O_2, the $SiO_2@Co_3O_4$ core-shell nanorattles show almost six times higher affinity compared to Co_3O_4 nanoparticles and six times lower affinity compared to HRP. Higher concentration of H_2O_2 and lower concentration of TMB are the best conditions to achieve maximum peroxidase-like activity using the $SiO_2@Co_3O_4$ core-shell nanorattles. The higher activity of the nanorattles compared to HRP is attributed to the availability of more active sites on the surface of $SiO_2@Co_3O_4$ core-shell nanorattles compared to HRP, which has only one active site (iron (II)) [80,90].

In order to compare the peroxidase-like activity of $SiO_2@Co_3O_4$ core-shell nanorattles (S2) with that of natural peroxidase (HRP) and pure Co_3O_4 nanoparticles, turnover number (k_{cat}) values were also estimated (Table 6.3.1). The k_{cat} value for $SiO_2@Co_3O_4$ core-shell nanorattles is much higher than that of pure Co_3O_4 and HRP. These results suggest that the $SiO_2@Co_3O_4$ core-shell nanorattles can be used as highly efficient peroxidase mimic compared to pure Co_3O_4 nanoparticles and HRP [78,90]. The ratio of k_{cat}/K_m is often referred to as specificity constant; a higher specificity constant value indicates higher peroxidase-like activity of the material. The k_{cat}/K_m values estimated for $SiO_2@Co_3O_4$ core-shell nanorattles (S2) are given in Table 6.3.1. In the present study, the $SiO_2@Co_3O_4$ core-shell nanorattles show higher specificity constant compared to pure Co_3O_4 and HRP for TMB. With respect to H_2O_2, the $SiO_2@Co_3O_4$ core-shell nanorattles show two orders of magnitude higher specificity compared to pure Co_3O_4 nanoparticles and the specificity is similar to that of HRP [90]. These results demonstrate that the $SiO_2@Co_3O_4$ core-shell nanorattles show higher peroxidase-like activity compared to Co_3O_4 nanoparticles and HRP.

Table 6.3.1: Comparison of the kinetic parameters for $SiO_2@Co_3O_4$ core-shell nanorattles with those for Co_3O_4 nanoparticles and HRP.

Catalyst	*[E]/ M	Substrate	K_m /mM	V_{max}/ Ms^{-1} (10^{-8})	k_{cat}/ s^{-1}	k_{cat}/K_m ($M^{-1}s^{-1}$)	Reference
$SiO_2@Co_3O_4$ (S2)	7.54×10^{-11}	TMB	0.087±0.0028	0.012±0.00056	1.49×10^{4}	1.75×10^{8}	Present work
$SiO_2@Co_3O_4$ (S2)	7.54×10^{-11}	H_2O_2	25.2±1.28	0.015±0.00035	1.96×10^{4}	8.08×10^{5}	Present work
Co_3O_4 NPs	3.43×10^{-10}	TMB	0.037	6.27	1.83×10^{2}	4.94×10^{6}	[78]
Co_3O_4 NPs	3.43×10^{-10}	H_2O_2	140.07	12.1	3.53×10^{2}	2.52×10^{3}	″
HRP	2.50×10^{-11}	TMB	0.434	10.0	4.00×10^{3}	9.22×10^{6}	[90]
HRP	2.50×10^{-11}	H_2O_2	3.70	8.71	3.48×10^{3}	9.40×10^{5}	″

* [E] = The concentration of catalyst (e.g. $SiO_2@Co_3O_4$) or the concentration of enzyme (HRP).

6.3.4 Proposed mechanism for the peroxidase-like activity of $SiO_2@Co_3O_4$ core-shell nanorattles on TMB

The proposed mechanism for the peroxidase-like activity of $SiO_2@Co_3O_4$ core-shell nanorattles on TMB is given in Scheme 6.3.2 [78,87,88]. Neither H_2O_2 nor $SiO_2@Co_3O_4$ core-shell nanorattles alone was found to exhibit peroxidase-like activity. The presence of $SiO_2@Co_3O_4$ and H_2O_2 together are important for the peroxidase-like activity on tetramethyl benzidine. When $SiO_2@Co_3O_4$, H_2O_2 and TMB are present, the TMB molecules adsorb on the surface of $SiO_2@Co_3O_4$ and increases the electron density by donating the lone pair electrons of the amino groups [78,91]. The $SiO_2@Co_3O_4$ core-shell nanorattles induce electrochemical reduction of H_2O_2 producing OH^- and $OH^\bullet$ species which involve in the oxidation of TMB to produce $TMB^{\bullet+}$ (a charge transfer complex which is blue in colour). Mu et al. have reported electrochemical reduction of H_2O_2 using pure Co_3O_4 nanoparticles [78]. In the case of core-shell nanorattles, there is an assembly of Co_3O_4 nanoparticles on the surface of SiO_2 spheres. The TMB molecules undergo less steric hindrance to reach the catalytic active centers (cobalt) in the case of $SiO_2@Co_3O_4$ core-shell nanorattles compared to pure Co_3O_4 nanoparticles. This increases the electron density on the core-shell nanorattles and facilitate the electron transfer. The enhancement in the peroxidase-like activity of $SiO_2@Co_3O_4$ core-shell nanorattles compared to pure Co_3O_4 nanoparticles is due to increased surface area and also due to increase in the electron density. Sample S2 shows higher activity than S1 and this is due to the presence of more number of catalytic active centers in S2 compared to S1 but sample S3 consists of free Co_3O_4 nanoparticles in addition to $SiO_2@Co_3O_4$ nanorattles which leads to lower activity compared to S2.

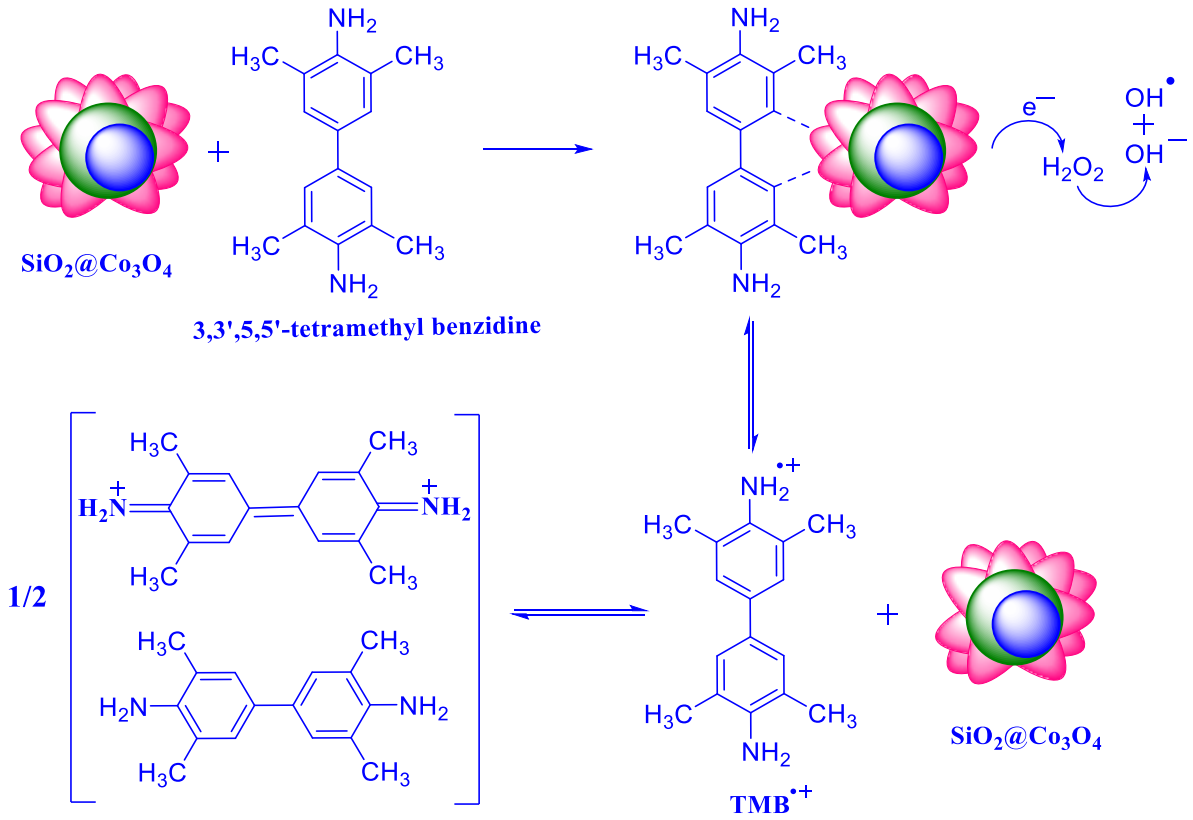

Scheme 6.3.2: Proposed mechanism for the peroxidase-like activity of $SiO_2@Co_3O_4$ core-shell nanorattles on TMB.

6.4 Adsorption of mixture of rhodamine B and methylene blue in an aqueous solution using SiO_2@Ni-Co mixed metal oxide core-shell nanorattles

6.4.1 Introduction

Removal of industrial waste is very important for environmental safety and various methods such as adsorption, membrane separation, oxidation, reduction, coagulation and flocculation, and biological treatment have been used for the removal of organic waste from the water resources [92–96]. Among all the methods, adsorption plays an important role due to its ease of operation, low cost and it is most widely used in industries for the removal of various contaminants. Different adsorbents such as red mud, fly ash, clay, banana peel, coconut shell, orange peel, peanut hulls, sugar cane bagasse, rice husk, saw dust, and activated carbon have been reported [97–102]. Zhou et al. have explored C@Al_2O_3 core-shell rattles as adsorbent for the removal of orange-II [103]. Liang et al. have used Fe_3O_4@mesoporous carbon core-shell nanoparticles as adsorbent for the removal of rhodamine B [104]. Zheng et al. have used Fe_2O_3@SiO_2 yolk-shell nanoparticles as adsorbent for the removal of methylene blue [105]. Xie et al. have explored Fe_3O_4@polydopamine-Ag core-shell nanoparticles as adsorbent for the removal of methylene blue [57]. Li et al. have used TiO_2/graphene oxide core-shell nanoparticles as adsorbent for the removal of congo red [106]. Pradhan et al. have explored Fe/Al_2O_3-MCM-41 nanoparticles as adsorbent for the adsorption of mixture of methylene blue and methyl orange [107]. Till date, the use of nanoparticles with core-shell, yolk-shell, and nanorattle morphology as adsorbents for the adsorption of the mixture of dyes has not been reported. In the present study, SiO_2@Ni-Co mixed metal oxide core-shell nanorattles have been explored as adsorbents for the removal of mixture of rhodamine B and methylene blue from an aqueous solution.

6.4.2 Experimental details

Stock solutions of the dyes (rhodamine B and methylene blue) were prepared at a concentration of 100 mg/L, and subsequently the test solutions were prepared by sequential dilution of the stock solutions with Millipore water®. The dye solution mixtures (RhB and MB) were prepared by mixing solutions of rhodamine B and methylene blue at desired concentrations. The concentration of the dyes (RhB and MB) in the aqueous solution after the adsorption was determined using a Shimadzu UV-2450

UV-Visible spectrophotometer by measuring the absorbance at the corresponding λ_{max} (664 nm for MB and 554 nm for RhB). In the case of binary mixture of dyes A and B, the individual dye concentrations were determined by measuring the absorbance values at their maximum wavelengths λ_{max1} and λ_{max2}, respectively using the following equations [108].

$$A_{\lambda 1} = \varepsilon_{11} C_1 l + \varepsilon_{12} C_2 l \quad (4)$$

$$A_{\lambda 2} = \varepsilon_{21} C_1 l + \varepsilon_{22} C_2 l \quad (5)$$

Where, $A_{\lambda 1}$ and $A_{\lambda 2}$ are the corresponding absorbance values at λ_{max1} and λ_{max2}, respectively. ε_{11} and ε_{21} are the absorbance coefficients of dye A at wavelength λ_{max1} and λ_{max2}, respectively. ε_{12} and ε_{22} are the absorbance coefficients of dye B at wavelengths λ_{max1} and λ_{max2}, respectively and l is the path length.

For the preliminary adsorption studies, 100 mL of dye mixture (1×10^{-5} M of each dye) was used. About 50 mg each of the adsorbent (e.g. SiO_2@Ni-Co mixed metal oxide core-shell nanorattles (M1, M2, and M3), SiO_2@Co_3O_4 core-shell nanorattles, SiO_2@NiO core-shell nanorattles, SiO_2, $NiCo_2O_4$, Co_3O_4, NiO, physical mixtures (NiO:Co_3O_4 ratio = 7:3, 5:5, and 3:7)) was added into 100 mL of the dye mixture in a 250 mL beaker covered with an aluminium foil and stirred in dark at 25 ^oC for 30 min. Aliquots (about 4 mL) were taken at periodic time intervals, centrifuged, and the supernatant solutions were analyzed using UV-Visible spectroscopy. The effect of varying the pH, amount of adsorbent, and concentration of the initial dye mixture on the adsorption was investigated. To study the effect of pH, 25 mg of the adsorbent (M1) was dispersed in 50 mL of the dye mixture (1×10^{-5} M) and the pH was varied between 3 and 13. To study the effect of amount of adsorbent, the concentration of dye mixture was kept as 1×10^{-5} M and the amount of adsorbent (M1) was varied between 5 mg and 25 mg. For studying the effect of initial dye concentration, the concentration of dye mixture was varied from 1×10^{-5} M to 5×10^{-5} M while keeping the amount of adsorbent as 25 mg. The adsorption capacity of the adsorbent towards MB and RhB was calculated using the following equation [98,101].

$$Q_e = \frac{C_o - C_e}{W} \times V \quad (6)$$

Where Q_e is the amount of dye adsorbed (mg/g), C_o and C_e are the initial and equilibrium concentrations of dye (mg/L), W is the mass of adsorbent (g), and V is the volume of dye solution (L).

6.4.3 Results and discussion

6.4.3.1 Preliminary adsorption studies

Preliminary adsorption studies were carried out using 100 mL of mixture of rhodamine B and methylene blue (1×10^{-5} M each) with 50 mg powder of each of the adsorbent (e.g. SiO_2, $NiCo_2O_4$, Co_3O_4, NiO, physical mixtures (e.g. NiO:Co_3O_4 ratio = 7:3, 5:5, and 3:7), SiO_2@Ni-Co mixed metal oxide core-shell nanorattles (M1, M2, and M3), SiO_2@Co_3O_4, and SiO_2@NiO core-shell nanorattles). The adsorption of dyes using different adsorbents was monitored using UV-Visible spectroscopy and the results are shown in Figure 6.4.1. Pure SiO_2 shows preferential adsorption of methylene blue over rhodamine B where as pure $NiCo_2O_4$, Co_3O_4, NiO nanoparticles, and the physical mixtures show incomplete adsorption of both methylene blue and rhodamine B. The SiO_2@Co_3O_4 and SiO_2@NiO core-shell nanorattles show complete adsorption of methylene blue and appreciable adsorption of rhodamine B (70-75 %). The SiO_2@Ni-Co mixed metal oxide core-shell nanorattles (M1) show complete adsorption of both methylene blue as well as rhodamine B from the mixture whereas the other two SiO_2@Ni-Co mixed metal oxide core-shell nanorattle samples (M2 and M3) show complete adsorption of methylene blue and about 92-95 % adsorption of rhodamine B.

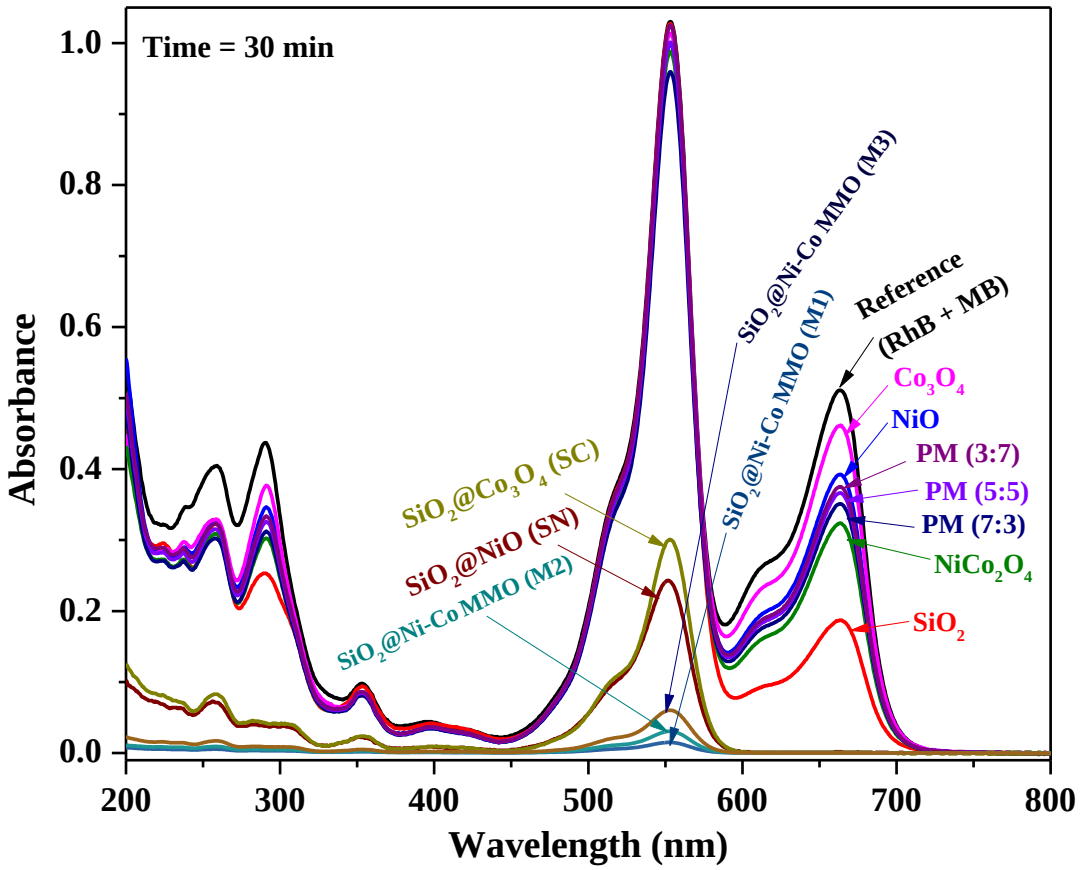

Fig. 6.4.1: UV-Vis spectra for monitoring the adsorption of mixture of rhodamine B and methylene blue from an aqueous solution using different adsorbents (e.g. SiO_2, $NiCo_2O_4$, Co_3O_4, NiO, physical mixtures (Co_3O_4:NiO as 3:7, 5:5, and 7:3), SiO_2@Ni-Co mixed metal oxide core-shell nanorattles (M1, M2, and M3), SiO_2@Co_3O_4, and SiO_2@NiO core-shell nanorattles).

For a better understanding of the adsorption, kinetic studies were performed using all the adsorbents and the results are shown in Figure 6.4.2. The results clearly indicate that SiO_2@Ni-Co mixed metal oxide nanorattles (M1) show complete adsorption of methylene blue and rhodamine B from their mixture within 2 min while the other samples M2 and M3 show complete adsorption of methylene blue and about 92-95 % adsorption of rhodamine B in the same time period. The dye removal efficiency results of different adsorbents are shown in Figures 6.4.2c and 6.4.2d. The SiO_2@Ni-Co mixed metal oxide core-shell nanorattles (M1, M2 and M3) show enhanced adsorption efficiency of dyes from the mixture compared to all the other adsorbents.

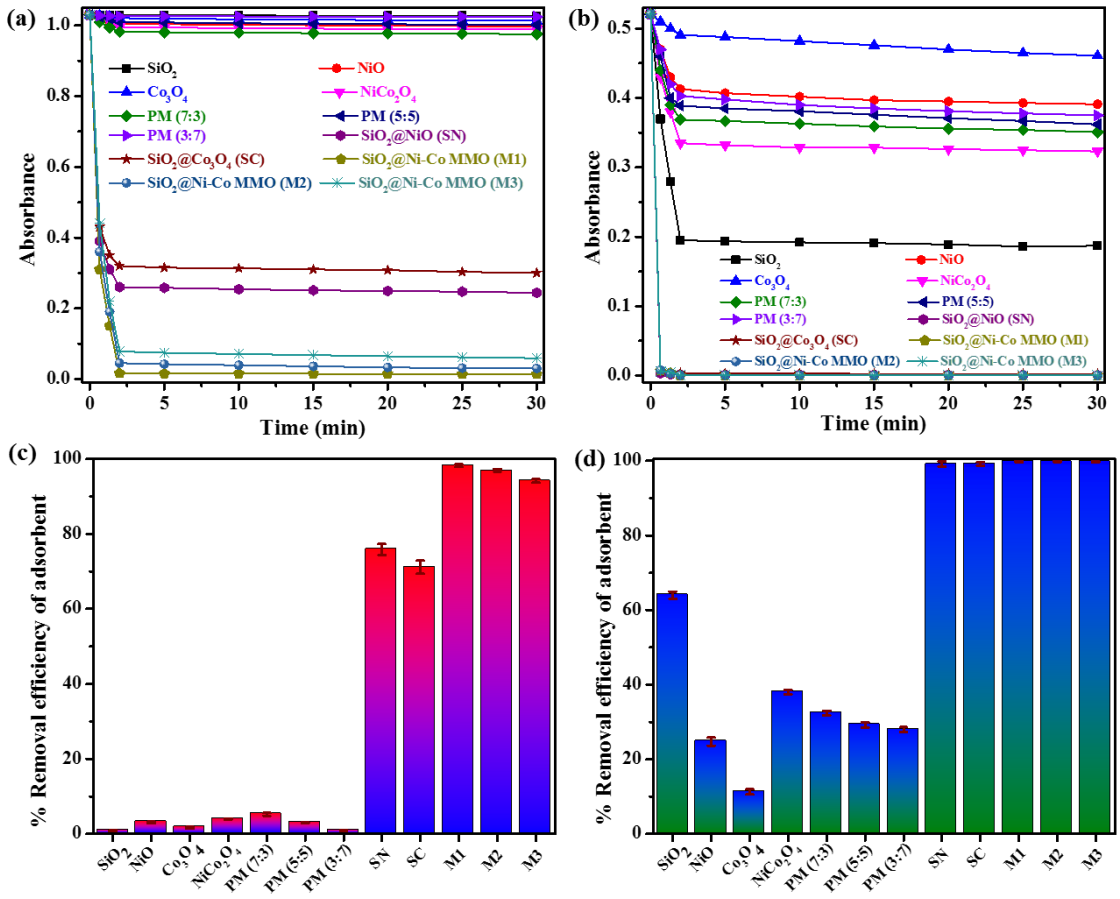

Fig. 6.4.2: (a and b) Kinetics of adsorption of rhodamine B and methylene blue from their mixture in an aqueous solution using different adsorbents; **(c and d)** comparison of rhodamine B and methylene blue removal efficiency from their mixture using different adsorbents.

The adsorption efficiency depends on factors such as amount of adsorbent, initial dye concentration and pH of the medium. A series of experiments were carried out by varying these factors and the results are discussed below. For these studies, SiO_2@Ni-Co mixed metal oxide core-shell nanorattles (M1) was chosen as the adsorbent since it exhibits the highest adsorption efficiency.

6.4.3.2 Effect of external factors on adsorption

6.4.3.2.1 Amount of adsorbent

In order to study the effect of amount of adsorbent on the adsorption efficiency, a series of adsorption studies were carried out by varying the amount of adsorbent (M1) from 5 mg to 25 mg in 20 mL solution of mixture of dyes (1×10^{-5} M each) which was stirred in dark up to 30 min at room temperature and the results are shown in Figure 6.4.3a. The

results indicate that, increasing the amount of adsorbent from 5 to 25 mg, leads to complete adsorption of both the dyes (methylene blue and rhodamine B). 10 mg of the adsorbent (M1) exhibits maximum removal efficiency of both the dyes (about 98.5 % of rhodamine B and 100 % of methylene blue) and therefore 10 mg of the adsorbent was used for further studies.

6.4.3.2.2 Initial dye concentration

The effect of initial concentration of mixture of rhodamine B and methylene blue was studied using 20 mL solutions of different dye mixtures (8-40 mg/L; 1×10^{-5} M to 5×10^{-5} M), 10 mg of the adsorbent (M1), pH = 6.75, and the results are shown in Figure 6.4.3b. On increasing the initial concentration of mixture of dyes from 8 mg/L to 40 mg/L, the percent removal of methylene blue is decreased from 99.5 to 83.2 and the removal of rhodamine B is drastically decreased from 99.4 % to 20.3 %. At lower concentration of mixture of dyes, the cationic dye (methylene blue) adsorbs on the surface of the negatively charged adsorbent while at higher concentration of mixture of dyes, the surface of adsorbent is occupied with a large number of methylene blue molecules which retards the adsorption of rhodamine B (zwitterionic dye) due to presence of bulky groups. This results in decrease in the adsorption of rhodamine B from the dye mixture at higher concentration of the mixture of dyes.

6.4.3.2.3 Effect of pH

To investigate the effect of pH on the adsorption efficiency, adsorption studies were carried out using 20 mL solution of mixture of dyes (1×10^{-5} M) at different pH (e.g. 3-13), and 10 mg of adsorbent (M1) was used. The results are shown in Figure 6.4.3c. On increasing the pH from 3 to 13, the percent removal of methylene blue increases from 70 to 100 while the removal of rhodamine B drastically decreases from 95 to 14 %. The zeta potential values of SiO_2@Ni-Co mixed metal oxide core-shell nanorattles (M1) at different pH values are shown in Figure 6.4.3d. In an acidic medium, the negatively charged carboxylate groups of rhodamine B get adsorbed on the surface of adsorbent through electrostatic interaction while in a basic medium (e.g. pH = 7-14), the surface of adsorbent possesses negative charge which is favourable for the adsorption of positively charged N-ethyl groups of methylene blue through electrostatic attraction.

Similar behaviour has been reported by several researchers for different adsorbents [100,109,110].

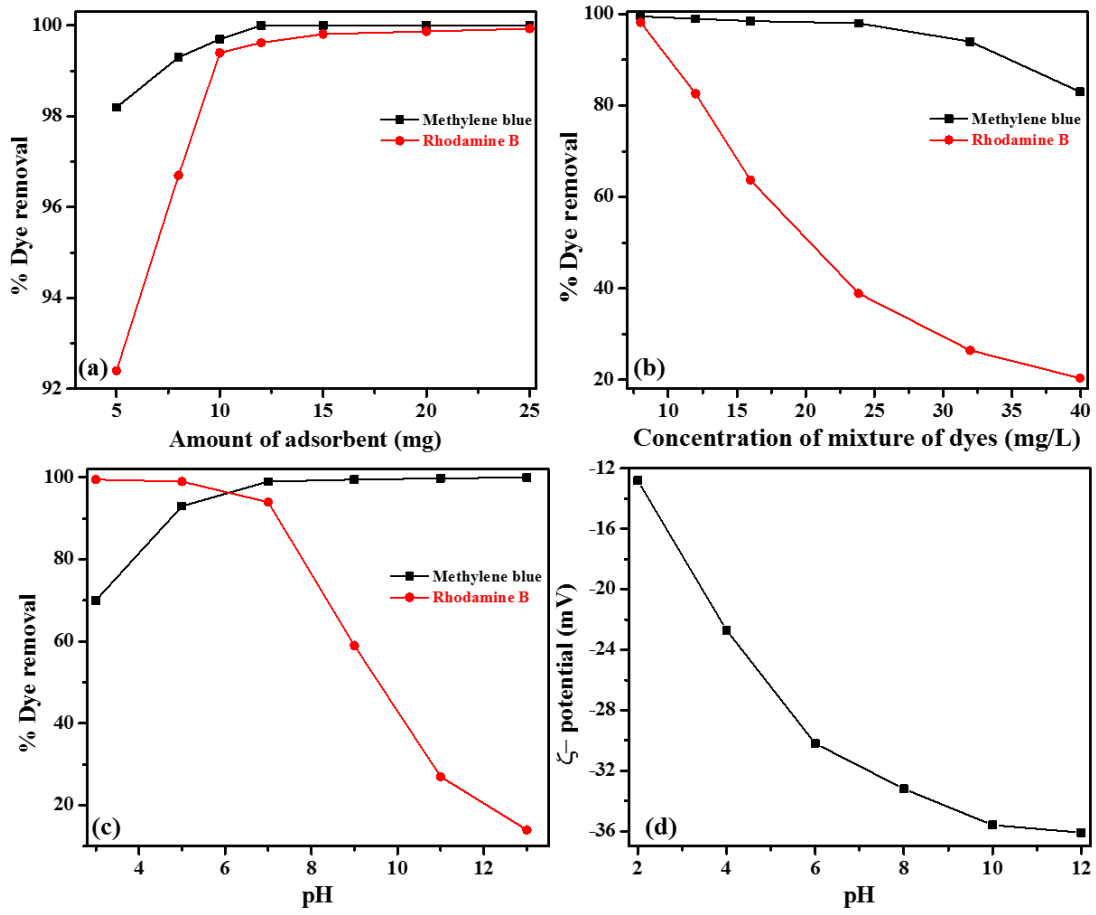

Fig. 6.4.3: Effect of external factors on the adsorption of rhodamine B and methylene blue dye mixture on SiO_2@Ni-Co mixed metal oxide core-shell nanorattles (M1); **(a)** the amount of adsorbent, **(b)** initial concentration of mixture of rhodamine B and methylene blue, **(c)** pH and **(d)** zeta potential of sample M1 at different pH values.

6.4.3.3 Adsorption isotherm studies

Adsorption isotherm studies play an important role in measuring adsorption capacity of the adsorbent. They also demonstrate how an adsorbate interacts with the adsorbent at a particular temperature. Different models (e.g. Langmuir, Freundlich, Temkin, Sips, etc) have been proposed to explain the adsorption [100,101]. Among these, Langmuir and Freundlich models are the most versatile and commonly used ones. In the present study, Langmuir and Freundlich models were used to describe the adsorption of methylene blue and rhodamine B on SiO_2@Ni-Co mixed metal oxide core-shell nanorattles.

6.4.3.3.1 Langmuir isotherm

The Langmuir isotherm assumes monolayer coverage of adsorbate on the surface of the adsorbent and all the adsorption sites are considered to be energetically identical [98]. The model also assumes that the adsorbent possesses homogeneous adsorption sites on its surface and the adsorbate selectively adsorbs on these sites [15]. The linear form of Langmuir isotherm can be expressed as

$$\frac{C_e}{q_e} = \frac{C_e}{q_{max}} + \frac{1}{q_m K_L} \quad (7)$$

where q_e is the amount of either rhodamine B or methylene blue adsorbed at equilibrium (mg/g), q_{max} is the maximum monolayer adsorption capacity of SiO_2@Ni-Co mixed metal oxides (mg/g), K_L is the Langmuir adsorption constant (L/mg) and C_e is the equilibrium concentration of the either rhodamine B or methylene blue (mg/L).

6.4.3.3.2 Freundlich isotherm

Freundlich model is applicable for multilayer non-ideal adsorption on a heterogeneous surface [100,111]. The linear form of Freundlich equation can be expressed as

$$lnq_e = lnK_F + 1/n\ lnC_e \quad (8)$$

where K_F is the Freundlich equilibrium constant (L/g), n is the empirical constant, q_e is the amount of either rhodamine B or methylene blue adsorbed at equilibrium (mg/g) and C_e is the equilibrium concentration of either rhodamine B or methylene blue (mg/L).

In the case of adsorption of individual dye systems (rhodamine B and methylene blue), the adsorption parameters were calculated using Langmuir and Freundlich models and the parameters are given in Table 6.4.1. The adsorption isotherms for individual dyes (rhodamine B and methylene blue) show L-type curves (Figures 6.4.4a and 6.4.4b) which indicate higher affinity of the adsorbate for the adsorbent [15]. The maximum adsorption capacity (q_{max}) has a significant role in deciding the applicability of the adsorbent; higher value of q_{max} indicates higher adsorption capacity of the adsorbent [100]. The Langmuir constant (K_L) relates to the heat of adsorption and affinity of the adsorption sites. The maximum adsorption capacity (q_{max}) and Langmuir constant (K_L) for SiO_2@Ni-Co mixed metal oxide core-shell nanorattles (M1, M2, and M3) were

calculated from the slope and intercept of the linear plots between C_e/q_e and C_e, respectively (Figures 6.4.4c and 6.4.4d). Among all the samples, SiO_2@Ni-Co mixed metal oxide core-shell nanorattles M1 show the highest adsorption capacity (79.1 mg/g and 83.5 mg/g for rhodamine B and methylene blue, respectively).

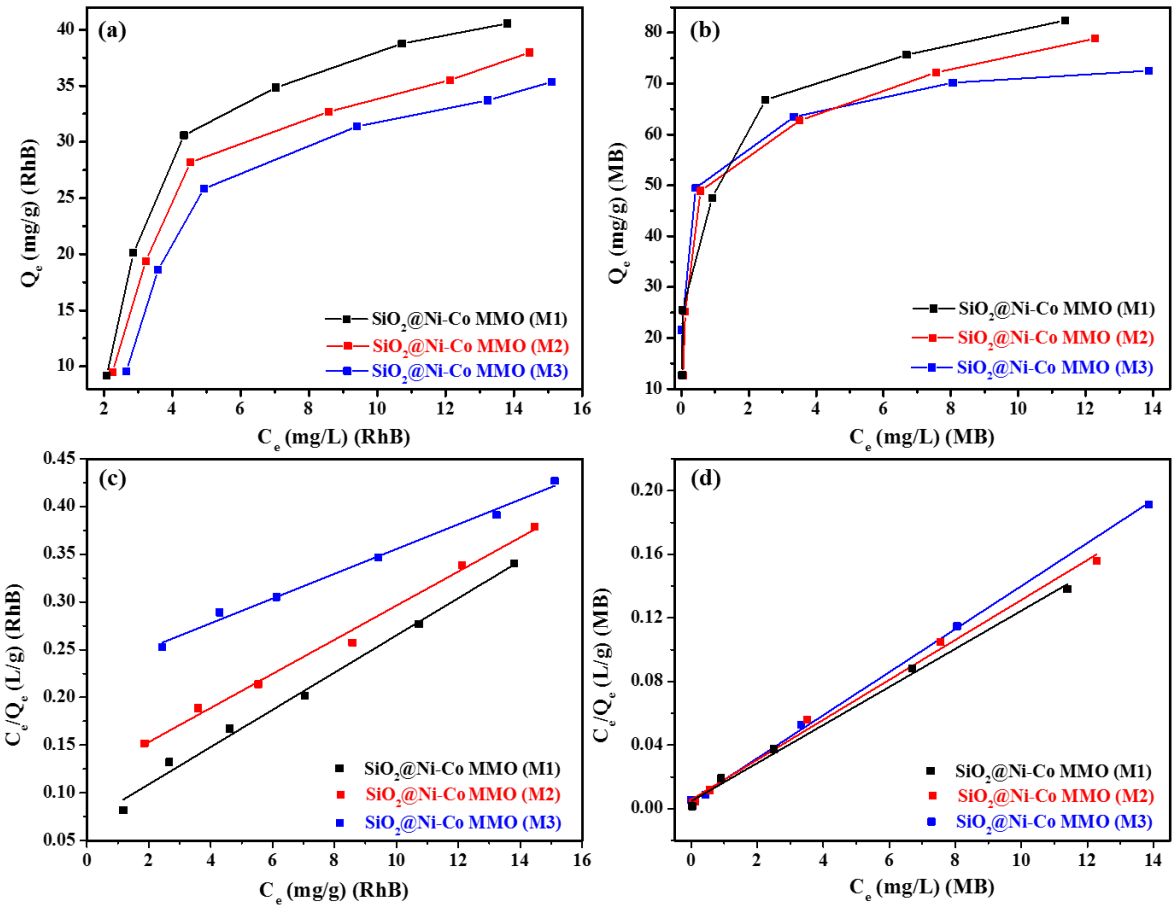

Fig. 6.4.4: Langmuir isotherms for the adsorption of rhodamine B **(a and c)** and methylene blue **(b and d)** from pure aqueous solutions using SiO_2@Ni-Co mixed metal oxide core-shell nanorattles.

The Freundlich parameter K_F indicates adsorption capacity of the adsorbent similar to q_{max} in the Langmuir isotherm, and parameter n demonstrates strength of the adsorption and a higher value of n indicates strong bonding between the adsorbate and the adsorbent [100,111]. The Freundlich constant (K_F) and the empirical constant (n) were calculated from the slope and intercept of the linear plots between lnq_e and lnC_e, respectively (Figure 6.4.5a and 6.4.5b). Among the adsorbents, the SiO_2@Ni-Co mixed metal oxide core-shell nanorattle sample M1 shows the highest Freundlich equilibrium constant (K_F) values (13.56 L/g and 47.11 L/g for rhodamine B and methylene blue,

respectively). All the samples show that the value of n is greater than 1 which indicates strong bonding between the adsorbate and the adsorbent. The adsorption data fits well with both Langmuir as well as Freundlich models. The linear regression correlation coefficient (r^2) values are about 0.99 and 0.98 for Langmuir isotherm and Freundlich isotherm (Table 6.4.1), respectively.

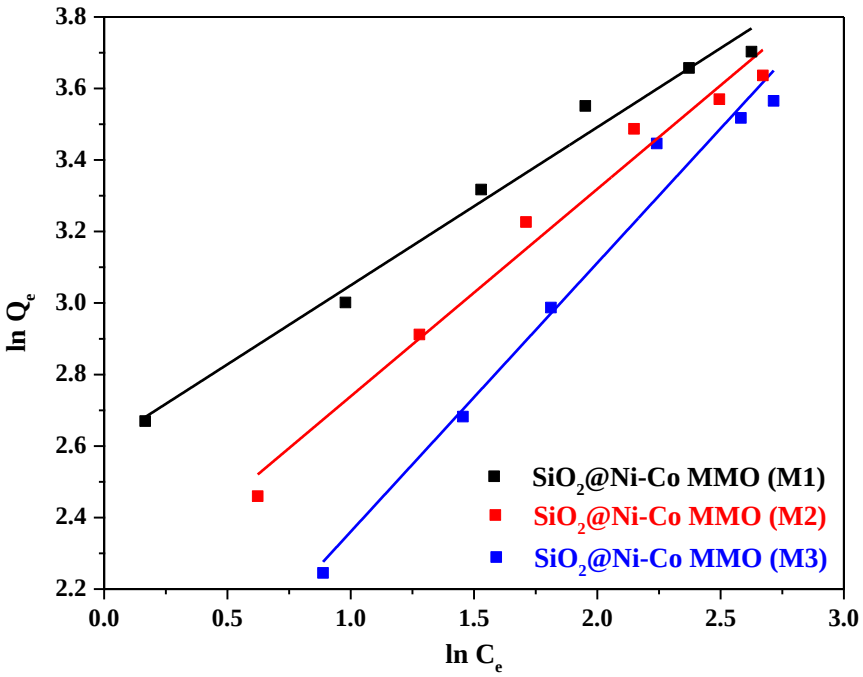

(a)

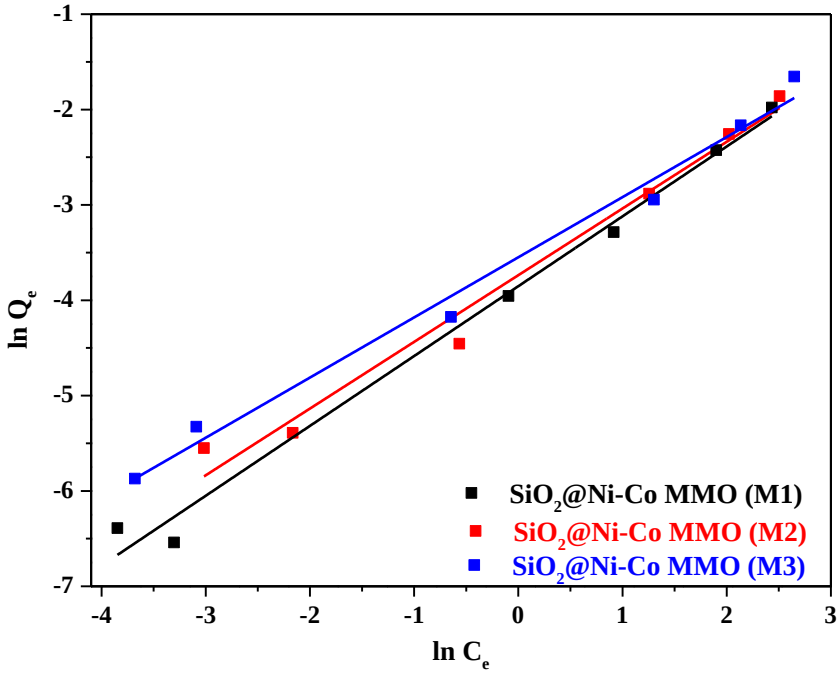

(b)

Fig. 6.4.5: Freundlich isotherms for the adsorption of **(a)** rhodamine B and **(b)** methylene blue from pure aqueous solutions using SiO_2@Ni-Co mixed metal oxide core-shell nanorattles.

Table 6.4.1: Langmuir and Freundlich adsorption isotherm parameters for rhodamine B and methylene blue in single dye systems using SiO_2@Ni-Co mixed metal oxide core-shell nanorattles.

Dye	Adsorbent	Langmuir model			Freundlich model		
		q_{max} (mg/g)	K_L (L/mg)	r^2	K_F (L/g)	n	r^2
RhB	M1	79.11±1.21	0.28±0.01	0.9952	13.56±0.27	2.26±0.15	0.9797
	M2	57.37±1.39	0.44±0.02	0.9914	8.67±0.34	1.73±0.13	0.9728
	M3	51.25±1.89	0.55±0.04	0.9938	4.99±0.37	1.33±0.10	0.9709
MB	M1	83.47±0.88	2.55±0.12	0.9944	47.11±1.04	1.36±0.08	0.9887
	M2	79.61±2.65	2.22±0.06	0.9952	41.98±1.10	1.43±0.12	0.9771
	M3	73.85±2.77	2.924±0.17	0.9992	31.45±0.78	1.67±0.19	0.9851

In the case of mixture of dyes, competitive adsorption occurs and this limits the number of adsorption sites. The adsorption of adsorbate molecules on the surface of an adsorbent depends upon the interaction between the adsorbate and the adsorbent [15]. The binary Langmuir model assumes that the surface of the adsorbent is homogeneous with respect to the energy of adsorption and all the adsorption sites are equally available to all the adsorbate molecules [15,112,113]. The competitive binary Langmuir equations can be expressed as follows.

$$q_{e1}= \frac{q_{max1}K_{L1}C_{e1}}{1 + K_{L1}C_{e1} + K_{L2}C_{e2}} \quad (9)$$

$$q_{e2}= \frac{q_{max2}K_{L2}C_{e2}}{1 + K_{L1}C_{e1} + K_{L2}C_{e2}} \quad (10)$$

where q_{max1} and q_{max2} are the maximum adsorption capacity for rhodamine B and methylene blue, respectively, and K_{L1} and K_{L2} are the Langmuir constants for rhodamine B and methylene blue, respectively.

The adsorption isotherms for the binary system (mixture of dyes) are shown in Figure 6.4.6a and 6.4.6b. The adsorption isotherms of the binary system also show L-type curves similar to that of single systems which indicate higher affinity of the adsorbate for the adsorbent [15] and the estimated Langmuir parameters are given in Table 6.4.2. For a binary system, the maximum adsorption capacity (q_{max}) and the Langmuir constant (K_L) were calculated from the slope and intercept of the linear plot between C_e/q_e and C_e, respectively (Figure 6.4.6c and 6.4.6d). The SiO_2@Ni-Co mixed metal oxide core-shell nanorattles M1 shows the highest maximum adsorption capacity and the values are 66.7 mg/g and 72.6 mg/g for rhodamine B and methylene blue, respectively. These values are lower than that for the individual dye systems which indicate competitive adsorption between the rhodamine B and methylene blue. The competitive Langmuir model follows the same assumption as that for single component system and it must be noted that, these assumptions are rarely accomplished in real systems because of surface heterogeneity and interaction between the adsorbate molecules [15].

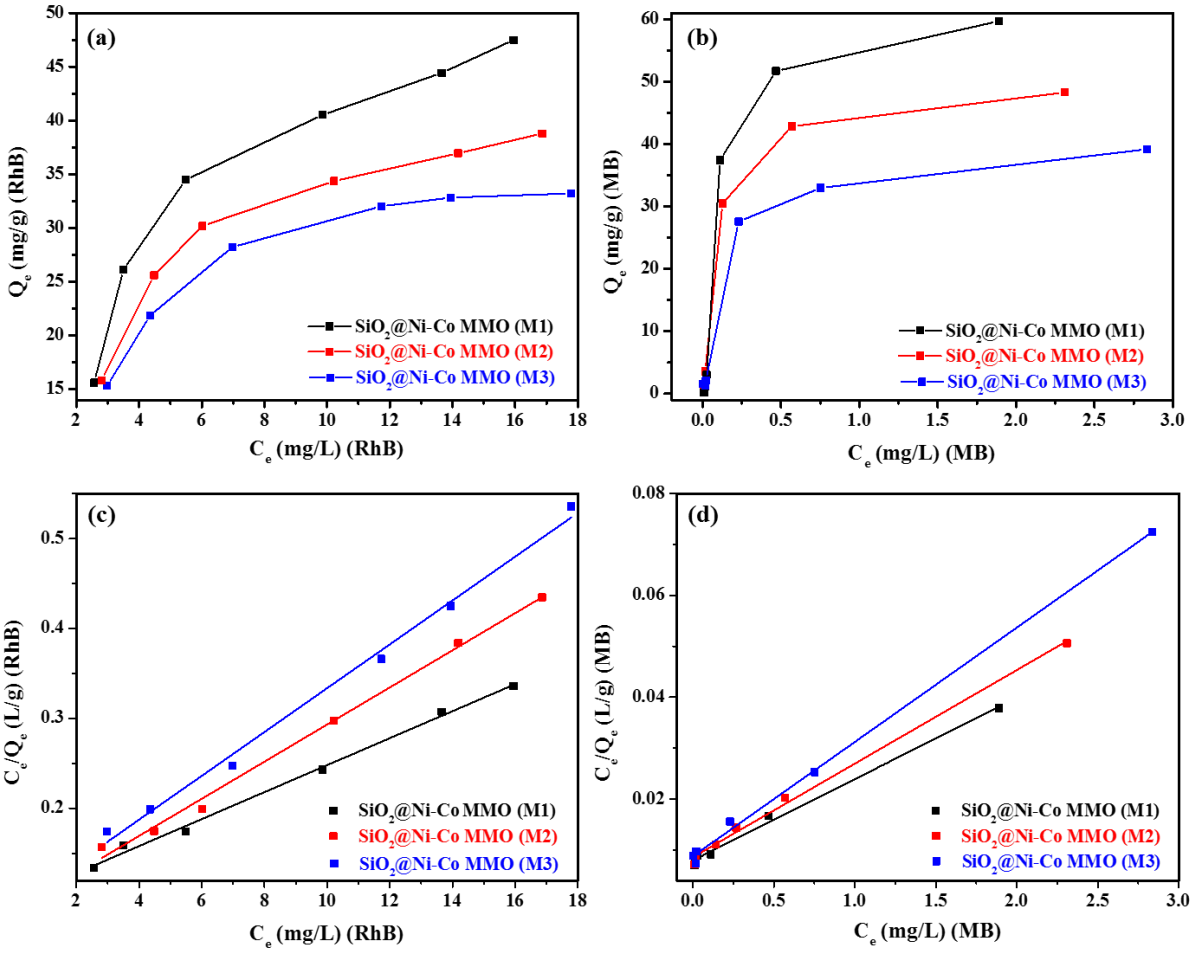

Fig. 6.4.6: Langmuir isotherms for the adsorption of rhodamine B **(a and c)** and methylene blue **(b and d)** from a mixture using SiO_2@Ni-Co mixed metal oxide core-shell nanorattles.

Table 6.4.2: Langmuir adsorption isotherm parameters using a competitive binary Langmuir model for the adsorption of rhodamine B and methylene blue from a mixture in an aqueous solution using SiO_2@Ni-Co mixed metal oxide core-shell nanorattles.

Adsorbent	Competitive binary Langmuir Model (RhB)			Competitive binary Langmuir Model (MB)		
	q_{max1} (mg/g)	K_L (L/mg)	r^2	q_{max2} (mg/g)	K_L (L/mg)	r^2
M1	66.71±1.55	0.15±0.01	0.9948	72.61±1.01	2.01±0.12	0.9935
M2	48.47±1.68	0.24±0.03	0.9939	54.40±1.68	2.14±0.14	0.9952
M3	41.06±2.14	0.27±0.02	0.9928	44.54±2.61	2.56±0.18	0.9974

6.4.3.4 Adsorption kinetics

In the present study, pseudo-first-order and pseudo-second-order kinetic models were tested for the adsorption of individual dye systems as well as the mixed dye systems. The Lagergren pseudo-first-order model is expressed as follows [101,102].

$$ln(q_e - q_t) = lnq_e - \frac{k_1}{2.303}\, t \qquad (11)$$

where q_e and q_t are the adsorption capacity of the adsorbent at equilibrium (mg/g) and at time t (mg/g), k_1 is the pseudo first-order rate constant (min^{-1}) and t is the time (min).

The pseudo-second-order rate equation is expressed as follows [111,114].

$$\frac{t}{q_t} = \frac{1}{k_2 q_e^2} + \frac{1}{q_e}\, t \qquad (12)$$

where q_e and q_t are the adsorption capacity of the adsorbent at equilibrium (mg/g) and at time t (mg/g), k_2 is the pseudo second-order rate constant (g mg^{-1} min^{-1}) and t is the time (min).

The calculated kinetic parameters assuming pseudo-first-order and pseudo-second-order kinetic models are given in Table 6.4.3. The rate constant (k_1) and q_e values of the pseudo-first-order kinetic model were calculated from the slope and intercept of the liner plot between $ln(q_e - q_t)$ versus time (t). When the pseudo first order kinetics was used, the linear regression correlation coefficient values are lower than 1 and also the experimental q_e values deviate much from the calculated q_e values which indicate that the adsorption does not follow pseudo-first-order kinetics [101]. Most of the authors have reported that the adsorption follows pseudo-second-order kinetics [98–101]. The experimental data was fitted using the pseudo-second-order equation. For single and binary systems, the plot of t/q_t versus t gives linear regression correlation coefficient close to 1 and the plots are shown in Figures 6.4.7a to 6.4.7c. The adsorption capacity at equilibrium (q_e) and pseudo-second-order rate constant (k_2) were calculated from the slope and intercept of the plots. The experimental q_e values are close to the calculated q_e values which indicate that the adsorption follows pseudo-second-order kinetics.

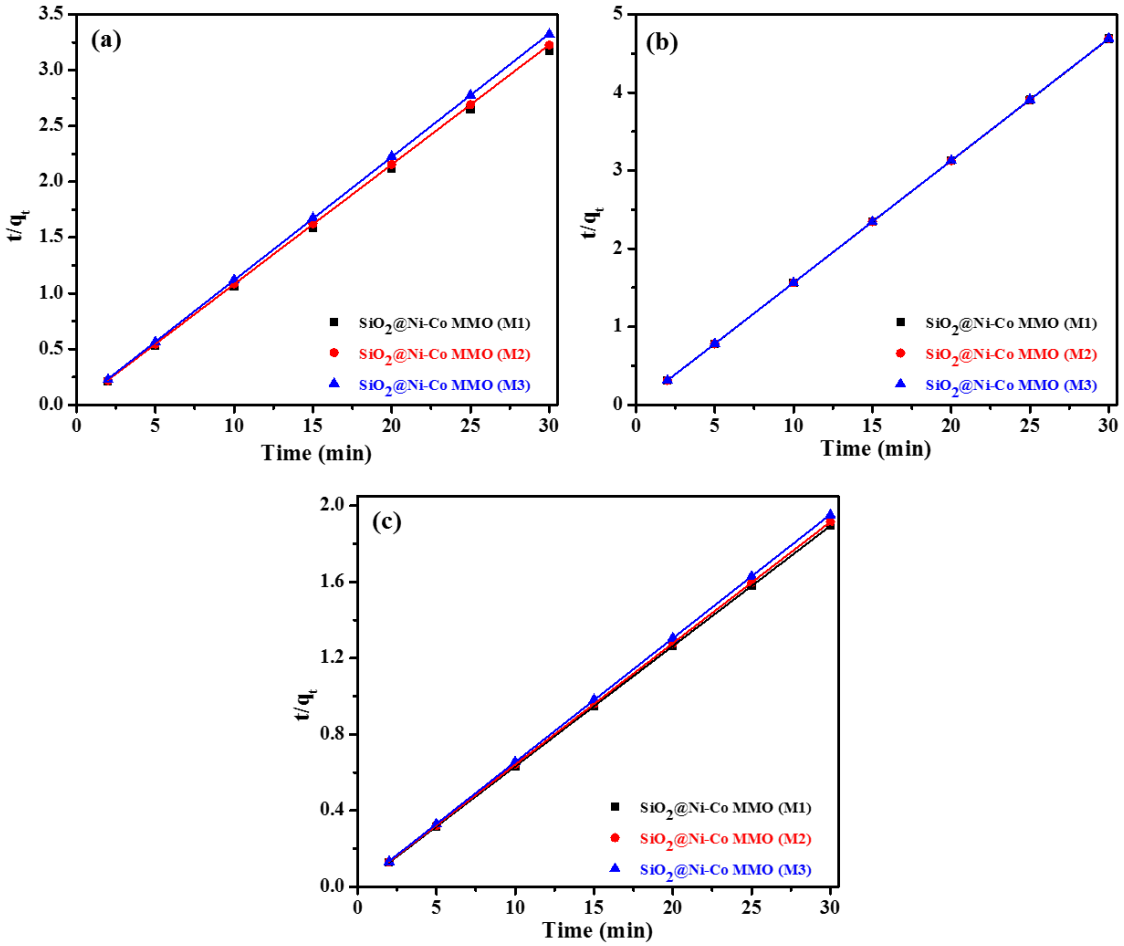

Fig. 6.4.7: Pseudo second order kinetics of adsorption of **(a)** rhodamine B, **(b)** methylene blue and **(c)** mixture of rhodamine B and methylene blue using SiO_2@Ni-Co mixed metal oxide core-shell nanorattles.

Table 6.4.3: Kinetic parameters for the adsorption of rhodamine B and methylene blue in a single and mixed dye systems using SiO_2@Ni-Co mixed metal oxide core-shell nanorattles.

Dye	Adsorbent	q_e (exp) (mg/g)	Pseudo first order kinetic model			Pseudo second order kinetic model		
			k_1 (min^{-1})	q_e (cal) (mg/g)	R^2	k_2 ($gmg^{-1}min^{-1}$)	q_e (cal) (mg/g)	R^2
RhB	M1	9.45	0.31±0.06	13.40±1.62	0.8242	1.53±0.07	9.45±0.02	1.0000
	M2	9.30	0.26±0.03	4.60±0.14	0.9309	1.43±0.05	9.31±0.03	0.9999
	M3	9.03	0.18±0.02	4.42±0.35	0.9548	1.11±0.04	9.04±0.04	0.9999
MB	M1	6.40	0.19±0.02	17.86±0.24	0.9688	1.86±0.08	6.40±0.01	1.0000
	M2	6.39	0.18±0.02	4.61±0.10	0.9416	1.37±0.05	6.40±0.01	1.0000
	M3	6.39	0.22±0.03	4.36±0.13	0.9282	1.24±0.05	6.39±0.01	1.0000
Binary dye mixture	M1	15.83	0.31±0.06	28.08±0.43	0.8279	1.77±0.08	15.83±0.03	1.0000
	M2	15.67	0.26±0.04	4.13±0.60	0.9341	1.29±0.04	15.69±0.03	1.0000
	M3	15.37	0.18±0.02	3.96±0.82	0.9547	0.99±0.03	15.39±0.04	0.9999

6.4.4 Mechanism for adsorption of dyes on SiO_2@Ni-Co mixed metal oxide core-shell nanorattles

A possible mechanism is proposed for the adsorption of rhodamine B and methylene blue from an aqueous solution based on the experimental results (Scheme 6.4.1). In general, the adsorption of dyes on the surface of an adsorbent involves several stages [16,100,111]. In the first stage, the dye molecules adsorb instantaneously on external surface of the adsorbent through electrostatic attraction. In the second stage, the dye molecules adsorb on the pores of the adsorbent gradually due to intraparticle diffusion of dye molecules and in the final stage, the dye molecules occupy all the active sites on the adsorbent and reach an equilibrium stage. Metal oxides possess negative charge on their surface which is favourable for the removal of most of the cationic dyes and the dyes are chemisorbed on the surface of metal oxides through electrostatic interaction [109–111,114]. The zeta potential measurements on SiO_2, $NiCo_2O_4$ and SiO_2@Ni-Co mixed metal oxide core-shell nanorattle samples indicate negative charge on their surface. The zeta potential values were found to be -25.1 and -3.9 mV for pure SiO_2 and $NiCo_2O_4$ while the SiO_2@Ni-Co mixed metal oxide core-shell nanorattles possess -31.9, -26.3 and -23.1 mV for M1, M2 and M3, respectively.

Among all the samples, sample M1 possesses more negative charge (-31.9 mV). Pure cationic dye (methylene blue) contains diethylamine group which possesses positive charge whereas rhodamine B (zwitterionic dye) contains carboxylate group as well as diethylamine group [110]. In the case of binary dye adsorption, competition occurs between methylene blue and rhodamine B, but methylene blue dominates the adsorption because of its cationic nature [107]. The SiO_2@Ni-Co mixed metal oxide core-shell nanorattles possess negative charge on their surface which instantaneously form a bond with positively charged methylene blue through electrostatic interaction. Then, the methylene blue molecules slowly diffuse into the pores of the core-shell nanorattles *via* external diffusion/ intraparticle diffusion. At the same time, the zwitterionic dye (rhodamine B) adsorbs on the surface of adsorbent as well as the cationic dye (methylene blue) through electrostatic interaction [107]. After a certain time, the methylene blue molecules completely adsorb on all the active sites and tends to reach an equilibrium stage. At higher concentration of mixture of dyes, the surface of the adsorbent is

occupied with a large number of methylene blue molecules which retards further adsorption of rhodamine B [107,113].

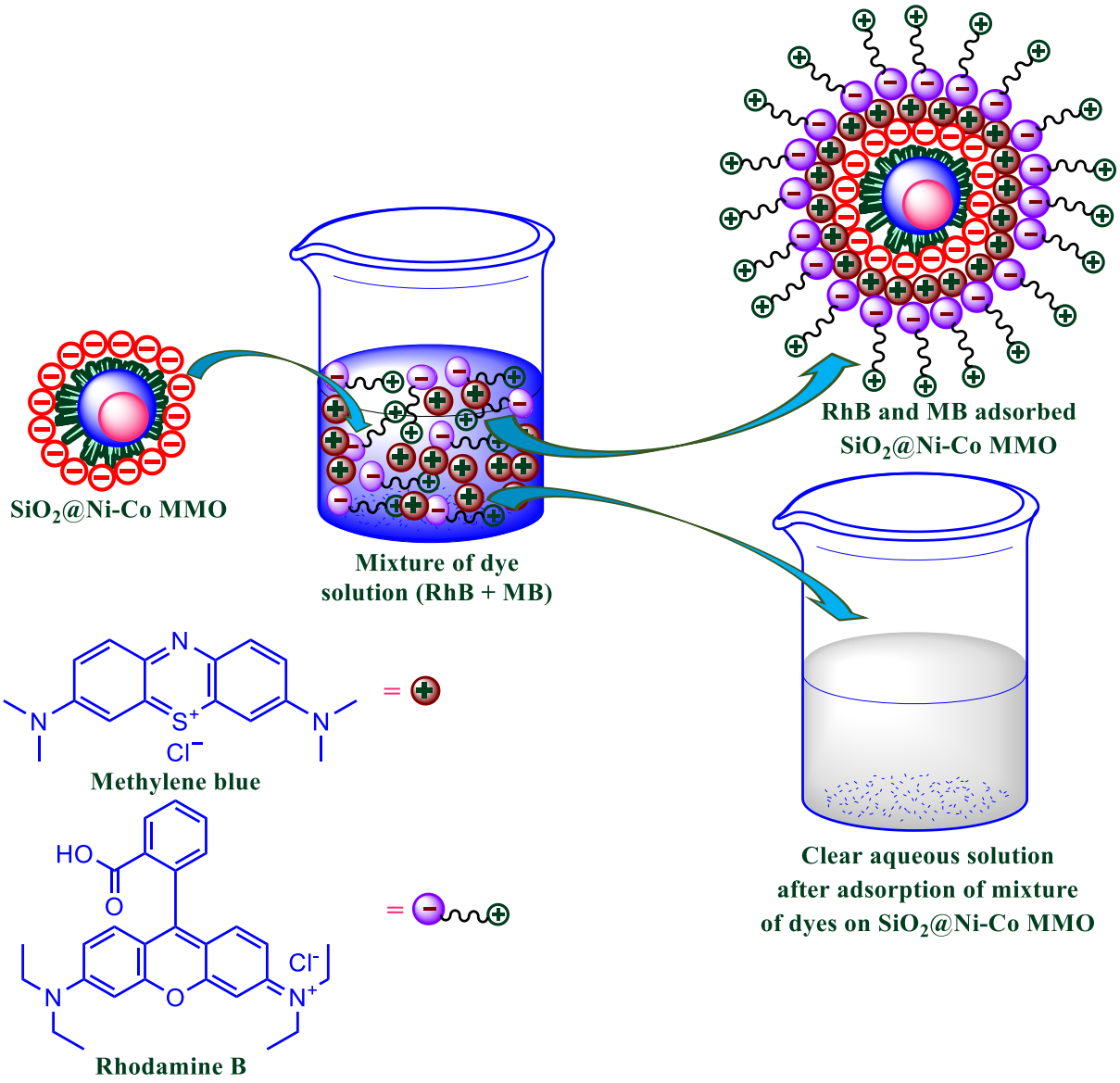

Scheme 6.4.1: Proposed mechanism for the adsorption of rhodamine B and methylene blue from an aqueous medium on SiO_2@Ni-Co mixed metal oxide core-shell nanorattles.

After adsorption of the mixture of dyes on the surface of the adsorbent, FT-IR analysis was carried out to understand the adsorption mechanism which shows the presence of FT-IR bands due to both rhodamine B and methylene blue along with the bands due to silica and Ni-Co mixed metal oxide (Figure 6.4.8) [98,110]. The IR results suggests that the dye molecules are adsorbed on the adsorbent through electrostatic interaction.

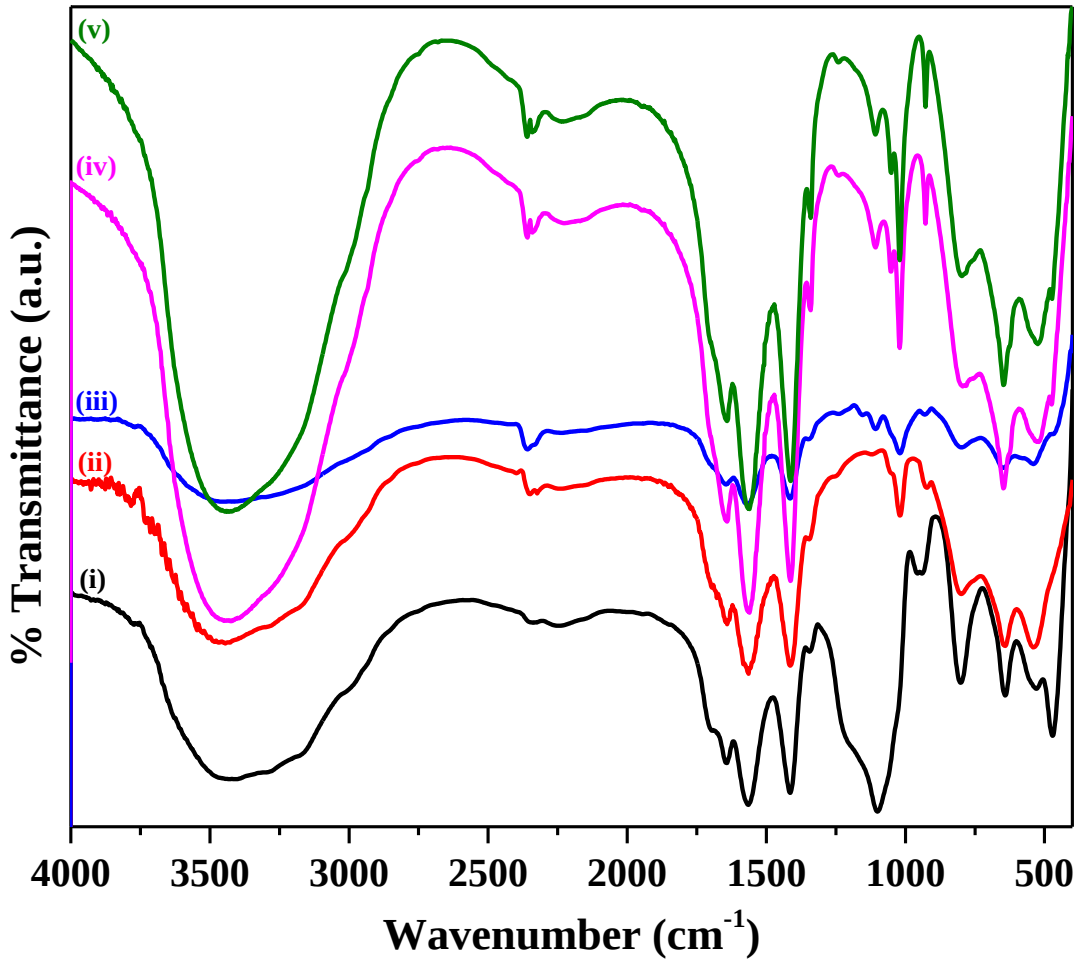

Fig. 6.4.8: FT-IR spectra of **(i)** SiO_2, **(ii)** $NiCo_2O_4$, and **(iii-v)** SiO_2@Ni-Co mixed metal oxide core-shell nanorattles after the adsorption of mixture of rhodamine B and methylene blue from an aqueous solution.

The higher adsorption capacity of SiO_2@Ni-Co mixed metal oxide core-shell nanorattles is attributed to more negative charge on their surface and as well as higher surface area due to their porous shell structure.

6.4.5 Reusability of SiO_2@Ni-Co mixed metal oxide core-shell nanorattles for the adsorption of rhodamine B and methylene blue

Reusability of the adsorbent was tested for five times and the removal of the dyes (rhodamine B and methylene blue) from the surface of the best adsorbent (M1), after the adsorption, was carried out using 10 % acetic acid in methanol. Only a marginal decrease in the adsorption efficiency was observed (3 % in the case of rhodamine B and 0.2 % in the case of methylene blue) which indicates that the adsorbent is reusable.

6.5 Conclusions

Various applications such as photocatalysis, reduction, peroxidase-like activity and adsorption using the synthesized core-shell nanoparticles/nanorattles were demonstrated. ZnO@CdS and ZnO@Ag core-shell heteronanostructures exhibit better photocatalytic activity in the photodegradation of methylene blue in aqueous solutions compared to their counter parts. Cu_2O@Ag polyhedral core-shell nanoparticles show enhanced catalytic activity in the reduction of 4-nitrophenol and methylene blue in aqueous solutions compared to their individual constituents as well as previously reported literature. SiO_2@Co_3O_4 core-shell nanorattles exhibit enhanced peroxidase-like activity compared to pure Co_3O_4 nanoparticles and HRP. SiO_2@Ni-Co mixed metal oxide core-shell nanorattles show higher adsorption capacity in the adsorption of mixture of rhodamine B and methylene blue in aqueous solutions as compared to pure NiO and Co_3O_4 nanoparticles as well as physical mixtures of NiO and Co_3O_4 nanoparticles.

References

1. Shi W., Lu D., Wang L., Teng F., Zhang J., 'Core–shell structured Fe_3O_4@SiO_2@CdS nanoparticles with enhanced visible-light photocatalytic activities', *RSC Advances,* **5**, 106038–106043 (2015).

2. Yang P., Xu Y., Chen L., Wang X., Zhang Q., 'One-pot synthesis of monodisperse noble metal@resorcinol-formaldehyde (M@RF) and M@carbon core–shell nanostructure and their catalytic applications', *Langmuir,* **31**, 11701–11708 (2015).

3. Murugadoss A., Okumura K., Sakurai H., 'Bimetallic AuPd nanocluster catalysts with controlled atomic gold distribution for oxidative dehydrogenation of tetralin', *The Journal of Physical Chemistry C,* **116**, 26776–26783 (2012).

4. Zu G., Shen J., Wang W., Zou L., Lian Y., Zhang Z., Liu B., Zhang F., 'Robust, highly thermally stable, core–shell nanostructured metal oxide aerogels as high-temperature thermal superinsulators, adsorbents, and catalysts', *Chemistry of Materials,* **26**, 5761–5772 (2014).

5. Xia X., Zhang J., Lu N., Kim M. J., Ghale K., Xu Y., McKenzie E., Liu J., Ye H., 'Pd–Ir core–shell nanocubes: A type of highly efficient and versatile peroxidase mimic', *ACS Nano,* **9**, 9994–10004 (2015).

6. Jiang G., Zhu H., Zhang X., Shen B., Wu L., Zhang S., Lu G., Wu Z., Sun S., 'Core/shell face-centered tetragonal FePd/Pd nanoparticles as an efficient non-Pt catalyst for the oxygen reduction reaction', *ACS Nano,* **9**, 11014–11022 (2015).

7. Zhu L., Chang Z., Wang Y., Chen B., Zhu Y., Tang W., Wu Y., 'Core–shell MnO_2@Fe_2O_3 nanospindles as a positive electrode for aqueous supercapacitors', *Journal of Materials Chemistry A,* **3**, 22066–22072 (2015).

8. Chen G., Damasco J., Qiu H., Shao W., Ohulchanskyy T. Y., Valiev R. R., Wu X., Han G., Wang Y., Yang C., Ågren H., Prasad P. N., 'Energy-cascaded upconversion in an organic dye-sensitized core/shell fluoride nanocrystal', *Nano Letters,* **15**, 7400–7407 (2015).

9. Fan Y., Huang X., Wang G., Jiang P., 'Core-shell structured biopolymer@$BaTiO_3$

nanoparticles for biopolymer nanocomposites with significantly enhanced dielectric properties and energy storage capability', *The Journal of Physical Chemistry C*, **119**, 27330–27339 (2015).

10. Liao C., Tang L., Gao X., Xu R., Zhang H., Yu Y., Lu C., Cui Y., Zhang J., 'Bright white-light emission from Ag/SiO_2/CdS–ZnS core/shell/shell plasmon couplers', *Nanoscale*, **7**, 20607–20613 (2015).

11. Yu H., Fan H., Yadian B., Tan H., Liu W., Hng H. H., Huang Y., Yan Q., 'General approach for MOF-derived porous spinel AFe_2O_4 hollow structures and their superior lithium storage properties', *ACS Applied Materials and Interfaces*, **7**, 26751–26757 (2015).

12. Rai P., Yoon J. W., Kwak C. H., Lee J. H., 'Role of Pd nanoparticles in gas sensing behaviour of Pd@In_2O_3 yolk–shell nanoreactors', *Journal of Materials Chemistry A*, **4**, 264–269 (2016).

13. Nanayakkara C. E., Larish W. A., Grassian V. H., 'Titanium dioxide nanoparticle surface reactivity with atmospheric gases , CO , SO and NO_2: Roles of surface hydroxyl groups and adsorbed water in the formation and stability of adsorbed products', *The Journal of Physical Chemistry C*, **118**, 23011–23021 (2014).

14. Liu X., Liu H. L., Fang N., Li X. M., Guo W. H., Wu J. H., Zhao M. X., 'Facile synthesis of multifunctional $La_{1-x}Sr_xMnO_3$@Au core–shell nanoparticles for biomedical applications', *RSC Advances*, **5**, 95454–95462 (2015).

15. Atar N., Olgun A., Wang S., Liu S., 'Adsorption of anionic dyes on boron industry waste in single and binary solutions using batch and fixed-bed systems', *Journal of Chemical and Engineering Data*, **56**, 508–516 (2011).

16. Gupta V. K., Kumar R., Nayak A., Saleh T. A., Barakat M. A., 'Adsorptive removal of dyes from aqueous solution onto carbon nanotubes: A review', *Advances in Colloid and Interface Science*, **193-194**, 24–34 (2013).

17. Huang X., Tan C., Yin Z., Zhang H., '25th anniversary article: Hybrid nanostructures based on two-dimensional nanomaterials', *Advanced Materials*, **26**, 2185–2204 (2014).

18. Khin M. M., Nair A. S., Babu V. J., Murugan R., Ramakrishna S., 'A review on nanomaterials for environmental remediation', *Energy and Environmental Science,* **5**, 8075–8109 (2012).

19. Mclaren A., Valdes-Solis T., Li G., Tsang S. C., 'Shape and size effects of ZnO nanocrystals on photocatalytic activity', *Journal of the American Chemical Society,* **131**, 12540–12541 (2009).

20. Zhang L., Tian L., Tan T., Liu Y., Liu D., Wang C., 'Synthesis of tapered tetragonal nanorods of anatase TiO_2 with enhanced photocatalytic activity *via* a sol-hydrothermal process mediated by H_2O_2 and NH_3', *Journal of Materials Chemistry A*, **3**, 15265–15273 (2015).

21. Kar A., Sain S., Kundu S., Bhattacharyya A., Swapan K. P., Patra A., 'Influence of size and shape on the photocatalytic properties of SnO_2 nanocrystals', *ChemPhysChem,* **16**, 1017–1025 (2015).

22. Huang S., Lin Y., Yang J., Li X., Zhang J., Yu J., Shi H., Wang W., Yu Y., 'Enhanced photocatalytic activity and stability of semiconductor by Ag doping and simultaneous deposition: The case of CdS', *RSC Advances,* **3**, 20782–20792 (2013).

23. Tak Y., Kim H., Lee D., Yong K., 'Type-II CdS nanoparticle-ZnO nanowire heterostructure arrays fabricated by a solution process: Enhanced photocatalytic activity', *Chemical Communications,* 4585–4587 (2008).

24. Khanchandani S., Kundu S., Patra A., Ganguli A. K., 'Shell thickness dependent photocatalytic properties of ZnO/CdS core-shell nanorods', *The Journal of Physical Chemistry C,* **116**, 23653–23662 (2012).

25. Li H., Yao C., Meng L., Sun H., Huang J., Gong Q., 'Photoelectrochemical performance of hydrogenated ZnO/CdS core-shell nanorod arrays', *Electrochimica Acta,* **108**, 45–50 (2013).

26. Lu W., Gao S., Wang J., 'One-pot synthesis of Ag/ZnO self-assembled 3D hollow microspheres with enhanced photocatalytic performance', *The Journal of Physical Chemistry C,* **112**, 16792–16800 (2008).

27. Zheng Y., Zheng L., Zhan Y., Lin X., Zheng Q., Wei K., 'Ag/ZnO heterostructure nanocrystals: Synthesis, characterization, and photocatalysis', *Inorganic Chemistry*, **46**, 6980–6986 (2007).

28. Wu Z., Xu C., Wu Y., Yu H., Tao Y., Wan H., Gao F., 'ZnO nanorods/Ag nanoparticles heterostructures with tunable Ag contents: A facile solution-phase synthesis and applications in photocatalysis', *CrystEngComm*, **15**, 5994–6002 (2013).

29. Ren C., Yang B., Wu M., Xu J., Fu Z., lv Y., Guo T., Zhao Y., Zhu C., 'Synthesis of Ag/ZnO nanorods array with enhanced photocatalytic performance', *Journal of Hazardous Materials*, **182**, 123–129 (2010).

30. Lin S. L., Hsu K. C., Hsu C. H., Chen D. H., 'Hydrogen treatment-improved uniform deposition of Ag nanoparticles on ZnO nanorod arrays and their visible-light photocatalytic and surface-enhanced Raman scattering properties', *Nanoscale Research Letters*, **8**, 325/1–9 (2013).

31. Shan G., Zheng S., Chen S., Chen Y., Liu Y., 'Multifunctional ZnO/Ag nanorod array as highly sensitive substrate for surface enhanced Raman detection', *Colloids and Surfaces. B, Biointerfaces*, **94**, 157–162 (2012).

32. Sun F., Tan F., Wang W., Qiao X., Qiu X., 'Facile synthesis of Ag/ZnO heterostructure nanocrystals with enhanced photocatalytic performance', *Materials Research Bulletin*, **47**, 3357–3361 (2012).

33. Ramachandra T. V, Jain R., Krishnadas G., 'Hotspots of solar potential in India', *Renewable and Sustainable Energy Reviews*, **15**, 3178–3186 (2011).

34. Tonda S., Kumar S., Kandula S., Shanker V., 'Fe-doped and -mediated graphitic carbon nitride nanosheets for enhanced photocatalytic performance under natural sunlight', *Journal of Materials Chemistry A*, **2**, 6772–6780 (2014).

35. Liu S., Li C., Yu J., Xiang Q., 'Improved visible-light photocatalytic activity of porous carbon self-doped ZnO nanosheet-assembled flowers', *CrystEngComm*, **13**, 2533–2541 (2011).

36. Zhang C. F., Qiu L. G., Ke F., Zhu Y. J., Yuan Y. P., Xu G. S., Jiang X., 'A novel

magnetic recyclable photocatalyst based on a core–shell metal–organic framework Fe_3O_4@MIL-100(Fe) for the decolorization of methylene blue dye', *Journal of Materials Chemistry A*, **1**, 14329–14334 (2013).

37. Zhao W., Bai Z., Ren A., Guo B., Wu C., 'Sunlight photocatalytic activity of CdS modified TiO_2 loaded on activated carbon fibers', *Applied Surface Science*, **256**, 3493–3498 (2010).

38. Kim H., Tak Y., Senthil K., Joo J., Jeon S., Yong K., 'Novel heterostructure of CdS nanoparticle/WO_3 nanowhisker: Synthesis and photocatalytic properties', *Journal of Vacuum Science and Technology B*, **27**, 2182–2186 (2009).

39. Pawar R. C., Lee C. S., 'Single-step sensitization of reduced graphene oxide sheets and CdS nanoparticles on ZnO nanorods as visible-light photocatalysts', *Applied Catalysis B: Environmental*, **144**, 57–65 (2014).

40. Zhu J., Yang D., Geng J., Chen D., Jiang Z., 'Synthesis and characterization of bamboo-like CdS/TiO_2 nanotubes composites with enhanced visible-light photocatalytic activity', *Journal of Nanoparticle Research*, **10**, 729–736 (2008).

41. Li J., Yan J., Liu C., Dong L., Lv H., Sun W., Xing S., 'Manipulation on ZnO heterostructures: From binary ZnO–Ag to ternary ZnO–Ag–polypyrrole', *CrystEngComm*, **16**, 10943–10948 (2014).

42. Saravanan R., Khan M. M., Gupta V. K., Mosquera E., Gracia F., Narayanan V., Stephen A., 'ZnO/Ag/CdO nanocomposite for visible light-induced photocatalytic degradation of industrial textile effluents', *Journal of Colloid and Interface Science*, **452**, 126–133 (2015).

43. Voisin C., Fatti N. D., Christofilos D., Vallée F., 'Ultrafast electron dynamics and optical nonlinearities in metal nanoparticles', *The Journal of Physical Chemistry B*, **105**, 2264–2280 (2001).

44. Chen X., Zheng Z., Ke X., Jaatinen E., Xie T., Wang D., Guo C., Zhao J., Zhu H., 'Supported silver nanoparticles as photocatalysts under ultraviolet and visible light irradiation', *Green Chemistry*, **12**, 414–419 (2010).

45. Shifu C., Yunguang Y., Wei L., 'Preparation, characterization and activity evaluation of TiN/F-TiO_2 photocatalyst', *Journal of Hazardous Materials*, **186**, 1560–1567 (2011).

46. Yu J., Wang B., 'Effect of calcination temperature on morphology and photoelectrochemical properties of anodized titanium dioxide nanotube arrays', *Applied Catalysis B: Environmental*, **94**, 295–302 (2010).

47. Hao Y., Shao X., Li B., Hu L., Wang T., 'Mesoporous TiO_2 nanofibers with controllable Au loadings for catalytic reduction of 4-nitrophenol', *Materials Science in Semiconductor Processing*, **40**, 621–630 (2015).

48. Le X., Dong Z., Zhang W., Li X., Ma J., 'Fibrous nano-silica containing immobilized Ni@Au core-shell nanoparticles: A highly active and reusable catalyst for the reduction of 4-nitrophenol and 2-nitroaniline', *Journal of Molecular Catalysis A: Chemical*, **395**, 58–65 (2014).

49. Malik A. H., Hussain S., Kalita A., Iyer P. K., 'Conjugated polymer nanoparticles for the amplified detection of nitro-explosive picric acid on multiple platforms', *ACS Applied Materials and Interfaces*, **7**, 26968–26976 (2015).

50. Batzli K. M., Love B. J., 'Formation of platinum-coated templates of insulin nanowires used in reducing 4-nitrophenol', *Materials Science and Engineering C*, **48**, 103–111 (2015).

51. Zheng Y., Shu J., Wang Z., 'AgCl@Ag composites with rough surfaces as bifunctional catalyst for the photooxidation and catalytic reduction of 4-nitrophenol', *Materials Letters*, **158**, 339–342 (2015).

52. Demirci U. B., 'How green are the chemicals used as liquid fuels in direct liquid-feed fuel cells?', *Environment International*, **35**, 626–631 (2009).

53. Pang M., Wang Q., Zeng H. C., 'Self-generated etchant for synthetic sculpturing of Cu_2O-Au, Cu_2O@Au, Au/Cu_2O, and 3D-Au nanostructures', *Chemistry - A European Journal*, **18**, 14605–14609 (2012).

54. Zhang P., Shao C., Li X., Zhang M., Zhang X., Su C., Lu N., Wang K., Liu Y., 'An electron-rich free-standing carbon@Au core-shell nanofiber network as a highly active

and recyclable catalyst for the reduction of 4-nitrophenol', *Physical Chemistry Chemical Physics*, **15**, 10453–10458 (2013).

55. Dong Z., Yu G., Le X., 'Gold nanoparticle modified magnetic fibrous silica microspheres as a highly efficient and recyclable catalyst for the reduction of 4-nitrophenol', *New Journal of Chemistry*, **39**, 8623–8629 (2015).

56. Wang S., Zhang M., Zhang W., 'Yolk-shell catalyst of single Au nanoparticle encapsulated within hollow mesoporous silica microspheres', *ACS Catalysis*, **1**, 207–211 (2011).

57. Xie Y., Yan B., Xu H., Chen J., Liu Q., Deng Y., Zeng H., 'Highly regenerable mussel-inspired Fe_3O_4@polydopamine-Ag core-shell microspheres as catalyst and adsorbent for methylene blue removal', *ACS Applied Materials and Interfaces*, **6**, 8845–8852 (2014).

58. Yao T., Cui T., Wang H., Xu L., Cui F., Wu J., 'A simple way to prepare Au@polypyrrole/Fe_3O_4 hollow capsules with high stability and their application in catalytic reduction of methylene blue dye', *Nanoscale*, **6**, 7666–7674 (2014).

59. Liu C. H., Liu J., Zhou Y. Y., Cai X. L., Lu Y., Gao X., Wang S. D., 'Small and uniform Pd monometallic/bimetallic nanoparticles decorated on multi-walled carbon nanotubes for efficient reduction of 4-nitrophenol', *Carbon*, **94**, 295–300 (2015).

60. Kang H., Kim M., Park K. H., 'Effective immobilization of gold nanoparticles on core–shell thiol-functionalized GO coated TiO_2 and their catalytic application in the reduction of 4-nitrophenol', *Applied Catalysis A: General*, **502**, 239–245 (2015).

61. Muthuchamy N., Gopalan A., Lee K. P., 'A new facile strategy for higher loading of silver nanoparticles onto silica for efficient catalytic reduction of 4-nitrophenol', *RSC Advances*, **5**, 76170–76181 (2015).

62. Mignani A., Fazzini S., Ballarin B., Boanini E., Cassani M. C., Maccato C., Barreca D., Nanni D., 'Mild fabrication of silica-silver nanocomposites as active platforms for environmental remediation', *RSC Advances*, **5**, 9600–9606 (2015).

63. Zhu M., Wang C., Meng D., Diao G., 'In situ synthesis of silver nanostructures on

magnetic Fe_3O_4@C core-shell nanocomposites and their application in catalytic reduction reactions', *Journal of Materials Chemistry A*, **1**, 2118–2125 (2013).

64. Jiang Z. J., Liu C. Y., Sun L. W., 'Catalytic properties of silver nanoparticles supported on silica spheres', *The Journal of Physical Chemistry B*, **109**, 1730–1735 (2005).

65. Guo X. H., Ma J. Q., Ge H. G., 'Synthesis and characterization of Cu_2O/Au and its application in catalytic reduction of 4-nitrophenol', *Russian Journal of Physical Chemistry A*, **89**, 1374–1380 (2015).

66. Panigrahi S., Basu S., Praharaj S., Pande S., Jana S., Pal A., Ghosh S. K., Pal T., 'Synthesis and size-selective catalysis by supported gold nanoparticles: Study on heterogeneous and homogeneous catalytic process', *The Journal of Physical Chemistry C*, **111**, 4596–4605 (2007).

67. Xu X., Tian B., Kong J., Zhang S., Liu B., Zhao D., 'Ordered mesoporous niobium oxide film: A novel matrix for assembling functional proteins for bioelectrochemical applications', *Advanced Materials*, **15**, 1932–1936 (2003).

68. Shi W., Zhang X., He S., Huang Y., '$CoFe_2O_4$ magnetic nanoparticles as a peroxidase mimic mediated chemiluminescence for hydrogen peroxide and glucose', *Chemical Communications*, **47**, 10785–10787 (2011).

69. Chen W., Chen J., Feng Y. Bin, Hong L., Chen Q. Y., Wu L. F., Lin X. H., Xia X. H., 'Peroxidase-like activity of water-soluble cupric oxide nanoparticles and its analytical application for detection of hydrogen peroxide and glucose', *Analyst*, **137**, 1706–1712 (2012).

70. Zhang L., Han L., Hu P., Wang L., Dong S., 'TiO_2 nanotube arrays: Intrinsic peroxidase mimetics', *Chemical Communications*, **49**, 10480–10482 (2013).

71. Ray C., Dutta S., Sarkar S., Sahoo R., Roy A., Pal T., 'Intrinsic peroxidase-like activity of mesoporous nickel oxide for selective cysteine sensing', *Journal of Materials Chemistry B*, **2**, 6097–6105 (2014).

72. Nie G., Zhang L., Lei J., Yang L., Zhang Z., Lu X., Wang C., 'Monocrystalline VO_2 (B) nanobelts: Large-scale synthesis, intrinsic peroxidase-like activity and application in

biosensing', *Journal of Materials Chemistry A*, **2**, 2910–2914 (2014).

73. Mandal S. S., Navratna V., Sharma P., Gopal B., Bhattacharyya A. J., 'Titania nanotube-modified screen printed carbon electrodes enhance the sensitivity in the electrochemical detection of proteins', *Bioelectrochemistry*, **98**, 46–52 (2014).

74. Wang H., Shrestha T. B., Basel M. T., Pyle M., Toledo Y., Konecny A., Thapa P., Ikenberry M., Hohn K. L., Chikan V., Troyer D. L., Bossmann S. H., 'Hexagonal magnetite nanoprisms: Preparation, characterization and cellular uptake', *Journal of Materials Chemistry B*, **3**, 4647–4653 (2015).

75. Zhang W., Liu X., Walsh D., Yao S., Kou Y., Ma D., 'Caged-protein-confined bimetallic structural assemblies with mimetic peroxidase activity', *Small*, **8**, 2948–2953 (2012).

76. Dong J., Song L., Yin J. J., He W., Wu Y., Gu N., Zhang Y., 'Co_3O_4 nanoparticles with multi-enzyme activities and their application in immunohistochemical assay', *ACS Applied Materials and Interfaces*, **6**, 1959–1970 (2014).

77. Sun H., Jiao X., Han Y., Jiang Z., Chen D., 'Synthesis of Fe_3O_4-Au nanocomposites with enhanced peroxidase-like activity', *European Journal of Inorganic Chemistry*, **2013**, 109–114 (2013).

78. Mu J., Wang Y., Zhao M., Zhang L., 'Intrinsic peroxidase-like activity and catalase-like activity of Co_3O_4 nanoparticles', *Chemical Communications*, **48**, 2540–2542 (2012).

79. Mu J., Zhang L., Zhao G., Wang Y., 'The crystal plane effect on the peroxidase-like catalytic properties of Co_3O_4 nanomaterials', *Physical Chemistry Chemical Physics*, **16**, 15709–15716 (2014).

80. Gao L., Zhuang J., Nie L., Zhang J., Zhang Y., Gu N., Wang T., Feng J., Yang D., Perrett S., Yan X., 'Intrinsic peroxidase-like activity of ferromagnetic nanoparticles', *Nature Nanotechnology*, **2**, 577–583 (2007).

81. Chen H., Li Y., Zhang F., Zhang G., Fan X., 'Graphene supported Au-Pd bimetallic nanoparticles with core-shell structures and superior peroxidase-like activities', *Journal of Materials Chemistry*, **21**, 17658–17661 (2011).

82. Chen X., Tian X., Su B., Huang Z., Chen X., Oyama M., 'Au nanoparticles on citrate-

functionalized graphene nanosheets with a high peroxidase-like performance', *Dalton Transactions*, **43**, 7449–7454 (2014).

83. Chen L., Sun B., Wang X., Qiao F., Ai S., '2D ultrathin nanosheets of Co–Al layered double hydroxides prepared in L-asparagine solution: Enhanced peroxidase-like activity and colorimetric detection of glucose', *Journal of Materials Chemistry B*, **1**, 2268–2274 (2013).

84. Cai K., Lv Z., Chen K., Huang L., Wang J., Shao F., Wang Y., Han H., 'Aqueous synthesis of porous platinum nanotubes at room temperature and their intrinsic peroxidase-like activity', *Chemical Communications*, **49**, 6024–6026 (2013).

85. Nie G., Zhang L., Lu X., Bian X., Sun W., Wang C., 'A one-pot and in situ synthesis of CuS-graphene nanosheet composites with enhanced peroxidase-like catalytic activity', *Dalton Transactions*, **42**, 14006–14013 (2013).

86. Wang H., Li S., Si Y., Sun Z., Li S., Lin Y., 'Recyclable enzyme mimic of cubic Fe_3O_4 nanoparticles loaded on graphene oxide-dispersed carbon nanotubes with enhanced peroxidase-like catalysis and electrocatalysis', *Journal of Materials Chemistry B*, **2**, 4442–4448 (2014).

87. Song C. O., Lee J. W., Choi H. S., Kang J. K., 'Two-step synthesis of agglomeration-free peroxidase-like Co_3O_4 nanoparticles–carbon nitride nanotube hybrids enabling a high redox activity', *RSC Advances*, **3**, 20179–20185 (2013).

88. Xie J., Cao H., Jiang H., Chen Y., Shi W., Zheng H., Huang Y., 'Co_3O_4-reduced graphene oxide nanocomposite as an effective peroxidase mimetic and its application in visual biosensing of glucose', *Analytica Chimica Acta*, **796**, 92–100 (2013).

89. Nice J. A., Wright H., 'A model of peroxidase activity with inhibition by hydrogen peroxide', *Enzyme and Microbial Technology*, **21**, 302–310 (1997).

90. Zhang X. Q., Gong S., Zhang Y., Yang T., Wang C. yu, Gu N., 'Prussian blue modified iron oxide magnetic nanoparticles and their high peroxidase-like activity', *Journal of Materials Chemistry*, **20**, 5110–5116 (2010).

91. Song Y., Qu K., Zhao C., Ren J., Qu X., 'Graphene oxide: Intrinsic peroxidase catalytic

activity and its application to glucose detection', *Advanced Materials*, **22**, 2206–2210 (2010).

92. Sojka-Ledakowicz J., Zylla R., Mrozinska Z., Pazdzior K., Klepacz-Smolka A., Ledakowicz S., 'Application of membrane processes in closing of water cycle in a textile dye-house', *Desalination*, **250**, 634–638 (2010).

93. Ling K. S., Wang S., Peng Y., 'Oxidative degradation of dyes in water using Co^{2+}/H_2O_2 and Co^{2+}/peroxymonosulfate', *Journal of Hazardous Materials*, **178**, 385–389 (2010).

94. Khajeh M., Laurent S., Dastafkan K., 'Nanoadsorbents: Classification, preparation, and applications (with emphasis on aqueous media)', *Chemical Reviews*, **113**, 7728–7768 (2013).

95. Szpyrkowicz L., 'Hydrodynamic effects on the performance of electro-coagulation/electro-flotation for the removal of dyes from textile wastewater', *Industrial and Engineering Chemistry Research*, **44**, 7844–7853 (2005).

96. You S. J., Damodar R. A., Hou S. C., 'Degradation of reactive black 5 dye using anaerobic/aerobic membrane bioreactor (MBR) and photochemical membrane reactor', *Journal of Hazardous Materials*, **177**, 1112–1118 (2010).

97. Wang S., Ang H. M., Tadé M. O., 'Novel applications of red mud as coagulant, adsorbent and catalyst for environmentally benign processes', *Chemosphere*, **72**, 1621–1635 (2008).

98. Schiewer S., Iqbal M., 'The role of pectin in Cd binding by orange peel biosorbents: A comparison of peels, depectinated peels and pectic acid', *Journal of Hazardous Materials*, **177**, 899–907 (2010).

99. Valtchev V., Tosheva L., 'Porous nanosized particles: Preparation, properties, and applications', *Chemical Reviews*, **113**, 6734–6760 (2013).

100. Ahmad A., Rafatullah M., Sulaiman O., Ibrahim M. H., Hashim R., 'Scavenging behaviour of meranti sawdust in the removal of methylene blue from aqueous solution', *Journal of Hazardous Materials*, **170**, 357–365 (2009).

101. Ghaedi M., Pakniat M., Mahmoudi Z., Hajati S., Sahraei R., Daneshfar A., 'Synthesis

of nickel sulfide nanoparticles loaded on activated carbon as a novel adsorbent for the competitive removal of methylene blue and safranin-O', *Spectrochimica Acta Part A: Molecular and Biomolecular Spectroscopy*, **123**, 402–409 (2014).

102. Ali I., 'New generation adsorbents for water treatment', *Chemical Reviews*, **112**, 5073–5091 (2012).

103. Zhou J., Tang C., Cheng B., Yu J., Jaroniec M., 'Rattle-type carbon-alumina core-shell spheres: Synthesis and application for adsorption of organic dyes', *ACS Applied Materials and Interfaces*, **4**, 2174–2179 (2012).

104. Liang L., Zhu Q., Wang T., Wang F., Ma J., Jing L., Sun J., 'The synthesis of core-shell Fe_3O_4@mesoporous carbon in acidic medium and its efficient removal of dye', *Microporous and Mesoporous Materials*, **197**, 221–228 (2014).

105. Zheng J., Cheng C., Yan R., Fang W., Chen C., Huai H., Wang C., 'Synthesis of yolk–shell magnetic magnesium silicate with tunable yolk morphology for removal of methylene blue in water', *Journal of Alloys and Compounds*, **596**, 5–9 (2014).

106. Li L., Li X., Duan H., Wang X., Luo C., 'Removal of congo red by magnetic mesoporous titanium dioxide-graphene oxide core-shell microspheres for water purification', *Dalton Transactions*, **43**, 8431–8438 (2014).

107. Pradhan A. C., Parida K. M., 'Facile synthesis of mesoporous composite Fe/Al_2O_3-MCM-41: An efficient adsorbent/catalyst for swift removal of methylene blue and mixed dyes', *Journal of Materials Chemistry*, **22**, 7567–7579 (2012).

108. Chiou M. S., Chuang G. S., 'Competitive adsorption of dye metanil yellow and RB15 in acid solutions on chemically cross-linked chitosan beads', *Chemosphere*, **62**, 731–740 (2006).

109. Salleh M. A. M., Mahmoud D. K., Karim W. A. W. A., Idris A., 'Cationic and anionic dye adsorption by agricultural solid wastes: A comprehensive review', *Desalination*, **280**, 1–13 (2011).

110. Natarajan T. S., Bajaj H. C., Tayade R. J., 'Preferential adsorption behavior of methylene blue dye onto surface hydroxyl group enriched TiO_2 nanotube and its

photocatalytic regeneration', *Journal of Colloid and Interface Science*, **433**, 104–114 (2014).

111. Abramian L., El-Rassy H., 'Adsorption kinetics and thermodynamics of azo-dye Orange II onto highly porous titania aerogel', *Chemical Engineering Journal*, **150**, 403–410 (2009).

112. Rigoberto T. G., Ma. del Rosario M. V., Jaime M. P., Adrian B. P., Virginia H. M., Carlos J. D. V., 'Analysis of synergistic and antagonistic adsorption of heavy metals and acid blue 25 on activated carbon from ternary systems', *Chemical Engineering Research and Design*, **93**, 755–772 (2015).

113. Zolgharnein J., Asanjrani N., Bagtash M., Azimi G., 'Multi-response optimization using Taguchi design and principle component analysis for removing binary mixture of alizarin red and alizarin yellow from aqueous solution by nano γ-alumina', *Spectrochimica Acta Part A: Molecular and Biomolecular Spectroscopy*, **126**, 291–300 (2014).

114. Ge F., Ye H., Li M., Zhao B., 'Efficient removal of cationic dyes from aqueous solution by polymer-modified magnetic nanoparticles', *Chemical Engineering Journal*, **198-199**, 11–17 (2012).

Chapter-7

Overall Summary and Future Prospects

The present chapter deals with an overall summary of the present study and future prospects. In the thesis, different types of core-shell nanoparticles such as (i) SiO_2@CdS (type-I) and ZnO@CdS (type-II), (ii) semiconductor-metal based core-shell nanoparticles (ZnO@Ag and Cu_2O@Ag), and (iii) nanorattle type core-shell nanoparticles (SiO_2@Co_3O_4 and SiO_2@Ni-Co mixed metal oxides) were successfully synthesized. A few applications of the synthesized core-shell nanoparticles/nanorattles were also explored. A detailed summary on the synthesis, characterization, properties and various applications of the core-shell nanoparticles/ nanorattles, presented in the thesis, along with their future prospects are discussed individually.

Chapter-1: *Introduction*

In this chapter, a brief perspective of nanotechnology, an introduction to core-shell nanoparticles, classification, and their various synthetic methods have been discussed. Different examples elucidating the optical, magnetic and electrochemical properties of core-shell nanoparticles have been discussed. At the end, some of the multifunctional applications of core-shell nanoparticles in different fields have been presented.

Chapter-2: *Experimental techniques*

In this chapter, the set of analytical techniques which were used to characterize the core-shell nanoparticles and their sample preparation methods have been discussed. The analytical techniques include powder X-ray diffraction, Fourier transform infrared spectroscopy, thermal gravimetric analysis, field emission scanning electron microscopy, energy dispersive X-ray analysis, transmission electron microscopy, X-ray photoelectron spectroscopy, zeta potential and BET surface area analysis. Optical properties of the core-shell nanoparticles were studied using UV-Visible diffuse reflectance spectroscopy and photoluminescence spectroscopy.

Chapter-3: *Synthesis of SiO_2@CdS (Type-I) and ZnO@CdS (Type-II) core-shell nanoparticles via a novel thermal decomposition approach*

This chapter contains two sub sections and summary on each of them is as follows.

Synthesis of SiO_2@CdS (Type-I) core-shell nanoparticles via a novel thermal decomposition approach

The thermal decomposition approach has been used to prepare the SiO_2@CdS core-shell nanoparticles for the first time. SiO_2@CdS core-shell nanoparticles with different shell thicknesses have been successfully synthesized *via* thermal decomposition approach. First,

SiO_2 microspheres were synthesized according to StÖber process and calcined at 500 ^oC for 3 h to get activated SiO_2. In the second step, CdS shell was deposited on the surface of SiO_2 microspheres by thermal decomposition of cadmium acetate and thiourea along with as prepared SiO_2 or activated SiO_2 in ethylene glycol. Four different SiO_2@CdS core-shell nanoparticle samples were prepared by varying the concentration of cadmium acetate and thiourea ($[Cd^{2+}]:[S^{2-}]$ = 0.125:0.125 and 0.25:0.25) and nature of SiO_2. Among the four samples, two samples were prepared using as prepared SiO_2 and another two samples were prepared using activated SiO_2. The present method is superior, facile and has several advantages. There is no need for surface functionalization of silica core and uniform CdS shell with different thicknesses on silica can be achieved in 60 min.

XRD results indicate the presence of CdS in all the SiO_2@CdS samples and the crystallite size of CdS is about 2 nm. FT-IR results show IR band at 950 cm^{-1} in the as prepared silica and this band is absent in the activated SiO_2 which indicate the absence of surface hydroxyl groups. SEM and TEM results clearly show the deposition of CdS on the SiO_2 microspheres. SiO_2@CdS samples prepared using unactivated silica show uniform deposition of cadmium sulfide nanoparticles on silica compared to SiO_2@CdS samples prepared using activated silica. The uniform deposition of CdS in the case of as prepared SiO_2 is attributed to strong interaction between cadmium ions (Cd^{2+}) and surface silanol groups (vicinal and geminal) of silica. EDX results confirm the presence of silicon, oxygen, cadmium and sulfur in all the SiO_2@CdS samples. To understand the deposition of CdS on SiO_2 better, the effect of temperature, thermal decomposition time and sonication was investigated. SEM results indicate that sonication of the reaction contents before the reaction, and thermal decomposition at 180 ^oC for 60 min leads to uniform deposition of CdS on SiO_2 spheres. SAED patterns indicate polycrystalline nature of CdS in the SiO_2@CdS samples and HRTEM images show characteristic lattice spacing of CdS in all the SiO_2@CdS samples. The SiO_2@CdS core-shell nanoparticles show an increase in the band gap of CdS and a blue shift in the band gap absorption as compared to bulk CdS due to quantum size effect. PL results show an enhancement in the intensity of near band edge emission of CdS due to immobilization of CdS nanoparticles on the surface of silica and also by reducing the surface trap states in the SiO_2@CdS core-shell nanoparticles. Finally, mechanism has been proposed for the deposition of CdS shell on the SiO_2 microspheres. The present synthetic method can be extended to prepare other core-shell nanomaterials with type-I band alignment.

Synthesis of ZnO@CdS (Type-II) core-shell heteronanostructures via a novel thermal decomposition approach

ZnO@CdS core-shell heteronanostructures have been successfully synthesized by a simple, economical thermal decomposition approach. The CdS shell thickness in ZnO@CdS core-shell heteronanostructures could be controlled by varying the concentration of precursors used during the thermal decomposition. First, hexagonal ZnO nanorods were synthesized by homogeneous precipitation method. After that, the surface of ZnO nanorods was functionalized using citric acid. Finally, CdS shell is deposited on hexagonal ZnO nanorods *via* thermal decomposition of cadmium acetate and thiourea along with surface functionalized hexagonal ZnO nanorods in ethylene glycol at 180 ^{o}C. Three different ZnO@CdS core-shell heteronanostructured samples were prepared by varying the concentration of cadmium acetate and thiourea ($[Cd^{2+}]$:$[S^{2-}]$ = 0.125:0.125, 0.1:0.1 and 0.075:0.075). The synthesized ZnO@CdS core-shell heteronanostructures were characterized using a set of analytical techniques.

XRD results show peaks due to both ZnO and CdS in all the ZnO@CdS samples. The crystallite size of ZnO decreases after the formation of CdS shell on the ZnO and the crystallite size of CdS was difficult to calculate in the ZnO@CdS samples due to less intense and broad XRD peaks of CdS. This suggests the presence of small CdS nanoparticles in the ZnO@CdS samples. FT-IR results show IR bands due to citrate ions in the surface modified ZnO which prove the surface functionalization of ZnO. SEM images show the hexagonal morphology of ZnO nanorods. SEM and TEM results confirm the deposition of CdS on the ZnO nanorods. EDX analysis results indicate the presence of zinc, oxygen, cadmium and sulfur in all the ZnO@CdS samples. The effects of reaction temperature, thermal decomposition time and surface modification of ZnO nanorods on the quality of CdS coating in the ZnO@CdS core-shell heteronanostructures were studied. SEM results indicate that good deposition of CdS is possible at 180 ^{o}C for 60 min with surface modified ZnO nanorods. SAED patterns of ZnO and CdS confirm the single crystalline nature of ZnO and polycrystalline nature of CdS. The SAED patterns of ZnO@CdS core-shell heteronanostructures confirm the crystalline nature of all the ZnO@CdS samples. HRTEM images show clear interface between ZnO core and the CdS shell. DRS results show red shift of the band gap of ZnO and blue shift of the band gap of CdS in the ZnO@CdS core-shell heteronanostructures compared to pure ZnO and CdS nanoparticles. The blue shift in the band gap of CdS shell is attributed to quantum size effect. Photoluminescence spectroscopy results show disappearance of UV emission band and reduction in the intensity of visible emission in the ZnO@CdS core-shell heteronanostructures

and this is attributed to synergistic interaction between ZnO core and CdS shell in the ZnO@CdS core-shell heteronanostructures. Finally, the mechanism for the deposition of a CdS shell on the ZnO nanorods has been proposed.

Chapter-4: *Synthesis of semiconductor-metal (ZnO@Ag and Cu_2O@Ag) core-shell nanoparticles via a novel thermal decomposition approach*

This chapter contains two parts and each of them is summarized as follows.

Synthesis of ZnO@Ag core-shell nanoparticles via a novel thermal decomposition approach

ZnO@Ag core-shell heteronanostructures were synthesized *via* a facile, economical, and simple thermal decomposition approach. The particle size of silver nanoparticles on the ZnO nanorods could be controlled simply by varying the concentration of silver acetate during the thermal decomposition. Initially, ZnO nanorods were synthesized *via* homogeneous precipitation method. Silver was then deposited on the ZnO nanorods by thermal decomposition of silver acetate along with ZnO in diphenyl ether at 220 ^{o}C. The particle size of silver on ZnO nanorods was controlled by varying the concentration of silver acetate ([Agac] = 0.10, 0.l5 and 0.25). The synthesized ZnO@Ag core-shell heteronanostructures were characterized by various analytical techniques.

XRD results indicate the presence of ZnO and silver in all the ZnO@Ag samples. The crystallite size of silver is about 24-31 nm in the ZnO@Ag samples. FE-SEM images show the deposition of silver nanoparticles on the surface of ZnO nanorods. EDX results confirm the presence of zinc, oxygen and silver in all the ZnO@Ag samples. TEM results clearly show strongly adhered silver nanoparticles on the surface of ZnO nanorods. The broad particle size distribution of silver nanoparticles on the ZnO nanorods is attributed to site-selective positioning of silver on the ZnO nanorods. SAED patterns indicate the polycrystalline nature of ZnO@Ag samples. XPS results confirm metallic nature of silver in the ZnO@Ag samples. DRS results show the absorption bands due to both ZnO and Ag nanoparticles in ZnO@Ag samples. PL results of ZnO@Ag samples show emission bands with reduced intensity as compared to pure ZnO which is attributed to effective charge separation at the interface of ZnO and Ag nanoparticles. The mechanism for the deposition of Ag nanoparticles on the surface of ZnO nanorods has been proposed. To understand the deposition of Ag on ZnO nanorods better, thermal decomposition reaction time and temperatures were varied. SEM results

suggest that the thermal decomposition time of 60 min and temperature of 220 ^{o}C leads to uniform deposition of silver nanoparticles on the surface of ZnO nanorods. The reported synthetic method can be extended to prepare other metal-semiconductor heteronanostructured materials for various functional applications.

Synthesis of Cu_2O@Ag polyhedral core-shell nanoparticles via a novel thermal decomposition approach

Cu_2O@Ag polyhedral core-shell nanoparticles were prepared by a novel thermal decomposition approach. First, Cu_2O with different morphologies such as rhombicuboctahedron, cuboctahedron, truncated octahedron and octahedron were synthesized *via* a solution route. Then, silver was deposited on Cu_2O with different morphologies by thermal decomposition of silver acetate at 220 ^{o}C followed by at 150 ^{o}C in diphenyl ether. The concentration of silver acetate used was 0.075 mM. The synthesized Cu_2O@Ag polyhedral core-shell nanoparticles were characterized using various techniques.

XRD results confirm the presence of Cu_2O and Ag in all the Cu_2O@Ag samples. The crystallite size of silver is 21-30 nm in the Cu_2O@Ag samples. FT-IR spectral results indicate Cu(I)-O stretching in all the Cu_2O samples. TGA results indicate different oxidation onset temperatures for Cu_2O with different shapes. The Cu_2O samples with octahedron morphology show higher oxidation temperature indicating that Cu_2O octahedron is more stable than the other morphologies of Cu_2O. SEM images confirm rhombicuboctahedron, cuboctahedron, truncated octahedron and octahedron morphologies of Cu_2O. SEM results also show the deposition of silver on Cu_2O with various morphologies. EDX analysis confirms the presence of copper, oxygen and silver in all the Cu_2O@Ag samples. To understand the nature of deposition of silver nanoparticles on Cu_2O polyhedral microcrystals better, the nucleation time (N_t), the growth time (G_t) and the concentration of silver acetate were varied during the synthesis. Deposition of silver nanoparticles on Cu_2O polyhedral microcrystals is observed only on decreasing the nucleation time, growth time and concentration of silver acetate. TEM images show the deposition of silver nanoparticles on Cu_2O with various morphologies. SAED patterns prove polycrystalline nature of silver in Cu_2O@Ag samples and no diffraction due to Cu_2O was observed which indicates the formation of thick silver shell on the surface of Cu_2O microcrystals. Cu_2O@Ag samples show marginally higher surface area compared to pure Cu_2O microcrystals due to the deposition of silver nanoparticles on the Cu_2O polyhedral microcrystals. DRS results show band gap absorptions due to both Cu_2O and Ag in all the

Cu_2O@Ag samples. A mechanism has been proposed for the deposition of silver shell on Cu_2O polyhedral microcrystals. The current synthetic approach can be extended to prepare other metal-semiconductor core-shell materials for various functional applications.

Chapter-5: *Synthesis of SiO_2@Co_3O_4 and SiO_2@Ni-Co mixed metal oxide core-shell nanorattles via homogeneous precipitation method*

This chapter contains two sections and a summary on each of the sections is as follows.

Synthesis of SiO_2@Co_3O_4 core-shell nanorattles via homogeneous precipitation method

SiO_2@Co_3O_4 core-shell nanorattles with uniform Co_3O_4 porous shell over the silica core have been synthesized using a self-template route by the calcination of SiO_2@α-$Co(OH)_2$ at 500 ^oC. First, SiO_2 microspheres were synthesized according to StÖber process. In the second step, SiO_2 microspheres was mixed with cobaltous nitrate and urea and the reaction contents were stirred at 85 ^oC for 6 h to deposit α-$Co(OH)_2$ shell on the SiO_2 microspheres. The shell thickness was controlled by varying the concentration of cobaltous nitrate ($[Co^{2+}]$ = 5, 10 and 15 mM) during the synthesis. The obtained samples were calcined in air at 500 ^oC to get Co_3O_4 shell coated SiO_2 microspheres. The synthesized samples were characterized using various analytical techniques.

XRD patterns of α-$Co(OH)_2$ and SiO_2@α-$Co(OH)_2$ samples indicate the presence of α-$Co(OH)_2$. Co_3O_4 and SiO_2@Co_3O_4 samples indicate the presence of Co_3O_4. SiO_2@Co_3O_4 samples show poor crystallinity compared to pure Co_3O_4 nanoparticles. FT-IR spectra confirms the presence of Co(II)–O stretching and Co(III)–O stretching in all the SiO_2@Co_3O_4 samples. The TGA patterns of SiO_2@α-$Co(OH)_2$ samples show weight loss features due to both SiO_2 and α-$Co(OH)_2$ and the all the SiO_2@α-$Co(OH)_2$ samples are converted to SiO_2@Co_3O_4 at 500 ^oC. FE-SEM images show flower-like morphology for SiO_2@α-$Co(OH)_2$ and SiO_2@Co_3O_4 core-shell samples. EDX analysis confirms the presence of silicon, oxygen and cobalt in all the SiO_2@α-$Co(OH)_2$ and SiO_2@Co_3O_4 core-shell nanoparticles. TEM results clearly show the formation of nanorattle morphology for SiO_2@Co_3O_4 samples. The SAED patterns show spots/rings indicating polycrystalline nature of the samples. BET surface area analysis shows enhanced surface area for SiO_2@Co_3O_4 samples as compared to pure SiO_2 microspheres

and Co_3O_4 nanoparticles which is attributed to the nanorattle morphology composed of porous Co_3O_4 shell. DRS results show band gap absorptions due to charge transfer transitions of $O^{2-} \rightarrow Co^{3+}$ and $O^{2-} \rightarrow Co^{2+}$ in all the $SiO_2@Co_3O_4$ core-shell nanorattle samples. $SiO_2@Co_3O_4$ samples show blue shift with respect to pure Co_3O_4 nanoparticles which is attributed to quantum confinement effect and smaller particle size of Co_3O_4 in the $SiO_2@Co_3O_4$ core-shell nanorattle samples. Compared to other preparation methods, this approach does not require any surface modification of silica and the method is facile, and inexpensive. This method can be extended to prepare other metal oxide core-shell nanorattles for various functional applications.

Synthesis of SiO_2@Ni-Co mixed metal oxide core-shell nanorattles via homogeneous precipitation method

SiO_2@Ni-Co mixed metal oxide core-shell nanorattles have been synthesized, for the first time, *via* a novel, economical, and facile self-template route. First, SiO_2 microspheres were synthesized according to StÖber process. After that, SiO_2 microspheres were mixed with different ratios of nickel nitrate and cobaltous nitrate with urea and the contents were stirred at 85 ^oC for 6 h to get SiO_2@Ni-Co mixed metal layered double hydroxides. The obtained LDHs were calcined at 500 ^oC in air to get a SiO_2@Ni-Co mixed metal oxide core-shell nanorattles. The composition of Ni-Co mixed metal oxides was tuned by varying the concentration of nickel nitrate and cobaltous nitrate ($[Ni^{2+}]$: $[Co^{2+}]$ = 7:3, 5:5, 3:7; total concentration = 10 mmol) during the synthesis. The synthesized samples were characterized using various techniques.

XRD patterns show peaks due to α-$Co(OH)_2$ and α-$Ni(OH)_2$ in SiO_2@Ni-Co LDH samples and SiO_2@Ni-Co mixed metal oxide samples show peaks due to NiO, Co_3O_4 and $NiCo_2O_4$ which indicate the formation of mixed metal oxides in the SiO_2@Ni-Co mixed metal oxide samples. FT-IR results indicate characteristic metal-oxygen vibrations in all the SiO_2@Ni-Co mixed metal oxide samples. TGA patterns show different weight loss features in SiO_2@Ni-Co LDH samples due to the presence of different amounts of α-$Co(OH)_2$ and α-$Ni(OH)_2$. FE-SEM images show hierarchical flower-like morphology in the case of SiO_2@Ni-Co LDH and SiO_2@Ni-Co mixed metal oxide samples. EDX results confirm the presence of silicon, oxygen, nickel and cobalt in all the SiO_2@Ni-Co LDH and SiO_2@Ni-Co mixed metal oxide samples. TEM images clearly show the formation of nanorattles in the case of SiO_2@Ni-Co mixed metal

oxides. SAED patterns of SiO_2@Ni-Co mixed metal oxide samples show ring patterns which suggest polycrystalline nature of the Ni-Co mixed metal oxides on the SiO_2 spheres. BET surface area analysis results show higher surface area for SiO_2@Ni-Co mixed metal oxide samples which is attributed to the nanorattle morphology. DRS results show band gap absorptions due to NiO, Co_3O_4 and $NiCo_2O_4$ in the SiO_2@Ni-Co mixed metal oxides. A clear understanding on the deposition of Ni-Co mixed metal oxides on the surface of SiO_2 microspheres is elaborated using TEM analysis on the products obtained at different times. The current method can be extended to prepare other mixed metal oxide core-shell nanorattles for various multifunctional applications.

Chapter-6: *Applications of core-shell nanoparticles/nanorattles*

In the present study, photocatalytic degradation of methylene blue (MB) in an aqueous solution, catalytic reduction of 4-nitrophenol (4-NP) and MB in aqueous solution, peroxidase-like activity, and adsorption of mixture of rhodamine B (Rh B) and methylene blue in aqueous solution have been demonstrated.

ZnO@CdS and ZnO@Ag core-shell heteronanostructures were explored as photocatalysts for the photodegradation of methylene blue in an aqueous solution under sun light. ZnO@CdS core-shell heteronanostructures show complete degradation of methylene blue in 120 min whereas the ZnO@Ag core-shell heteronanostructures show the complete degradation of methylene blue in 90 min. Both the ZnO@CdS and ZnO@Ag core-shell heteronanostructures show higher pseudo first order apparent rate constant (k_{app}) than their counter parts. The higher photocatalytic activity observed in the case of ZnO@CdS and ZnO@Ag core-shell heteronanostructures is attributed to effective charge separation at the interface.

Cu_2O@Ag polyhedral core-shell nanoparticles were explored as catalysts for the reduction of 4-nitrophenol and methylene blue in the presence of $NaBH_4$ in aqueous solutions. Cu_2O@Ag polyhedral core-shell nanoparticles complete the reduction of 4-nitrophenol to 4-aminophenol within 6-13 mins whereas complete reduction of methylene blue to leucomethylene blue occurs within 5-9 mins. In both the cases, Cu_2O@Ag polyhedral core-shell nanoparticles show higher first order rate constant (k_{app}) than pure Cu_2O microcrystals, silver nanoparticles and physical mixture of Cu_2O octahedra and silver nanoparticles. The Cu_2O@Ag polyhedral core-shell nanoparticles show higher turnover frequency and activity parameter (k_{act}) than previously reported

catalysts in the case of 4-nitrophenol reduction. Reusability studies indicate higher stability and applicability of Cu_2O@Ag core-shell nanoparticles for practical applications.

SiO_2@Co_3O_4 core-shell nanorattles were explored as an artificial peroxidase-like enzyme mimic. The SiO_2@Co_3O_4 core-shell nanorattles show enhanced intrinsic peroxidase-like activity compared to pure Co_3O_4 nanoparticles and horseradish peroxidase (HRP), a natural enzyme. The SiO_2@Co_3O_4 core-shell nanorattles show higher turnover number (k_{cat}) and specificity constant (k_{cat}/K_m) values compared to pure Co_3O_4 and HRP indicating their applicability as an artificial enzyme mimic in biomedicine and bio-sensing. The higher peroxidase-like activity in the case of SiO_2@Co_3O_4 core-shell nanorattles is due to increased surface area and increased electron density as compared to pure Co_3O_4 nanoparticles.

SiO_2@Ni-Co mixed metal oxide core-shell nanorattles were explored as effective adsorbents for the removal of mixture of rhodamine B and methylene blue in aqueous solutions. SiO_2@Ni-Co mixed metal oxide core-shell nanorattles completely adsorb rhodamine B and methylene blue within 2 min. SiO_2@Ni-Co mixed metal oxide core-shell nanorattles show higher adsorption capacity in the case of single dye adsorption than mixed dye adsorption indicating competitive adsorption of rhodamine B and methylene blue. The adsorption follows both Langmuir and Freundlich isotherms in the case of single dye adsorption and binary Langmuir model in the case of adsorption of mixed dyes. The adsorption kinetics follows pseudo second order kinetics. The higher adsorption capacity of SiO_2@Ni-Co mixed metal oxide core-shell nanorattles is attributed to negative charge on their surface and as well as high surface area due to their porous shell structure. Reusability studies show only a marginal decrease in the adsorption efficiency after five cycles indicating that the adsorbents are reusable for various practical applications.